Transactions of the ASME

Journal of Heat Transfer

Published Quarterly by The American Society of Mechanical Engineers
VOLUME 103 • NUMBER 2 • May 1981

ANNOUNCEMENTS

TECHNICAL PAPERS

(*Contents continued on page 211*)

EDITORIAL STAFF
Editor, **J. J. JAKLITSCH, JR.**
Production Editor,
STELLA ROBINSON
Editorial Prod. Asst.,
BETH DARCHI

HEAT TRANSFER DIVISION
Chairman, **C. L. TIEN**
Secretary, **C. J. CREMERS**
Senior Technical Editor, **K. T. YANG**
Technical Editor, **B. T. CHAO**
Technical Editor, **D. K. EDWARDS**
Technical Editor, **M. EPSTEIN**
Technical Editor, **J. S. LEE**
Technical Editor, **V. E. SCHROCK**
Technical Editor, **R. SIEGEL**

POLICY BOARD, COMMUNICATIONS
Chairman and Vice-President
I. BERMAN

Members-at-Large
J. W. LOCKE
J. E. ORTLOFF
M. J. RABINS
W. J. WARREN

Policy Board Representatives
Basic Engineering, **F. LANDIS**
General Engineering, **C. F. PHILLIPS**
Industry, **J. E. ORTLOFF**
Power, **R. E. REDER**
Research, **G. P. COOPER**
Codes and Stds., **L. L. ELDER**
Nom. Com. Rep.,
J. W. LOCKE

Business Staff
345 E. 47th St.
New York, N. Y. 10017
(212) 644-7789
Mng. Dir., Publ., **J. J. Frey**

OFFICERS OF THE ASME
President, **CHARLES E. JONES**
Deputy Exec. Dir. & Asst. Sec'y,
PETER CHIARULLI
Treasurer, **ROBERT A. BENNETT**

Journal of Heat Transfer (ISSN 0022-1481) is edited and published quarterly at the offices of The American Society of Mechanical Engineers, United Engineering Center, 345 E. 47th St., New York, N. Y. 10017. ASME-TWX No. 710-581-5267, New York. *Second-class postage paid at New York, N. Y., and at additional mailing offices.*

CHANGES OF ADDRESS must be received at Society headquarters seven weeks before they are to be effective. Please send old label and new address.

PRICES: To members, $30.00, annually; to nonmembers, $60.00. Single copies, $20.00 each. Add $5.00 for postage to countries outside the United States and Canada.

STATEMENT from By-Laws. The Society shall not be responsible for statements or opinions advanced in papers or . . . printed in its publications (B7.1, para. 3).

COPYRIGHT © 1980 by the American Society of Mechanical Engineers. Reprints from this publication may be made on condition that full credit be given the TRANSACTIONS OF THE ASME, JOURNAL OF HEAT TRANSFER, and the author, and date of publication be stated.

INDEXED by the Engineering Index, Inc.

Downloaded 04 Feb 2011 to 194.85.80.107. Redistribution subject to ASME license or copyright; see http://www.asme.org/terms/Terms_Use.cfm

TECHNICAL NOTES

J. G. van Leersum[1]
Research Scientist,
Division of Mechanical Engineering,
Commonwealth Scientific and Industrial Research Organisation,
Highett, Victoria, Australia

C. W. Ambrose
Senior Lecturer,
Department of Mechanical Engineering,
Monash University,
Clayton, Victoria, Australia

Comparisons between Experiments and a Theoretical Model of Heat and Mass Transfer in Rotary Regenerators with Nonsorbing Matrices

A mathematical model of condensation, evaporation and heat transfer in a regenerator having a non sorbing matrix is derived. Good agreement between heat and moisture effectivities predicted by a simulation of the model, and corresponding results from an independently derived equilibrium model is shown for a particular case. Details of an experimental facility for testing the performance of a rotary regenerator are given, and a comparison between results obtained from the facility and those produced by the model are given.

1 Introduction

Regenerators in which purely sensible heat transfer occurs have been in use for many years and more recently, a theory of their operation, as applied to air conditioning, has been given by Dunkle and Maclaine-cross [1]. In these regenerators, energy is transferred cyclicly to or from a matrix which rotates between two air streams, thus effecting a transfer from one fluid stream to another. So long as the dew point temperature of the inlet air state having the higher temperature is less than the dry bulb temperature of the other air inlet state, only sensible heat transfer occurs. However, if this is not so, condensation may occur in the regenerator. Hausen [2] considered the problem of condensation in regenerators, but, in general, his results are not in a suitable form to compare with those presented here. Because of approximations used, they are more relevant to the type of model used in van Leersum and Banks [3].

Holmberg [4] has described numerical experiments with a model of heat and mass transfer in rotary regenerators having nonhygroscopic matrix materials. His model is less restrictive than the one used in the following, in that it allows for both condensate and ice forming on the matrix, and considers the matrix to have a finite thermal resistance in the fluid flow direction. However, no details are given of the way in which his numerical simulation traverses wet/dry interfaces in the matrix. Neither Hausen nor Holmberg have compared their numerical models with experimental results. In this paper, a series of experimental results from a regenerator in which condensation occurs are shown to agree well with corresponding results from a computer based simulation of the process. The simulation is also shown, for a small number of cases, to yield very similar results to those of the model described in [4].

2 The Mathematical Model

The following assumptions were made in setting up the mathematical model of the regenerator:

1 Equal mass flow rates of moist air flow at the same constant velocity through equal facial areas in each period.

2 The regenerator matrix consists of a homogeneous substance of density P and constant porosity ϵ, completely impervious to moisture.

3 Air flows through the matrix transferring heat to or from the matrix and moisture to or from the undrained matrix surface.

Numerical estimates in [3] of the moisture film thickness suggest the assumption of a thin undrainable moisture film on the matrix surface, at the matrix temperature, is a reasonable one.

4 The thermal conductivity of the matrix in the fluid flow direction is negligible, as is the thermal gradient through the matrix at right angles to the flow direction. Corresponding assumptions were made in [1].

Assumptions 3 and 4 allow a lumped parameter heat transfer coefficient to be used in the model, and since the only mass transfer takes place at an air-water-interface, the Lewis number was assumed to be unity giving the heat and mass transfer coefficient identical values.

The differential equations describing moisture and enthalpy conservation in the regenerator, on those parts of the matrix where a moisture film is present are, from Banks, et al. [5], but nondimensionalized

$$\frac{\partial h_f}{\partial \zeta} + \frac{\partial H}{\partial \tau} = 0 \tag{1}$$

$$\frac{\partial w_f}{\partial \zeta} + \frac{\partial W}{\partial \tau} = 0 \tag{2}$$

where

$$\zeta = \frac{Jx}{v} \text{ and } \tau = J\left(\theta - \frac{x}{v}\right) \Big/ \mu$$

The associated rate equations are

$$\frac{\partial t_f}{\partial \zeta} = (t_m - t_f) \tag{3}$$

$$\frac{\partial w_f}{\partial \zeta} = (w_m - w_f) \tag{4}$$

where the moist air enthalpy, h is

$$h = c_p t + c_{pv} t w + h_v w \tag{5}$$

and the matrix enthalpy H is

$$H = c_s t_m + c_w W t_m \tag{6}$$

Subscripts f and m refer to the relevant parameters being evaluated at fluid (air) or matrix states respectively. When a moisture film is present on the matrix, the air in equilibrium with the matrix is necessarily saturated, so:

$$w_m = w_m(t_m) \tag{7}$$

---

[1] Formerly, Department of Mechanical Engineering, Monash University, Clayton, Victoria, Australia.

Contributed by the Heat Transfer Divsion for publication in the JOURNAL OF HEAT TRANSFER. Manuscript received by the Heat Transfer Division January 23, 1980.

In this case, $w_m = 0.622\ P_m/(P_T - P_m)$ where $P_m = 23.28199 - 3780.82/t_m - 225805/t_m{}^2$ and P_T = total air pressure, after [6]; i.e. the saturation humidity ratio is an explicit function of the matrix temperature. When the matrix is dry, the equations (1–4) reduce to

$$\frac{\partial t_f}{\partial \zeta} + \sigma \frac{\partial t_m}{\partial \tau} = 0 \qquad (8)$$

$$\sigma \frac{\partial t_f}{\partial \zeta} = (t_m - t_f) \qquad (9)$$

where σ is the ratio of specific heats, matrix to fluid.

When equations (5) and (6) are substituted into equation (1), the results, together with equations (2, 3, 4) and (7) describe heat and mass transfer in a regenerator in which moisture is either condensing on, or evaporating from the matrix surface. Equations (8) and (9) describe heat transfer to and from those parts of the matrix which have dried out. All of these equations, together with the boundary conditions [3, 4], and [7] allow, in principle, a numerical model of the regenerator to be constructed.

Lambertson [7], Holmberg [4] and Maclaine-cross with justification [8], have all omitted the term Jx/v from the co-ordinate τ. The arguments used in [8] for air conditioning regenerators, justify it in the present case and this leads to a relatively simple finite difference formulation of the problem.

2.1 Dimensionless Independent Variables for the Regenerator Model. It is desirable to express the performance (heat and mass transfer effectivities in this case) of the regenerator in terms of dimensionless parameters. The two dimensionless parameters, $\Lambda = JL/v$ (dimensionless length) and $C_r = 2L(1 + \mu\sigma)/v\theta_p$ (dimensionless speed) completely determine the temperature effectivities of a regenerator in which heat transfer only occurs, provided that the mass of air flowing through the matrix in period 1 is equal to that flowing through the matrix in period 2. Similar, if not identical parameters were used in [1, 2, 5] and [7]. Dimensionless speed was used in [3] and its physical meaning is discussed there. When condensation occurs, the amount of mass transfer is very much dependent upon the regenerator inlet states' proximity to the saturation line. No satisfactory dimensionless group of inlet parameters, which, together with Λ and C_r would determine completely the regenerator's performance, could be found. For this reason, the inputs to the mathematical model are Λ and C_r, together with the temperatures and humidity ratios of both inlet states. These are sufficient to determine the enthalpy, moisture, and temperature effectivities, as well as mean outlet states in each period.

2.2 The Finite Difference Solution. The finite difference grid used to solve the equations (1–9) was identical with that used by Lambertson [7] for his heat transfer only solution, and Holmberg [4] for his solution to the problem when condensation and icing occur. The method of applying the equations to the finite difference grid was essentially the same as Holmberg's [4] and the iterative method of numerically cycling the solution to the steady state as employed by Lambertson and Holmberg was used.

At wet-dry transitions, an estimate of the "drying out point" inside the grid was made, and the grid split into two subgrids, one in which heat and mass transfer occurs and one where heat transfer only occurs. The first subgrid was then treated similary to its parent grid, and the process repeated until a consistent transition point was obtained. Usually, less than three iterations were required to establish this, after which the outlet states at the two subgrids were combined to give a single outlet state for the parent grid.

The relevant grid states at the outlet end of the regenerator were averaged to obtain the mean outlet regenerator states. From these,

Nomenclature

c_p = specific heat of dry air (1005 J/kg °C)
c_{pv} = specific heat of steam (1868 J/kg °C)
c_s = specific heat of dry matrix (Mylar: 1160 J/kg °C)
c_w = specific heat of water (4182 J/kg °C)
C_r = dimensionless speed = $2L\ (1 + \mu\sigma)/(v\theta_p)$ (dimensionless)
f = friction factor (dimensionless)
h = specific fluid enthalpy (J/kg)
h_v = latent heat of vaporization of water at datum temperature 0°C. (2500800 J/kg)
H = specific enthalpy of matrix (J/kg)
J = lumped parameter film transfer coefficient (s^{-1})
L = length of matrix (m)
M_t = air mass flow rate through heater and humidifier (Fig. 2.) (kg/s)
M_0 = air mass flow rate through inlet nozzle (Fig. 2) (kg/s)
M_{cd} = air mass flow rate through regenerator during period 1 (Fig. 2) (kg/s)
M_{ab} = air mass flow rate through regenerator during period 2 (Fig. 2) (kg/s)
NTU = number of transfer units = JL/2v (dimensionless)
P = density of matrix material (Mylar 1395 kg/m^3)
St = Stanton number (dimensionless)
t = temperature (°C)
t_{f0} = fluid temperature at inlet to period 1 (°C)
t_{fp} = fluid temperature at inlet to period 2 (°C)
$\bar{t}_1$ = mean outlet temperature of air leaving period 1 (°C)
v = velocity of air in regenerator passages (m/s)
w = air humidity ratio (kg water/kg dry air)
w_{f0} = air humidity ratio at start of period 1 (kg water/kg dry air)
w_{fp} = air humidity ratio at start of period 2 (kg water/kg dry air)
$\bar{w}_1$ = humidity ratio of mean outlet air state leaving period 1 (kg water/kg dry air)
W = moisture content of matrix (kg water/kg matrix)
x = distance down matrix (m)
ζ = dimensionless "x" co-ordinate = $\dfrac{Jx}{v}$ (dimensionless)
ϵ = interstitial volume of matrix per unit total volume (Mylar: 0.923 dimensionless)
η_h = enthalpy effectivity. |Time averaged outlet air enthalpy for one period—corresponding inlet air enthalpy|/|difference between two relevant inlet air enthalpies| (dimensionless)
η_t = temperature effectivity. Same as η_h except temperature replaces enthalpy
η_w = moisture effectivity. Same as η_h except water content replaces enthalpy
Λ = dimensionless length = $\dfrac{JL}{v}$ (dimensionless)
$\mu = P(1 - \epsilon)/(\rho\epsilon)$ (dimensionless)
θ = time from beginning of period
θ_p = time for one regenerator cycle (s)
ρ = air density (1.16 kg/m^3 at 20°C)
σ = specific heat ratio: dry matrix to air (1.15 dimensionless)
τ = dimensionless "θ" co-ordinate = $J\left(\theta - \dfrac{x}{v}\right)/\mu \simeq \dfrac{J\theta}{\mu}$ (see 1.3) (dimensionless)

Subscripts

1, 2 = period 1, period 2
a, b, c, d = indicate positions as shown in Fig. 2
f = evaluated at air stream temperature
m = evaluated at matrix state

Prefix

Period 1 = period which has air at the higher temperature and humidity ratio entering its inlet, (condensation usually occurs)
Period 2 = period which has air at the lower temperature and humidity ratio entering its inlet, (evaporation usually occurs)
E = calculated error estimates
P = results from numerical simulation, $P\{\ \}$. Results from numerical simulation of parameter within braces
X = experimental results, $X\{\ \}$. Experimental results of parameter within braces

temperature, moisture and enthalpy effectivities were computed. Numerical simulation of the regenerator continued until the difference between period 1 and period 2 enthalpy effectivities was smaller than 10^{-4}. This signified that an energy balance had been obtained, and, under these circumstances, the difference between corresponding moisture effectivities was less than 10^{-4}, indicating mass conservation.

Extrapolation to zero mesh size as described by Carnahan, et al. [9] was carried out to ensure that the best possible estimates of regenerator performance could be obtained. A visual check on the variation of effectivities with mesh sizes showed no erratic tendencies.

2.3 Checks on the Numerical Simulation Results. In [3], a method of deriving regenerator effectivities when heat and mass transfer coefficients are infinite was given. For large transfer coefficients, regenerator effectivities predicted by the above model should approach those resulting from the independently derived model in [3]. For a particular set of operating conditions, Table 1 shows this to be the case since the claimed accuracy of the results in [3] is only 4 percent.

Graphs in [4] show regenerator effectivities as functions of a restricted range of inlet states, characterized by relative humidity and dry bulb temperature as well as dimensionless speeds and lengths. The two significant figure accuracy in reading these graphs was sufficient to transpose the inlet states to dry bulb temperature and humidity ratio, using a psychrometric chart. This enabled the model described above to be run, using inlet states and operating conditions described by the graphs in [4]. Comparisons between the predicted regenerator performances using the results in [4] for inlet states above 0°C and the model described above showed close agreement, typified by the three results given in Table 2. The estimates of moisture effectivities from the model are a little higher than those from [4] in all three cases. One possible explanation of the discrepancy is that in [4], enthalpy is assumed to be a linear function of temperature and humidity ratio, whereas the authors used a nonlinear function which gives a slightly different relationship between the three variables. It is also conjectured that there are likely to be small differences between functions used in each case to relate saturation air humidity ratio to temperature.

3 Description of Experimental Apparatus and Instrumentation

The experimental test rig ran with one of the inlet states at ambient condition with the onset of condensation subject to the vagaries of the weather. Consequently, some of the results, although characterized by condensation occurring, are not typical of those which might be found in real air conditioning applications. The aim of the exercise was to test the mathematical model developed in previous sections, so this was not important. Some of the inlet states tested were, however, similar to those which might occur if a regenerator were used for heat recovery in a tropical climate.

Table 1 Variation of effectivities with NTU for C_r = 2.9; t_{fo} = 34.44°C; t_{f_p} = 21.11°C; w_{fo} = 0.0210; w_{fp} = 0.0086

NTU	2.5	7.5	12.5	17.5	25	50	∞*
η_h	0.24	0.35	0.38	0.39	0.40	0.42	0.45
η_w	0.06	0.16	0.19	0.20	0.22	0.23	0.27

* These values result from the independently derived equilibrium model [3].

3.1 Description of Test Rig. The matrix material of the test regenerator presented an array of closely spaced parallel passages to the air flow as shown diagrammatically in Fig. 1. This was constructed by spirally winding a 102 mm wide ribbon of 0.076 mm thick polyethylene terephthalate (Mylar) under tension. Spacers inserted in the spokes during winding provided for the fixed 0.836 mm gap between layers as well as maintaining the tension. Apart from producing a regenerator with a high ratio of effectivity to pressure drop (i.e., a high St/f), the laminar fluid flow velocity and pressure drop, in this parallel passage geometry have been measured [10, 11] and compare favourably with corresponding analytical solutions.

When wound, the 1.27 m dia regenerator was placed in the test rig which is shown diagrammatically in Fig. 2. Under test, air was drawn through the 381 mm dia entry nozzle which had been calibrated to measure the mass flow. This was followed by a diffuser transition length from circular to rectangular section where pressure measurements were made on the upstream side of the regenerator. A transition piece of constant cross sectional area from rectangular to semi-circular admitted the supply air to the upstream face of the regenerator. On the downstream face, after a similar transition piece from semi-circular to rectangular, the downstream side station for pressure measurements was located. This downstream flow of the supply air was next heated, turned through 180 deg and humidified to present the return air flow to the upstream face of the second half of the regenerator. Again, similar transition pieces were used after and before the pressure measuring stations. All air was exhausted through a constant speed centrifugal fan where, if necessary, the flow rate could be varied by restricting the outlet area.

The heating used was by electrical resistance in which the arrangement of switching gave nine steps. The resistive wires were wound uniformly across the duct section. Humidification was achieved by supplying steam at nominal atmospheric pressure via a header located under the ductwork and connected to a series of six 25.4 mm dia vertical tubes evenly spaced and spanning the duct from top to bottom. Each had a series of 10 pairs of holes 3.18 mm dia drilled approximately 45 deg either side of the stagnation point to produce considerable mixing in the wake of the cylinders.

While the average state of air on the downstream face of the regenerator is steady with time, there are distinct spatial variations across the duct. Since this air is returned to the second half of the regenerator, steps were taken to mix this air prior to heating and humidification. This was effected by attaching to the duct walls swirl plates, each 200 mm × 150 mm, which generated two counter rotating vortices.

3.2 Measurement Procedure. Prior to the test, extensive flow and pressure drop measurements were made on the test rig. These included leakage tests on the rig, seal leakages in the regenerator, calibration of the flow nozzle and pressure drop measurements across the regenerator. The results were reported in [11], and for the dimensionless pressure drop over the possible range of 2:1 in Reynolds number, agreement of ±2.35 percent between the experimental results and theoretical prediction was established. Such confirmation was considered necessary, prior to predicting theoretically, the lumped

Table 2 Comparison with results in [4]

C_r = 5; Λ = 10
t_{f0} = 20.0°C; w_{f0} = 0.0058 (relative humidity 40 percent)
t_{fp} = 0.0°C; w_{f_p} = 0.0029 (relative humidity 75 percent)
η_w (from [4]) 0.29; η_w (authors) 0.31
η_t (from [4]) 0.82; η_t (authors) 0.82

C_r = 2; Λ = 10
t_{f0} = 20.0°C; w_{f0} = 0.0058 (relative humidity 40 percent)
t_{fp} = 0.0°C; w_{fp} = 0.0029 (relative humidity 75 percent)
η_w (from [4]) 0.19; η_w (authors) 0.20
η_t (from [4]) 0.79; η_t (authors) 0.78

C_r = 5; Λ = 10
t_{f0} = 24.0°C; w_{f0} = 0.0075 (relative humidity 40 percent)
t_{fp} = 0.0°C; w_{fp} = 0.0029 (relative humidity 75 percent)
η_w (from [4]) 0.48; η_w (authors) 0.49
η_t (from [4]) not given; η_t (authors) 0.81

transfer coefficients in the heat and mass transfer model reported in the earlier sections.

At the inlet and outlet of each stream, four thermocouple pairs were placed, each in the center of equal sectors, with each pair comprising an adjacent dry bulb and wet bulb thermocouple. At each station the dry bulb and wet bulb thermocouples were formed into thermopiles with eight sets served to a multi channel chart recorder which was coupled in parallel to a digital volt meter having a resolution of 1μv. Average inlet and outlet dry and wet bulb temperatures could thus be found and used to calculate regenerator enthalpy, temperature and moisture effectivities using standard psychrometric equations [12].

Wet bulb thermocouples do not measure, accurately, adiabatic saturation temperatures because the Lewis number is not exactly unity and radiation errors occur. The rig was run without rotation of the regenerator and only the heater operating. By measuring the wet and dry bulb temperatures before and after such a process, which is one of constant humidity ratio, one can calculate directly the effective psychrometer constant as fully outlined in [13]. Unfortunately, but as expected, the psychrometer constant varied by up to 10 percent depending upon the air temperatures involved so that an average value of the psychrometer constant was used to calculate directly the air humidity ratio at each station. Such methods mean inevitably that experimental moisture transfer results will not agree closely with theory, however, an error analysis was carried out on each experimental run so that likely errors in all calculated parameters could be quantified.

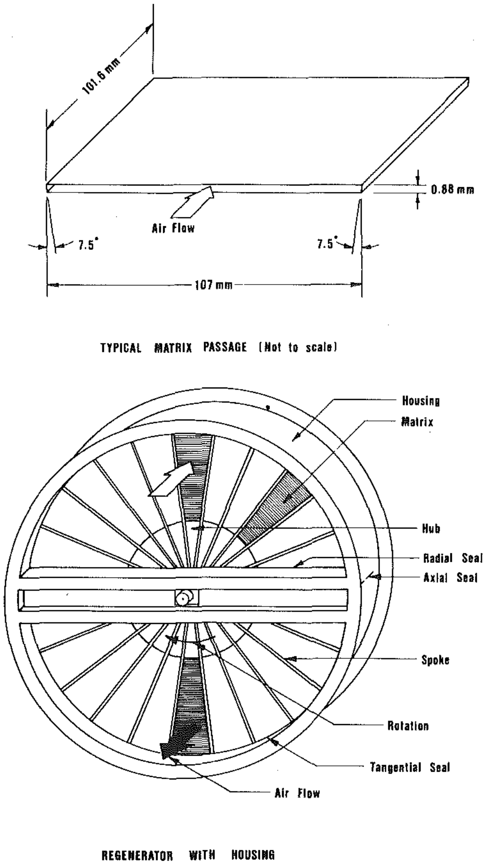

TYPICAL MATRIX PASSAGE (Not to scale)

REGENERATOR WITH HOUSING

Fig. 1 Rotary regenerator and passage

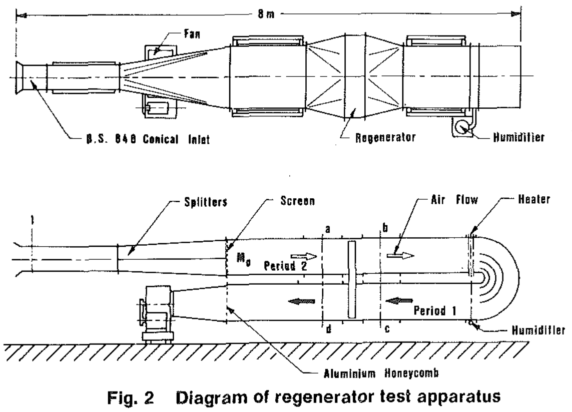

Fig. 2 Diagram of regenerator test apparatus

4 Experimental Results

A compact form of presenting a large range of comparisons between the results from the numerical simulation of the model and the experimental results has not been possible because no satisfactory method of nondimensionalising regenerator inlet states has been found as discussed in Section 2.3. Instead, the results of 23 separate tests on the regenerator in which condensation occurs are presented in column (X), Table 3 and the corresponding simulation results in column (P). The third column, ($E\pm$), shows estimates of the maximum probable error in t_{f0}, t_{fp}, η_{h1}, η_{h2}, η_{w1} and η_{w2}. These were based on an estimated accuracy of reading the wet and dry bulb thermocouples of 0.1°C and of ± 0.00003 in the psychrometer constant.

Ideally, the sum of the estimated errors for the experimental values of η_{h1} and η_{h2} should be greater than $|\eta_{h1} - \eta_{h2}|$, and $(\eta_{h1} + \eta_{h2})/2$ should not deviate from the corresponding theoretical value by more than the average of the maximum errors in η_{h1} and η_{h2}. Similar criteria should also apply for temperature and moisture effectivities.

5 Discussion of Experimental Results

5.1 Runs 1 and 2. Runs 1 and 2 are for heat transfer only when $C_r \ll 1$. It can be seen that $\eta_t > C_r$ in both cases whereas in [14] it is shown that $\eta_t = C_r$ when $C_r \ll 1$ and Ntu $\rightarrow \infty$. If Ntu is finite, $\eta_t < C_r$, contrary to the experimental results. Operation at such low values of C_r were characterised by extreme spatial variation of temperatures coming off the wheel at station b (Fig. 2). The mixing vanes, described in Section 3.1, only reduced this variation at station c to 7°C in runs 1 and 2; hence the inconsistent results. However, regenerators used in air conditioning applications operate with $C_r > 1$ for which condition the temperature variation in the experimental test facility at cross section c was of the order 1°C. The effect therefore caused no significant errors in the remaining tests.

The limitations of wet bulb thermocouples are demonstrated clearly by the negative experimental moisture content effectivities obtained for runs 1 and 2. The regenerator inlet states for these runs are such that no condensation can possibly take place, so η_w must be zero.

5.2 Runs 3–19. For each of runs 3–19, excepting run 12, theoretical enthalpy and moisture content effectivities lie within the error envelopes surrounding the corresponding experimental effectivities, thus meeting the criteria discussed in Section 4. All the period 1 mean outlet states are at, or very close to saturation, as predicted by the model simulation.

In run 12, a comparatively large difference of about 0.05 between period 1 and period 2 temperature effectivities is noted when compared with correspondingly smaller differences <0.02 for all other runs. This suggests a misreading of one of the dry bulb temperatures which consequently invalidates the error envelope for the experimental effectivity of the enthalpy.

It is surprising to note that on runs other than run 12, both theory and experiment predict differences up to 0.02 between period 1 and period 2 temperature effectivities. This reflects the non linearity of the system.

5.3 Runs 20–22. The experimental temperature effectivities for runs 20–22 lie as close to their theoretical counterparts as do those in runs 3–19, but neither the experimental enthalpy nor moisture effectivities meet the criteria for theoretical/experimental agreement discusssed in Section 4. In addition, the error envelopes for these three runs are generally smaller than for previous runs, exhibiting decreasing behavior as moisture effectivities increase. Since enthalpy is a function of temperature and humidity ratio only, and theoretical/experimental temperature effectivity agreement is acceptable for these runs, it would appear that errors in humidity ratio measurement, or in the estimating of humidity ratio error bounds are causing discrepancies.

Table 3 Experimental results

	1			2			3			4		
	P	X	E(±)	P	X	E(±)	P	X	E(±)	P	X	E(±)
t_{f_o}	23.27	23.27	.0112	26.12	26.12	.01	39.62	39.62	.01	42.25	42.25	.01
t_{f_p}	15.08	15.08	1.01	14.95	14.95	.01	17.09	17.09	.01	16.69	16.69	.01
w_{f_o}	.0093	.0093	.0095	.0096	.0096		.0176	.0176		.0170	.0170	
w_{f_p}	.0055	.0055	.0054	.0054	.0054		.0072	.0072		.0067	.0067	
η_{h_1}	.1738	.1642	.0769	.2857	.2736	.0651	.3480	.3409	.0317	.3983	.3899	.0315
η_{h_2}		.1793	.0807		.2818	.0756		.3273	.0478		.3719	.0510
η_{w_1}	0	-.0491	.1751	0	-.0634	.1721	.0021	-.0073	.0783	.0095	.0080	.0851
η_{w_2}		-.0230	.1720		-.0363	.1735		-.0247	.0894		.0744	.0978
η_{t_1}	.3731	.4106		.5508	.5864		.7369	.7302		.7801	.7637	
η_{t_2}	(.3748)	.4157		(.5552)	.5817		(.7513)	.7350		(.7952)	.7748	
$\bar{t}_1$	20.32	19.90		19.97	19.57		23.02	23.17		22.31	22.72	
$\bar{w}_1$	.0093	.0095		.0096	.0099		.0176	.0176		.0169	.0169	
C_r	.38	.38		.57	.57		1.03	1.03		1.33	1.33	
Λ	13.24	13.24		13.19	13.19		13.44	13.44		13.40	13.40	

	5			6			7			8		
	P	X	E(±)	P	X	E(±)	P	X	E(±)	P	X	E(±)
t_{f_o}	52.84	52.84	.01	24.26	24.26	.01	28.42	28.42	.01	51.69	51.69	.01
t_{f_p}	16.26	16.26	.01	16.41	16.41	.01	14.80	14.80	.01	17.71	17.71	.01
w_{f_o}	.0162	.0162		.0178	.0178		.0149	.0149		.0189	.0189	
w_{f_p}	.0060	.0060		.0067	.0067		.0055	.0055		.0060	.0060	
η_{h_1}	.5075	.5026	.0304	.1010	.1132	.0242	.2917	.2917	.0300	.4726	.5002	.0279
η_{h_2}		.5099	.0600		.0843	.0350		.2797	.0442		.9962	.0534
η_{w_1}	.0124	.0250	.1116	.0590	.0717	.0382	.0698	.0820	.0579	.0761	.1486	.0793
η_{w_2}		.0441	.1228		.0398	.0527		.0694	.0763		.1494	.1001
η_{t_1}	.8422	.8292		.2444	.2547		.6656	.6365		.8381	.8352	
η_{t_2}	(.8603)	.8436		(.2505)	.2419		(.6768)	.6460		(.8570)	.8322	
$\bar{t}_1$	21.96	22.50		22.34	22.26		19.35	19.76		23.21	23.31	
$\bar{w}_1$	.0161	.0160		.0171	.0170		.0142	.0142		.0179	.0170	
C_r	3.28	3.28		.50	.50		1.19	1.19		4.21	4.21	
Λ	13.24	13.24		13.37	13.37		13.33	13.33		13.28	13.28	

	9			10			11			12		
	P	X	E(±)	P	X	E(±)	P	X	E(±)	P	X	E(±)
t_{f_o}	43.72	43.72	.01	40.53	40.53	.01	51.45	51.45	.01	24.98	24.98	.01
t_{f_p}	16.56	16.56	.01	17.11	17.11	.01	18.46	18.46	.01	16.34	16.34	.01
w_{f_o}	.0187	.0187		.0205	.0205		.0209	.0209		.0195	.0195	
w_{f_p}	.0066	.0066		.0074	.0074		.0074	.0074		.0067	.0067	
η_{h_1}	.4309	.4415	.0275	.3801	.4080	.0260	.4827	.5185	.0265	.1945	.2144	.0214
η_{h_2}		.4421	.0469		.3957	.0407		.5129	.0509		.2324	.0280
η_{w_1}	.1064	.1369	.0690	.1280	.1741	.0567	.1329	.2024	.0714	.1656	.1940	.0335
η_{w_2}		.1391	.0853		.1537	.0703		.2123	.0935		.2067	.0420
η_{t_1}	.7817	.7717		.7208	.7225		.8290	.8319		.2958	.2844	
η_{t_2}	(.7979)	.7860		(.7370)	.7370		(.8476)	.8276		(.3044)	.3308	
$\bar{t}_1$	22.49	22.17		23.65	23.61		24.10	24.03		22.42	22.52	
$\bar{w}_1$	.0174	.0170		.0188	.0182		.0191	.0182		.0174	.0170	
C_r	2.06	2.06		1.70	1.70		4.19	4.19		.96	.96	
Λ	13.45	13.45		13.18	13.18		13.24	13.24		13.37	13.37	

	13			14			15			16		
	P	X	E(±)	P	X	E(±)	P	X	E(±)	P	X	E (±)
t_{f_o}	42.13	42.13	.01	50.31	50.31	.01	44.37	44.37	.01	28.55	28.55	.01
t_{f_p}	17.21	17.21	.01	17.59	17.59	.01	16.41	16.41	.01	14.68	14.68	.01
w_{f_o}	.0212	.0212		.0215	.0215		.0203	.0203		.0174	.0174	
w_{f_p}	.0073	.0073		.0067	.0067		.0065	.0065		.0055	.0055	
η_{h_1}	.4314	.4672	.0245	.4986	.5361	.0242	.4707	.4981	.0244	.3487	.3822	.0242
η_{h_2}		.4519	.0411		.5074	.0473		.4782	.0436		.3534	.0346
η_{w_1}	.1927	.2502	.0531	.2033	.2722	.0608	.2670	.2592	.0572	.2145	.2665	.0430
η_{w_2}		.2244	.0708		.2282	.0845		.2252	.0713		.2252	.0571
η_{t_1}	.7525	.7575		.8206	.8217		.7848	.7815		.6271	.6207	
η_{t_2}	(.7694)	.7727		(.8395)	.8280		(.8019)	.7952		(.6397)	.6306	
$\bar{t}_1$	23.38	23.27		23.46	23.31		22.43	22.52		19.85	19.94	
$\bar{w}_1$	.0185	.0177		.0185	.0174		.0174	.0167		.0148	.0142	
C_r	2.34	2.34		4.30	4.30		2.80	2.80		1.70	1.70	
Λ	13.08	13.08		13.33	13.33		13.46	13.46		13.48	13.48	

	17			18			19			20		
	P	X	E(±)	P	X	E(±)	P	X	E(±)	P	X	E(±)
t_{f_o}	37.69	37.69	.01	44.99	44.99	.01	45.29	45.29	.01	31.59	31.59	.01
t_{f_p}	18.91	18.91	.01	16.61	16.61	.01	16.18	16.18	.01	14.60	14.60	.01
w_{f_o}	.0216	.0216		.0224	.0224		.0259	.0259		.0243	.0243	
w_{f_p}	.0065	.0065		.0066	.0066		.0069	.0069		.0055	.0055	
η_{h_1}	.4399	.4853	.0240	.4969	.5408	.0218	.5748	.6038	.0175	.5400	.6066	.0158
η_{h_2}		.4474	.0393	.2832	.5132	.0400		.5800	.0342		.5527	.0217
η_{w_1}	.2580	.3217	.0433	.2832	.3575	.0474	.4372	.4787	.0352	.4848	.5663	.0261
η_{w_2}		.2759	.0623		.3112	.0686		.4439	.0566		.4934	.0338
η_{t_1}	.7915	.8026		.7823	.7847		.7869	.7960		.6810	.7082	
η_{t_2}	(.8092)	.7974		(.8004)	.8001		(.8054)	.8080		(.7000)	.7229	
$\bar{t}_1$	22.83	22.62		22.79	22.72		22.38	22.14		20.01	19.55	
$\bar{w}_1$	.0177	.0168		.0179	.0168		.0170	.0168		.0152	.0136	
C_r	4.20	4.20		3.29	3.29		4.23	4.23		2.99	2.99	
Λ	13.26	13.26		13.46	13.46		13.46	13.46		13.44	13.44	

	21			22			23		
	P	X	E(±)	P	X	E(±)	P	X	E(±)
t_{f_o}	33.11	33.11	.01	34.95	34.95	.01	Program would not converge.	46.00	
t_{f_p}	14.60	14.60	.01	14.43	14.43	.01		10.00	
w_{f_o}	.0270	.0270		.0306	.0306			.0510	
w_{f_p}	.0054	.0054		.0054	.0054			.0055	
η_{h_1}	.6065	.6596	.0141	.6660	.7080	.0121		.8255	
η_{h_2}		.6362	.0192		.6679	.0165		.7850	
η_{w_1}	.5622	.6288	.0229	.6360	.6872	.0194		.8403	
η_{w_2}		.5969	.0295		.6369	.0245		.7686	
η_{t_1}	.7241	.7391		.7510	.7630			.7673	
η_{t_2}	(.7421)	.7603		(.7709)	.7730			.8477	
$\bar{t}_1$	19.71	19.43		19.41	19.17			18.36	
$\bar{w}_1$	.0149	.0134		.0146	.0132			.0128	
C_r	3.65	3.65		4.26	4.26			4.58	
Λ	13.60	13.60		13.66	13.66			14.18	

η_t values in brackets are not extrapolated to zero mesh size but are the results for the smallest mesh used.

The various values of psychrometric constant were determined experimentally at ambient humidity ratio only and showed a variation of psychrometric constant with temperature. A further variation could be expected with changes in humidity ratio, however, because of the rig design, there was no way of determining quantitatively this effect which was not included in the psychrometric constant error estimate. In runs 20–22, the inlet states to period 1 had high humidity ratios, as well as being close to the saturation line. Since moisture content and temperature effectivities were high, there were large moisture content and temperature differences between inlet states and mean outlet states, and hence comparatively large differences in the corresponding psychrometric constant.

Runs 20–22 therefore do not meet the error criteria in section 4, due to the variation of psychrometric constant with humidity ratio not having been considered. This is further supported by Table 3, which shows consistently that the experimental period 1 moisture effectivities deviate more from their theoretical counterparts than do the period 2 effectivities. Because all air states in the regenerator during period 2 lie closer to ambient than do those in period 1, the above explanation is consistent with the observed effect. This is noticeable to a lesser extent in runs 3–19. The discrepancies discussed above are small in magnitude and do not really conflict with the general conclusion that the model predicts the performance of the sensible heat regenerator very well, when condensation occurs.

5.4 **Runs 23.** In run 23, regenerator operating conditions were such that a large amount of water was observed in the transparent outlet pipe exhausting air from the rig via the fan. Eventhough the chart recorder showed that system steady state had been reached, large water droplets still formed on the outlet pipe walls at such a rate that the droplets eventually flowed down the pipe and back into the fan casing. The system had thus reached a steady state condition where more water appeared to be condensing in period 1 than evaporating in period 2 with $\eta_{h1} \neq \eta_{h2}$ and $\eta_{w1} \neq \eta_{w2}$. The excess water appeared to be blown physically out of the matrix into the outlet pipe. When run for these particular operating conditions, the computer simulation of the model would not converge. Instead, it showed numerically that more and more water would condense in period 1, with the enthalpy and moisture effectivities varying very little after the system appeared to have settled down. Moisture effectivities were unequal for each period.

Trends such as those observed in run 23 were noticed in situations where the warmer regenerator inlet state was very near saturation. Decreasing the dimensionless speed in such a situation, resulted in both the regenerator and the numerical model showing normal operation. From this, it can be concluded that for certain combinations of regenerator operating conditions, the system will not reach steady state, large amounts of water being deposited continuously on the regenerator matrix per cycle. This conclusion is supported by similar findings in Holmberg [4], who observed the phenomenon numerically.

5.5 Other Sources of Error. The only sources of error not taken into account in the error analysis were errors in C_r, Λ and heat losses/gains through the rig walls.

The only measured parameter likely to affect C_r was the period cycle time, which was measured by dividing the time for a large number of regenerator revolutions by the number of revolutions. Little error is introduced into C_r, using this method.

Λ was found from pressure drop and air flow measurements on the rig [11]. The manometers used to monitor pressure drop across the parallel plates of the regenerator were calibrated correctly and showed steady readings during regenerator operation. Account was taken of leakage flows through regenerator seals, analysis showing typically that $m_{ab} \simeq m_{cd} \simeq 0.9\, m_0$ (Fig. 2) so balanced flow always occurred. Any errors in Λ could therefore be associated only with the errors in flow measurements. The flow nozzle was constructed to BSS:848, calibrated, and the error is estimated to be less than 2 percent. In addition, at the values of Λ used, the model was found to be relatively insensitive to errors less than 10 percent in Λ, so any errors in the flow measurements would be unlikely to show up as significant errors in effectivities.

The ducting on all parts of the test apparatus subject to higher air temperatures than ambient was well insulated, making heat losses through duct walls negligible.

6 Comparison with Heat Transfer Alone

The computer program developed by Maclaine-cross [6] for a linear model of heat transfer only, was run for each of the pairs C_r, Λ, obtained from the experimental results (Table 3). The resulting temperature effectivities, together with corresponding averages of period 1 and period 2 temperature effectivities from Table 3 column P, are shown in Table 4.

In all cases, the temperature effectivity for heat transfer only is greater than the corresponding effectivity when condensation occurs, showing that moisture transfer is achieved at the expense of heat transfer. Discrepancies between corresponding temperature effectivities vary greatly, depending on the amount of mass transfer occurring, or, equivalently, the proximity of the regenerator inlet states to the saturation line. Nevertheless, the maximum enthalpy that can be transferred for given inlet states is greater when condensation occurs, as discussed in [3], eventhough generally high values of C_r and/or Λ are needed to approach this situation.

7 Concluding Remarks

Lack of a fully nondimensional model precludes the drawing of very broad and general conclusions, without a large number of experimental results. However, the close agreement between the comparatively few experimental results and the corresponding results from the model simulation suggests that the model is a good representation of the regenerator. Further agreement between the simulation of the model for three randomly chosen operating conditions and corresponding results from a similar independently derived model [4] reinforce the model's integrity.

Table 4 Comparison with heat transfer alone

C_r	Λ	η_t (R)	η_t (Mc)
1.03	13.44	.7441	.7780
1.33	13.40	.7877	.8161
3.28	13.24	.8513	.8587
.50	13.37	.2477	.4974
1.19	13.33	.6712	.8017
4.21	13.28	.8476	.8627
2.06	13.45	.7898	.8472
1.70	13.18	.7289	.8347
4.19	13.24	.8383	.8632
.96	13.37	.3001	.7621
2.34	13.08	.7610	.8488
2.80	13.46	.7933	.8572
4.30	13.33	.8300	.8635
1.70	13.48	.6334	.8373
4.20	13.26	.8003	.8625
3.29	13.46	.7914	.8606
4.23	13.46	.7962	.8643
2.99	13.44	.6905	.8585
3.65	13.60	.7331	.8635
4.26	13.66	.7610	.8660

(R) Numerical simulation of condensation and evaporation in regenerators
(Mc) Maclaine-cross's Heat transfer only results

For certain operating conditions, the regenerator can exhibit unstable behaviour, in that a net build up of water occurs on the matrix in period 1. In the practical situation, this water is blown off the matrix by the airflow. The numerical simulation of the corresponding model does not converge, and also shows a net build up of water on the matrix. *Shifting the period 1 inlet state away from the saturation line,* and/or decreasing the dimensionless speed sufficiently, results in both the regenerator returning to normal operation, and the numerical model converging.

Condensation in regenerators is a function of the regenerator inlet air states, and unless these can be controlled independently, it is unavoidable in certain situations. For some applications, the extra total heat transfer obtained when condensation takes place is beneficial, but for other applications, the associated moisture transfer is undesirable. In the latter cases, the user has no option but to try to control one of the inlet states, so that only sensible heat transfer occurs in the regenerator.

References

1 Dunkle, R. V., and Maclaine-cross, I. L., "Theory and Design of Rotary Regenerators for Air Conditioning," *Mechanical and Chemical Engineering Transactions, Institution of Engineers, Australia*, Vol. 6, 1970, pp. 1–6.

2 Hausen, H., Wärmeübertragung im Gegenstrom, Gleichstrom und Kreuzstrom, Springer, Berlin, 1950.

3 van Leersum, J. G., and Banks, P. J., "Equilibirum Heat and Mass Transfer in Regenerators in which Condensation Occurs," *International Journal of Heat and Mass Transfer*, Vol. 20, 1977, pp. 927–934.

4 Holmberg, R. B., "Heat and Mass Transfer in Rotary Heat Exchangers with Nonhygroscopic Rotor Materials," ASME JOURNAL OF HEAT TRANSFER, Vol. 99, 1977, pp. 196–202.

5 Banks, P. J., Close, D. J., and Maclaine-cross, I. L. "Coupled Heat and Mass Transfer in Fluid Flow through a Porous Media—An Analogy with Heat Transfer," *Heat Transfer* 1970, *Proceedings of the 4th International Transfer Conference*, Versailles, Sept., 1970, Vol. VII, paper T3, 1, Elsevier, Amsterdam, 1970.

6 Maclaine-cross, I. L., "Heat and Mass Transfer in Regenerators," Ph.D. Thesis, Department of Mechanical Engineering, Monash University, Victoria, Australia, 1974.

7 Lambertson, T. J. "Performance Factors of a Periodic Flow Heat Exchanger," ASME JOURNAL OF HEAT TRANSFER, 80, 1959, pp. 586–592.

8 Maclaine-cross, I. L., "Effect of Interstitial Fluid Heat Capacity on Regenerator Performance," Accepted for publication, ASME JOURNAL OF HEAT TRANSFER, 1980.

9 Carnahan, B., Luther, H. A., Wilkes, J. O., *Applied Numerical Methods*, 1st ed., Wiley, New York, 1969.

10 Beavers, G. S., Sparrow, E. M., and Magnuson, R. A., "Experiments on Hydrodynamically developing Flow in Rectangular Ducts of Arbitrary Aspect Ratio," *International Journal Heat Mass Transfer*, Vol. 13, pp 689–702.

11 Maclaine-cross, I. L., and Ambrose, C. W., "Pressure Drop in Parallel Rotary Regenerators," ASME *Journal of Fluids Engineering*, Vol. 102, No. 1, Mar 1980, pp. 59–63.

12 Dunkle, R. V., and Norris, D. J., "General Analysis of Regenerative

Evaporative Cooling Systems," XII International Congress of Refrigeration, Madrid Paper 6A.06, 1967.

13 van Leersum, J. G., "Heat and Mass Transfer in Regenerators," Ph.D. Thesis, Department of Mechanical Engineering, Monash University, Victoria, Australia, 1975.

14 Maclaine-cross, I. L., and Banks, P. J., "Coupled Heat and Mass Transfer in Regenerators. Prediction using an Analogy with Heat Transfer," *International Journal of Heat and Mass Transfer*, Vol. 15, 1972, pp. 1225–1242.

Heishichiro Takahama
Professor,
Department of Mechanical Engineering,
Faculty of Engineering,
Nagoya University,
1, Furo-cho, Chikusa-ku,
Nagoya, 464, Japan

Hajime Yokosawa
Research Associate,
College of General Education,
Nagoya University

Energy Separation in Vortex Tubes with a Divergent Chamber

The vortex tube is a simple device for separating a compressed gaseous fluid stream into two flows of high and low temperature. In order to produce a high temperature separation effect, the use of a sufficiently long tube with a smooth inner surface has been standard procedure up until now. However, since such a device requires a large installation space, an attempt was made to shorten the length of the vortex chamber without any fall in the temperature separation effect by using some divergent tubes as the vortex chamber. Experimental data obtained in these vortex chambers were compared with those in the commonly used straight vortex chambers. Observation indicates that a divergent tube with a small angle of divergence is effective in obtaining a higher temperature separation and makes possible a shortening of the chamber length.

Introduction

The vortex tube is a simple device that separates a compressed gaseous fluid stream into two flows of high and low temperature. The complexity of this phenomenon despite its simple structure (it has no moving parts) has attracted interest from various points of view [1–5]. Taking advantage of this simple operation for continuous and extensive change of outflowing stream temperatures, the vortex tube has been applied to air-cooled suits used in high temperature work environments. It has also been used as a cooling device for cutting tools [6]. Moreover, its application to such things as shortening the start-up time of steam power units [7] and its use as gas-processing tool [8] have also been examined.

According to the literature [9, 10], the use of a relatively long tube with a smooth inner surface is required to maintain the swirling motion in the vortex chamber from the nozzle outlet to as far downstream as possible, in order to obtain high-energy separation performance. Practically speaking, however, this requires in turn a large installation space, which makes the utilization of the device difficult. Consequently, it is important to find a way to shorten the length of the chamber without lowering its energy separation performance.

Few reports, however, have dealt with this matter of shortening vortex chambers. Parulekar [11], Otten [12], and Raiskii and Tunkel [13] used divergent tubes for all or a part of their vortex chambers in an attempt to shorten the chamber and improve energy separation performance. In contrast, Metenin [14] set straighteners of various shapes at various locations in vortex chambers in order to discover which shape was most efficient and where it should best be positioned. But these reports focus attention only on the rise and fall of temperatures in the outflowing streams; the measurement of swirling flow is not considered. Both effects of the shape of the vortex chamber on the internal flow as well as the causes of change in performance remain unknown.

The swirling motion in the flow itself is capable of being adopted in the industrial field, for example, in the augmentation of heat transfer, combustion control, and the concentration of uranium. Moreover, the swirling flow in the vortex chamber of the vortex tube device has attracted additional interest since it accompanies the temperature separation and high rate of back flow. Hence it is also important to understand through experimentation the effects that differences in the geometrical shape of the chamber have on the swirling flow. No detailed investigation of the effects of length and angle of divergence on the swirling flow and the energy distributions in the counter-flow vortex tube is available, although Lay [15] reports the results in vortex tubes of various lengths withdrawing no cold stream, and other reports [16–18] differ among themselves in the particular length of the vortex tube used in experiments.

The purpose of the present study is to examine the possibility of shortening the chamber length without any fall in energy separation performance, and to present data on the internal flow for the counter flow vortex tube which has not previously been available. In order to quicken the decay in swirling flow, a divergent vortex chamber was chosen. The swirling flows in the divergent vortex chambers of different lengths and tapers were measured and compared with straight chambers of the same lengths. Next, the energy separation performance of these vortex chambers was compared, enabling a final discussing of optimum conditions for shortening the vortex chamber length.

Experiments

Figure 1 shows a schematic diagram of the layout of the experiment. Air, compressed by the two compressors (CP), together with water and oil droplets removed by the filter (F) and water separator (WS), is jetted into the vortex chamber (VC) through four tangential nozzles (N). These nozzles are arranged peripherally at one end of the VC in order to produce a high speed swirling flow. An air cooler (C) and relief valve (RV) are utilized to keep the inlet temperature and pressure constant. As the axial pressure gradient is created in the central portion of the chamber by a radial drop in pressure that is inversely proportional to the decay of the swirl velocity, a back flow is generated and flows out through the cold end orifice (CO) as a cold air stream. On the other hand, the annular flow, which follows along the chamber wall, passes out through the cone-shaped valve regulating the rate of flow (CV) as a hot air stream.

The mass rates of flow for the outflowing cold air (G_{co}) and inlet air (G_t) are measured by standard pipe flow orifices (O), and their ratio, or cold-flow fraction ($\xi = G_{co}/G_t$) is changed by regulating the CV opening. A marked energy separation occurs in the vicinity of $\xi = 0.5$; and, although the axial velocity changes to some degree, the variations in other physical values are small, depending on changes in the value of ξ. Therefore, measurements of the flow in vortex chambers were made keeping ξ at 0.5. The mass flow-rate and the

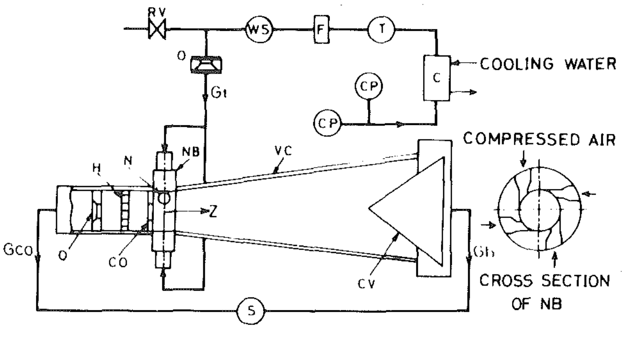

Fig. 1 Schematic diagram of experimental layout: CP, air compressor; C, air cooler; T, tank; F, filter; WS, water separator; RV, relief valve; O, pipe flow orifice; NB, nozzle block; N, nozzle; CO, cold end orifice; VC, vortex chamber; CV, flow rate regulating valve; S, silencer; H, straightener.

Contributed by the Heat Transfer Division for publication in the JOURNAL OF HEAT TRANSFER. Manuscript received by the Heat Transfer Division August 25, 1980.

stagnation temperature of the inlet air before the nozzle inlet (G_t and T_{tn1}) were regulated to 0.172 (±0.002) kg/s and 317 (±0.5) K, respectively. Mach numbers (M_{n2}) of jets at the nozzle outlet, which change to some degree according to the type of vortex chambers, were nearly equal to 0.6. A cylindrical pitot tube equipped with a stagnation temperature probe with an outside diameter of 3 mm was used to carry out measurements of swirling flows inside the chambers. The diameter of the two pressure taps was 0.3 mm, and the angle between pressure taps, 81.0 deg. The angle corresponding to a surface pressure equal to the static pressure was measured [10, 18], and the recovery factor of the stagnation temperature probe was calibrated by means of a jet from a tank nozzle.

Putting the pitot tube through vortex chambers along the diameter, the angle of flow (α), the total and static pressure (p_t and p), and the stagnation temperature (T_t) were measured respectively with a protractor, Hg manometers, and a copper-constantan thermocouple. The maximum likely errors in these measurements can be approximated as follows: $\alpha = \pm 0.25$ deg; $p_t = \pm 0.67$ kPa; $p = \pm 1.33$ kPa; $T_t = \pm 1.5$ K. With measured values, and using the following equations

$$M = \sqrt{\frac{2}{\kappa - 1}\left\{\left(\frac{p_t}{p}\right)^{(\kappa-1)/\kappa} - 1\right\}} \tag{1}$$

$$T_t/T = 1 + (\kappa - 1)M^2/2 \tag{2}$$

$$V_s = \sqrt{\kappa R T} \tag{3}$$

$$V = M V_s \tag{4}$$

$$v = V\cos\alpha, \quad w = V\sin\alpha \tag{5}$$

the static temperature (T), absolute velocity (V), tangential velocity (v), and axial velocity (w) were calculated at each radial position. The following equation, which is taken from the equation of continuity for the steady, axially symmetrical flow, was used to calculate radial velocity at a given radial position (r_1).

$$u_{r=r_1} = -\left\{\frac{\partial}{\partial z}\int_0^{r_1} \rho w r dr\right\}\Big/ \rho_1 r_1 \tag{6}$$

where ρ_1 is the density of air at $r = r_1$.

In order to compare the energy separation performances in the vortex chambers used in the experiments, performance tests were run in the range of $0.25 \leq \xi \leq 0.7$ under the same inlet air conditions as the flow measurements. Mach numbers (M_{n2}) of the jets varied, depending on the type of vortex chambers and the values of ξ, and $M_{n2} = 0.5$–0.7.

Table 1 Main dimensions of test chambers

Chambers	Taper	θ°	L mm	L/D_0	F_t/F_1
D 1	3/100	1.72	900	17	2.25
D 2			2000	38	4.58
D 4			4000	76	10.69
T 6			6000	114	19.45
T 2	9/100	5.15	2000	38	
T 1	15/100	8.58	1200	23	
S 1	straight tube		1000	19	1.0
S 2			2000	38	
S 4			4000	76	
S 6			6000	114	

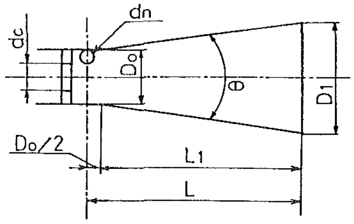

$D_0 = 52.8$, $d_c = 23.5$, $d_n = 11.01$ (mm)
Taper $= (D_1 - D_0)/L_1$, $F_t = \pi D_1^2/4$, $F_1 = \pi D_0^2/4$

Table 1 shows the main dimensions of the test chambers. The tapers of divergent vortex chambers were determined by referring to the optimum angle at which the divergent tube would incur the minimum loss of enlargement where there is no rotational motion. In order to examine the effects of chamber length on separation performance, chambers D1, D2, D4, and T6, all of which have the same taper (3/100) but different lengths, were used. Moreover, to examine the effects of the divergent angle on separation performance, T6, T2, and T1, all of which have different divergent angles but the same ratio between the cross-sectional area at the inlet of the divergent portion and that at its outlet, were used. Four straight chambers of the same length, which is equal to those of the aforementioned divergent vortex chambers, were also tested and the results compared.

The nozzle block used for both divergent and straight chambers was designed in accord with the following dimensional ratios, considered optimal for a 52.8 mm i.d. straight chamber [10].

Nomenclature

C_p = specific heat at constant pressure, J/kg·K
D_0 = inner diameter of vortex chamber at $Z = 0$ ($= 2r_{w0}$), mm
d_c = diameter of cold end orifice, mm
d_n = diameter of nozzle outlet, mm
G = mass rate of flow, kg/s
h_t = specific stagnation enthalpy, J/kg
h = specific static enthalpy, J/kg
$(\Delta h)_j$ = dynamic enthalpy of jet ($= U^2/2$), J/kg
$(\Delta h)_{cs}$ = isentropic enthalpy drop between the state of nozzle outlet and p_{co}, J/kg
L = length of vortex chamber, mm
M = Mach number
N = number of nozzles
p_t = total pressure, Pa
p = static pressure, Pa
R = gas constant of air, J/kg·K
r = radius, radial position, mm
$r' = r/r_w$
S = swirl intensity
T_t = stagnation temperature, K
T = static temperature, K
$(\Delta T)_j = (\Delta h)_j/C_p$, K
$(\Delta T)_{cs} = (\Delta h)_{cs}/C_p$, K
U = reference velocity defined by equation (10), m/s
u, v, w = radial, tangential, and axial velocity, m/s
$u' = u/U$, $v' = v/U$, $w' = w/U$
V = absolute velocity, m/s
V_s = velocity of sound, m/s
V_{ns} = velocity obtained by an isentropic expansion in nozzle, m/s
Z = axial distance from nozzle opening, mm
$z' = Z/r_{wo}$
α = angle of flow, deg
β = constant determined from chamber dimensions (= 0.963)
η = efficiency of energy separation defined by equation (11)
η_l = adiabatic efficiency defined by equation (8)
Θ = angle of divergence, deg
κ = specific-heat ratio
λ = coefficient of decrease
ξ = cold flow fraction ($= G_{co}/G_t$)
ρ = density, kg/m^3
ϕ = kinetic energy, J
ϕ_n = velocity coefficient of nozzle
ψ = deceleration coefficient of jet (= 0.98)

Subscripts

a = annular flow
c = back flow
co = outflowing cold air
h = outflowing hot air
i = interface between back flow and annular flow regions
m = mixed-mean value
$n1$ = values at nozzle inlet
$n2$ = values at nozzle outlet
t = inlet air
w = values at wall of vortex chamber

$$\left.\begin{array}{l} d_n/D_0 \leqq 0.20,\ d_c < D_0 - 2d_n \\ Nd_n{}^2/D_0{}^2 = 0.16\text{–}0.20,\ d_c{}^2/Nd_n{}^2 \leqq 2.3 \end{array}\right\} \quad (7)$$

Considering the effects of error due to heat conduction, divergent chambers were made of stainless steel sheet (1 mm thickness) and the straight chambers of polycarbonate. The vortex chambers were thermally insulated with glass wool and felt. The adiabatic efficiency of thermal insulation used for the estimation of the heat loss can be defined as follows:

$$\eta_l = \{\xi h_{tco} + (1 - \xi)h_{th}\}/h_{tn1} \quad (8)$$

Since air has nearly the same characteristics as an ideal gas under experimental conditions, equation (8) can be rewritten as

$$\eta_l = \{\xi T_{tco} + (1 - \xi)T_{th}\}/T_{tn1} \quad (9)$$

η_l is sufficiently large ($\eta_l > 0.997$) to disregard error due to heat loss.

Results and Discussion

Reference Velocity. The velocity of the jet at the nozzle outlet can be calculated as $V_{n2} = \phi_n V_{ns}$. According to the experimental results [19], the swirling flow in the cross-section at the nozzle opening ($z' = 0$) is axially asymmetric. Therefore, the mean velocity of annular flow at $z' = 0$ must be corrected as

$$U = \psi V_n = \psi \phi_n V_{ns} \quad (10)$$

where ψ (= 0.98) is the deceleration coefficient of the jet considered to result from the partial admission of the nozzle on the velocity field [19].

Efficiency of Energy Separation. In order to compare the energy separation performance in vortex tube devices, it is possible to define certain efficiencies based on various criteria in the light of the drop in the stagnation enthalpy of the cold air stream. As a criterion, $(\Delta h)_j = U^2/2$ is applicable to the comparison of performances in a specific vortex tube device (e.g., operated under the various inlet gas conditions). It is not suitable, however, for comparing the performances in several vortex tube devices of different geometrical proportions, in that it does not take into account the loss of the pressure head which is bound to occur in flowing through the vortex chamber.

Taking into account such geometrical differences and the initial available energy of the jet at $z' = 0$, the efficiency of energy separation (η) may be defined as:

$$\eta = (h_{tn1} - h_{tco})/\{(\Delta h)_j + (\Delta h)_{cs}\} \quad (11)$$

or, since the air under the experimental conditions has nearly the same characteristics as an ideal gas,

$$\eta = (T_{tn1} - T_{tco})/\{(\Delta T)_j + (\Delta T)_{cs}\} \quad (12)$$

where $(\Delta h)_{cs} = C_p(\Delta T)_{cs}$ is the isentropic enthalpy drop to be obtained between the state at the nozzle outlet and the pressure at the cold air outlet. Changes in η value depending on ξ in the tested vortex chambers are shown in Fig. 2, with the stagnation temperature and mass flow rate of inlet air as constant values ($T_{tn1} = 317$ K and $G_t = 0.172$ kg/s). The changes in value for the relatively long, straight tube (S8, $L/D_0 = 150$, and using the same nozzle block as other tube tested), that has so far been taken as optimal, are indicated in the figure with a solid line.

In straight chambers, the effect of chamber length (L/D_0) on η is noteworthy: the shorter the length, the lower the value of η. It is clear from the values of chamber S6 that length does have some influence on η, however slight, even at $L \geqq 100D_0$.

In the case of divergent chambers, however, each chamber tested showed a better performance than its corresponding straight chamber of the same length. Among chambers D1, D2, D4, and T6, all of which have the same divergent angle, D2 showed the best values over a wide range of ξ. The drop in the value of η for the comparatively long chambers D4 and T6 at $\xi > 0.4$ are remarkable. Among chambers T6, T2, and T1, all of which have different divergent angles, T2 showed the largest η value and had nearly the same performance as D2. The level of performance drops in T1 which has large divergent angle. As mentioned above, this leads us to conclude that the divergent chamber with the divergent taper 3/100–9/100 (Θ = 1.7–5.1 deg) and a chamber length of $L = 38D_0$ is optimal.

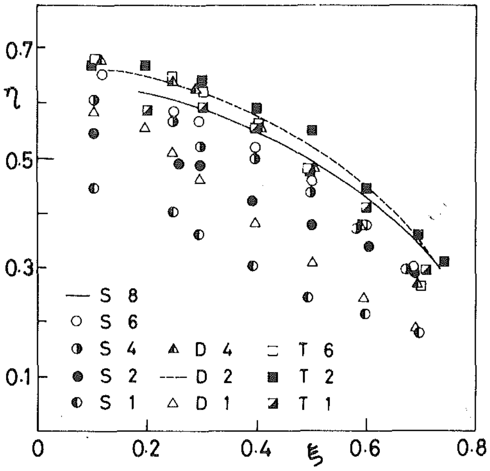

Fig. 2 Efficiency of energy separation

It would be helpful to compare the present results with those of other experiments [11–13] using the efficiency formula given above, but sufficient data has not been provided. Moreover, energy separation in vortex tubes is strongly influenced by the geometrical proportion of the chamber as well as by the state of the inlet gas. A simple comparison, therefore, would be misleading. We shall leave this matter for discussion at a later date.

Velocity Profiles. Swirling flows in the vortex chambers were measured in several cross-sections at different axial distances, and radial, tangential, and axial velocity components were calculated. Typical resultant values are given in Figs. 3, 4, and 5.

Air velocity varies from a value of zero at the surface of the chamber wall to a specific finite value at a point some distance away from the wall. The thickness of this region of the high velocity gradient, which is influenced by the retarding effect of the surface, may become thinner in accord with the effect of the swirl.

As shown in Fig. 5, a back flow ($w < 0$) obtains in the central portion of all the vortex chambers with the ratio of its radius (r_i) to that of the vortex chamber (r_w) decreasing gradually.

As shown in the tangential velocity profiles of Fig. 4, a notable difference appears in the back flow region owing to chamber type. Angular velocities in straight chambers are slightly higher in the back flow region, and shortening the chamber length increases this tendency. In the case of divergent chambers, the regions of forced vortex profiles are a little larger and, in some cases, extend into the region of annular flow. In chambers with the same divergent angle, the effect of chamber length on angular velocity is not found in T6, D4, and D2, but is noticeable only in D1. With an increase in the divergent angle, the region of the forced vortex profile extends into the annular flow region, and the region of lower angular velocity appears in the central portion of the back flow ($r' < 0.3$) in the cross-section adjacent to the nozzle ($z' = 0.5$).

When the chambers are long, profiles for both straight and divergent chambers of the same length show no noticeable difference. A difference shows up only with a decrease in chamber length. In the short vortex chambers (S1, D1, and T1) the profiles of the annular flow regions tend to be the same as that of a free vortex in cross-sections near the hot end.

Since the rate of flow in the outflowing cold air was kept constant in the experiments, in short vortex chambers a larger quantity of air had to be moved from the area of annular flow to that of the back flow per unit of distance and also accelerated so as to reach the velocity of the outflow at the cold end. The pressure level in the chamber, therefore, tends to be high and the radial and axial pressure gradients

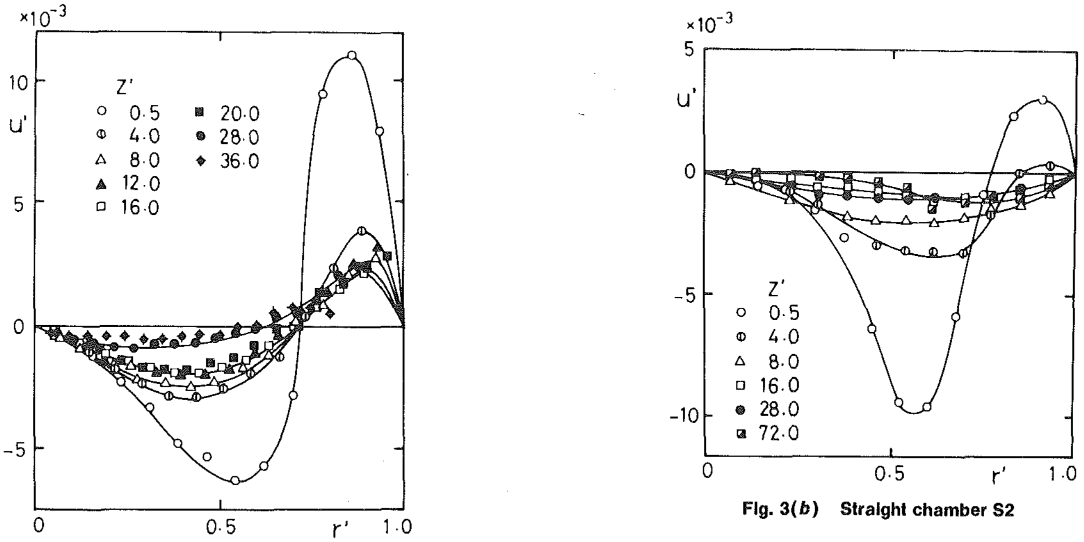

Fig. 3(*a*) Divergent chamber D2

Fig. 3(*b*) Straight chamber S2

Fig. 3 Radial velocity profiles

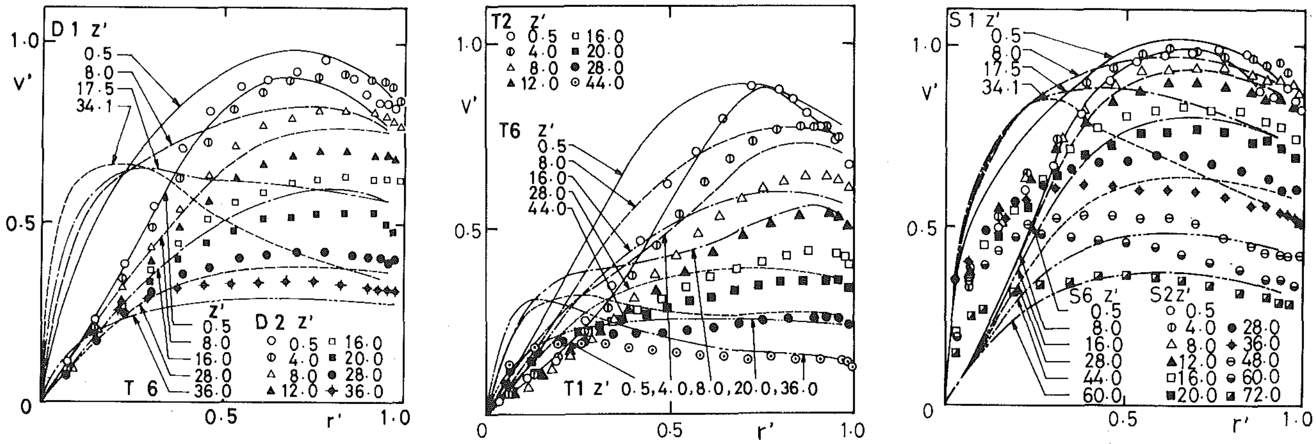

Fig. 4(*a*) Divergent chambers D1, D2, T6

Fig. 4(*b*) Divergent chambers T1, T2, T6

Fig. 4(*c*) Straight chambers S1, S2, S6

Fig. 4 Tangential velocity profiles

to be steep, and these in turn cause changes in the pattern of flow.

As shown in Fig. 5, the axial velocity profiles in divergent chambers are slightly different from those in straight chambers. In all of the straight chambers, axial velocities have small absolute values near the axis, and this tends to show up with a decrease in chamber length. On the other hand in the case of divergent chambers, this tendency appears only in the short chambers T1 and D1. This is due to the fact that the large angular velocity in the back flow region causes a relatively large pressure drop near the axis. At the cross-section nearest to the cold end orifice ($z' = 0.5$), $|w|$ has a larger value in divergent chambers than in straight ones; and, as detailed below, the quantity of back flow in divergent chambers is much greater than that in straight chambers.

In straight chambers, the shorter the chamber length is, the higher the radial velocity, although $|u/U|$ does not exceed 0.01. Since the radius of a divergent vortex chamber increases in an axial direction, the direction of the flow is not parallel to the axis. Therefore, the direction of radial velocity is outward (towards the chamber wall) in the annular flow region, and inward (towards the chamber axis) in the back flow region.

Decay of Tangential Velocity. Distributions of the tangential velocities near the wall (v_w') along the axial direction are given in Fig. 6 in order to indicate the decay of the swirling flow.

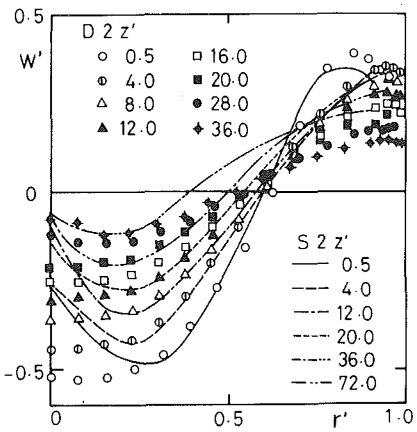

Fig. 5 Axial velocity profiles

In a long, straight vortex chamber, the decay, which is mainly influenced by the wall friction, is expressed as [20, 21]:

$$v_{ws}' = \beta \exp(-\lambda z'^{6/7}) \tag{13}$$

The constant β can be determined from the chamber dimensions at the nozzle opening as $\beta = 0.963$; the constant λ, from the experimental results in the longest of the straight chambers tested (S6) as $\lambda = 0.0313$. Equation (13) can be rewritten as:

$$v_{ws}' = 0.963 \exp(-0.0313 z'^{6/7}) \tag{14}$$

The values resultant from equation (14) are indicated in the figure by a solid line. The experimental data for the shorter chambers S1 and S2 are slightly greater than these values.

In addition to wall friction, the effect of an increase in the cross-sectional area appears in the decay of v_w' in the divergent chambers. The chamber radius (r_w) at any value of z' can be formulated, using the divergent angle (Θ), as follows:

$$\left.\begin{aligned} 0 \leqq z' \leqq z_0' &: r_w = r_{w0} \\ z' > z_0' &: r_w = r_{w0}\{1 + (z' - z_0') \tan(\Theta/2)\} \end{aligned}\right\} \tag{15}$$

where $z_0' = Z_0/r_{w0}$ (= 1.0), that is, at the entrance position of the divergent chamber. If we suppose that angular momentum remains constant throughout changes in the cross-sectional area of the chamber, the decay in divergent chambers may be given as:

$$\left.\begin{aligned} 0 \leqq z' \leqq z_0' &: v_w' = v_{ws}' \\ z' > z_0' &: v_w' = v_{ws}' r_{w0}/r_w \\ &\qquad = v_{ws}'/\{1 + (z' - 1) \tan(\Theta/2)\} \end{aligned}\right\} \tag{16}$$

Substituting equation (14), and the values of Θ corresponding to the divergent chambers tested, into equation (16), v_w' can be calculated. Results are indicated in Fig. 6 with solid lines: **a** for taper 3/100, **b** for 9/100, and **c** for 15/100. Although in part the experimental results in the shorter chambers, D1 and D2, are greater than what has been calculated from equation (16), the equation generally expresses the tendency of the decay. It is apparent from the data that the loss of angular momentum due to the enlargement of the area is quite small in the vicinity of the chamber wall.

Swirl Intensity. The swirl intensity of the swirling flow at a given cross section in the chamber is expressed as the ratio of angular momentum to axial momentum. Since the swirling flow in the vortex chamber has a relatively large quantity of back flow, it may be reasonable to distinguish between annular and back flow. The swirl intensity of the annular flow (S_a) may be calculated according to the following equation:

$$S_a = \int_{ri}^{r_w} \rho w v r^2 dr \bigg/ \left[\{(r_i + r_w)/2\} \int_{ri}^{r_w} \rho w^2 r dr\right] \tag{17}$$

Equation (17) is integrated numerically, taking into account the region of retarded velocity adjacent to the wall. The same procedure is followed in calculations in the following sections.

Figure 7 shows the representative values of S_a obtained by substituting the measured values in each vortex chamber into equation (17). S_a increases rapidly for $z' < 4$. This is caused by the deflection of the gravitational center of the annular flow to the axis of the chamber near the nozzle opening, as shown in Fig. 5. This deflection is brought about by the inward radial velocity of the jet at the nozzle opening. The increase of the axial velocities at $z' = 0.5$ proportionate to the increase of the divergent angle makes the magnitude of S_a small. In straight chambers, each velocity component decreases for $z' > 4$, but it is a decreasing rate of angular momentum, larger than that of axial momentum, that causes the decays in S_a. In divergent chambers, on the other hand, an increase in the cross-sectional area of the annular flow causes a rapid decay of axial momentum, which in turn brings about the increase in S_a observed from the results in chambers T1 and T2, which have a slightly larger divergent angle. In chambers D2, D4, and T6, which have a relatively small angle of divergence, however, since the increasing ratio of the annular flow area is low, we find a tendency similar to that for straight chambers, due to the lower rate of increase in the flow area.

Stagnation Temperature Profiles. Figure 8 shows the representative stagnation temperature profiles in several cross sections in chambers D2, S2, and T2. The ordinate is $t_t' = (T_t - T_{tw})/(U^2/2C_p)$, where T_{tw} is the stagnation temperature near the wall corresponding

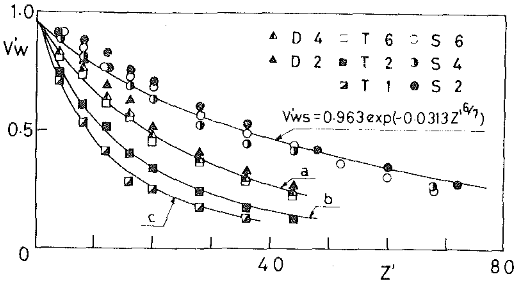

Fig. 6 Decay of tangential velocity

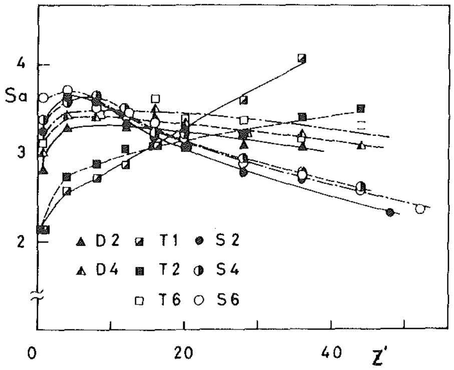

Fig. 7 Swirl intensity

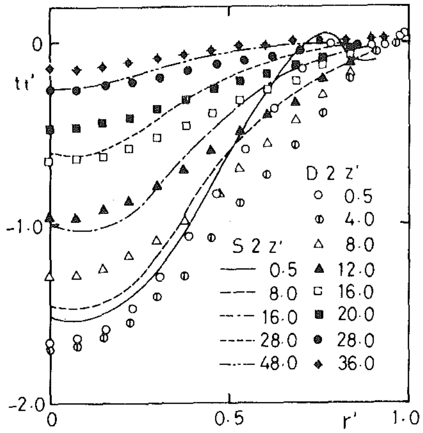

Fig. 8(*a*) S2, D2

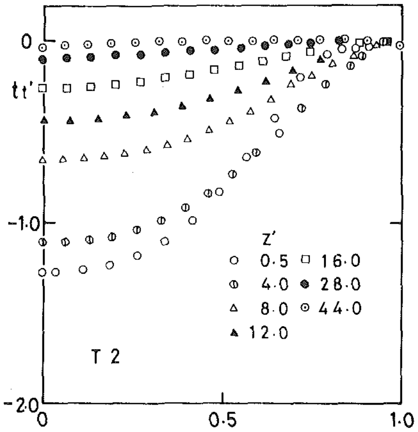

Fig. 8(*b*) T2

Fig. 8 Stagnation temperature profiles

to the cross-sections measured. The stagnation temperature decreases toward the center of the swirling flow at each cross section, and in any vortex chamber the value of $|dt_t'/dr'|$ decreases axially. The radial gradient of t_t' is large in the back flow region—except near the axis—and small in the annular flow region of straight chambers. With divergent chambers, the radial gradient is steep near the border between the back flow and annular flow regions. The radial stagnation temperature distributions have similar profiles at all the measured cross-sections, except the section nearest to the nozzle opening ($z' = 0.5$). The radial gradient decays toward the hot end more rapidly in divergent chambers than it does in straight ones. Therefore, the energy separation processes are completed in a shorter axial distance in divergent chambers than in straight ones.

In straight chambers, the amount of stagnation temperature drop in the center of the chamber, at the cross section nearest to the nozzle ($z' = 0.5$), increases with an increase in chamber length. In divergent chambers with the same divergent angle, the drop is greatest in D2, and decreases gradually from D1 to D4 to T6. Chamber length also has a slight influence on the distribution profiles of t_t'.

Distribution profiles of the stagnation temperature correspond to those of the tangential velocity. This means that the decrease in the radial gradient of the stagnation temperature and its corresponding axial decay become greater with an increase in the divergent angle. Moreover, the stagnation temperatures in the central portions of divergent chambers tend to have nearly the same value.

Back Flow Amount. Figure 9 shows the axial distributions of the amount of back flow (G_c) calculated as:

$$G_c = \int_0^{r_i} 2\pi|w|\rho r dr \tag{18}$$

Ideally, in order to improve energy-separation performance, all injected air should flow down toward the hot end after leaving the nozzle and $(G_c)_{z'=0} = G_{co}(G_c/G_{co} = 1)$ at the nozzle opening ($z' = 0$). Thus it is apparent that $(G_c)_{z'=0} < G_{co}$ both in D1, D2, D4, and T6, all of which have small divergent angle, and in all straight chambers. As a result, the lack of cold air flow is compensated for by a part of the injected air that flows out directly through the cold end orifice, without contributing to the energy-separation process. The part of the injected air that exits immediately upon entering the chamber has a high stagnation temperature and causes a rise in the back flow temperature. Divergent chambers have a great deal of back flow at each axial position, so that only a small portion of the flow from the nozzle exits immediately. Since the amount of back flow increases with an increase in the angle of divergence, divergent chambers have an advantage over straight chambers. In the shortest chambers, D1 and S1, chamber length was seen to exert a strong influence on G_c, while it had only a slight influence for $L \geqq 38D_0$ in both divergent and straight chambers.

Distributions of Kinetic Energy and Stagnation Enthalpy. The mean kinetic energies and the stagnation enthalpies of the annular and back flow per unit weight at each cross section measured represented respectively by ϕ_{ma}, ϕ_{mc}, and h_{tma}, h_{tmc}, can be calculated, assuming an axially symmetrical flow, as follows:

$$\left.\begin{aligned} \phi_{ma} &= \int_{r_i}^{r_w} 2\pi\rho w(V^2/2)rdr/G_a \\ \phi_{mc} &= \int_0^{r_i} 2\pi\rho|w|(V^2/2)rdr/G_c \end{aligned}\right\} \tag{19}$$

$$\left.\begin{aligned} h_{tma} &= \int_{r_i}^{r_w} 2\pi\rho w C_p T_t rdr/G_a \\ h_{tmc} &= \int_0^{r_i} 2\pi\rho|w|C_p T_t rdr/G_c \end{aligned}\right\} \tag{20}$$

where

$$G_a = \int_{r_i}^{r_w} 2\pi\rho w r dr \tag{21}$$

These values were nondimensionalized using the mean static enthalpy of the annular flow at the nozzle opening, h_{n2}, and the reference velocity, U, as:

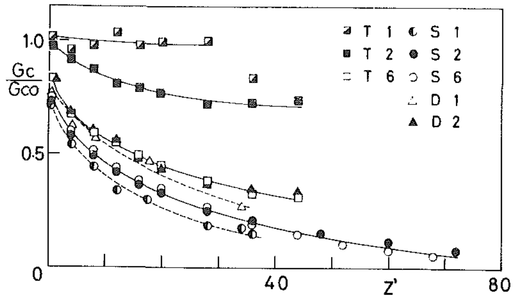

Fig. 9 Back flow amount

$$\phi_{ma}' = \phi_{ma}/(U^2/2),\ \phi_{mc}' = \phi_{mc}/(U^2/2) \tag{22}$$

$$\left.\begin{aligned} h_{tma}' &= (h_{tma} - h_{n2})/(U^2/2) \\ h_{tmc}' &= (h_{tmc} - h_{n2})/(U^2/2) \end{aligned}\right\} \tag{23}$$

where $h_{n2} = h_{tn1} - (U^2/2)$. These values were calculated by using the measurement results of ρ, V, w, and T_t at each measured cross section, and are shown in Figs. 10 and 11.

In Fig. 10, the kinetic energy of the annular flow (ϕ_{ma}') decays because of the wall friction and the exchange of momentum with the back flow. In divergent chambers, in that kinetic energy is converted into pressure due to an increase in the cross-sectional area, the decay tends to be rapid in chambers having a large divergent angle. On the other hand, the kinetic energy of the back flow (ϕ_{mc}') increases in the direction of flow. While the axial velocity of the back flow is higher in divergent chamber than in straight chambers, the difference in the increase in tangential velocity is not so great. Therefore, the value of ϕ_{mc}' are smaller in divergent chambers than in straight ones, and this tendency becomes marked with an increase in the angle of divergence.

Although the annular flow initially has a low temperature because of adiabatic expansion in the nozzles, an axial increase in its static enthalpy is brought about by the heat that is generated through the wall friction, and by the heat exchange with the back flow that occurs through turbulent mixing at the border between the back and annular flows. The increase in static enthalpy exceeds the decrease in kinetic energy, with the result that stagnation enthalpy increases axially. In the back flow, on the other hand, since the decrease in static enthalpy exceeds the increase in kinetic energy, stagnation enthalpy (h_{tmc}') decreases in the direction of the flow.

The stagnation enthalpy of the annular flow (h_{tma}') increases rapidly in the interval of $0 < z' < 20$. The energy separation process tends to be accomplished in a shorter distance in a chamber with a larger divergent angle.

The stagnation enthalpy of the back flow (h_{tmc}'), like that of the annular flow, decreases rapidly near the nozzle opening in the direction of the flow. In both divergent and straight chambers, the rate of change in h_{tmc}' is greatest in the longer chambers and in those with a larger angle of divergence.

Conclusions

The results of the experiments explained above lead to the following major conclusions:

1 In order to obtain a high energy-separation performance in straight chambers, it is necessary that $L \geqq 100D_0$ (L = the chamber length, D_0 = the inner diameter of the chamber): the shorter the chamber length, the lower the performance. The efficiency of energy-separation in divergent chambers was higher than that in straight chambers of the same length.

2 In divergent chambers, when the taper of divergence equals 3/100, chamber length made only a very slight difference in efficiency where $L \geqq 38D_0$. Moreover, the divergent chamber where $L = 38D_0$ showed a higher performance than the straight chamber heretofore considered to be the optimum shape, in comparison with the optimum straight chamber, maximum performance improvement reached 10 percent. The divergent chamber with a taper 9/100 and a length of

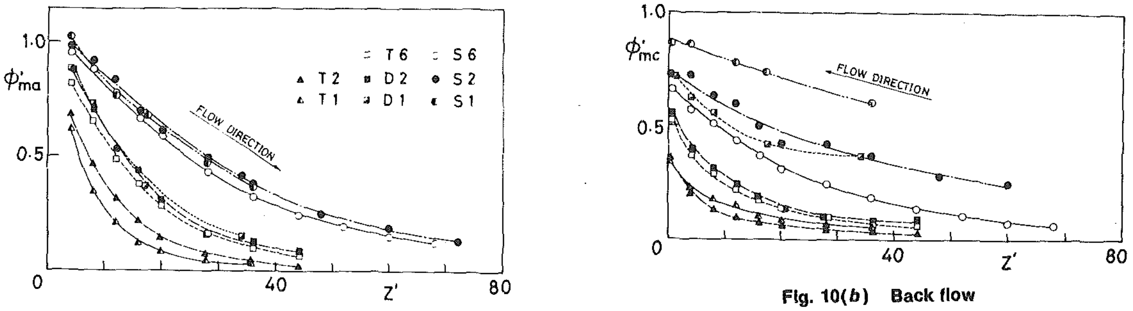

Fig. 10(*a*) **Annular flow**

Fig. 10(*b*) **Back flow**

Fig. 10 **Kinetic energy distributions**

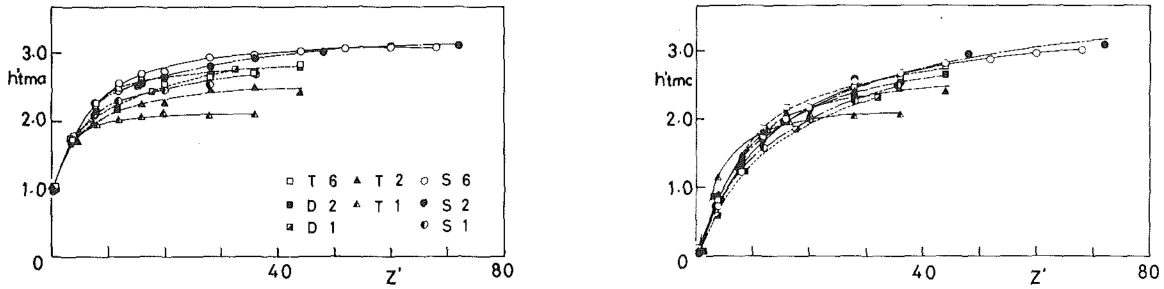

Fig. 11(*a*) **Annular flow**

Fig. 11(*b*) **Back flow**

Fig. 11 **Distributions of stagnation enthalpy**

$38D_0$ showed nearly the same performance as the chamber with a taper of 3/100 and a length of $38D_0$. Hence, in the case of divergent chambers, a shortening of the vortex chamber is possible.

3 In straight chambers, the length of the chamber showed a pronounced influence on velocity profiles, especially on the tangential velocity profile: the shorter the chamber length, the higher the angular velocity near the center of the back flow. The same tendency was observed in shorter divergent chambers (with tapers of 3/100 and 15/100, and a length of approximately $20D_0$), but was not noticeable in the longer chambers (with a taper of 3/100 and a length equal to or greater than $38D_0$). In contrast, to straight chambers, the region of the forced vortex tends to widen in divergent chambers.

4 The intensity of the swirl decreases in the direction of the flow in straight chambers, but increases in divergent chambers with relatively large divergent angles.

5 The rates of change in both the velocity components and the stagnation temperature in the direction of the flow are large in the divergent chambers, so that the process of energy-separation progresses rapidly: the greater the length and the larger the taper, the more marked this tendency.

6 At the cross section nearest to the nozzle opening, the magnitudes of the stagnation temperature drop t_t' and the stagnation enthalpy h_{tmc}' differed little between divergent and straight chambers, but the work of compression required to inject the same amount of air was smaller in the case of divergent chambers.

7 At each axial position, the amount of back flow was greater in divergent chambers than in straight ones and the rise in the stagnation temperature at the cold end resulting from the part of jet, that exits from the nozzle immediately upon entering the chamber, was less. For these reasons, and those stated in the preceding paragraph, the energy-separation efficiency η improves in divergent chambers.

Acknowledgment

The authors wish to express their thanks to Mr. T. Ohara, a former graduate student of Nagoya University, for help in measurements made during these experiments.

References

1 Soni, Y., and Thomson, W. J., "Optimal Design of the Ranque-Hilsch Vortex Tube," ASME JOURNAL OF HEAT TRANSFER, Vol. 97, No. 2, May 1975, pp. 316–317.

2 Collins, R. L., and Lovelace, R. B., "Experimental Study of Two-Phase Propane Expanded through the Ranque-Hilsch Tube," ASME JOURNAL OF HEAT TRANSFER, Vol. 101, No. 2, May 1979, pp. 300–305.

3 Marshall, J., "Effect of Operating Conditions, Physical Size and Fluid Characteristics on the Gas Separation Performance of a Linderstrom-Lang Vortex Tube," *International Journal of Heat Mass Transfer*, Vol. 20, No. 3, Mar. 1977, pp. 227–231.

4 Landecker, K., "A Two-Stage Refrigeration and Power Producing Arrangement Consisting of a "Vortex" Cooling Tube and a Thermoelectric Stage," *Energy Conversion*, Vol. 17, No. 2–3, 1977, pp. 119–122.

5 Williams, A., "Cooling of Methane with Vortex Tubes," *Journal of Mechanical Engineering Science*, Vol. 13, No. 6, Dec. 1971, pp. 369–375.

6 Aronson, R. B., "The Vortex Tube: Cooling with Compressed Air," *Machine Design*, Vol. 48, No. 28, Dec. 1976, pp. 140–143.

7 Takahama, H., et al., "Performance Characteristics of Energy Separation in a Steam-Operated Vortex Tube," *International Journal of Engineering Science*, Vol. 17, No. 6, 1979, pp. 735–744.

8 Fekete, L. A., "Vortex Tube is Intriguing Separator," *The Oil and Gas Journal*, Vol. 68, No. 24, June 1970, pp. 71–73.

9 Hilsch, R., "The Use of Expansion of Gases in a Centrifugal Field as a Cooling Process," *Review of Scientific Instruments*, Vol. 18, No. 2, 1947, pp. 108–113.

10 Takahama, H., and Kawashima, K., "An Experimental Study of Vortex Tubes," *Memoirs of the Faculty of Engineering, Nagoya University*, Vol. 12, No. 2, 1960, Nagoya University, pp. 227–245.

11 Parulekar, B. B., "The Short Vortex Tube," *Journal of Refrigeration*, Vol. 4, 1961, pp. 74–80.

12 Otten, E., "Producing Cold Air—Simplicity of the Vortex Tube Method," *Engineering*, Vol. 186, 1958, pp. 154–156.

13 Raiskii, Yu. D., and Tankel', L. E., "Influence of Vortex-Tube Configuration and Length on the Process of Energetic Gas Separation," *Journal of Engineering Physics*, Vol. 27, No. 6, Dec. 1974, pp. 1578–1581.

14 Metenin, V. I., "Investigation of Vortex Temperature Type Compressed Gas Separators," *Soviet Physics—Technical Physics*, Vol. 5, 1961, pp. 1025–1032.

15 Lay, J. E., "An Experimental and Analytical Study of Vortex-Flow Temperature Separation by Superposition of Spiral and Axial Flows Part 1," ASME JOURNAL OF HEAT TRANSFER, Vol. 81, No. 3, Aug. 1959, pp. 202–212.

16 Hartnett, J. P., and Eckert, E. R. G., "Experimental Study of the Velocity

and Temperature Distribution in a High-Velocity Vortex-Type Flow," *Trans. ASME*, Vol. 79, May 1957, pp. 751–758.

17 Scheper, G. W., "The Vortex Tube—Internal Flow Data and a Heat Transfer Theory," *Refrigerating Engineering*, Vol. 59, No. 10, 1951, pp. 985–989, 1018.

18 Bruun, H. H., "Experimental Investigation of the Energy Separation in Vortex Tubes," *Journal of Mechanical Engineering Science*, Vol. 11, No. 6, 1969, pp. 567–582.

19 Takahama, H., and Soga, N., "Studies on Vortex Tubes (2nd Report, Reynolds Number. The Effects of the Cold Air Rate and the Partial Admission of Nozzle on the Energy Separation)," *Bulletin of Japan Society of Mechanical Engineers*, Vol. 9, No. 33, 1966, pp. 121–130.

20 Takahama, H., "Studies on Vortex Tubes (3rd Report, Variations of Velocity, Temperature and Energy with Axial Distance, and Mechanism of Energy Separation)," *Transactions of the Japan Society of Mechanical Engineers*, Vol. 32, No. 235, 1966, pp. 503–510.

21 Murakami, M., and Heya, N., "Stress Calculation on Swirling Flow in Suction Pipe of a Centrifugal Pump," *Transactions of the Japan Society of Mechanical Engineers*, Vol. 31, No. 228, 1965, pp. 1222–1229.

Mass Transfer from a Rotating Inclined Plate

Hitoshi Koyama
Professor,
Department of Mechanical Engineering,
Faculty of Engineering,
Shizuoka University,
Hamamatsu, Japan

Sei-ichi Ohsawa
Research Scientist,
Tokyo Sanyo Electric Corporation,
Oh-Izumi, Gunma, Japan

Akira Nakayama
Research Assistant,
Department of Mechanical and
Industrial Engineering,
University of Illinois at Urbana-Champaign,
Urbana, Ill. 61801

An extensive experimental investigation using the Naphthalene Sublimation Technique, has been carried out to explore the mass transfer processes on inclined flat plates at rotation. It has been found that the flows responsible for the transfer processes can be classified into three types, namely, flow without a separated region, flow with a separated region located near the leading edge, and flow with a separated region all over the surface. A wind tunnel experiment on stationary flat plates has been also performed so as to isolate the effects of incidence angle from the rotational effects. A tremendous increase in transfer rate has been observed for the surface of the rotational system exposed to a wake flow.

1 Introduction

The exploration of heat transfer processes associated with the boundary layers developed on rotating systems, has been a hard task for many years, yet a task of critical importance for the thermal design of various types of fluid-mechanical devices and systems. In such systems, the boundary layers usually exhibit complex three-dimensional natures due to the secondary flows induced by Coriolis and centrifugal forces. It also has been realized that these rotational effects play a significantly important role in the heat transfer processes in the view of the enhancement of the heat transfer coefficient.

On bodies of revolution such as spheres, cones, and cylinders, many experimental as well as analytical works are available at the present time. However, the experimental data on rotating systems, in general and especially on rotating blades in the presence of angle of attack, are so scarce that considerably more experimental investigations should be required so as to fully understand the complex phenomena, namely, flow separation and reattachment, laminar-turbulent transition, and local heat transfer from the blades, all of which are influenced by the presence of angle of attack as well as the three-dimensional effects due to the rotation.

McCroskey [1] observed laminar flow separation as well as the laminar-turbulent transition on helicopter blades, and has obtained the streamlines traced on the blade surfaces. Through experimental investigation, he concluded that the presence of the centrifugal force has rather minor effects on the development of the boundary layers. Theoretical studies on the flow field over rotating blades have been made at a zero angle of attack [2–4] and some of them have been extended to the heat transfer problems [5, 6]. Heat transfer measurements on rotating blades at zero incidence have been successfully carried out by Eisele, et al. [6]. They have reported that the body forces due to rotation can work favorably over the heat transfer processes when relatively short blades are used.

Measurements of heat transfer may lead to uncertainties as to the data since they involve extraneous heat losses, either by conduction through supports and instrumentation, or by radiation. The situation could be extremely aggravated when one has to deal with a rotating system because of the difficulties in providing the interface between the rotating system and measuring devices. In response to these difficulties and uncertainties, the sublimation mass transfer system has been used in place of heat transfer system to solve a number of complex heat transfer problems.

The present paper reports the experimental investigations on the rotating inclined flat plates by means of the naphthalene sublimation technique, carried out at Shizuoka University, Japan. The experiments have been performed at various angular velocities with changing angle of attack. The measurements on stationary flat plates have also been carried out to isolate the effects of incidence angle from those of body forces resulted from rotation.

2 Experimental Procedure

2.1 Experimental Apparatus and Procedure Figure 1(*a*) shows a cross section of the plate which is made of 6.5 mm thick brass. Naphthalene is coated smoothly over the upper surface of the plate. Leading and trailing edges are shaped into 45 deg half wedge (Flow development may be significantly altered by a different choice of edge angle). Chord lengths of plates used for the present study are $C = 30$, 50 and 70 mm. The schematic diagram of the rotating system is shown in Fig. 1(*b*) along with the coordinate system employed in the study. A pair of flat plates are mounted on a 100 mm dia hub in such a manner that naphthalene surface of one plate meets the plane normal to the axis of rotation at an angle of α, while that of the other plate meets the plane at an angle of $-\alpha$. Throughout the study, the surface at positive incidence angle associated with a favorable pressure gradient is to be called the "front" surface, and that at negative angle, the "back" surface. The tips of the plates are kept at 250 mm radius. The shaft is rotated by an electric motor with a speed range from 60 to 1200 rpm. No wake interactions have been observed from the rotating system with four blades by Eisel, et al. [6]. For the present system with two blades, the interactions among the rotating blades are expected to be completely eliminated.

All the test runs have been carried out in a sufficiently large room (100 m^3) where the temperature can be controlled anywhere from 28

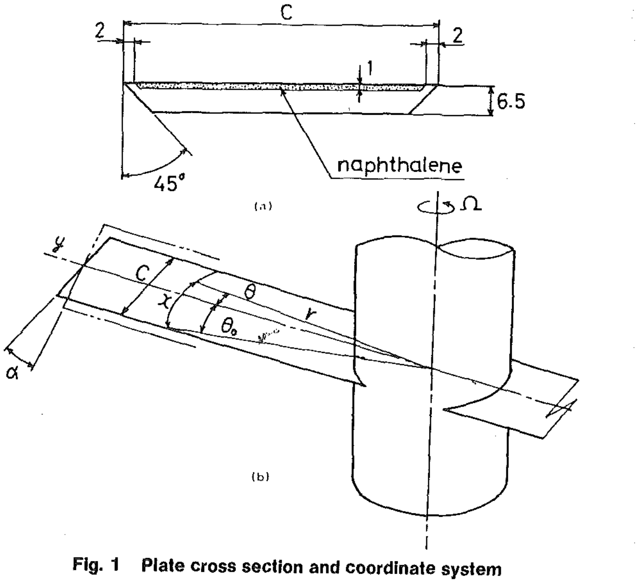

Fig. 1 Plate cross section and coordinate system

Contributed by the Heat Transfer Division for publication in the JOURNAL OF HEAT TRANSFER. Manuscript received by the Heat Transfer Division April 14, 1980.

Table 1 Experimental conditions in rotating system

C m	n rpm	$\alpha°$
0.07	60, 100, 200, 400, 800	0, ±2.5, ±5, ±10 ±20, ±45, ±90
0.05	60, 100, 200, 400, 800, 1200	
0.03	60, 100, 200, 400, 800	

Table 2 Experimental conditions in uniform air stream

C m	U_∞ m/s	$\alpha°$
0.07	1.5 7.9	0, ±2.5, ±5, ±10, ±20, ±45, ±90

to 30°C. Continuously measuring the room temperature with thermocouples, the temperature variation during each test run, has been strictly kept within 0.5°C.

Before and after the run, naphthalene surface level is measured to an accuracy of 1 μm by use of an electric micro-meter at the measuring points spaced either 2 or 4 mm apart in the chord-wise direction, and either 10 or 20 mm apart in the span-wise direction. The duration of the test run is chosen such that the sublimation takes place resulting the height loss of at least 0.05 mm and at most 0.25 mm over the naphthalene surface. Possible naphthalene sublimation occurred during the surface measurement can be estimated less than 1.5 μm, and, therefore, is to be neglected through the data reduction described below. The operating condition for the experiments done in the sealed laboratory is summarized in Table 1 while Table 2 lists the operating condition for the wind-tunnel experiments done separately on stationary flat plates.

2.2 Data Reduction Procedure. The rate of mass transfer m from surface area A, can be written in terms of either mass transfer coefficient K_c or the measured rate of height loss on naphthalene surface d as follows.

$$m = K_c \cdot A(C_{vs} - C_{v\infty}) = \gamma \cdot d \cdot A \qquad (1)$$

where γ is density of coated naphthalene, and C_v is the concentration of naphthalene vapor while subscripts s and ∞ stand for naphthalene surface and ambient.

Since the partial pressure of naphthalene vapor P_{vs} is very small compared with the atmospheric pressure P_∞, and the vapor covering the naphthalene surface is to be saturated at the surface temperature T_s, the naphthalene vapor concentration, C_{vs} can be approximated well by the Perfect Gas law, namely,

$$C_{vs} = P_{vs}/(R_v \cdot T_s) \qquad (2)$$

where R_v is naphthalene vapor gas constant. Dropping $C_{v\infty}$ due to the fact that the accumulation of naphthalene vapor is negligibly small provided the room is sufficiently large, the equation (1) can be reduced to give the following equation for the data reduction,

$$K_c = m/(A \cdot C_{vs}) = (\gamma \cdot d \cdot R_v \cdot T_s)/P_{vs} \qquad (3)$$

where the naphthalene vapor pressure is calculated using the following $P_{vs} - T_s$ correlation [7],

$$\log_{10} P_{vs} = 13.9046 - 3812.34/T_s - 0.02593 \log_{10} T_s \; (P_a, \mathrm{K}) \qquad (4)$$

In order to account for the temperature drop associated with naphthalene sublimation [7], the surface temperature T_s under the vapor pressure 1 atm, is reduced by,

$$T_s = T_\infty - 0.1(\mathrm{K}) \qquad (5)^1$$

The diffusivity of naphthalene vapor to be used for Sherwood number reduction is calculated by,

$$D_v = 0.520\,(T_\infty/273.15)^2/P_\infty \; (m^2/s, \mathrm{K}, P_a) \qquad (6)$$

For the presentation of experimental results below, the arc length $x = r(\theta + \theta_0)$ where $\theta_0 = \sin^{-1}(C/2r)$ (See Fig. 1(b)), is replaced by the straight distance from the leading edge in the chord-wise direction since they can be used inter-changeably provided the radius r is not small. In fact, the maximum error due to this practice, can be found to be less than 5 percent, therefore, the experimental results presented here may well be compared with existing predictions which are usually based on the cylindrical coordinate system. Moreover, it is noted that, for the convenience of graphical presentations, the negative x is assigned for back surface results (i.e., negative incidence angle data) in some of the figures.

3 Experimental Results

3.1 Mass Transfer from Stationary Plates. The preliminary investigation of laminar flow over the stationary inclined flat plate by a flow visualization technique using aluminum particles in water stream, has revealed that the flows over the plate can be classified into three types, namely,

Type I	flow without a separated region (See Fig. 2(b))
Type II	flow with a separated region located near the leading edge (See Fig. 2(a))
Type III	flow with a separated region all over the surface (See Fig. 2(c))

One may expect that flows of type I, even in the presence of angle of attack, may exhibit behavior similar to the laminar flow over a parallel flat plate, namely, the transfer coefficient K_c approaches infinity at the leading edge, then decreases downstream at the rate of $x^{-1/2}$ (wedge flow solution, $K_c \propto x^{(m-1)/2}$ where m is angle parameter shown as $m = \beta/(2 - \beta)$ and β is the full equivalent wedge angle measured as a fraction of the straight angle π, may describe flows of type I collectively, provided the singular point stays at the leading edge and the equivalent wedge angle is correctly estimated. Due to the presence of inert leading edge, the mass diffusion boundary layer does not develop exactly from the leading edge. However, the expression above may still be relevant if the inert portion is small since initial errors

Nomenclature

A = surface area
C = chord length
C_v = concentration of naphthalene vapor
d = rate of height loss on naphthalene surface
D_v = mass diffusion coefficient
K_c = mass transfer coefficient
m = rate of mass transfer from surface area
n, Ω = rotational speed
p = pressure
R_v = gas constant of naphthalene vapor
r = radius
T = absolute temperature
U = reference velocity
x = distance from the leading edge in the chord wise direction
y = coordinate normal to the chord line
α = incidence angle
γ = density of naphthalene coated on the surface
θ = angular coordinate measured from the plate center line
ν = kinematic viscosity
Nu = Nusselt number
Pr = Prandtl number
Sc = Schmidt number
Sh = Sherwood number
Re = Reynolds number = $U_\infty \cdot x/\nu$ or $r\Omega x/\nu$

Subscripts and Superscripts

ch = chord
cr = critical
∞ = ambient
s = naphthalene surface
v = naphthalene vapor
— = average

---

[1] One of referees has carefully checked equation (5) and pointed out that the correct temperature drop is 0.2 K. However, no corrections have been made in the present report since the error would be about one percent of the correlations.

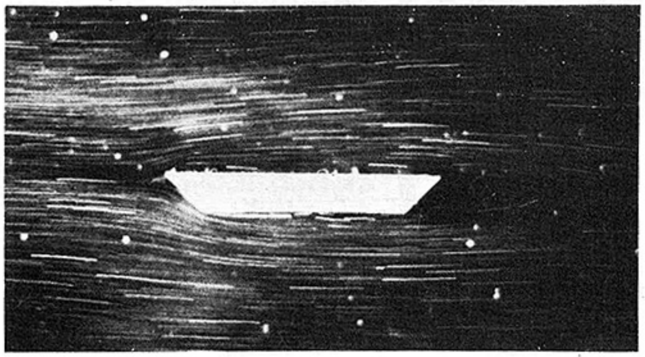

Fig. 2(*a*) $\alpha = 0$ deg

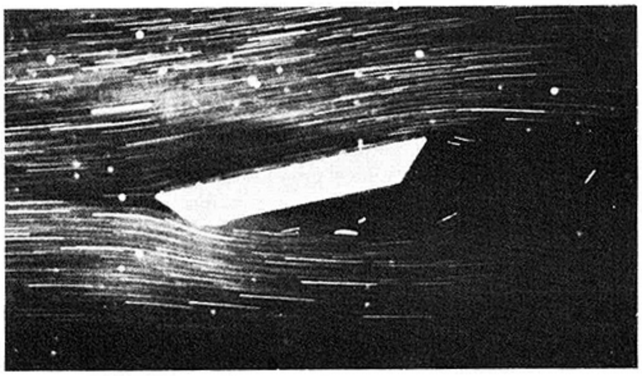

Fig. 2(*b*) $\alpha = +8$ deg

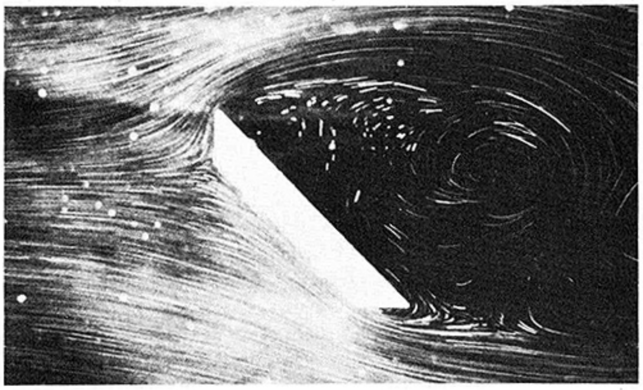

Fig. 2(*c*) $\alpha = -45$ deg

Fig. 2 Flow patterns on the stationary plate

will diminish at downstream due to the parabolic nature of boundary layer).

One of interesting features associated with flow type II is that the point of the maximum transfer rate is commonly observed near the reattachment point.

Flow of type III consist of wake flows having very low momentum, therefore one cannot expect much from convection processes over the surfaces exposed to these flows (The situation however becomes different for the case of rotating system.)

Mass transfer experiments have been carried out in the wind tunnel on the stationary plate to study the effects of incidence angle over the mass transfer rate without rotational effects.

Figure 3 shows local mass transfer coefficients obtained from the flat plate of chord length $C = 70$ mm, exposed to the free-stream velocity $U_\infty = 7.9$ m/s. The data of front surface at $\alpha = 0$ and 5 deg clearly show the behavior associated with flow Type II; i.e., flow with a separated region located near the leading edge, rather than flow type I. This rather surprising result may have been brought by the fact that the plates used in the present study are relatively thick (6.5 mm) and have a large leading edge angle (45 deg). The figure also shows that

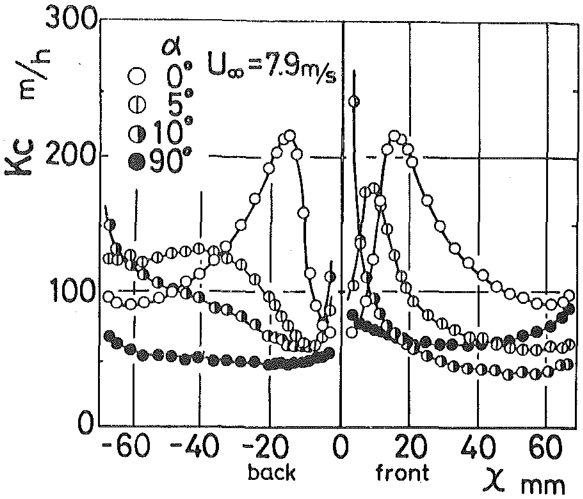

Fig. 3 Local mass transfer coefficient on the stationary plate in uniform air stream

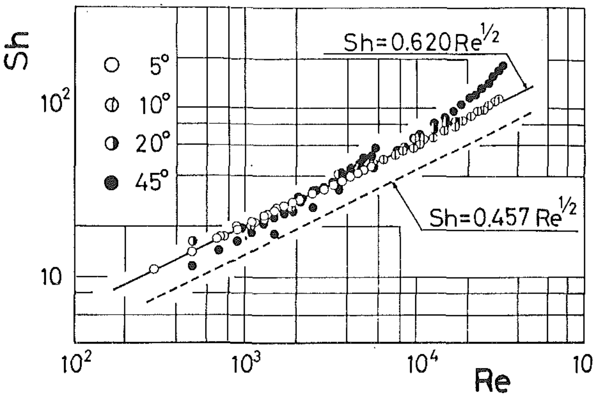

Fig. 4 Local Sherwood number on the stationary plate in uniform air stream

the flow changes from type II to type I as α reaches 10 deg. The experimental results obtained for $U_\infty = 1.5$ m/s, which are not given here, have revealed that, for this case, the flow at $\alpha = 5$ deg already falls into type I while the flow at $\alpha = 0$ deg still remains as type II. This may indicate that flow type II tends to dominate the wider range of incidence angle α as the free-stream velocity increases. Moreover, a comparison of the data for $\alpha = 0$, 5 and 10 deg in the figure, leads to the fact that the location of maximum K_c, hence, the reattachment point, moves closer to the leading edge with increasing α. On the other hand, all the back surface data, i.e., $\alpha < 0$ deg, show the trend of the leeward increase in transfer rate. This can be taken as a typical behavior associated with flow type III. The flow over the front surface at $\alpha = 90$ deg exhibits nearly constant mass transfer rate. This phenomenon is particular to the stagnation flow associated with the fact that the boundary layer thickness stays almost constant over the plate surface. All the data in Fig. 3 show abrupt increase in K_c near the trailing edge. This can be attributed to the vortex shedding from the trailing edge.

Experimental data are reduced into local Sherwood number, and are plotted in Fig. 4. Although the wedge flow solution indicates Sh $\propto x^{(m+1)/2}$, no appreciable change in slope can be observed except $\alpha = 45$ deg for which the wedge flow solution would give Sh $\propto x^{2/3}$ when the equivalent wedge angle, for the first approximation, is taken to be twice the incidence angle α. In fact, the following $\frac{1}{2}$ power correlation for a moderate α can be obtained through the least square fit using the data of flow type I at 5 deg $\lesssim \alpha \lesssim$ 20 deg,

$$\mathrm{Sh} = 0.620\ \mathrm{Re}^{1/2} \quad (\text{Type I; } 5\text{ deg} \lesssim \alpha \lesssim 20\text{ deg}) \tag{7}$$

where $\mathrm{Re} = U_\infty x/\nu$ is local Reynolds number and $\mathrm{Sh} = K_c \cdot x/D_v$ is local Sherwood number. Blasius' solution for a flat plate along with Colburn's analogy when Sc = 2.6 leads to,

$$\mathrm{Sh} = \tfrac{1}{2}\cdot C_f \cdot \mathrm{Re} \cdot S_c{}^{1/3} = 0.332\, S_c{}^{1/2} \cdot \mathrm{Re}^{1/2}$$
$$= 0.457\ \mathrm{Re}^{1/3}\ (\text{type I};\ \alpha = 0\ \text{deg}) \qquad (8)$$

where C_f is local friction coefficient. Experimental correlation (7) gives a transfer rate roughly 36 percent greater than equation (8). Although there is some possibility that the wind-tunnel turbulence may have enhanced the mass transfer rate to some extent, the authors feel that one should be aware of the fact that a direct application of friction analogy to mass transfer is likely to underestimate the transfer coefficient.

Mass transfer coefficient averaged over the chord, $\overline{K_{cch}}$ is plotted in Fig. 5 to see the effects of indicence angle and free stream velocity. The flow at $\alpha = 0$ deg yields the highest value of $\overline{K_{cch}}$, and the minimum point of $\overline{K_{cch}}$ occurs at $\alpha = 10$ deg for $U_\infty = 7.9$ m/s, i.e., $\overline{\mathrm{Re}}_{ch} = 3.45 \times 10^4$ when the reattachment point reaches toward the leading edge. For the case of $U_\infty = 7.9$ m/s, the maximum value at $\alpha = 0$ deg is just about twice as large as the minimum value at $\alpha = 10$ deg. As α goes further beyond 20 deg, the mass transfer rate on front surface tends to increase, which is similar to what may be observed for wedge flows. On the back surface, on the otherhand, $\overline{K_{cch}}$ becomes insensitive to α when $|\alpha| > 20$ deg.

3.2 Local Mass Transfer from Rotating Plates. Figures 6(*a*, *b*) and (*c*) show the contour maps of equal mass transfer rate on the plates at $\alpha = 0$ deg, rotated at the same speed $n = 60$ rpm with different chord lengths, 70, 50 and 30 mm, respectively. If the tail-up behavior due to vortex shedding and tip effects are ignored, map patterns of plates with chord lengths $C = 50$ and 30 mm shown in Figs. 6(*b*) and (*c*) can be found to be almost identical reproductions of the corresponding portions of the map pattern of $C = 70$ mm shown in Fig. 6(*a*).

The effects of incidence angle over the contour maps are shown in Fig. 7 for the case of chord length $C = 70$ mm and rotational speed $n = 800$ rpm. Figures 7(*a*, *b*) and (*c*) again show that the ridge of the maximum transfer rate moves closer to the leading edge as the incidence angle α increases, and the flow eventually exhibits flow type I all over the surface when α reaches to 20 deg as seen in Fig. 7(*c*). Knowing that the half power correlation, equation (7), is valid for the stationary plates, a rough estimation for the rotating system can be made simply by replacing the free-stream velocity U_∞ with the peripheral velocity $r\Omega$, which leads to the relation for the contour lines, namely $r \propto x$. The contour lines shown in Fig. 7(*c*) are seen to exhibit this behavior. Both Figs. 7(*a*) and (*b*) indicate that the flow falls into flow type I where the peripheral velocity is small and changes into type II near the tip where the peripheral velocity becomes large. The fact that the increase in the incidence angle as well as the decrease in the velocity outside of boundary layer work to change the flow from type II to type I is consistent with what has been observed from the wind-tunnel experiment on the stationary plates already discussed in the preceding section. Contour maps on the back surface are shown in Figs. 7(*d*) and (*e*). A typical map pattern of flow type III may be observed in Fig. 7(*e*). The magnitude of transfer rate, however, has been found to be considerably greater than that observed for the stationary case. The similarlity between the map pattern of Fig. 7(*d*) for $\alpha = -10$ deg and that of Fig. 7(*a*) for $\alpha = 0$ deg may be surprising since it indicates that the flow at a negative incidence angle can fall into flow type II (separation followed by reattachment) rather than type III (wake flow). The situation above is quite possible if the incidence angle is not far from zero. The phenomenon can only be explained by considering the three-dimensional effects due to the rotation since it is unlikely to happen for stationary flat plates.[2] One of the major effects of rotation is to induce the secondary flow which works as boundary layer suction, hence maintaining relatively thin boundary layer. Another effect is to decrease the absolute value of the "effective angle of attack." The authors believe that the interaction of these rotational effects is responsible for what is observed in Fig. 7(*d*).

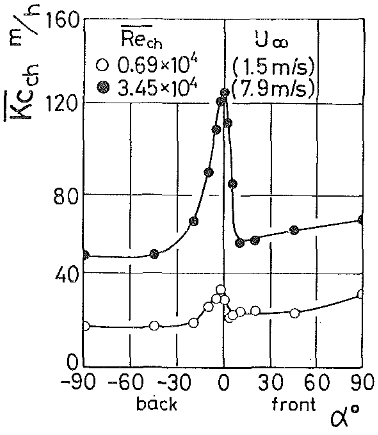

Fig. 5 Average mass transfer coefficient on the stationary plate in uniform air stream

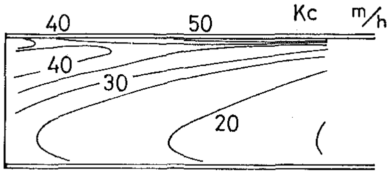

Fig. 6(*a*) $\alpha = 0$ deg, $C = 0.07$m

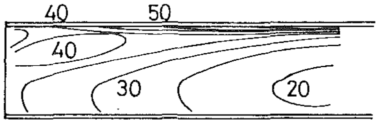

Fig. 6(*b*) $\alpha = 0$ deg, $C = 0.05$m

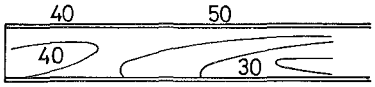

Fig. 6(*c*) $\alpha = 0$ deg, $C = 0.03$m, $n = 60$ rpm

Fig. 6 Contour maps of mass transfer coefficient on rotating plates of various chord lengths

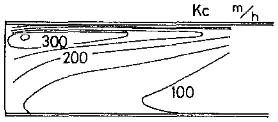

Fig. 7(*a*) $\alpha = 0$ deg

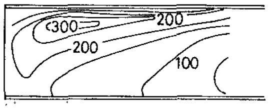

Fig. 7(*d*) $\alpha = -10$ deg,

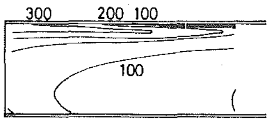

Fig. 7(*b*) $\alpha = +10$ deg

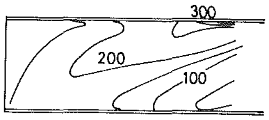

Fig. 7(*e*) $\alpha = -45$ deg
$C = 0.07$m, $n = 800$ rpm

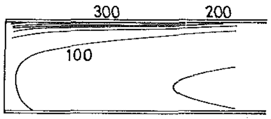

Fig. 7(*c*) $\alpha = +20$ deg

Fig. 7 Contour maps of mass transfer coefficient on rotating plates at various incidence angles

---

[2] One of referees pointed out that the phenomenon is not inherent in rotating systems and it can happen even on the stationary flat plates without chamfer.

Experimental data obtained from rotating flat plates are plotted in Fig. 8 in terms of local Sherwood number and local Reynolds number based on peripheral velocity $r\Omega$. The figure shows that the data from rotating plates fall right on correlation (7) which was originally obtained for the stationary plates. In fact, correlation (7) has been found valid for front surfaces of rotating plates at moderate incidence angle 5 deg $\lesssim \alpha \lesssim$ 20 deg within an error of 20 percent. Eisele, et al. reported an interesting analysis for flow type I at zero incidence using an integral method. After transforming two momentum equations into two "ordinary" differential equations for momentum thickness and shear stress ratio through the magnitude analysis, they obtained the following closed form expression for local Nusselt number with the aid of Reynolds' analogy.

$$\mathrm{Nu} = 0.3233 \cdot \mathrm{Re}^{1/2} \cdot \mathrm{Pr}^{1/3}\{1 + [1.453(\theta + \theta_0)]^2\}^{1/2} \quad \text{(type I; } \alpha = 0 \text{ deg)} \quad (9)$$

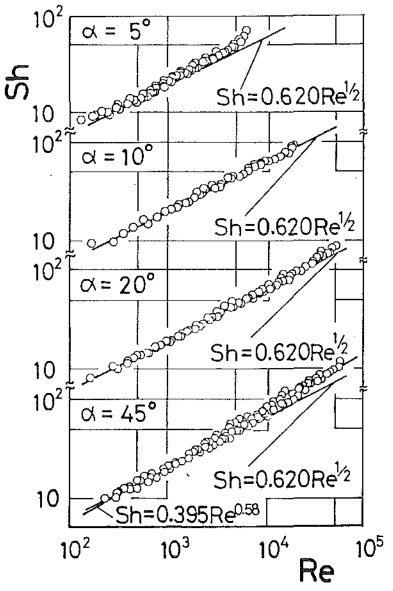

Fig. 8 Local Sherwood number on rotating plates

The equation indicates that the transfer rate from the rotating plate is to be greater than that from the stationary plate exposed to the freestream velocity equal to the peripheral velocity by the factor of $\{1 + [1.453(\theta + \theta_0)]^2\}^{1/2}$. For example, at the point located midway along the chord of 70 mm at r = 85 mm, the equation gives a 15 percent increase in transfer rate. No such effect due to rotation is observed in Fig. 8. Stagnation flow data, i.e., α = 90 deg, are not shown in the figure since it is obvious that the appropriate length scale for Re is no longer x. A semi-empirical correlation for the heat transfer from the back surface of stationary flat plate at α = −90 deg, has been reported by Igarashi [8]. An attempt to relate the present data to the correlation by Igarashi has failed because of tremendous increase in transfer rate observed on the back surface due to rotational effects. Almost all of the theoretical predictions available for rotating blades at the present, are based on integral techniques. It should, however, be emphasized here that the problem is fully elliptic three-dimensional flow associated with leading edge separation, reattachment, redevelopment, and vortex shedding. The presence of vortex shedding makes the problem even more formidable, time-dependent. Realistic predictions can only be made by means of numerical simulations solving unsteady fully elliptic three-dimensional Navier-Stokes equation. The last comment on Fig. 8 should be made for the case of α = 45 deg. The least square fit gives the correlation below which is valid within the error of 20 percent.

$$\mathrm{Sh} = 0.395\ \mathrm{Re}^{0.58} \quad \text{(type I; } \alpha = 45 \text{ deg)} \qquad (10)$$

The increase in slope is again observed here for a large incidence angle, the value of exponent is however much lower than the corresponding wedge flow solution, namely $\frac{2}{3}$.

In order to compare the rotating system with the stationary system, the data which correspond to the Reynolds number based on the chord length C and the peripheral velocity $r\Omega$, $\overline{\mathrm{Re}}_{ch}$ = 3.39 × 10^4 (n = 400 rpm, r = 185 mm) are plotted in Fig. 9 along with the data obtained from stationary plates at U_∞ = 7.9 m/s which gives roughly same value of Reynolds number based on free-stream velocity, $\overline{\mathrm{Re}}_{ch}$ = 3.45 × 10^4. Drastic increase in transfer rate due to rotation is observed from the back surface data. Moreover, Fig. 9(b) clearly shows that both front and back surfaces at α = ±10 deg are exposed to the flows of type II.

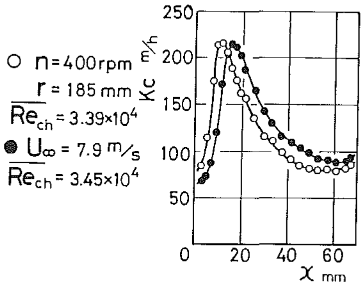

Fig. 9(*a*) α = 0 deg

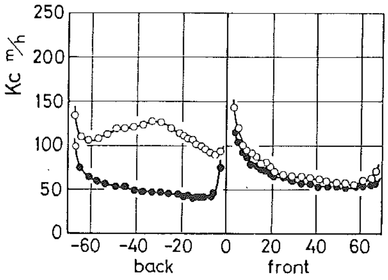

Fig. 9(*c*) α = 45 deg

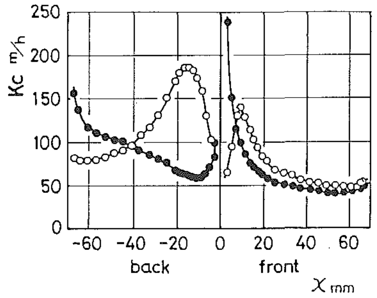

Fig. 9(*b*) α = 10 deg

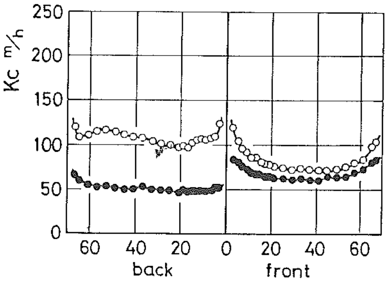

Fig. 9(*d*) α = 90 deg

Fig. 9 Comparison of mass transfer coefficient between stationary and rotational systems

Effects of incidence angle on the location of the maximum transfer rate is shown in Fig. 10 for r = 180 mm. No influences due to the change of chord length is observed. The figure also substantiates the fact that the increase in incidence angle leads the location of the maximum transfer rate closer to the leading edge.

3.3 ***Overall Mass Transfer from Rotating Plates.*** The integration of equation (9) gives average Nusselt number as function of the radius r as follows,

$$\overline{\mathrm{Nu}} = 0.6466\overline{\mathrm{Re}}_{ch}{}^{1/2}\cdot \mathrm{Pr}^{1/3}[1 + 0.1B^2 - 0.01388B^4 + \ldots\ldots] \qquad (\text{type I}; \alpha = 0) \qquad (11)$$

where $B = 2.906\,\theta_0$. When r = 85 mm and C = 70 mm, the equation gives roughly 11 percent increase in $\overline{\mathrm{Nu}}$ due to rotational effects. However, since no such increase has been found in local transfer rate, the overall transfer rate is to be correlated collectively in terms of Sherwood number averaged over the chord $\overline{\mathrm{Sh}}_{ch}$ and Reynolds number based on chord length $\overline{\mathrm{Re}}_{ch}$ for each angle of incidence. Figure 11(a) shows front surface flow at α = 0 deg, the data are well represented by the following correlation valid for flow type II (See also Fig. 7(a)).

$$\overline{\mathrm{Sh}}_{ch} = 0.237\,\overline{\mathrm{Re}}_{ch}{}^{0.71} \quad (\text{type II}) \qquad (12)$$

The correlation obtained by integration equation (7) valid for flow type I is also shown in the figure, that is,

$$\overline{\mathrm{Sh}}_{ch} = 1.240\,\overline{\mathrm{Re}}_{ch}{}^{1/2} \quad (\text{type I}) \qquad (13)$$

In Fig. 11(b), the data on the front surface at α = 20 deg except those obtained near the tip, fall well on equation (13), indicating that flow type I prevails over the entire surface (See also Fig. 9(c)). The front surface data at α = 45 deg, which are not shown here, have been found to be well represented by the integrated of equation (10), i.e. $\overline{\mathrm{Sh}}_{ch} = 0.681\,\overline{\mathrm{Re}}_{ch}{}^{0.58}$. A transition curve can be observed for the front surface at α = 5 deg as shown in Fig. 11(c). As the figure shows, the transition takes place around $10^4 < \overline{\mathrm{Re}}_{ch} < 4 \times 10^4$. For the case of α = 10 deg, which is not shown here, the critical Reynolds number can be taken as $\overline{\mathrm{Re}}_{chcr} \simeq 3 \times 10^4$, which implies that the flow changes from type I to type II at $n{\cdot}r \simeq 65$[rpm·m], for example, n = 800 rpm gives $r_{cr} \simeq$ 80 mm. This estimation can be also appreciated by observing directly the contour map in Fig. 7(b). Back surface flow at $\alpha = -90$ deg is also plotted in Fig. 11(d). The figure shows nearly constant transfer rate over the surface.

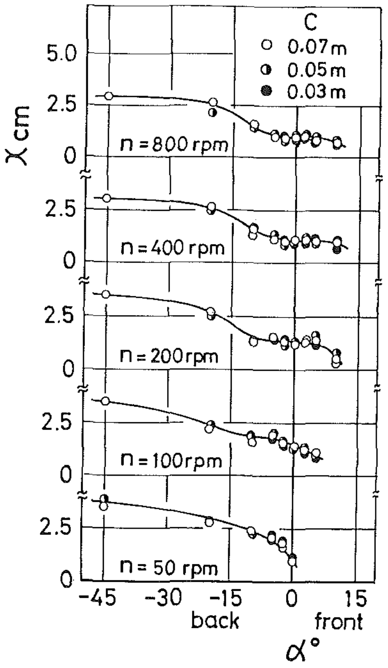

Fig. 10 Effects of incidence angle on the location of maximum transfer rate

Figure 12 shows the overall mass transfer rate from the surface of blade span 80 $\lesssim r \lesssim$ 250 mm as function of incidence angle. The effects of incidence angle on the front surface can be found essentially identical to what has been already observed for the case of the stationary plate shown in Fig. 5, namely, transfer rate initially diminishes as α increases from 0 deg bringing the reattachment point closer to the leading edge, consequently, the transfer rate reaches to the minimum point as the entire surface is covered by the flow of type I. Once this flow type I prevail over the surface, any additional increase in

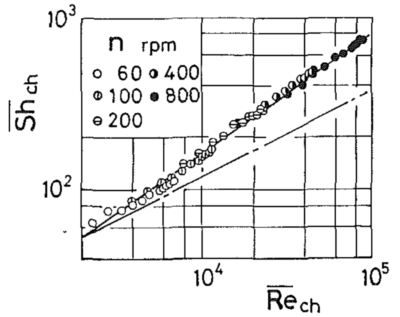

Fig. 11(*a*) α = 0 deg

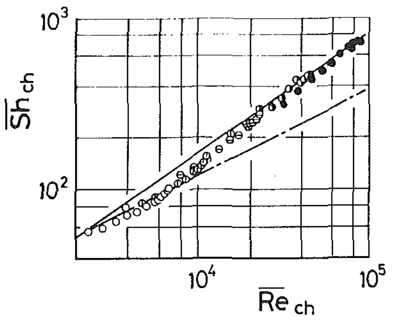

Fig. 11(*c*) α = +5 deg

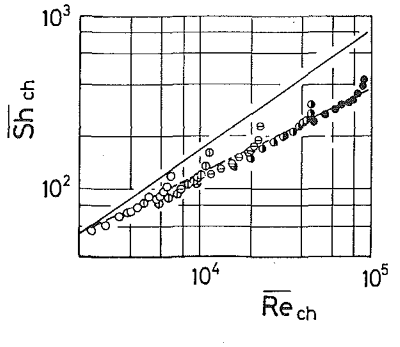

Fig. 11(*b*) α = +20 deg

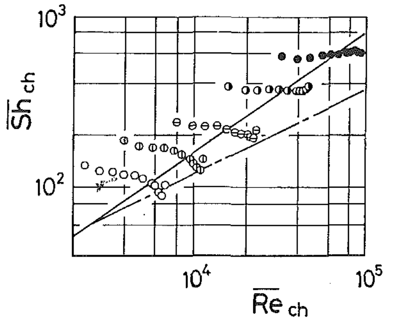

Fig. 11(*d*) α = −90 deg

Fig. 11 Sherwood number averaged over the chord

incidence angle works only to enhance the transfer rate. Transfer rate on the back surface of rotational system, however, exhibits the behavior quite different from that of stationary system. The strong amplification of transfer rate takes place on the back surface of rotational system, yielding the maximum peak around $\alpha \doteqdot -20$ deg. The rotational effects are solely responsible for this amplification on the back surface.

The data in Fig. 12 are replotted in Figs. 13, 14 and 15 in terms of overall Sherwood number and Reynolds number based on the peripheral velocity at the blade tip and the chord length. From Fig. 13, the following correlation can be obtained to represent the total mass transfer from a front surface at $\alpha = 20$ deg.

$$\mathrm{Sh} = 0.860\,\overline{\mathrm{Re}}^{1/2} \qquad (\text{type I}; \alpha = 20 \text{ deg}) \tag{14}$$

Equation (14) has been established using all the data over the blade span $80 \lesssim r \lesssim 250$ mm, including those possibly amplified by the tip effects as well as vortex shedding from the trailing edge. The data of flow type II obtained from the front surface at small incidence $0 \text{ deg} \lesssim \alpha \lesssim 5$ deg are also shown in Fig 13. In equation (12), $\overline{\mathrm{Sh}}_{ch}$ is proportional to the 0.71 power of $\overline{\mathrm{Re}}_{ch}$. However, the overall Sherwood number for flow type II, in fact, has been found to vary approximately in proportion to the $\frac{3}{4}$ power of $\overline{\mathrm{Re}}$. This increase in the exponent is again due to the tip and trailing edge effects discussed above. The data of the other two chord lengths, 30 and 50 mm, which are not shown here, have indicated that these effects become more significant for the plates of smaller chord length, therefore giving further increase in the overall transfer rate. Back surface data of flow type III are shown in Fig. 14. The figure reveals that the overall Sherwood number for this type varies in proportion to the $\frac{2}{3}$ power of $\overline{\mathrm{Re}}$. The exponent $\frac{2}{3}$ happens to be the same as that of wedge flow solution for $\alpha = 45$ deg. The $\frac{2}{3}$ power correlation for stationary plate rearward transfer has been reported by several workers, e.g., Igarashi [8]. Figure 15 shows the transition from flow type I to type II which takes place at $\alpha = 10$ deg, as angular velocity increase. Critical Reynolds numbers have been evaluated as 1×10^4 for $C = 30$ mm, 1.5×10^4 for $C = 50$ mm and 3×10^4 for $C = 70$ mm.

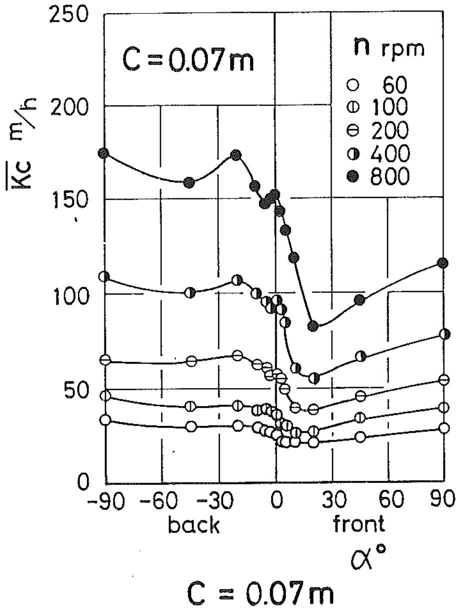

Fig. 12 Mass transfer coefficient averaged over the surface

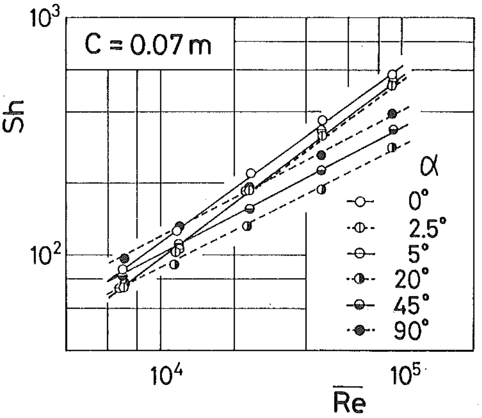

Fig. 13 Sherwood number averaged over front surface

4 Conclusions

1 The flows on inclined flat plates with or without rotation can be classified into three types, namely,

Type I	flow without a separated region
Type II	flow with a separated region located near the leading edge
Type III	flow with a separated region all over the surface.

2 Transfer rate from plates decreases as increasing α from 0 deg (type II) until the reattachment point reaches to the leading edge (the minimum transfer rate), then increases as α increases further (type I). Moreover, flows of type III gain tremendous transfer rate increase by rotation.

3 The following correlations identical to those for stationary plates are valid for rotating plates exposed to flows of type I at $5 \text{ deg} \lesssim \alpha \lesssim 20$ deg.

$$\mathrm{Sh} = 0.620\,\mathrm{Re}^{1/2}$$

$$\overline{\mathrm{Sh}}_{ch} = 1.24\,\overline{\mathrm{Re}}_{ch}{}^{1/2}$$

4 Flow type II at $0 \lesssim \alpha \lesssim 20$ deg can be correlated in terms of Sherwood number averaged over the chord as,

$$\overline{\mathrm{Sh}}_{ch} = 0.237\,\overline{\mathrm{Re}}_{ch}{}^{0.71}$$

5 Transfer rate averaged over the entire surface can be correlated

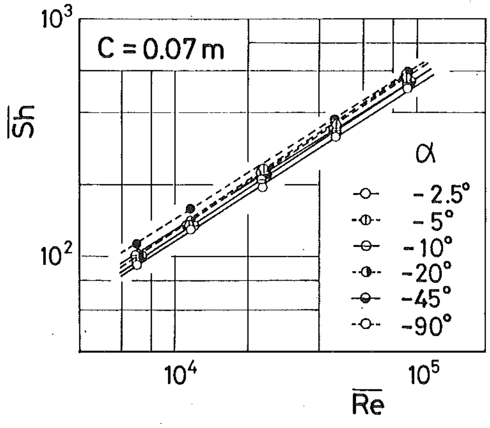

Fig. 14 Sherwood number averaged over back surface

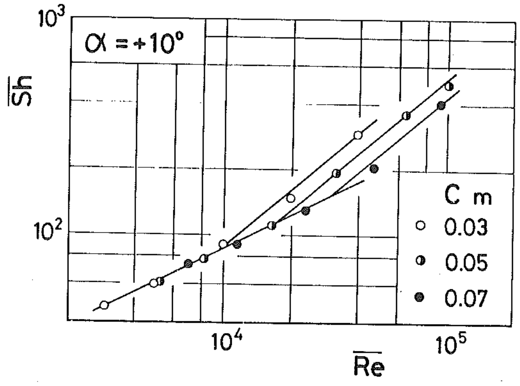

Fig. 15 Sherwood number averaged over front surface at $\alpha = 10$ deg

by following power laws,

$$\overline{\mathrm{Sh}} \propto \overline{\mathrm{Re}}^{1/2} \quad \text{(type I; 5 deg} \lesssim \alpha \lesssim \text{20 deg)}$$

$$\overline{\mathrm{Sh}} \propto \overline{\mathrm{Re}}^{3/4} \quad \text{(type II)}$$

$$\overline{\mathrm{Sh}} \propto \overline{\mathrm{Re}}^{2/3} \quad \text{(type III)}$$

Acknowledgment

The authors would like to express sincere thanks to Mr. E. Makita for his invaluable suggestions over this experimental study. Thanks are also due to a number of individuals in Thermal Science Division at Shizuoka University.

References

1 McCroskey, W. J., "Measurements of Boundary Layer Transition, Separation and Streamline Direction on Rotating Blades," NASA, TN. D-6321, 1971.

2 Toyokura, T., and Harada, K., "Boundary Layer on a Rotating Thin Blade," *Journal of JSME,* Vol. 72, No. 609, 1969, pp. 56–66.

3 Yamamoto, K., and Toyokura, T., "Analysis of the Boundary Layer on a Workless Rotating Thin Blade," *Trans. JSME,* Vol. 39, No. 328, 1973, pp. 3662–3668.

4 Lakshminarayana, B., Jabbari, A., and Yamaoka, H., "Turbulent Boundary Layer on a Rotating Herical Blade," *Journal of Fluid Mechanics,* Vol. 51, Part 3, 1972, pp. 545–569.

5 Millsaps, K., and Pohlhausen, K., "Heat Transfer by Laminar Flow from a Rotating Plate," Journal of Aerospace Science, Vol. 19, No. 2, 1952, p. 120.

6 Eisele, E. H., Leidenfrost, W., and Muthunayagam, A. E., "Studies of Heat Transfer from Rotating Heat Exchangers," *Progress Heat and Mass Transfer,* Vol. 2, Pergamon Press, pp. 483–499.

7 Fukui, S., and Morishita, T., "Measurements of Heat Transfer Coefficient by Sublimation of Naphthalene" *Journal of JSME,* Vol. 65, No. 525. 1962, p. 1483.

8 Igarashi, T., Hirata, M., and Nishiwaki, N., "Heat Transfer in Separated Flows (1st Report, Experiments on Local Heat Transfer from the Rear of an Inclined Flat Plate to Air Stream)," *Trans. JSME,* Vol. 39, No. 322, 1973, pp. 1881–1889.

S. Mochizuki
Department of Mechanical Engineering,
Tokyo University of Agriculture and Technology,
Koganei, Tokyo, Japan

Wen-Jei Yang
Department of Mechanical Engineering and
Applied Mechanics,
University of Michigan,
Ann Arbor, Mich 48109

Heat Transfer and Friction Loss in Laminar Radial Flows through Rotating Annular Disks

Heat transfer and pressure drop performance are experimentally studied for laminar radial flow through a stack of corotating annular disks. The disk surfaces are heated by condensing steam to create constant surface temperature condition. The traditionally defined friction factor is modified to include the effect of centrifugal force induced by the rotation of the heat transfer surface on core pressure drop. Empirical equations are derived for the heat transfer and friction factors at zero rotational speed. Test results are obtained for various rotational speeds. It is disclosed that (1) The transition in the radial flow through rotating parallel disk passages occurs at the Reynolds number (based on the hydraulic diameter of the flow passage) of 3000 at which stall propagation occurs in the rotor. (2) In the laminar flow regime, its heat transfer performance at zero rotational speed is superior to forced convection in the triangular, square, annular, rectangular and parallel-plane geometries. (3) The effects of disk surface rotation are twofold: a significant augmentation in heat transfer accompanied by a very substantial reduction in friction loss. (4) These rotational effects decrease with an increase in the fluid flow rate until the transition Reynolds number where the effects of centrifugal and Coriolis forces diminish is reached. (5) Heat transfer performance at low through flows is superior to that of high-performance surfaces for compact heat exchangers.

Introduction

In many gas-liquid heat exchangers, heat transfer performance is controlled by thermal resistance on the gas side. Two remedies are available to reduce this resistance: by increasing heat transfer area through implementation of fins, and by enhancing the heat transfer coefficient through increasing the bulk flow or generating secondary flows. Various means have been applied to produce secondary flows, for example oscillation of the bulk flow, vibration or rotation of the surface, introduction of acoustic waves into the bulk flow, etc. In vehicular applications, emphasis on compactness and low weight discourages not only surface addition but also flow increase as the latter will result in an increase in the operating pressure, thus requiring the reinforcement of tube or duct walls. Rotation is one way to achieve heat transfer enhancement without suffering power losses in the ducts or weight and volume increases.

Leidenfrost and his associates [1] studied both experimentally and analytically the heat transfer and friction loss performance of rotating-blade heat exchangers. A rotating flat plate was used as a model. Theoretical results and test data were obtained in both laminar and turbulent flow regimes. The main effect of rotation was to promote flow transition which occurs at a Reynolds number (based on the blade chord as the characteristic length) of approximately 10,000. Three-dimensional effects on heat transfer performance were insignificant in both flow regimes. At zero pitch angle, the performance equations were found to be

$$\mathrm{Nu} = 0.646\ \mathrm{Re}^{1/2}$$

$$f = 1.293\ \mathrm{Re}^{-1/2}$$

for laminar flow and

$$\mathrm{Nu} = 0.036\ \mathrm{Re}^{0.8}$$

$$f = 0.072\ \mathrm{Re}^{-0.2}$$

for turbulent flow. Here, Nu, Re and f denote the Nusselt and Reynolds number, and Fanning friction factor, respectively.

A radial-flow shear-force pump was first applied as an air-cooled condenser in the Rankine-cycle vehicular power plant by Doerner, et al. [2]. Instead of rotating a blade to generate lift forces to accelerate the fluid in a conventional pump, the shear flow pump utilizes the velocity difference between fluid and shear surfaces to produce shear forces for accelerating the fluid. The rotor consisted of a package of closely spaced disks with openings in the center. The pump fluid entered along the axis of the disk package and proceeded radially into the spaces between the disks where it was accelerated by the shear forces generated by the slip between the disks and the fluid. In its flow to the outside, the fluid was pressurized. When the pump was used as a condenser rotating at approximately 2500 rpm, the disks functioned as fins with 24 condenser tubes installed equally spaced on a circumference close to the outer edge of the disks. Condensate returned to the boiler simply by centrifugal action. Test results disclosed that for the same power per unit area, the rotary viscous drag condenser has a heat transfer coefficient about 1.5 times that of the conventional automobile radiator. No attempt was made to explore heat transfer characteristics in the rotating system. Mochizuki, et al. [3] modified the rotary condenser by utilizing the disks as a primary heat transfer surface rather than fins. Details of the modified unit will be presented in the succeeding section. The study concluded that (1) When "stall propagation" [4] (a regular, periodic, and relatively simple type of flow pulsation) occurred in the pump condenser, the heat exchanger effectiveness defined as $(T_{c\ \mathrm{out}} - T_{c\ \mathrm{in}})/(T_w - T_{c\ \mathrm{in}})$ exceeded unity. $T_{c\ \mathrm{out}}$ and $T_{c\ \mathrm{in}}$ represent the outlet and inlet air temperatures, respectively, while T_w is the disk surface temperature. (2) For the same heat duty, the rotary condenser requires 30 percent less heat transfer area to exchanger volume ratio than a compact plate-finned type heat exchanger.

A substantial effort has been directed toward the development of high-performance heat transfer surfaces [5]. Since augmentation is achieved through disruption of thermal boundary layers or generation of secondary flows, most techniques are not useful in laminar flow regime but become fully effective beyond the onset of transition. Thus, in many instances (for example, [6]), increases in j and f are accompanied by the problem of noise generation and surface vibration. Reference [7] disclosed that high-porosity perforations induce a second laminar flow regime in which significant increase in heat transfer and friction factors were achieved. The present study represents one instance in which a substantial increase in j accompanied by a significant reduction of f are achieved in the laminar flow regime.

Contributed by the heat transfer division for publication in the JOURNAL OF HEAT TRANSFER. Manuscripts received by the Heat Transfer Division February 6, 1980.

It constitutes an experimental investigation of laminar radial flow in a stack of corotating annular disks. Heat transfer and pressure drop performance are measured. Results are correlated on the basis of area goodness factor and volume goodness factor and compared with those of high-performance heat transfer surfaces.

The definition of friction factor is modified to include the effect of centrifugal force induced by the rotation of the heat transfer surface. However, when stall propagation [4] occurs in the rotor, a self-excited, large-amplitude reverse flow at the disk periphery causes the core pressure drop to change from a positive value to a negative one. As a result, the magnitude of friction factor changes from positive to negative. This unusual physical phenomenon of negative friction factor is unique to the rotating system which is called "shear pump". One must also realize that air is supplied to the rotor in two different ways: (1) "self supply" from the ambient as the rotor works, and (2) "forced supply" with the aid of an external agent such as a turbo fan. The latter means must be employed should high mass flows through the rotor be required.

Experimental Apparatus and Procedure

The heat transfer system under consideration consisted of multiple disks with openings in the center, as shown in Fig. 1, which rotates as a unit. Each disk was made of aluminum 0.5 mm in thickness with 160 mm i.d. (d_1) and 310 mm o.d. (d_2). Alternate spacings between disks were enclosed by an inner and outer ring of 0.8 mm thickness, forming the condensation space. The remaining alternate spaces formed radial flow passages for the cooling air. Fifteen such condensing spaces were assembled coaxially at 1.5 mm spacing on the air side by fastening them to a base disk to form a rotor, i.e. an annular disk assembly. The condensation spaces were interconnected by tubes parallel to the axis of rotation; sixteen equally spaced near the center of rotation to distribute the vapor and eight near the outer periphery to remove the condensate. The rotor was assembled by an aluminum-blazing technique in a vacuum chamber. A tray-shaped disk was bolted to the base disk. Within this tray was located a rotating steam supply tube and a stationary condensate scoop, as shown schematically in the right part of Fig. 1. The arrows indicate the flow directions of the respective fluids.

Air entered through a bellmouth, flowed along the drive shaft, and progressed radially into the spaces between the disks. It was accelerated by shear forces and discharged from the rotor to the surroundings. Steam supplied from a stationary pipe entered into a rotating hollow shaft via a rotating seal. Condensation of the steam took place inside the hollow disks. The condensate together with uncondensed steam were forced by centrifugal force through the eight condensate tubes into the space enclosed by the tray-shape disk. The condensate accumulated in the space was extracted by the scoop and removed via the stationary pipe. The heat released by condensing steam was transferred through the disk walls by conduction and then into the air in the passages by convection. In order to maintain a uniform and constant disk wall temperature, complete condensation was prevented by releasing uncondensed steam into the atmosphere through a pipe inserted into the middle of the tray-shaped disk. Figure 2 shows a cross section of the unit as designed and constructed.

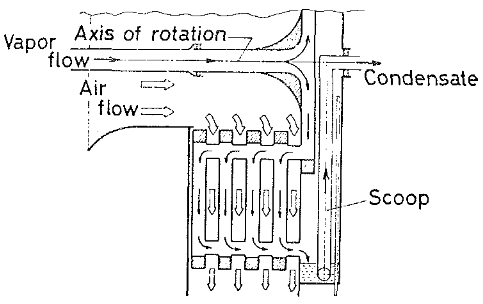

Fig. 1 Fluid flows through rotating annular disk assembly

The entire experimental setup is schematically illustrated in Fig. 3. Steam supplied from the boiler (1) was regulated by both the main valve (2) and the bypass valve (3) and was fed into the rotor core after being slightly superheated by the electric heater (4). Steam temperature and pressure were monitored by the thermocouple (5) and the U-tube manometer (6), respectively. After being cooled to near room temperature, a graduated cylinder and a stopwatch were employed to determine the rate of condensation from which the rate of heat release was evaluated. The rotating speed of the rotor was adjusted by the variable-speed motor (7) and measured using the photoelectric pulse detector (8). Air was supplied to the rotor from the turbo fan (9) through a calming chamber. A Pitot tube was used to measure the air velocity distribution in a suction duct upstream from the turbo fan. The inlet air temperature $T_{c\ \mathrm{in}}$ was measured by the thermocouple (10) located upstream from the rotor. The damper (11) was installed upstream from the turbo fan to regulate the rate of forced air supply. The static pressure drop across the rotor was measured between a static pressure proble located upstream from the rotor and the ambient

Nomenclature

A = heat transfer area = $2N\pi(R_2^2 - R_1^2)$, m^2
$a = 2S$
Cp = specific heat of air at constant pressure J/(kg.K)
D_H = hydraulic diameter = $2S$, m
d = rotor diameter = $2R$, m; d_1, inner; d_2, outer
E_{STD} = flow friction power =

$$\frac{1}{2g_c}\left(\frac{\mu^3}{\rho^2}\right)_{\mathrm{STD}}(f\,\mathrm{Re}^2/D_H{}^3),\ kW/m^2$$

f = *Fanning friction* = $\Delta P_f'/(2\rho\bar{u}^2\,L/D_H)$ as defined by equation (11)
G = mass velocity = $\rho\bar{u}, kg/(\mathrm{m}^2\mathrm{s})$
G_z = Graetz number = Re Pr D_H/L
g_c = conversion factor, 1.0 (kg.m)/N.s^2)
h = heat transfer coefficient as defined by equation (1), W/(m^2.k)
h_{STD} = heat transfer power =

$$\left(\frac{C_p{}^{\mu}}{Pr^{2/3}}\right)_{STD} j\,Re/D_H, (\mathrm{W/m^2K})$$

j = heat transfer factor = $(h/G\,Cp)\mathrm{Pr}^{2/3}$
K_c = entrance loss coefficient as defined by equation (4)
K_e = exit loss coefficient as defined by equation (5)
k = thermal conductivity of air, W/(m.k)
L = flow length $(d_2 - d_1)/2$, m
N = number of hollow disks
Nu = Nusselt number
n = rotational speed of rotor, Hz
P = static pressure N/m^2
ΔP = static pressure drop, N/m^2
Pr = Prandtl number
q = rate of heat released by condensing steam, W
Re = Reynolds number = GD_H/μ
R = rotor radius, m; R_1, inner; R_2, outer
r = radial coordinate
S = disk spacing (width of air flow passage) in rotor core, m
T = temperature, C; $T_{c\ \mathrm{in}}$, of inlet air; $T_{c\ \mathrm{out}}$, of outlet air; = T_s, of condensing steam; T_w, of heat transfer (disk) surface
Ta = Taylor number = $\omega\rho S^2/\mu$
u = velocity component in the r direction; $\bar{u}$, mean value as defined by equation (2), m/s
V = heat exchanger core volume, m^3
$\dot{V}$ = volume flow rate of air in each passage, m^3/s
v = velocity component in the θ direction, m/S; v_1, at core inlet
z = axial coordinate
θ = circumferential coordinate
μ = absolute viscosity of air, N.s/m^2
σ = frontal porosity of rotor core
τ_r = wall shear stress, N/m^2
ω = angular velocity of rotor = $2n\pi$, rad/s
ρ = density of air, kg/m^3

Subscripts

0 = location of static pressure tap upstream from rotor
1 = inlet to rotor core
2 = exit of rotor core
STD = standard condition at 293 K and 1 atmospheric pressure

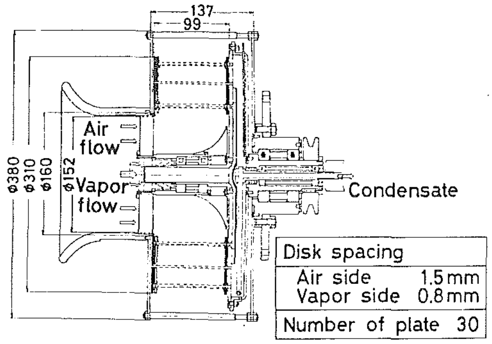

Fig. 2 Test core

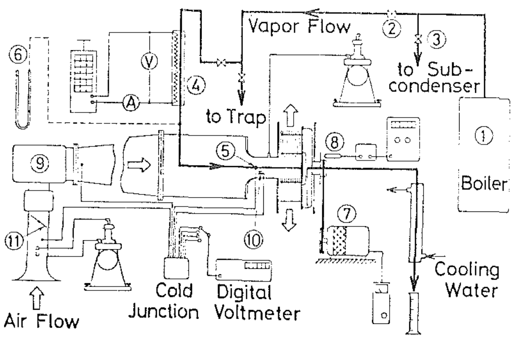

Fig. 3 A schematic diagram of experimental setup

Experimental Results and Discussion

Experiments were performed under the following operating conditions: rotor speed n = 0 to 50 Hz which is equivalent to Taylor number Ta = 0 to 37.5; inlet steam gage pressure = 540 to 850 mm Aq (1 mm Aq = 9.81 Pa); steam condensation temperature T_s = 99.9 to 101.6°C; inlet air temperature $T_{c\ \mathrm{in}}$ = 15.2 to 21.5°C; air flow rate = 51.5 to 867.6 m^3/hr; and heat transfer rate = 1410 to 15170 k cal/hr. The flow length hydraulic diameter ratio L/D_H for this core was 25. The condensing steam temperature is the average value between the saturated steam temperature corresponding to pressure at the rotor inlet and that at the ambient pressure which was different by less than 2°C. Because of higher thermal conductivity of aluminum and high condensation heat transfer coefficient, the disk surface temperature on the air side T_w is equated to T_s. The air-side heat transfer coefficient is defined, based on the lagarithmic mean temperature difference, as

$$h = \frac{q \ln \dfrac{T_w - T_{c\ \mathrm{out}}}{T_w - T_{c\ \mathrm{in}}}}{A(T_{c\ \mathrm{out}} - T_{c\ \mathrm{in}})} \tag{1}$$

The hydraulic diameter of air flow passages is twice the disk spacing S, while the mean radial air velocity is defined, based on the integral average, as

$$\bar{u} = \frac{\dot{V} \ln d_2/d_1}{\pi S(d_2 - d_1)} \tag{2}$$

Using Fig. 10 in reference [8], it was confirmed that the radially outward throughflows covered in the study were within laminar range.

The friction factor f was determined in the following way: Let ΔP_r indicate the static pressure drop across the rotor between a static pressure probe upstream from the rotor (P_0) and the rotor core exit (P_2). ΔP_r consists of

$$\Delta P_r = \Delta P_{01} + \Delta P_1 + (P_1 - P_2) - \Delta P_2 + \Delta P_{2\infty} \tag{3}$$

Here, ΔP_{01} = pressure drop between the static pressure probe at the rotor core inlet, $P_0 - P_1$, ΔP_1 = entrance pressure drop, ΔP_2 = exit pressure rise, $\Delta P_{2\infty}$ = pressure drop between the rotor core exit and the ambient.

Both ΔP_{01} and $\Delta P_{2\infty}$ can be dropped from equation (3) since their magnitude is very small compared to the other terms on the RHS of the equation. One can write [8]

$$\Delta P_1 = \frac{1}{2}\rho\left(\frac{\dot{V}}{\pi d_1 S}\right)^2 (1 - \sigma^2 + K_c) \tag{4}$$

$$\Delta P_2 = \frac{1}{2}\rho\left(\frac{\dot{V}}{dS}\right)^2 \left(\frac{d_1}{d_2}\right)^2 (1 - \sigma^2 - K_e) \tag{5}$$

in which σ denotes the frontal porosity, i.e. core free-flow to frontal-area ratio. K_c denotes the abrupt contraction, or entrance, coefficient while K_e is the abrupt expansion, or exit, coefficient. K_c and K_e are functions of contraction and expansion geometry and, in some cases, of the Reynolds number in the flow passages. In the present study, Fig. 5-3 of reference [8] indicates that K_c and K_e may vary in the ranges of 0.42 ~ 0.72 and 0.12 ~ 0.26, respectively. In the following data correlations, K_c = 0.5 and K_e = 0.2 will be employed.

In order to make the analysis mathematically tractable, an assumption is imposed that both the radial and tangential velocities, u and v, respectively, are uniform in the axial direction. In radial flows between parallel disks, the effect of velocity distribution in the axial direction on the momentum change in the radial direction was found to be insignificant [9]. Even for two extreme cases, the parabolic velocity profile yields the momentum change approximately 35 percent higher than that in the uniform velocity distribution. In the present study, flows within the rotor are still in a developing stage and the velocity profiles are in between the two extreme cases. Therefore, the assumption will not lead to an important error in the results. With the origin of cylindrical coordinates (γ, θ, z) fixed on the rotating axis midway between two parallel disks, the momentum equation in the radial direction reads

$$\frac{dP}{dr} = -\frac{1}{Sr}\frac{d}{dr}\left(r\int_{-a}^{a} \rho u^2 dz\right) + \frac{1}{S}\int_{-a}^{a} \rho \frac{v^2}{r} dz - \frac{2\tau_r}{S} \tag{6}$$

where S is disk spacing; a, one-half of disk spacing; and τ_r, wall shear stress. The integration of the above equation from the inlet to the exit of the rotor core yields

$$P_1 - P_2 = -\Delta P_m + \Delta P_f - \Delta P_c \tag{7}$$

Here, ΔP_m = pressure recovery due to momentum reduction

$$= -\frac{\rho}{8}\left(\frac{\dot{V}}{\pi S}\right)^2 \left(\frac{1}{R_1{}^2} - \frac{1}{R_2{}^2}\right) \tag{8}$$

ΔP_f = pressure drop in the rotor core due to wall friction

$$= \int_{R_1}^{R_2} \frac{2\tau_r}{S} dr \tag{9}$$

ΔP_c = pressure rise due to centrifugal force

$$= \int_{R_1}^{R_2} \frac{\rho v^2}{r} dr \tag{10}$$

Now, define the friction coefficient as

$$f = \frac{\Delta P_f{}'}{2\rho \bar{u}^2 L/D_H} \tag{11}$$

where

$$\Delta P_f{}' = \Delta P_f - \Delta P_c \tag{12a}$$

In the absence of disk rotation, i.e. for a radial flow through parallel disks, ΔP_c diminishes and $\Delta P_f{}'$ becomes identical with ΔP_f. Then equation (11) is reduced to the traditional definition for f. In other words, the definition of f in equation (11) includes the effect of centrifugal force which induces a pressure rise in the rotor core. As a consequence, f drops with rotational speed which will be observed later in the section.

With the substitution of equations (3) and (7), one can rewrite equation (12a) as

$$\Delta P_f{}' = \Delta P_r + \Delta P_m - \Delta P_1 + \Delta P_2 \tag{12b}$$

or

$$\Delta P_f' = \Delta P_r - 2.6 \times 10^5 \rho \dot{V}^2 \qquad (12c)$$

Equation (12c) results from the use of equations (4) and (5) together with $K_c = 0.5$, $K_e = 0.2$ and $\sigma = 0.455$ corresponding to the core geometry employed in the present study. ΔP_r was experimentally measured, while $\dot{V}$ was calculated from the measurements of the pitot tube.

For heat transfer calculations, all physical properties of air were evaluated at the arithemetic mean temperature between the inlet and the exit. Test data were plotted in Figs. 4, 5 and 6 in two typical forms for performance comparison: the heat transfer factor j, the friction factor f and their ratio versus the Reynolds number Re and the heat transfer power h_{STD} against the flow friction power E_{STD}. These factors are defined in the Nomenclature.

1 **General Data Correlations.** Rice and his associates [11] disclosed the existence of an entrance region followed by an asymptotic region in laminar flows between corotating disks. In the case of radially outward throughflow, the flow in the entrance region depends on the inlet velocity profile and three-dimensionless parameters Re, Ta and $v_1/(R_1\omega)$ where v_1 denotes the tangential component of air velocity at the inner radius of the rotor. However, the parameter $v_1/(R_1\omega)$ may be eliminated for the case of prewhirl since its values are approximately zero. The flow in the asymptotic region depends only on Re and Ta. For forced convection in the fully developed laminar flow between the corotating disks, Kreith [12] obtained Nu as a function of Re, Ta, Pr and $S^2/(d_2{}^2 - d_1{}^2)$ which is the dimensionless geometrical parameter. Summarizing these results, one may conclude that the f and Nu performance in radially outward laminar developing flow between corotating disks depends on the inlet velocity profile, Re, Ta, Pr (for j only), and $S^2/(d_2{}^2 - d_1{}^2)$. The last parameter consists of D_H/L and $D_H/\bar{d}$. $\bar{d}$ is a mean diameter of the rotor, which may be an arithmatic or logarithmic mean value. Therefore, for the same inlet velocity distribution, Nu can be correlated in the form

$$\mathrm{Nu} \propto \mathrm{Re}^a Ta^b \mathrm{Pr}^c (D_H/L)^d (D_H/\bar{d})^e \qquad (13)$$

where a, b, c, d and e are constants to be determined empirically. At zero rotation, b is zero. In many flow systems, for example the Graetz problems and the Leveque solution [13], a, c and d take the same value say 1/3 [13, 14]. Then, for a given $D_H/\bar{d}$, it reduces to

$$\mathrm{Nu} \propto \mathrm{Gz}^{1/3} \qquad (14)$$

f can be correlated in the form of

$$f \propto \mathrm{Re}^B (D_H/L)^F \qquad (15)$$

at zero rotation, where B and F are empirical constants.

2 **No Rotation (as Annular Disks).** It is seen in Fig. 4 that at zero rotating speed and under constant wall temperature, the heat transfer and friction loss performance can be expressed as

$$j = 1.15\,\mathrm{Re}^{-2/3} \quad \text{or} \quad \mathrm{Nu} = 0.394\,\mathrm{Gz}^{1/3} \qquad (16)$$

and

$$f = 1.40\,\mathrm{Re}^{-0.222} \qquad (17)$$

respectively. In comparison, a study on heat transfer for source flow between two parallel disks by Kreith]12] yields

$$\mathrm{Nu} = \mathrm{Gz} D_H/(4L) \qquad (18)$$

which is equivalent to

$$j = 1.03 \times 10^{-4}$$

for $L/D_H = 25$. The physical system and thermal boundary condition are identical with those in the present work. The only difference between the two studies is in their hydrodynamic conditions: The former deals with a fully developed source flow, while the latter includes the entrance effects. Equations (16) and (17) are also compared with those for laminar flows through parallel plates. For fully developed flow case, Sieder and Tate [15] obtained

$$\mathrm{Nu} = 1.85\,\mathrm{Gz}^{1/3} \qquad (19)$$

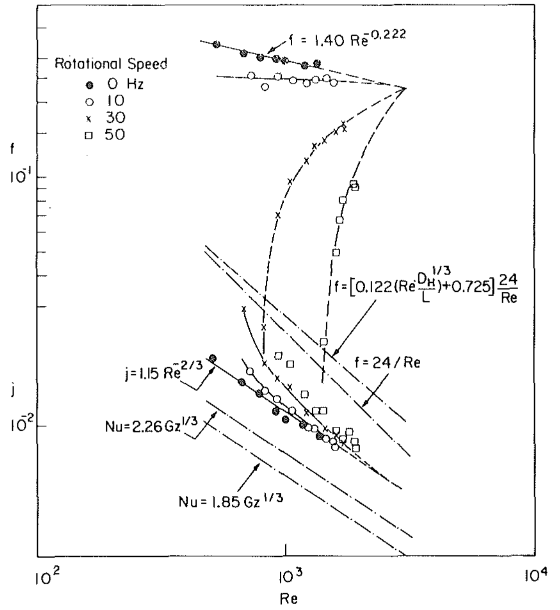

Fig. 4 Heat transfer and friction factors versus Reynolds number

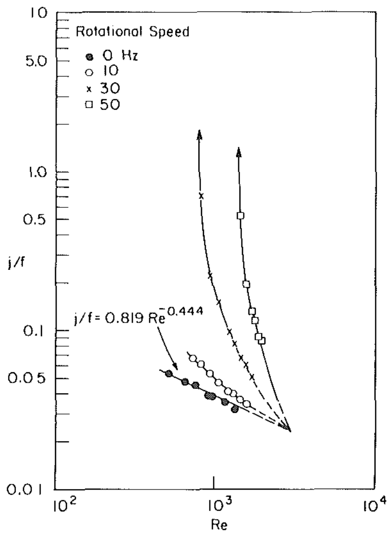

Fig. 5 Heat transfer to friction factor ratio versus Reynolds number

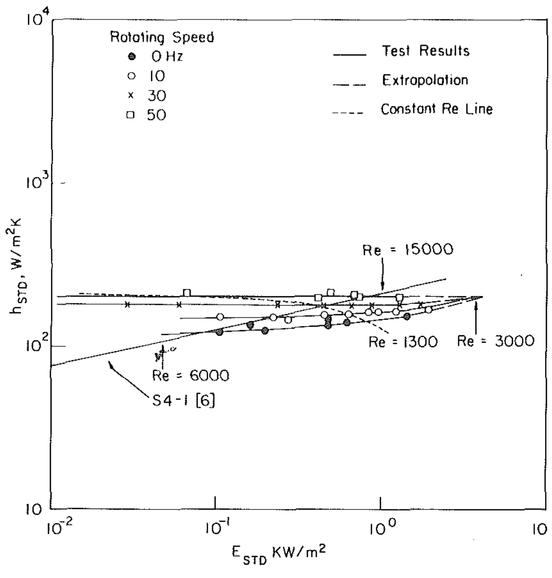

Fig. 6. Heat transfer power versus flow friction power

The corresponding friction factor is [16]

$$f = 24/\mathrm{Re} \tag{20}$$

When entrance effects are included, Bunditkul and Yang [14] gave

$$\mathrm{Nu} = 2.26\ \mathrm{Gz}^{1/3} \tag{21}$$

$$f = 0.12\left(\mathrm{Re}\frac{D_H}{L}\right)^{1/3} + 0.725\frac{24}{\mathrm{Re}} \tag{22}$$

while Sparrow [17] got

$$\mathrm{Nu} = \frac{0.664\ \mathrm{Gz}^{1/2}}{\mathrm{Pr}^{1/2}F_1}\left[1 + 7.3\left(\frac{\mathrm{Pr}}{\mathrm{Gz}}\right)^{1/2}\right]^{1/2} \tag{23}$$

where F_1 is equal to about 1.2 for air. In the absence of rotation one may conclude that the present system yields much higher heat transfer performance than the parallel-plane system which is known to be the best in laminar heat transfer performance among various simple geometries [8]. As illustrated in Fig. 7, it is comparable to high-performance compact plate-fin surfaces of plain, louvered and strip type, respectively in Fig. 10-26, 10-44 and 10-52 of reference [8]. These surfaces were all made of 0.152 mm thick aluminum with 11.1 fins per 2.54 cm (in.), 6.35 mm of plate spacing, 3.08 mm of flow passage hydraulic diameter, fin area to total heat transfer area ratio of 0.756 and compactness (total transfer area/volume between plates) of 112 $\mathrm{m}^2/\mathrm{m}^3$ (367 $\mathrm{ft}^2/\mathrm{ft}^3$).

3 **Effect of Rotation.** It is seen in Fig. 4 that as the rotational speed or Taylor number increases, heat transfer performance is enhanced while friction loss decreases. The latter phenomenon is one important feature of a shear-force pump. That is, if the pump through flow is increased, the velocity difference between fluid and shear surface increases causing a steady drop in pump head with increasing flow. At the same Ta, the increase in j and decrease in f become more prominent as Re is reduced. When Ta is sufficiently high, the f factor falls sharply with a reduction in the inlet flow rate Re and eventually becomes negative—occurrence of stall propagation. When the j and f data points are extrapolated, they meet at the same Reynolds number of 3000 which represents the critical Re for the onset of transition. The transition Reynolds number for parallel-plane systems is about 4000 [6, 7]. In the laminar flow regime, heat transfer enhancement and friction loss reduction due to rotation diminish as Re approaches 3000. This observation is in agreement with the conclusion that the efficiency of multiple disk-friction pump degrades as Re increases toward the threshold of transition flow [11].

Most heat transfer augmentation devices are effective only in the transition and turbulent flow regimes. The uniqueness of the present unit is an enhancement in the laminar regime and consequently operation is at a very low noise level because of no flow separation.

Figure 5 is a plot of the area goodness factor j/f versus Re. It is interesting to note that the value of j/f may far exceed 0.5, the limiting value in turbulent heat transfer according to the Reynolds analogy. A steep increase in j/f toward infinity (changing from plus infinity to minus one as f changes from positive to negative) signifies the occurrence of stall propagation, i.e. a self-excited, large-amplitude, reverse flow through the disk periphery into the rotor core. At zero rotor speed, the goodness factor can be expressed as

$$j/f = 0.819\ \mathrm{Re}^{-0.444} \tag{24}$$

Again, the data points are extrapolated to meet at Re of 3000.

A volume goodness factor comparison is given in Fig. 6. When the system is in rotation at high speed, the heat transfer power h_{STD} is practically independent of the flow friction power E_{STD}. It is observed that h_{STD} increases with the rotor speed. But as Re increases the effect of centrifugal and Coriolis forces on heat transfer diminishes. An extrapolation of these data points meets at Re of 3000. The performance of a perforated heat transfer surface S4-1 [6] is superimposed in the figure for comparison. Perforation produces no effect on heat transfer performance when the flow is laminar. The perforated surface exhibits high performance only in transition and turbulent flow ranges accompanied by high-pitch noise and surface vibration. The locations of Re = 6000 and 15,000 are indicated by an arrow. It is seen that the heat transfer power of the present unit at low Reynolds number is higher than that of the perforated surface in turbulent flows.

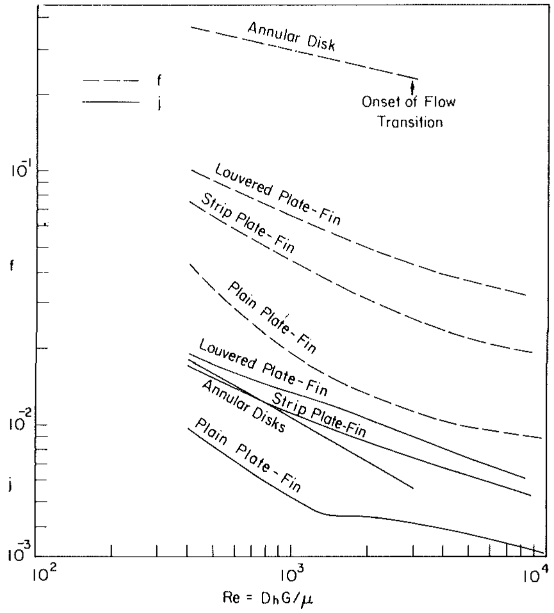

Fig. 7 Performance comparison with other high-performance compact surfaces

4 **Error Analysis of data.** An error analysis was carried out to determine the uncertainties in the test data using the method described in [18]. The factor taken into account included the uncertainties in the physical constants, geometric measurement of rotor core, temperature and pressure measurement. The uncertainties in f and j were estimated to be about 4 percent and 6 percent, respectively.

Conclusions

An experimental study was performed to determine the changes in heat transfer and friction loss performance in laminar radial flows caused by the rotation of disk walls. It is concluded from the study that

1 In the range of high rotational speed and low Reynolds number, a significant heat transfer enhancement is achieved by rotating parallel disks without noise or vibration. In the absence of rotation, annular disks are better than those of simple goemetries and comparable to compact finned surfaces in heat transfer performance.
2 Transition from laminar to turbulent flow occurs at a Reynolds number of approximately 3000.
3 Equations (16) and (17) describe the performance at zero rotor speed for laminar flows of Re within 3000.
4 At low Reynolds number, both heat transfer and friction loss performance are significantly changed by the action of centrifugal and Coriolis forces. However, the effects are reduced with flow and diminish at the transition Reynolds number.
5 The occurrence of stall propagation is evidenced by a very low or negative value of f and a very high value of the j/f ratio.

More experimental work is needed by varying core geometry (d_1/S, d_2/S) to confirm the generality of equations.

References

1 Eisele, E. H., Leidenfrost, W., and Muthunayagam, A. E., "Studies of Heat Transfer from Rotating Heat Exchangers," in *Progress in Heat and Mass Transfer,* Vol. 2 edited by T. F. Irvine, Jr., Ibele, W. E., Hartnett, J. P. and Goldstein, R. J., Pergamon Press, London, 1969, pp. 483–499.

2 Doerner, W. A., Dietz, R. J., Van Buskirk, O. R., Levy, S. B., Rennolds, P. J., and Bechtold, M. F., "A Rankine Cycle Engine with Rotary Heat Exchangers," Society of Automotive Engineers Paper No. 720053, 1972.

3 Mochizuki, S., Yagi, Y., and Honma, N., "Research on Rotary Heat Exchangers," Japan Society of Mechanical Engineers Paper No. 780-16, 1978.

4 Mochizuki, S. and Tanida, Y., "Unsteady Flow Phenomena in Multiple Disk Fans," ASME Paper No. 79-FE-10, 1979.

5 Bergles, A. E., "Survey and Evaluation of Techniques to Augment Convective Heat and Mass Transfer, "Progress in Heat and Mass Transfer, Vol. 1, 1969.

6 Liang, C. Y., and Yang, Wen-Jei, "Heat Transfer and Friction Loss Performance of Perforated Heat Exchanger Surfaces," ASME JOURNAL OF HEAT TRANSFER, Vol. 97, pp. 9–15, 1975.

7 Lee, C. P. and Yang, Wen-Jei, "Augmentation of Convective Heat Transfer from High-Porosity Perforated Surfaces," *Heat Transfer 1978*, Toronto, Canada, Vol. 2, pp. 589–594, 1978.

8 Kays, W. M., and London, A. L., *Compact Heat Exchangers*, Second Ed., McGraw-Hill, New York, 1964.

9 Moller, P. S., "Radial Flow without Swirl between Parallel Discs," *The Aeronautical Quarterly*, Vol. 14, pp. 163–186 (1963).

10 Jackson, J. D., and Symmons, G. R., "An Investigation of Laminar Radial Flow between Two Parallel Disks," *Applied Scientific Research*, Vol. 15, pp. 59–75 (1965).

11 Pater, L. L., Crowther, E. and Rice, W., "Flow Regime Definition for Flow Between Corotating Disks," ASME *Journal of Fluids Engineering*, Vol. 96, pp. 29–34, 1974.

12 Kreith, F., "Transfert de Chaleur et de Masse dans un Ecoulement Radial entre Deux Disques Paralleles Fixes, ou Tourant a la meme Vitesse," *International Journal of Heat Mass Transfer*, Vol. 9, pp. 265–282, 1966.

13 Knudsen, J. G., and Katz, D. L., *Fluid Dynamics and Heat Transfer*, McGraw-Hill, New York, 1958.

14 Bunditkul, S., and Yang, Wen-Jei, "Laminar Transport Phenomena in Parallel Channels with a Short Flow Constriction," ASME JOURNAL OF HEAT TRANSFER, Vol. 101, pp. 217–221, 1979.

15 Sieder, E. N., and Tate, G. E., "Heat Transfer and Pressure Drop of Liquids in Tubes," *Industrial Engineering and Chemistry*, Vol. 28, p. 1429, 1936.

16 Whan, G. A., and Rothfus, R. R., "Characteristics of Transition Flow Between Parallel Plates," *AIChE Journal*, Vol. 5, pp. 204–208, 1959.

17 Sparrow, E. M., "Analysis of Laminar Forced-Convection Heat Transfer in Entrance Region of Flat Rectangular Ducts," NACA TN 3331, 1955.

18 Kline, S. J., and McClintock, F. A., "Describing Uncertainty in Single Sample Experiments," *Mechanical Engineering*, Vol. 75, p. 3, 1953.

E. M. Sparrow
Fellow ASME

S. Acharya

Department of Mechanical Engineering,
University of Minnesota,
Minneapolis, Minn 55455.

A Natural Convection Fin with a Solution-Determined Nonmonotonically Varying Heat Transfer Coefficient

A conjugate conduction-convection analysis has been made for a vertical plate fin which exchanges heat with its fluid environment by natural convection. The analysis is based on a first-principles approach whereby the heat conduction equation for the fin is solved simultaneously with the conservation equations for mass, momentum, and energy in the fluid boundary layer adjacent to the fin. The natural convection heat transfer coefficient is not specified in advance but is one of the results of the numerical solutions. For a wide range of operating conditions, the local heat transfer coefficients were found not to decrease monotonically in the flow direction, as is usual. Rather, the coefficient decreased at first, attained a minimum, and then increased with increasing downstream distance. This behavior was attributed to an enhanced buoyancy resulting from an increase in the wall-to-fluid temperature difference along the streamwise direction. To supplement the first-principles analysis, results were also obtained from a simple adaptation of the conventional fin model.

Introduction

In the conventional heat transfer analysis of fins, it is standard practice to assume that the heat transfer coefficient for convection at the fin surfaces is uniform all along the fin. There is, however, evidence in the literature demonstrating that the heat transfer coefficient can experience substantial variations along the fin surfaces (e.g., [1–3]). These variations may be caused by nonuniformities in both the velocity and temperature fields in the fluid adjacent to the fin. When natural convection is involved, the nonuniformity of the fin surface temperature will affect the buoyancy force which drives the natural convection flow, with a resulting impact on the heat transfer coefficient.

The present paper is concerned with fins which transfer heat to or from a surrounding fluid by natural convection. A special feature of the analysis is that the magnitude and surface distribution of the heat transfer coefficient is not prescribed in advance but rather is an outcome of the solution.

Natural convection heat transfer coefficients for a fin are established by a highly coupled interaction between the fin and the surrounding fluid. The root of the interaction is the temperature-driven nature of the fluid flow, which causes the flow field to be specific to the temperature distribution in the fin. Since the flow field has a strong influence on the convective heat transfer coefficient which, in turn, strongly affects the fin temperature distribution, the tightness of the coupling is apparent.

Any first-principles analysis of fins must deal with both the energy conservation equation in the fin and the equations of mass, momentum, and energy conservation in the fluid. For forced convection flows where thermophysical property variations can be neglected, the fluid flow problem can be solved prior to the analysis of the coupled heat transfer problem for the fluid and the fin. On the other hand, for natural convection, the fluid flow must be solved simultaneously with the fluid-fin heat transfer problem. In this light, the first-principles solution of natural convection fins is more complex than is that for forced convection fins.

As will be illustrated shortly, the problem to be analyzed here involves a vertical plate fin situated in an otherwise quiescent environment. Owing to the aforementioned coupling between the fin and the fluid, the present analysis is fundamentally different from the extensive literature on natural convection about a vertical plate (see [4] for a representative sampling of the literature). That literature deals, in the main, with plates having thermal boundary conditions which yield similarity solutions. These include the isothermal plate, the uniform heat flux plate, and plate surface temperatures which vary as a power law of the distance from the leading edge—with the leading-edge temperature being either infinite or equal to the ambient temperature. In addition, solutions are available in the literature for specific prescribed variations of plate temperature or heat flux which do not yield a similarity solution.

For the vertical plate fin studied here, the resulting variations of surface temperature and surface heat flux do not yield similarity solutions, nor are they of the elementary forms that have been dealt with in published nonsimilarity analyses. Indeed, the resulting thermal boundary conditions have yielded the rather unconventional finding alluded to in the title of the paper, namely, that the local heat transfer coefficient at first decreases with increasing distance from the leading edge, attains a minimum, and then increases.

A schematic diagram of the vertical plate fin is presented in Fig. 1 to illustrate the physical situation and the nomenclature needed for the analysis. The figure shows two possible thermal configurations. The fin in the left-hand part of the diagram is attached at its upper end to a base surface whose temperature T_0 exceeds the ambient temperature T_∞. In this case, there is an upward flow along the plate fin. On the other hand, the right-hand portion of the diagram pictures a fin whose lower end is attached to a base surface for which $T_0 < T_\infty$,

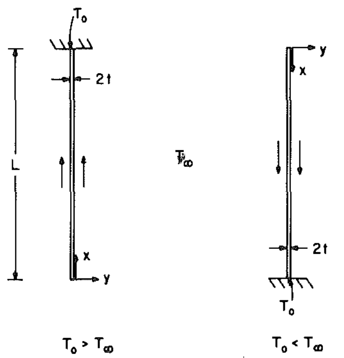

Fig. 1 Vertical plate fin

Contributed by The Heat Transfer Division for publication in the JOURNAL OF HEAT TRANSFER. Manuscript received by the Heat Transfer Division November 21, 1981.

resulting in a downward flow along the fin. Aside from certain changes in sign, the analyses for the two thermal configurations are identical and, for concreteness, attention will be focused on the case at the left (i.e., the upflow case).

The analysis will encompass the simultaneous solution of the heat conduction equation for the fin and the boundary layer equations for the adjacent fluid. The solutions are governed by two parameters, one of which will be termed the conduction-convection number and the other of which is the Prandtl number. Values of the conduction-convection number were selected to cover the entire range of practically realistic operating conditions. The Prandtl number was set equal to 0.7 for all cases to reflect the frequent use of natural convection fins in air.

Results were obtained for the overall fin heat transfer, and these are presented both in terms of physical variables and in terms of the fin efficiency. Distributions along the fin of the surface temperature, local heat flux, and local heat transfer coefficient are also presented.

In addition to the results of the first-principles analysis, an alternative set of results was generated on the basis of a seemingly naive application of the classical fin heat transfer formula. Comparisons will be made of the two sets of results and their relationship elucidated.

A search of the literature revealed only one reference which bears directly on the present work. That paper, [3], was also concerned with a vertical fin attached at one of its ends to a base surface. In [3], by the adroit selection of a fin with a tapered power-law contour which has zero thickness at the tip, the natural convection boundary layer was, in effect, uncoupled from the conduction problem for the fin. In fact, the resulting natural convection boundary layer yielded similarity solutions which could be obtained without reference to the fin. These similarity solutions corresponded to the power-law fin surface-temperature distribution $T_{wx} - T_\infty = (T_0 - T_\infty)(x/L)^n$, with $n > 0$. For this distribution, the temperature at the fin tip is equal to the ambient temperature.

Neither the tapered contour nor the power-law temperature distribution of [3], along with their special tip conditions, bears a significant relation to the geometrical and thermal configuration considered here. In particular, the present problem is a truly coupled problem, and it must be solved as one.

With regard to experiments, the literature contains several reported experiments on natural convection fins in air (e.g., [3, 5–8]). Aside from [3], the geometric configurations of the experiments differed significantly from that studied here, thereby eliminating the possibility of comparison. The experiments of [3] were specific to the conditions of the analysis set forth there and are, therefore, not able to serve for comparisons here.

Analysis

Governing Equations. As was already noted, the formulation of a first-principles analysis for the natural convection fin involves the energy conservation equation for the fin and the boundary layer equations for the fluid. For the fin, there is ample evidence based on finite-difference solutions that a one-dimensional model for the temperature distribution is fully adequate (e.g., [9, 10]). Since the fin temperature at any station x also serves as the wall temperature for the adjacent fluid, it will be denoted as T_{wx}.

The energy equation for the fin may be written in either of two forms depending on how the coupled fin–boundary layer problem is to be solved. The method to be used here involves a succession of consecutive solutions for the fin and the boundary layer, with the sequence continued until there are no changes (within a preset tolerance) between the nth cycle and the $(n - 1)$ cycle. Within each cycle of such a method, information must be transferred from the boundary layer solution that is current for that cycle for use as input to the upcoming fin solution. This information may either be in the form of the local natural convection heat flux $q(x)$ or in the form of the local natural convection heat transfer coefficient $h(x)$. Both $q(x)$ and $h(x)$ would be available from the current boundary layer solution.

The two forms of the fin energy equation that respectively correspond to these options are

$$d^2T_{wx}/dx^2 = q/k_f t \tag{1}$$

$$d^2T_{wx}/dx^2 = (h/k_f t)(T_{wx} - T_\infty) \tag{2}$$

where k_f is the fin thermal conductivity and t is the half thickness of the fin (Fig. 1). For the solution of either equations (1) or (2) at a given cycle of the iterative procedure, h and q can be regarded as known.

At first glance, it would appear advantageous to use equation (1) rather than equation (2) because it is easier to solve. Notwithstanding this, equation (2) was employed in the solution scheme. This choice was made on the basis of prior experience which has shown that at any stage of an iterative scheme, h is closer to the final converged result than is q. Thus, equation (2) was chosen with a view to obtaining rapid convergence of the iterative procedure, and this objective was satisfactorily fulfilled, as will be documented shortly.

Equation (2) was recast in dimensionless form by the substitutions

$$X = x/L, \quad \theta_{wx} = (T_{wx} - T_\infty)/(T_0 - T_\infty) \tag{3}$$

so that

$$d^2\theta_{wx}/dX^2 = \hat{h} N_{cc} \theta_{wx} \tag{4}$$

where N_{cc} is the conduction-convection number[1]

$$N_{cc} = (kL/k_f t)\mathrm{Gr}_L{}^{1/4}, \quad \mathrm{Gr}_L = g\beta(T_0 - T_\infty)L^3/\nu^2 \tag{5}$$

The quantity $\hat{h}$ is a dimensionless form of the natural convection heat transfer coefficient, the values of which are fed to equation (4) from the boundary layer solution that is current at a given cycle of the iteration.

To develop the equation for $\hat{h}$, dimensionless variables are introduced as follows

$$\theta = (T - T_\infty)/(T_0 - T_\infty), \quad Y = (y/L)\mathrm{Gr}_L{}^{1/4} \tag{6}$$

in which $T(x,y)$ is the temperature distribution in the fluid, and

---

[1] The Biot number is not an appropriate parameter in the present problem because the heat transfer coefficient varies with x and is also unknown prior to the initiation of the computations.

Nomenclature

Gr_L = Grashof number, $g\beta(T_0 - T_\infty)L^3/\nu^2$
g = acceleration of gravity
h = local heat transfer coefficient
$\hat{h}$ = dimensionless local heat transfer coefficient, $hL/k\mathrm{Gr}_L{}^{1/4}$
h^* = uniform heat transfer coefficient for simple model
k = fluid thermal conductivity
k_f = fin thermal conductivity
L = fin length
m = dimensional group, $(h^*/k_f t)^{1/2}$
N_{cc} = conduction-convection number, $(kL/k_f t)\mathrm{Gr}_L{}^{1/4}$
Pr = Prandtl number
Q = overall fin heat transfer rate
q = local natural-convection heat flux
T = temperature
T_0 = root temperature
T_{wx} = local fin temperature
$\overline{T}_{wx}$ = average fin temperature
T_∞ = ambient temperature
t = fin half thickness
U, V = dimensionless velocities, equation (9)
u, v = velocity components
X = dimensionless coordinate, x/L
Y = dimensionless coordinate, $(y/L)\mathrm{Gr}_L{}^{1/4}$
x, y = coordinates
β = thermal expansion coefficient
η = fin efficiency
θ = dimensionless temperature, $(T - T_\infty)/(T_0 - T_\infty)$
ν = kinematic viscosity

$\theta(X,Y)$ is its dimensionless counterpart. Then, from the definition of the local heat transfer coefficient

$$h = -k(\partial T/\partial y)_{wx}/(T_{wx} - T_\infty) \quad (7)$$

so that

$$\hat{h} = hL/k\mathrm{Gr}_L{}^{1/4} = -(\partial\theta/\partial Y)_{wx}/\theta_{wx} \quad (8)$$

The right-hand member of equation (8) is readily evaluated at any streamwise station by employing the boundary layer solution that is most current.

Attention will now be turned to the governing equations for the boundary layer. These equations may be recast in dimensionless form by using the definitions of X, θ, and Y from equations (3) and (6) along with the following dimensionless velocities

$$U = u/(g\beta(T_0 - T_\infty)L)^{1/2}, \quad V = v/(g\beta(T_0 - T_\infty)\nu^2/L)^{1/4} \quad (9)$$

In terms of the new variables, the boundary layer equations for mass, momentum, and energy become

$$\partial U/\partial X + \partial V/\partial Y = 0 \quad (10)$$

$$U(\partial U/\partial X) + V(\partial U/\partial Y) = \theta + \partial^2 U/\partial Y^2 \quad (11)$$

$$U(\partial\theta/\partial X) + V(\partial\theta/\partial Y) = (1/\mathrm{Pr})(\partial^2\theta/\partial Y^2) \quad (12)$$

These equations contain only one parameter, the Prandtl number. Despite the transformation, equations (10–12) remain as partial differential equations because the thermal boundary conditions do not admit a similarity solution.

Equations (4) and (10–12) constitute the governing equations of the problem. They contain N_{cc} and Pr as prescribable parameters. Since Pr will be taken equal to 0.7, N_{cc} remains as the only active parameter.

The aforementioned governing equations are supplemented by thermal and velocity boundary conditions. At the fluid-solid interface $y = 0$ (i.e., the surface of the fin), it is required that the local temperature T_{wx} and the local heat flux q be the same in the fluid and in the solid; furthermore, the velocities u and v are zero. The fluid temperature T and the streamwise velocity u are respectively equal to T_∞ and to zero, both at the leading edge of the plate ($x = 0$) and in the region beyond the edge of the boundary layer ($y \to \infty$). For the fin, the tip ($x = 0$) is regarded as adiabatic while the temperature at the root ($x = L$) is T_0. The manner in which these boundary conditions participate in the solution scheme will be described shortly.

It may be observed that in the foregoing description of the boundary conditions, no mention was made of the velocity conditions at the base surface to which the fin is attached. This omission is actually required by the boundary layer equations. Once conditions have been specified at the leading edge of the plate ($x = 0$), the solution yields the velocity field at all $x > 0$ and, therefore, does not permit the specification of velocity boundary conditions at any $x > 0$. The nonaccounting of hydrodynamic effects related to the presence of the base surface should not materially affect the fin heat transfer results provided that the fin length L is large compared with the boundary layer thickness at $x = L$.

Solution Methodology. In its overall pattern, the solution begins by solving the natural convection boundary layer problem for an isothermal plate with $T_{wx} = T_0$ (i.e., $\theta_{wx} = 1$) for all X. The dimensionless heat transfer coefficients $\hat{h}(X)$ determined from this solution in accordance with equation (8) are then used as input to the fin heat conductance equation (4); but note that θ_{wx} which appears on the right-hand side of equation (4) is treated as an unknown (i.e., θ_{wx} from the boundary layer solution is not transferred to equation (4)). With N_{cc} prescribed, the differential equation (4) is then solved to yield $\theta_{wx}(X)$.

To begin the next cycle of the iterative procedure, the just-determined θ_{wx} is imposed as the thermal boundary condition for the natural convection boundary layer problem, the solution to which yields a new $\hat{h}(X)$ distribution which is used as input to the fin heat conduction equation. This procedure of alternately solving the boundary layer problem and the fin conduction problem was continued until convergence was attained.

To track the approach to convergence, the (dimensionless) overall rate of heat transfer from the fin was monitored. When the cycle-to-cycle change in this quantity was less than one in the fifth significant figure, convergence was deemed to have been attained. The number of cycles needed for convergence ranged from four to six, depending on the value of N_{cc}. This rapid convergence validates the selection of the heat transfer coefficient $\hat{h}$ as the transferred quantity from the boundary layer problem to the heat conduction problem.

The boundary layer solutions were obtained by a marching procedure, starting at the leading edge (i.e., at the fin tip) where $X = 0$ and proceeding downstream step-by-step until $X = 1$ (the root) is reached. The actual computations were carried out by the Patankar-Spalding method [11]. This is an implicit finite-difference scheme, a special feature of which is that a dimensionless stream function $\omega = (\psi - \psi_i)/(\psi_o - \psi_i)$ is used as the cross-stream coordinate. The quantities ψ_i and ψ_o respectively denote the values of the stream function at the inner and outer edges of the boundary layer. In the present problem, $\psi_i = 0$ (i.e., the plate is impermeable), but ψ_o varies with X as the boundary layer entrains fluid in the course of its development (the calculation of the entrainment rates is described in [11]). The finite-difference grid spans the range $0 \leq \omega \leq 1$ at all X, so that as the boundary layer thickness varies, the grid automatically follows the variations.

To ensure high accuracy, a step-size study was performed prior to the initiation of the main calculations. The final grid pattern encompassed 500 points in the cross-stream (ω) direction and 4000 points in the streamwise (X) direction. There was a denser concentration of points near the leading edge (small X) to accommodate the initial rapid growth of the boundary layer (i.e., relatively large derivatives). In addition, at all X, the points were more densely concentrated near the plate surface. The distribution of the points in the streamwise direction was determined by the computer program itself in order to accommodate a given input value for the rate of fluid entrainment at the edge of the boundary layer. For the transverse grid points, the coordinates ω_i were determined from the relation $\omega_i = [(i - 1)/(N - 1)]^{2.75}$, where $N = 500$.

As an accuracy test, the computer program was used to solve for the Nusselt numbers for the isothermal vertical plate. These results were compared with the literature value that had been obtained from a similarity solution. The deviation between the results was one or two in the fourth significant figure (0.03–0.06 percent), but it is an open question whether the similarity solution is accurate to that level.

The Patankar-Spalding method requires that velocity and temperature profiles be given at the streamwise station at which the marching procedure was initiated. For this purpose, algebraic-form profile expressions were taken from the integral momentum-energy solution ([12] pp. 312–315) and applied at $X = 6 \times 10^{-10}$, which was the starting point of the marching solution. In view of this very small value of X, the possible approximations in the input profiles had no influence on the results at downstream stations, as was verified in the aforementioned accuracy test.

The boundary conditions employed in the boundary layer solutions were that $U = V = 0$ and $\theta = \theta_{wx}$ at the plate surface, with $\theta_{wx} = 1$ for the first pass and θ_{wx} taken from the immediately preceding fin solution for all subsequent passes. At the edge of the boundary layer, $\theta = 0$ and $U = 0$. It was not necessary to explicitly impose conditions at the leading edge since, as noted in the foregoing, the solutions were initiated just downstream of the leading edge.

Consideration may next be given to the fin heat conduction equation (4). This equation was discretized by a control volume approach. The fin length $0 \leq X \leq 1$ was subdivided into approximately 1600 control volumes. A typical control volume i had an axial length ΔX_i and spanned the thickness of the fin. Each control volume was laid out so that its faces were midway between the immediately adjacent grid points. Thus, if the coordinates of three adjacent grid points are X_{i-1}, X_i, and X_{i+1}, the intermediate control volume faces are at

$$(X_{i-1}+X_i)/2, \quad (X_i+X_{i+1})/2 \tag{13}$$

and the axial length ΔX_i is

$$\Delta X_i = (X_{i+1} - X_{i-1})/2 \tag{14}$$

Furthermore, the temperature derivatives at the respective control volume faces are accurately represented via central differences as

$$(\theta_i - \theta_{i-1})/(X_i - X_{i-1}), \quad (\theta_{i+1} - \theta_i)/(X_{i+1} - X_i) \tag{15}$$

With these considerations, equation (4) takes on the discretized form

$$a_i\theta_i = b_i\theta_{i+1} + c_i\theta_{i-1} \tag{16}$$

where

$$a_i = (X_{i+1} - X_i)^{-1} + (X_i - X_{i-1})^{-1} + \hat{h}_i N_{cc}(X_{i+1} - X_{i-1})/2 \tag{17}$$

$$b_i = (X_{i+1} - X_i)^{-1}, \quad c_i = (X_i - X_{i-1})^{-1} \tag{18}$$

Equations (16–18) represent the discretized conduction equation at all fin grid points except $X = 0$ (tip) and $X = 1$ (root). At the root, the fin temperature is equal to T_0, so that $\theta_{wx} = 1$. In light of this, a difference equation is not written at $X = 1$. At the tip, the adiabatic boundary condition is applied and an energy balance written for the usual surface-adjacent control volume (i.e., a control volume whose grid point is at the surface). This energy balance yields an algebraic relationship between the tip grid point and the fin grid point adjacent to it.

All told, about 1600 fin grid points were used. The grid point deployment was somewhat nonuniform, but the largest control-volume length did not exceed $\Delta X = 10^{-3}$. The solution of the algebraic equations (16), plus the tip equation, was carried out by the tridiagonal matrix algorithm (Thomas algorithm). As a test of the discretization scheme and the computer program, solutions were obtained for input values of $\hat{h}$ = constant. Agreement with the corresponding exact solution was found to be, at the very worst, to within one in the fifth significant figure.

For most of the fin length, $2.8 \times 10^{-3} \le X \le 1$, the X coordinates of the fin grid points were matched with those of the boundary layer. For smaller X, a finer X subdivision was needed for the boundary layer solution. The nonalignment of the two sets of grid points for $X < 2.8 \times 10^{-3}$ was taken into account in the transfer of information from the boundary layer to the fin and vice versa. For $\hat{h}$, equation (8) was evaluated using mean values of $(\partial\theta/\partial Y)_{wx}$ and θ_{wx} with respect to the control volume length ΔX_i. When transferring θ_{wx} from the fin solution to the boundary layer solution, interpolation was employed.

Representations for the Results. The quantity of most immediate practical interest is the overall rate of heat transfer Q from (or to) the fin as a whole. Numerical values of Q can be obtained from the solutions either by integrating the local convective flux at the fin surface or from the heat conducted from the fin into the base surface at $X = 1$. Both approaches were used, and the corresponding Q values were found to be in excellent agreement. To motivate the dimensionless representation for Q, the integrated convection will be evaluated. In dimensional terms,

$$Q = 2\int_0^L -k(\partial T/\partial y)_{wx}dx \tag{19}$$

where the factor of two is inserted to account for heat transfer from both faces of the fin. When dimensionless variables are introduced, there follows

$$Q/k(T_0 - T_\infty)\mathrm{Gr}_L{}^{1/4} = 2\int_0^1 (-\partial\theta/\partial Y)_{wx}dX \tag{20}$$

The group on the left-hand side will be employed to convey the dimensionless heat transfer results.

For a fin of infinite thermal conductivity, $\theta_{wx} = 1$. Since such a fin is isothermal, $(\partial\theta/\partial Y)_{wx}$ can be evaluated from the available similarity solution for the boundary layer, and the integral on the right-hand side of equation (20) is equal to 0.4709 for $\mathrm{Pr} = 0.7$. The fin efficiency η compares the heat transfer for a real fin with that for a fin of infinite thermal conductivity, with all other controllable parameters held fixed. (Note that the natural convection heat transfer coefficient is not the same for the real fin and the corresponding fin of infinite conductivity.) With the foregoing as background, it follows that

$$\eta = (1/0.4709)\int_0^1 (-\partial\theta/\partial Y)_{wx}dX \tag{21}$$

Results will also be reported for the distribution of the local convective heat transfer coefficient h along the length of the fin. The dimensionless form for these results, borrowed from equation (8), is

$$hL/k\mathrm{Gr}_L{}^{1/4} = -(\partial\theta/\partial Y)_{wx}/\theta_{wx} \tag{22}$$

Also to be reported is the distribution of the local convective heat flux q, the dimensionless form of which is

$$qL/k(T_0 - T_\infty)\mathrm{Gr}_L{}^{1/4} = -(\partial\theta/\partial Y)_{wx} \tag{23}$$

The dimensionless fin temperature distribution $(T_{wx} - T_\infty)/(T_0 - T_\infty)$ will also be presented.

Simplified Analysis. In the absence of the first-principles analysis that has been described in the foregoing sections of the paper, it would have been necessary somehow to adapt conventional fin theory to the natural convection case. An approach toward such an adaptation will now be described, and results will be obtained for comparison with those from the first-principles analysis.

The overall fin heat transfer rate based on conventional fin theory can be recast in the form

$$Q/k(T_0 - T_\infty)\mathrm{Gr}_L{}^{1/4} = 2(mL/N_{cc})\tanh mL \tag{24}$$

where

$$m = (h^*/k_f t)^{1/2} \tag{25}$$

The form of equation (24) was chosen so that the dimensionless representation of Q (left-hand side) corresponds to that on the left-hand side of equation (20). Equation (24) is based on the assumption that the heat transfer coefficient h^* is uniform along the fin, which is, in general, not true. For natural convection, the quandary about how to determine h^* for insertion into equation (25) is compounded because the heat transfer coefficients depend on the temperature variation along the fin.

Perhaps the most naive assumption that can be made is that h^* is equal to the average heat transfer coefficient corresponding to the base-to-ambient temperature difference $(T_0 - T_\infty)$. From the boundary layer similarity solution for $\mathrm{Pr} = 0.7$, h^* then follows as

$$h^* = (0.4709k/L)\mathrm{Gr}_L{}^{1/4} \tag{26}$$

so that, for this case,

$$mL = (0.4709N_{cc})^{1/2} \tag{27}$$

and

$$Q/k(T_0 - T_\infty)\mathrm{Gr}_L{}^{1/4} = (1.372/N_{cc}{}^{1/2})\tanh(0.4709N_{cc})^{1/2} \tag{28}$$

Equation (28) provides a simple predictive formula for the fin heat transfer as a function of the conduction-convection number N_{cc}.

The seemingly extreme naivete of basing h^* on $(T_0 - T_\infty)$ motivates the need for some refinement. Instead, let h^* be the average coefficient based on $(\overline{T}_{wx} - T_\infty)$, where $\overline{T}_{wx}$ is a mean fin temperature. Then,

$$h^* = (0.4709k/L)\mathrm{Gr}_L{}^{1/4}\,\bar{\theta}_{wx}{}^{1/4} \tag{29}$$

and

$$\begin{aligned} &Q/k(T_0 - T_\infty)\mathrm{Gr}_L{}^{1/4} \\ &\quad = (1.372\,\bar{\theta}_{wx}{}^{1/8}/N_{cc}{}^{1/2})\tanh(0.4709N_{cc}\bar{\theta}_{wx}{}^{1/4})^{1/2} \end{aligned} \tag{30}$$

Furthermore, if

$$\overline{T}_{wx} = \int_0^1 T_{wx}d(x/L) \tag{31}$$

then by using the fin temperature distribution from conventional fin theory, there follows

$$\bar{\theta}_{wx} = (1/mL)\tanh mL \qquad (32)$$

where

$$mL = (0.4709 N_{cc} \bar{\theta}_{wx}{}^{1/4})^{1/2} \qquad (33)$$

For the numerical evaluation of the dimensionless heat transfer rate from equation (30), the value of $\bar{\theta}_{wx}$ at a given N_{cc} is needed. Equations (32) and (33), taken together, provide a means for computing $\bar{\theta}_{wx}$, but these equations are too complex to permit a direct solution. They were, instead, solved by iteration, and the resulting $\bar{\theta}_{wx}$ for each given N_{cc} was introduced into equation (30) for the evaluation of the heat transfer. The results obtained from this approach will be presented shortly.

Results and Discussion

Overall Heat Transfer. The presentation of results will begin with the overall rate of heat transfer Q from the fin as a whole. The results for Q will be presented in two forms, both dimensionless. One of these, $Q/k(T_0 - T_\infty)\mathrm{Gr}_L{}^{1/4}$, involves physical variables explicitly, while the other is the fin efficiency η. Both of these groups are plotted as a function of the conduction-convection parameter $(kL/k_ft)\mathrm{Gr}_L{}^{1/4}$ in Fig. 2. The figure contains three curves. The solid line corresponds to the first-principles solution, while the single and double dot-dashed lines represent the results from the foregoing simple model based on conventional fin theory, respectively for a uniform heat transfer coefficient h^* corresponding to $(T_0 - T_\infty)$ and to $(\bar{T}_{wx} - T_\infty)$.

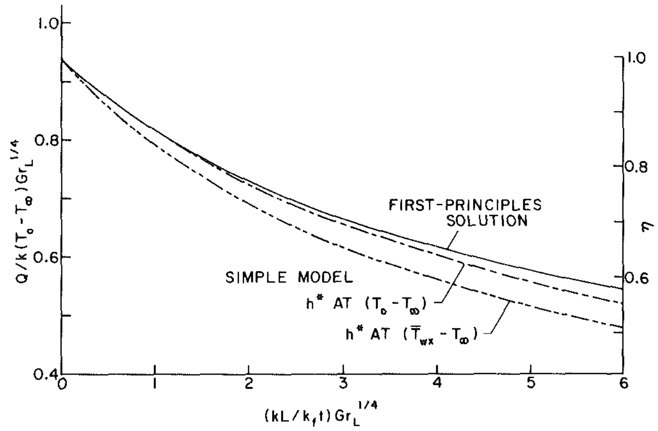

Fig. 2 Overall heat transfer and fin efficiency

If the curves are first regarded as a representation of the fin efficiency η, then their downsloping nature is readily rationalized. In this regard, it may be noted that, fundamentally, the fin efficiency is a measure of the departure of the fin temperature distribution from a uniform value T_0. Such departures are favored by higher convective heat transfer coefficients (i.e., by higher k and Gr_L), greater fin lengths L, and by lower fin conductances k_ft. Therefore, larger values of $(kL/k_ft)\mathrm{Gr}_L{}^{1/4}$ promote greater fin temperature nonuniformities and lower values of the efficiency η.

When the curves are viewed as representing the dimensionless heat transfer group of the left-hand ordinate, then trends with respect to fin-related parameters are readily identified. However, because Gr_L appears in both the ordinate and abscissa groups, the identification of natural-convection-related trends requires greater care. The downsloping trend of the curves indicates that, as expected, the fin heat transfer is increased as the fin conductance k_ft increases. Also, since the product of the ordinate and abscissa groups

$$[Q/k(T_0 - T_\infty)\mathrm{Gr}_L{}^{1/4}][(kL/k_ft)\mathrm{Gr}_L{}^{1/4}] \qquad (34)$$

increases with $(kL/k_ft)\mathrm{Gr}_L{}^{1/4}$, it follows that the heat transfer rate increases with the Grashof number, also not an unexpected result.

What is totally unexpected is the close proximity of the curves for the simple models to that for the first-principles analysis. Equally surprising is that the more naive version of the simple model, that in which h* corresponds to the root-to-ambient temperature difference $(T_0 - T_\infty)$, produces results closer to the first-principles curve than does the seemingly more rational evaluation of h^* at $(\bar{T}_{wx} - T_\infty)$. Indeed, it is easier to cite ample reasons to explain why such good agreement should *not* exist than to explain why it does exist. Two basic reasons can be cited which favor an absence of agreement: (1) the heat transfer coefficient is not uniform along the fin surface and (2) the evaluation of the heat transfer coefficient h^* at the root-to-ambient temperature difference should substantially overestimate the general level of the coefficient. Notwithstanding these, good agreement does prevail, as witnessed by Fig. 2. The possible reasons for the agreement will be examined as the local results are presented.

Local Heat Transfer Coefficients. The distribution of the local natural convection heat transfer coefficient along the fin surface is presented in Figs. 3–6 for representative values of the conduction-convection parameter $N_{cc} = (kL/k_ft)\mathrm{Gr}_L{}^{1/4} = 0.05, 0.75, 3$, and 6. The ordinate variable is the dimensionless group $hL/k\mathrm{Gr}_L{}^{1/4}$, all ingredients of which, other than the heat transfer coefficient, are independent of x; the abscissa variable is the dimensionless distance along the fin. Each figure contains five curves, although in some of the figures all curves are not fully distinct because of overlap. The legend given in Fig. 4 (the first of the set of figures where the curves are decisively distinct) applies to all of the figures.

The solid line conveys the results for the first-principles solution. To give perspective for these results, two curves have been plotted which are based on the similarity solution for uniform wall temperature for Pr = 0.7. That solution gives

$$h_{uwt} = (0.3532k/x)(g\beta\Delta T x^3/\nu^2)^{1/4} \qquad (35)$$

For the long-dashed curve, ΔT is taken equal to $(T_0 - T_\infty)$, whereas for the short-dashed curve ΔT was evaluated at the local temperature difference $(T_{wx} - T_\infty)$ given by the solution of the first-principles model. There are, in addition, two horizontal lines on each figure. These depict the h^* values for the simple model, respectively for h* corresponding to $(T_0 - T_\infty)$ and $(\bar{T}_{wx} - T_\infty)$.

Attention will first be focused on the results from the first-principles solution as displayed in the successive figures (i.e., the solid lines). In this regard, it may be recalled that increasing values of the conduction-convection number N_{cc} are indicative of larger variations of the temperature along the fin. It should also be noted that the fin temperature variation is such that the temperature increases in the flow direction (i.e., from the tip to the root). Thus, the successive figures, Figs. 3–6, show the response of the natural convection heat transfer coefficient to increasing streamwise variations of the fin temperature.

In Fig. 3, where N_{cc} is very nearly zero, the distribution of the heat transfer coefficient along the fin closely approximates the h versus x distribution for an isothermal plate. As seen from the figure, h decreases monotonically from the tip to the root, with the variations being relatively rapid near the tip and more gradual near the root. In Fig. 4, the heat transfer coefficient (solid line) displays a behavior that is quite unusual for natural convection boundary layer flows, namely, downstream of an initial sharp drop, the coefficient tends to level off and take on a constant value.

The behavior of the coefficient at higher values of the conduction-convection number (Figs. 5 and 6, solid lines) is even more unusual. In these figures, the h versus x distribution is characterized by an initial sharp drop which becomes more and more gradual with increasing x and ultimately leads to the attainment of a minimum, after which h increases steadily with x. As the conduction-convection number increases, the location of the minimum shifts toward the tip and the extent of the downstream rise becomes greater. Thus, for example, for $N_{cc} = 6$ (Fig. 6), the majority of the fin length is in a region of streamwise-increasing heat transfer coefficient.

Nonmonotonic distributions of the natural convection heat transfer coefficient characterized by a minimum and a subsequent streamwise increase are rarely encountered (the authors are not aware of similar

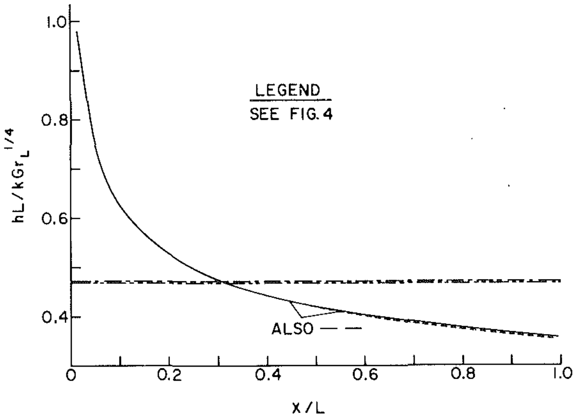

Fig. 3 Local heat transfer coefficients for $(kL/k_f t)\mathrm{Gr}_L{}^{1/4} = 0.05$

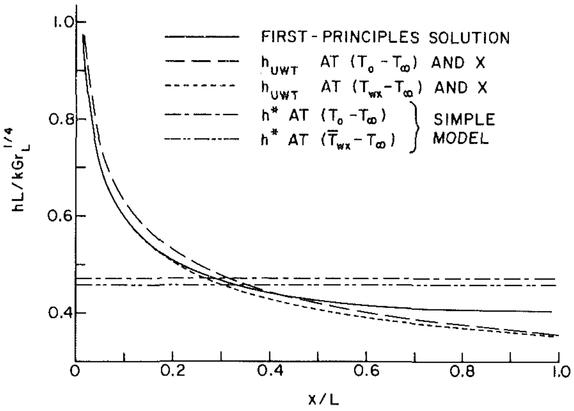

Fig. 4 Local heat transfer coefficients for $(kL/k_f t)\mathrm{Gr}_L{}^{1/4} = 0.75$

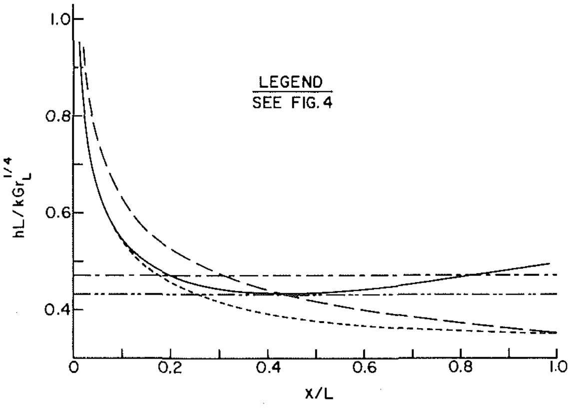

Fig. 5 Local heat transfer coefficients for $(kL/k_f t)\mathrm{Gr}_L{}^{1/4} = 3$

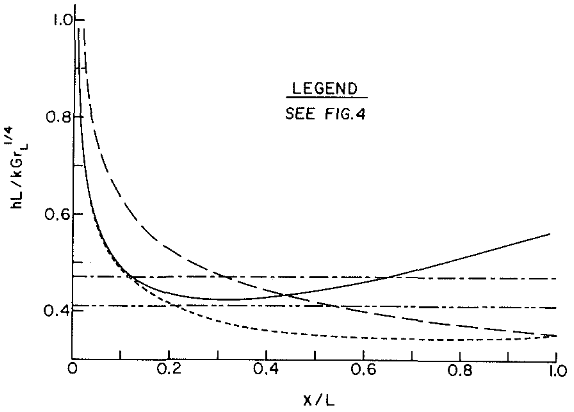

Fig. 6 Local heat transfer coefficients for $(kL/k_f t)\mathrm{Gr}_L{}^{1/4} = 6$

results in the published literature). The basic cause of this behavior is the streamwise increase of the temperature of the fin, which serves as the bounding wall for the natural convection flow. The wall temperature increase causes a streamwise increase in the buoyancy force which, in turn, gives rise to an additional acceleration of the flow.

The effects of this acceleration were examined by considering the quantities $U_{\max}/X^{1/2}$ and $Y_{\max}/X^{1/4}$, where $U_{\max}$ is the dimensionless maximum velocity in the boundary layer at a given station X, and $Y_{\max}$ is the dimensionless distance from the wall where $U_{\max}$ occurs. For a similarity solution, $U_{\max}/X^{1/2}$ and $Y_{\max}/X^{1/4}$ are independent of X. However, in the present problem, owing to the aforementioned additional acceleration, $U_{\max}/X^{1/2}$ was found to increase with X, while $Y_{\max}/X^{1/4}$ decreased. These findings signal the presence of enhanced velocities relatively close to the bounding wall, and it is this combination of factors which causes the downstream rise in the h versus x distribution. It is expected that this rise, which is attributable to buoyancy, would not be encountered in a forced convection boundary layer flow subjected to the same wall temperature variations.

Attention will now be turned to the relationship between the first-principles h versus x results and the others shown in Figs. 3–6. The two curves in each figure based on the h equation (35) for uniform wall temperature have been included to dramatize the uniqueness of the h versus x distribution from the first-principles solution. The h_{uwt} curve corresponding to $\Delta T = (T_0 - T_\infty)$, the long-dashed curve, displays a $X^{-1/4}$ variation and is, therefore, monotonically decreasing. When h_{uwt} is based on the local $\Delta T = (T_{wx} - T_\infty)$, the resulting (short-dashed) curve does show a leveling-off tendency close to the root for the larger values of N_{cc}. Indeed, at $N_{cc} = 6$ (the largest N_{cc} value used in the calculations), the short-dashed curve actually displays a shallow minimum and increases gradually thereafter. Note, however, that the short-dashed curve in each figure lies below that for the first-principles solution. Therefore, the local application of the uniform wall temperature formula underestimates the local heat transfer coefficient.

Consider next the dot-dashed horizontal lines in Figs. 3–6 which represent the uniform h^* values used as input for the simple model. Whereas these lines do not faithfully reproduce the details of the h versus x distributions from the first-principles solutions, they tend to lie in the same magnitude range, except at small x. It is interesting to note that, in general, the horizontal lines appear to deviate less from the h versus x distributions at larger N_{cc} than at very small N_{cc}, and it is the aforementioned additional buoyancy which is responsible for this tendency. Of the two horizontal lines in each figure, that corresponding to $(T_0 - T_\infty)$ appears to bear a closer kinship with the h versus x distribution.

We will now consider how the results of Figs. 3–6 can be used to rationalize the highly accurate predictions of the overall heat transfer Q from the simple model. To begin, it may be noted that

$$Q \sim \int_0^L h\theta_{wx}dx \tag{36}$$

For small values of N_{cc}, $\theta_{wx} \sim 1$, so that

$$Q \sim \int_0^L hdx, \quad \text{or} \quad Q \sim (1/L)\int_0^L hdx \tag{37}$$

Thus, for small N_{cc}, Q is proportional to the average heat transfer coefficient. If reference is made to Fig. 3, it may be verified that the horizontal lines correspond to the average of the h versus x distribution from the first-principles solution. Therefore, for small N_{cc}, the highly accurate Q predictions of the simple model are readily understood.

At large N_{cc}, a satisfactory rationalization is more difficult to achieve. For the condition that the same heat transfer rate Q is predicted by the first-principles solution and the simple model based on $(T_0 - T_\infty)$, equation (36) requires that

$$h^* = \int_0^L h\theta_{wx}dx \Big/ \int_0^L \theta^*{}_{wx}dx \tag{38}$$

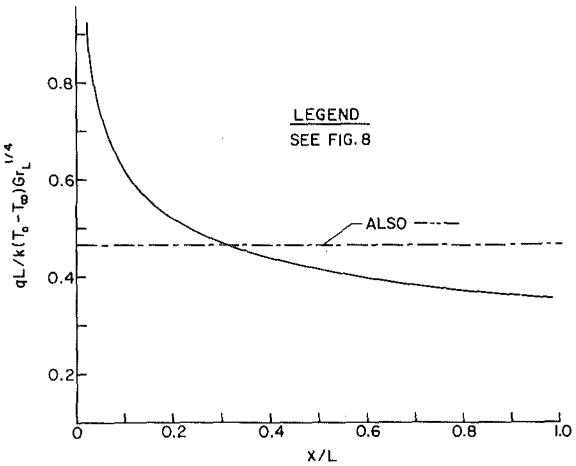

Fig. 7 Local convective heat flux distributions for $(kL/k_f t)\mathrm{Gr}_L^{1/4} = 0.05$

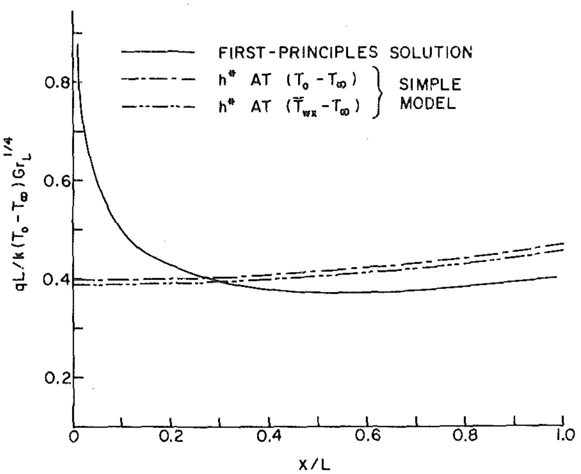

Fig. 8 Local convective heat flux distributions for $(kL/k_f t)\mathrm{Gr}_L^{1/4} = 0.75$

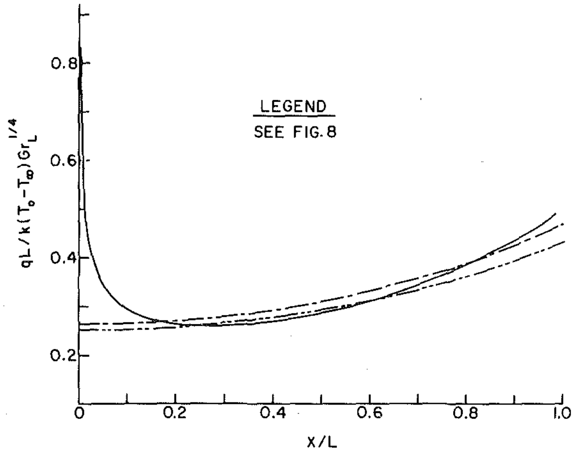

Fig. 9 Local convective heat flux distributions for $(kL/k_f t)\mathrm{Gr}_L^{1/4} = 3$

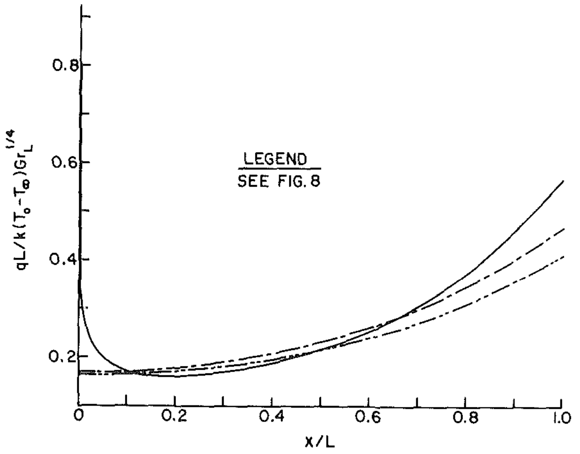

Fig. 10 Local convective heat flux distributions for $(kL/k_f t)\mathrm{Gr}_L^{1/4} = 6$

where θ^*_{wx} is the temperature distribution for the simple model. Equation (38) shows that to achieve the condition of equal Q values, it is inappropriate that h^* merely be the average of h, and this observation is valid even if $\theta^*_{wx} \simeq \theta_{wx}$ for all x. Therefore, the h distribution curves alone are not sufficient to explain the accurate Q predictions of the simple model. The rationalization must be sought elsewhere—specifically from the local heat flux results.

Local Heat Flux. Distributions of the dimensionless local convective heat flux at the fin surface are plotted in Figs. 7–10 as a function of x/L, respectively for $N_{cc} = 0.05, 0.75, 3$, and 6. Each figure contains three curves that are defined in the legend of Fig. 8. These include the first-principles solution and the simple model respectively based on h^* corresponding to $(T_0 - T_\infty)$ and $(\overline{T}_{wx} - T_\infty)$.

Figure 7 shows that at small N_{cc}, the heat flux distribution for the simple model is very nearly constant, whereas that from the first-principles solution yields high values of flux near the tip and lower values near the root. This finding stands in contrast to the conventional perception that the highest rates of convective heat transfer always occur adjacent to the root.

As N_{cc} increases, the simple model appears to track the heat flux distributions of the first-principles solution more faithfully. The precision of the tracking is different for different portions of the fin length and also depends on N_{cc}. In the neighborhood of the tip, the tracking is generally unsatisfactory and at large N_{cc}, deviations reemerge near the root.

The fact that there is general agreement at intermediate and large N_{cc} between the first-principles solution and the simple model can be attributed to the nature of the heat transfer coefficient distributions that emerge from the first-principles solutions. It is, in fact, the unexpected characteristics of the h versus x distribution that are decisive. In particular, the leveling off of the distribution encountered at intermediate N_{cc} and the downstream increase at larger N_{cc} are the essential features. Had h versus x been monotonic decreasing, there would have been a significant mismatch of the q results at all N_{cc} (similar to that shown in Fig. 7).

Since

$$Q = \int_0^L q dx \tag{39}$$

the remarkable accuracy of the simple model can be understood in terms of Figs. 7–10. The simple model underpredicts the convective heat transfer for certain portions of the fin and overpredicts it in other portions, but the overpredictions and underpredictions very nearly balance out. The additional buoyancy which shapes the h versus x distribution and brings the respective q distributions closer together must be given credit for the agreement of the Q predictions.

Fin Temperature Distributions. Representative results for the fin temperature distribution are presented in Fig. 11. As in the preceding figures for the heat flux, three curves are given for each value of N_{cc}. These curves encompass that for the first-principles solution and those for the simple model.

Figure 11 shows the expected trend whereby the fin temperature decreases monotonically from the root to the tip. The figure also confirms the prior assertions that larger values of N_{cc} give rise to larger fin temperature variations.

The most remarkable aspect of Fig. 11 is the close agreement between the temperature distributions of the first-principles solution and that of the simple model based on h^* corresponding to $(T_0 - T_\infty)$. The temperature distributions plotted in Fig. 11 can be thought of as solutions of equation (2) corresponding to given input values of h from Figs. 3–6. There are clear differences in evidence in those figures between the h^* lines and the h versus x distributions of the first-

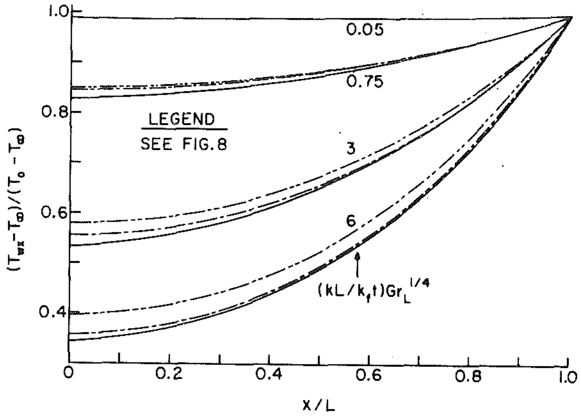

Fig. 11 Fin temperature distributions

principles solution. Yet, the temperature solutions of Fig. 11 are insensitive to these differences.

For explaining this finding, small values of N_{cc} may be regarded as indicative of a large overall thermal resistance, while large N_{cc} indicates a relatively small overall thermal resistance. When the thermal resistance is large, the temperature solution should be insensitive to the detailed nature of the h distribution. On the other hand, when the resistance is relatively low, a greater sensitivity can be expected. However, for the larger N_{cc}, the additional buoyancy works to reduce the differences between the h versus x distribution and h^*.

Concluding Remarks

The analysis that has been performed here has yielded a number of unexpected results. Natural-convection boundary layer heat transfer coefficients were encountered which do not decrease monotonically in the streamwise direction, as is customary. Rather, the coefficient decreased at first, attained a minimum, and then increased with increasing downstream distance. This behavior was attributed to an enhanced buoyancy associated with an increase in the wall-to-fluid temperature difference along the streamwise direction.

Another group of surprising findings was encountered when a simple adaptation of the conventional fin model was employed to provide heat transfer and temperature distribution results for comparison with the first-principles solution. The highly accurate predictions of the simple model were altogether unforeseen, and only in hindsight could they be reasonably rationalized.

If the relative magnitudes of T_∞ and T_0 were to be reversed from those shown in Fig. 1, then the direction of fluid flow would also reverse. Correspondingly, the wall-to-fluid temperature difference would decrease along the streamwise direction and, in all likelihood, the heat transfer coefficient would display a monotonic variation.

Acknowledgment

The research reported here was performed under the auspices of the National Science Foundation.

References

1 Sparrow, E. M., Baliga, B. R., and Patankar, S. V., "Forced Convection Heat Transfer from a Shrouded Fin Array with and without Tip Clearance," ASME JOURNAL OF HEAT TRANSFER, Vol. 100, 1978, pp. 572–579.

2 Stachiewicz, J. W., "Effect of Variation of Local Film Coefficients on Fin Performance," ASME JOURNAL OF HEAT TRANSFER, Vol. 91, 1969, pp. 21–26.

3 Lock, G. S. H. and Gunn, J. C., "Laminar Free Convection from a Downward-Projecting Fin," ASME JOURNAL OF HEAT TRANSFER, Vol. 90, 1968, pp. 63–70.

4 Ede, A. J., "Advances in Free Convection," in *Advances in Heat Transfer*, Vol. 4, 1967, pp. 1–64.

5 Starner, K. E. and McManus, H. N., Jr., "An Experimental Investigation of Free Convection Heat Transfer from Rectangular Fin Arrays," ASME JOURNAL OF HEAT TRANSFER, Vol. 85, 1963, pp. 273–278.

6 Welling, J. R. and Wooldridge, C. B., "Free Convection Heat Transfer Coefficients from Rectangular Vertical Fins," ASME JOURNAL OF HEAT TRANSFER, Vol. 87, 1965, pp. 439–444.

7 Chaddock, J. B., "Free Convection Heat Transfer from Vertical Rectangular Fin Arrays," *ASHRAE Journal*, Vol. 12, August, 1970, pp. 53–60.

8 Sparrow, E. M. and Bahrami, P. A., "Experiments on Natural Convection from Vertical Parallel Plates with Either Open or Closed Edges," ASME JOURNAL OF HEAT TRANSFER, Vol. 102, 1980, pp. 221–227.

9 Sparrow, E. M. and Hennecke, D. K., "Temperature Depression at the Base of a Fin," ASME JOURNAL OF HEAT TRANSFER, Vol. 92, 1970, pp. 204–206.

10 Sparrow, E. M. and Hsu, C. F., "Analytically Determined Fin-Tip Heat Transfer Coefficients," ASME JOURNAL OF HEAT TRANSFER, Vol. 103, No. 1, pp. 18–25.

11 Patankar, S. V. and Spalding, D. B., *Heat and Mass Transfer in Boundary Layers*, second ed., Intertext Books, London, 1970.

12 Eckert, E. R. G. and Drake, R. M., *Heat and Mass Transfer*, McGraw-Hill, New York, 1959.

G. S. Shiralkar
Graduate Assistant.

C. L. Tien
Professor.

Department of Mechanical Engineering,
University of California,
Berkeley, Calif. 94720

A Numerical Study of Laminar Natural Convection in Shallow Cavities

Heat transfer by natural convection in a horizontal cavity with adiabatic horizontal walls and isothermal side walls is investigated numerically for high aspect ratios (width/height). Comparison is made with existing analytical and experimental results. Agreement is generally good at moderate and high Prandtl numbers to which most previous works have been restricted. Improvements of the existing correlation have been proposed in regions of discrepancy. Extension to the low Prandtl number case, including the range of liquid metals, has been made on the basis of an analytical model for high Rayleigh numbers as well as by numerical solution of the full equations. The agreement between the two is found to be very good. A correlation for the heat transfer is proposed for each of the two different cases of high and low Prandtl number.

Introduction

A fairly extensive literature exists for enclosure heat transfer for small and intermediate aspect ratios and has been reviewed by Ostrach [1] and Catton [2]. Numerical work in this area is readily available [3–5]. Work on large aspect ratios (B = width/height ≥ 10), however, has been rather limited. In a series of papers, Cormack, et al. [6–9] investigated this problem by means of an asymptotic theory for very large B, applicable for all finite Prandtl numbers, and some numerical results and experiments applicable to moderate and high Prandtl numbers. The asymptotic theory was developed considerably by Bejan and Tien [10] into an approximate theory for large but finite aspect ratios, to cover the three regimes of $\mathrm{Ra} \rightarrow 0$, Ra intermediate and large Ra. The present work includes a numerical solution of the full equations for large but finite ($B \geq 10$) aspect ratios for varying Rayleigh and Prandtl numbers. Generally good agreement is found for moderately high Prandtl numbers but at lower Prandtl numbers in the boundary layer regime there is a clear dependence of the heat transfer on the Prandtl number, a conclusion that does not agree with the theory of Bejan and Tien. It is shown that this theory is more appropriate at high Prandtl numbers for finite aspect ratios. A model is proposed to account for the Prandtl number effect and the results are compared with the results of the present numerical study, with excellent agreement.

The Problem Formulation

The geometry of the problem is illustrated in Fig. 1. The enclosure is of a rectangular cross-section, with isothermal hot and cold vertical sides. The top and bottom walls are insulated. The flow is assumed laminar and two-dimensional. The fluid within is assumed to have constant properties except insofar as the buoyancy is concerned, i.e., the Boussinesq approximation of linear temperature dependence of density is utilized. The governing equations may be written in nondimensional form as:

$$\frac{1}{\alpha_\omega}\frac{\partial \omega}{\partial \tau} + \frac{\partial}{\partial x}\left(u\omega - \frac{\partial \omega}{\partial x}\right) + \frac{\partial}{\partial y}\left(v\omega - \frac{\partial \omega}{\partial y}\right) = \mathrm{Gr}\frac{\partial \theta}{\partial x} \tag{1}$$

$$\frac{1}{\alpha_\theta}\frac{\partial \theta}{\partial \tau} + \frac{\partial}{\partial x}\left(u'\theta - \frac{\partial \theta}{\partial x}\right) + \frac{\partial}{\partial y}\left(v'\theta - \frac{\partial \theta}{\partial y}\right) = 0 \tag{2}$$

$$\frac{1}{\alpha_\psi}\frac{\partial \psi}{\partial \tau} + \frac{\partial^2 \psi}{\partial x^2} + \frac{\partial^2 \psi}{\partial y^2} = -\omega \tag{3}$$

$$u = \partial\psi/\partial y, \; v = -\partial\psi/\partial x \tag{4a}$$

$$u' = u\mathrm{Pr}, \; v' = v\mathrm{Pr} \tag{4b}$$

where

$$x = X/h, \; y = Y/h$$

$$u = u''h/\nu, \; v = v''h/\nu$$

$$\theta = (T - T_c)/(T_H - T_c)$$

The boundary conditions are

$$\begin{aligned} &\psi = 0, u = v = 0, \theta = 1 && \text{at } x = 0 \\ &\psi = 0, u = v = 0, \theta = 0 && \text{at } x = \mathrm{B} \\ &\psi = 0, u = v = 0, \partial\theta/\partial y = 0 && \text{at } y = 0, 1 \end{aligned} \tag{5}$$

The heat transfer rate is given by:

$$\text{Local heat flux:} \quad \mathrm{Nu}_x = -(\partial\theta/\partial x)_{x=0} \tag{6}$$

$$\text{Total heat flux:} \quad \mathrm{Nu} = -\int_0^1 (\partial\theta/\partial x)_{x=0}\,dy \tag{7}$$

It will be noticed that a false diffusivity term has been added in equation (3) so that it may be cast in a false transient form suitable for numerical solution. Also the diffusivities in equations (1–2) do not correspond to their natural values of one and Pr^{-1}, respectively, but are selected according to the needs for convergence speed and stability of the numerical computation.

General Numerical Approach

A simple and rapidly converging method has been developed capable of studying high aspect ratio situations. It combines the use of the unconditionally stable 'exponential' differencing scheme with a mesh size that can be varied in either direction. Also, the method uses the alternating direction implicit (ADI) procedure for iteration in conjunction with under-relaxation. The equations themselves are solved in false transient form so that, effectively, different time steps are used for the different equations.

Each of the fields θ, ω, ψ is advanced one at a time until the following convergence criteria are all met for all variables ϕ:

$$|(\phi_{i,j}^{m+1} - \phi_{i,j}^{m})/(\phi_{i,j}^{m})|_{\max} < \epsilon_1 \tag{8}$$

$$|(\phi_{i,j}^{m+1} - \phi_{i,j}^{m})/(\phi_{i,j}^{m})|_{\max}/\Delta\tau_\phi < \epsilon_2 \tag{9}$$

and an overall energy balance is satisfied:

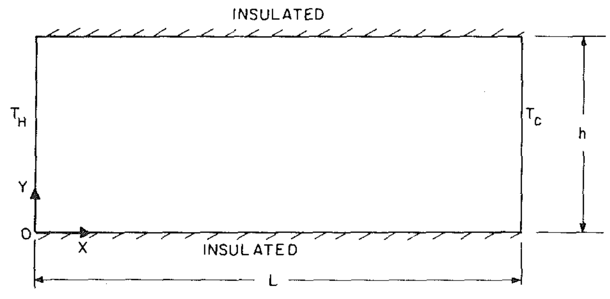

Fig. 1 Enclosure geometry

Contributed by the Heat Transfer Division for publication in the JOURNAL OF HEAT TRANSFER. Manuscript received by the Heat Transfer Division April 2, 1980.

$$\left|\frac{(\mathrm{Nu})_{x=0} - (\mathrm{Nu})_{x=B}}{(\mathrm{Nu})_{x=0}}\right| < \epsilon_3 \tag{10}$$

Typically, $\epsilon_1 = 10^{-4}$, $\epsilon_2 = 10^{-2}$ and $\epsilon_3 = 10^{-4}$. Also, since the problem possesses 'centrosymmetry', a visual check is made at the end of each run that

$$\theta(x - B/2, y) \simeq 1 - \theta(B/2 - x, -y) \tag{11}$$

$$u(x - B/2, y) \simeq -u(B/2 - x, -y) \tag{12}$$

$$v(x - B/2, y) \simeq -v(B/2 - x, -y) \tag{13}$$

This serves as a very useful check not only on the convergence but also on the ultimate correctness of the solution. For finite differencing equations (1–2) the exponential differencing scheme (EDS), put forward by Raithby and Torrance [11] and Spalding [12], was used. Although the EDS is unconditionally stable for single equations, the nonlinear coupling of the governing equations does lead to instabilities for large time steps. These could be overcome by additional under-relaxation for equation (1) and over-relaxation for equation (3). The optimum parameters were found to be 0.6 and 1.2 so that

$$\psi_{i,j}^{m+1} = \lambda\psi_{i,j}\Big|_{\mathrm{ADI}} + (1 - \lambda)\,\psi_{i,j}^{m},\ \lambda = 1.2 \tag{14}$$

$$\omega_{i,j}^{m+1} = \lambda\omega_{i,j}\Big|_{\mathrm{ADI}} + (1 - \lambda)\,\omega_{i,j}^{m},\ \lambda = 0.6 \tag{15}$$

With these optimum values of the relaxation parameter, a time step $\Delta\tau$ as large as 0.01 for the vorticity equation (1) could be used for the large majority of cases, although at high Rayleigh numbers (6×10^6) this had to be reduced to $\Delta\tau = 0.003$. The corresponding time steps for the energy and stream function equations were 5000 and 1000 times as large. Newell and Schmidt [13] varied the grid spacing by a coordinate transformation which was then finite differenced. In the present work the alternative of imposing a variable-sized grid directly on the original equations was selected, Fig. 2.

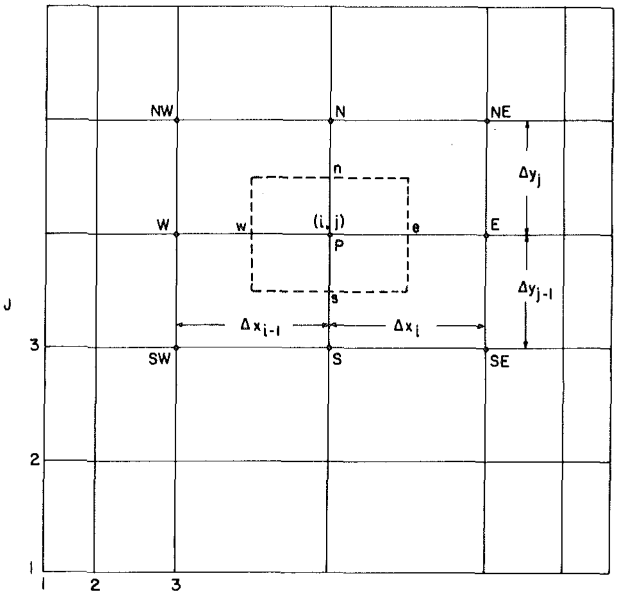

Fig. 2 Mesh outlay

For the boundary condition on the vorticity, the following form was used:

$$\omega_{i,1} = -2(\psi_{i,2} - \psi_{i,1})/\Delta y_1^2 \tag{16}$$

Moderate and High Prandtl Number Case

Numerical results have been obtained for a Prandtl number of unity and $1 \leqslant \mathrm{B} \leqslant 40$ and $\mathrm{Ra} \leqslant 6 \times 10^6$. Table 1 shows partial results for the Nusselt number obtained for a wide range of the Rayleigh number for varying aspect ratios for the case of Pr = 1. For B = 1, we find our results in very good agreement with those of Marshall, et al. [3]. Table 2 indicates the relative independence of the heat transfer on the

Table 1 Variations of the Nusselt number[a] for various Rayleigh numbers and aspect ratios (Pr = 1)

B	$\mathrm{Ra} = 10^3$	10^4	10^5	10^6	6×10^6
1	1.131	2.277	4.687	9.012	
10	0.104	0.303	2.442	6.987	12.26
	(0.102)	(0.225)	(2.059)	(7.573)	(13.11)
20	0.050	0.096	1.413	5.832	11.16
	(0.050)	(0.073)	(0.806)	(5.549)	(11.83)
30	0.033	0.056	0.781	5.003	10.62
	(0.033)	(0.041)	(0.392)	(4.121)	(10.65)
40	0.025	0.039	0.536	4.254	9.96
	(0.025)	(0.029)	(0.221)	(3.114)	(9.59)

[a] Numbers in parentheses are those based on the predictions of equation (17).

Table 2 Variations of the Nusselt number for different Prandtl numbers and Rayleigh numbers (B = 10)

Pr	$\mathrm{Ra} = 10^3$	10^4	10^5	10^6
0.01	0.102	0.196	0.796	2.533
0.03	0.103	0.262	1.320	3.636
0.06	0.103	0.290	1.699	4.394
0.10	0.103	0.301	1.865	4.951
0.30	0.103	0.309	2.318	6.039
1.0	0.104	0.303	2.442	6.987
10.0	0.102	0.316	2.544	7.352
100.0	0.102	0.327	2.625	7.502

Nomenclature

a = dimensionless temperature stratification, equation (22)
$B = L/h$ = aspect ratio
C = constant, equation (23)
g = gravitational acceleration
$\mathrm{Gr} = g\beta h^3\Delta T/\nu^2$ = Grashof number
h = enclosure height, Fig. 1
K_1 = constant of core flow
k = fluid thermal conductivity
L = enclosure width, Fig. 1
Nu = Nusselt number, equation (7)
Nu_x = local Nusselt number, equation (6)
Nu_∞ = asymptotic value of Nu
$\mathrm{Pr} = \nu/\sigma$ = Prandtl number
Ra = GrPr = Rayleigh number
T = temperature
T_c = cold wall temperature, Fig. 1
T_H = hot wall temperature, Fig. 1
$\Delta T = T_H - T_c$ = temperature difference
t = time
u'', v'' = velocities in x, y directions
u', $v' = u\mathrm{Pr}$, $v\mathrm{Pr}$ = dimensionless velocities
u, $v = u''h/\nu$, $v''h/\nu$ = dimensionless velocities
X, Y = Cartesian coordinates, Fig. 1
x, $y = X/h$, Y/h = dimensionless Cartesian coordinates
Δx, Δy = mesh spacing in x, y directions
α = general nondimensional fluid diffusivity
β = thermal expansion coefficient of fluid
γ = constant, equation (18)
γ_1, γ_2 = functions of B, equations (20, 21)
δ = boundary layer thickness
$\theta = (T - T_c)/\Delta T$ = dimensionless temperature
λ = relaxation factor
ν = fluid kinematic viscosity
$\psi = \psi'/\nu$ = dimensionless stream function
ψ' = stream function
σ = fluid thermal diffusivity
$\tau = \nu t/h^2$ = dimensionless time
$\Delta\tau$ = dimensionless time step
ω = dimensionless vorticity, equation (3)
$\omega' = \omega\mathrm{Pr}$ = dimensionless vorticity

Subscripts

ADI = alternating direction implicit
i, j = column, row number of a mesh point, Fig. 2
max = maximum
v = pertaining to velocity
℄ = centerline
ϕ, ω, θ, ψ = pertaining to variables ϕ, ω, θ, ψ, respectively

Superscripts

m = number of numerical iteration

Prandtl number for $\mathrm{Pr} > 1$. Table 1 also shows the corresponding Nusselt number predicted by Bejan and Tien [10]. The agreement is better at high Ra and at low Ra. In the intermediate range the agreement is somewhat worse. In our notation their correlation is

$$\mathrm{Nu} = \frac{1}{B}\left[1 + \left\{\left[\frac{(\mathrm{Ra}/B)^2}{362{,}880}\right]^n + [0.623\,\mathrm{Ra}^{0.2}B]^n\right\}^{1/n}\right] \tag{17}$$

where $n = -0.386$. Here, the boundary layer regime solution was predicted to be

$$\mathrm{Nu} = 0.623\,\gamma\,\mathrm{Ra}^{0.2} \tag{18}$$

The analysis for this equation, however, more accurately predicts the local heat flux at the cavity midheight, $y = 0.5$. Moreover, the quantity γ was chosen to be a constant equal to unity, a shrewd guess made on an order-of-magnitude basis. The present results indicate that it may be more appropriate to replace $\gamma = 1$ by $\gamma = \gamma(B)$, at large but finite B so as to account for the fact, Fig. 3, that the shape of the local heat flux variation along the wall varies (slightly) with B so that if $\mathrm{Nu} = (\mathrm{Nu})_{y=0.5}F$, then $F = F(B)$ for finite values of Ra and B.

The prediction of the theory, that at $y = 0.5$, near the wall $x = 0$,

$$\theta = 1 - 0.5(1 - e^{-2\mathrm{Nu}_{\not{c}}x} \cos 2\mathrm{Nu}_{\not{c}}x) \tag{19a}$$

was found to be in fairly good agreement with the present numerical results, Fig. 4. The predictions of Cormack, et al. [6] are also confirmed with respect to the structure of the flow in the center of the cavity called the core region. The core reveals essentially parallel streamlines (except near the center line $y = 0.5$ where streamlines close in). The profile of the horizontal velocity for the core, equation (19b) is shown in Fig. 5.

$$u = -K_1\mathrm{Gr}\,(y^3/6 - y^2/4 + y/12) \tag{19b}$$

Experimental data in this area are limited. Most of them [8] deal with parameters out of the range of the present computations such as $B \geqslant 50$, $\mathrm{Ra} = 10^7$, etc. We can, however, make the comparison with the experiment of Smart, Hollands and Raithby [14] for the case of low emissivities. While the temperature boundary conditions on the horizontal walls were not identical to those considered here, they noted that the form of the flow field outlined by [10] was probably applicable to their experiments. They were able to fit the form of the equation (17) for air as

$$\mathrm{Nu} = \frac{1}{B}[1 + \{[(\mathrm{Ra}/B)^2\,\gamma_1]^n + [\gamma_2\,\mathrm{Ra}^{0.2}\,B]^n\}^{1/n}] \tag{20}$$

where $n = -0.386$ and $\gamma_1(B)$ and $\gamma_2(B)$ for $B = 10$ were found to be 3.952×10^{-6} and 0.502, respectively. The results of the present study are compared in Table 3 with these experimental results. It is seen that the agreement is good to about 20 percent.

Based on the present study the following modification to equation (17) is proposed for $\mathrm{Pr} \geqslant 1$, $B \geqslant 10$:

$$\mathrm{Nu} = \frac{1}{B}\left[1 + \left\{\left[\left(\frac{\mathrm{Ra}}{B}\right)^2 \frac{\gamma_1(\mathrm{B})}{362{,}880}\right]^n + [\gamma_2(B)\mathrm{Ra}^{0.2}\,B]^n\right\}^{1/n}\right] \tag{21a}$$

where $n = -0.386$ and

$$\gamma_1(B) = (0.811 - 6.433 \times 10^{-3}B)^{-2.5907} \tag{21b}$$

$$\gamma_2(B) = (1.2425 + 4.5 \times 10^{-4}B)^{-2.5907} \tag{21c}$$

The mean deviation from the numerical data is 3.5 percent and the maximum deviation is 12.9 percent. Some numerical data are shown in Fig. 6 for graphical representation.

Low Prandtl Number Case

For low Prandtl number fluids, particularly in the liquid metal range, $\mathrm{Pr} \leqslant 0.06$, there is a clear dependence on the Prandtl number. It is evident that the theory of Bejan and Tien [10] does not apply as well to cases with low Pr as it does to high Pr. At low Pr, inertia effects will be significant. For $\mathrm{Pr} \ll 1$, it is possible to split up the end wall boundary layer into two regions, an inner region right next to the wall where friction is comparable in magnitude to inertia and an intermediate region a little further away where inertia is dominant.

In this boundary layer, the quantity $\partial\theta/\partial y$ is considered to be im-

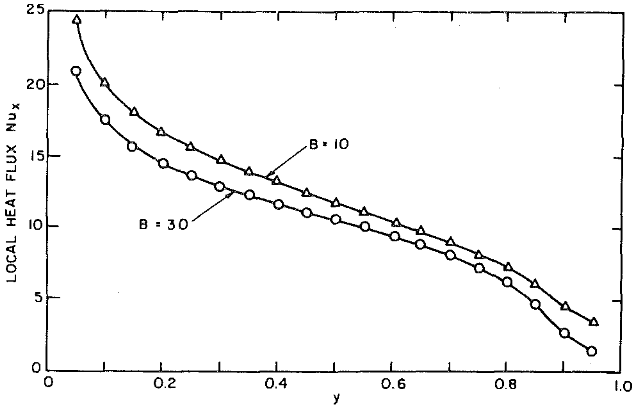

Fig. 3 Local heat flux along the hot wall for $\mathrm{Ra} = 6 \times 10^6$, $\mathrm{Pr} = 1$

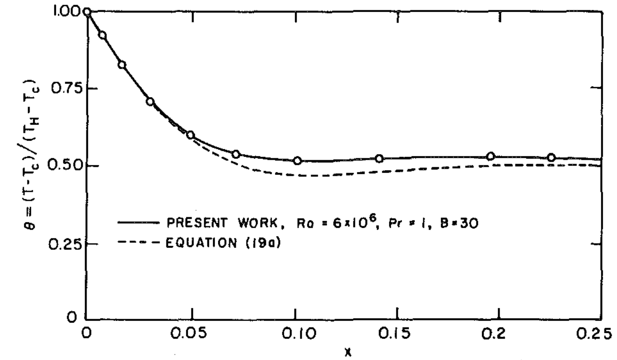

Fig. 4 Temperature profile near hot wall at $y = 0.5$ in the high Ra range

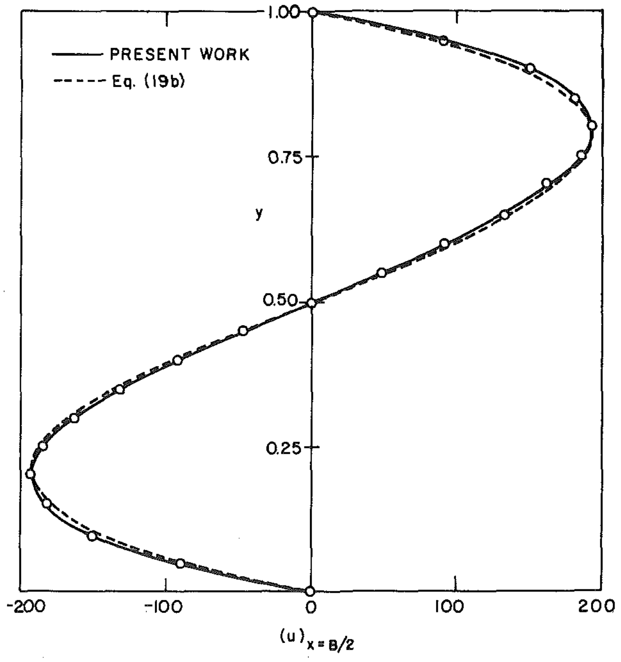

Fig. 5 Profile of horizontal velocity at cavity mid-section for $\mathrm{Ra} = 6 \times 10^6$, $\mathrm{Pr} = 1$, $B = 30$

Table 3 Comparison of the Nusselt number for air ($\mathrm{Pr} = 0.71$) found numerically with experiment [14], ($B = 10$)

Ra =	10^3	10^4	10^5	10^6	6×10^6
Nu [14]*	0.103	0.252	2.015	6.452	10.75
Nu [present]	0.103	0.310	2.407	6.701	11.85

* From equation (20).

posed by the core region at the midheight, in the manner of Gill [15] and Bejan and Tien [10]. In a similar way, the quantity $\partial\omega'/\partial y$ is replaced in the intermediate region of the boundary layer by the average value across it so that for the intermediate region

$$\partial\theta/\partial y = (\partial\theta/\partial y)_{\text{core}} = a,\ a > 0 \tag{22}$$

$$\partial\omega'/\partial y = \text{constant} = C \tag{23}$$

Following an order-of-magnitude analysis we may write for the intermediate region

$$(C/\text{Pr})v' = \text{Ra}\,\partial\theta/\partial x \tag{24}$$

$$a\ v' = \partial^2\theta/\partial x^2 \tag{25}$$

subject to the boundary condition $v' \rightarrow 0, \theta \rightarrow 0.5$ as $x \rightarrow \infty$. Since the objective here is to determine the functional dependence of Nu on Ra and Pr, it suffices to include only one of the inertia terms. In the inner region of the vertical boundary layer, energy convection is negligible so that

$$\partial^2\theta/\partial x^2 = 0 \tag{26a}$$

$$\frac{\partial^3 v'}{\partial x^3} - \frac{v'}{\text{Pr}}\frac{\partial\omega'}{\partial y} + \text{Ra}\frac{\partial\theta}{\partial x} = 0 \tag{26b}$$

with the boundary condition $v' = 0, \theta = 1$ at $x = 0$. The solution for the intermediate region is

$$v' = C_0 e^{a\text{RaPr}(x/C)},\ C < 0 \tag{27a}$$

$$\theta = \frac{C_0C^2}{(\text{RaPr})^2a}e^{a\text{RaPr}(x/C)} + 0.5 \tag{27b}$$

where C_0 is the characteristic velocity and the quantity $C/(-a\text{RaPr})$ plays the role of the boundary layer x scaling length. For the inner region, we may write

$$\theta = 1 - (\text{Nu})x \tag{28}$$

The matching between the regions for θ gives

$$C_0C^2/(\text{RaPr})^2a = 0.5 \tag{29a}$$

$$\text{Nu} = -(a\text{RaPr}/2C) \tag{29b}$$

From equation (27a) and $\omega' = \partial v'/\partial x$ is obtained $\omega' = C_0\ (a\text{RaPr}/C)\ e^{a\text{RaPr}(x/C)}$. Since x and y are independent coordinates, it is possible to first average ω' across the intermediate region and then differentiate with respect to y, in order to obtain C. Thus $C \simeq d/dy\ (C_0/\delta)$ where $\delta = -C/(a\text{RaPr})$.

The assumption is made that the characteristic scaling length for the velocity equation in the y direction is the height of the cavity, independent of Ra and Pr. The implication is that if $C_0/\delta \sim \text{Ra}^{m1}\text{Pr}^{n1}$, then $d(C_0/\delta)/dy \sim \text{Ra}^{m1}\text{Pr}^{n1}$, also. There follows

$$C \sim (C_0/\delta) \sim C_0\text{Nu} \tag{30}$$

In this and the following discussion, the ~ sign is taken to denote local power dependence on Ra and Pr, and not simply orders of magnitude. The exponents of Ra and Pr for Nu, for example, are the local slopes of the log Nu-log Ra curve and the log Nu-log Pr curve respectively, and may in general be variable. Balancing the powers on two sides of an equation is then equivalent to requiring that the equation be satisfied over the whole range of considered Ra and Pr.

Combining equations (29a, 29b) and (30) we obtain

$$\text{Nu} \sim (\text{RaPr})^{1/4}\,a^{1/2} \tag{31}$$

The quantity a represents the coupling between the end region boundary layers and the core, and can thus only be obtained from a consideration of the flow in the core. If the enclosure is assumed shallow enough so that a flow of the fully developed type is established, this leads to, by matching with the core, [10]:

$$a = (\partial\theta/\partial y)_{y=0.5} = K_1{}^2\text{Ra}/384$$

where $K_1 > 0$ is a constant of the flow equal to the axial temperature gradient so that equation (31) becomes $\text{Nu} \sim K_1\text{Ra}^{3/4}\,\text{Pr}^{1/4}$. Also, from [10], a consideration of the core flow gives, neglecting conduction, $\text{Nu} = (K_1{}^3\text{Ra}^2)/362{,}880$. Combining these two results yields

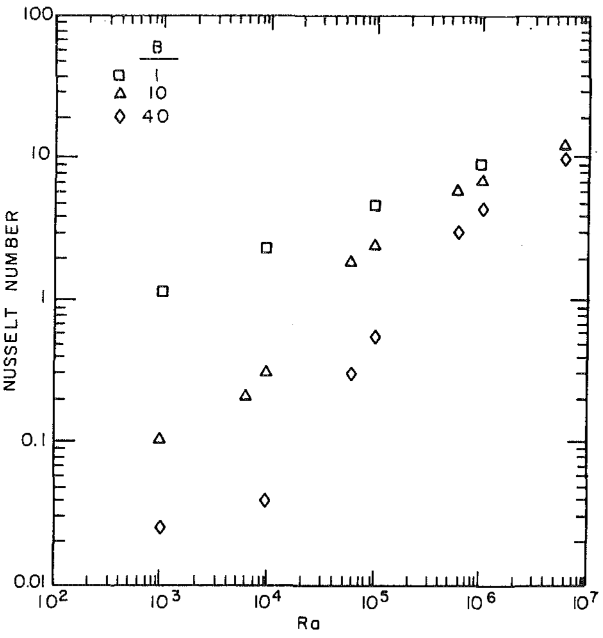

Fig. 6 Nusselt number for various aspect ratios (Pr = 1)

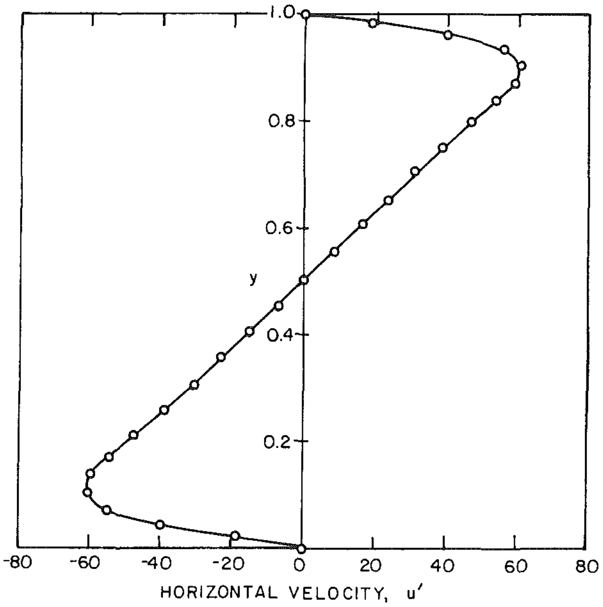

Fig. 7 Core velocity profile for Ra = 10^6, Pr = 0.01, B = 10

$$\text{Nu} \sim \text{Ra}^{1/8}\,\text{Pr}^{3/8} \tag{32}$$

Equation (32) remains to be verified. Comparison with the numerical results for B = 10, indicates that even at this large aspect ratio, at Ra = 10^6, the core flow is not fully developed; on the contrary, the core contains forming velocity boundary layers along the horizontal walls, Fig. 7. For low Pr, B must be exceedingly large for a fully developed type of flow to exist in the core. The case of boundary layers in the core is considered below.

For the central part of the core (y near 0.5), on the assumption of scales for x, y as $x = 0(B)$ and $y = 0(1)$, the equations can be simplified, following an order of magnitude analysis, to

$$1/\text{Pr}\ u'\ \partial\omega'/\partial x = \text{Ra}\,\partial\theta/\partial x \tag{33a}$$

$$\partial^2\theta/\partial y^2 = 0 \tag{33b}$$

where $\omega' \simeq -\partial u'/\partial y$. Again, only one inertia term has been included. The boundary conditions are $u' = 0, \theta = 0.5$ at $y = 0.5$. In the horizontal boundary layer next to the bottom wall, the following equations apply:

$$\frac{1}{\text{Pr}} u' \frac{\partial \omega'}{\partial x} = \text{Ra} \frac{\partial \theta}{\partial x} - \frac{\partial^3 u'}{\partial y^3} \tag{34a}$$

$$\partial^2\theta/\partial y^2 = 0 \tag{34b}$$

and with the boundary condition $u' = 0, \partial\theta/\partial y = 0$ at $y = 0$. The solution to equations (33a) and (33b) after matching with the boundary layer is

$$u' = b_2(x)\,(y - 0.5),\ b_2(x) > 0 \tag{35a}$$

$$\theta = 0.5 + a(x)\,(y - 0.5),\ a(x) > 0 \tag{35b}$$

such that $b_2\, db_2/dx = -\text{RaPr}\, da/dx$. For the boundary layer near $y = 0$:

$$\theta = (1 - a)/2 \tag{36a}$$

For the boundary layer near $y = 1$, similarly

$$\theta = (1 + a)/2 \tag{36b}$$

The quantity a in equation (31) is now seen to represent the temperature difference between the upper hotter and lower colder wall in the core, since in the boundary layer regime the core temperature gradient da/dx is negligible, being orders of magnitude less than $1/B$. Our numerical results clearly indicate that a is an increasing function of Ra, but increasing slower at higher Ra. This is not unexpected, for a should gradually increase with Ra and asymptotically approach 1 as Ra → ∞ for a given (low) Pr. In the asymptotic behavior for high Ra and low Pr, therefore, we expect $a \rightarrow 1$ so that from equation (31)

$$\text{Nu}_\infty \sim \text{Ra}^{1/4}\,\text{Pr}^{1/4} \tag{37}$$

where Nu_∞ is the asymptotic value of Nu.

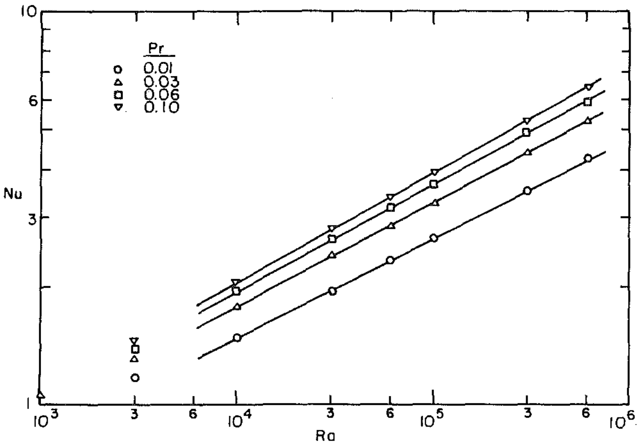

Fig. 8 Nusselt number for low Prandtl number as a function of Ra

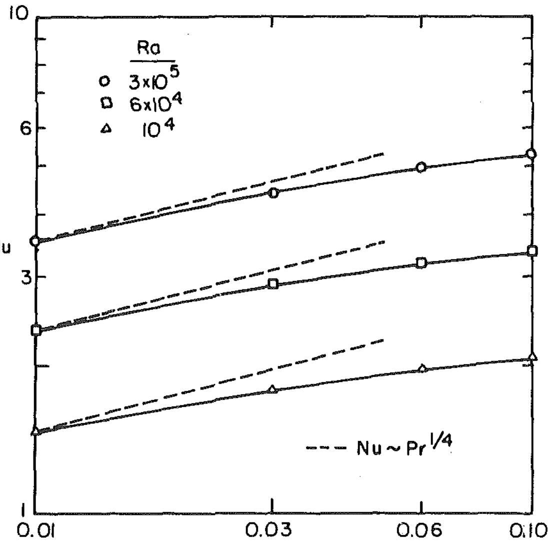

Fig. 9 Nusselt number as a function of (low) Pr

Results and Discussion

Results obtained for $B = 10$ and $0.1 \geq \text{Pr} \geq 0.01$, Table 2, show a slope of almost 0.5 on a log (Nu) – log (Ra) plot. However, this high slope is due to the flow at this point being in transition into the core boundary layer regime, and far from the asymptotic limit. For Pr = 0.01 and Ra = 10^6 for example, the temperature of the midpoint of the upper hotter plate is only 0.59. In order to further investigate the asymptotic behavior of Nu, the numerical calculations were extended to $B = 1$. While the enclosure is no longer shallow, it is expected that some of the qualitative features would be preserved. Thus, we anticipate that the flow would be more 'into' the core boundary layer regime, and so closer to the asymptotic behavior in that the momentum generated at the end walls would be so great as to overpower the enclosure flow resistance with a consequent independence of the heat transfer on the aspect ratio. The numerical results for B = 1, $0.01 \leq \text{Pr} \leq 0.1$ and $10^3 \leq \text{Ra} \leq 6 \times 10^5$ are shown in Figs. 8 and 9. For $B = 1$, Ra = 10^5, Pr = 0.01 for example, the temperature at the midpoint of the upper wall is already 0.80 indicating that the penetration into the regime characterized by core boundary layers is substantial. The asymptotic trend as Ra increases and Pr decreases can be seen from Figs. 8 and 9. This flow regime, in accordance with the prediction, equation (31), is not characterized by a simple power law behavior, and Nu approaches Nu_∞ only asymptotically. An interesting feature of this regime is that for a given low Pr, the asymptotic trend towards $m_1 = 0.25$ (for $\text{Nu} \sim \text{Ra}^{m_1}$) is from values of m_1 greater than 0.25 as Ra increases, and from values of n_1 less than 0.25 (for $\text{Nu} \sim \text{Pr}^{n_1}$) as Pr → 0 for a given value of Ra. Thus it would be difficult to correlate the heat transfer according to $\text{Nu} \sim (\text{RaPr})^{m_1}$ for any value of m_1 not very close to 0.25.

The changing in the exponent within this one regime corresponds to a changing of the extent of the coupling between the vertical end wall boundary layer region and the core. The effect of increasing Ra (or decreasing Pr) is to increase the relative importance of inertia with respect to flow resistance of the enclosure. In this asymptotic process, therefore, the sensitivity to the aspect ratio should continuously decrease, so that if $\text{Nu} \sim B^{-n_1}$, then n_1 should be a decreasing function of Ra. As Ra → ∞, for a given low Pr, the end regions become independent of the core, and also of B.

The following correlations are proposed for the heat transfer for $B = 1$ based on the numerical results:

$$\text{Pr} = 0.01;\ \text{Nu} = 0.1344\ \text{Ra}^{0.259} \tag{38}$$

$$\text{Pr} = 0.03;\ \text{Nu} = 0.1521\ \text{Ra}^{0.266} \tag{39}$$

$$\text{Pr} = 0.06;\ \text{Nu} = 0.1613\ \text{Ra}^{0.271} \tag{40}$$

$$\text{Pr} = 0.10;\ \text{Nu} = 0.1605\ \text{Ra}^{0.277} \tag{41}$$

The correlations are each based on six points between $10^4 \leq \text{Ra} \leq 6 \times 10^5$ and have a mean deviation of less than 0.6 percent. It can be seen that the effect of lowering Pr is to bring the exponent on Ra closer to its asymptotic value of 0.25.

The numerical results also show that the highest Pr dependence occurs at the lowest Pr, increasing slightly at higher Ra. Thus, at Ra = 3×10^5, $\text{Nu} \sim \text{Pr}^{0.202}$ between Pr = 0.01 and Pr = 0.03, while at Ra = 6×10^4, between Pr = 0.06 and Pr = 0.1, this is only $\text{Nu} \sim \text{Pr}^{0.122}$. Accounting for this variation at the low end of the Pr results, and at the high end of the Ra results, and extrapolating, the following correlation is proposed for the asymptotic heat transfer:

$$\text{Nu}_\infty = 0.35\ \text{Ra}^{0.25}\text{Pr}^{0.25} \tag{42}$$

This is expected to be applicable for shallow and square enclosures, independent of B.

Summary

Heat transfer in shallow ($B \geqslant 10$) enclosures has been investigated numerically for both moderate and low Prandtl numbers. For the moderate Pr case, comparison with earlier work has been made, and a new correlation for the heat transfer proposed, accounting for the aspect ratio dependence. Based on the numerical results, a model has been proposed for the low Pr case, which agrees very well with the final results for the heat transfer behavior. Correlations for the heat transfer for low Pr have been given.

Acknowledgment

The authors wish to acknowledge the support of the National Bureau of Standards Center for Fire Research through Grant No. 809253.

References

1 Ostrach, S., "Natural Convection in Enclosures," *Advances in Heat Transfer*, Vol. 8, 1972, pp. 161–227.

2 Catton, I., "Natural Convection in Enclosures," Keynote Paper, 6th International Heat Transfer Conference, Toronto, 1978, Vol. 6, 1979, pp. 13–43.

3 Marshall, R. S., Heinrich, J. C., and Zienkiewicz, O. C., "Natural Convection in a Square Enclosure by a Finite Element Penalty Function Method Using Primitive Fluid Variables," *Numerical Heat Transfer*, Vol. 1, 1978, pp. 315–330.

4 Jones, I. P., "A Numerical Study of Natural Convection in an Air-Filled Cavity: Comparison with Experiment," *Numerical Heat Transfer*, Vol. 2, 1979, pp. 193–214.

5 Wilkes, J. O., and Churchill, S. W., "The Finite Difference Computation of Natural Convection in a Rectangular Enclosure," *AIChE Journal*, Vol. 12, 1966, pp. 161–178.

6 Cormack, D. E., Leal, L. G., and Imberger, J., "Natural Convection in a Shallow Cavity with Differentially Heated End Walls. Part 1: Asymptotic Theory," *Journal of Fluid Mechanics*, Vol. 65, 1974, pp. 209–229.

7 Cormack, D. E., Leal, L. G. and Seinfeld, J. H., "Natural Convection in a Shallow Cavity with Differentially Heated End Walls. Part 2: Numerical Solutions," *Journal of Fluid Mechanics*, Vol. 65, 1974, pp. 231–246.

8 Imberger, J., "Natural Convection in a Shallow Cavity with Differentially Heated End Walls. Part 3: Experimental Results," *Journal of Fluid Mechanics*, Vol. 65, 1974, pp. 247–260.

9 Cormack, D. E., Stone, G. P. and Leal, L. G., "The Effect of Upper Surface Conditions on Convection in a Shallow Cavity with Differentially Heated End Walls," *International Journal of Heat and Mass Transfer*, Vol. 18, 1975, pp. 635–648.

10 Bejan, A., and Tien, C. L., "Laminar Natural Convection Heat Transfer in a Horizontal Cavity with Different End Temperatures," ASME JOURNAL OF HEAT TRANSFER, Vol. 100, 1978, pp. 641–647.

11 Raithby, G. D., and Torrance, K. E., "Upstream-Weighted Differencing Schemes and Their Application to Elliptic Problems Involving Fluid Flow," *Computers and Fluids*, Vol. 2, 1974, pp. 191–206.

12 Spalding, D. B., "A Novel Finite Difference Formulation for Differential Expressions Involving Both First and Second Derivatives," *International Journal of Numerical Methods in Engineering*, Vol. 4, 1972, pp. 551–559.

13 Newell, M. E., and Schmidt, F. W., "Heat Transfer by Laminar Natural Convection within Rectangular Enclosures," ASME JOURNAL OF HEAT TRANSFER, Vol. 92, 1970, pp. 159–168.

14 Smart, D. R., Hollands, K. G. T., and Raithby, G. D., "Free Convection Heat Transfer Across Rectangular-Celled Diathermous Honeycombs," presented at ASME Winter Annual Meeting, New York, N.Y., Dec 2–7, 1979.

15 Gill, A. E., "The Boundary-Layer Regime for Convection in a Rectangular Cavity," *Journal of Fluid Mechanics*, Vol. 26, 1966, pp. 515–536.

C. E. Hickox
Sandia National Laboratories,[1]
Albuquerque, N.M. 87185
Mem. ASME

Thermal Convection at Low Rayleigh Number from Concentrated Sources in Porous Media

A simple mathematical theory is proposed for the analysis of natural convective motion, at low Rayleigh number, from a concentrated source of heat in a fluid-saturated porous medium. The theory consists of retaining only the leading terms of series expansions of the dependent variables in terms of the Rayleigh number, is thus linear, and is valid only in the limit of small Rayleigh number. Based on fundamental results for a variety of isolated sources, superposition is used to provide solutions for situations of practical interest. Special emphasis is given to the analysis of sub-seabed disposal of nuclear waste.

Introduction

It has been suggested by Bishop and Hollister [1] that the mid-plate, mid-gyre regions of the major oceanic basins be investigated as possible repositories for high level radioactive waste. It was proposed that solidified nuclear waste be encapsulated in suitably designed containers and implanted in the seabed below the surface of the sedimentary layer. This scheme would provide a series of barriers to the release of radionuclides into the environment.

One such potential barrier is the seabed material itself which, although composed primarily of very fine, compacted clay, is still sufficiently permeable to permit interstitial pore water migration. An implanted container of waste material, which is generating heat, can cause an upward migration of pore water due to thermally induced convective motion. Interstitial water motion is a key parameter in studies of radionuclide transport which can ultimately determine the effectiveness of the seabed as a barrier to the release of radionuclides into the water column.

In this paper, a simple mathematical model is proposed for the analysis of thermal convection from a concentrated source of heat in a fluid-saturated porous medium of low permeability. It is assumed that the Rayleigh number (Ra) associated with the natural convection process is small enough so that the temperature distribution is unaffected by the fluid motion and is established by thermal conduction. This assumption is shown to be reasonable for parameters typical of the seabed. The temperature field is then used to predict the associated velocity distribution through use of Darcy's law and the Boussinesq approximation. In essence, the theory is developed by retaining only the leading terms of series expansions of the dependent variables in terms of the Rayleigh number. This general approach has been utilized previously by several authors. Yamamoto [2] used a Rayleigh number expansion to obtain a solution for the steady natural convection induced by a constant temperature sphere embedded in an infinite porous medium. Steady thermal convection induced by a variety of concentrated sources was studied by Hickox [3] for the limiting case of small Rayleigh number, $\mathrm{Ra} \to 0$. Bejan [4] presented solutions, in terms of power series in Ra, for transient and steady natural convection induced by a concentrated heat source in an infinite porous medium. Most recently, Hodgkinson [5] obtained solutions for thermal convection associated with an idealized spherical nuclear waste repository in a permeable rock mass, also for the limiting case of small Rayleigh number.

Simple, algebraic solutions are obtained for the steady-state thermal and flow fields induced by point and line sources as well as those resulting from a constant temperature sphere embedded in a semi-infinite, fluid-saturated, porous region below a horizontal, permeable boundary on which the temperature and pressure are constant. Based on the work of Bejan, the transient response to an embedded point source is also analyzed for the same geometry. Application of these results to the sub-seabed disposal of nuclear waste is considered. A solution which describes the steady natural convection due to a point source situated at the base of a semi-infinite region is also presented. All solutions are valid only for the limiting case of small Rayleigh number.

Basic Theory

In this section, a mathematical model is developed for the description of axisymmetric free convection produced by a concentrated source in a fluid-saturated porous medium. The porous medium is assumed to be rigid, homogeneous, and isotropic and the fluid incompressible, with density changes occurring only as a result of changes in the temperature according to

$$\rho = \rho_\infty [1 - \beta(T - T_\infty)], \tag{1}$$

where ρ is the density, T is the temperature, β is the coefficient of thermal expansion, and the subscripts refer to reference conditions. In accordance with the usual Boussinesq approximation, density changes are accounted for only in the buoyancy term in the equations of motion. It is also assumed that the fluid and porous matrix are in thermal equilibrium and that the fluid motion can be adequately described by Darcy's law. Permeability, viscosity, thermal conductivity, thermal capacity, and the coefficient of thermal expansion are assumed constant and dispersion effects are neglected.

The equation of continuity, Darcy's law, and the energy equation are then

$$\operatorname{div} \mathbf{v} = 0, \tag{2}$$

$$\frac{\mu}{k}\mathbf{v} = -\operatorname{grad} P - \rho g \operatorname{grad} z, \tag{3}$$

$$(\rho c_p)_e \frac{\partial T}{\partial t} + \rho_\infty c_p \mathbf{v} \cdot \operatorname{grad} T = \kappa_e \operatorname{div} (\operatorname{grad} T), \tag{4}$$

where $\mathbf{v}$, k, μ, κ_e, P, g, ρ, and c_p are, respectively, the velocity vector, permeability, dynamic viscosity, effective thermal conductivity, pressure, acceleration due to gravity, density, and specific heat. The subscript e refers to effective values. The elevation z is measured vertically upward.

Since only axisymmetric convection is to be considered, it is convenient for purposes of analysis to write equations (2–4) in terms of spherical polar coordinates (R, Φ) with associated velocity components (v_R, v_Φ). In subsequent developments, it will be helpful to also make use of the cylindrical polar coordinates (r, z) with associated velocity components (v_r, v_z). The relationship between the two coordinate systems is illustrated in Fig. 1. The continuity relation given by equation (2) is identically satisfied through the introduction of an appropriately defined stream function ψ, and the pressure is eliminated by the cross-differentiation of the components of equation (3) after substituting for the density from equation (1).

Contributed by the Heat Transfer Division for publication in the JOURNAL OF HEAT TRANSFER. Manuscript received by the Heat Transfer Division July 31, 1980.

[1] A U.S. Department of Energy Facility.

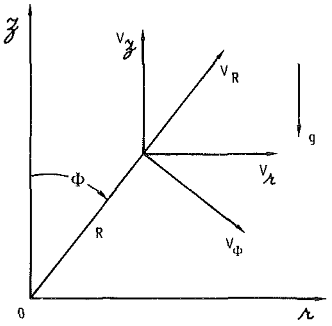

Fig. 1 Axisymmetric coordinate systems

After implementation of the procedure described above, it is also convenient to write the resulting equations in nondimensional form through the introduction of the nondimensional parameters

$$r = R/L, \quad \mathfrak{z}' = \mathfrak{z}/L, \quad \tau = t\kappa_e/(\rho c_p)_e L^2,$$

$$(V_R, V_\Phi) = \frac{\rho_\infty c_p L}{\kappa_e}(v_R, v_\Phi), \quad \Psi = \frac{\rho_\infty c_p}{\kappa_e L}\psi,$$

$$\theta = \frac{\kappa_e L}{Q}(T - T_\infty), \tag{5}$$

where Q is the rate of energy release from the concentrated source and L is an appropriately chosen length scale. For those situations in which there is no obvious physical length scale (e.g., point source in an infinite region), it is usually convenient to set $L = k^{1/2}$. Equations (1–4) can now be written in final, non-dimensional form, as

$$\frac{1}{r^2}\frac{\partial}{\partial\Phi}\left(\frac{1}{\sin\Phi}\frac{\partial\Psi}{\partial\Phi}\right) + \frac{1}{\sin\Phi}\frac{\partial^2\Psi}{\partial r^2} = \text{Ra}\left(\cos\Phi\frac{\partial\theta}{\partial\Phi} + r\sin\Phi\frac{\partial\theta}{\partial r}\right), \tag{6}$$

$$\frac{\partial\theta}{\partial\tau} + \frac{1}{r^2\sin\Phi}\left(\frac{\partial\Psi}{\partial\Phi}\frac{\partial\theta}{\partial r} - \frac{\partial\Psi}{\partial r}\frac{\partial\theta}{\partial\Phi}\right) = \frac{1}{r^2}\frac{\partial}{\partial r}\left(r^2\frac{\partial\theta}{\partial r}\right) + \frac{1}{r^2\sin\Phi}\frac{\partial}{\partial\Phi}\left(\sin\Phi\frac{\partial\theta}{\partial\Phi}\right), \tag{7}$$

where Ra is the Rayleigh number

$$\text{Ra} = \frac{k\rho_\infty{}^2 c_p g\beta Q}{\kappa_e{}^2\mu}, \tag{8}$$

and the velocities are related to the stream function by

$$V_R = \frac{1}{r^2\sin\Phi}\frac{\partial\Psi}{\partial\Phi}, \quad V_\Phi = -\frac{1}{r\sin\Phi}\frac{\partial\Psi}{\partial r}. \tag{9}$$

In the limit of small Rayleigh number, solutions to equations (6) and (7) can be sought through expansion of the dependent variables in power series in Ra, viz

$$\Psi = \Psi_0 + \text{Ra}\Psi_1 + \text{Ra}^2\Psi_2 + \ldots,$$

$$\theta = \theta_0 + \text{Ra}\theta_1 + \text{Ra}^2\theta_2 + \ldots. \tag{10}$$

The zeroth-order functions correspond to a state of pure conduction, hence there is no fluid motion and $\Psi_0 = 0$. The zeroth-order temperature distribution is obtained from the solution of

$$\frac{\partial\theta_0}{\partial\tau} = \frac{1}{r^2}\frac{\partial}{\partial r}\left(r^2\frac{\partial\theta_0}{\partial r}\right) + \frac{1}{r^2\sin\Phi}\frac{\partial}{\partial\Phi}\left(\sin\Phi\frac{\partial\theta_0}{\partial\Phi}\right). \tag{11}$$

The first non-zero contribution to the stream function is then found from the solution of

$$\frac{1}{r^2}\frac{\partial}{\partial\Phi}\left(\frac{1}{\sin\Phi}\frac{\partial\Psi_1}{\partial\Phi}\right) + \frac{1}{\sin\Phi}\frac{\partial^2\Psi_1}{\partial r^2} = \cos\Phi\frac{\partial\theta_0}{\partial\Phi} + r\sin\Phi\frac{\partial\theta_0}{\partial r}. \tag{12}$$

In the examples which follow, only solutions to the linear system comprised of equations (11) and (12) will be considered. The linearity of this system can be used to advantage in that superposition of certain basic solutions is thus allowed. However, all solutions are then, of necessity, limited to cases for which the Rayleigh number is small ($\text{Ra} \to 0$).

Also, in the cases to be considered subsequently, thermal energy is released continuously at a finite rate from a concentrated source. Hence, in the absence of any bounding surfaces which can inhibit motion, any deviation from an isothermal state will result in fluid motion. Therefore, no lower limit for the occurrence of natural convective motion is expected.

Fundamental Solutions

In this section, certain fundamental solutions to equations (11) and (12) are identified for concentrated sources in an unbounded region. These results then form the basis for superposition models involving more complex boundary geometries. Since it is a straightforward exercise to verify that the quoted results satisfy the appropriate differential equations, details of the solution procedure are omitted.

Steady-State Point Source. When a point source of strength Q is located at the origin of the coordinate system, the appropriate steady-state solutions for the temperature and stream function are

$$\theta_0 = \frac{1}{4\pi r}, \quad \Psi_1 = \frac{1}{8\pi}r\sin^2\Phi. \tag{13a,b}$$

From this result, it is apparent that there is a singularity at the origin, and $(T - T_\infty)$ as well as the velocity components approach zero for large r. Additional terms in the series expansion are available in the paper by Bejan. Also, a numerical solution for this situation based on the use of similarity transformations, and valid for any Rayleigh number, is presented by Hickox and Watts [6].

Transient Point Source. If a point source of strength Q is placed at the origin at time $\tau = 0$, Bejan has shown that the transient response

Nomenclature

a = radius of sphere
c_p = specific heat
D = burial depth for heat source
g = acceleration of gravity
H = length of line source
k = permeability
L = reference length
P = pressure
Q = strength of heat source
R = radial distance, spherical coordinates
r = normalized spherical radial coordinate
$\mathfrak{r}$ = radial distance, cylindrical coordinates
Ra = Rayleigh number
s = integration variable for line source
T = temperature
t = time
$\mathbf{v}$ = velocity vector
v_R, v_Φ = velocity components in spherical coordinates
V_R, V_Φ = nondimensional velocity components in spherical coordinates
$v_{\mathfrak{r}}$, $v_{\mathfrak{z}}$ = velocity components in cylindrical coordinates
$V_{\mathfrak{r}}$, $V_{\mathfrak{z}}$ = nondimensional velocity components in cylindrical coordinates
$\mathfrak{z}$ = vertical coordinate
β = coefficient of thermal expansion
η = nondimensional parameter $(r/2\tau^{1/2})$
θ = nondimensional temperature difference
κ = thermal conductivity
μ = viscosity
ρ = density
τ = nondimensional time
Φ = spherical coordinate
ψ = stream function
Ψ = nondimensional stream function

Subscripts

a = refers to sphere radius
e = effective value
0, 1, 2, . . . = indicates terms in power series
∞ = reference condition

Superscript

$'$ = quantity normalized by division by L

is expressed by

$$\theta_0 = \frac{1}{4\pi r}\,\mathrm{erfc}\,\eta, \tag{14a}$$

$$\Psi_1 = \frac{1}{8\pi}\,\tau^{1/2}\sin^2\Phi\left[2\eta\,\mathrm{erfc}\eta + \frac{1}{\eta}\,\mathrm{erf}\eta - \frac{2}{\pi^{1/2}}\exp\left(-\eta^2\right)\right], \tag{14b}$$

where $\eta = r/2\,\tau^{1/2}$, erf is the error function, and erfc is the complementary error function. This solution is also singular at the origin and the far-field behavior is the same as that described for the steady-state case.

Steady-State Line Source. The steady-state solution for a vertical line source of length H, coincident with the vertical axis, symmetrically located about the origin, and with strength per unit length Q/H can be obtained from superposition of the fundamental results for a point source as given in equations (13). Converting to cylindrical polar coordinates and assuming all lengths have been normalized with respect to the length scale L, allows the temperature and stream function to be expressed by the integrals

$$\theta_0 = \frac{1}{4\pi H'}\int_{-H'/2}^{H'/2}\left[\mathfrak{r}'^2 + (\mathfrak{z}' - s')^2\right]^{-1/2} ds' \tag{15a}$$

$$\Psi_1 = \frac{1}{8\pi H'}\int_{-H'/2}^{H'/2}\mathfrak{r}'^2\left[\mathfrak{r}'^2 + (\mathfrak{z}' - s')^2\right]^{-1/2} ds' \tag{15b}$$

where primes denote that the indicated quantities have been normalized by division by the length scale L (i.e., $H' = H/L$, $\mathfrak{r}' = \mathfrak{r}/L$, $\mathfrak{z}' = \mathfrak{z}/L$, $s' = s/L$), and s' is an integration variable.

Integration then provides the results

$$\theta_0 = \frac{1}{4\pi H'}\ln\left\{\frac{\mathfrak{z}' + H'/2 + [(\mathfrak{z}' + H'/2)^2 + \mathfrak{r}'^2]^{1/2}}{\mathfrak{z}' - H'/2 + [(\mathfrak{z}' - H'/2)^2 + \mathfrak{r}'^2]^{1/2}}\right\}, \tag{16a}$$

$$\Psi_1 = \frac{1}{8\pi H'}\,\mathfrak{r}'^2\ln\left\{\frac{\mathfrak{z}' + H'/2 + [(\mathfrak{z}' + H'/2)^2 + \mathfrak{r}'^2]^{1/2}}{\mathfrak{z}' - H'/2 - [(\mathfrak{z}' - H'/2)^2 + \mathfrak{r}'^2]^{1/2}}\right\}. \tag{16b}$$

These results exhibit a singularity along the portion of the z-axis occupied by the line source and have the same far-field behavior previously discussed in conjunction with the point source solution. For solutions expressed in terms of cylindrical polar coordinates, the velocity components are obtained from the nondimensional relations

$$V_{\mathfrak{r}} = \frac{1}{\mathfrak{r}'}\frac{\partial\Psi}{\partial\mathfrak{z}'}, \quad V_{\mathfrak{z}} = -\frac{1}{\mathfrak{r}'}\frac{\partial\Psi}{\partial\mathfrak{r}'}. \tag{17a,b}$$

Steady-State, Constant-Temperature Sphere. Yamamoto has analyzed the natural convection process associated with an isothermal sphere of radius a and surface temperature T_a embedded in an infinite porous medium. Retaining only the leading terms of his solution provides

$$\theta_0 = \frac{1}{4\pi r}, \tag{18a}$$

$$\Psi_1 = \frac{1}{8\pi}\left[\frac{Lr}{a} - \left(\frac{Lr}{a}\right)^{-1}\right]\sin^2\Phi, \tag{18b}$$

where the center of the sphere is coincident with the origin, and the energy release rate from the sphere is $4\pi a\kappa_e(T_a - T_\infty)$. Hence, it is readily deduced that equations (18) yield a temperature of T_a on the surface of the sphere. The stream function takes on the value zero on the surface of the sphere and velocities approach zero for large r.

Steady-State Point Source at the Base of a Semi-Infinite Region. For a point source situated on the lower, insulated, boundary below a semi-infinite region, the temperature and stream function are given by

$$\theta_0 = \frac{1}{2\pi r}, \tag{19a}$$

$$\Psi_1 = \frac{r}{4\pi}\cos\Phi\left[(\tan\Phi + 1)^{-1/2} - 1\right], \tag{19b}$$

where the source is, as usual, located at the origin and the behavior for large r is as previously described for a point source. A numerical solution for this case is also presented in the paper by Hickox and Watts.

Although this case is not used in the superposition models described subsequently, it is included for completeness. In order to illustrate the solution for this configuration, isotherms and streamlines obtained from equations (19) are plotted in Fig. 2.

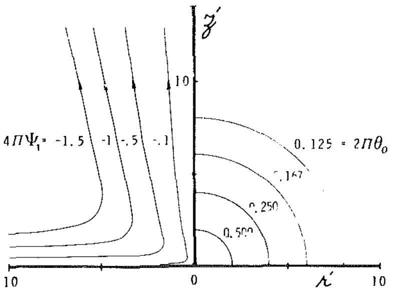

Fig. 2 Steady-state streamlines and isotherms for a point source at the base of a semi-infinite region ($L = k^{1/2}$)

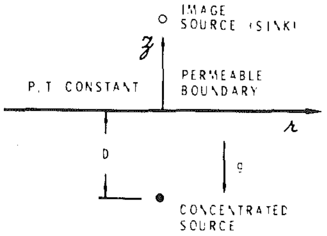

Fig. 3 Concentrated source below a permeable boundary

Concentrated Sources Below a Permeable Boundary

Thermal and Flow Fields. If a thermally active container of nuclear waste material is emplaced in the sediment below the seabed, the situation resembles that depicted in Fig. 3 where a concentrated source is located in the sediment a distance D below the sediment-water interface. The interface is represented as a horizontal, permeable boundary on which the pressure and temperature are both constant.

For small Rayleigh number, the thermal and flow fields associated with the concentrated source can be determined approximately through superposition of the solutions to the linear system described by equations (11) and (12), in the previous section. The boundary conditions at the interface are satisfied by locating an appropriate image of the concentrated source at the mirror image point above the boundary. The image is thus a source of negative strength (sink) located a distance D above the interface. The direction of gravity is also reversed in the image plane.

In Figs 4–7, nondimensional representations are presented for solutions obtained by the superposition principle described above. In all cases, a permeable boundary on which pressure and temperature are constant has been assumed. Figure 4 depicts isotherms and streamlines for steady flow induced by a point source located a distance D below the interface. As an example of the transient behavior associated with a point source, isotherms and streamlines are plotted in Fig. 5 for a Rayleigh number of 0.5 and a nondimensional time of 0.1. For large time, the isotherm and streamline patterns approach those of Fig. 4. In Fig. 6, results for a line source of length H are presented. In this figure, the top of the line source is located a distance D below the interface. Finally, in Fig. 7, results for a constant temperature sphere buried a distance D below the interface are presented.

Note on Velocities. Explicit relations for the velocity components associated with a concentrated source can be obtained by differentiation of the formulas for the stream functions given in the previous section. The relations between velocity components and stream function in spherical and cylindrical polar coordinates are given by

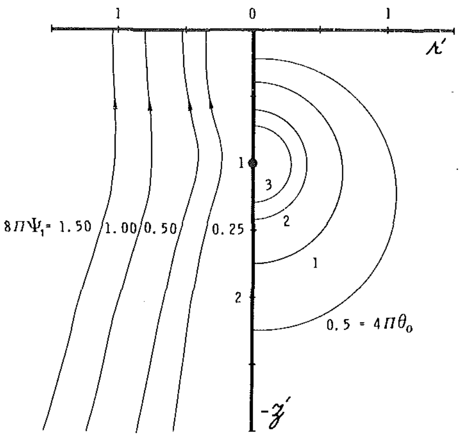

Fig. 4 **Steady-state streamlines and isotherms for a point source located below a permeable boundary ($L = D$)**

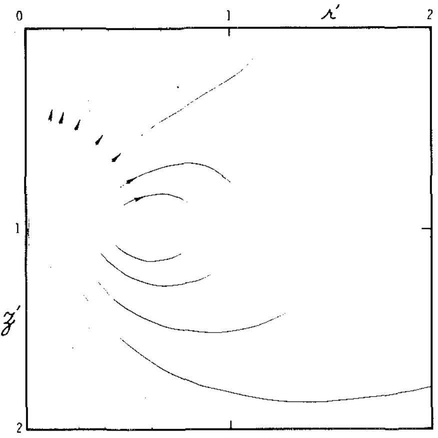

Fig. 5(*a*) **Transient streamlines for a point source located below a permeable boundary (Ra = 0.5, $\tau = 0.1$, $L = D$; $\Psi_1 \times 10^3 = 0.25, 0.5, 1, 2, 3, 4, 4.5$)**

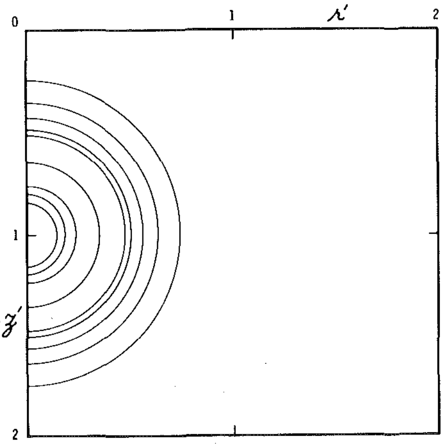

Fig. 5(*b*) **Transient isotherms for a point source located below a permeable boundary (Ra = 0.5, $\tau = 0.1$, L = D; $\theta_0 \times 10^2 = 1, 2, 3, 4, 5, 10, 20, 30, 40$)**

equations (9) and (17), respectively. Once formulas for the velocities are derived for individual sources, superposition can be used to predict velocities for the geometries treated in this section. These results can then be used to predict the fluid particle paths produced by a particular concentrated source, thus providing an estimate of the maximum distance traversed by a fluid particle in a given time interval. This latter result is of some importance in evaluating the potential for convective transport of radionuclides, a topic considered briefly in the following section.

Application to Sub-Seabed Disposal of Nuclear Waste

As an example of the application of the ideas developed in the previous section, brief consideration will be given to the prediction of the flow field associated with the sub-seabed disposal of nuclear waste. Currently, it is conjectured that such a disposal scheme would consist of emplacing a cylindrical canister of nuclear waste material at a depth of approximately 30 m below the sediment-water interface. Suggested canister dimensions are 3 m in length and 0.3 m in diameter. Thermal considerations for the canister design require the initial thermal output to be no greater than 1.5 kW. A generic disposal site, located in the Central North Pacific is currently under study. The water depth and bottom temperature in this region are approximately 6000 m and 1.5°C, respectively.

Referring to Fig. 3, it is assumed that the situation described above can be represented by the transient solution for a point source located a given distance below the sediment-water interface. Using current estimates for the thermophysical properties of the sediment, an initial Rayleigh number of approximately 10^{-3} is predicted. The condition

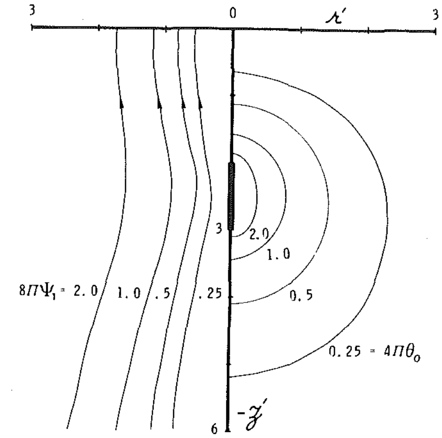

Fig. 6 **Steady-state streamlines and isotherms for a line source located below a permeable boundary ($L = H$, $D/H = 2$)**

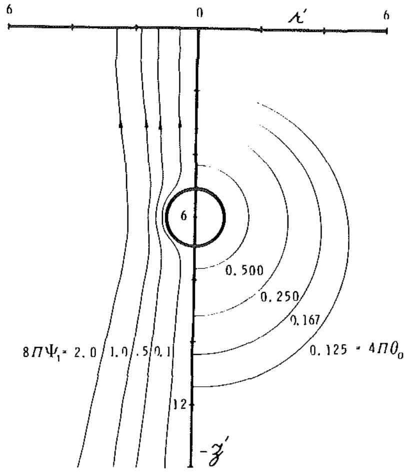

Fig. 7 **Steady-state streamlines and isotherms for a constant temperature sphere located below a permeable boundary ($L = a$, $D/a = 6$)**

of small Rayleigh number, required by the theory, is thus easily satisfied. For a burial time of one year, the corresponding non-dimensional time τ is approximately 4.8×10^{15}. Assuming that the power output remains constant over the time period of interest, the associated streamline pattern at the end of one year is illustrated in Fig. 8. Thermal properties are such that, at a distance of 3 m from the source, the temperature rise is only approximately 5°C. Hence the thermal field is relatively uninteresting and is not reproduced.

Analyses using models such as the one just described can provide useful information for studies of the transport of radionuclides inadvertently released from emplaced canisters. In general, the transport of radionuclides in a fluid-saturated porous medium involves the four fundamental processes: convection, diffusion-dispersion, sorption, and radioactive decay. Assuming only weak concentrations of radionuclides in the pore water, the analysis of this section can provide estimates of the fluid velocity necessary to evaluate the convective transport. If the sorption process is temperature dependent, then predictions of the thermal field based on simple models will also prove useful.

The analyses discussed apply only to regions sufficiently far removed from the thermal source so that the physical processes are relatively unaffected by the geometry of the canister. Indications are that this distance need be no greater than a few canister lengths.

Discussion

Subject to the small Rayleigh number limit, Ra → 0, solutions have been presented which describe the thermal and flow fields produced by an isolated, concentrated, thermal source in a fluid-saturated porous medium. A variety of concentrated sources were considered. All solutions presented were obtained by retaining only the leading terms in expansions of the dependent variables in power series in the Rayleigh number, resulting in a system of linear partial differential equations for the description of the processes involved.

The linearity of the basic system allowed the use of superposition to obtain solutions for concentrated sources embedded in a semi-infinite region below a permeable boundary on which the pressure and temperature were held constant. This particular geometry was used as a model for the subseabed disposal of nuclear waste. Although attention was focused on a particular geometry in this paper, the principle of superposition can be used in conjunction with the various fundamental solutions to provide descriptions for a variety of geometries.

Aside from the assumption of small Rayleigh number, the assumptions most likely to introduce errors into the analysis are those associated with the Boussinesq approximation and the assumed rigidity of the porous matrix. The rapid heating of a liquid confined in a rigid porous matrix of low permeability can actually produce a rather high transient pore pressure [7]. As a result of the assumptions invoked, this behavior is not evidenced by the solutions presented in this paper. If the porous matrix is composed of clay particles, as is the case for marine sediments, then it is likely that some local deformation of the matrix will occur in regions of high heating rates. The resulting deformation need not necessarily be large since only a small deformation is required to relieve the pressure in a liquid-saturated porous medium. Some investigators (e.g., Chavez and Dawson [8]) have suggested that it is possible for certain deformable porous media to deform continuously in response to local heating, thereby providing a mechanism for the movement of an emplaced container of thermally active nuclear waste. However, questions regarding the deformational behavior of marine sediments cannot be answered conclusively until the rheological properties of marine sediments have been accurately determined. A calculational procedure must then be developed which properly accounts for the anticipated behavior.

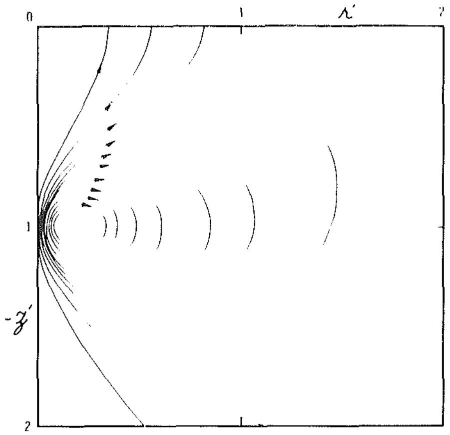

Fig. 8 Transient streamlines at one year for sub-seabed disposal of nuclear waste (Ra = 10^{-3}, $\tau = 4.8 \times 10^{15}$, $L = D$; $\Psi_1 \times 10^{-4} = 1, 2, 3, 4, 5, 6, 8, 10, 12, 14$)

Additional comments are perhaps in order regarding the applicability of the results for small but finite values of the Rayleigh number. For a point source embedded in an infinite porous medium, Hickox and Watts have shown that the thermal field is relatively unaffected by convection for Rayleigh numbers less than unity. Hence, the results of this paper are expected to provide accurate descriptions for natural convective flows so long as the Rayleigh number remains less than unity. For the sub-seabed disposal of radioactive waste, a Rayleigh number of only 10^{-3} is anticipated.

Hodgkinson has indicated that Rayleigh numbers on the order of 10^{-2} are expected for disposal of radioactive wastes in a hard rock depository. Hence, it is expected that the current results may find application in the analysis of proposed nuclear waste disposal schemes other than the one treated in this paper. Also, the possibility of applications in the analysis of geothermal systems should not be overlooked.

Acknowledgments

I wish to thank W. D. Sundberg for providing some of the numerical results presented in this paper. This work was supported by the U.S. Department of Energy under contract DE-AC04-76DP00789.

References

1 Bishop, W. P., and Hollister, C. D., "Sea-bed Disposal—Where to Look," *Nuclear Technology*, Vol. 24, 1974, pp. 425–443.

2 Yamamoto, K., "Natural Convection About a Heated Sphere in a Porous Medium," *Journal of the Physiological Society of Japan*, Vol. 37, No. 4, 1974, pp. 1164–1166.

3 Hickox, C. E., "Steady Thermal Convection at Low Rayleigh Number from Concentrated Sources in Porous Media," Report SAND77-1529, Sandia National Laboratories, Albuquerque, NM, 1977.

4 Bejan, A., "Natural Convection in an Infinite Porous Medium with a Concentrated Heat Source," *Journal of Fluid Mechanics*, Vol. 89, Part 1, 1978, pp. 97–107.

5 Hodgkinson, D. P., "A Mathematical Model for Hydrothermal Convection Around a Radioactive Waste Depository in Hard Rock," Report AERE-R9149, AERE Harwell, Oxfordshire, July, 1979.

6 Hickox, C. E. and Watts, H. A., "Steady Thermal Convection from a Concentrated Source in a Porous Medium," ASME JOURNAL OF HEAT TRANSFER, Vol. 102, No. 2, May 1980, p. 248.

7 Eaton, R. R., et al., "Calculated Hydrogeologic Pressure and Temperatures Resulting from Radioactive Waste in the Eleana Argillite," *Proceedings International Symposium on the Scientific Basis for Nuclear Waste Management*, Materials Res. Soc., Plenum Press, Mar, 1980.

8 Chavez, P. F., and Dawson, P. R., "Thermally Induced Motion of Marine Sediments Resulting from Disposal of Radioactive Wastes," Sandia National Laboratories Report (in press), Albuquerque, NM, 1980.

Adrian Bejan
Department of Mechanical Engineering,
University of Colorado,
Boulder, CO 80309,
Assoc. Mem. ASME

Lateral Intrusion of Natural Convection into a Horizontal Porous Structure

This article illustrates the fundamental features of lateral penetration of natural convection into a horizontal porous layer in lateral communication with a heat reservoir. It is found that the important group governing the fluid mechanics of the phenomenon is the Darcy-modified Rayleigh number Ra based on longitudinal (horizontal) permeability and on transversal (vertical) thermal diffusivity. It is shown that the buoyancy-driven flow has flattened C-shaped streamlines and isotherms. The flow penetrates laterally to a distance of order H $Ra^{1/2}$, where H is the height of the porous layer. The net heat exchange between the porous structure and the lateral heat reservoir is described by a Nusselt number result of the type $Nu \sim Ra^{1/2}$. The effect of horizontal wall temperature gradient on penetration length and heat transfer is discussed. The engineering importance of these findings is illustrated by examples related to the conceptual design of porous winding structures for rotating superconducting electric machines.

Introduction

The objective of this paper is to document the phenomenon of *lateral* penetration of free convection into a fluid-saturated porous medium. The model employed in this study consists of a horizontal (two-dimensional) porous layer bounded on three sides by impermeable isothermal surfaces; the fourth side (one of the lateral vertical surfaces) is permeable and communicates with a heat reservoir of a different temperature. The fundamental questions addressed in this study are:

- What is the distance to which reservoir fluid travels into the porous structure?
- What is the net heat exchange between the impermeable walls and the reservoir?
- What are the relevant dimensionless groups which govern the heat transfer and fluid mechanics of the phenomenon? In other words, what are the necessary conditions for an effective thermo-fluid interaction between the porous structure and the lateral reservoir?

In recent years we have witnessed a growing interest in the fundamentals of buoyancy-driven flows in fluid-permeated porous structures. This interest is motivated by important applications in energy-engineering and geophysics. A number of these applications are related directly to the emerging technology of geothermal energy, as demonstrated in Cheng's comprehensive review [1]. Other applications are found in the area of thermal insulation engineering, where the horizontal porous layer is one of the basic configurations [2, 3].

My own interest in the phenomenon of lateral intrusion of free convection into a porous structure was triggered by a critical engineering problem encountered in the thermal design of rotating superconducting windings [4]. One design philosophy advocates the use of an annular porous winding structure permeated by helium at supercritical pressures (single phase). For example, Fig. 1 shows a cutaway view through the 21 cm diameter winding structure of an experimental generator constructed at MIT [5]. During steady operation, the main heat input to the structure takes place along the cylindrical surfaces which, at cryogenic temperatures, are not perfectly insulated. Since the rotor is usually long, the coolant can only be ducted to the winding radius at *discrete* locations along the rotor axis. The thought is that, once cold fluid is deposited at one point on the axis, natural convection will take over and spread the cold fluid longitudinally through the porous structure. Of critical importance to the survival of the superconducting state is the relationship between the winding-coolant temperature difference and the distance (penetration length) to which the cooling effect will be felt. It is also important to know how this relationship can be affected by other geometric parameters present in the structural design of the winding.

At this time, there are no means of predicting the behavior of a porous structure in contact with a lateral heat reservoir of a different temperature. It is the mission of this paper to present the first analytical results and physical description of the ensuing free convection phenomenon.

Mathematical Formulation

Consider the two-dimensional space of height H and total length L shown in Fig. 2. The impermeable walls of the space are at a temperature T_0^* while the reservoir to the right of the horizontal layer is at a temperature T_∞^*. It is convenient to assume from the outset that the walls are colder than the lateral reservoir ($T_0^* < T_\infty^*$). This as-

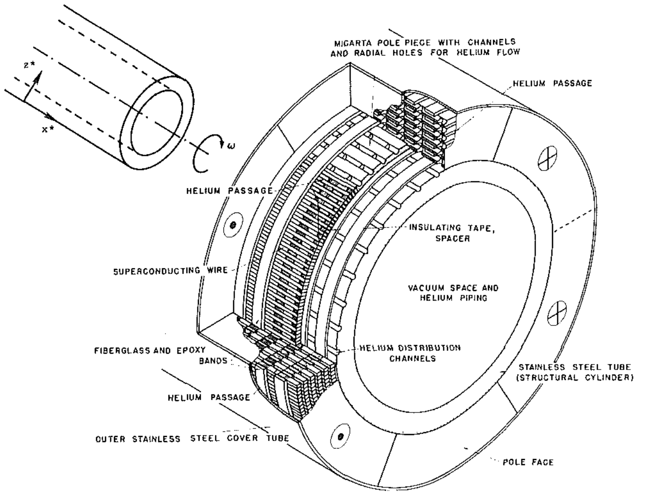

Fig. 1 Isometric drawing showing the porous structure of a rotating superconducting winding

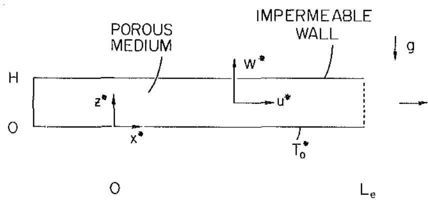

Fig. 2 Schematic of horizontal porous structure in communication with a lateral heat reservoir

---

Contributed by the Heat Transfer Division for publication in the JOURNAL OF HEAT TRANSFER. Manuscript received by the Heat Transfer Division June 16, 1980.

sumption does not restrict the generality of the analysis which, as can be easily verified, applies to the reverse situation where the gap is warmer than the reservoir. Such an arrangement was mentioned in the Introduction in connection with the lateral cooling of porous superconducting windings saturated with single phase helium.

When the horizontal impermeable walls are colder than the right extremity of the porous structure, we expect a buoyancy-driven flow in which warm fluid sinks through the structure, being first drawn from the right along the top wall and later driven back to the right along the bottom wall. If the horizontal space is extremely slender, $H \ll L$, the free convection effect will be limited to an "entrance region" of length L_e which is smaller than the actual horizontal dimension of the porous structure, L. One of the objectives of this study is to determine the penetration length L_e.

The equations governing the conservation of mass, momentum and energy in the Cartesian system $x^* - z^*$ of Fig. 2 are

$$\frac{\partial u^*}{\partial x^*} + \frac{\partial w^*}{\partial z^*} = 0 \tag{1}$$

$$u^* = -\frac{K_x}{\mu}\frac{\partial P^*}{\partial x^*}, \; w^* = -\frac{K_z}{\mu}\left(\frac{\partial P^*}{\partial z^*} + \rho g\right) \tag{2, 3}$$

$$\rho c_p\left(u^*\frac{\partial T^*}{\partial x^*} + w^*\frac{\partial T^*}{\partial z^*}\right) = \lambda_x\frac{\partial^2 T^*}{\partial x^{*2}} + \lambda_z\frac{\partial^2 T^*}{\partial z^{*2}} \tag{4}$$

where u^*, w^*, P^*, T^* are the velocity components, the pressure and the temperature. The momentum equations are based on the Darcy flow model. The governing equations account also for the fact that the permeability and thermal conductivity in the longitudinal direction (K_x, λ_x) may differ from the values measured in the transversal direction (K_z, λ_z). The fluid-saturated porous structure is treated as a homogeneous porous medium (see, for example, Elder [6]): the fluid and the solid matrix are locally in thermal equilibrium, with μ, ρ, c_p and λ representing the fluid viscosity, density, specific heat at constant pressure and thermal conductivity of the fluid/porous matrix composite. Equations (1–3) are based also on the Boussinesq approximation, whereby the variation of density with temperature is accounted for only in the body force term of the momentum equation, where $\rho \cong \rho_0[1 - \beta(T^* - T_0^*)]$. Eliminating the pressure terms between equations (2, 3) yields a unique momentum conservation statement,

$$\frac{\partial u^*}{\partial z^*} - \frac{K_x}{K_z}\frac{\partial w^*}{\partial x^*} = -\frac{\beta g K_x}{\nu}\frac{\partial T^*}{\partial x^*} \tag{5}$$

In this expression β is the volumetric coefficient of thermal expansion.

In the region of interest, $0 < x^* < L_e$, the appropriate boundary conditions along the horizontal impermeable walls are

$$w^* = 0 \text{ and } T^* = T_0^* \text{ at } z^* = 0, H \tag{6}$$

Dimensional Analysis

Let ℓ be the unknown horizontal length scale of the flow field in the entrance region of interest ($x^* \sim \ell$). In the same region, z^* is of order H, and $(T^* - T_0^*)$ is of the same order as the temperature difference driving the flow, $T_\infty^* - T_0^*$. If the entrance region is slender enough so that the longitudinal conduction term is negligible relative to the transversal conduction term, i.e., if

$$\frac{\lambda_x}{\lambda_z}\left(\frac{H}{l}\right)^2 \ll 1, \tag{7}$$

the balance of convection and transversal conduction implied by the energy equation yields

$$0(u^*) = \frac{\lambda_z \ell}{\rho c_p H^2}. \tag{8}$$

Turning to the momentum equation (5), the second term on the left hand side is negligible compared with the first when the flow region is slender enough so that

$$\frac{K_x}{K_z}\left(\frac{H}{\ell}\right)^2 \ll 1. \tag{9}$$

In this limit, the momentum equation (5) yields an alternate order-of-magnitude estimate for the same longitudinal velocity u^*,

$$0(u^*) = \frac{g\beta K_x(T_\infty^* - T_0^*)}{\nu}\frac{H}{\ell}. \tag{10}$$

Comparing equations (8, 10) we conclude that the unknown horizontal length scale ℓ must be

$$\ell = H\,\mathrm{Ra}^{1/2}, \tag{11}$$

where Ra is the Rayleigh number based on longitudinal permeability (K_x) and on transversal thermal diffusivity [$\alpha_z = \lambda_z/(\rho c_p)$],

$$\mathrm{Ra} = \frac{g\beta K_x H\,(T_\infty^* - T_0^*)}{\alpha_z \nu}. \tag{12}$$

The characteristic time interval associated with a fluid packet entering and leaving the structure (the residence time) is $t^* = \ell/u^* = H^2/\alpha_z$. Therefore, the fluid residence time is of the same order as the characteristic response time to transient heat conduction in the z direction through the fluid-saturated porous structure.

The chief conclusion of the above scaling is that natural convection will penetrate laterally into the fluid-bathed porous structure to a distance which is proportional to $H\,\mathrm{Ra}^{1/2}$. Consequently, the correct dimensionless variables for this problem are

$$x = \frac{x^*}{H\,\mathrm{Ra}^{1/2}}, \quad z = \frac{z^*}{H} \tag{13, 14}$$

$$u = \frac{u^* H}{\alpha_z\,\mathrm{Ra}^{1/2}}, \quad w = \frac{w^* H}{\alpha_z} \tag{15, 16}$$

$$T = \frac{T^* - T_0^*}{T_\infty^* - T_0^*} \tag{17}$$

The corresponding conservation statements for mass, momentum and energy are

$$\frac{\partial u}{\partial x} + \frac{\partial w}{\partial z} = 0$$

$$\frac{\partial u}{\partial z} = -\frac{\partial T}{\partial x} \tag{19}$$

Nomenclature

A = wall temperature gradient parameter, equation (36)
c_p = specific heat at constant pressure
g = gravitational acceleration
H = vertical dimension of porous structure
K_x = horizontal permeability
K_z = vertical permeability
ℓ = horizontal length scale of penetrative flow
L = horizontal dimension of porous structure
L_e = length of entrance (penetration) region
P^* = pressure
Q = heat transfer rate per unit width
Ra = Rayleigh number, equation (12)
T = dimensionless temperature
T^* = temperature
T_0^* = temperature of impermeable walls
T_∞^* = temperature of heat reservoir
u = dimensionless horizontal velocity
u^* = horizontal velocity
w = dimensionless vertical velocity
w^* = vertical velocity
x = dimensionless horizontal position
x^* = horizontal position
z = dimensionless vertical position
z^* = vertical position
α_z = vertical thermal diffusivity
β = coefficient of thermal expansion
θ = temperature profile function
λ_x = horizontal thermal conductivity
λ_z = vertical thermal conductivity
μ = viscosity
ν = kinematic viscosity
ρ = fluid density
ϕ = streamfunction profile
ψ = streamfunction

$$u\frac{\partial T}{\partial x} + w\frac{\partial T}{\partial z} = \frac{\partial^2 T}{\partial z^2} \tag{20}$$

with boundary conditions

$$w = T = 0 \text{ at } z = 0,1 \tag{21}$$

Recalling conditions (7, 9), the momentum and energy equations (19, 20) are valid provided

$$\mathrm{Ra} \gg \max\left(\frac{\lambda_x}{\lambda_z}, \frac{K_x}{K_z}\right). \tag{22}$$

If the porous medium is isotropic, as might be the case in a geothermal or thermal insulation application, the necessary condition (22) becomes

$$\mathrm{Ra} \gg 1. \tag{23}$$

Solution and Numerical Results

Introducing the streamfunction ψ defined as $u = \partial\psi/\partial z$ and $w = -\partial\psi/\partial x$, the momentum and energy equations (19, 20) become

$$\frac{\partial^2\psi}{\partial z^2} = -\frac{\partial T}{\partial x} \tag{24}$$

$$\frac{\partial\psi}{\partial z}\frac{\partial T}{\partial x} - \frac{\partial\psi}{\partial x}\frac{\partial T}{\partial z} = \frac{\partial^2 T}{\partial z^2}. \tag{25}$$

The solution presented below is based on the observation that equations (24, 25) admit solutions $\psi(x, z)$, $T(x, z)$ of the form

$$\psi(x, z) = x\phi(z) \tag{26}$$

$$T(x, z) = x^2\theta(z). \tag{27}$$

Performing transformation (26, 27) on equations (24, 25) leads to a system of coupled equations in $\phi(z)$ and $\theta(z)$

$$\phi'' = -2\theta \tag{28}$$

$$2\phi'\theta - \phi\theta' = \theta'' \tag{29}$$

where $(\ )' = d/dz$. The boundary conditions (21) become

$$\phi = 0, \theta = 0 \text{ at } z = 0, 1. \tag{30}$$

From this point on the streamfunction and temperature profiles ϕ, θ were determined numerically. The z interval [0, 1] was divided into N segments by considering a total of $N - 1$ equidistant nodes between $z = 0$ and $z = 1$. The finite difference version of equations (28, 29) permits the calculation of streamfunction and temperature at the ith node, based on ϕ, θ information at the two preceeding nodes. The integration of equations (28, 29) was started from $z = 0$ where $\phi_0 = \theta_0 = 0$. A "shooting scheme" was employed, whereby the starting slopes (ϕ_1, θ_1) were adjusted by trial and error until the top wall boundary conditions were met, $\phi_N = \theta_N = 0$.

The resulting $\phi(z)$ and $\theta(z)$ solution is displayed graphically in Fig. 3. This solution was obtained using $N = 1500$ and a shooting success criterion ϕ_N, $\theta_N < 10^{-5}$. The streamfunction profile has a maximum $\phi_{\max} = 7.147$ situated at $z = 0.55$. The temperature profile has a maximum $\phi_{\max} = 39.925$ at $z = 0.653$. Figure 3(*b*) shows also the velocity profile, ϕ'; as expected, warm fluid creeps in the negative x direction along the top wall, and flows toward the warm end along the bottom wall. Since $\psi = x\phi$, hence $w = -\phi < 0$, the fluid always "falls" through the porous structure.

We can now discuss how this natural counterflow, whose intensity increases in the x direction, "fits" between the cold impermeable walls and the warm heat reservoir. At $x \leq 0$ the fluid *stagnates*, as its temperature equals that of all three impermeable walls. At the warm end, $x = L_e/\ell$, the structure draws warm fluid from the warm reservoir ($T = 1$). To account for the supply of warm fluid to the porous structure, it is appropriate to assign the reservoir temperature ($T = 1$) to the point of highest temperature in the two-dimensional space [7]. This point is located at $x = L_e/\ell$ and $z = 0.653$; hence, from equation (27),

$$1 = \left(\frac{L_e}{\ell}\right)^2 \Theta_{\max}. \tag{31}$$

In conclusion, the actual penetration length L_e is shorter than the order-of-magnitude estimate (11),

$$L_e = (\theta_{\max})^{-1/2} H\, \mathrm{Ra} = 0.158\, H\, \mathrm{Ra}^{1/2}. \tag{32}$$

Figure 4 shows streamlines and isotherms in the flow region $0 < x^*/L_e < 1$. The graphic construction of the contours is based on combining the numerical profiles (Fig. 3) with expressions (26, 27). It is evident that the temperature effect of the reservoir is felt over a distance which is relatively shorter than the fluid penetration effect.

Heat Transfer

The Nusselt Number. The net heat exchange effected by the buoyancy-driven flow between the porous structure and the lateral heat reservoir, can be calculated by summing up the heat flux over the isothermal impermeable walls.

$$Q = \lambda_z \int_0^{L_e} \left[\left(\frac{\partial T^*}{\partial z^*}\right)_{z^*=0} - \left(\frac{\partial T^*}{\partial z^*}\right)_{z^*=H}\right] dx^*. \tag{33}$$

Symbol Q denotes the net heat exchange per unit width in the direction perpendicular to the plane of Fig. 2. Integral (33) can be carried out and rearranged in dimensionless form as

$$\mathrm{Nu} = \frac{\theta'_{z=0} - \theta'_{z=1}}{3\,\theta_{\max}^{3/2}} \mathrm{Ra}^{1/2} = 0.319\, \mathrm{Ra}^{1/2} \tag{34}$$

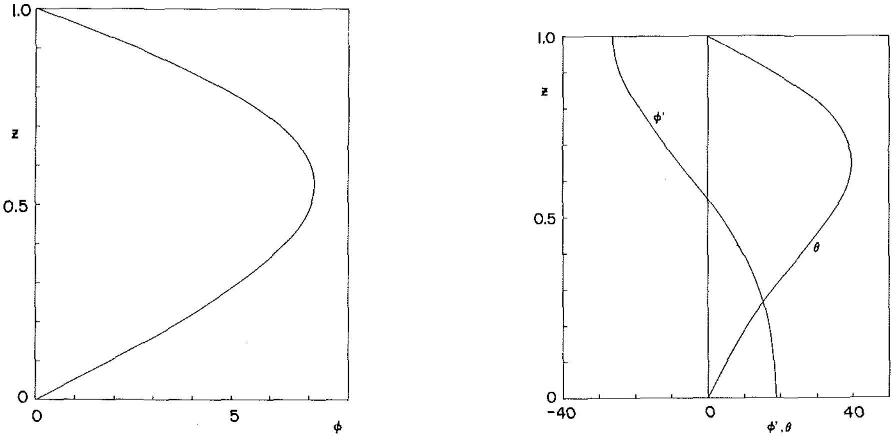

Fig. 3(*a*) Streamfunction profile $\varphi(z)$ **Fig. 3(*b*)** Temperature profile $\theta(z)$ and horizontal velocity profile $\varphi'(z)$.

Fig. 3 Numerical results

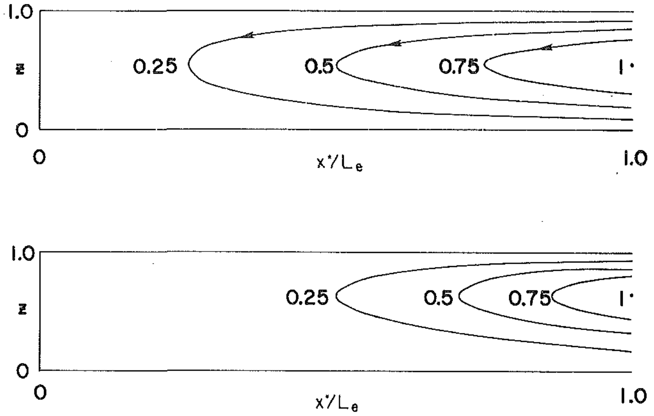

Fig. 4 Streamlines and isotherms in the region penetrated by natural convection

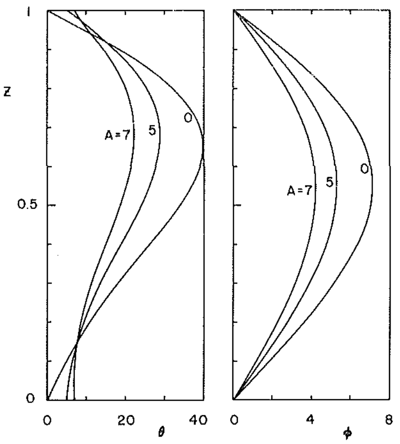

Fig. 5 Effect of wall temperature gradient on streamfunction and temperature profiles

Table 1 Summary of numerical solutions for streamfunction, temperature and heat transfer

A	$\theta'_{y=0}$	$\theta'_{y=1}$	$\Theta_{\max}(z)$	$\phi_{\max}(z)$	$\mathrm{Nu}/\mathrm{Ra}^{1/2}$
0	48.913	−191.86	39.925(.653)	7.147(.550)	0.319
1	40.109	−183.15	37.887(.657)	6.806(.551)	0.319
5	7.286	−137.12	28.837(.677)	5.297(.551)	0.311
7	−7.900	−98.18	22.294(.694)	4.199(.549)	0.286

where the Nusselt number is $\mathrm{Nu} = Q/\lambda_z(T_\infty^* - T_0^*)$. We note that the $\mathrm{Nu} \sim \mathrm{Ra}^{1/2}$ proportionality is similar to the result encountered in other porous configurations differentially heated in the horizontal direction [2, 8, 9].

For actual engineering calculations equation (34) can be written as

$$Q = 0.319 \left(\lambda_z K_x H \frac{g\beta\rho c_p}{\nu}\right)^{1/2} (T_\infty^* - T_0^*)^{3/2} \qquad (35)$$

This form shows that the heat transfer rate is proportional to the group $(\lambda_z K_x)^{1/2}$. This observation has implications in the conceptual design of superconducting winding structures, where designing for high longitudinal permeability K_x runs against the ability to achieve a high transversal conductivity λ_z. Result (35) shows that in such applications the structural designer must seek to augment the *product* of K_x and λ_z.

The Effect of Wall Temperature Gradient. The fact that the porous medium temperature is proportional to x^2, equation (27), demonstrates that the heat flux from the porous structure to the impermeable wall is highest near the $x^* = L_e$ end of the system. In an engineering situation, the uneven distribution of heat flux has the effect of pulling the horizontal wall temperature up closer to the temperature of the lateral reservoir. This leads to a longitudinal temperature gradient along the impermeable walls, so far assumed isothermal ($T = 0$). The wall temperature gradient can also be caused by direct conduction from the reservoir in the negative x direction.

Whatever its cause, a finite wall temperature gradient has the effect of decreasing the "effective" temperature difference driving the penetrative flow, thus inhibiting the flow. This effect can be evaluated using the finite difference solution described in the preceding section, assuming a wall temperature of the form

$$T = Ax^2, \text{ at } z = 0,1. \qquad (36)$$

Parameter A accounts for how close the horizontal wall temperature (at $x^* = L_e$) approaches the reservoir temperature ($A < \theta_{\max}$). The only change in the numerical scheme is that the temperature boundary condition, equation (30), is now replaced by

$$\theta = A \text{ at } z = 0, 1. \qquad (37)$$

Numerical results for a series of discrete values of wall gradient parameter A are presented in Fig. 5. Important features of the streamfunction and temperature profiles are summarized in Table 1.

The effect of increasing A is represented by a decrease in net mass flow drawn from the reservoir into the structure, $\psi_{\max}$ (Fig. 5). Another effect is the decrease in the numerical coefficient of the $\mathrm{Nu} \sim \mathrm{Ra}^{1/2}$ proportionality (see Table 1). Finally, we note that $\theta_{\max}$ decreases as A increases: this means that the penetration distance L_e *increases* as the horizontal walls respond thermally to the presence of the lateral heat reservoir (see equation (32)). This observation suggests that one way of enhancing the spreading of natural convection through a porous structure is by increasing the longitudinal thermal conductance, not through the porous structure itself, rather, through the structural longitudinal walls.

As indicated by the temperature profile $\theta(z)$ plotted on the left side of Fig. 5, the temperature variation in the vertical direction becomes less pronounced as the wall temperature gradient (A) increases. For example, if $A = 7$, in the lower quarter ($0 < z < 1/4$) of the structure the temperature is practically independent of vertical position; also, the temperature gradient at $z = 0$ is negative, meaning that when A is sufficiently large, the lower branch of the C-shaped flow *gains* heat from the lower wall, contrary to the effect present when the horizontal walls are isothermal ($A = 0$). The "stretching" exhibited by the temperature profile as A increases is responsible for the disappearance of this solution above a threshold value of A. Setting $A = 10, 20$ (and, presumably, for higher values of A), I was unable to determine solutions which satisfy all boundary conditions at $z = 0, 1$.

Engineering Examples

It is instructive to consider at this point two numercial examples of engineering calculations based on the preceeding theory.

1 **Superconducting Winding Structure.** One of the more recent porous structures of the type shown in Fig. 1 was described by Ito [10]. The structure is saturated with supercritical helium (40 atm, 10K) which has the following properties: $c_p = 4.6$ J/gK, $\rho = 147$ kg/m^3, $\nu = 3.7 \times 10^{-8}$ m^2/s, $\beta = 4.5 \times 10^{-3}$ K^{-1}. The structure itself has the following parameters: $K_x = K_z = 10^{-9}$ m^2, $\lambda_x = 500$ W/mK, $\lambda_z = 0.25$ W/mK, $L = 2$m, $H = 10$ cm. The radius of the annular structure is 0.4 m, hence, at a speed $\omega = 3600$ rpm, the structure is suspended in the transversal "gravitational" field $g = 7.1 \times 10^4$ m/s^2.

The Rayleigh number corresponding to this design is

$$\mathrm{Ra} = 2.3 \times 10^6 \frac{\Delta T}{1K},$$

where ΔT is the temperature difference between the longitudinal (horizontal) walls and the coolant (helium) deposited at one longitudinal location. Since $K_x/K_z = 1$ and $\lambda_x/\lambda_z = 2000$, Ra must be greater than 2000 if we are to use the present theoretical results. We find that $\mathrm{Ra} > 2000$ when $\Delta T > 10^{-3}$ K. Since the lateral penetration effect is needed to control temperature variations of the order of 0.1

K (which could affect the superconducting state), we conclude that the Rayleigh number of interest will always be greater than 2000. Using equation (32), the penetration length L_e can be calculated as a function of overall temperature difference ΔT.

ΔT[K]	L_e[m]
0.001	0.76
0.01	2.4
0.1	7.6

This calculation proves that the coolant will travel the entire length of the structure ($L = 2$ m) as soon as ΔT exceeds 0.007 K.

The numerical results presented in this example will change appreciably if we consider the behavior of the same structure at lower angular speeds: since $L_e \sim \mathrm{Ra}^{1/2}$ and $g \sim \omega^2$, the penetration length will decrease *linearly* with the angular speed.

2 **Building Insulation.** In a fibrous insulation of the type used in buildings, the permeability ($K_x = K_z$) is of order 10^{-9} m², while the thermal diffusivity of the air-saturated porous medium is of order 5×10^{-5} m²/s [11]. The Rayleigh number based on air properties at 16°C is

$$\mathrm{Ra} = 0.11 \frac{H}{1\,\mathrm{m}} \frac{\Delta T}{1\,\mathrm{K}},$$

which shows that, if $\Delta T = 30$ K, the vertical dimension H must be in excess of 0.3 m (condition (23)). Therefore, the lateral intrusion phenomenon is likely to be present in porous spaces characterized as "large," for example, in underground rock beds proposed for solar energy storage, and silos for the storage of grain.

Conclusions

In order to shed light on the phenomenon of lateral intrusion of free convection into a porous structure, this study focused on the interaction of a horizontal permeable space with a heat reservoir positioned laterally (Fig. 2). The following conclusions were reached:

1 The penetrative flow consists of flattened C-shaped streamlines and isotherms, as shown in Fig. 4.

2 The important dimensionless group is the Darcy-modified Rayleigh number based on height, overall temperature difference, *longitudinal* permeability and *transversal* conductivity (equation (12)).

3 The penetration length L_e is proportional to $H^{3/2}$ and $\Delta T^{1/2}$ i.e., $L_e \sim H\,\mathrm{Ra}^{1/2}$ (equation (32)).

4 The net heat exchange between the impermeable walls and the lateral reservoir is described by a proportionality of the type $\mathrm{Nu} \sim \mathrm{Ra}^{1/2}$ (equation (34)). The actual heat transfer rate is proportional to $\Delta T^{3/2}$ and $(\lambda_z K_x H)^{1/2}$ (equation (35)).

5 If the horizontal wall temperature gradually approaches the reservoir temperature in the vicinity of the reservoir (increasing A in Fig. 5 and Table 1), the heat and mass exchange decrease, while the penetration length increases.

It is important to keep in mind the extent of the parametric domain in which this study and its conclusions are valid. First, as summarized in inequality (22), the Rayleigh number must exceed (λ_x/λ_z) or (K_x/K_z), whichever is greater. This condition accounts for the assumption that the flow pattern is *slender* in the horizontal direction. The second condition follows from comparing the penetration length L_e with the physical length of the porous structure L: the intrusion flow unveiled in this study required $L_e < L$. This second condition amounts to a geometric upper-bound for the Rayleigh number. In conclusion, the Rayleigh number range covered by this study is

$$\max\left(\frac{\lambda_x}{\lambda_z}, \frac{K_x}{K_z}\right) \ll \mathrm{Ra} < \theta_{\max}\left(\frac{L}{H}\right)^2 \tag{38}$$

where $\theta_{\max}$ is listed in Table 1. In an isotropic porous medium with isothermal horizontal surfaces, the Ra range is

$$1 \ll \mathrm{Ra} \leq 40\left(\frac{L}{H}\right)^2. \tag{39}$$

An additional boundary to this domain comes from considering the validity of the Darcy flow model used in this study. According to Muskat [12], the Darcy flow model is applicable in cases where the Reynolds number based on pore diameter D is less than a number of order one. Using the order-of-magnitude estimated obtained for u^* earlier, equations (8, 10), the pore Reynolds number criterion dictates

$$\mathrm{Ra} < \left(\frac{H}{D}\right)^2 \left(\frac{\nu}{\alpha_z}\right)^2 \tag{40}$$

as an added condition for the validity of the present theory. It is interesting to note in (40) the presence of ratio (ν/α_z) which can be viewed as the equivalent "Prandtl number" of the fluid-saturated porous medium. Reading criterion (40) from right to left, we learn that the porous medium Prandtl number must exceed a critical value, $\mathrm{Ra}(D/H)^2$, before we can neglect fluid inertia, i.e., before we can treat the flow as a Darcy-flow. This observation agrees qualitatively with the known fact that in free convection in enclosures filled with fluid (without porous matrix) the fluid inertia plays only a minor role when the fluid Prandtl number is greater than a number of order unity [13].

Regarding the practical use of the theoretical results developed in this paper, the designer must keep in mind that the present theory assumes the existence of a two-dimensional flow pattern. The extent to which this simplifying assumption is valid must be established in future studies, numerically or experimentally.

Acknowledgment

This work was carried out under the auspices of NSF Grant ENG-78-20957.

References

1 Cheng, P., "Heat Transfer in Geothermal Systems," *Advances in Heat Transfer*, Vol. 14, 1979.

2 Bejan, A., and Tien, C. L., "Natural Convection in a Horizontal Porous Medium Subjected to an End-to-End Temperature Difference," ASME JOURNAL OF HEAT TRANSFER, Vol. 100, 1978, pp. 191–198.

3 Walker, K. L., and Homsy, G. M., "Convection in a Porous Cavity," *Journal of Fluid Mechanics*, Vol. 87, 1978, pp. 449–474.

4 Bejan, A., "Improved Thermal Design of the Cryogenic Cooling System for the Rotor of a Superconducting Generator," Ph.D. Thesis, Massachusetts Institute of Technology, Cambridge, Mass., Feb. 1975.

5 Bejan, A., "Superconductive Field Winding for a 2MVA Synchronous Generator," M. S. Thesis, Massachusetts Institute of Technology, Cambridge, Mass., May 1972.

6 Elder, J. W., "Steady Free Convection in a Porous Medium Heated from Below," *Journal Fluid Mechanics*, Vol. 27, 1966, pp. 29–48.

7 Lighthill, M. J., "Theoretical Considerations on Free Convection in Tubes," *Journal of Mechanics and Applied Mathematics*, Vol. 6, 1953, pp. 398–439.

8 Weber, J. E., "The Boundary Layer Regime for Convection in a Vertical Porous Layer," *International Journal of Heat and Mass Transfer*, Vol. 18, 1975, pp. 569–573.

9 Klein, I. S., "Natural Convection in a Porous Bed with a Permeable Boundary," *Fluid Dynamics*, Vol. 13, No. 4, 1979, pp. 606–609, translated from Russian.

10 Ito, T., Private Communication, February 1977, University of California, Berkeley.

11 Rohsenow, W. M., and Choi, H. Y., *Heat, Mass and Momentum Transfer*, Prentice-Hall, Englewood Cliffs, N.J., 1961, p. 517.

12 Muskat, M., *The Flow of Homogeneous Fluids Through Porous Media*, J. W. Edwards, Mich. 1946.

13 Ostrach, S., "Natural Convection in Enclosures," *Advances in Heat Transfer*, Vol. 8, 1972, p. 161.

Y. T. Chan
Graduate Student.

S. Banerjee
Professor.

Department of Chemical and Nuclear Engineering,
University of California, Santa Barbara,
Santa Barbara, Calif. 93106

Analysis of Transient Three-Dimensional Natural Convection in Porous Media

Transient multidimensional natural convection in porous media has been studied using a numerical method based on the simplified marker and cell technique with local cancellation of low order, diffusional truncation errors. The conservation equations and boundary conditions were phrased in terms of the primitive variables, velocity and temperature. Differences in temperature between the fluid and the solid matrix are considered. Heat transfer between the solid and liquid phases was modelled by representing the porous medium as an assemblage of spherical particles, and solving the conduction problem within the spheres at every time step. Nusselt numbers at walls were calculated from the temperature and velocity profiles. Numerical results for heat transfer through fluid saturated porous media heated from below are in good agreement with published experiments. Consideration of heat transfer between the solid and fluid phase leads to Nusselt numbers that vary with the thermophysical properties of the solid material, even when the Rayleigh number and fluid thermophysical properties are kept constant. This is also observed in experiments. The calculations also show convective instabilities of the right period at high Rayleigh numbers.

Introduction

The analysis of multidimensional natural convection in porous media is of importance in many industrial and geophysical problems. Two examples are the study of natural convection cooling of nuclear fuel in shipping flasks, and mixed convection cooling in water filled fuel storage bays. Cooling has to be analyzed not only during routine operation of these facilities but also in postulated accidents. These situations can be simulated to some extent by considering them as fluid saturated media with appropriate porosity and boundary conditions. The purpose of this paper is to discuss the development and validation of a numerical procedure for solving such problems. In addition, the separate temperatures of the fluid and solid matrix are taken into account. As shown later, there is good reason for this.

Combarnous and Bories [1] have extensively reviewed the state of the art on natural convection in porous media. Experiments have been conducted in both Hele-Shaw cells and porous layers bounded by horizontal isothermal plates. The types of cells observed were polyhedral for low Rayleigh numbers and oscillatory two-dimensional for high Rayleigh numbers. Heat transfer coefficients have also been measured for various Rayleigh numbers and types of materials. Buretta and Berman [2] performed experiments to determine heat transfer for Rayleigh numbers in the range 10–1000, with porous media both uniformly heated from below and locally heated. His results for natural convection induced by uniform heating from below were in good agreement with the analytical upper bound estimates obtained by Gupta and Joseph [3]. Both authors observed a change of slope in the Nusselt number curve when the Rayleigh number is approximately seven times the critical value.

Zebib and Kassoy [4] did a weakly nonlinear analysis for the nondimensionalized conservation equations to obtain a two-term expansion for the Nusselt number. They found that the two-dimensional roll configuration transferred heat more efficiently than did the three dimensional pattern of motion at low Rayleigh numbers. Straus and Schubert [5,6] investigated stability for three-dimensional convection in a cube and two-dimensional multicellular convection in a square by the Galerkin technique. For two-dimensional calculations, their results show that convection is unsteady when Rayleigh number is greater than 300 in single-cell flow, 650 in double-cell flow and 800 in triple-cell flow, while for three-dimensional calculations, instability occurred when Rayleigh number is greater than 300. Horne and O'Sullivan [7] studied the stability of natural convective flows in two-dimensional porous layers heated both uniformly and non-uniformly from below. Using forward differencing in time for the parabolic portion of the equations and an odd-even reduction method for the elliptic stream function portion of the equations, they were able to find a relation between the oscillatory period and the Rayleigh number. Horne [8], formulating the equations with the vector potential, demonstrated that more than one mode of convection is possible for any particular physical configuration and Rayleigh number. In some cases, a particular flow situation may be stable even though it does not maximize the heat transfer across the system. For a cubic region he found that the flow pattern at a particular value of Rayleigh number was not unique and was determined by the initial conditions. In some cases, there exists four alternatives, two and three-dimensional, steady and unsteady.

There have been several numerical investigations of natural convection in porous media, e.g., Holst and Aziz [9]. The numerical technique most closely related to that used in this paper is that of Chan and Banerjee [10] who used a modified Marker and Cell (MAC) numerical scheme to study natural convection of pure fluids in a rectangular erclosure with different velocity and temperature bounday conditions. The MAC technique was used with "donor cell" differencing of the advective terms. It was recognized that this could be inaccurate for natural convection problems. This could be due to numerical diffusion, and because the energy conservation equation is written in nonconservative form to decouple the velocity field calculation at each time step from the temperature field at that time step. They were able to achieve satisfactory accuracy by using unequal mesh spacing in the wall regions as demonstrated in their convergence studies.

The objective of the present work is to investigate natural convection phenomena in porous media, in relatively simple geometries, through numerical studies also using the modified MAC technique. The conservation equations in primitive form, together with empirical relations for effects like friction are used as the basis for the finite difference equations. In addition, heat transfer between the solid and liquid phases is considered explicitly by representing the porous medium as an assemblage of spherical particles and solving the conduction problem in them. As will be shown later, explicit consideration of solid-fluid heat transfer is necessary to obtain agreement with experiments using different solid materials, even at low Rayleigh numbers in the natural convection range. The effect becomes even

---

Contributed by the Heat Transfer Division for publication in the JOURNAL OF HEAT TRANSFER. Manuscript received by the Heat Transfer Division May 28, 1980.

more pronounced when convective instabilities occur. Agreement with experimental results could not be obtained in our investigation until we incorporated the solid-fluid heat transfer model.

With regard to the numerical method two significant changes were made compared to the technique used by Chan and Banerjee [10]. First the energy equations for the fluid was used in conservation law form. This was necessary to assure energy conservation at high Rayleigh numbers, but did not affect the results at Rayleigh numbers below 300. Second, a significant increase in accuracy was achieved by using a technique for local cancellation of low order truncation errors (see also Rivard [11]). This reduces numerical diffusion effects. However, the order of the finite difference equations generally remains unchanged since all the low order errors, other than those related to diffusion, remain unchanged. The cancellation of low order truncation error is especially important at high Rayleigh numbers. This became evident when the numerical procedure was compared to experiments.

Mathematical Modelling

Mathematical modelling of convective phenomena in porous medium is usually based on the methodology used in continuum mechanics. Hence, the partial differential equations have a familiar form provided averaging is done over representative elementary volumes (R.E.V.). A discussion of the literature in this area and various forms of the conservation equations may be found in Chan [12].

For natural convection flows with small density changes, the conservation equations may be simplified by the Boussinesq approximation. The fluid density is considered constant except in the buoyancy force term that drives the natural convection. To simplify matters we will consider that the porous medium is homogeneous and isotropic in its physical properties, including fluid permeability and thermal conductivity, both of which are assumed to stay approximately constant with changes in temperature. These assumptions may be relaxed if necessary, without severe problems arising from the numerical solution viewpoint.

For incompressible flow the continuity equation can be written as

$$\nabla \cdot \bar{V} = 0 \tag{1}$$

To describe the motion of the fluid phase in an isotropic medium, the momentum equation is

$$\frac{\rho}{\phi}\frac{\partial \bar{V}}{\partial t} + \frac{\rho}{\phi^2}(\bar{V}\cdot\nabla)\bar{V} = -\nabla P + \rho\bar{g} - \mu\frac{\bar{V}}{K}, \tag{2}$$

where K is the permeability of the medium. The inertial term is associated with microscale inertial effects and is negligible if the Reynolds number based upon interstitial velocity and pore length or grain size is small. On the other hand, neglect of the inertial term has unknown mathematical consequences, especially at high Rayleigh numbers, and we will therefore retain it in the finite difference formulation.

For any geometrical point and its associated representative elementary volume, we can define two average temperatures, T_s for the solid phase and T_f for the fluid phase. T_s and T_f characterize the thermal state of each phase in the same elementary volume. For the mathematical modelling of heat transfer, two alternate methods are possible, depending on the magnitude of the difference between T_s and T_f.

1 The difference between the two temperatures is assumed to be negligible. Then the medium can be considered as equivalent to a unique continuum and the thermal behavior is described by a single equation for the average temperature $T = T_s = T_f$, i.e.,

$$(\rho C)\frac{{}^{*}\partial T}{\partial t} = \nabla(k^{*}\nabla T) - (\rho C)_f\bar{V}\nabla T \tag{3}$$

This "equivalent diffusivity" model is commonly used, and is valid when the filtration velocity is not too high and both phases are well-dispersed.

Note that in this case the average vertical heat transfer can be shown to depend on the Rayleigh number and the height by length ratio of the roll cells. Therefore, no difference in Nusselt number would be obtained for different solid-fluid materials combinations provided the Rayleigh number and system dimensions were kept constant.

2 The second method is used when it is not possible to assume that the difference between T_s and T_f is negligible. This may occur for certain ranges of thermophysical properties and in transients. It is then necessary to explicitly describe interphase heat transfer. The medium may be considered as equivalent to two continua, and two sets of equations are usually required to describe the phenomenon. These are

$$\nabla(k_s^{*}\nabla T_s) = (1-\phi)(\rho C)_s\frac{\partial T_S}{\partial t} + h(T_s - T_f) \tag{4a}$$

$$\nabla(k_f^{*}\nabla T_f) - (\rho C)_f\nabla\bar{V}T_f = \phi(\rho C)_f\frac{\partial T_f}{\partial t} + h(T_f - T_s) \tag{4b}$$

In the first term of each equation, fictitious thermal conductivities appear, k_s^{*} takes into account the dispersed structure of the solid matrix, and k_f^{*} includes the effect of hydrodynamical dispersion.

It should be noted that a mathematical model based on equation (4) is difficult to apply because an estimate is needed for three unknown quantities h, k_s^{*}, k_f^{*}. However, the model can be simplified by using equation (4b), together with an assumption regarding the structure of the porous medium and an empirical relation for the heat

Nomenclature

a = solid particle surface area per unit volume
$\mathrm{Bi} = \frac{hR}{k}$ = Biot number
C = specific heat capacity
C_x = Courant number in x direction
D = diameter
g = gravitational acceleration
h = heat transfer coefficient
H = height
$j_H = \frac{h_{\mathrm{loc}}}{C^{*}\rho|v|}\left(\frac{C\mu}{k}\right)_f^{2/3}$ = Colburn number
K = permeability
m = number of cells in x-direction
n = number of cells in y-direction
$\mathrm{Nu}^{*} = \frac{\dot{q}H}{k_f^{*}\Delta T}$ = filtration Nusselt number
p = pressure
p'' = pressure fluctuation
$\dot{q}$ = heat flux
R = radius
$\mathrm{Ra}^{*} = \frac{g\beta(\rho c)_f K\Delta TH}{\nu_k{}^{*}}$ = filtration Rayleigh number
$\mathrm{Re} = \frac{\rho V}{a\mu_f\psi}$ = Reynolds number
S = surface area
t = time
T = temperature
V = filtration velocity
α = thermal diffusivity
β = volumetric expansion coefficient
γ = parameter defining amount of upwind differencing
k = conductivity
λ_n = eigenvalue
μ = viscosity
ν = kinematic viscosity
ρ = density
ϕ = porosity
ψ = shape factor

Subscripts

f = fluid phase
loc = local value
o = reference value
p = particles
s = solid phase
∞ = value of quantity far from boundary

Superscripts

n = nth time step
$*$ = equivalent value

transfer coefficient. In the present work the porous medium is modelled as an assemblage of spheres as discussed in detail in the following section.

A model of this type leads to Nusselt numbers that depend not only on the Rayleigh number and height to length ratio for the rolls but also on the ratio of the solid to fluid thermal diffusivities and a dimensionless group involving solid-fluid heat transfer.

Assemblage of Spheres Model

In order to obtain the temperature of the solid phase, T_s, a physical model for a representative elementary volume (R.E.V.) is required. Obviously, T_s depends on the thermal properties and temperature history of the phases. In this model the simplifying assumption is made, that in a R.E.V., the solid phase consists of spheres that go through identical temperature transients. Thus, the surface temperature of the solid phase can be approximated by the surface temperature of one representative sphere for each R.E.V.

Initially, each sphere has a uniform temperature of T_0 and the fluid has a temperature of T'_∞. The analysis for the temperature profile in the sphere after $\Delta t'$ is available and is outlined, for example, in Arpaci [13]. However, if the fluid phase temperature T'_∞ is changed to T''_∞ after $\Delta t'$, the analysis to be carried out is similar except that the initial condition should be changed to

$$T(r, \Delta t') - T''_\infty$$

In general, the temperature profile at time, t^{n+1}, is

$$T(r, t^{n+1}) = T_\infty^{n+1} + \sum_{p=1}^{\infty} A_p^{n+1} \exp\left(-\alpha \lambda_p^{n+1^2} \Delta t^{n+1}\right) \sin \lambda_p^{n+1} r / r \quad (5)$$

where

$$A_p^{n+1} = \frac{2(T_\infty^n - T_\infty^{n+1})\left(\frac{\sin \lambda_p^{n+1} R}{\lambda_p^{n+1}}\right) - R\cos\lambda_p^{n+1}R) + \lambda_p^{n+1} \sum_{q=1}^{\infty} A_q^n \exp\left(-\alpha \lambda_q^{n^2}\, \Delta t^n\right) I_{q,p}}{\lambda_p^{n+1} R - \sin \lambda_p^{n+1} R \cos \lambda_p^{n+1} R}$$

and

$$I_{q,p} = \begin{cases} \dfrac{\sin(\lambda_q^n - \lambda_p^{n+1})R}{\lambda_q^n - \lambda_p^{n+1}} - \dfrac{\sin(\lambda_q^n + \lambda_p^{n+1})}{\lambda_q^n + \lambda_p^{n+1}} & \text{if } \lambda_q^n \neq \lambda_p^{n+1} \\ R - \dfrac{\sin \lambda_p^{n+1} R \cos \lambda_p^{n+1} R}{\lambda_p^{n+1}} & \text{if } \lambda_q^n = \lambda_p^{n+1} \end{cases}$$

if $n > 1$

and

$$A_p^n = \sum_q^{\infty} \frac{2(T_0 - T_\infty^n)\left(\frac{\sin \lambda_q^n R}{\lambda_q^n} - R \cos \lambda_q^n R\right)}{\lambda_q^n R - \sin \lambda_q R \cos \lambda_q^n R}$$

if $n = 1$

where the eigenvalues λ_n are given by

$$\lambda_n R \cos \lambda_n R = (1 - \mathrm{Bi}) \sin \lambda_n R$$

$T(R, t^{n+1})$ is then used as the temperature of the solid phase in the R.E.V. at the $n + 1$ th time step.

The permeability which is also required is computed from the Kozeny-Carmen relation:

$$K = \frac{D_p^2 \phi^3}{36 s (1 - \phi)^2}$$

where s is the shape factor of the constituting particles. In the case of a porous medium made up of identical spherical beads, D_p is the diameter, and s is about 4.8, Wyllie [14]. According to Bird, et al. [15], this relation is limited to homogeneous porous media of porosity less than 0.5, in which the channeling effect is negligible, and the mean particle diameter is small compared with the dimensions of the container.

The heat transfer coefficient between solid and fluid phases in a packed layer is generally defined as a local value representative of a cross section through the bed. A large amount of experimental information on heat and mass transfer in packed layers has been analyzed to arrive at the following empirical correlation, Bird, et al. [15]:

$$j_H = 0.91\ \mathrm{Re}^{-0.51}\psi \quad \mathrm{Re} \leq 50$$

$$j_h = 0.61\ \mathrm{Re}^{-0.41}\psi \quad \mathrm{Re} > 50$$

The quantity ψ is equal to unity for a porous layer consisting of spherical particles.

The heat transfer coefficient between the solid and fluid phases will depend on the local velocity even when the thermophysical properties are kept constant. Therefore, the heat transfer between the solid and fluid phases will vary with position (and with time in transients).

Numerical Technique and Calculational Procedure

The field is discretized into cells of size Δx, Δy, and Δz with cell centers being designated by i, j, k in the x, y, z direction, respectively. The x-component of velocity (U) is located at the left and right faces of the cell, y-component of velocity (V) at the upper and lower faces, z-component of velocity (W) at the front and back faces, while the pressure, and temperatures are located at the cell center.

The frictional or Darcy term is written half in the nth and half in the $n + 1th$ time step to stabilize the scheme as well as to reduce truncation errors. The finite difference equations are similar in form to that used in Chan and Banerjee [10] and are described in detail in Chan [12]. The difference is in the use of the conservation law form of the energy equation. As discussed later, this is necessary to conserve energy.

Thus, one difference in comparison to the work of Chan and Banerjee is the use of $(\rho C)_f \nabla \overline{V} T_f$ as the second term in equation (4b) instead of $(\rho C)_f \overline{V} \nabla T_f$. This leads to finite differences for terms of the type $\partial/\partial x\,(UT)$ rather than $U \partial T/\partial x$. These are written as $\partial/\partial x\,(UT)_{i,j,k} = 0.5[(T_{i+1,j,k} + T_{i,j,k})U_{i+1/2,j,k} + |U_{i+1/2,j,k}|(T_{i,j,k} - T_{i+1,j,k}) - (T_{i,j,k} + T_{i-1,j,k})U_{i-1/2,j,k} - |U_{i-1/2,j,k}|(T_{i-1,j,k} - T_{i,j,k})]/\Delta x$.

In addition, local truncation error cancellation (TEC) is used to reduce diffusional errors. The most important part of the TEC method is to calculate the amount of truncation error introduced by the finite difference equation analytically. Once the amount of truncation error is known, the low-order, diffusional truncation errors can be cancelled locally.

Only the diffusional truncation errors for the y-component of the momentum equation are derived: the diffusional truncation errors in the other components and energy equation can be derived similarly.

Define

$$DE(V) = \frac{\partial V}{\partial t} + \phi \frac{\partial p''}{\partial y} + \frac{1}{\phi}\left(U \frac{\partial V}{\partial x} + V \frac{\partial V}{\partial y} + W \frac{\partial V}{\partial z}\right) + \beta g \phi \Delta T + \frac{\nu \phi}{K} V = 0$$

$$FD(V) = \frac{V_{i,j+1,2,k}^{n+1} - V_{i,j+1/2,k}^{n}}{\Delta t} + \frac{(p''_{i,j+1,k} - P''_{2,j,k})\phi}{\Delta y}$$

$$+\frac{FVX + FVY + FVZ}{\phi} + \beta g \phi \Delta t + \frac{1}{2}\frac{\nu\phi}{K}(V^{n+1}_{i,j+1/2,k} + V^{n}_{i,j+1/2,k}) = 0$$

where FVX is $U\partial V/\partial x\,|^{n}_{i,j+1/2,k}$, and FVY and FVZ are related to the y and z components of velocity.

With the Taylor series expansion of V for the *nth* time step and point $i, j+\frac{1}{2}, k$, and p'' for i, j, k, the $FD(V)$ becomes

$$FD(V) = DE(V) - \frac{1}{2\phi}\left(|U|\Delta x(\gamma - C_x)\frac{\partial^2 V}{\partial x^2} + |V|\Delta y(\gamma - C_y)\frac{\partial^2 V}{\partial y^2}\right.$$
$$\left. + |W|\Delta z\left(\gamma - C_z\frac{\partial^2 V}{\partial z^2}\right)\right) + 0(\Delta t, \Delta x) = 0$$

where

$$C_x = \frac{|U|}{\phi}\frac{\Delta t}{\Delta x},$$

and similarly for C_y and C_z. The quantity γ defines the amount of upwind differencing used for the advective terms. When it is 1, the difference approximations are pure "donor cell."

In order to reduce the diffusional truncation errors, $A_x + A_y + A_z$ is added to the $FD(V)$, where

$$A_x = \begin{cases}(1-\xi)\epsilon_x, & \epsilon_x \geq 0\\ (1+\xi)\epsilon_x, & \epsilon_x < 0\end{cases}$$

with

$$\epsilon_x = \frac{1}{2}\frac{|U|}{\phi}\Delta x(\gamma - C_x)\frac{\partial^2 V}{\partial x^2} \quad \text{and } 0 \leq \xi \leq 1$$

A_y and A_z are similarly defined, and ξ is used to control the amount of effective diffusion after the low order diffusional truncation errors are exactly cancelled.

To proceed, the necessary boundary conditions are imposed by considering the whole porous region to be surrounded by a single layer of fictitious cells in which the variables are specified (as in Chan and Banerjee [10]) according to whether the wall cells are free slip or no slip, and adiabatic or isothermal. For no slip walls, equation (2) has to be modified to include a term containing $\mu\,\nabla^2\bar{V}$. This is only necessary if it is desired to approach the correct limit as the porosity tends to unity. For the cases considered here the differences between no slip and free slip results are negligible.

To calculate velocities, pressures and temperatures at a new time step from values at the previous time step, the following computational cycle is followed.

1 Compute estimate for the new velocity field from the momentum equations. This is done for all cells.

2 Adjust the new velocity field iteratively to satisfy the mass conservation equation by changing the cell pressures. If the divergence, D, of a cell is negative, this corresponds to a net flow of mass into the cell, the cell pressure is then increased to eliminate the net inflow. Likewise, the cell pressure can be decreased to eliminate net outflow if D is positive. If the pressure of one cell is adjusted, then the adjustment must be done iteratively. The details may be found in Chan [12].

3 When the new velocity field has been calculated, the average surface temperature field of the solid phase is calculated using equation (5). This is done for each cell.

4 The fluid temperature field is then calculated using the energy equation.

5 The velocity and pressure fields are then used as the starting values for the next step cycle.

Numerical Stability and Computational Time

Numerical calculations often develop large, high frequency oscillations in space, time or both. This behavior is usually referred to as a numerical instability, especially if the physical problem being studied is known not to have unstable solutions. For accuracy, the mesh increments must be chosen small enough to resolve the expected spatial variations in all dependent variables. When this is impossible because of limitations imposed by computing time or memory requirements, special care must be exercised in interpreting computational results. Once a mesh has been chosen, the choice of the time increment necessary for stability is governed by the usual Courant number criterion, i.e.

$$\Delta t \leq \min\left(\frac{\phi}{|U|}\Delta x, \frac{\phi}{|V|}\Delta y, \frac{\phi}{|W|}\Delta z\right),$$

where the minimum is with respect to every cell in the mesh. The proper choice of γ, which is related to the amount of upwind differencing for the advective terms, has been found from tests to be

$$1 \geq \gamma \geq \max(C_x, C_y, C_z) \geq 0.3$$

This has been determined from stability tests carried out for different combinations of γ and ξ. It is found that for $\gamma < 0.3$, the scheme is unstable, even if $\xi = 1$. On the other hand, for $\gamma \geq 0.3$, the scheme is stable, even if $\xi = 0$. Calculations based on the two extremes in γ(0.3 and 1.0) differ by less than 10 percent.

The problem computation time required per time increment depends, in general on (1) the number of cells, (2) the cell size, (3) the time step and (4) the convergence criterion set for the velocity field iteration to satisfy the continuity equation. The cell size and time step size are interrelated by stability conditions. In general, we have found for transient calculations that, on the average, about (7.67 + 0.15 × number of iterations) ms CPU time is required per cell per time step on the McMaster Cyber 170 machine.

Calculations and Comparisons

In order to gain confidence in the numerical procedure used it is very important to compare calculations with experimental results. The system geometry used in a calculation, to check the numerical method, is similar to that of Combarnous and Bories [1]. It is a horizontal porous layer saturated with water and the whole layer is enclosed in a rectangular box consisting of impervious isothermal or adiabatic plates. The vertical plates are adiabatic and the horizontal plates are isothermal. The temperature of the bottom plate is higher than the temperature of the top plate. The porous layer is made of spherical beads of diameter 0.4 mm ($\phi = 0.37$), to simplify estimation of the permeability of the layer. The height of the porous layer is chosen to be 5.35 cm for comparison purposes. Calculations have been performed at Rayleigh numbers of 36, 83, 100, 150, 250, 490, 550, 800 and the corresponding average Nusselt numbers are estimated according to

$$\mathrm{Nu}^{*}_{j+1/2}(y) = \frac{H}{mn\Delta T}\sum_{ik=1}^{mn}\left(\frac{\partial T_{i,j+1/2,k}}{\partial y} + \frac{(\rho C)}{k^*}T_{i,j+1/2,k}V_{i,j+1/2,k}\right)$$

or

$$\mathrm{Nu}^{*}_{j+1/2}(y) = \frac{H}{mn\Delta T}\sum_{ik=1}^{mn}\left(\frac{k^*_s}{k^*}\frac{\partial T_{si,j+1/2,k}}{\partial y} + \frac{k^*_f}{k^*}\frac{\partial T_{fi,j+1,k}}{\partial y}\right.$$
$$\left. + \frac{(\rho C)_{i,j+1/2,k}}{k^*}T_{i,j+1/2,k}V_{i,j+1/2,k}\right)$$

depending on whether the equal or separated temperature formulation is used. For each vertical volume of cells, the cubic spline technique is applied to the numerical solution of the temperature field to give a third order polynomial fit. The temperatures and temperature gradients for the corresponding level are then obtained from the fitted polynomial and its first derivative respectively, see [12].

Steady-state is achieved if the total heat flow across any horizontal layer is constant. In other words, when the Nu*(y) is independent of y. The variation of average Nusselt number with respect to y is indicated in Fig. 1 after a fairly long real time run. As evident, there is still some variation in the average Nusselt number. Figure 2 shows the transient values of the average Nusselt number. When the average Nusselt number does not change with respect to time then steady state may be considered to have been achieved for the purpose of comparison with experiments.

Figure 3 shows the numerical results as compared with the experimental results of Combarnous [1]. The Nusselt numbers found for the three different solid phase materials are in good agreement with those obtained from experiments, when the model for heat transfer

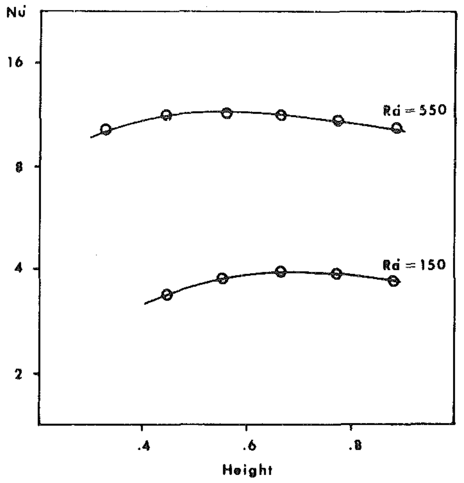

Fig. 1 Variations of average Nusselt number with height for $R_a{}^* = 150$ and 550

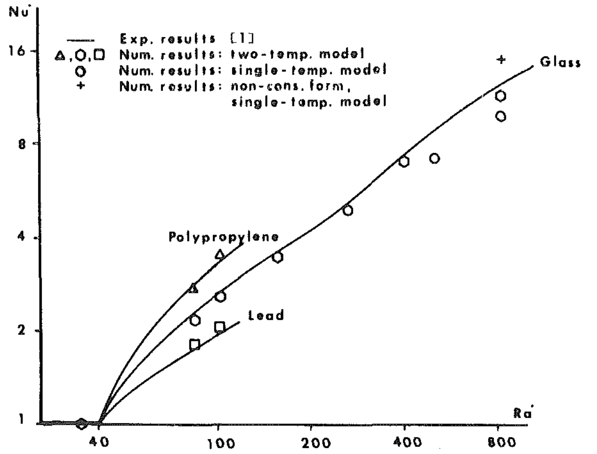

Fig. 3 Numerical results compared with the experimental results of Combarnous and Bories [1]

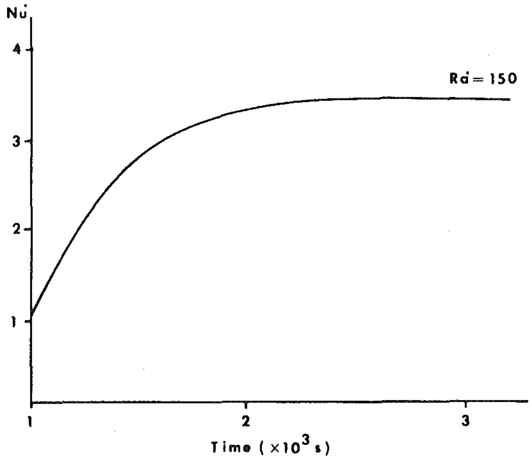

Fig. 2 Transient values of the average Nusselt number at $R_a^* = 150$

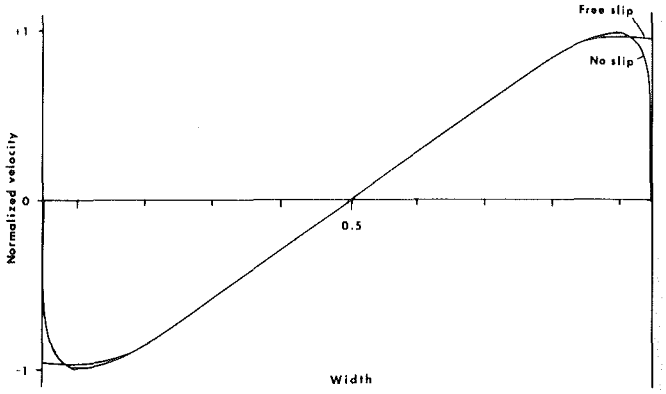

Fig. 4 Comparison of velocity profiles in a middle plane using "slip" and "no slip" boundary conditions

between solid and fluid, described previously, is used. Use of an equivalent thermal diffusivity not only fails to predict the effect of different solid materials on the average Nusslet number, but also underestimates the Nusselt number at high Rayleigh numbers even for the glass beads-water combination, for which this representation predicted the data reasonably well at the lower Rayleigh numbers. On the other hand, the solid-fluid heat transfer model used leads to Nusselt numbers that are in agreement with data for different solid materials, and over the range of Rayleigh numbers studied (up to 800 for glass-water). Calculations were not done for all the solid-fluid combinations at high Rayleigh numbers because of computer cost, and because the correct trends were observed at the lower Rayleigh numbers.

In addition, Fig. 3 illustrates the effect of using the nonconservative form of the energy equation at a Rayleigh number of 800 for the equivalent diffusivity (single temperature) model. The nonconservative form gives a higher Nusselt number than the conservative form because energy is lost. In fact, the misleading impression is left that the calculations with the equivalent diffusivity model agree with the data, when they actually do not. The nonconservative form leads to satisfactory energy conservation at the lower Rayleigh numbers, and no difference is observed in comparison to results obtained with the conservative form.

Another interesting observation with regard to the numerical results was that they were very similar whether the free slip or no slip condition was used at the wall. The Nusselt numbers changed by less than 1 percent and the temperature profiles were also nearly identical. The only difference was in the velocity profiles in the wall region. This is illustrated in the calculated velocity profiles shown in Fig. 4 for the slip and no slip boundary conditions. (Note that if the no slip boundary condition is used, a term containing $\mu \nabla^2 \overline{V}$ must be added to equation (2) and this will then lead to the correct limits as porosity approaches unity.)

Other typical numerical results on velocity and temperature fields are displayed in the following graphs, see also [12]. Results simulating free convection in finite and infinite enclosures are presented. For Ra* ≤ 300, the vortex observed inside a cubic box is a two-dimensional roll with the axis of rotation oriented with the diagonal of the box, as shown in Fig. 5. It is, of course, equally likely to have the axis of rotation aligned with the other diagonal of the box. The initial conditions used are zero velocity and a constant reference temperature throughout the box. Figure 6 shows the top view of a typical velocity field at Ra* = 150 in a larger geometry. Vortex structures, except those near the walls, are of the polyhedral type. This type of cell has a hexagonal horizontal cross section and was found experimentally by Combarnous [1]. Linear theory predicted that the reduced aspect ratio is 0.75 for this type of convective cell. Our numerical solutions are in agreement with this. The bi-dimensional roll type of convective cell, as observed near the wall, is most likely due to the temperature boundary condition used.

At higher Rayleigh numbers, convective instabilities were found. Typical variations in Nusselt number with time are shown in Fig. 7. The period is 120 s. If the period is nondimensionalized by the thermal diffusion time from one wall to the other, then the non-dimensional period is in agreement with Schubert and Straus [6]. Also the explicit consideration of heat transfer, between the solid and liquid, leads to typical differences in fluid and solid surface temperatures shown in Fig. 8.

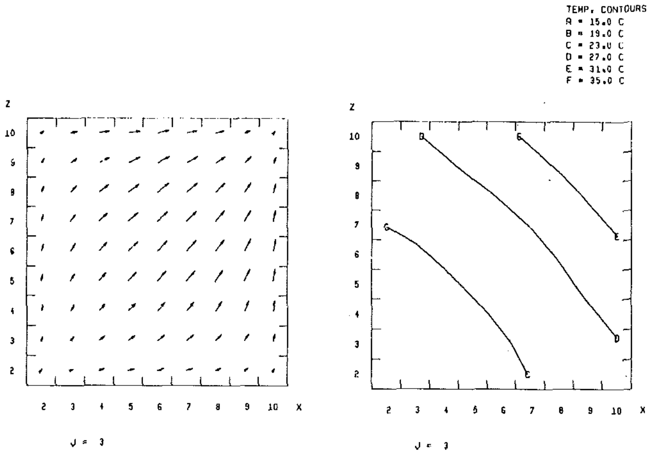

Fig. 5 Top view of a typical velocity and temperature field in a cubic box (9 × 9 × 9, $\Delta x = \Delta y = \Delta z =$ 0.594 cm), $R_a^* = 150$

Conclusion

A numerical scheme based on the simplified MAC technique has been applied to the study of free convective flow in fluid saturated porous medium in rectangular enclosures. Local cancellation of low order, diffusional truncation errors, and use of the conservative form of the energy equation were needed to increase accuracy of the solutions. The numerical results at the higher Rayleigh numbers deviate from experiment in both Nusselt numbers and flow patterns if this technique is not used. Cases with different Rayleigh number, ranging from 36 to 800 have been studied and the solutions are compared with experiments. The solid phase was modeled as an assemblage of spheres, and the temperature profiles obtained within the spheres analytically. The comparisons, including the Nusselt number and vortex structure, between experiments and calculations are satisfactory. Explicit consideration of heat transfer between the solid and fluid was important even at relatively low Rayleigh numbers in order to predict the effect of different solid materials on Nu*. For high Rayleigh number (and transient calculations) this type of model is also necessary to obtain correct Nusselt numbers even for the cases for which the equivalent diffusivity concept works well at low Rayleigh numbers. The numerical method and heat transfer model also predict convective instabilities at high Rayleigh numbers that have a period in agreement with Schubert and Straus [6].

Additional features, such as in and out-flow boundary conditions and internal heat generation are easy to add to the numerical procedure, and have already been used to calculate convective flow in the moderator of Canadian reactor systems, and in designing fuel storage pools. The numerical technique can also accommodate nonuniform porosity and anisotropic porous media. In these cases, the limitations are not on the calculational aspects, but on the physical models needed to predict solid-fluid heat transfer and frictional losses, which must be based on experimental results.

References

1 Combarnous, M. A., and Bories, S. A., "Hydrothermal Convection in Saturated Porous Media," *Advances in Hydroscience*, Vol. 10, 1975, pp. 231–307.

2 Buretta, R. J., and Berman, A. S., "Convective Heat Transfer in a Liquid Saturated Porous Layer," *Journal of Applied Mechanics*, 1976, pp. 249–253.

3 Gupta, V. P., and Joseph, D. D., "Bounds for Heat Transport in a Porous Layer," *Journal of Fluid Mechanics*, Vol. 57, 1973, pp. 491–514.

4 Zebib, A., and Kassoy, D. R., "Three-Dimensional Natural Convection Motion in a Confined Porous Medium," *Physics of Fluids*, Vol. 21, 1978, pp. 1–3.

5 Straus, J. M., and Schubert, G., "3-D Convection in a Cubic Box of Fluid-Saturated Porous Material," *Journal of Fluid Mechanics*, Vol. 91, 1979, pp. 155–165.

6 Schubert, F., and Straus, J. M., "3-D and Multicellular Steady and Unsteady Convection in Fluid-saturated Porous Media at High Rayleigh

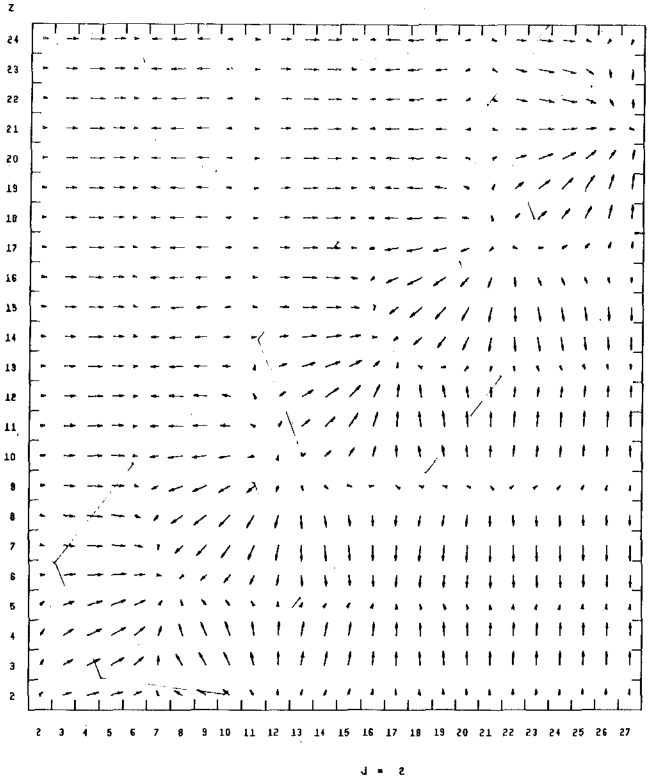

Fig. 6 Top view of typical velocity field in a large geometry (26 × 5 × 23, $\Delta x = \Delta y = \Delta z =$ 1.07 cm), $R_a^* = 150$

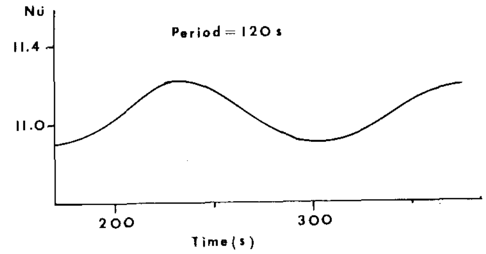

Fig. 7 Typical variations in average Nusselt number with time at $R_a^* = 800$

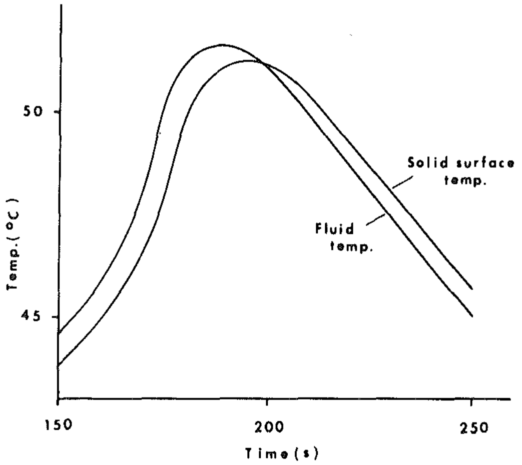

Fig. 8 Typical differences in fluid and solid surface temperatures near the bottom plate at $R_a^* = 800$

Numbers," *Journal of Fluid Mechanics*, Vol. 94, 1979, pp. 25–38.

7 Horne, R. N., and O'Sullivan, J. J., "Oscillatory Convection in a Porous Medium Heated from Below," *Journal of Fluid Mechanics*, Vol. 66, 1974, pp. 339–352.

8 Horne, R. N., "3-D Natural Convection in a Confined Porous Medium Heated from Below," *Journal of Fluid Mechanics*, Vol. 92, 1979, pp. 751–766.

9 Holst, P. H., and Aziz, K., "Transient Three-Dimensional Natural Convection in Confined Porous Media," *International Journal of Heat Mass Transfer*, Vol. 15, 1972, pp. 73–90.

10 Chan, A. M. C. and Banerjee, S., "3-D Numerical Analysis of Transient Natural Convection in Rectangular Enclosures," ASME JOURNAL OF HEAT TRANSFER, Vol. 101, 1979, pp. 114–119.

11 Rivard, W. C., Farmer, O. A., Butler, T. D. and O'Rourke, P. J., "A Method for Increased Accuracy in Eulerian Fluid Dynamics Calculations," LA-5426-MS, Los Alamos, 1973.

12 Chan, Y. T., "Numerical Investigation of Natural Convection in Porous Media," M. Eng. Thesis, McMaster University, 1980.

13 Arpaci, V. S., *Conduction Heat Transfer*, Addison Wesley, 1966.

14 Wyllie, M. J. R., and Gregory, A. R., "Fluid Flow Through Unconsolidated Porous Aggregates," *Industrial Engineering Chemistry*, Vol. 47, 1955, pp. 1379–1388.

15 Bird, R. B., Stewart, W. E. and Lightfoot, E. N., *Transport Phenomena*, J. Wiley, 1960.

W. W. Yousef[1]
Research and Development Engineer,
Canadian General Electric,
Peterborough, Ont., Canada
K9J 7B5

J. D. Tarasuk
Associate Professor,
Faculty of Engineering Science,
The University of Western Ontario,
London, Ont., Canada
N6A 5B9

An Interferometric Study of Combined Free and Forced Convection in a Horizontal Isothermal Tube

A Mach-Zehnder interferometer was employed to determine the three-dimensional temperature field, and the circumferential and average Nusselt numbers for laminar flow of air in the entrance region of an isothermal horizontal tube where the velocity and the temperature profiles were developing simultaneously. The influence of free convection due to buoyancy on forced convection heat transfer was investigated. The Reynolds numbers ranged from 120 to 1200, the Grashof numbers ranged from 0.8×10^4 to 8.7×10^4, and the ratio L/D was varied from 6 to 46. The free convection increases, substantially, the average Nusselt number, by up to a factor of 2.0 from the analytical predictions, which account for forced convection only, near the tube inlet. Far from the tube inlet the free convection tends to decrease the average Nusselt number below the analytical predictions.

Introduction

Laminar flow convective heat transfer in tubes has many diverse industrial and engineering applications. Some of these applications are: compact heat exchangers designed for gas flowing at a high temperature, heat exchangers designed for viscous liquids in chemical processes and oil coolers [1, 2], and the heating of oil flowing through pipelines. Applications can also be extended to study the solidification or freezing processes [4].

In forced convection heat transfer, the fluid is set in motion entirely by the external forces (such as pressure gradient or magnetic flux forces).

In free convection heat transfer, the fluid is set in motion by the gravitational or the buoyancy forces. These gravitational forces are due to the density differences arising from differences in temperature. The influence of free convection on forced convection can be significant and in many practical situations both free and forced convection effects are of comparable order of magnitude. Buoyancy force, due to density differences, is characterized by the Grashof number, Gr, and the forced flow by the Reynolds number, Re. The ratio $Gr/Re^{2.5}$ may be representative of the relative magnitudes of the free and forced convection effects.

When heat is transferred through the wall of a horizontal tube, the density of the fluid near the wall decreases and the buoyancy forces due to this density change cause the warmer fluid to move upward along the side walls. By continuity, then, the heavier fluid near the center of the tube flows downward. As a result, two vortices are formed which are symmetrical about the vertical plane passing through the axis of the tube. Thus a circulation is established which is superimposed on the main forced flow and results in the formation of two symmetrical spiral-like motions. This secondary flow not only increases the rate of heat transfer but also distorts the velocity and temperature profiles which would exist for an isothermal flow.

Two thermal boundary conditions are generally considered for laminar flow heat transfer in tubes: uniform wall heat flux and uniform wall temperature. For the uniform wall heat flux boundary condition there is a constant wall-minus-fluid temperature difference downstream of the thermal entrance region; thus the free convection effects persist throughout the tube. For the uniform wall temperature boundary condition the secondary flow develops to a maximum intensity and then diminishes downstream provided the tube is long enough. Thus the free convection effects are important only in the thermal entrance region of an isothermally heated tube, since the effects disappear as the fluid bulk temperature approaches the wall temperature in the fully developed region.

The problem considered herein is one with uniform wall temperature, which approximates the majority of industrial application and occurs in evaporators, condensers, and in any heat exchanger where one fluid has a much higher capacity rate than the other.

The analytical investigations, which deal with the uniform wall temperature, include series expansions [5–7], finite difference methods [8–11], and boundary layer analysis [12].

The literature studied shows an abundance of experimental results for the uniform heat flux boundary condition, undoubtedly because it affords a more accurate determination of the local heat flux [13, 14]. On the other hand, experimental data for the uniform wall temperature boundary condition are rather scarce, especially for relatively short tubes, i.e., $L/D < 30$.

The published experimental studies which deal with the uniform wall temperature [1–3] were mainly directed toward developing a correlation which predicts the heat transfer for different fluids. These studies do not have a direct bearing on the present work. A review of the available analytical and experimental studies is given in reference [15].

The Mach-Zehnder interferometer has been used exclusively [16–18] to study one (or two) dimensional thermal boundary layers. Chu and Goldstein [16] and Kuehn and Goldstein [17] utilized the time exposure technique to obtain time-spatial averaged interferograms which were analyzed to determine the contours of constant temperature in turbulent convection situations. Franke [19] showed that the Mach-Zehnder interferometer can be used to obtain accurately the average temperature and the average rate of heat transfer with temperature variation along the light beam in a two-dimensional field.

Panknin, et al. [20] used a holographic interferometer to measure the circumferential heat transfer coefficient for forced convection in closely spaced circular tube bundles. In the present study the Mach-Zehnder interferometer was used to study the three-dimensional field which develops due to the combined effect of free and forced convection in the entrance region of an isothermal horizontal tube.

This study includes: (1) The determination of both the radial and axially averaged temperature profiles. (2) The determination of the circumferential and the average Nusselt Numbers with special emphasis on free convection effects.

---

[1] Present address: Advance Engineering Branch, Chalk River Nuclear Laboratories, Chalk River, Ontario, Canada K0J 1J0.

Contributed by the Heat Transfer Division for publication in the JOURNAL OF HEAT TRANSFER. Manuscript received by the Heat Transfer Division September 22, 1980.

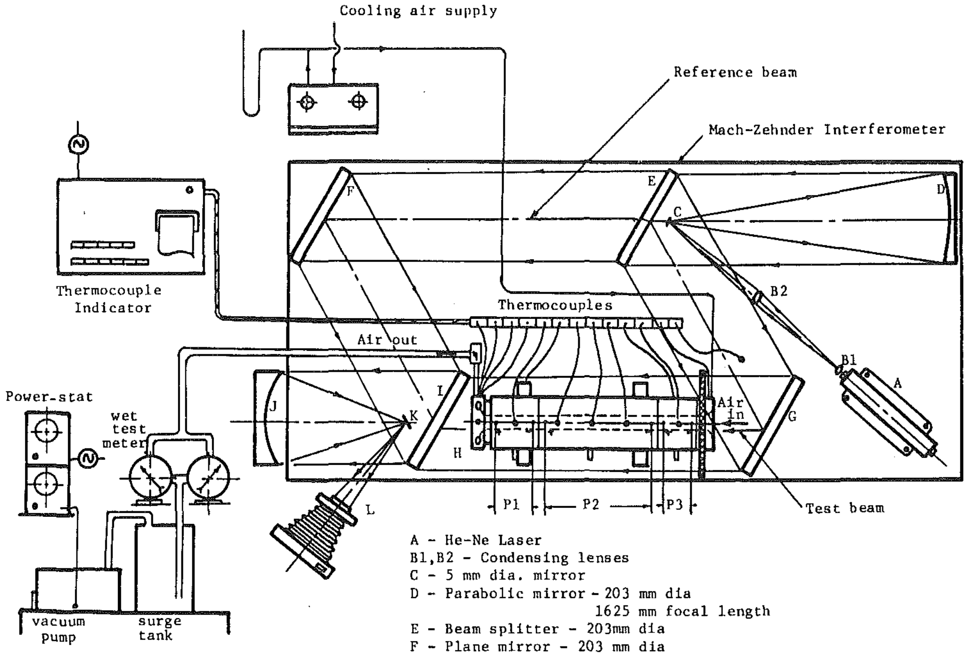

A - He-Ne Laser
B1,B2 - Condensing lenses
C - 5 mm dia. mirror
D - Parabolic mirror - 203 mm dia
1625 mm focal length
E - Beam splitter - 203mm dia
F - Plane mirror - 203 mm dia
G - Plane mirror 203 mm dia
H - Model
I - Beam splitter 203 mm dia
J - Spherical mirror 203 mm dia, 787 mm focal length
K - 10 mm dia mirror
L - Camera
P1,P2,P3 - dc power supplies

Fig. 1 Schematic layout of the test apparatus

Test Apparatus

A schematic layout of the test apparatus is shown in Fig. 1. The main piece of equipment in the test apparatus was the Mach-Zehnder interferometer.

Laminar air flow, with minimum air disturbance at tube entrance, was produced by withdrawing the air through the tube by a variable speed vacuum pump. The volumetric air flow was measured by a precision wet-test gas meter which had a capacity range of 1.13 – 11.33 liter/min, a resolution of 0.01 liter, and an accuracy of ±0.5 percent of the measured volume. Before passing through the flow meters, the air passed through a surge tank of approximately 45.5 L capacity to dampen any flow or pressure fluctuations, especially at low flow rates.

Air and tube wall temperatures were measured by 28-gauge copper-constantan thermocouples which were either shielded against radiation when used to measure air temperature, or electrically insulated to protect against stray current produced in the tube wall which is heated by a d-c current. The ambient air temperature was measured at two different locations: near the tube entrance and at the reference beam. This was done to check the uniformity of the room

Nomenclature

a = tube radius, $D/2$
C_p = specific heat at constant pressure
D = inside tube diameter
Gr = Grashof number, $g\beta D^3(\Delta t_{\mathrm{lm}})/\nu^2$
g = gravitational acceleration
h_ϕ = axially averaged heat transfer coefficient at an angle ϕ
h_{lm} = average heat transfer coefficient based on Δt_{lm}
K = Gladstone-Dale constant, equation (6)
k = thermal conductivity
L = tube length
$\dot{m}$ = mass flow rate
N_t = total fringe shift
$N_{\max}$ = maximum fringe shift
$\overline{\mathrm{Nu}}$ = circumferential average Nusselt number, $1/\pi \int_0^\pi \mathrm{Nu}_\phi \cdot d\phi$
Nu_ϕ = axially averaged Nusselt number at a given ϕ, $h_\phi D/k$
Nu_m = average Nusselt number, $h_{lm}D/k$
n = refractive index
Pr = Prandtl number, $C_p\ \mu/k$
Re = Reynolds number, $4\ \dot{m}/\pi D\mu$
r = radial distance measured from tube wall
t = axially-averaged fringe temperature at a location r, ϕ
t_1 = air bulk temperature at tube inlet
t_2 = air bulk temperature at tube exit
t_w = tube wall temperature
t_b = air mean bulk temperature, equation (3)
$\bar{t}_b$ = air mean bulk temperature as determined by interferogram analysis, equation (2)
t_c = core fringe temperature
Δt_{lm} = logarithmic mean temperature difference (LMTD), $\dfrac{t_2 - t_1,}{ln\dfrac{t_w - t_1}{t_w - t_2}}$
u = axially-averaged velocity at a location r, ϕ
X = nondimensional axial distance, $\dfrac{\mathrm{L/D}}{\mathrm{RePr}}$
X_t = nondimensional axial distance where thermal boundary layer coalesce
$\overline{X_d}$ = nondimensional axial distance where average Nusselt number becomes constant
β = coefficient of thermal expansion
λ_0 = wave length of the light source
θ = temperature difference, $t - t_c$
θ_1 = temperature difference, $t - t_1$
θ_w = temperature difference, $t_w - t_1$
Θ = nondimensional fringe temperature, $\Theta = \dfrac{\theta_1}{\theta_w} = \dfrac{t - t_1}{t_w - t_1}$
μ = dynamic viscosity
ρ = density
ϕ = circumferential angle measured from the tube top, in degrees

Subscripts

1 = inlet conditions
2 = outlet conditions
b = evaluated at mean bulk temperature
m = mean value
w = evaluated at wall temperature
ϕ = evaluated at an angle ϕ

temperature. All thermocouple leads were directly connected to a Doric Digitrend 220 data acquisition system.

The test section was basically comprised of three parts: the inlet section, the tube, and the exit section.

The tube was made of aluminum of 25.1028 mm i.d. and 25.00 mm wall thickness. The inside tube surface was honed circular to ±0.0076 mm (i.e., $D = 25.1028 \pm 0.0076$ mm), with the tube axis parallel to within ±0.020 mm over the total tube length of 1200 mm. The tube is formed of interchangeable segments bolted together. Segment lengths were 50, 100, 150, 200, 300, and 400 mm, which, when assembled in different combinations, could give L/D ratios of approximately $2, 4, 6, \cdots, 46, 48$. Particular care was taken during each assembly to make all segments perfectly coaxial. The tube segments were heated electrically through an AerOcoax electric heating cable which was wrapped tightly around the tube.

The inlet section was designed so as to prevent flow separation at the tube inlet by having the radius of curvature at the tube inlet of the same order of magnitude as the tube diameter. The inlet section was thermally insulated from the rest of the tube in order to prevent heating the air prior to the tube inlet [15]. The exit section was designed to insure good mixing and even withdrawal of air. A very short exit section was used in order to minimize the disturbance caused to the light beam. The maximum error in fringe temperature due to the end effects was estimated to be +1.5 percent.

To achieve isothermal heating, the tube segments at both ends of the tube were heated independently by a power supply. A dc current was employed and up to three d-c power supplies were used for furnishing the necessary current.

At midway of each tube segment, three thermocouple wells were drilled radially 90 deg apart and 3 mm from the inside tube wall. A detailed description of the test section is given in reference [15].

Operating Procedure and Measurements

Through proper focusing by the use of mirror J and the camera screen in Fig. 1, a well-defined model tube edge was obtained which was checked later under the travelling microscope. The fringes were brought to a focus at one-third the distance from the exit plane of the test section. This should result in the minimum possible refraction error according to a study done by Mehta and Black [21].

With the interferometer set up for the infinite fringe field, the fringes represent isotherms in a two-dimensional field or the average temperature along the light path in a three-dimensional field. The infinite fringe setting was found to be more convenient when compared with the wedge fringe setting [17, 22] in determining the temperature gradient at all points on the model surface.

The experiment proceeded by increasing the flow rate at constant wall temperature. Holding the tube wall at constant temperature while varying the flow rate necessitated a fine adjustment for the electrical current especially in segments at both ends of the tube. A period of about three hours was allowed for warm-up and a period of 30 min was required to reach steady-state conditions for each run without affecting the infinite fringe setting.

Upon reaching steady-state conditions, room temperature, tube wall temperature, inlet and exit air temperatures, barometric pressure and electric power input were recorded. At least two exposures, or interferograms, were made of the same situation.

The position of the centre of each fringe was measured by viewing the film negative on a travelling microscope. Destructive interference fringes were used as they appeared sharper and narrower on the negatives. The tube edge was first located and by traversing radially, the positions of fringes centre were then recorded. The opposite tube edge was also located and thus the scale factor was determined by comparing the tube diameter as measured on the negative with the actual tube diameter. Measurements were taken every 30 deg around the tube circumference and on only half of the interferogram due to symmetry of fringes.

In the present study the authors have developed a technique in which the main flow is parallel to the light beam. This technique allows for the study of the three-dimensional temperature field in developing laminar flows in ducts and pipes. This technique can be applied equally to study a forced convection situation in which the free convection effects are negligible.

Presentation and Discussion of Results

The influence of buoyancy forces on temperature profiles and heat transfer has been studied for a wide range of L/D, namely, 6, 10, 14, 18, 24, 30, 38 and 46 which were labeled A, B, C, D, E, F, G and H, respectively. The wall-minus-air temperatures, $\theta_w = t_w - t_1$, were taken as 12.0, 23.0, 33.0, 49.0, 63.0, 81.0 and 102.0°C and were identified by the numerals 1, 2, 3, 4, 5, 6 and 7, respectively. The Reynolds numbers ranged from 120 to 1200. The range of Grashof numbers was from 0.8×10^4 to 8.7×10^4. The average Nusselt number was determined independently by two methods: (1) by an interferogram analysis, and (2) by an energy balance.

A typical interferogram, with the infinite fringe setting, for $L/D = 6$ is shown in Fig. 2.

Temperature Distributions. The developing nondimensional temperature profiles along the planes $\phi = 0 - 180$ deg, $30 - 150$ deg, $60 - 120$ deg and $90 - 90$ deg were determined at various axial locations [15]. Because of symmetry, measurements were taken on only half of the interferogram. Thus the angle $\phi = 210$ deg was replaced by the angle $\phi = 150$ deg and so on. The developing temperature profile along the vertical plane, $\phi = 0 - 180$ deg, is shown in Fig. 3.

It should be made clear that the fringe temperature, t, at a given location (ϕ, r) represents an average integrated value along the tube length. As a consequence of free convection, the temperature profiles differ considerably from the Poiseuille parabolic profile. A common feature in the temperature profiles at different angular positions is that the location of the minimum temperature seems to be invariant and occurs at a distance $a\text{-}r/a \simeq 0.55$ on the bottom of the tube. The temperature profile across the tube maintains its shape as the flow proceeds; it only decreases gradually.

The temperature profile along the vertical centreline as determined numerically by Ou and Cheng [9], at $X = 0.04$ and $\mathrm{Gr} \cdot \mathrm{Pr} = 0.704 \times 10^4$ is plotted on Fig. 3. The temperature profile by Ou and Cheng [9] represents the local temperature rather than the average for the tube length and that explains why Ou and Cheng's profile gives a higher temperature at the same distance X.

A fully developed temperature profile is reached when it becomes invariant with the tube length. The criterion for fully developed temperature profiles as presented by Kays [23] is realized when the local heat transfer coefficient becomes constant.

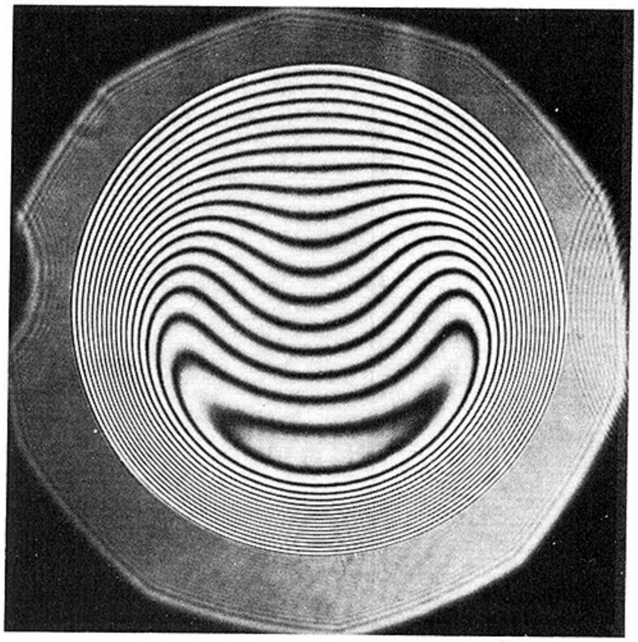

Fig. 2 Interferogram showing isotherms at $X = 0.0143$: $L/D = 6$, Re = 602, Gr = 6.3×10^4, $\theta_w = 101.1$°C, $\overline{\mathrm{Nu}} = 12.14$, Run A-7-5

The equivalent nondimensional distance, $\overline{X}_d$, where the temperature represents an axially averaged value, rather than the local value, is the distance at which the average Nusselt number becomes constant. The value of $\overline{X}_d$ was determined to be 0.255 [15]. Thus in Fig. 3, for $X \geq 0.255$ the averaged temperature profile may be considered as fully developed.

The axial development of temperature, expressed as $\Theta = t\text{-}t_1/t_w - t_1$, in the vertical plane passing through the tube center-line at a distance of $a\text{-}r/a = 0.3$, 0.7 and 0.9 from both top ($\phi = 0$ deg) and bottom ($\phi = 180$ deg) of the tube are shown in Fig. 4. Also shown on the same figure is the axial development of the core-fringe temperatures (the core-fringe represents a zone of minimum temperature in the tube cross-section) whose center lies at a distance of $a\text{-}r/a \cong 0.54 - 0.56$ from tube bottom for all the test runs. Temperatures at the locations $a\text{-}r/a = 0.3$ and 0.7 from the tube bottom were identical, which indicates that the same fringe passes through the two locations for all values of X. Grigull and Tratz [11] solved numerically the energy and momentum equations by assuming a fully developed flow at the tube entrance and by neglecting the free convection term in the energy equation. The temperature as determined by Grigull and Tratz [11] at $a\text{-}r/a = 0.7$ and 0.9 agree quite well with the corresponding experimental results of this study at the tube top, $\phi = 0$ deg, where free convection has the least effect. Discrepancies between results near the tube entrance or at low values of X are mainly due to the assumption of a parabolic velocity profile made in Grigull and Tratz's study.

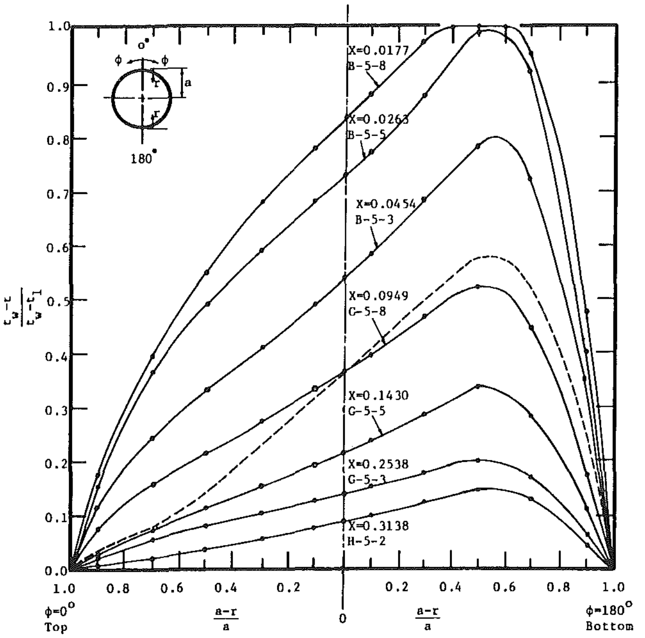

Fig. 3 Development of temperature profile at the vertical plane, $\phi = 0 - 180$ deg, $\theta_w \simeq 63.0°C$, Gr $= 3.0 \times 10^4 - 6.3 \times 10^4$, $X = L/D/\text{Re} \cdot \text{Pr}$, - - - Ou and Cheng's [9] theoretical solution at $X = 0.040$, Gr $\cdot$ Pr $= 0.704 \times 10^4$

The three-dimensional temperature profiles at the vertical plane are shown in Fig. 5. The temperature profile does not change its shape in either the vertical or the horizontal plane; it only decreases gradually as the flow proceeds.

Since the buoyancy force is proportional to the temperature difference $(t_w - t)$, it would be desirable to see how the temperature gradient, expressed as $\partial\Theta/\partial X$, varies with the nondimensional axial distance X. The gradient $\partial\Theta/\partial X$, as approximated by $\Delta\Theta/\Delta X$, expresses the change in free convection intensity with the distance X.

Figure 6 illustrates the variation of free convection intensity along the tube at $a\text{-}r/a = 0.9$ and $\phi = 0$, 90 and 180 deg. A negative $\partial\Theta/\partial X$ value indicates an increase in the intensity of free convection. At $\partial\Theta/\partial X = 0$ the free convection intensity reaches a maximum. As can be seen from both Figs. 4 and 6, the free convection effect reaches a maximum at

$$X_{\text{maximum free convection}} \simeq 0.0180 \cdots\cdots \qquad (1)$$

at which $1\text{-}\Theta = (t_w - t)/(t_w - t_1)$ is a maximum and $\partial\Theta/\partial X$ is zero. Further downstream, the ratio $(t_w - t)/(t_w - t_1)$ and $\partial\Theta/\partial X$ decreases monotonically and the free convection intensity diminishes gradually.

Mean Bulk Temperature. The mean bulk temperature as expressed by

$$\bar{t}_b = \frac{\displaystyle\sum_{\phi=0}^{2\pi}\sum_{i=0}^{N_t}\left[\rho\, C_p\left(\frac{t_i+t_{i+1}}{2}\right)\left(\frac{u_i+u_{i+1}}{2}\right)(r_{i+1}^2-r_i^2)\right]_\phi}{\displaystyle\sum_{\phi=0}^{2\pi}\sum_{i=0}^{N_t}\left[\rho\, C_p\left(\frac{u_i+u_{i+1}}{2}\right)(r_{i+1}^2-r_i^2)\right]_\phi} \cdots \qquad (2)$$

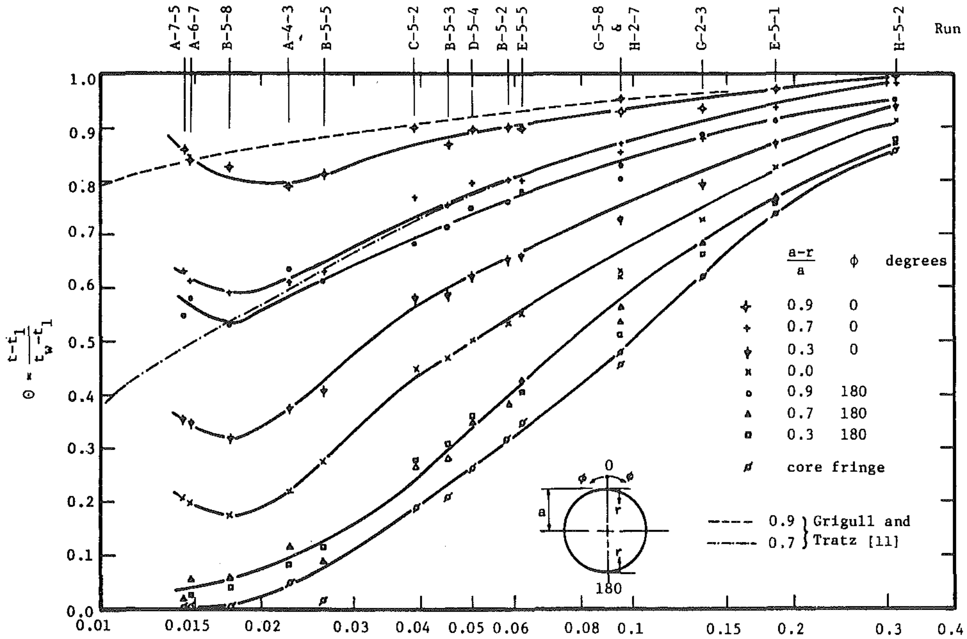

Fig. 4 Axial development of temperature at the vertical plane $\phi = 0 - 180$ deg

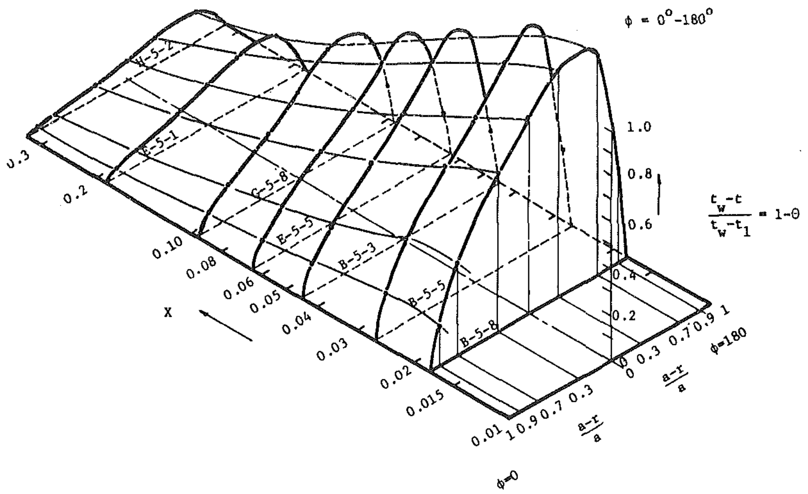

Fig. 5 Temperature profile in the thermal entry region of an isothermal horizontal tube. The vertical plane, $\theta_w \simeq 63.0°C$, Gr $= 3.0 \times 10^4 - 6.3 \times 10^4$

was determined numerically from interferogram analysis. An inherent advantage in the interferogram analysis is the capability of including the physical properties of the fluid when the summations in equation (2) are carried out. This advantage could be very useful when using fluids which have considerable variation in their physical properties, such as heavy oils. For fluids with Prandtl number close to unity, like most gases, the nondimensional axial velocity profile may be considered similar to the nondimensional temperature profile at a given angle ϕ [23]. This similarity between the velocity and temperature profiles was utilized to carry out the summations in equation (2). Density ρ and specific heat C_p were both evaluated at an average temperature $(t_i + t_{i+1})/2$ where i represents the fringe shift.

The mean bulk temperature t_b based on the LMTD is expressed by

$$t_b = t_w - \Delta t_{lm} \cdots\cdots \qquad (3)$$

In spite of the many simplifying assumptions that have been made in the derivation of the LMTD [24], the difference between temperatures as determined from equation (2) and equation (3) was within ±4 percent.

The nondimensional mean bulk temperature variation with X is shown on Fig. 7, where the solid line represents the best-fit curve.

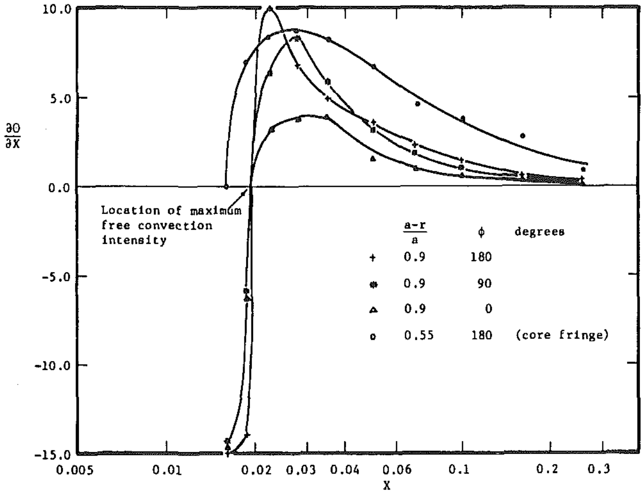

Fig. 6 Variation of free convection intensity along the tube

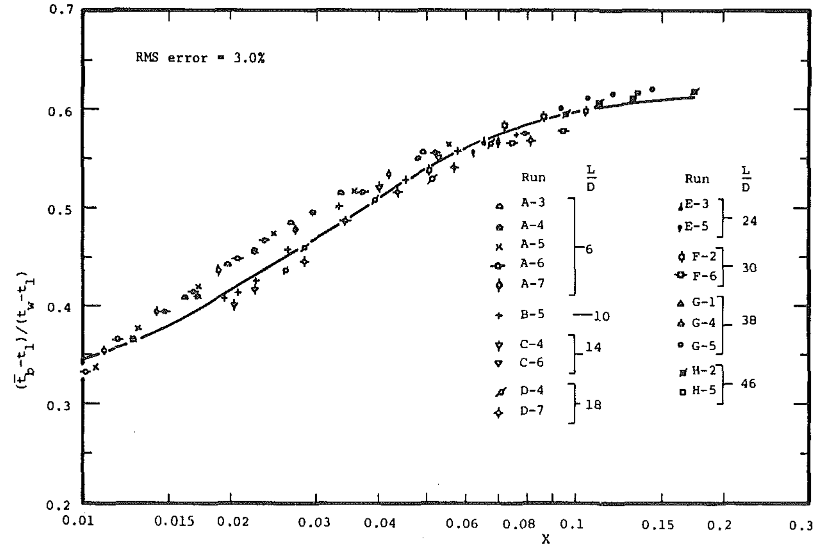

Fig. 7 Axial variation of mean bulk temperature in an isothermal horizontal tube

Fringe Shift Variation. In combined free and forced convection, like the problem considered in this study, the total fringe shift for a given light source, working fluid, and reference temperature depends upon L, Θ_w and Re, thus

$$N_t = f(L, \Theta_w, \mathrm{Re}) \cdots\cdots \tag{4}$$

Experimental results from the current investigation showed that the total fringe shift, N_t, increased as the Reynolds number increased and approached asymptotically a maximum value. The fringe shift reached a maximum when the core fringe was at the room temperature.

The maximum fringe shift, $N_{\max}$, indicates that the thermal boundary layer edges just merge at the tube exit section. The nondimensional distance for this condition is labeled X_t. A further increase in the flow rate results in a thinner thermal boundary layer at the tube exit. The core fringe in this case represents the edges of the thermal boundary layer at tube exit.

Figure 8 shows the variation in total fringe shift with Reynolds number, where the total fringe shift N_t refers to the order of the fringe (or fraction of the fringe) next to the tube wall. The total fringe shift gradually reaches the maximum value $N_{\max}$, as determined from

$$N_{\max} = \frac{T_w - T_1}{T_w} \cdot \frac{L}{\lambda_0} (n_1 - 1) \cdots\cdots\cdot \tag{5}$$

where n_1 is the refractive index at room temperature and was evaluated by the Gladstone-Dale equation [22]:

$$\frac{2(n_1 - 1)}{3\rho_1} = K \cdots\cdots\cdot \tag{6}$$

At this point the temperature of the core fringe becomes the same as the ambient temperature. Any further increase in the Reynolds number would simply reduce the thermal boundary layer thickness at the tube exit but N_t remains unchanged as it would be equal to $N_{\max}$. The axial location X_t at which $N_t = N_{\max}$ was determined as

$$X_t = 0.0212 \cdots\cdots\cdot \tag{7}$$

Equation (7) gives an average value for X_t with a maximum deviation of +14.6 percent and −11.0 percent.

In pure forced convection, the location at which the boundary layer meets at the tube center may be considered the location of the fully developed temperature profile [25]. Thus for pure forced convection, $X_t = 0.05$, which, when compared with equation (7), one concludes that the free convection reduces X_t by more than 50 percent.

Circumferential Nusselt Number. The circumferential Nusselt number, Nu_ϕ, was determined from the following relation

$$\mathrm{Nu}_\phi = \frac{h_\phi \cdot D}{k} = -\frac{D \cdot \left[\left(\frac{\partial \theta}{\partial r}\right)_w\right]_\phi}{\Delta t_{lm}} \cdots\cdots\cdot \tag{8}$$

where Nu_ϕ represents an axially averaged Nusselt number at a given angle ϕ.

The variation of Nusselt number, Nu_ϕ, over the tube perimeter for different values of the nondimensional axial distance X is illustrated in Fig. 9.

A strong secondary flow is indicated by a relatively high $\mathrm{Gr/Re}^{2.5}$. The circumferential Nusselt number tends to become even over a considerable arc at both the top and bottom surfaces of the tube as shown in Fig. 9.

Since a strong secondary flow tends to flatten Nu_ϕ distribution at the top and the bottom regions of the tube, most of the change in Nu_ϕ in runs with relatively high $\mathrm{Gr/Re}^{2.5}$ takes place between $\phi = 60$ deg and $\phi = 120$ deg.

The rate of change of the circumferential Nusselt number with respect to angle ϕ as expressed by $\partial \mathrm{Nu}_\phi / \partial \phi$ is plotted against angle ϕ on Fig. 10. As the ratio $\mathrm{Gr/Re}^{2.5}$ increases, the distribution curve becomes more flattened. This means that a strong secondary flow tends to minimize the variation in the circumferential Nusselt number, as mentioned earlier. The important feature of Fig. 10 is that $\partial \mathrm{Nu}_\phi / \partial \phi$ reaches a maximum at approximately an angle $\phi = 75$ deg. This can be explained as follows: As the secondary flow develops, the thermal boundary layer builds up as the flow moves upward along the tube side wall, with the result of a lower temperature gradient and a corresponding lower circumferential Nusselt number as ϕ decreases. At approximately an angle $\phi = 75$ deg, the secondary flow spirals separate from the wall and the rate of decrease of the circumferential Nusselt number begins to slow down. The point at which the secondary flow separates corresponds to the inflection point on the distribution curve in Fig. 9.

The variation of the circumferential Nusselt number with X, at $\phi = 0$, 30, 60, 90, 120 and 180 deg is shown on Fig. 11.

The average Nusselt number, $\overline{\mathrm{Nu}}$, as expressed by

$$\overline{\mathrm{Nu}} = \frac{1}{\pi} \int_0^\pi \mathrm{Nu}_\phi \cdot d\phi \cdots\cdots \tag{9}$$

is also shown in Fig. 11. Because Nu_ϕ represents an axially averaged Nusselt number at a given angle ϕ, the integration (9) over the tube circumference gives an overall average Nusselt number $\overline{\mathrm{Nu}}$ which is referred to as "average Nusselt number" for simplicity.

Figure 11 shows that, at a given X, the ratio $\mathrm{Nu}_{180}/\mathrm{Nu}_0$ reached a value as high as 5.0. This is a considerable variation in Nusselt number over the tube perimeter.

Figure 11 shows also that while the average Nusselt number becomes twice the value predicted analytically by Kays [23] at points near the tube inlet ($X < 0.04$), the average Nusselt number becomes lower than the asymptotic value, Nu_∞, of 3.66 at points further downstream ($X > 0.15$), for an isothermal tube. This is due mainly to omission of free convection effects in the analytical solution of Kays [23].

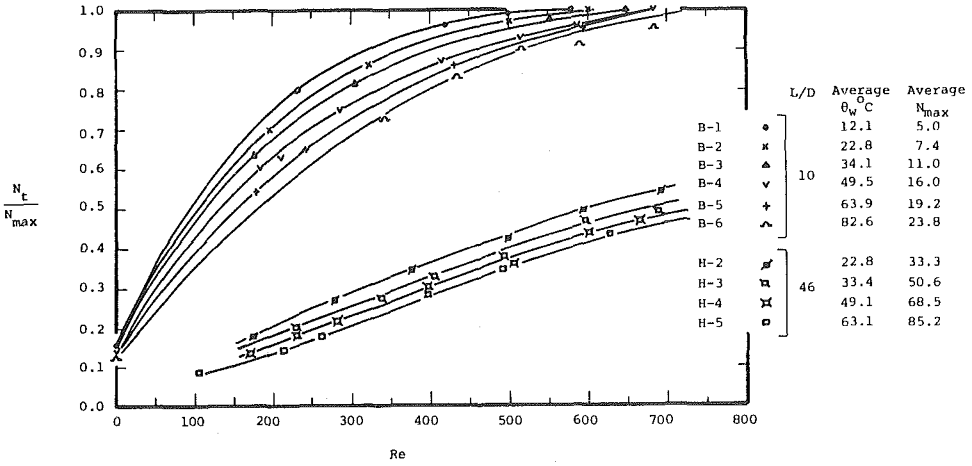

Fig. 8 Variation of total fringe shift with Reynolds number

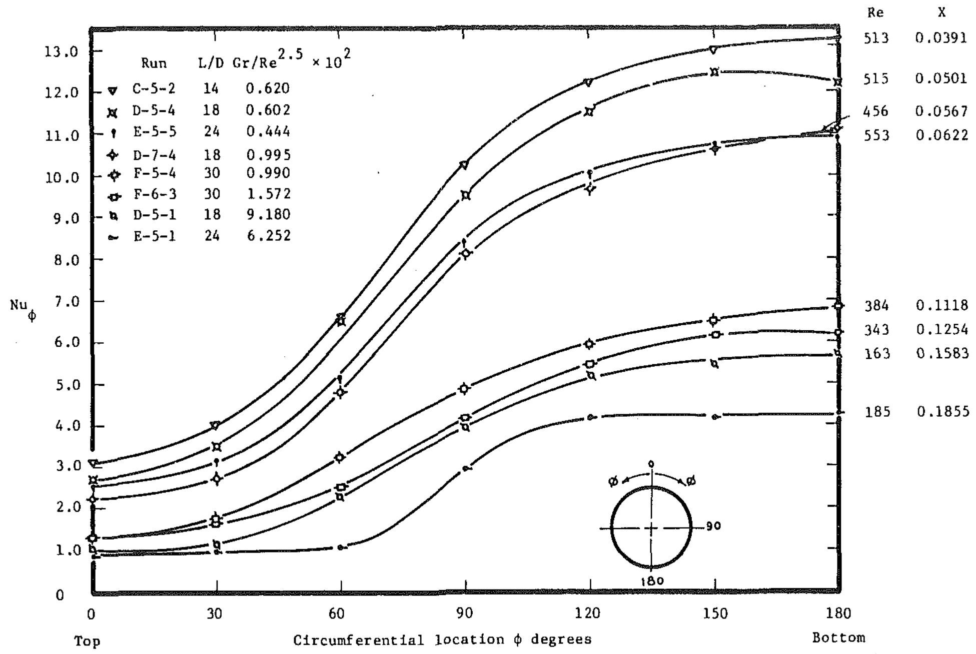

Fig. 9 Circumferential variation of Nusselt number — Runs *C*,*D*,*E* and *F*

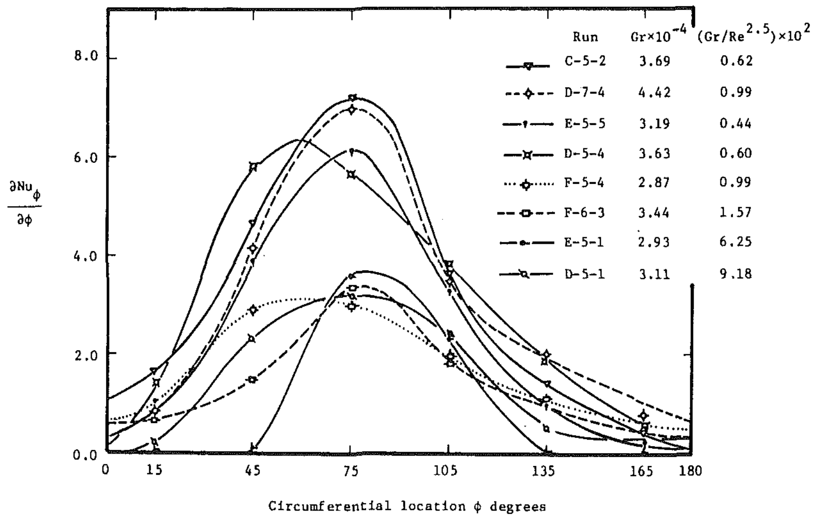

Fig. 10 Rate of change of circumferential Nusselt number versus angle *ϕ*

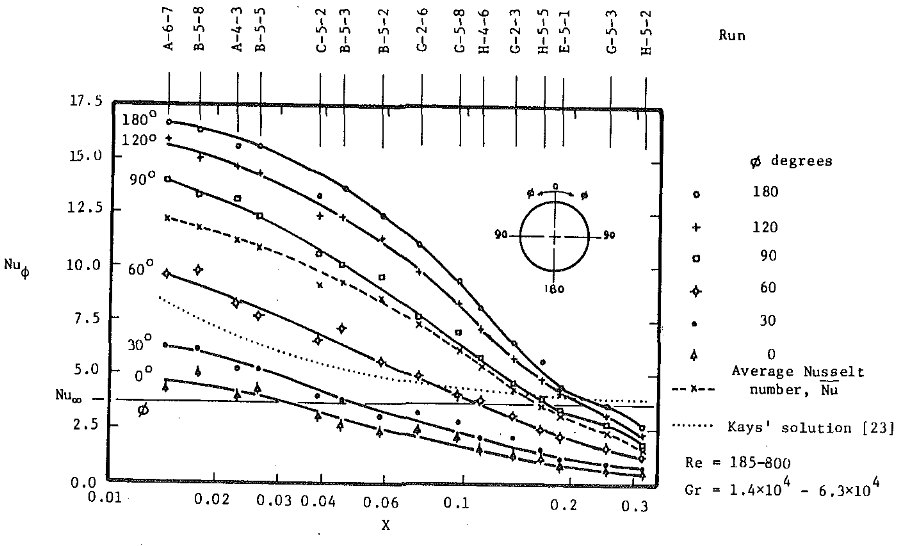

Fig. 11 Axial variation of the circumferential Nusselt number

The average Nusselt number was determined independently by an energy balance and was labeled Nu_m, where

$$\mathrm{Nu}_m = \frac{h_{lm} D}{k} = \dot{m}\, C_p \frac{ln\left(\frac{t_w - t_1}{t_w - t_2}\right)}{\pi k L} \cdots\cdots \tag{10}$$

The percentage difference between $\overline{\mathrm{Nu}}$ as determined from the interferogram analysis and Nu_m as determined from the energy balance was found to be within ±7% for $X > 0.03$ [15]. This good agreement supports the method of analysis.

For more details on the work described in this paper the reader may refer to reference [15].

Summary and Conclusions

The Mach-Zehnder interferometer was employed to determine the three-dimensional temperature field and the Nusselt number for laminar flow of air in the entrance region of an isothermal horizontal tube.

The technique developed in this study has proven to yield accurate reliable, and consistent results when used to study three-dimensional temperature fields. The interferogram analysis gave a precise value to the mean bulk temperature which compared quite well (within ±4 percent) with that based on thermocouple measurements and the use of log-mean temperature difference. The average Nusselt numbers as determined from the interferogram analysis for $X > 0.030$ were in good agreement with the corresponding values determined by an energy balance.

This study has elucidated the influence of free convection on laminar flow of air in an isothermal horizontal tube, which is summarized below.

1 The secondary flow, due to buoyancy, causes a significant change in the temperature profile from that of pure force convection. The minimum temperature occurs approximately midway between tube center and wall in the bottom half of the tube.

2 The secondary flow causes a considerable variation in the circumferential Nusselt number. The Nusselt number at the bottom of the tube can be as high as five times the Nusselt number at the top.

3 The intensity of the free convection reaches a maximum near the tube inlet (i.e., at $X = 0.018$) and then diminishes gradually as the flow proceeds. While the free convection increases substantially the average Nusselt number, by up to a factor of 2.0 from the analytical predictions near the tube inlet ($X < 0.04$), it tends to decrease the average Nusselt number below the analytical predictions far from the tube inlet ($X > 0.15$).

Acknowledgment

This research was supported by the Natural Sciences and Engineering Research Council of Canada. The authors are grateful to W. R. Tarasuk, D. E. Teed and M. Barns of the Canadian General Electric of Peterborough for useful discussions.

References

1 Depew, C. A., and August, S. E., "Heat Transfer Due to Free and Forced Convection in a Horizontal and Isothermal Tube," ASME JOURNAL OF HEAT TRANSFER, Vol. 93, 1971, pp. 380–384.

2 Oliver, D. R., "The Effect of Natural Convection on Viscous-Flow Heat Transfer in Horizontal Tubes," *Chemical Engineering Science*, Vol. 17, 1962, pp. 335–350.

3 Brown, A. R., and Thomas, M. A., "Combined Free and Forced Convection Heat Transfer for Laminar Flow in Horizontal Tubes," *Journal of Mechanical Engineering Science*, Vol. 7, No. 4, 1965, pp. 440–443.

4 Cheng, K. C., and Ou, J. W., "Maximum Density Effects on Forced Laminar Convection in Horizontal Water Pipes with Near Freezing Temperature," *Heat Transfer 1978, Proceedings of the Sixth International Heat Transfer Conference*, MC. 12, Vol. 1, Toronto 1978, pp. 67–72.

5 Yao, L. S., "Free-Forced Convection in the Entry Region of a Heated Straight Pipe," ASME JOURNAL OF HEAT TRANSFER, Vol. 100, 1978, pp. 212–219.

6 Graetz, L., "Über die Wärmeleitungsfähigkeit von Flüssigkeiten," *Annalen der Physik*, Vol. 25, 1885, pp. 337–357.

7. Sellars, J. R., Tribus, M., and Klein, J. S., "Heat Transfer to Laminar Flow in a Round Tube or Flat Conduit—The Graetz Problem Extended," *Trans. ASME*, Vol. 78, 1956, pp. 441–448.

8 Kays, W. M., "Numerical Solutions for Laminar-Flow Heat Transfer in Circular Tubes," *Trans. ASME*, Vol. 77, 1955, pp. 1265–1274.

9 Ou, J. W. and Cheng, K. C., "Natural Convection Effects on Graetz Problem in Horizontal Isothermal Tube," *International Journal of Heat and Mass Transfer*, Vol. 20, 1977, pp. 953–960.

10 Ulrichson, D. L., and Schmitz, R. A., "Laminar-Flow Heat Transfer in the Entrance Region of Circular Tubes," *International Journal of Heat and Mass Transfer*, Vol. 8, 1965, pp. 253–258.

11 Grigull, U., and Tratz, H., "Thermischer Einlauf in Ausgebildeter Laminarer Rohrströmung," *International Journal of Heat and Mass Transfer*, Vol. 8, 1965, pp. 669–678.

12 Hieber, C. A., and Sreenivasan, S. K., "Mixed Convection in an Isothermally Heated Horizontal Pipe," *International Journal of Heat and Mass Transfer*, Vol. 17, 1974, pp. 1337–1348.

13 Mori, Y., Futagami, K., Tokuda, S., and Nakamura, M., "Forced Convective Heat Transfer in Uniformly Heated Horizontal Tubes," *International Journal of Heat and Mass Transfer*, Vol. 9, 1966, pp. 453–463.

14 Bergles, A. E., and Simonds, R. R., "Combined Forced and Free Convection for Laminar Flow in Horizontal Tubes with Uniform Heat Flux," *International Journal of Heat and Mass Transfer*, Vol. 14, 1971, pp. 1989–2000.

15 Yousef, W. W., "An Interferometric Study of Laminar Combined Free and Forced Convective Heat Transfer in the Entrance Region of an Isothermal Horizontal Tube," Ph.D. Thesis, Faculty of Engineering Science, The University of Western Ontario, 1980.

16 Chu, T. Y., and Goldstein, R. J., "Turbulent Convection in a Horizontal Layer of Water," *Journal of Fluid Mechanics*, Vol. 60, 1973, pp. 141–159.

17 Kuehn, T. H., and Goldstein, R. J., "An Experimental Study of Natural Convection Heat Transfer in Concentric and Eccentric Horizontal Cylindrical Annuli," ASME JOURNAL OF HEAT TRANSFER, Vol. 100, 1978, pp. 635–640.

18 Meyer, B. A., Mitchell, J. W., and El-Wakil, M. M., "Natural Convection Heat Transfer in Moderate Aspect Ratio Enclosures," ASME JOURNAL OF HEAT TRANSFER, Vol. 101, 1979, pp. 655–659.

19 Franke, M. E., "Interferometer Measurements in Free Convection on a Vertical Plate with Temperature Variation in Light-beam Direction," *Heat Transfer 1970, Proceedings of the Fourth International Heat Transfer Conference*, N.C. 1.2, Vol. 4, Paris 1970, pp. 1–12.

20. Panknin, W., Jahn, M., and Reineke, H. H., "Forced Convection Heat Transfer in the Transition from Laminar to Turbulent in Closely Spaced Circular Tube Bundles," *Heat Transfer 1974, Proceedings of the Fifth International Heat Transfer Conference*, F.C. 8.7, Vol. 2, Tokyo 1974, pp. 325–329.

21 Mehta, J. M., and Black, W. Z., "Errors associated with Interferometric Measurements of Convective Heat Transfer Coefficients," *Applied Optics*, Vol. 16, No. 6, 1977, pp. 1720–1726.

22 Hauf, W., and Grigull, U., "Optical Methods ir Heat Transfer", in *Advances in Heat Transfer*, Hartnett, J. P., and Irvine, T. F., Jr. (Editors), Academic Press, New York, Vol. 6, 1970, pp. 131–366.

23 Kays, W. M., *Convective Heat and Mass Transfer*, McGraw-Hill, New York, 1966, pp. 118–128.

24 Chapman, A. M. *Heat Transfer*, *Macmillan*, New York, Third Edition, 1974, pp. 510–514.

25 Eckert, E. R. G., and Drake, R. M. Jr., *Analysis of Heat and Mass Transfer*, McGraw-Hill, New York, 1972, pp. 333–342.

A. Moutsoglou
T. S. Chen
Department of Mechanical and Aerospace Engineering,
University of Missouri-Rolla, Rolla, MO 65401

K. C. Cheng
Department of Mechanical Engineering,
University of Alberta,
Edmonton, Alberta, Canada

Vortex Instability of Mixed Convection Flow over a Horizontal Flat Plate

The vortex instability of laminar, mixed-convection flow over an isothermal, horizontal flat plate is investigated analytically by the linear stability theory. In the analysis, the main flow and thermal fields are treated as non-parallel and the disturbances are assumed to have the form of a stationary longitudinal vortex roll that is periodic in the spanwise direction. Numerical results for the critical Grashof and Reynolds numbers that predict the first occurrence of the vortex rolls are obtained for fluids with Prandtl numbers of 0.7 and 7. It is found that the flow becomes more susceptible to vortex mode of instability as the buoyancy force increases. The present results are compared with available experimental data and also with analytical results from the wave mode of instability.

Introduction

In laminar forced convection flow over a heated, horizontal flat plate, the buoyancy force effects may become significant and influence the flow regime such that laminar flow becomes unstable and transition to turbulent flow takes place. Of the two modes of instability that may arise in laminar mixed convection flow over a horizontal flat plate, the wave mode of instability was studied by Chen and Moutsoglou [1], and the vortex mode by Wu and Cheng [2]. In their study, however, Wu and Cheng treated the vortex instability problem by approximating the mainflow as the Blasius flow without the buoyancy force effect and then proceeded to solve the disturbance equations. Their model of Blasius flow approximation of the mainflow in the vortex instability analysis is not proper, because the term solely responsible for the possible occurence of the vortex rolls and hence of the instability of the flow is the buoyancy force term that appears in the mainflow equation. Without the presence of the buoyancy force in the mainflow, vortex instability of the flow cannot be expected to occur.

The present paper deals with an analysis of the vortex instability of laminar, mixed-convection flow over an isothermal, horizontal flat plate for the situations in which the fluid is either heated from below or cooled from above. The governing equations for the coupled main flow and thermal fields are transformed into a dimensionless form and then solved by an efficient finite-difference method. In the stability analysis, the resulting eigenvalue problem is solved by Runge-Kutta integration scheme along with a Newton-Raphson shooting method. Critical Grashof numbers and critical Reynolds numbers for the onset of the instability of the flow are presented for fluids having Prandtl numbers of 0.7 and 7. The present analytical results are compared with the experimental data of Hayashi, et al. [3] for air and Gilpin, et al. [4] for water. They are also compared with the analytical results from the wave mode of instability [1]. From such a comparison, it is possible to determine which of the two modes is responsible for the first onset of the instability of laminar horizontal flow under the effect of buoyancy forces.

Analysis

The Main Flow and Thermal Fields. The problem of laminar mixed-convection flow over an isothermal, semi-infinite horizontal plate was recently studied by Chen, et al. [5]. The governing differential equations for such a flow, as shown in [5], can be expressed by the following dimensionless form:

$$F''' + \frac{1}{2}FF'' + \frac{1}{2}\xi\left(\eta\theta + \int_\eta^\infty \theta d\eta + \xi\int_\eta^\infty \frac{\partial\theta}{\partial\xi}d\eta\right) = \frac{1}{2}\xi\left(F'\frac{\partial F'}{\partial\xi} - F''\frac{\partial F}{\partial\xi}\right) \quad (1)$$

$$\frac{1}{\mathrm{Pr}}\theta'' + \frac{1}{2}F\theta' = \frac{1}{2}\xi\left(F'\frac{\partial\theta}{\partial\xi} - \theta'\frac{\partial F}{\partial\xi}\right) \quad (2)$$

$$F(\xi, 0) = F'(\xi, 0) = 0, \theta(\xi, 0) = 1, F'(\xi, \infty) = 1, \theta(\xi, \infty) = 0 \quad (3)$$

In the foregoing equations $\xi(x) = \mathrm{Gr}_x/\mathrm{Re}_x{}^{5/2}$ is the buoyancy force parameter, $\eta(x, y) = y(U_\infty/\nu x)^{1/2}$ is the pseudo-similarity variable, Gr_x is the local Grashof number, Re_x is the local Reynolds number, Pr is the Prandtl number, $F(\xi, \eta)$ is the reduced stream function, and $\theta(\xi, \eta)$ is the dimensionless temperature, as are defined in the nomenclature. The primes in equations (1–3) denote partial differentiation with respect to η.

Formulation of the Stability Problem. To demonstrate the formulation of the equations governing the disturbances, it suffices to mention its highlights. The perturbation quantities u', v', w', p', and t' are superimposed on the main flow quantities U, V, $W = 0$, P, and T to obtain the resultant velocity components $\hat{u}$, $\hat{v}$, and $\hat{w}$ in the x, y, and z directions, the resultant static pressure $\hat{p}$ and the resultant temperature $\hat{t}$ as:

$$\begin{aligned} \hat{u} &= U(x, y) + u'(y, z) \\ \hat{v} &= V(x, y) + v'(y, z) \\ \hat{w} &= w'(y, z) \\ \hat{p} &= P(x, y) + p'(y, z) \\ \hat{t} &= T(x, y) + t'(y, z) \end{aligned} \quad (4)$$

The form of the perturbation quantities is for disturbances that are stationary and neutrally stable [6]. To proceed, equation (4) is first substituted into the Navier-Stokes equations and the energy equation for incompressible, three-dimensional steady fluid flow. This is followed by subtraction of the mainflow and linearization of the disturbance quantities. This operation leads to the following system of equations:

$$u'\frac{\partial U}{\partial x} + v'\frac{\partial U}{\partial y} + V\frac{\partial u'}{\partial y} = \nu\left(\frac{\partial^2 u'}{\partial y^2} + \frac{\partial^2 u'}{\partial z^2}\right) \quad (5)$$

$$u'\frac{\partial V}{\partial x} + v'\frac{\partial V}{\partial y} + V\frac{\partial v'}{\partial y} = -\frac{1}{\rho}\frac{\partial p'}{\partial y} + g\beta t' + \nu\left(\frac{\partial^2 v'}{\partial y^2} + \frac{\partial^2 v'}{\partial z^2}\right) \quad (6)$$

$$V\frac{\partial w'}{\partial y} = -\frac{1}{\rho}\frac{\partial p'}{\partial z} + \nu\left(\frac{\partial^2 w'}{\partial y^2} + \frac{\partial^2 w'}{\partial z^2}\right) \quad (7)$$

$$u'\frac{\partial T}{\partial x} + v'\frac{\partial T}{\partial y} + V\frac{\partial t'}{\partial y} = \kappa\left(\frac{\partial^2 t'}{\partial y^2} + \frac{\partial^2 t'}{\partial z^2}\right) \quad (8)$$

The system of equations (5–8) is then nondimensionalized by introducing the following dimensionless quantities.

$$(X, Y, Z) = (x, y, z)/L, \ (u^+, v^+, w^+) = (u', v', w')/U_\infty,$$

Contributed by the Heat Transfer Division for publication in the JOURNAL OF HEAT TRANSFER. Manuscript received by the Heat Transfer Division March 23, 1980.

$$p^+ = p'/(\rho U_\infty{}^2/\mathrm{Re}_L),\ t^+ = t'/(T_w - T_\infty) \tag{9}$$

With the characteristic length $L(x)$ defined by $L = (\nu x/U_\infty)^{1/2}$, it follows that $Y = \eta$ and $\mathrm{Re}_L = \mathrm{Re}_x{}^{1/2}$. Next, after the elimination of the pressure terms, the dimensionless disturbance equations are further simplified by assuming that the stationary longitudinal vortices are periodic in the spanwise direction, with amplitude functions depending only on Y. Thus, with

$$(u^+, v^+, w^+, t^+) = [u(y), v(y)/\mathrm{Re}_L, w(y), t(y)]e^{i\alpha z} \tag{10}$$

the disturbance equations along with their boundary conditions can be cast in the following final form

$$[(D^2 - \alpha^2) - C_1 D + C_2]u = F''v \tag{11}$$

$$[(D^2 - \alpha^2)^2 - C_1(D^3 - \alpha^2 D) - C_2(D^2 - \alpha^2)]v = \alpha^2\xi\mathrm{Re}_x t - \alpha^2 C_3 u \tag{12}$$

$$[(D^2 - \alpha^2) - \mathrm{Pr}C_1 D]t = \mathrm{Pr}(\theta' v - C_4 u) \tag{13}$$

$$u = v = Dv = t = 0 \text{ at } \eta = 0 \tag{14a}$$

$$u = v = Dv = t \to 0 \text{ as } \eta \to \infty \tag{14b}$$

In equations (11) to (14), $D^n = d^n/d\eta^n$, α is the dimensionless wavenumber of the disturbances, and C_1, C_2, C_3, C_4 are the mainflow quantities that can be obtained from solution of equations (1) to (3). The expressions for C_1, C_2, C_3, and C_4 are

$$C_1(\xi, \eta) = \frac{1}{2}\left(\eta F' - F - \xi\frac{\partial F}{\partial \xi}\right) \tag{15}$$

$$C_2(\xi, \eta) = \frac{1}{2}\left(\eta F'' - \xi\frac{\partial F'}{\partial \xi}\right) \tag{16}$$

$$C_3(\xi, \eta) = \frac{1}{4}\left(F - \eta F' - \eta^2 F'' + 2\eta\xi\frac{\partial F'}{\partial \xi} - \xi\frac{\partial F}{\partial \xi} - \xi^2\frac{\partial^2 F}{\partial \xi^2}\right) \tag{17}$$

$$C_4(\xi, \eta) = \frac{1}{2}\left(\eta\theta' - \xi\frac{\partial \theta}{\partial \xi}\right) \tag{18}$$

and the boundary condition $Dv = 0$ results from $w^+ = 0$ along with $\partial v^+/\partial Y + \partial w^+/\partial Z = 0$. It is noted here that the term $\alpha^2 C_3 u$ in equation (12), which corresponds to $u'\,\partial V/\partial x$ in equation (6), was neglected in the work of [2]. In addition, the terms containing $\xi\partial/\partial\xi$ in equations (15–18) do not appear in [2].

The mathematical system consisting of the coupled differential equations (11) to (13) along with the boundary conditions, equation (14), constitutes an eigenvalue problem of the form

$$E(\mathrm{Re}_x, \alpha; \xi, \mathrm{Pr}) = 0 \tag{19}$$

In determining the neutral stability curve for a given buoyancy force parameter ξ and a given Prandtl number Pr, the value of Re_x or α satisfying equation (19) is sought as the eigenvalue for a prescribed value of α or Re_x.

Numerical Method of Solution

The solutions to the main flow and thermal fields, as described by the system of equations (1–3), were obtained by a finite-difference scheme similar to, but modified from that described in [7], to provide the mainflow quantities that are needed in the stability calculations. In this connection, it is noted here that equation (1) was differentiated with respect to η once to remove the integral terms in the equation. This gave rise to a fourth-order equation and necessitated an additional boundary condition $F'''(\xi, 0)$ which was obtained by evaluating equation (1) at $\eta = 0$.

The equations describing the stability problem, equations (11–14), were solved numerically by a fourth-order Runge-Kutta integration scheme. This eigenvalue problem is best solved by starting the integration of equations (11–13) from $\eta = \infty$ to $\eta = 0$ (at the wall). Thus, to proceed with the integration, the boundary conditions (14b) at $\eta = \infty$ need to be replaced by approximate conditions that are obtained from the asymptotic solutions of equations (11–13) at $\eta = \eta_\infty$ (the edge of the boundary layer). The asymptotic solutions for u, v, and t consists of four sets of independent solutions (u_i, v_i, t_i), with $i = 1, 2, 3$, and 4. They can be obtained as

$$u_2 = e^{-m\eta_\infty},\ u_1 = u_3 = u_4 = 0 \text{ at } \eta = \eta_\infty \tag{20a}$$

$$v_1 = e^{-\alpha\eta_\infty},\ v_2 = e^{-m\eta_\infty},\ v_3 = e^{-r\eta_\infty},\ v_4 = \eta_\infty e^{-m\eta_\infty} \text{ at } \eta = \eta_\infty \tag{20b}$$

$$t_3 = e^{-r\eta_\infty},\ t_1 = t_2 = t_4 = 0 \text{ at } \eta = \eta_\infty \tag{20c}$$

where

$$m = \frac{-C_1(\xi, \eta_\infty) + \sqrt{[C_1(\xi, \eta_\infty)]^2 + 4\alpha^2}}{2},$$

$$r = \frac{-C_1(\xi, \eta_\infty)\mathrm{Pr} + \sqrt{[C_1(\xi, \eta_\infty)\mathrm{Pr}]^2 + 4\alpha^2}}{2} \tag{21}$$

Thus, the complete solutions for u, v, and t at any $\eta = Y$ can be expressed by

$$\begin{aligned} u(\eta) &= k_1 u_1(\eta) + k_2 u_2(\eta) + k_3 u_3(\eta) + k_4 u_4(\eta) \\ v(\eta) &= k_1 v_1(\eta) + k_2 v_2(\eta) + k_3 v_3(\eta) + k_4 v_4(\eta) \\ t(\eta) &= k_1 t_1(\eta) + k_2 t_2(\eta) + k_3 t_3(\eta) + k_4 t_4(\eta) \end{aligned} \tag{22}$$

where k_1, k_2, k_3, and k_4 are constants and each of the independent solutions (u_i, v_i, t_i) satisfies the system of equations (11–14).

For prescribed values of ξ and Pr, and with a pre-assigned value of, say, α, equations (11–13) are numerically integrated from $\eta = \eta_\infty$ to $\eta = 0$, starting with the asymptotic values given by equation (20). The remaining eigenvalue Re_x is then determined by a Newton-Raphson differential-correction iteration scheme until the boundary conditions at the wall, equations (14a), are satisfied within a certain tolerance. This is accomplished by evaluating three of the four wall boundary conditions along with a normalizing condition at the wall, $D^2 v = 1$ at $\eta = 0$, to determine the four unknown constants k_1, k_2, k_3, and k_4.

Nomenclature

$D^n = d^n/d\eta^n$, differential operator
$F = \psi(x, y)/(\nu U_\infty x)^{1/2}$, reduced stream function
g = gravitational acceleration
$\mathrm{Gr}_x = g\beta(T_w - T_\infty)x^3/\nu^2$, local Grashof number
$L = (\nu x/U_\infty)^{1/2}$, characteristic length
p' = perturbation pressure
P = mainflow pressure
Pr = Prandtl number
$\mathrm{Re}_x = U_\infty x/\nu$, local Reynolds number
$\mathrm{Re}_L = U_\infty L/\nu$, Reynolds number based on L
t' = perturbation temperature
T = mainflow temperature
T_w = wall temperature
u', v', w' = axial, normal, and spanwise components of velocity disturbances
U, V, W = axial, normal, and spanwise velocity components of mainflow
x, y, z = axial, normal, and spanwise coordinates
X, $Y = \eta$, Z = dimensionless axial, normal, and spanwise coordinates
$\alpha = 2\pi/\lambda$, dimensionless wavenumber
β = coefficient of thermal expansion
$\eta = y(U_\infty/\nu x)^{1/2}$, pseudo-similarity variable
η_∞ = dimensionless boundary-layer thickness
$\theta = (T - T_\infty)/(T_w - T_\infty)$, dimensionless temperature
κ = thermal diffusivity of fluid
λ = dimensionless wavelength
ν = kinematic viscosity
$\xi = \mathrm{Gr}_x/\mathrm{Re}_x{}^{5/2}$, buoyancy force parameter
ρ = density of fluid
ψ = stream function

Superscripts

+ = dimensionless disturbance quantity
* = critical condition

Subscript

∞ = condition at free stream

These four constants are then substituted back to the remaining wall boundary condition to check if the last condition is fulfilled.

In the numerical integration of the stability equations, it was determined that a step size of 0.04 was more than adaquate for all the parameters that were investigated. The step size for the solution of the mainflow was then chosen as 0.02. During the course of the investigation, it was found that for smaller values of the wavenumber α, sufficiently larger values of the boundary layer thickness η_∞ had to be used for the stability results to reach a converged value which was independent of η_∞. Thus, as α was varied from 0.5 to 0.00005 the value of η_∞ had to be increased from 10 to 330. This indicates that, although η_∞ values of about 10 are all that are needed to provide a very accurate mainflow solution, much larger η_∞ values are required in the stability calculations, particularly when α is very small. As a result, for the present problem, care must be exercised in selecting the η_∞ values that are based on the stability calculations and not on the mainflow calculations, as is customarily done in the literature.

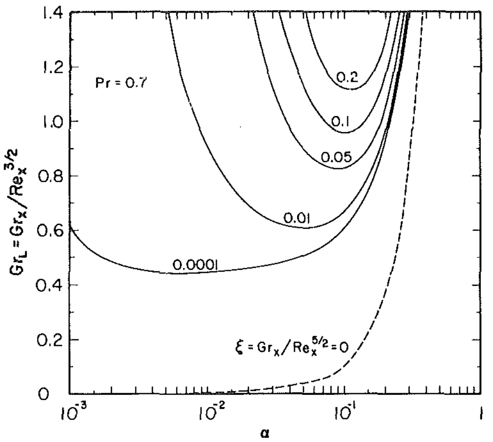

Fig. 1 Representative neutral stability curves, Pr = 0.7

Table 1 Critical stability characteristics for Prandtl number of 0.7

$Gr_x/Re_x^{5/2}$	$Re_x{}^*$	$Gr_x{}^*$	α^*
1×10^{-7}	4.34×10^6	3.93×10^9	0.0010
5×10^{-7}	8.69×10^5	3.52×10^8	0.0015
1×10^{-6}	4.35×10^5	1.25×10^8	0.0020
5×10^{-6}	8.73×10^4	1.12×10^7	0.0030
1×10^{-5}	4.37×10^4	4.00×10^6	0.0035
5×10^{-5}	8.85×10^3	3.68×10^5	0.0055
7.5×10^{-5}	5.93×10^3	2.03×10^5	0.0070
1×10^{-4}	4.46×10^3	1.33×10^5	0.0075
2.5×10^{-4}	1.82×10^3	3.53×10^4	0.0100
5×10^{-4}	930.9	1.32×10^4	0.0135
7.5×10^{-4}	631.4	7.51×10^3	0.0150
1×10^{-3}	485.8	5.20×10^3	0.025
2.5×10^{-3}	209.8	1.59×10^3	0.030
5×10^{-3}	110.2	637.5	0.040
7.5×10^{-3}	77.30	394.0	0.045
1×10^{-2}	60.92	289.7	0.060

Table 2 Critical stability characteristics for Prandtl number of 7

$Gr_x/Re_x^{5/2}$	$Re_x{}^*$	$Gr_x{}^*$	α^*
1×10^{-7}	4.33×10^6	3.91×10^9	0.0008
5×10^{-7}	8.67×10^5	3.50×10^8	0.0010
1×10^{-6}	4.33×10^5	1.23×10^8	0.0020
5×10^{-6}	8.67×10^4	1.11×10^7	0.0030
1×10^{-5}	4.34×10^4	3.92×10^6	0.0035
5×10^{-5}	8.69×10^3	3.53×10^5	0.0050
1×10^{-4}	4.35×10^3	1.25×10^5	0.0060
5×10^{-4}	878.0	1.14×10^4	0.010
1×10^{-3}	441.8	4.10×10^3	0.013
5×10^{-3}	91.09	395.9	0.026
1×10^{-2}	46.64	148.5	0.036

Results and Discussion

Numerical results were obtained for fluids with Prandtl numbers of 0.7 and 7 which are typical for air and water, respectively. The buoyancy force parameter $Gr_x/Re_x{}^{5/2}$ in the computations ranged from 1×10^{-7} to 0.1.

Figure 1 shows the neutral stability curves for air, for several representative values of the buoyancy force parameter ξ. In the figure, the parameter $Gr_L = \xi Re_x = Gr_x/Re_x{}^{3/2}$ is plotted against the wavenumber α so that the recalculated stability results of the Blasius flow ($\xi = 0$) can be incorporated for comparisons. The present results for $\xi = 0$ are shown by the dotted line which is different from that given by Wu and Cheng [2]. The discrepancy arises from a numerical error in their work and a negligence in their part to account for the effect of η_∞ on the accuracy of the numerical results. It is worthwhile to mention here that the present results for $\xi = 0$ were also verified by solving the disturbance equations by the finite-difference method of Thomas as used in [2]. The critical Reynolds numbers $Re_x{}^*$ and the critical Grashof numbers $Gr_x{}^*$ for air can be found from the minima of the neutral stability curves in Fig. 1. As seen from the figure, the minima of the neutral stability curves shift to larger critical values as the buoyancy force parameter ξ increases. Thus, for the Blasius flow ($\xi = 0$), the flow is stable to the vortex mode of instability. This is because the buoyancy force term in the mainflow, which is responsible for the possible onset of the vortex instability of the flow, does not exist when $\xi = 0$. The neutral stability curves for Pr = 7 are similar in shape to those for Pr = 0.7 and, to conserve space, they are not shown. The critical Reynolds numbers $Re_x{}^*$ along with the corresponding critical Grashof numbers $Gr_x{}^*$ and the critical wavenumbers α^* are listed in Tables 1 and 2, respectively, for Pr = 0.7 and 7 for representative values of the $Gr_x/Re_x{}^{5/2}$ parameter that were investigated. It can be seen from the tables that the flow becomes more susceptible to the vortex instability as the buoyancy force parameter increases.

The critical Reynolds numbers $Re_x{}^*$ are plotted against the critical Grashof numbers $Gr_x{}^*$ in Figs. 2 and 3, respectively, for Prandtl numbers of 0.7 and 7. This $Re_x{}^*$ versus $Gr_x{}^*$ curve plotted as a solid line in each figure separates the stable flow regime from the unstable one with respect to vortex instability. Thus, as labeled in each figure, any flow condition determined by any combination of Re_x and Gr_x that lies below the solid line represents an unstable situation for the vortex mode of instability, whereas any point lying above the line represents a stable one. In the same figure, the critical neutral stability results from the wave mode of disturbances [1] are plotted with a dotted line. As far as the wave mode of instability of the flow is concerned, any flow combination of Re_x and Gr_x that lies inside the region enclosed by the dotted line represents a stable flow situation, while any point lying outside that region represents an unstable one. Thus, from Figs. 2 and 3 one can conclude that for both Pr = 0.7 and 7, the flow is less susceptible to the vortex disturbances and the first onset of instability is due to the wave mode of disturbances when the Reynolds numbers are larger than 8.42×10^4. On the other hand, when $Re_x < 8.42 \times 10^4$ the first instability of the flow is due to vortex disturbances. Physically, one would expect this behavior to prevail, because at higher Reynolds numbers the buoyancy force effect under a given temperature difference would tend to diminish, thus making the flow less susceptible to vortex mode of instability.

It is also of interest to compare the present analytical results with available experimental data. In an experimental study on forced convection of air over a heated, horizontal flat plate, Hayashi, et al. [3] arrived at the following equation for the onset of the vortex instability of the flow

$$Gr_x{}^*/Re_x{}^{*1.5} = 192 \qquad (23)$$

This equation is shown by a solid-dotted line in Fig. 2. The vortex instability results from the present analysis as shown by the solid line in the same figure can be correlated as

$$Gr_x{}^*/Re_x{}^{*1.496} = 0.461 \qquad (24)$$

For all engineering purposes, equation (24) can be approximated as

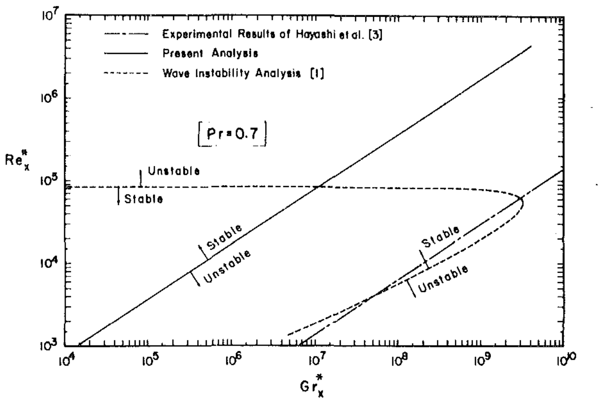

Fig. 2 Critical Reynolds number versus critical Grashof number, Pr = 0.7

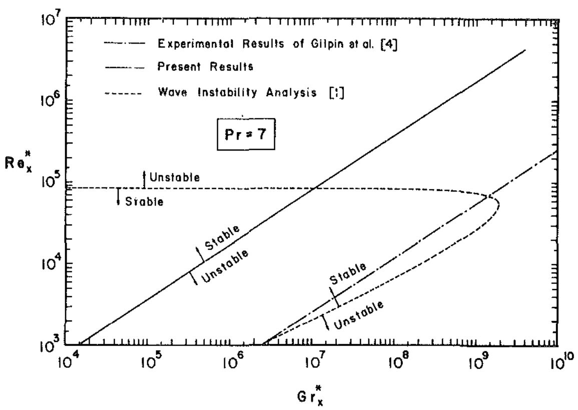

Fig. 3 Critical Reynolds number versus critical Grashof number, Pr = 7

$$Gr_x^*/Re_x^{*1.5} = 0.447 \qquad (25)$$

in the range of critical Reynolds numbers between 10^3 and 10^7. Thus, for a given Reynolds number, the linear stability theory predicts a lower critical Grashof number than that observed in the experiments. This is to be expected, because in all known results for *natural disturbances* in boundary layer flows, appreciable growth of any disturbances takes place before they can be detected experimentally. Similar findings have also been reported in vortex instability of natural convection flows [6, 8].

From their experimental study on the vortex instability of water flow over a heated, horizontal flat plate, Gilpin, et al. [4] arrived at the correlation equation

$$Gr_x^*/Re_x^{*1.5} = c_1, \quad 46 < c_1 < 110 \qquad (26)$$

for the onset of the instability of the flow. Their results based on an average value of $c_1 = 78$ are shown with a solid-dotted line in Fig. 3. On the other hand, the vortex instability results from the present analysis for a Prandtl number of 7, drawn as a solid line in the same figure, can be correlated by the equation

$$Gr_x^*/Re_x^{*1.499} = 0.438 \qquad (27)$$

For the range of Reynolds numbers between 10^3 and 10^7, equation (27) can be approximated as

$$Gr_x/Re_x^{*1.5} = 0.434 \qquad (28)$$

Again, as can be seen from Fig. 3, the linear stability theory predicts a lower critical Grashof number than that observed in the experiments.

In Fig. 4, the critical Reynolds numbers versus the critical Grashof numbers from the present analysis are plotted for the lower range of Reynolds numbers. As can be seen from the figure, water (Pr = 7) is slightly more susceptible to the vortex mode of instability than air (Pr = 0.7). This trend has also been confirmed from experiments (compare Figs. 2 and 3 or equations (23) and (26)). The deviation in the flow instability between air and water, however, diminishes as the Reynolds number increases. In the wave instability analysis for flow over a horizontal flat plate [1] water was also found to be less stable than air to wave type of small disturbances for flow above a heated plate or below a cooled plate (buoyancy assisting flow). However, for the case of flow above a cooled plate or below a heated plate (buoyancy opposing flow), the trend is reversed. Of course, for the opposing flow situation, the flow is thermally stable and vortex instability does not occur.

It is of interest to show the streamlines and isotherms for the secondary flow. With the dimensionless stream function for the disturbances, ψ^+, defined such that it satisfies the continuity equation $\partial v^+/\partial y + \partial w^+/\partial z = 0$, one has

$$v^+ = \frac{\partial \psi^+}{\partial z}, \; w^+ = -\frac{\partial \psi^+}{\partial y} \qquad (29)$$

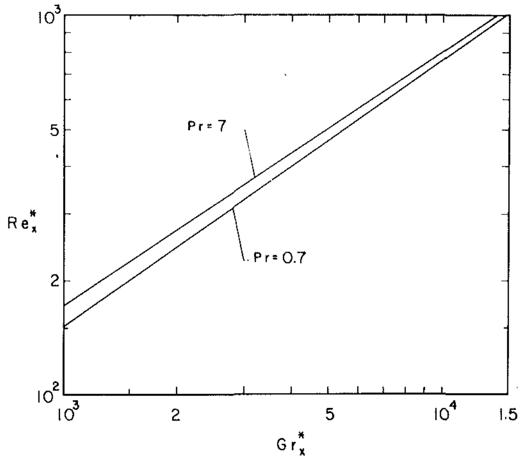

Fig. 4 A comparison of the critical instability results between Pr = 0.7 and 7 for low Reynolds numbers

With the aid of equations (10) and (29), it can be shown that the real part of ψ^+, which represent the physical quantity of interest, has the form

$$\psi_r^+ = \frac{v(y)}{\alpha Re_L} \sin \alpha z \qquad (30)$$

Similarly, from equation (10), one obtains the real part of temperature disturbances t^+ as

$$t_r^+ = t(y) \cos \alpha z \qquad (31)$$

With the magnitude of the maximum disturbance quantities taken to be 1 for both velocity and temperature disturbances, one can determine the normalized streamlines and isotherms for the secondary flow as

$$\frac{\psi_r^+}{\psi_{r_{\max}}^+} = \frac{v(y)}{v(y)_{\max}} \sin \alpha z, \; \frac{t_r^+}{t_{r_{\max}}^+} = \frac{t(y)}{t(y)_{\max}} \cos \alpha z \qquad (32)$$

These results at the onset of instability for Prandtl number of 0.7 and $Gr_x^*/Re_x^{*5/2} = 0.04$ are plotted against αZ in Fig. 5 by solid and dotted lines, respectively. As can be seen from equation (32), the phase angle between the streamlines and the isotherms is $\pi/2$.

Conclusions

In analyzing the vortex instability of laminar mixed-convection flow over a horizontal isothermal plate, it has been found that the flow becomes more susceptible to vortex mode of disturbances as the buoyancy force increases and that air is slightly less susceptible to the vortex mode of instability than water. A comparison of the present results with those for the Tollmien-Schlichting wave mode of instability shows that the flow is more susceptible to the wave mode of instability for Reynolds numbers larger than 8.42×10^4 for both air

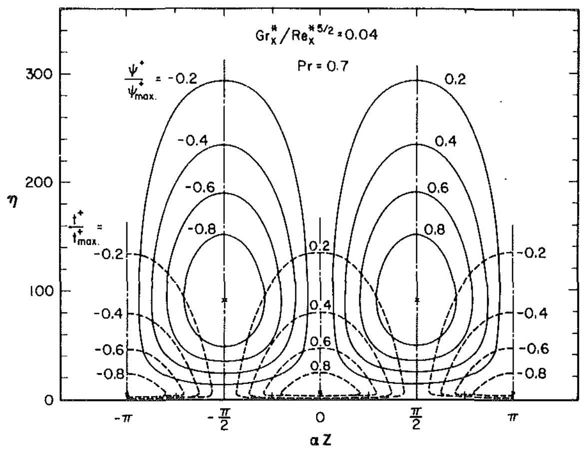

Fig. 5 Secondary flow streamlines and isotherms at the onset of vortex instability, Pr = 0.7 and $\xi = 0.04$

and water, whereas the first onset of the instability is due to the vortex mode for Reynolds numbers less than 8.42×10^4. In addition, it is found that the linear analysis predicts the occurrence of longitudinal vortex rolls at a much smaller Grashof number than that observed experimentally.

Acknowledgment

This study was supported by a grant (NSF ENG 75-15033 A01) from the National Science Foundation.

References

1 Chen, T. S., and Moutsoglou, A., "Wave Instability of Mixed Convection Flow Over a Horizontal Flat Plate," *International Journal of Heat and Mass Transfer*, Vol. 22, 1979, pp. 185–196.

2 Wu, R. S., and Cheng, K. C., "Thermal Instability of Blasius Flow Along Horizontal Plates," *International Journal of Heat and Mass Transfer*, Vol. 19, 1976, pp. 907–913.

3 Hayashi, Y., Takimoto, A., and Hori, K., "Heat Transfer in Laminar, Mixed Convection Flow Over a Horizontal Flat Plate," (in Japanese), *Proceedings of the 14th Japan Heat Transfer Symposium*, 1977, pp. 4–6.

4 Gilpin, R. R., Imura, H., and Cheng, K. C., "Experiments on the Onset of Longitudinal Vortices in Horizontal Blasius Flow Heated from Below," ASME JOURNAL OF HEAT TRANSFER, Vol. 100, 1978, pp. 71–77.

5 Chen, T. S., Sparrow, E. M., and Moutsoglou, A., "Mixed Convection in Boundary Layer Flow on a Horizontal Plate," ASME JOURNAL OF HEAT TRANSFER, Vol. 99, 1977, pp. 66–71.

6 Haaland, S. E. and Sparrow, E. M., "Vortex Instability of Natural Convection Flow on Inclined Surfaces," *International Journal of Heat and Mass Transfer*, Vol. 16, 1973, pp. 2355–2367.

7 Cebeci, T. and Bradshaw, P., *Momentum Transfer in Boundary Layers*, Chapter 7, Hemisphere Publishing, Washington, D.C., 1977.

8 Hwang, G. J. and Cheng, K. C., "Thermal Instability of Laminar Natural Convection Flow on Inclined Isothermal Plates," *Canadian Journal of Chemical Engineering*, Vol. 51, 1973, pp. 659–666.

Heat Transfer During Wind Flow over Rectangular Bodies in the Natural Environment

F. L. Test
Professor.

R. C. Lessmann
Associate Professor.

A. Johary
Graduate Assistant.

Department of Mechanical Engineering
and Applied Mechanics, University of
Rhode Island, Kingston, RI 02881

An experimental investigation has been performed to determine the constant temperature heat transfer behavior on the upper surface of a rectangular plate with a chord length of 122 cm (48 in.), a width of 81.3 cm (32 in.) and a thickness aspect ratio of 6/1. Special side attachments were made in order to maintain approximately two-dimensional flow over the finite width body when exposed to varying wind directions. The angle of attack was 40 deg or greater. Quasi-local values of $ST\sqrt{Re}$ *were found to be 200 percent higher than wind tunnel values and 300 percent higher than analytical predictions. The disturbance intensity of the wind flow was in the range of 20 to 50 percent and is thought to be related to the increase in heat transfer since the flow over the plate was found to be laminar.*

Introduction

This paper represents a continuation of the work discussed by Sam, Lessmann and Test [1] and Test and Lessmann [2]. The purpose of the research presented in this series of papers is the study of convective heat transfer from the upper surface on a body of rectangular cross section in two-dimensional flow. One of its goals is to determine whether or not wind tunnel studies can be used to predict behavior in the natural environment. This paper discusses the results of experiments in the natural environment and compares them to the previous wind tunnel results.

One of the important conclusions presented in [2] states that the experimental heat transfer coefficients, determined in the wind tunnel, were about 50 percent higher than those predicted by a Smith-Spalding analysis [3]. This difference was due to freestream disturbances caused by wake oscillations which appeared to have the same effect as freestream turbulence in the favorable pressure gradient laminar flow following a stagnation line. These findings have considerable significance for this study as the amount of freestream disturbance in the natural environment can be quite high and consequently one should expect heat transfer in the natural environment to be higher than in a low turbulence level wind tunnel.

Kowalski and Mitchell [4] observed this when they found that the average convection coefficients on spheres in a naturally turbulent outdoor environment were up to 2.2 times greater than the coefficients obtained in standard low turbulence intensity wind tunnel experiments. A similar finding results from the present study.

To the contrary Sparrow and Tien [5] produced heat transfer results for an inclined and yawed square plate by running tests in a low turbulence wind tunnel. Based on their results the authors concluded that current standard computational methods [6, 7] lead to a substantial overestimation of wind-related convection losses from flat surfaces. The present paper will attempt to show that prediction methods based on low turbulence intensity wind tunnel tests significantly underestimate the heat transfer due to wind flow in the natural environment.

The environmental experiments were conducted out of doors with a test surface having a chord to height ratio of 6 (as did the wind tunnel models) but a finite span (width to cord ratio of 2 to 3). Without modification this relatively short span would have led to unacceptibly large three dimensional effects and prevented any meaningful comparison with the wind tunnel data. Therefore a model study was undertaken in an attempt to mitigate the problem by the addition of suitable side fins to the basic experimental plate.

Two Dimensional Flow Considerations

The prototype plate, shown in Fig. 1(*a*), for outdoor experiments was 122 cm (48 in.) long (*C*), 81.3 cm (32 in.) wide (*W*) and 20.3 cm (8 in.) high (*H*). A model of $^1/_8$ size was constructed for use in the wind tunnel. The problem was to determine the type of edges that should be placed on the three-dimensional model in order to approximate the pressure coefficients, and hence the chord wise velocity variations, that were obtained in [1] for the two-dimensional case. The model had nine equally spaced pressure taps along its centerline as the heat transfer data on the prototype was to be taken at mid span. It was mounted in the wind tunnel on a vertical shaft so it could be rotated in yaw and positioned at an angle of attack (α), shown in Fig. 1(*b*) of 40 deg. At this angle there was no separation on the upper surface and the stagnation point was very close to the leading edge. Some testing was also done at a 50 deg angle. The various geometrical edge shapes considered are shown in Fig. 2. All of these continued for the full chord length. Figure 2(*a*) represents the basic three dimensional box.

In evaluating the effectiveness of a particular edge shape, account had to be taken of its performance in yaw. It was desired that the centerline flow in the natural environment remain approximately two dimensional even as the wind varied in direction within reasonable limits.

A comparison of the different schemes is shown in Fig. 3. All of the cases from Fig. 2 that are not shown in Fig. 3 fall between the lines for Case A, three dimensional flow, and case *H*, 45 deg attachment of

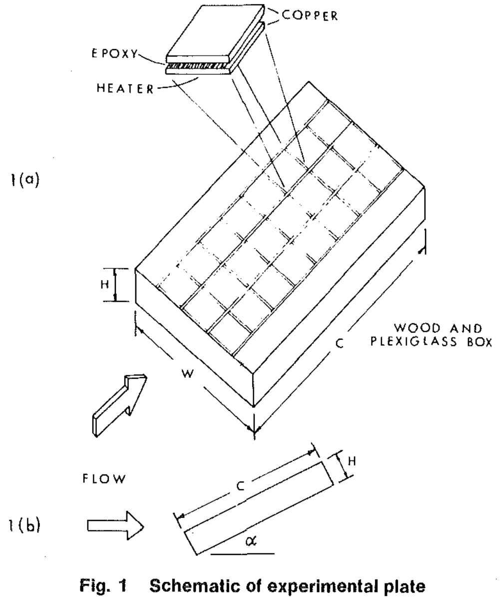

Fig. 1 Schematic of experimental plate

Contributed by the Heat Transfer Division for publication in the JOURNAL OF HEAT TRANSFER. Manuscript received by the Heat Transfer Division August 18, 1980.

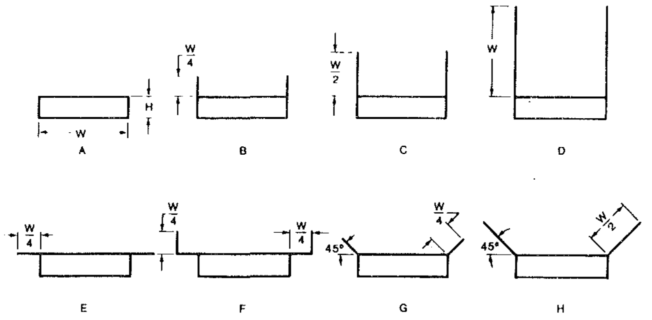

Fig. 2 Types of side attachments

length $W/2$. Case D most closely simulates the $2D$ results, however the problem of varying wind direction remains to be considered.

Experiments were run with varying yaw up to 20 deg on both configurations D and H. In the vertical side case the Cp curve for 20 deg yaw paralleled that for the two-dimensional case but was low by about $Cp = 0.05$ over the entire chord. This represents a 83 percent decrease in the velocity at 10 percent chord and a 5 percent decrease in velocity at 90 percent of the chord. The 45 percent sides gave results which were essentially in agreement with the $2D$ case from 30 to 70 percent of the chord and were low by $Cp = 0.02$ at 10 percent chord and high by an equal amount at 90 percent chord. The corresponding velocities were 30 percent low and 2 percent high. This together with the fact that if the yaw increased beyond 20 percent the vertical side case deteriorated rapidly due to separation from the fin tops indicated case H, 45 deg attachments of width $W/2$ to be the better choice.

The ultimate purpose of this work was to study heat transfer behavior, therefore the influence of the side attachments on pressure coefficient is only important in so far as it affects heat transfer. The pressure coefficients from the model study were used in a Smith-Spalding analysis [3] as used in [2] to predict the variation of $\mathrm{ST}\sqrt{\mathrm{Re}}$ and the results are shown in Fig. 4. It can be seen that the value of $\mathrm{ST}\sqrt{\mathrm{Re}}$ for 45 deg attachments is usually within 5 percent of the two-dimensional case over most of the chord length where the case without attachments (three-dimensional) is normally only within 20 percent of the two-dimensional case.

Finally, sides of width $W/2$ at an angle of 45 deg were placed on the prototype and static-pressure measurements were taken at several positions along the center chord. In the wind tunnel the upstream static pressure can easily be obtained for reference purposes in determining the pressure coefficient. This cannot easily be done in the natural environment due to the varying wind direction. Therefore the reference was taken to be the static pressure at the center of the top surface of the prototype. If this point was assumed to have the same C_p as the wind tunnel model at its center, the C_p's at the other points on the prototype could be determined from the static pressure readings. The results of this are shown in Fig. 5. Considering the possible yaw effect, it can be seen that the C_p's for the prototype agree quite well with those from the wind tunnel model.

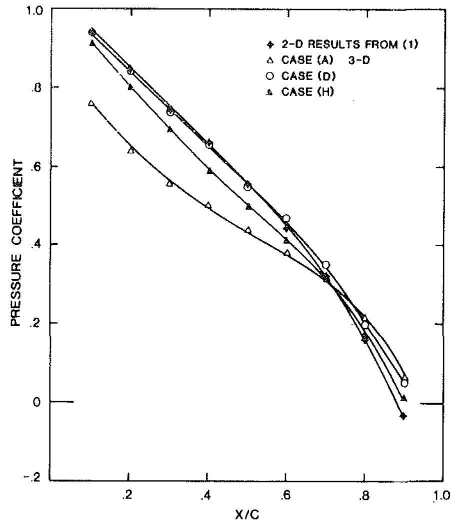

Fig. 3 Comparison of attachment schemes, 40 deg angle — no yaw

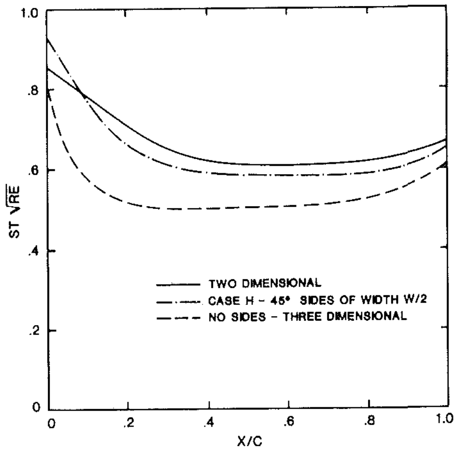

Fig. 4 Effect of side attachments on heat transfer

Wind Measurements

A crucial element in this experiment was the measurement and interpretation of wind flow past the prototype. This was accomplished using a Gill uvw anemometer [8] which is a triaxial array of helicoid propellers each driving a small d-c generator. The individual propellers are 19 cm in diameter and are located one third of a meter from a common origin. The array of sensors was positioned on a mast about a meter above the experimental surface oriented with one axis vertical and a second parallel to the test surface pointing across the span (see Fig. 6). The anemometer mast was rigidly attached to the plate support in such a way that the entire experiment could be rotated to face the remaining propeller sensor in the direction of the mean wind.

Nomenclature

C = chord, length of rectangular plate
C_p = nondimensional pressure coefficient
$DI = \dfrac{\sigma_v\, 100}{\bar{V}}$
g = gravitational acceleration
$\mathrm{Gr}_x = g\,\beta(T_w - T_\infty)x^3/\nu^2$
h = quasi-local surface convection heat transfer coefficient
H = thickness of plate
$\mathrm{Re} = \bar{u}_e\, x/\nu$
$\mathrm{Re}_L = \bar{u}\, L/\nu$
S_t = quasi-local Stanton number based on $\bar{u}_e$
$TI = \bar{\sigma}\, 100/\bar{V}$
T_w = surface temperature
T_∞ = free stream temperature
u = velocity component in the time average mean wind direction
U_e = local freestream velocity
v = horizontal velocity component that is perpendicular to u
$\bar{V}$ = wind speed = $(u^2 + v^2 + w^2)^{1/2}$
w = vertical velocity component
W = width of rectangular plate
x = distance from leading edge parallel to the chord direction
α = angle of attack
β = volumetric coefficient of thermal expansion
ν = kinematic viscosity
$\sigma_v = V_{\mathrm{rms}}$
$\bar{\sigma} = (\frac{1}{3}(u_{\mathrm{rms}}{}^2 + v_{\mathrm{tms}}{}^2 + w_{\mathrm{rms}}{}^2))^{1/2}$

Subscript

rms = root mean square

Superscript

$^-$ = time averaged value

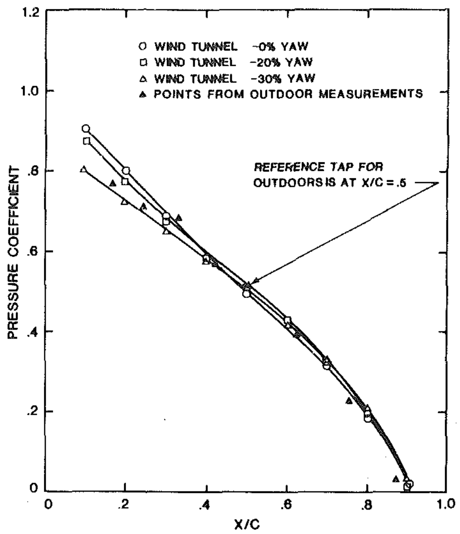

Fig. 5 Comparison of pressure coefficients measured in wind tunnel and outdoors, 45 deg sides of width W/2

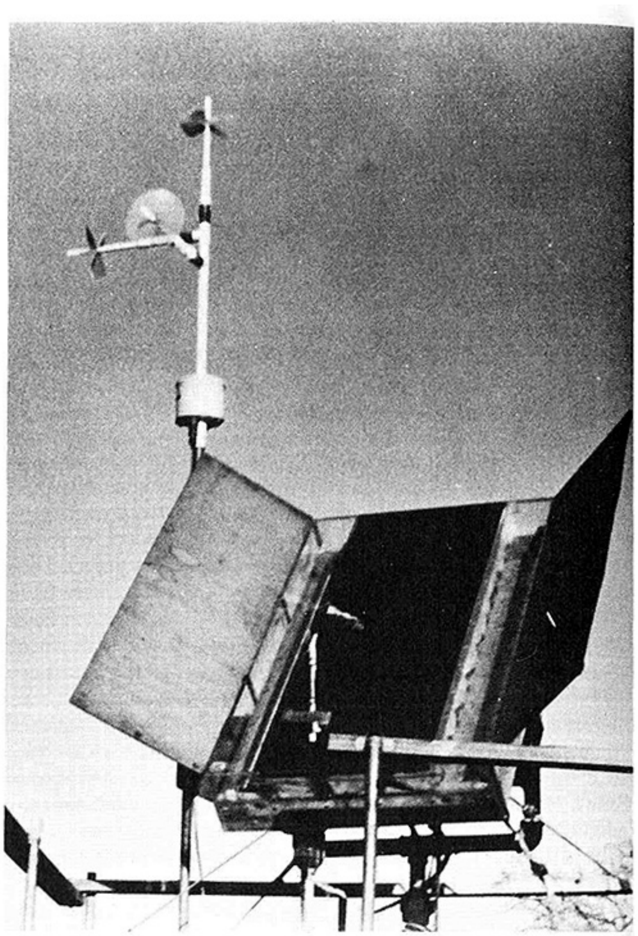

Fig. 6 Photograph of rectangular plate with sides and anemometer

The helicoid propeller design offers several advantages. It is a primary measuring instrument which requires no calibration as such a propeller passes a given volume of air for each revolution (30 cm of wind/rev). Also the response of each sensor is linear above 1.0 m/s and the light polystyrene fabrication gives a response threshold of 0.2 m/s.

The primary error encountered in using the Gill anemometer is noncosine response [9]. Each sensor responds only to that component of the wind which is parallel to its axis but, depending upon the orientation of the velocity vector, this will not be given exactly by the direction cosine. The noncosine correction factors provided by the manufacturer were determined adequate for all three sensors employed in this experiment by independent wind tunnel tests.

In order to insure the desired experimental conditions of approximate two-dimensionality, heat transfer data were only acceptable when recorded during periods such that the output of the vertical sensor was essentially zero (on the average) and simultaneously the output of the cross span sensor indicated the yaw angle of the wind was within ±20 deg.

Outputs from each sensor were recorded on a multipoint recorder with a frequency of 1 per second. Typically data would be recorded for 10 min for the mean flow sensor after which data from the cross flow sensors would be sampled for 2 min at a time. This procedure introduces some additional uncertainty into the final results primarily because of digital filtering and the necessity of extrapolating the average value of the mean wind into periods where only cross flow data were recorded.

A separate study of the dynamic response of the anemometer [10] was conducted to evaluate these uncertainties. The anemometer has a time constant which is a function of wind speed [9] varying from 0.3 s at 3 m/s to 0.1 s at 9 m/s. ($\tau = 0.95/\bar{u}$). The greatest sensitivity is obtained by sampling at 2 time constants however sampling rates of up to 10 s yielded variations in the calculated averages of less than 7 percent. Considering that the thermal time constant of the experimental surface was estimated at 30 min, a digitation rate of 1 s was considered acceptable.

Also, the effect of averaging time on the calculation of turbulent intensities was studied. Average values of the ratio of rms fluctuations to the average wind speed for ten min intervals were calculated using averaging times between 15 s and the full 600 s. Over this range the turbulence intensity varied by as much as 53 percent but its standard deviation varied by upward of 300 percent. The standard errors for these calculations all overlapped indicating a clear progression toward a more accurate determination. Usually very little change was noted after averaging times of about 120 s with the standard deviation falling rapidly to zero for larger averaging times. Consequently 10 min were deemed sufficient for an accurate determination of turbulence intensity.

Accounting for all of these effects: non-cosine response, threshold error, digital filtering, averaging time, and extrapolation of average wind speed, results in an estimated uncertainty of ±4 percent for the mean wind speed and ±12 percent for fluctuations measured by the cross flow sensors.

Experimental Apparatus and Technique

Figure 1(*a*) is a sketch of the experimental apparatus and Fig. 6 is a photograph of the prototype apparatus in position on its mount. The top surface of the rectangular box contained three rows of heating units and there were eight units in each row. The prototype could be placed at any angle of attack and at any desired azimuth angle. The plexiglass divider between the center row of heaters and one of the outer rows had several static pressure taps for the measurements of surface pressure variation. All of the heat transfer data were taken with the center row of heating units, the outer two rows serving as guard heaters.

The heating units consisted of two 0.635 cm (0.25 in.) thick copper pieces, with the space between the copper pieces filled with 0.635 cm (0.25 in.) of Stycast 3050, a low viscosity electrical grade epoxy manufactured by Emerson and Cuming, Inc. Each heating unit was calibrated to determine its thermal resistance after the epoxy had cured between the copper pieces. These measurements were made on the heating units before and after use. Resistance values did not change by more than 3 percent.

Individual copper units had a top surface that was 15.2 cm (5.97 in.) by 14.8 cm (5.83 in.) and there was a 0.32 cm ($^1/_8$ in.) thick plastic spacer between each unit in a given row. The top copper surface was plated with 0.005 cm (0.001 in.) of polished chrome in order to reduce radiation effects. Since data were only taken at night, radiation accounted for between 1 and 3 percent of the total heat loss depending on the local convective heat transfer coefficient, surface temperature, and ambient temperature.

A thick 160 ohm heater was attached, by means of pressure sensitive adhesive, to the bottom side of each copper plate. A copper constantan thermocouple was imbedded in the center of the copper plates by peening. All leads were brought out through small grooves in the copper. For the anticipated conditions of the experiments a two dimensional finite difference heat transfer analysis indicated that the temperature difference between the upper and lower surface of each copper piece would not exceed 0.01°C (0.02°F); and that the temperature variation in the direction of flow in the upper copper plate would not exceed 0.25°C (0.5°F).

The temperature difference between each top plate and the air and between each top and bottom plate was recorded for a total of 48 readings, by a Digitec Datalogger 2000 using a 25 mv d-c signal conditioning card. The accuracy of this instrument is ±0.00625 mv ±0.00015 percent of the reading. When this is combined with the thermocouple calibration curve the accuracy of the temperature readings was ±0.16°C (0.28°F).

The power to each of the 24 heaters was regulated by an individual rheostat so that the top surface temperature of every heater would be the same. This function, which was performed by hand, was more difficult than in the wind tunnel because of the variable nature of the wind and the large thermal capacity of the copper plates. Even though the experiments were nominally considered to be conducted with an isothermal surface the best that could be done was to keep the top plates within ±1.1°C (±2°F) of each other.

Because of the basic variability of the environment and consequent nonrepeatability of the experiment a single sample approach was taken to estimate uncertainty in the final results. The accuracies of all the instrumentation, as already discussed, plus estimates of the effects not directly measured were propagated through the formulas for calculating the heat transfer coefficient and $ST\sqrt{Re}$. Specifically the heat transfer coefficient was calculated from the temperature difference between the two copper plates, the thermal resistance of the epoxy, and the difference between the upper plate temperature and the ambient air. Considering the uncertainty in the temperature measurements, epoxy resistance, and estimation of radiation and conduction losses the possible uncertainty in the experimental heat transfer coefficient is ±6 percent. Most of the results are reported in the form of $ST\sqrt{Re}$ where the velocity is the local freestream velocity at the outside of the boundary layer. The local freestream velocity was determined from the wind speed and the pressure coefficient for the particular plate angle. Considering the uncertainty in these quantities, in addition to that in heat transfer coefficient, the possible error in $ST\sqrt{Re}$ is about ±9 percent near the leading edge of the plate decreasing to about ±7 percent near the trailing edge.

All data were taken at night in order to avoid any solar radiation inputs. This presented a difficulty in that night winds were usually very light and there were normally only about three or four nights a month when winds were high enough to avoid free convection effects and persistent enough to achieve steady state conditions. On the basis of a paper by Mucoglu and Chen [11] and a personal communication with Chen [12] the free convection effects are negligible if Gr_x/Re^2 is less than 0.1. It was not always possible to meet this requirement and consequently it is necessary to account for buoyancy effects in some of the final results.

A sample of data points for a particular run is shown in Fig. 7. If the wind held a mean value for a long period of time it was possible to arrive at a steady state in 2 hr. However as seen by the wind speed plot in Fig. 7, this was not the case. Each point on this plot represents an average over a 10 min period. The thermal capacity of the plates made them insensitive to variations with frequencies higher than two cycles per hour. Fortunately it was found that the experimental determination of $ST\sqrt{Re}$ varied very little (±5 percent) during the long term (1 hr or more) temperature oscillations that coincided with the long term changes in mean wind speed. For this reason quasi steady state conditions exist during the long term variations. In a data record, such as in Fig. 7, one could evaluate the mean heat transfer coefficient and mean $ST\sqrt{Re}$ for each plate during the time interval from 19:30 to 22:30 with good confidence.

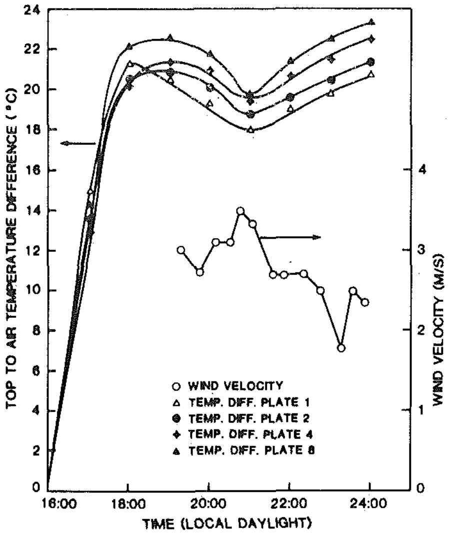

Fig. 7 Typical data sample

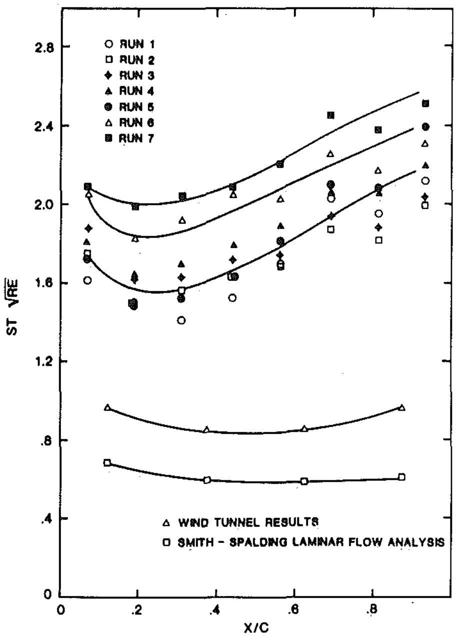

Fig. 8 Results for 40 deg angle of attack

Discussion of Results

All of the results except for one run were at an angle of attack of 40 deg and Fig. 8 compares them with the wind tunnel results and a Smith-Spalding analysis [3]. The wind tunnel results given in [2] at a particular angle did not change significantly with velocity over the range of 9 to 22 m/s (30 to 70 ft/s). The values of $ST\sqrt{Re}$ are quasi-local in that they are the mean over each of the eight plates and are considered to be the value at the center of the plate. Information appropriate to the outdoor results at a 40 deg angle, runs 1 to 7, is shown in Table 1.

Data were also taken at an angle of 50 deg and compared with the wind tunnel results. The quasi-local values of $ST\sqrt{Re}$ for 50 deg and negligible free convection were about 10 percent higher than the mean line for 40 deg. This was about the same percent change that occurred in the wind tunnel results reported in [2].

In order to fully describe the results that are presented in Fig. 8 there are at least four questions that must be answered: (1) What is the justification for considering the runs in the natural environment to be laminar and thus comparable to the wind tunnel and analytical

Table 1

Run	Mean Wind Speed (M/s)	Mean Surface to Air Temp. Diff (°C)	Mean Value of Gr_x/Re^2	Re_L* 10^{-3}
1	2.2	13	.11	183
2	4.6	37	.073	382
3	3.2	20.5	.093	266
4	2.9	23	.11	242
5	5.6	16	.0095	465
6	2.3	42	.34	192
7	1.5	22	.44	125

Mean values reported in this table correspond to averages over the entire test periods which were typically on the order of four hours (see Fig. 7).

Table 2

Run	10 min average wind $\overline{u}$(m/s)	u_{rms}	v_{rms}	w_{rms}	$\frac{\overline{\sigma}\text{x}100}{\overline{u}}$	** *TI*	** *DI*
*1	2.43	0.96	0.97	—	40	34	31
2+6	4.27	1.19	1.16	0.45	23	20	25
3	7:30 PM 3.05	1.09	0.69	0.57	27	29	29
	11:00 PM 2.13	0.79	0.71	0.55	33	27	30
*4	3.05	1.56	1.49	—	50	39	36
*5	6.71	2.66	1.93	—	35	31	31
7	1.28	0.87	0.79	0.72	62	46	39
			averages		45	38	37

* Intensities calculated assuming $w_{rms} = (u_{rms} + v_{rms})/2$.
** These values calculated approximately using the methods in reference [15].

results? (2) What is the reason for the scatter in the various outdoor runs? (3) Why is the variation with length at bit stronger for the outdoor runs than for the wind tunnel results? (4) Why should the results for the outdoor runs be at least twice the magnitude of the wind tunnel results?

Considerable discussion was given in [2] as to why the wind tunnel results for angles of attack greater than 30 deg were for laminar flow conditions. The length Reynolds number for the wind tunnel results varied from 135 × 10^3 to 315 × 10^3. It can be seen from Table 1 that the range of length Reynolds numbers of the outdoor tests is essentially the same as that for the wind tunnel. Further verification of laminar flow conditions can be seen in Fig. 9. The experimental values of the heat transfer coefficient for Run No. 2 are shown in comparison with those obtained from a Smith-Spalding laminar analysis [3] and an Ambrok turbulent analysis [13] using the appropriate pressure coefficient. The experimental distribution of heat transfer coefficient with length parallels the laminar analysis but is opposite that of the turbulent analysis. It is felt that the above evidence demonstrates that the laminar flow exists in the boundary layer over the upper surface of the outdoor prototype.

It can be seen in Fig. 8 that there is quite a spread in the outdoor experimental values of $ST\sqrt{Re}$ for different velocities whereas differing free stream speeds caused very little effect on the wind tunnel results. If a mean line is drawn through results of the runs 1–5 it is seen that the data points for these runs fall within ±10 percent of the line, which is about the overall experimental accuracy. The results of runs 6 and 7 are significantly above those of the other outdoor runs, with run 7 higher than run 6. The reason for this can be seen from the values of Gr_x/Re^2 in Table 1. For runs 1–5 the parameter is about 0.1 or less but it is considerably higher for runs 6 and 7 so that free convection effects result in higher heat transfer coefficients for these runs.

Figure 8 shows that both the wind tunnel and outdoor results form a concave shaped curve with length but the outdoor results have a significantly stronger variation toward the aft end than do the wind tunnel results. This is thought to be due to velocity effects resulting from the fact that even with the side attachments the outdoor flow conditions were not two-dimensional.

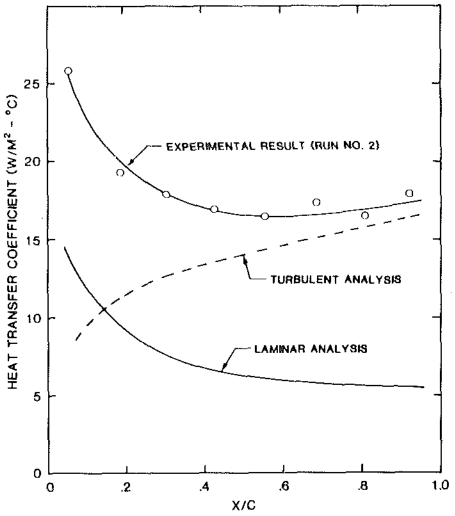

Fig. 9 Experimental comparison with laminar and turbulent analyses

In the earlier wind tunnel studies [2] it was observed that free stream disturbances (caused by wake oscillations) dramatically increased heat transfer. A disturbance level of 2.5 percent compared to average speed resulted in a general elevation in heat transfer coefficients of 50 to 60 percent. These results were in line with those reported from other wind tunnel work such as that of Junkhan and Serovy [14].

The present data again shows a dramatic increase in heat transfer coefficients on the order of 200 percent higher than in the wind tunnel and 300 percent higher than theory would predict. An equally dramatic increase in environmental disturbance level also may be seen in Table 2.

This table shows values of fluctuation levels for the several heat transfer runs and the corresponding 10 minute average wind speed from the output of the horizontal propeller sensor which was oriented into the wind ($\overline{u}$).

Since the thermal response of the test surface is such that it is in a quasi steady state over 10 min intervals such time windows should be adequate to characterize the turbulence intensity of each run. Furthermore the choice of a particular window is not critical (although usually taken at mid run) as can be seen by the very small difference between the reported value at the beginning and end of run 3.

This has to be qualified however as the environment is not stationary in the mean. Thus it is possible to encounter inconsistencies such as in the case for runs 2 and 6. Here the selected windows give essentially the same ten min average wind as reported in Table 2, but the long term average speed shown in Table 1 differs considerably for these two runs. Thus, in this type of experiment, care must be taken to relate data which are averaged over the same time period.

When fluctuation levels become large (compared to mean values), the calculation of turbulence intensity becomes complicated. Turbulence intensity (*TI*) is taken to mean the ratio of the average rms fluctuations to the average wind speed. However large fluctuations themselves contribute significantly to the average velocity magnitude ($\overline{V}$). It has been suggested by Lessmann [15] that an alternative measure, the disturbance intensity (*DI*), defined as the ratio of rms variation in the magnitude of the wind divided by the average speed may be preferable to turbulence intensity in the presence of large scale disturbances.

Both of these measures, together with the average fluctuations ratioed to $\overline{u}$ are given in Table 2. The important thing to note is that even though the various measures of disturbance level vary somewhat both across the several runs, and with each other for the same run, they all are at least an order of magnitude greater than the disturbance level in the wind tunnel. At the same time, within the experimental uncertainty, all of these runs yield essentially the same heat transfer results.

Therefore, it is reasonable to assume that the 2 to 3 fold increase in heat transfer, compared to the wind tunnel tests, is correlated in some way with this order of magnitude increase in disturbance level.

This conclusion agrees with the work of Kowalski and Mitchell [4] who observed similar behavior for the average Nusselt number from spheres.

Sufficiently detailed information about this physical situation is not yet available to make a definitive statement concerning the mechanisms behind this enhancement. It may be, as has been suggested by McCormack, et al. [16], that the effect results from streamwise directed vortices forming near the surface in the laminar stagnation region. Whatever the operative mechanisms, it appears that the enhancement may peak at some disturbance level as it does not show any significant sensitivity to variations in fluctuation level between 20 and 40 percent of the average wind. At the same time it is most probable that the disturbance level alone, since it does not contain any frequency information about the turbulence, is insufficient to fully characterize the problem.

In a discussion of heat losses from flat plate solar collectors, Duffee and Beckman [6] give the equation:

$$h = 5.7 + 3.8\overline{V} \quad (1)$$

for the average convection heat transfer coefficient due to wind flow over the upper surface of the collector. The arithmetic average heat transfer coefficient for each of runs 1–5 was determined and a linear regression gives

$$h = (8.55 \pm .86) + (2.56 \pm .32)\overline{V} \quad (2)$$

The uncertainties in this equation are due to the statistical nature of the curve fitting process and the correlation coefficient is 0.978. Equations (1) and (2) give the same value for the heat transfer coefficient when the wind speed is 2.3 m/s (7.6 ft/s). Equation (2) is of course restricted to a 40 deg angle whereas equation (1) supposedly has no such restrictions. The purpose of the discussion in this paragraph is to indicate that the currently standard computational equation, while considerably in error by low turbulence intensity wind tunnel tests, is not necessarily in great error when compared with measurements in the natural environment.

Conclusions

1 This experiment showed that it is possible to make heat transfer measurements in the environment which may be related to carefully controlled wind tunnel tests. Specifically, this exterior experiment was configured to reasonably reproduce the two-dimensional character of a series of wind tunnel measurements and therefore has significance for nearly two-dimensional environmental flows.

2 Even though disturbance levels are at least an order of magnitude greater in the natural environment than in the wind tunnel the approximately two dimensional flow over the test surface mounted at a mean angle of attack of 40 deg was found to be laminar.

3 The experimental values of $ST\sqrt{Re}$ measured in the laminar flow following stagnation on the test surface were found to be twice the value reported from wind tunnel tests and three times that predicted by theory.

4 The observed enhancement of laminar flow heat transfer seems to correlate with the measured order of magnitude increase in disturbance intensity; however, it was insensitive to variations in disturbance levels of 20 percent of the mean velocity suggesting a possible peaking of the effect.

5 Until such time as the relationship between heat transfer enhancement and disturbance intensity is understood theoretically, existing empirical approaches appear reasonable for predicting average heat transfer coefficients for certain restricted conditions in the natural environment.

Acknowledgment

This research was performed under the auspices of NSF Grant ENG 16-18379. The help of J. Quinn Murphy and Bruce Rosen, undergraduate students at the University of Rhode Island, is gratefully acknowledged.

References

1 Sam, R. G., Lessmann, R. C., and Test, F. L., "An Experimental Study of Flow Over a Rectangular Body," ASME *Journal of Fluids Engineering*, Dec. 1979, pp. 443–448.

2 Test, F. L., and Lessmann, R. C., "An Experimental Study of Heat Transfer During Forced Convection Over a Rectangular Body," ASME JOURNAL OF HEAT TRANSFER, Feb. 1980, pp. 146–151.

3 White, F. M., *Viscous Fluid Flow*, McGraw-Hill, New York, 1974, pp. 326–329.

4 Kowalski, G. J., and Mitchell, J. W., "Heat Transfer From Spheres in the Naturally Turbulent, Outdoor Environment," ASME JOURNAL OF HEAT TRANSFER, Nov. 1976, pp. 649–653.

5 Sparrow, E. M., and Tien, K. K., "Forced Convection Heat Transfer at an Inclined and Yawed Square Plate—Application to Solar Collectors," ASME JOURNAL OF HEAT TRANSFER, Nov. 1977, pp. 507–512.

6 Duffee, J. A., and Beckman, W. A., *Solar Energy Thermal Processes*, Wiley, New York, 1974, p. 83.

7 ASHRAE, *1977 Fundamentals Handbook*, pp. 22.2.

8 Gill, G. C., "The Helicoid Anemometer," *Atmosphere*, Vol. 11, No. 4, 1973, pp. 145–155.

9 Horst, T. W., "Corrections for Response Errors in a Three Component Propeller Anemometer," *Journal of Applied Meteorology*, Vol. 12, No. 4, 1973, pp. 716–725.

10 Murphy, J. Q., "Wind Statistics," Senior Project Report, Dept. of Mechanical Engineering and Applied Mechanics, University of Rhode Island, June 1979.

11 Mucoglu, A., and Chen, T. S., "Mixed Forced and Free Convection on Inclined Surfaces," ASME paper 78-WA/HT-46.

12 Chen, T. S., personal communication, 1979.

13 Moretti, P. M., and Kays, W. M., "Heat Transfer to a Turbulent Boundary Layer with varying Free Stream Velocity and Varying Surface Temperature—an Experimental Study," *International Journal of Heat and Mass Transfer*, Vol. 8, 1965, pp. 1187–1202.

14 Junkhan, G. H., and Serovy, G. K., "Effects of Free Stream Turbulence and Pressure Gradient on Flat Plate Boundary Layer Velocity Profiles and on Heat Transfer," ASME JOURNAL OF HEAT TRANSFER, May 1967, pp. 164–179.

15 Lessmann, R. C., "Measuring Disturbance Intensity in the Natural Environment," submitted for publication, ASME *Journal of Fluids Engineering*.

16 McCormack, P. D., Walker, H., and Keller, M., "Taylor-Goertler Vortices and Their Effect on Heat Transfer," ASME JOURNAL OF HEAT TRANSFER, Feb. 1970, pp. 101–112.

E. M. Sparrow
Fellow ASME

S. C. Lau
Department of Mechanical Engineering,
University of Minnesota,
Minneapolis, Minn. 55455

Effect of Adiabatic Co-Planar Extension Surfaces on Wind-Related Solar-Collector Heat Transfer Coefficients

The heat transfer response to framing the thermally active cover surface of a flat plate solar collector with adiabatic co-planar extension surfaces has been investigated by wind tunnel experiments. Various framing patterns were employed (leading edge and/or trailing edge and/or side edge framing), along with frames of different width. The experiments were performed for various angles of inclination of the plate surface relative to the oncoming airstream and for a range of Reynolds numbers. It was found that the wind-related heat transfer coefficients can be substantially lower when the collector is framed than when it is unframed. An estimate of the possible reduction of the average heat transfer coefficient can be obtained from the equation $h/h^* = (L_c/L_f)^{1/2}$*, where h and h* respectively denote the coefficients in the presence and in the absence of the frame. The quantity* L_c *is a dimension that is characteristic of the thermally active area of the cover surface, while* L_f *is a characteristic dimension of the outer edges of the frame. With respect to the reduction of the heat transfer coefficient, framing along the side edges appears to be more beneficial than framing along the leading and trailing edges, as is framing along the trailing edge compared with framing along the leading edge.*

Introduction

The research reported here is concerned with a technique for diminishing wind-related forced convection heat transfer coefficients at the exposed surface of a flat plate solar collector. The effect of a decrease in the heat transfer coefficient would be to diminish the convective heat loss at the cover plate of the collector. Such a reduction in the convective heat loss tends to increase the collector efficiency, and it is this objective that has motivated the present work.

The approach to be used here to minimize the transfer coefficients is to frame the thermally active portion of the collector surface with adiabatic co-planar extension surfaces. With these extensions in place, the hydrodynamic dimensions of the collector are larger than are those of the convective heat transfer surface. One consequence of this arrangement is that the hydrodynamic edges of the collector (i.e., the outer edges of the frame) are displaced from the edges of the thermally active zone. There is evidence, based on the detailed measurements of [1], that relatively high local heat transfer coefficients occur adjacent to the hydrodynamic edges of plates oriented either normal or at an angle of inclination to an oncoming flow. Therefore, there are reasons to expect that displacing the hydrodynamic edges of the plate from the thermally active zone will reduce the average heat transfer coefficient.

Solar collectors framed by hydrodynamic extensions are commonly encountered in practice. This occurs, for example, when the area of a host surface (e.g., a roof of a building) is larger than the surface area of the collector. It has not been realized, however, that such an arrangement may have positive effects in decreasing extraneous heat losses. Indeed, heretofore, the only heat transfer coefficients available for estimating wind-related heat losses were for plates for which the hydrodynamic and thermal dimensions are coincident. The question of whether such heat transfer coefficients are applicable to hydrodynamically framed heat transfer surfaces seems not to have been raised in the past. This issue is dealt with here by comparing measured heat transfer coefficients for hydrodynamically framed surfaces with those for unframed surfaces.

Aside from the practical relevance of the results obtained, the present experiments constitute one of the few investigations of external flows with noncongruent thermally and hydrodynamically active surfaces. The prior work dealt mainly with the classical flow-aligned flat plate with an unheated starting length.

As will be described shortly, the experiments are wind tunnel studies in which the analogy between heat and mass transfer is employed to deduce heat transfer coefficients from mass transfer measurements. A wide variety of plate framing configurations were investigated with a view to obtaining a definitive conclusion as to the effect of hydrodynamic extensions on the heat transfer characteristics.

The Experiments

The experiments were performed by measuring the sublimation-related change of mass of naphthalene plates exposed to an airflow in the test section of a low-turbulence wind tunnel. The plates, whose shapes will be described shortly, were prepared by a casting process. Molten naphthalene was poured into a mold cavity formed between a flat, highly polished metal plate and a thin-walled hollowed-out block (both mold parts were of stainless steel). When the mold parts were separated, subsequent to pouring and cooling, the naphthalene face that had solidified adjacent to the polished plate was exposed, and it is this face that served as the test surface. Aside from the exposed face, the remainder of the casting remained housed in the hollowed-out block.

The rear face of the block was fitted with a fixture which facilitated its attachment to a support rod which was suspended from the upper wall of the wind tunnel. Since the naphthalene surface faced forward into the oncoming flow while the support was from the rear, the mass transfer results were not affected by the support structure. The angle of inclination of the naphthalene surface with respect to the oncoming flow was adjusted by swiveling the test plate in a socket situated at the forward end of the support rod, with the angle being read with the aid of a protractor.

Two molds were used during the course of the experiments. One of these produce a square naphthalene surface with dimensions of 7.62 × 7.62 cm (3 × 3 in.). The other produced a 5:2 aspect-ratio rectangular surface having dimensions of 12.7 × 5.08 cm (5 × 2 in.). The

---

Contributed by the Heat Transfer Division for publication in the JOURNAL OF HEAT TRANSFER. Manuscript received by the Heat Transfer Division September 17, 1980.

dimensions of the test surfaces were selected so that the blockage of the 61 × 30.5 cm (2 × 1 ft) cross section of the wind tunnel would be, at most, about three percent.

The rectangular plates were investigated in both the narrow-plate and wide-plate orientations when viewed from the vantage point of the oncoming airflow. These orientations are respectively illustrated at the upper right and in the lower diagram of Fig. 1; the square plate is shown at the upper left. The figure also serves to define the angle of attack α which was used to parameterize the experiments.

Attention will now be turned to the technique used for obtaining test plates where the active mass transfer surface is flanked by a coplanar hydrodynamic extension, with no mass transfer occurring on the extension surface. The key feature to be noted is that any area on a naphthalene surface can be instantaneously converted from an active region of mass transfer to a region of zero mass transfer. This is accomplished by affixing a piece of pressure-sensitive tape (3M Company no. 56, 0.005 cm (0.002 in.) thick) on the area. Auxiliary experiments affirmed that taping of a surface reduced the mass transfer to zero (or, at least, to a level below 10^{-4} g, which is the resolving power of the available analytical balance). Since zero mass transfer corresponds, via the analogy, to a thermally adiabatic surface, the adiabatic condition can be modeled by the naphthalene technique with remarkable ease.

In contrast, the attainment of a truly adiabatic surface in a heat transfer experiment is quite difficult owing to the imperfections of thermal insulators. Furthermore, any desired change in the size of a thermally insulated zone in a heat transfer experiment would require a substantial degree of fabrication—surely a much greater effort than the application or removal of a piece of tape. The clear advantage of the naphthalene technique in modeling an adiabatic surface is to be taken together with its other advantages relative to direct heat transfer experiments, namely, better control of boundary conditions, minimization of extraneous losses, and greater accuracy of measurement.

With the aforementioned taping procedure, test surfaces consisting of a mass transfer zone flanked by hydrodynamic extensions were readily obtained. Starting with either a freshly cast square or rectangular naphthalene surface as a basis, tape was affixed adjacent to one or more edges in accordance with the desired pattern of hydrodynamic extensions. Thus, the untaped part of the naphthalene surface modeled the thermally active zone while the taped portion modeled the adiabatic hydrodynamic extensions.

The various test plates employed during the course of the experiments are illustrated in Figs. 2 and 3. In each diagram, the white zone represents the region where mass transfer occurs, while the cross-hatched zone represents the taped region where there is no mass transfer. The configurations illustrated in Fig. 2 are based on the square naphthalene plate as a starting point, while those of Fig. 3 are based on the rectangular naphthalene plate. Designations A, B, . . . , H are employed to identify the respective cases. As pictured in Figs. 2 and 3, the lower edge of each plate corresponds to the edge which thrusts forward into the oncoming flow when the plate is inclined.

With regard to Fig. 2, cases A, B, and C pertain to framing arrangements which may be classified as narrow frames. Case A depicts side framing, case B depicts side and trailing-edge framing, and case C depicts all-sides framing. The width of each segment of the frame is one sixth of the overall dimension of the plate. Cases D, E, and F are simlar to A, B, and C, except that the framing arrangements will be classified as wide frames (each segment of the frame is one third of the overall plate dimension).

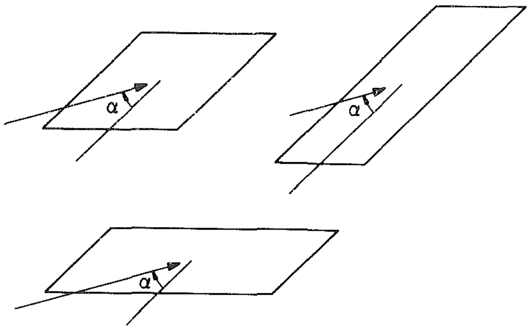

Fig. 1 Schematic diagram of the fluid flow configurations

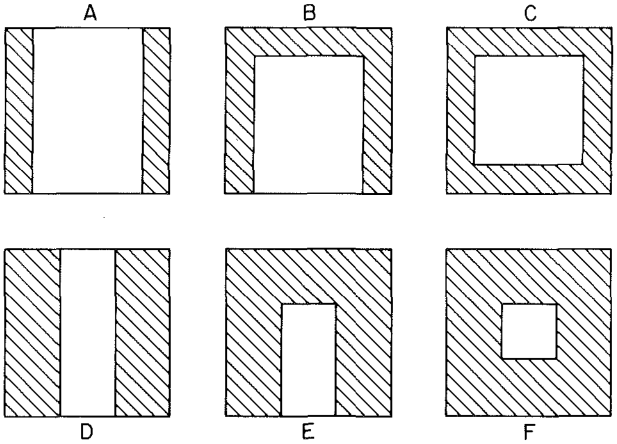

Fig. 2 Test plate configurations—overall square shapes

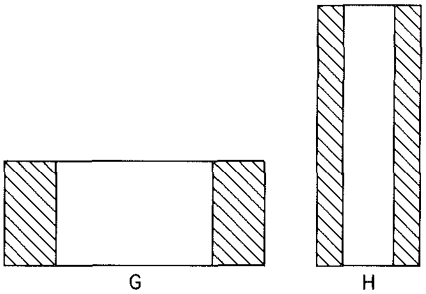

Fig. 3 Test plate configurations—overall rectangular shapes

The active transfer surfaces encompassed by the framing arrangements of Fig. 2 include squares and rectangles of various aspect ratios. From the standpoint of the oncoming flow, the rectangles appear to be longer than they are wide. The absence of relatively wide active zones from among those pictured in Fig. 2 is based on the findings of [2], where wide plates yielded results in close agreement with those for square plates. Some data for a moderately wide active zone were obtained for the frame configuration shown at the left of Fig. 3, and additional narrow-zone data were collected for the configuration at the right of the figure. For case G, each framing segment is one-fifth of the overall plate width; for case H, the narrow plate, the width of each framing segment is one-quarter that of the overall width of the plate.

Nomenclature

C = constant defined by equation (5)
c_p = specific heat at constant pressure
h = heat transfer coefficient for framed plate
h^* = heat transfer coefficient for unframed plate
j = j-factor, equations (1) and (2)
K = mass transfer coefficient
L = characteristic dimension, equation (3)
L_c = characteristic dimension for unframed collector
L_f = characteristic dimension for framed collector
Pr = Prandtl number
Re = Reynolds number, $U_\infty L/\nu$
Sc = Schmidt number
U_∞ = freestream velocity
α = angle of inclination of flow, Fig. 1
ν = kinematic viscosity
ρ = density

For each of the cases depicted in Fig. 2, data were obtained at three inclination angles α, namely, $\alpha = 90$ (normal impingement), 55, and 25 deg. At each angle, the Reynolds number was varied over the range from about 20,000 to 80,000, typically with six data points in the range. For the rectangular plates of Fig. 3, two angles were investigated, $\alpha = 90$ and 25 deg, over the same Reynolds number range. In addition to these, numerous runs were made to corroborate previously available data for unframed plates. All told, what with preliminary runs for verification of the experimental apparatus and procedure, about 175 data runs were made.

Each data run was preceded by the preparation of a new naphthalene test surface, with the casting being made with fresh (previously unused) reagent-grade naphthalene. Subsequent to the taping of the surface to obtain the desired framing pattern, the plate, capped by a protective, air-tight cover, was placed in the wind tunnel to attain thermal equilibrium with the airflow. Immediately prior to the data run, the mass of the plate was measured with an analytical balance having a smallest scale division of 0.1 mg. A similar measurement was made immediately after the termination of the run. Typically, the change of mass due to naphthalene sublimation during the data run was about 150 mg.

Results and Discussion

According to the analogy between heat and mass transfer, the j-factors for heat and mass are equal at any given Reynolds number. These factors are defined as

$$j = (h/\rho c_p U_\infty)\mathrm{Pr}^{2/3}, \qquad \text{heat transfer} \qquad (1)$$

$$j = (K/U_\infty)\mathrm{Sc}^{2/3}, \qquad \text{mass transfer} \qquad (2)$$

Equation (1) contains familiar heat-transfer-related symbols, while in equation (2) K denotes the mass transfer coefficient and Sc is the Schmidt number. Although the j-factors determined here are for mass transfer, they can be regarded as being equally applicable to heat transfer. Indeed, during the discussion of results, the phrases heat transfer and mass transfer will be used interchangeably.

The mass transfer coefficient K that appears in equation (2) was determined by making use of the measured rate of sublimation mass transfer $\dot{M}$. For each data run, the numerical value of K was found by dividing $\dot{M}$ by the active area for mass transfer (i.e., excluding the taped areas) and by the differences between the densities of naphthalene vapor at the plate surface and in the free stream. The latter vapor density is zero, while the former was found from the Sogin vapor pressure—temperature relation [3]. With regard to the Schmidt number $\mathrm{Sc} = \nu/\mathcal{D}$, the kinematic viscosity ν was evaluated as that of pure air and $\mathcal{D}$, the mass diffusion coefficient, was obtained via Skelland's formula [4]. For all of the operating conditions of the experiments, $\mathrm{Sc} \simeq 2.56$.

In addition to the j-factor, the Reynolds number was also evaluated for each data run. The characteristic length L appearing in the Reynolds number was based on the *hydrodynamic* dimensions of the surface, i.e., the length and width of the surface as measured along the outer edges of the frame. If L_1 and L_2 denote the hydrodynamic dimensions, then L was determined from

$$L = 2L_1L_2/(L_1 + L_2) \qquad (3)$$

This definition was evolved in [2] and its rationale is explained there. It was also shown in [2] that the thus-defined characteristic length is highly effective in bringing together mass (heat) transfer results for square and rectangular plates. With equation (3), the Reynolds number was evaluated from

$$\mathrm{Re} = U_\infty L/\nu \qquad (4)$$

For a square plate of side S, $L_1 = L_2 = S$, so that $L = S$.

For each framing arrangement and each angle of attack α, the j-factor was plotted as a function of the Reynolds number on logarithmic coordinates. The j, Re relation for each case was found to be of the form

$$j = C/\mathrm{Re}^{1/2} \qquad (5)$$

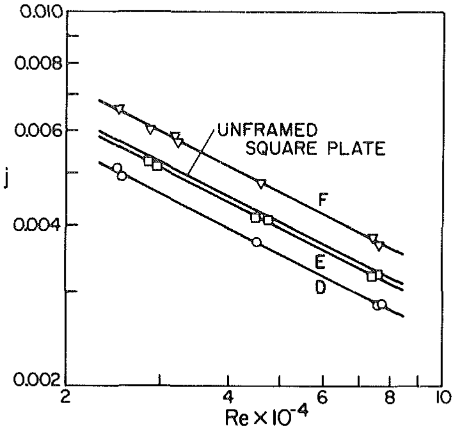

Fig. 4 Representative heat transfer results for hydrodynamically framed plates and for unframed plates

Table 1 Values of C for the relation $j = C/\mathrm{Re}^{1/2}$

Case	90 deg	55 deg	25 deg
A	0.884	0.841	0.823
B	0.839	0.830	0.879
C	0.803	0.837	0.887
D	0.825	0.783	0.791
E	0.807	0.835	0.885
F	0.701	0.980	1.031
G	0.886		0.909
H	0.831		0.702

Figure 4 has been prepared to illustrate this dependence. This figure shows data for cases D, E, and F at an inclination angle of $\alpha = 25$ deg. Also appearing in the figure is a straight line which represents the data of [5] for an unframed square plate; the equation of this line is $j = 0.905/\mathrm{Re}^{1/2}$. Figure 4 affirms that the inverse half-power relation between j and Re, which was encountered in [1, 2], and [5] for unframed square and rectangular plates, continues to apply for framed plates.

The existence of the power-law relationship (5) enables the data to be presented in terms of the Reynolds-number-independent constant C, thereby obviating the need for a detailed graphical or tabular presentation of the actual data for each case. The results for C, obtained via least-squares fits, are listed in Table 1 for the various framing configurations A through H for three angles of inclination $\alpha = 90$, 55, and 25 deg.

To provide perspective for the results of Table 1, it is relevant to take note of the C values for square and 5:2 rectangular plates. For the square plates of [5], the data for all α between 90 and 25 deg were correlated to within ±2½ percent by $C = 0.927$. The wide-plate configuration for the 5:2 rectangular plates of [2] yielded a C value of 0.939, virtually independent of α. The near equality of the aforementioned pair of C values is quite remarkable. For the narrow-plate 5:2 rectangle, C took on values of 0.937, 0.906, 0.843, and 0.769 for $\alpha = 90$, 45, 35, and 25 deg. A global correlation of all the results of [2] and [5] yielded

$$j = 0.86/\mathrm{Re}^{1/2} \qquad (6)$$

with deviations of ±10 percent.

Attention will now be turned to the characteristics of the results of Table 1 and to their mode of application. First, from an overall inspection of Table 1, it is seen that except for a few extreme cases (notably case F), the range of C is not too large. Furthermore, the mean value of C for the tabulation is 0.844, which is remarkably close to the value of 0.86 appearing in the correlation equation (6) for unframed plates. This suggests that as a first approximation, C be regarded as a universal constant. Such an assumption permits broad conclusions to be drawn about the effect of an adiabatic frame on the wind-related heat transfer coefficient for a solar collector.

Consider an unframed flat plate collector whose upper cover plate has dimensions L_{1c} and L_{2c} (i.e., L_{1c} and L_{2c} are dimensions of the thermally active zone). From these, a characteristic dimension L_c can be calculated with the aid of equation (3). Suppose that the collector is to be positioned within a co-planar frame (e.g., a roof surface) whose dimensions L_{1f} and L_{2f} are measured along the outer edges of the frame. A characteristic dimension L_f corresponding to L_{1f} and L_{2f} can then be evaluated from equation (3). The heat transfer coefficient for the frame plate will now be compared with that for the unframed plate at the same freestream velocity U_∞. The latter will be designated by an asterisk to distinguish it from the former.

When C is universal, then $j/j^* = (\mathrm{Re}^*/\mathrm{Re})^{1/2}$. If the definitions of the heat transfer j-factor and the Reynolds number are introduced, respectively from equations (1) and (4), and it is noted that U_∞ is the same for both cases, there is obtained

$$h/h^* = (L_c/L_f)^{1/2} \tag{7}$$

Since $L_f > L_c$, the presence of the frame will result in a heat transfer coefficient that is lower than that for the same plate without a frame.

The extent of the decrease depends on the square root of the ratio of the characteristic dimensions of the collector and the frame. If the frame is very large compared with the collector, major reductions in the heat transfer coefficient can result. For example, if $L_c/L_f = 1/3$, then the heat transfer coefficient will be only about 55 percent of that for a collector without a frame.

Concluding Remarks

The possibility of reducing wind-related heat losses due to the action of an adiabatic co-planar frame is one of the major findings of the present investigation. Another important result is conveyed in equation (7), which provides a remarkably simple means for estimating the extent of the reduction of the heat transfer coefficient. It is believed that this equation merits consideration for incorporation into the standard design procedure for flat plate solar collectors.

As a final matter, consideration may be given to the possibility of formulating guidelines for the positioning of a solar collector on a framing surface such as a roof. The use of such guidelines requires that it be possible to identify certain prevailing characteristics of the wind. In particular, the wind pattern has to be sufficiently regular so that specific edges of the collector can be designated as the leading, trailing, and side edges.

Once such an identification has been made, the following guidelines can be suggested on the basis of Table 1 and of the aforementioned summary of results for the unframed plate:

1 Framing along the side edges appears to have greater benefits than framing along the leading and trailing edges.

2 Framing along the trailing edge appears to be more beneficial than framing along the leading edge.

Acknowledgment

This research was performed under the auspices of the American Society of Heating, Refrigerating, and Air-Conditioning Engineers.

References

1 Tien, K. K., and Sparrow, E. M., "Local Heat Transfer and Fluid Flow Characteristics for Airflow Oblique or Normal to a Square Plate," *International Journal of Heat and Mass Transfer*, Vol. 22, 1979, pp. 349–360.

2 Sparrow, E. M., Ramsey, J. W., and Mass, E. A., "Effect of Finite Plate Width on Heat Transfer and Fluid Flow About an Inclined Rectangular Plate," ASME JOURNAL OF HEAT TRANSFER, Vol. 101, 1979, pp. 199–204.

3 Sogin, H. H., "Sublimation from Disks to Air Streams Flowing Normal to Their Surfaces," *Trans. ASME*, Vol. 80, 1958, pp. 51–59.

4 Skelland, A. H. P., *Diffusional Mass Transfer*, Wiley, New York, 1974, p. 51.

5 Sparrow, E. M., and Tien, K. K., "Forced Convection at an Inclined and Yawed Square Plate—Application to Solar Collectors," ASME JOURNAL OF HEAT TRANSFER, Vol. 99, 1977, pp. 507–512.

C. T. Avedisian
Sibley School of Mechanical
and Aerospace Engineering,
Cornell University, Ithaca, N.Y. 14853
Assoc. Mem. ASME

I. Glassman
Department of Mechanical
and Aerospace Engineering,
Princeton University, Princeton, N.J. 08544

High Pressure Homogeneous Nucleation of Bubbles within Superheated Binary Liquid Mixtures[1]

The limits of superheat of some binary normal paraffin mixtures were measured at pressures up to 2128 kPa using the floating droplet method. The variation of nucleation temperature with liquid phase mole fraction was found to be nearly linear for these n-paraffin solutions over the whole pressure range in which the experiments were performed. Homogeneous nucleation theory was used to predict the limits of superheat of the solutions tested. The vapor pressures of the mixtures were estimated by using the Peng-Robinson equation of state to evaluate the liquid and vapor phase fugacities, and the mixture surface tensions were calculated using an empirical adaptation of the van der Waals expression for the surface tension of a pure liquid near the critical point. The predicted and measured limits of superheat were found to be in good agreement over the entire pressure range for all liquid phase compositions. The results of the present work could be useful for predicting liquid phase temperatures and compositions at which the microexplosive or disruptive burning of droplets of fuel blends which are mixtures of volatile and nonvolatile liquids will be initiated during droplet combustion at high ambient pressures.

1 Introduction

The mixing of a cold volatile fluid and a hot nonvolatile liquid can lead to significant superheating, followed by the homogeneous nucleation of bubbles, within the volatile liquid. If the subsequent growth of these bubbles is sufficiently rapid, the resulting bulk phase transition could be manifested by an explosive type of boiling. For example, such explosive boiling has been observed in liquid natural gas spills on water [1] and during the combustion of droplets of certain fuel blends which are solutions of volatile and nonvolatile liquids [2]. Because of the hazards, and possible benefits, attendant to such explosive boiling, the importance of understanding and predicting the factors which initiate the explosive mechanism is self-evident.

In the absence of extraneous nucleation aids such as containing walls and particles, the formation of the initial vapor bubbles which are of a size such that they are in thermodynamic equilibrium with the surrounding liquid occurs by the random molecular processes proposed by homogeneous nucleation theory [3, 4]. The energy, rate of formation, and growth rate of such "critical size nuclei" strongly depends on the physical properties of the liquid in which the bubbles form. For pure liquids the important physical properties are relatively easy to predict, and the limits of superheat of such systems have been studied extensively from both a theoretical and experimental point of view [5, 6]. Experimental work on the homogeneous nucleation of bubbles within liquid-liquid mixtures has received much less attention [7–12], particularly experiments above atmospheric pressure [13], although some measurements of the nucleation pressures of liquid-gas solutions have been reported recently [14–17].

The physical properties of mixtures often cannot be predicted as accurately as the properties of pure liquids. The accuracy of such predictions has a very strong effect on the ability to obtain a meaningful estimate of the homogeneous nucleation temperature [11, 12, 18].

In the present work we report the results of an experimental and theoretical study of the effect of composition and ambient pressure on the limit of superheat of liquid-liquid mixtures. The limits of superheat of some selected binary liquid mixtures were measured over a range of ambient pressures. Methods for estimating the physical properties required to predict the temperature and pressure at which nucleation of bubbles occurs within these mixtures were also studied. The information obtained was used for predicting the conditions (liquid phase temperatures and compositions) under which the disruptive burning phenomenon or "micro-explosion" of fuel drops which are solutions of volatile and nonvolatile liquids was thought to be initiated during droplet combustion.

The mixtures used in our experiments were binary liquid-liquid solutions of the normal paraffins. Methods for estimating the physical properties of this class of hydrocarbons and their mixtures appear to be among the most well developed. If the homogeneous nucleation temperatures of such simple solutions could be accurately predicted at various liquid phase compositions and ambient pressures, then we believe that we will have established a basis for calculating the limits of superheat of a wider class of multicomponent liquid-liquid solutions.

2 Experiment

2.1 Description of the Apparatus. The experiments performed consisted of heating individual droplets of the test solutions by direct contact heat transfer between the test droplet and a surrounding immiscible field liquid which had a much higher boiling point. A small droplet of the test liquid solution was injected into the bottom of a column filled with a heavier immiscible nonvolatile field liquid. The field liquid was heated to produce a stable temperature profile which was hotter at the top of the column than at the bottom. As the droplet rose, it was progressively heated until it began to boil. By choosing a field liquid with a relatively high surface tension, low vapor pressure, and low mutual solubility with all components of the test solution, the probability for homogeneous nucleation within the bulk of the test droplet would be greater than at the interface between test drop and surrounding liquid [19]. The field liquid then serves only as a medium to transfer heat to the test drop and does not influence the ability of the droplet to intrinsically undergo a phase transition. This concept was first employed by Skripov and Kukushkin [7] for measuring the superheat limits of n-hexane/n-heptane mixtures at atmospheric pressure and by Skripov and Ermakov [20] for measuring the homogeneous nucleation temperatures of some pure liquids at high pressures.

A schematic diagram of the experimental installation is shown in Fig. 1. The test section consisted of a bubble column mounted inside

---

[1] Work performed at the Department of Mechanical and Aerospace Engineering, Princeton University, Princeton, N. J. 08544

Contributed by the Heat Transfer Division for publication in the JOURNAL OF HEAT TRANSFER. Manuscript received by the Heat Transfer Division, May 27, 1980.

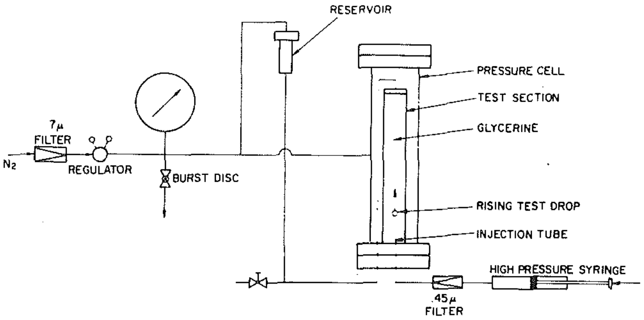

Fig. 1 Schematic of the apparatus

a pressure vessel. The bubble column was essentially a glass tube 55 cm long, 4.5 cm o.d., and 4.1 cm i.d. The tube was heated by an aluminum sleeve with variac-regulated electrical strip heaters and was attached along its length. The sleeve was placed around the glass tube and carefully pressed to the tube by using tie bolts. Vertical slits on opposite sides of the sleeve provided visual access to the interior of the tube. The test section assembly was mounted on the bottom cover plate of the pressure cell and sealed with a stainless steel cap via o-rings. Slotted windows on the pressure vessel with direct back lighting permitted observations of the interior of the test section. (The test section and pressure cell were connected to a small external reservoir in order to help condense vapors generated by both vaporization of the test drops and some vaporization of the field liquid.) Nitrogen gas was used for pressurizing the test section. The pressure was measured by a 0-3447 kPa (0–500 psi) Heise gage which was calibrated to ±6.9 kPa (1 psi). Temperature was measured by a digital volt meter connected to three thermocouples located at fixed positions in the test section 5.4 cm, 6.7 cm, and 9.2 cm from the top of the glass tube. The thermocouple lead and heater wires were passed through Conax "feedthrough" fittings screwed into the bottom cover plate.

The droplet injection system consisted of a high pressure syringe (High Pressure Equipment Co. pressure generator) connected to a glass capillary tube (a length of 3 mm o.d. pyrex tube about 3.8 cm long which had been drawn to an outside diameter of 0.1 to 0.15 mm at one end). This injection tube was mounted on the bottom cap of the test section by a Conax vacuum fitting. A high pressure Millipore filter holder containing a 0.45 micron filter was used to remove solid particles from the test liquid prior to introducing a drop into the test section. Individual droplets were introduced into the bottom of the test section by turning the handle on the syringe until a drop began to form on the tip of the capillary. Then, by suddenly withdrawing liquid in the capillary, droplets of any diameter in the range of 0.1 to 3 mm could be made to lift off of the capillary tip. In this manner it was possible to control reasonably well the size of the droplets entering the test section.

Power to the heaters was controlled in a manner such that rising droplets boiled at the vertical position in the column corresponding to the middle of the three thermocouples. When this procedure proved too time consuming, the temperature gradient in the field liquid was adjusted so that the droplets boiled between the top two thermocouples. The temperature at which boiling was observed was estimated by assuming a linear temperature gradient between the two thermocouples. The vaporization temperatures of ten droplets ranging in diameter from 0.5 to 1 mm were recorded for each mixture at a given pressure, and an average of the ten measurements was taken to be the limit of superheat of the test solution at the pressure on the field liquid. The pressure was then increased and the procedure repeated. In this way it was possible to measure the variation of nucleation pressure with temperature for a liquid solution of given composition. By changing the liquid phase composition of the mixture the variation of boiling temperature with composition at a given pressure could also be measured. Further discussion of the apparatus and procedure for obtaining the data are described in more detail elsewhere [19].

2.2 Selection of Liquids. The availability of physical property data for the pure liquids and mixtures we used was a major consideration in their selection. For this reason we used mixtures of the normal paraffins in our experiments. The most relevant physical property data are surface tension and bubble point pressures. However, no high temperature (>400 K) surface tension data could be located for such mixtures, and only limited vapor pressure data could be found at high temperatures. The only normal paraffin mixture whose components are liquid at room temperature for which equilibrium vapor pressure data up to the critical mixture point could be located were solutions of n-pentane and n-heptane [21]. Solutions of n-pentane and n-heptane were therefore used as model fuel mixtures Some limited measurements above atmospheric pressure were also made using n-pentane/n-octane and n-pentane/n-hexadecane mixtures.

To insure that boiling was initiated by bubble nucleation within the test mixture, the properties of the test liquid and field liquid (in which the droplets were heated) had to be such that nucleation within the bulk of the test droplet would be more probable than at the interface between the test droplet and field liquid. The basis for expecting nucleation of bubbles to occur within the bulk of the test droplet is determined by the interfacial forces acting on the microscopic vapor bubble and the energy of the critical size nucleus. If the surface tension of the nonvolatile field liquid is high enough that the test liquid spreads on the field liquid, bubble nucleation within the bulk of the field liquid will be more probable than at the interface between field and test liquids [19, 22, 23]. The relative success that others [8–10] have had in using glycerine as a field liquid to suppress boiling of droplets of the n-alkanes and their mixtures until the droplets reached temperatures as high as 90 percent of their respective

Nomenclature

a = Peng-Robinson constant, equation (15)
A = constant defined in equation (18)
b = Peng-Robinson constant, equation (17)
B = constant defined in equation (19)
d_{12} = empirical binary interaction parameter, equation (16)
f_i^v = vapor phase fugacity of component i
f_i^l = liquid phase fugacity of component i
J = nucleation rate
k = Boltzmann constant
k_f = total molecular evaporation rate
m_i = molecular mass of species i
n_i = number of moles of species i
n = total number of moles ($n = \Sigma_i n_i$)
N_0 = total number density of molecules within the liquid mixture
P = pressure of gas within the vapor nucleus ($P = \Sigma_i P_i$)
P_c = pure liquid critical pressure
P_0 = ambient pressure of liquid surrounding the vapor nucleus
P_e = equilibrium bubble point pressure of the mixture
P_i = partial pressure of component i within the vapor nucleus
P_{cm} = mole fraction average of the critical pressures of the components in solution
s_m = effective characterization parameter of the mixture
T = temperature
T_{bm} = mole fraction average of the normal boiling points of the components in solution
T_c = pure liquid critical temperature
T_{cm} = true mixture critical temperature
V = total volume
v = liquid molar volume of the mixture
v_{il} = partial molar volume of component i in the liquid mixture
x = liquid phase mole fraction
y = vapor phase mole fraction
Z = compressibility factor
β = surface tension proportionality constant, equation (5)
Γ = growth probability of a critical size nucleus
ΔA^* = energy of forming a critical size nucleus
σ = surface tension
μ = critical exponent

Subscripts

c = critical point
i = component i
e = saturation conditions
ie = saturation conditions for component i
m = mixture

critical temperatures (such temperatures are close to the theoretical limits of superheat of most liquids at atmospheric pressure) supports this hypothesis. The surface tension of glycerine is higher than that of the n-paraffin, and the glycerine/n-paraffin interfacial tension is low enough that the n-paraffin spreads on glycerine. As a result, glycerine was used as the field liquid in our experiments.

The n-hexadecane, n-heptane, and n-octane were obtained from Humphrey Chemical Co. with a stated purity of 99 percent. The n-pentane and glycerine were Fisher and Eastman "spectrograde" respectively and were used directly as received. The mixtures were prepared by combining appropriate volumes of the two liquids at room temperature to give the selected mole percent solution.

2.3 Experimental Observations and Results. Near atmospheric pressure, boiling of the liquid droplets was usually accompanied by a "popping" sound which was clearly audible through the walls of the pressure vessel. This effect was indicative of a high bubble growth rate within the droplet. In this case, there was little ambiguity about the vertical position in the column at which boiling was observed. However, between 377 and 653 kPa the bubble growth rate was apparently reduced sufficiently that droplet boiling was not accompanied by any audible sound. The position in the column at which boiling occurred was then detected by a sudden increase in the velocity and diameter of the rising drop. On further increasing the pressure in the test section, it became more difficult to detect the position in the column at which boiling commenced. For example, higher than around 2027 kPa, it was extremely difficult to observe a change in velocity of n-heptane droplets, even above a temperature at which they would have been expected to boil. A similar effect was also observed for dilute solutions of volatile and nonvolatile liquids: it was difficult to discern a change in velocity of n-pentane/n-hexadecane mixtures containing more than 30 mole percent n-pentane at pressures above 1216 kPa. Both these effects are probably due to a combination of high ambient pressure and/or to the possibility that the growth rate of the nucleated bubble is controlled by the rate of diffusion of the volatile species to the bubble surface as the mixture is increasingly diluted by the nonvolatile component. The accuracy of the measurements therefore probably decreased with increasing ambient pressure.

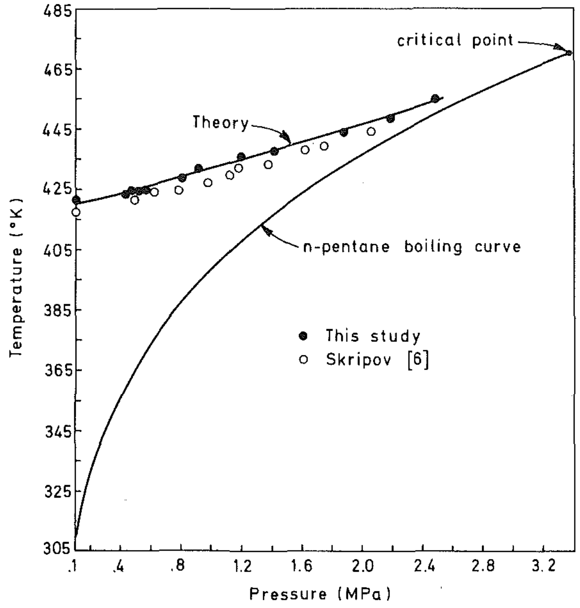

Fig. 2 Variation of the limit of superheat with ambient pressure of n-pentane

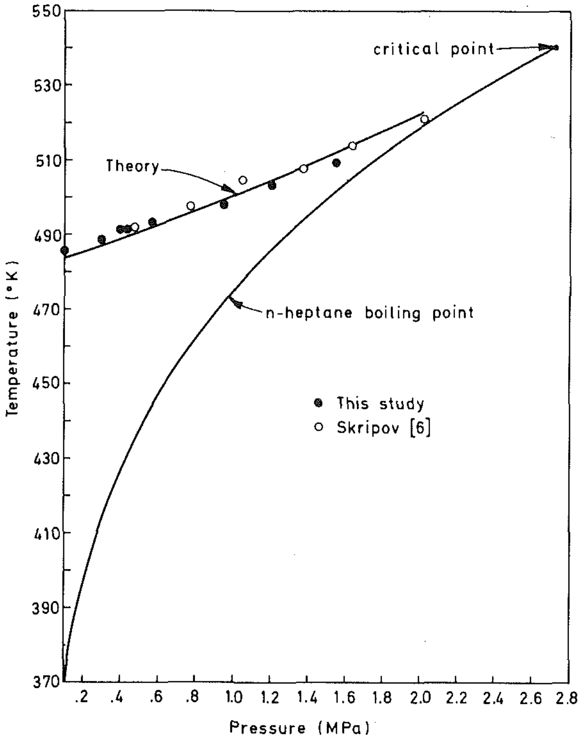

Fig. 3 Variation of the limit of superheat with ambient pressure of n-heptane

In order to verify our experimental procedures, the limits of superheat of pure n-pentane and n-heptane were measured at various pressures and the results were compared with data reported by Skripov [6]. Figures 2 and 3 show the results on a pressure-temperature diagram. The equilibrium vapor pressure curves of n-pentane

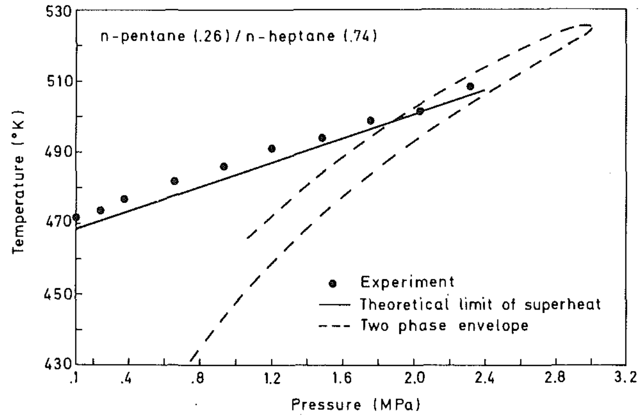

Fig. 4 The limit of superheat of a n-pentane/n-heptane mixture containing 26 mole percent n-pentane. The dotted line represents the locus of saturation states for this mixture which were experimentally measured by Cummings, et al. [21].

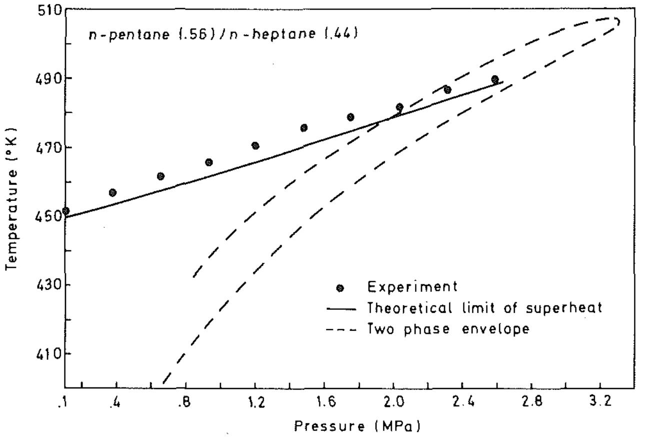

Fig. 5 The limit of superheat of a n-pentane/n-heptane mixture containing 56 mole percent n-pentane. The dotted line represents the locus of saturation states for this mixture which were experimentally measured by Cummings, et al. [21].

and n-heptane [24] are included in Figs. 2 and 3 to illustrate the extent of superheating of the liquid (the theoretical predictions are discussed in Section 3). The present measurements are consistent with Skripov's data. The atmospheric pressure data are also within 2 K of the measurements of Eberhart, et al. [8]. Compared to the variation of saturation temperature with pressure, the limit of superheat of a pure liquid is relatively insensitive to pressure as, for example, previously observed by Skripov [6].

The effect of ambient pressure on the limit of superheat of two n-pentane/n-heptane mixtures is shown in Figs. 4 and 5. The compositions of these two mixtures were chosen to coincide with the molar compositions used by Cummings, et al. [21] in their phase equilibrium measurements in order to understand more clearly the location of superheated liquid states on a phase diagram for a binary mixture. The boiling curves shown in Figs. 4 and 5 were obtained from their experimental results. (The locus of saturated states for a binary mixture separates into two branches on a pressure-temperature diagram—the dew point and boiling curves—which intersect at the mixture critical point.) The variation of limit of superheat with ambient pressure is similar to the variation of limit of superheat with ambient pressure observed for the individual components (Figs. 2 and 3). The nucleation temperature of the solution depends less strongly on pressure than does the mixture boiling curve, and the variation of nucleation temperature with pressure is nearly linear.

As the volatile component in the mixture is diluted, the limit of superheat increases at a fixed pressure. This behavior is illustrated on the temperature-composition diagrams displayed in Figs. 6 to 8. The variation of limit of superheat with liquid phase mole fraction is nearly linear over the whole pressure range in which the experiments were run. This observation, previously observed only at atmospheric pressure [7–10, 25], appears to be a characteristic for solutions of liquids from this homologous series.

3 Discussion

3.1 Theory of Homogeneous Nucleation. A homogeneous liquid-vapor phase transition is initiated by the formation of the aforementioned critical size nuclei within the bulk of a liquid. Such bubbles form within the liquid lattice structure by random fluctuations of density [3, 4] which produce cavities or holes within which the molecules are gas-like in terms of their molecular spacings and potential energies. The resulting vapor nuclei or bubbles are then considered to grow or decay in a more or less random manner by the acquisition or loss of single molecules until a critical size nucleus is produced which is in thermodynamic equilibrium with the surrounding liquid. These microscopic bubbles are unstable in that their energy is an extremum relative to larger or smaller nuclei [19], and they are the seeds which initiate the liquid-vapor phase transition. The onset of homogeneous nucleation of bubbles within a liquid is governed by the rate of formation (i.e., nucleation rate), or waiting time, of the critical size bubbles. The kinetic limit of superheat is usually defined as the mean temperature in the range in which the

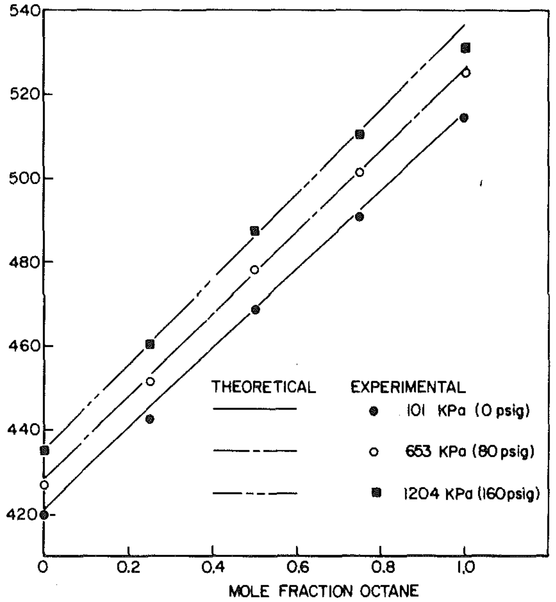

Fig. 7 The variation of limit of superheat of n-pentane/n-octane mixtures with liquid phase mole fraction at ambient pressures of 101 kPa, 653 kPa, and 1204 kPa

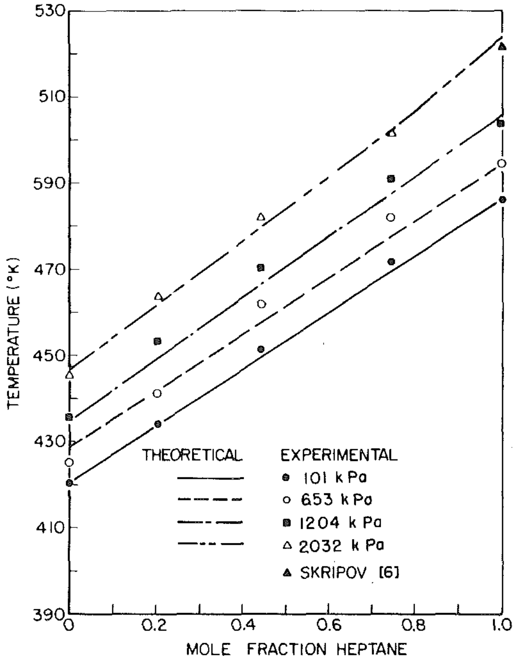

Fig. 6 The variation of limit of superheat of n-pentane/n-heptane mixtures with liquid phase mole fraction at various ambient pressures

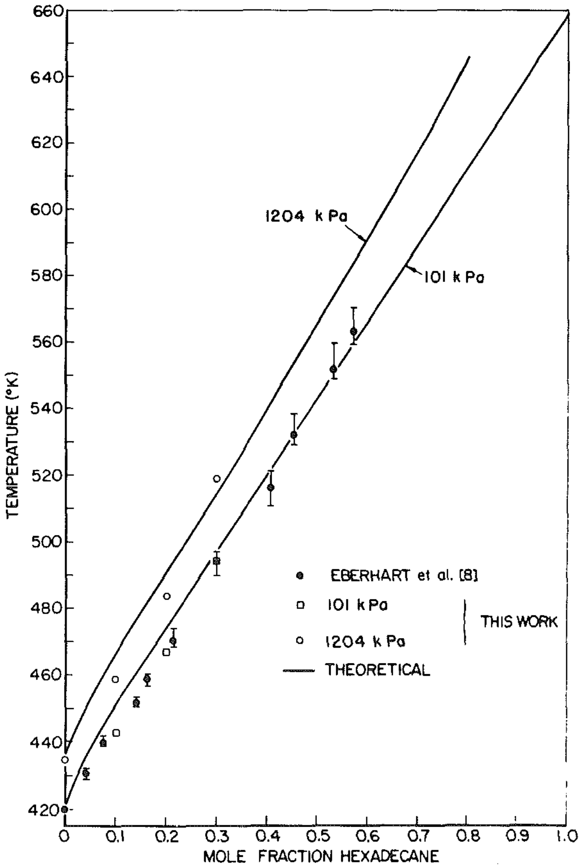

Fig. 8 The variation of limit of superheat of n-pentane/n-hexadecane mixtures at ambient pressures of 101 kPa and 1204 kPa.

nucleation rate changes from a negligible value to a very large value.

In its most elementary form, the nucleation rate is expressed by the product of the rate at which individual molecules evaporate into a critical size nucleus times the concentration of such nuclei, the latter usually being considered to follow a Boltzmann distribution. In this approximation, the kinetic limit of superheat can be written in the following form

$$T = \Delta A^* \left[k \ln \left(\frac{N_0 \Gamma k_f}{J}\right)\right]^{-1} \tag{1}$$

where the energy of the critical size nucleus is

$$\Delta A^* = \frac{16\pi\sigma^3}{3(P - P_0)^2} \tag{2}$$

The number density of molecules within the liquid solution, N_0, was approximated as

$$N_0 \simeq 6.023 \times 10^{23}/v \tag{3}$$

where v is the liquid molar volume of the mixture. k_f is the total evaporation rate of the individual molecular species. In a multicomponent liquid solution within which a spherical vapor nucleus forms, k_f was approximated as the sum of the ideal gas collision frequencies:

$$k_f = \frac{8P\sigma^2}{(P - P_0)^2} \left(\frac{2\pi}{kT}\right)^{1/2} \sum_i \left(\frac{y_i}{m_i^{1/2}}\right) \tag{4}$$

Γ essentially expresses the probability that a nucleus of critical size will grow by the evaporation of a single molecule of any chemical species within the liquid solution. In the above approximation $\Gamma = 1$ (i.e., all critical size nuclei continue to grow), but it may be more reasonable to expect that $\Gamma < 1$, and various approximations for Γ expressing this fact have been derived [12, 19]. The values of Γ so obtained typically range from 1 to 0.01. None of the expressions for Γ have yet been verified experimentally because of the microscopic dimensions of the critical size nuclei. However, differences in Γ of a few orders of magnitude will have an insignificant effect on the solution of equation (1) for the kinetic limit of superheat because the argument of the logarithmic term is on the order of 10^{29} to 10^{31}. Therefore, $\Gamma = 1$ was used in our work.

The limit of superheat is, however, very sensitive to the value of the energy of the critical size nucleus, ΔA^*, which in turn is strongly dependent on the vapor pressure and surface tension of the nucleus. These physical properties depend on the liquid phase composition as well as on temperature and ambient pressure, and must be estimated accurately to obtain a meaningful value of the homogeneous nucleation temperature. A major difficulty is that of estimating the relevant properties at a temperature which is higher than the critical temperature of one or more of the volatile components within the mixture. In the case of the vapor pressure, the problem is more computational than theoretical [26]. However, the problem of estimating the surface tension of a mixture of liquids requires further development as described in the next section. (These problems were recently addressed by Avedisian and Andres [11] and Holden and Katz [12] who presented the first accurate calculations of the limit of superheat of some binary liquid mixtures at atmospheric pressure.)

3.2 Surface Tension. If the surface tension of a liquid mixture is expressed in terms of the pure component surface tensions, the surface tension of the component whose critical temperature is exceeded is undefined and thus the method becomes unsuitable. The parachor mixing rule of Weinaug and Katz [27] is very sensitive to the value of the parachors of the components in solution and is sometimes difficult to use because of a lack of accurate vapor phase composition and density data of the mixture.

An empirical method which in principle avoids these difficulties is to apply to liquid solutions the functional dependence of the surface tension on temperature originally developed by van der Waals [28] for pure liquids. From the corresponding states principle, the surface tension of a pure liquid near its critical temperature can be written

$$\sigma = \beta P_c^{2/3} T_c^{1/3} \left[1 - \frac{T}{T_c}\right]^{\mu} \tag{5}$$

where the critical exponent μ is a constant which varies between 1.2 and 1.4 for a wide variety of nonpolar liquids. β should be a constant for all pure liquids which follow the corresponding states principle. However, examination of the available surface tension values of many pure nonpolar liquids reveals that β is not constant. This observation led Brock and Bird [29] to search for an empirical correlation for β in terms of some parameter characteristic of a liquid. They found that β could be correlated with the Riedel parameter, defined as

$$\frac{T_c}{P_c}\left(\frac{d \ln P}{dT}\right)_{T_c, P_c}.$$

However, use of various mixing rules in their correlation did not produce estimates of the surface tension of liquid mixtures sufficiently accurate for solving equation (1).

It was found that in some cases β could be correlated better with the characterization parameter which we defined for a mixture as

$$s_m = \frac{T_{cm} \ln (P_{cm})}{T_{cm} - T_{bm}} \tag{6}$$

This parameter represents the slope of a straight line connecting an appropriately defined normal boiling point and critical point of the mixture. It has been utilized in the past [24] to correlate the vapor pressure of pure nonpolar liquids. A correlation for β in terms of s_m was obtained by using mole fraction average values of T_{bm} and P_{cm}, and the true critical mixture temperature T_{cm} (as, for example, estimated by methods recommended by Reid, et al. [30]). The results of this approach for correlating β with s_m are shown in Fig. 9. The abscissa was obtained from available experimental surface tension data by taking an average value of β over the temperature range of the reported data for each substance at constant liquid composition. The critical exponent was held constant at a value of 11/9. The data were correlated by a second degree polynomial as

$$\beta = -0.4412 + 0.2003 s_m - 0.00516 s_m^2 \tag{7}$$

A limited test of the accuracy of equations (5) and (7) was made by

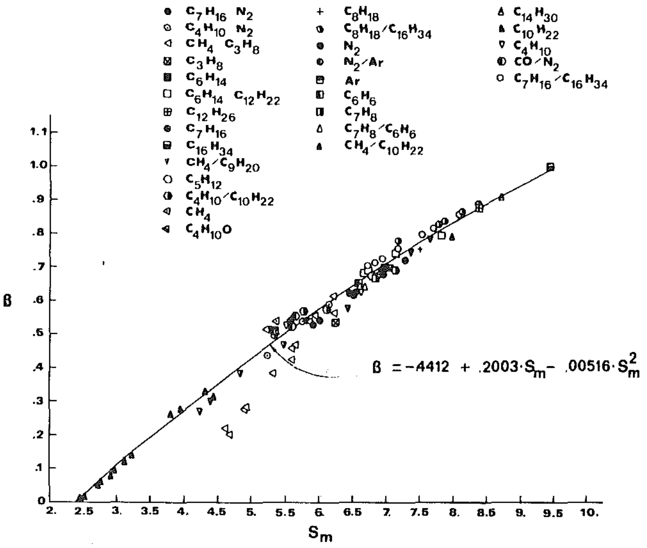

Fig. 9 Correlation of β in equation (5) with the characterization parameter for several nonpolar liquids and their mixtures.

Table 1 Correlations of surface tension with temperature

Liquid	$\beta P_c^{2/3} T_c^{1/3}$	μ	T_c(K)
n-pentane [35]	53.3	1.23	469.6
n-heptane [8]	55.13	1.28	540.2
n-octane [8]	55.72	1.30	568.8
n-hexadecane [35]	55.2	1.33	717.0

Avedisian [19]. The average absolute percent error for n-paraffin mixtures not containing methane as a component was under 3 percent. For pure liquids a slightly larger error of 6 percent was found. However, equation (7) was not used for predicting the surface tension of pure liquids because more accurate correlations for the pure liquid components we used were already available in the literature, as summarized in Table 1.

The substances included in the correlation leading to equation (7) were nonpolar mixtures from the same homologous series: n-alkane/n-alkane, aromatic/aromatic, etc. Equation (7) was found not to be very accurate for predicting surface tension of such mixtures as n-alkane/aromatic and n-alkane/alcohol.

3.3 Vapor Pressure. The vapor pressure P within the critical size nucleus was estimated by solving two problems. Firstly, the equilibrium vapor pressure P_e of the mixture was calculated by solving the basic set of phase equilibrium relations

$$f_i^{\upsilon}(P_e, T, y_{1e}, y_{2e}, \ldots) = f_i^{l}(P_e, T, x_1, x_2, \ldots) \qquad (8)$$

for P_e and the y_{ie}, given T and all the x_i. The fugacities were evaluated from the defining equation [26]

$$f_i^{\upsilon} = y_{ie} P_e \exp\left\{\frac{1}{RT}\int_{\infty}^{V}\left[\left(\frac{RT}{V} - \frac{\partial P_e}{\partial n_i}\right)_{T,V,n_j}\right] dV - RT\ln(Z)\right\}. \qquad (9)$$

A pressure explicit equation of state, $P = P(T, V, n_1, n_2, \ldots)$ is required in order to evaluate the integral in the above equation. The liquid phase fugacities, f_i^l, were determined by replacing y_{ie} by x_i in equation (9). Secondly, with P_e and the y_{ie} now known, the partial pressure of component i within the nucleus, which forms within the bulk of the liquid mixture under an ambient pressure P_0, was then obtained from the approximate relation (see Appendix)

$$P_i \simeq y_{ie} P_e \exp\left[\frac{\upsilon_{il}}{RT}\left(P_0 - P_e\right)\right], \qquad (10)$$

where the partial molar volume of component i in the liquid solution, υ_{il}, is defined as

$$\upsilon_{il} \equiv \frac{\left(\dfrac{\partial P_e}{\partial n_i}\right)_{T,V,n_j}}{\left(\dfrac{\partial P_e}{\partial V}\right)_{T,\text{all } n_i}} \qquad (11)$$

The fugacities and partial molar volumes were evaluated by using the Peng-Robinson [31] equation of state:

$$P_e = \frac{nRT}{(V - bn)} - \frac{an^2}{V^2 + 2bnV - n^2b^2} \qquad (12)$$

Equations (9) and (11) could then be expanded to yield

$$f_i^{\upsilon} = y_{ie} P_e \exp\left\{\frac{b_i}{b}(Z - 1) - \ln(Z - B) - \frac{A}{2\sqrt{2}B}\left(\frac{2\sum_{j=1}^{2} a_{ij} y_{je}}{a} - \frac{b_i}{b}\right)\ln\left(\frac{Z + 2.414B}{Z - .414B}\right)\right\} \qquad (13)$$

and

$$\upsilon_{il} \approx \frac{\dfrac{RT}{(\upsilon - b)^2}(\upsilon + b_i - b) + \dfrac{1}{(\upsilon^2 + 2b\upsilon - b^2)}\left(\dfrac{2a(\upsilon - b)b_i}{\upsilon^2 + 2b\upsilon - b^2} - 2\sum_{j=1}^{2} x_j a_{ij}\right)}{\dfrac{RT}{(\upsilon - b)^2} - \dfrac{2a(\upsilon + b)}{(\upsilon^2 + 2b\upsilon - b^2)^2}} \qquad (14)$$

where for a binary mixture,

$$a = a_1 y_{1e}^2 + 2y_{1e}y_{2e}a_{12} + a_2 y_{2e}^2 \qquad (15)$$

$$a_{12} = (a_1 a_2)^{1/2}(1 - d_{12}) \qquad (16)$$

$$b = y_{1e} b_1 + y_{2e} b_2 \qquad (17)$$

$$A = \frac{aP_e}{R^2T^2} \qquad (18)$$

and

$$B = \frac{bP_e}{RT} \qquad (19)$$

y_{1e} and y_{2e} are replaced by x_1 and x_2 respectively in equations (15) and (17) to evaluate υ_{il} from equation (14).

The parameters a_i and b_i were obtained from the pure component data, and d_{12} is an empirically determined interaction parameter characteristic of the binary 1–2 pair. For hydrocarbon mixtures Peng and Robinson [31] have found that $d_{12} = 0$. The compressibility factor, $Z \equiv PV/(nRT)$ in equation (13), was obtained by rewriting equation (12) in the form

$$Z^3 - (1 - B)Z^2 + (A - 3B^2 - 2B)Z - (AB - B^2 - B^3) = 0 \qquad (20)$$

The largest root of equation (20) is the vapor phase compressibility factor, and the smallest root is the liquid phase value. The molar volume of the liquid mixture, υ in equations (3) and (14), was evaluated from a correlation developed by Hankinson and Thomson [32].

For binary mixtures equations (8) are a set of two nonlinear algebraic equations for the unknowns y_{1e} and P_e. The equations were solved numerically [19], and the accuracy of the results were compared with some binary n-paraffin mixture data available in the literature. Such data are scarce at reduced temperatures typical of homogeneous bubble nucleation within mixtures $-T/T_{cm} > .9$. A relevant test of the accuracy of predicted bubble point pressures could only be made for the n-pentane/n-heptane mixtures we studied. Only for these mixtures could vapor-liquid equilibrium data be located at such high reduced temperatures [21]. As illustrated in Fig. 10, agreement between calculated and experimental vapor pressures is quite good, and there is no ambiguity in the method when the critical temperature of n-pentane is exceeded. (The relevant physical constants required in the calculation were taken from Reid, et al. [30].)

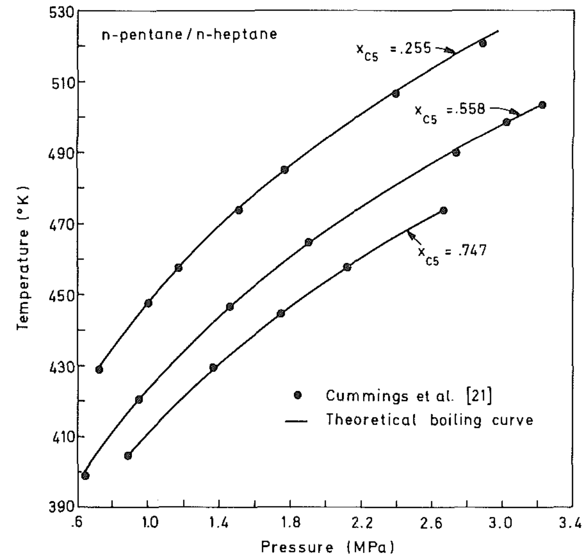

Fig. 10 Comparison of the boiling points of three n-pentane/n-heptane mixtures, as measured by Cummings, et al. [21], with calculated values obtained by solving the set of equations (8).

No data at high reduced temperatures could be located for the n-pentane/n-octane or n-pentane/n-hexadecane mixtures, although McGlashan and Williamson [33] reported some measurements of bubble point pressures of n-hexane/n-hexadecane mixtures at temperatures up to 333 K. The agreement between bubble point pressures calculated from equation (8) and their data was also found to be quite good. Notwithstanding the unavoidable criticism of using data at temperatures well below those characteristic of bubble nucleation within mixtures to justify our approach for predicting the gas pressure within the critical size nucleus, we feel that predicted bubble point pressures at high reduced temperatures are as accurate for solutions of volatile and nonvolatile liquids such as the n-pentane/n-hexadecane mixtures as they were found to be for n-pentane/n-heptane mixtures.

3.4 Results. Assuming that droplet boiling is the result of one bubble nucleating anywhere within the droplet, the nucleation rate can be estimated from the approximate expression $J = 1/(v_d t)$, where t is the mean lifetime of a superheated liquid droplet of volume v_d. From our experimental conditions, droplets traveling 4 cm/s over a distance of 1.3 cm spent an average of 0.3 s within a range of 2 K of the observed boiling temperature (a precise value of t is not too important). For droplet diameters ranging between 0.5 and 2 mm, the nucleation rate correspondingly varied from about 10^3 nuclei/cm^3-s to 10^5 nuclei/cm^3-s. This difference resulted in a less than 1 K change in the predicted limit of superheat.

Using the methods previously described for estimating the relevant physical properties, and a nucleation rate of 10^5 nuclei/cm^3-s, equation (1) was solved for T over the pressure range for which $P > P_0$. The results are shown by the theoretical lines in Figs. 2–8. The predicted limits of superheat of pure n-pentane and n-heptane (Figs. 2 and 3) are in very good agreement with both our data and those of Skripov [6] over the whole pressure range.

The theoretical limits of superheat of two n-pentane/n-heptane mixtures of fixed composition are shown as a function of pressure in Figs. 4 and 5. In these calculations, the possibility that the composition of the liquid in the vicinity of the nucleus is different from that in the bulk because of preferential vaporization and local depletion of the volatile species, as discussed by Pinnes and Mueller [18], was neglected. Reid [34] argues that such effects are negligible because the number of molecules within the vapor nucleus is small compared to the enormous number of molecules in the liquid. As shown in Figs. 4 and 5, the agreement between predicted and measured nucleation temperatures is quite good.

The effect of liquid phase composition (mole fraction) on the limit of superheat at fixed pressures is shown in Figs. 6–8 for the n-pentane/n-heptane, n-pentane/n-octane, and n-pentane/n-hexadecane mixtures, respectively. There is again very good agreement between predicted and measured limits of superheat over the whole pressure and composition range of the reported data. This observation shows that homogeneous nucleation was probably the cause of boiling in the majority of droplets tested.

The theoretical limits of superheat of the n-alkane mixtures varied nearly linearly with liquid phase mole fraction at both atmospheric and elevated pressures, as shown in Figs. 6–8. This fact was previously observed at atmospheric pressure [11, 12, 18]. However, this nearly linear variation of limit of superheat with mole fraction is by no means a universal result. Some liquid-liquid mixtures have been found to exhibit nonlinear variations of nucleation temperature with mole fraction. For example, Holden and Katz [12] found that the superheat limits at atmospheric pressure of benzene/n-hexane and benzene/cyclohexane mixtures varied nonlinearly with mole fraction. Those mixtures whose nucleation temperatures do vary nonlinearly with mole fraction are typically nonideal solutions which may exhibit a two-phase miscibility gap (e.g. mixtures of n-hexadecane and ethanol). The ability to correctly predict the limit of superheat of nonideal mixtures requires accurate vapor pressure and surface tension data of the mixture near the mixture critical temperature. Unfortunately, such data are scarce and methods for predicting them are not well developed. This fact is precisely why we choose to use normal alkane mixtures in our experiments. By showing that equation (1) could correctly predict experimentally measured limits of superheat of such relatively simple liquid-liquid mixtures as those made up of the normal alkanes over a range of pressures and liquid phase compositions, and at temperatures which may exceed the critical temperature of one of the components in the solution, we feel that the limits of superheat of more complicated mixtures may also be correctly predicted by using equation (1) once the required physical properties can be estimated accurately.

The above results may be useful for predicting the internal boiling or micro-explosion phenomenon which has been observed [2] in the combustion of fuel drops which are miscible solutions of volatile and nonvolatile liquids. Concentration gradients produced within the drop as a result of the diffusional processes attendant to droplet vaporization can result in locally superheated regions within the droplet interior. If the droplet burning temperature T_d surpasses the homogeneous nucleation temperature T at any point within the droplet interior, micro-explosions will be initiated by the formation of a critical size nucleus within the fuel blend. The subsequent growth of this initial vapor bubble will lead to the disruptive combustion of the droplet, if the bubble grows fast enough to fragment the drop before completion of burning. As ambient pressure is increased, or the volatile component within the solution is diluted, the bubble growth rate will be progressively reduced. Internal boiling may still be initiated at high pressures by formation of a critical size nucleus within the fuel blend $-T_d > T-$ but growth of this nucleus could be slowed enough that the time for the nucleus to grow sufficiently beyond its initial equilibrium size is longer than the droplet burning time. The method described here for predicting the nucleation temperature of a fuel blend which is a mixture of volatile and nonvolatile liquids may be useful, when coupled with accurate liquid phase temperature calculations of burning fuel droplets, for estimating if, when, and where within the fuel drop disruptive combustion will be initiated.

4 Conclusions

New measurements of the homogeneous nucleation temperature of some binary liquid n-alkane mixtures have been made at high pressures. The results showed that a mole fraction average of the limits of superheat of the individual components in solution at a given pressure could be used to estimate accurately the effect of pressure and composition on the limit of superheat of the mixture.

The theory of homogeneous nucleation of bubbles in liquids, as expressed by equation (1), was successfully used to accurately predict the experimentally measured nucleation temperatures at high pressures and over a range of compositions. Equation (1) was solved for temperature by using both the Peng-Robinson equation of state to evaluate the liquid and vapor phase fugacities of the mixture (and thereby the pressure of the gas within the vapor nucleus), and a new empirically based correlation for the liquid-vapor surface tension (applicable primarily to normal alkane mixtures).

Extension of the general procedures used in this work to other more nonideal liquid mixtures may be made only after the effects of vapor pressure and surface tension of the solution on the liquid phase composition and temperature can be predicted accurately at high temperatures.

References

1 Porteous, W. M., and Reid, R. C., "Light Hydrocarbon Vapor Explosions," *Chemical Engineering Progress*, Vol. 12, May 1976, pp. 83–89.

2 Lasheras, J. C., Fernandez-Pello, A. C., and Dryer, F. L., "Experimental Observations on the Disruptive Combustion of Free Droplets of Multicomponent Fuels," Paper No. 79-24, Spring Meeting of the Western States Section, Combustion Institute, Provo, Utah, Apr. 23–24, 1979.

3 Volmer, M., *Kinetik der Phasenbildung*, Translated by U.S. Department of Intelligence, refer to ATI No. 81935 (F-TS-7068-RE) from the Clearinghouse for Federal and Technical Information, 1939.

4 Frenkel, J., *Kinetic Theory of Liquids*, Oxford University Press, London, 1946.

5 Blander, M., and Katz, J. L. "Bubble Nucleation in Liquids," *AIChE Journal*, Vol. 21, No. 5, Sept. 1975, pp. 833–848.

6 Skripov, V. P., *Metastable Liquids*, John Wiley & Sons, New York, 1974.

7 Skripov, V. P., and Kukushkin, V. I., "Apparatus for Observing the Superheating Limits of Liquids," *Russian Journal of Physical Chemistry*, Vol. 35, No. 12, Dec. 1961, pp. 1393–1395.

8 Eberhart, J. G., Kremsner, W., and Blander, M., "Metastability Limits of Superheated Liquids: Bubble Nucleation Temperatures of Hydrocarbons and Their Mixtures," *Journal of Colloid and Interface Science*, Vol. 50, No. 2, Feb. 1975, pp. 369–378.

9 Renner, T. A., Kucera, G. H., and Blander, M., "Explosive Boiling of

Light Hydrocarbons and Their Mixtures," *Journal of Colloid and Interface Science*, Vol. 52, No. 2, Aug. 1975, pp. 391–396.

10 Porteous, W., and Blander, M., "Limits of Superheat and Explosive Boiling of Light Hydrocarbons, Halocarbons, and Hydrocarbon Mixtures," *AIChE Journal*, Vol. 21, No. 3, May 1975, pp. 560–566.

11 Avedisian, C. T., and Andres, R. P., "Bubble Nucleation in Emulsions and Mixtures," 175th National Meeting of the Americal Chemical Society, Anaheim, Calif, Mar. 12–17, 1978.

12 Holden, B. S., and Katz, J. L., "The Homogeneous Nucleation of Bubbles in Superheated Binary Liquid Mixtures," *AIChE Journal*, Vol. 24, No. 2, Mar. 1978, pp. 260–267.

13 Skripov, V., et al., "Superheated Liquids: Thermophysical Properties, Homogeneous Nucleation and Explosive Boiling-Up," ASME Paper No. 77-HT-87, AIChE-ASME Heat Transfer Conference, Salt Lake City, Utah, Aug. 15–17, 1977.

14 Mori, Y., Hijikata, K., and Nagatani, T., "Effect of Dissolved Gas on Bubble Nucleation," *International Journal of Heat and Mass Transfer*, Vol. 19, 1976, pp. 1153–1159.

15 Hijikata, K., Mori, Y., and Nagatani, T., "Experimental Study on Bubble Nucleation in the Oscillating Pressure Field," ASME JOURNAL OF HEAT TRANSFER, Vol. 100, Aug. 1978, pp. 460–465.

16 Forest, T. W., and Ward, C. A., "Effect of a Dissolved Gas on the Homogeneous Nucleation Pressure of a Liquid," *Journal of Chemical Physics*, Vol. 66, No. 6, Mar. 1977, pp. 2322–2330.

17 Forest, T. W., and Ward, C. A., "Homogeneous Nucleation of Bubbles in Solutions at Pressures above the Vapor Pressure of the Pure Liquid," *Journal of Chemical Physics*, Vol. 69, No. 5, Sept. 1978, pp. 2221–2230.

18 Pinnes, E. L., and Mueller, W. K., "Homogeneous Vapor Nucleation and Superheat Limits of Liquid Mixtures," ASME JOURNAL OF HEAT TRANSFER, Vol. 101, November 1979, pp. 617–621.

19 Avedisian, C. T., "Superheating and Boiling of Water in Hydrocarbons and of Hydrocarbon Mixtures," Ph.D. Thesis, Princeton University, 1980.

20 Skripov, V. P., and Ermakov, G. V., "Pressure Dependence of the Limiting Superheating of a Liquid," *Russian Journal of Physical Chemistry*, Vol. 38, No. 2, Feb. 1964, pp. 208–213.

21 Cummings, L. W. T., Stones, F. W., and Volante, M. A., "High Pressure Rectification: II. N-Pentane-N-Heptane System," *Industrial and Engineering Chemistry*, Vol. 25, No. 7, July 1933, pp. 728–732.

22 Apfel, R. E., "Vapor Cavity Formation in Liquids," Technical Memorandum No. 62, Acoustics Research Laboratory, Harvard University, Cambridge, Mass., Feb. 1970.

23 Jarvis, T. J., Donohue, M. D., and Katz, J. L., "Bubble Nucleation Mechanisms of Liquid Droplets Superheated in Other Liquids," *Journal of Colloid and Interface Science*, Vol. 50, No. 2, Feb. 1975, pp. 359–368.

24 Gómez-Nieto, M., and Thodos, G., "Generalized Vapor Pressure Equation for Nonpolar Substances," *Industrial and Engineering Chemistry Fundamentals*, Vol. 17, No. 1, 1978, pp. 45–51.

25 Blander, M., Hengstenberg, D., and Katz, J. L., "Bubble Nucleation in n-Pentane, n-Hexane, n-Pentane + Hexadecane Mixtures, and Water," *Journal of Physical Chemistry*, Vol. 75, No. 23, 1971, pp. 3613–3619.

26 Prausnitz, J. M., *Molecular Thermodynamics of Fluid-Phase Equilibria*, Prentice-Hall, Englewood Cliffs, N.J., 1969.

27 Weinaug, C. F., and Katz, D. L., "Surface Tensions of Methane-Propane Mixtures," *Industrial and Engineering Chemistry*, Vol. 35, No. 2, pp. 239–246.

28 Rowlinson, J. S., "Translation of J. D. van der Waals' 'The Thermodynamic Theory of Capillarity Under the Hypothesis of a Continuous Variation of Density'," *Journal of Statistical Physics*, Vol. 20, No. 2, 1979, pp. 197–244.

29 Brock, J. R., and Bird, R. B., "Surface Tension and the Principle of Corresponding States," *AIChE Journal*, Vol. 1, No. 2, June 1955, pp. 174–177.

30 Reid, R. C., Prausnitz, J. M., and Sherwood, T. K., *The Properties of Gases and Liquids*, 3rd ed., McGraw-Hill, New York, 1977.

31 Peng, D. Yu, and Robinson, D. B., "A New Two-Constant Equation of State," *Industrial and Engineering Chemistry Fundamentals*, Vol. 15, No. 1, 1976, pp. 59–64.

32 Hankinson, R. W., and Thomson, G. H., "A New Correlation for Saturated Densities of Liquids and Their Mixtures," *AIChE Journal*, Vol. 25, No. 4, July 1979, pp. 653–663.

33 McGlashan, M. L., and Williamson, A. G., "Thermodynamics of Mixtures of n-Hexadecane," *Transactions of the Faraday Society*, Vol. 57, Part 4, Apr. 1961, pp. 588–600.

34 Reid, R. C., "Superheated Liquids: A Laboratory Curiosity and, Possibly, an Industrial Curse. Part I: Laboratory Studies and Theory," *Chemical Engineering Education*, Spring 1978, p. 60.

35 Dickinson, E., "The Influence of Chain Length on the Surface Tension of Oligomeric Mixtures," *Journal of Colloid and Interface Science*, Vol. 53, No. 3, Dec. 1975, pp. 467–475.

Acknowledgments

The authors are very grateful for the many helpful discussions which they have had with Professor Ronald P. Andres throughout the course of this investigation. Conversations with Professors A. C. Fernandez-Pello and F. L. Dryer are also acknowledged. The assistance of Messrs. J. Sivo and D. Peoples in the construction of the experimental equipment was most appreciated. This work was supported under Department of Energy Contract No. ET-78-S-02-4920.A000.

APPENDIX

The vapor pressure P within a critical size nucleus which forms in a mixture under an ambient pressure P_0 (Fig. A-1(a)) is not the same as the equilibrium bubble point pressure P_e of the mixture at the same temperature and liquid phase composition (Fig. A-1(b)). The difference is due primarily to the curvature of the vapor nucleus. Given $T, P_0, x_1, x_2, \ldots$, we wish to estimate the vapor pressure within the nucleus.

Consider Fig. A-1(b). P_e is the equilibrium bubble point pressure of the mixture when the radius of curvature of the liquid-vapor interface is infinite. The fundamental equilibrium condition for component i is that

$$\mu_i^v (P_e, T, y_{1e}, y_{2e}, \ldots) = \mu_i^l (P_e, T, x_1, x_2, \ldots) \qquad \text{(A-1)}$$

where μ_i is the chemical potential of component i (not to be confused with critical exponent defined in equation (5)). With fugacity defined by the equation

$$\mu_i \equiv \mu_i^0 (T) + RT \ln (f_i), \qquad \text{(A-2)}$$

equation (A-1) may be expressed alternatively as

$$f_i^v (P_e, T, y_{1e}, y_{2e}, \ldots) = f_i^l (P_e, T, x_1, x_2, \ldots). \qquad \text{(A-3)}$$

The fugacities in equation (A-3) are experimentally accessible. They may also be estimated from a suitable equation of state (e.g., equation (12)): given T and liquid phase composition the set of simultaneous nonlinear algebraic equations implied by equation (A-3) can be solved numerically for P_e and the vapor phase composition.

A critical size nucleus (Fig. A-1(a)) is defined to be in thermodynamic equilibrium with the surrounding superheated liquid. Therefore, we may also write

$$\mu_i^v (P, T, y_1, y_2, \ldots) = \mu_i^l (P_0, T, x_1, x_2, \ldots) \qquad \text{(A-4)}$$

By combining equations (A-1), (A-2), and (A-4), the fugacity of component i within the vapor nucleus $f_i^v (P, T, y_1, y_2, \ldots)$, can be related to the fugacity of component i in the equilibrium configuration illustrated in Fig. A-1(b):

$$f_i^v (P, T, y_1, y_2, \ldots) = f_i^v (P_e, T, y_{1e}, y_{2e}, \ldots) \exp \left[\frac{\mu_i^l (P_0, T, x_1, x_2, \ldots) - \mu_i^l (P_e, T, x_1, x_2, \ldots)}{RT} \right] \qquad \text{(A-5)}$$

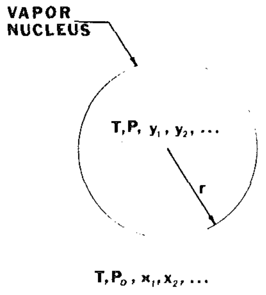

Fig. A-1(a)

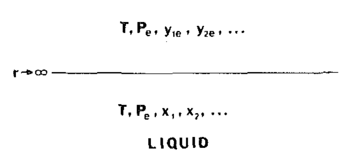

Fig. A-1(b)

Fig. A-1 Physical interpretation of difference between P and P_e

The exponential term in equation (A-5) can be further simplified by integrating the relation

$$v_{il} = \left(\frac{\partial \mu_i^l}{\partial P}\right)_{T,n_i,n_j} \tag{A-6}$$

from P_e to P_0, assuming v_{il} (e.g., equation (14)) is relatively insensitive to pressure. Combining the result with equation (A-5) gives

$$f_i^v(P, T, y_1, y_2, \ldots) = f_i^v(P_e, T, y_{1e}, y_{2e}, \ldots) \exp\left[\frac{v_{il}}{RT}(P_0 - P_e)\right] \tag{A-7}$$

The set of simultaneous equations implied by equation (A-7) may be solved numerically for $P, y_1, y_2, \ldots$ by first calculating $P_e, y_{1e}, y_{2e}, \ldots$ from the set of equations (A-3). However, equation (A-7) may be further simplified by assuming that

$$\phi_i^v (P, T, y_1, y_2, \ldots) \equiv \frac{f_i^v (P, T, y_1, y_2, \ldots)}{y_i P} \simeq \frac{f_i^v (P_e, T, y_{1e}, y_{2e}, \ldots)}{y_{ie} P_e} \equiv \phi_i^v (P_e, T, y_{1e}, y_{2e}, \ldots) \tag{A-8}$$

where the ϕ_i^v are defined as vapor phase fugacity coefficients. With this simplification equation (A-7) becomes

$$P_i \simeq P_e y_{ie} \exp\left(\frac{v_{il}}{RT}(P_0 - P_e)\right) \tag{A-9}$$

which is equation (10). The iterative solution implied by equation (A-7) for the nucleus vapor pressure P, once $P_e, y_{1e}, y_{2e}, \ldots$, are known is now replaced by equation (A-9) which provides an explicit expression for P_i in terms of P_e and y_{ie}.

Refilling and Rewetting of a Hot Horizontal Tube

Part I: Experiments

A. M. C. Chan[1]
S. Banerjee[2]
Mem. ASME.

Department of Engineering Physics,
McMaster University,
Hamilton, Ontario L8S 4M1

Experiments on refilling and rewetting of hot horizontal tubes indicate that gravitational effects are important and lead to flow stratification. The tube is quenched at a given location upwards from the bottom and there is a significant time lag before the top is quenched. The rewetting front is preceded by a liquid layer that is supported by film boiling and forms a "liquid tongue". Significant pre-cooling is observed at the bottom due to the presence of this tongue. No well defined rewetting temperature exists. The channel quenches at temperatures which can vary considerably between the top and bottom of the tube, and along the tube. The results cannot be explained by a conduction controlled rewetting model. Average rewetting velocities decrease with increases in initial wall temperature, and increase with increases in inlet flow rates and subcooling. These trends are consistent with other investigations in vertical reflood. For low inlet flows and low initial wall temperatures rewetting velocities can be higher than the constant inlet liquid flow velocity. This is due to the flow stratification effect that allows the front of the liquid tongue to move with a higher initial velocity than the inlet velocity.

Introduction

Refilling and rewetting is of fundamental importance for the reestablishment of normal and safe temperature levels following dryout in a loss of coolant accident (LOCA) in a water cooled nuclear reactor. In the event of a LOCA, fuel temperature in the reactor core rises rapidly due to poor heat transfer resulting from dryout and due to continuing decay heat generation. To prevent the fuel temperatures from rising too high and possibly damaging or melting the fuel rods, emergency core cooling (ECC) water is injected into the reactor core to arrest the temperature rise and restore a high heat transfer condition by quenching the hot surfaces.

The techniques used for emergency core cooling vary according to reactor designs. For the BWR- and PWR-type reactors with vertical fuel rods clustered in a reactor vessel, top spray cooling and/or bottom reflooding are used. In the CANDU PHR-type reactors, emergency cooling water is injected into individual horizontal fuel channels through the headers. Considerable experimental and theoretical work on top spray cooling and bottom reflooding now exists. However, very little work has been done on horizontal systems. Such experiments are needed so that the form of the conservation equations and constitutive relationships during the emergency core cooling phase of a postulated LOCA can be developed.

This is the first of a series of three papers reporting on a study on refilling and rewetting of a horizontal tube. Experimental facilities and results are discussed in this paper. Theoretical analyses are presented in subsequent papers.

Characteristics of Horizontal Channel Refilling and Rewetting

The actual process of surface rewetting is very complicated. It is still not well understood from a microscopic point of view. Macroscopically, rewetting is the re-establishment of continuous liquid contact with a hot dry surface. It has been found experimentally that rewetting always occurs when the temperature of the hot surface is below a certain value generally known as the rewetting, sputtering or Leidenfrost temperature (see, e.g., Godleski and Bell [1], Gottfried, et al. [2] and Patel and Bell [3]). However, for a hot surface with low thermal capacity, rewetting can also be initiated by the instability of the vapor film separating the hot surface and the liquid. This is discussed in a subsequent paper (Chan and Banerjee [4]).

The most important characteristic of refilling and rewetting of a hot horizontal system as opposed to vertical channels, is the stratified nature of the refilling liquid. Because of transverse gravitational effects, the flow is stratified; thus the channel will be quenched in the sequence bottom, mid-side and top at a given location.

From photographic studies (Chan [5]) and experimental evidence, which will be discussed later, the refilling and rewetting process in a horizontal channel can be visualized as sketched in Fig. 1. Three regions can be identified: the totally quenched, the partially quenched (or quenching) and the film boiling region. The local heat transfer processes are quite different in these regions.

In the totally quenched region (A-A′), the flow is single-phase or boiling liquid. The normal single-phase or two-phase pipe flow equations apply and the heat transfer mechanism will be forced convection and/or boiling heat transfer.

The quench front (Q_T-Q_B) is inclined in the quenching region. The shape of the quench front is determined by complicated local thermohydraulic conditions. The stratified length (which can be defined as the projection of Q_T-Q_B onto the flow direction) changes as the flow develops and the channel fills up. For low inlet flows, the leading edge (Q_B) can be more than 0.5 m ahead of Q_T, the trailing edge. In this region, since the bottom is quenched before the top for a given location, a large circumferential temperature gradient exists. Thus circumferential heat conduction may be important and has to be examined. Violent boiling exists at the quench front as it advances.

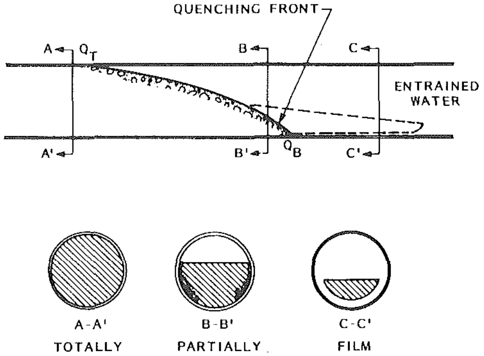

Fig. 1 Characteristics of horizontal channel rewetting

---

[1] Present address: Mechanical Research Department, Ontario Hydro, 800 Kipling Ave., Toronto, Ontario, M8Z 5S4 Canada.

[2] Present address: Department of Chemical and Nuclear Engineering, University of California, Santa Barbara, Calif. 93106.

Contributed by the Heat Transfer Division for publication in the JOURNAL OF HEAT TRANSFER. Manuscript received by the Heat Transfer Division June 12, 1980.

Upstream of the quench front, the local heat transfer mechanism can be nucleate boiling or single-phase forced convection heat transfer depending on whether the wall temperature is above or below the saturation temperature. Downstream of the quench front, the wall loses heat primarily by natural convection and radiation from the outer surface, by forced convection vapor flow inside the channel and by film boiling.

In the film boiling region, the excess water (which is proportional to the difference of flow rate and the rate at which the quench front can propagate) appears as a liquid tongue. This liquid mass is prevented from wetting the wall by a thin film of flowing vapor that supports the liquid. For areas not covered by the liquid tongue, the wall loses heat primarily by natural convection, radiation and vapor flow. Since film boiling is a more effective heat transfer mechanism than natural convection, radiation or forced convection vapor flow, the bottom region of the channel will be precooled significantly before the arrival of the quench front, whereas the top of the channel is affected to a much smaller extent. These pre-quench characteristics will be evident when experimental results are presented later.

Experimental Setup

The test loop for the study of the refilling and rewetting process is shown schematically in Fig. 2. The setup is simple, because the work was done at low pressures.

The test section is direct resistance heated. QAV1 is kept closed and QAV2 kept open, when the test section is being heated up, so that water by-passes the test section via QAV2. When the test section is at the desired temperature, QAV1 is opened and QAV2 closed simultaneously, forcing water into the test section. The steam, or steam-water mixture is discharged into a condenser which is kept at atmospheric pressure.

The test section is a 2-m long Zircaloy-2 tube with an outside diameter of 19.6 mm and a wall thickness of 0.898 mm. Zircaloy was chosen because of its relatively low thermal expansion coefficient. This is important because in horizontal channel rewetting, the bottom of the channel is expected to quench before the top and large circumferential temperature differences occur. With high thermal expansions, this differential quenching may result in high local stresses and damage the test section.

Inlet water was supplied either by a building water line or by a constant-water-level head tank. In the first case, a constant flow boundary condition was closely realized because of the large pressure drop across the regulating valve and negligible pressure build-up in the test section during the transients. Inlet water subcooling could be controlled by adjusting the cold and hot water supplies. We impressed a constant pressure boundary condition in the second case. Building tap water, as well as de-aerated and de-ionized water was used.

The test section was heated directly using a d-c motor generator (ANKER ELECTRIC). The unit is capable of delivering a maximum of 35 KVA d-c power. Its power output can be controlled using a manual variac. At the initiation of the refilling and rewetting transients, the power supply was either switched off or cut off using a circuit breaker. In the first case, the power input drops to zero exponentially and in the latter case, it drops instantaneously to zero.

The test section is instrumented with 38 glass-wrapped gauge 30 (0.254 mm) bare wire chromel-alumel thermocouples. The thermocouples were spot-welded onto the outside surface at twelve locations equally spaced along the test section. Locations of the wall thermocouples are shown in Fig. 3. The circumferential temperature variations were measured at five locations at which temperatures at the top, bottom and mid-sides were obtained.

Other thermohydraulic parameters measured during the transients included: (1) inlet and exit fluid temperatures, (2) inlet and exit differential pressures, (3) inlet water volumetric flow rates, (4) volume averaged void fractions at two locations using gamma densitometers and (5) total power input to the test section. Details are available in Chan [5].

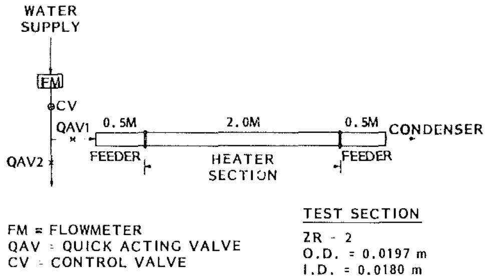

Fig. 2 Schematic diagram of rewetting facility

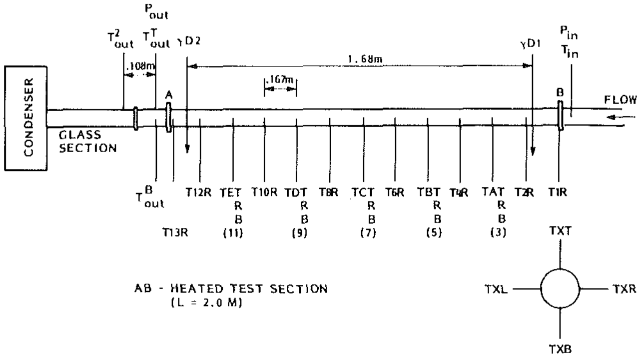

Fig. 3 Locations of transducers

The test section was not insulated in general so that void fraction measurements could be made with gamma densitometers. However, a few experiments were done with glass-wool insulation wrapped around the tube for comparison purposes.

During the transients, since the system parameters changed quite rapidly, an on-line computer was used for data acquisition. The data acquisition system scanned and processed 32 sensor inputs at a rate of 2000 channels per second. Details of the system are described in Chan [5].

Experimental Results and Discussion

A total of 200 runs have been done for different initial and boundary conditions. The runs can be put into six groups. The main parameters varied were the test section initial wall temperature (280–600°C) and the inlet water flow rate (35–110 ml/s). The operating conditions for each group are summarized in Table 1. Some of the more important results will be described below. Detailed results are presented in Chan [5] and data tapes, etc. are available on request.

Quenching Characteristics

The quenching of the channel for a typical experimental run is summarized in Figs. 4 and 5. The results are typical in the sense that the same general behavior is observed for all other experiments. Therefore, some general observations and conclusions can be drawn.

Figure 4 summarizes the quenching of the mid-side of the heated section. The locations of the thermocouples are as shown in Fig. 3. It can be seen that the initial dry wall temperature is almost uniform along the test section (500 ± 20°C). This means that the test section is fairly uniformly heated. T2R has a higher initial temperature because it is located in the collimation zone for the first gamma densi-

Nomenclature

QV = liquid volumetric flow rate
T = temperature
V = rewetting velocity

Subscripts

B = bottom of tube
S = mid-side of tube
T = top of tube
w = channel wall

Table 1 Matrix of experiments

Experimental Group	Inlet Flow Boundary	Power Input	Inlet Water Temperature	Water Supply	Test Section Insulation
I	Constant flow	switched off	8°C	tap water	no
II	Constant flow	switched off	45°C	tap water	no
III	Constant flow	cut off	8°C	tap water	no
IV	Constant pressure	cut off	7°C and 22°C	tap water	no
V	Constant pressure	cut off	22°C	de-aerated and de-ionized water	no
VI	Constant pressure	cut off	22°C	tap water	yes

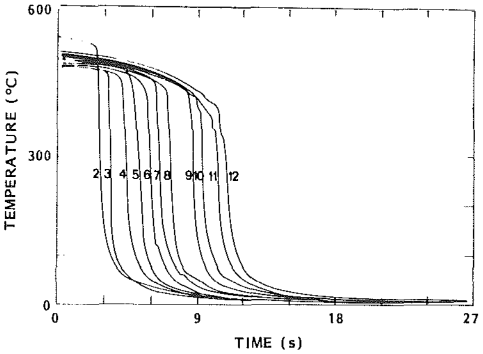

Fig. 4 Transient mid-side wall temperature

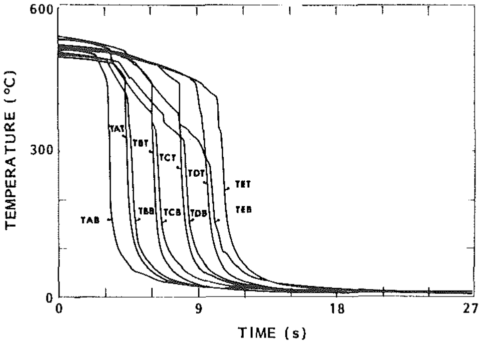

Fig. 5 Transient top and bottom wall temperature

tometer, the collimator cuts down heat losses to the surroundings and thus results in a somewhat higher wall temperature. Because of the residual power input (power is switched off at the start of the transient for Group I experiments resulting in an exponential drop in power input), constant wall temperature is maintained in the first few seconds. The details of the power decay curves for runs in this group are available in Chan [5]. The wall temperature then decreases slowly due to free convection and radiation heat losses until it is quenched. If power was cut off instantaneously at the start of the transient (Group III experiments), the wall temperature would drop steadily from the very beginning until it was quenched because there is no residual power input.

Figure 5 shows the quenching of the bottom (B) and top (T) of the channel. Again the locations of the thermocouples are as shown in Fig. 3. It can be seen that the quench front is highly stratified, the top of the channel at different locations always rewets later than the bottom. The difference in the pre-quench characteristics with regard to the bottom and top of the channel is clearly evident. The bottom region of the channel is precooled significantly before quenching because of stable film boiling. Regions with different heat transfer mechanisms can be easily identified from the different rates of wall temperature drop.

In the figure, it can also be seen that the temperature difference between the top and bottom can be large in the quench region. It can be as much as 400°C for an initial dry wall temperature of 500°C. Because of the large circumferential temperature difference, cooling at the top may occur due to circumferential heat conduction. However, no significant precooling of the top is observed. This is because the circumferential heat conduction process is relatively slow except in the immediate vicinity of the quench front. From analytical solutions (Chan [5]), it was found that it takes more than six seconds to lower the temperature at the top by 20°C by circumferential conduction alone when the lower portion of the channel is quenched to a level of $\frac{1}{4}$ D. Therefore, no significant precooling of the top due to circumferential conduction is observed when the difference in quench time for bottom and top is short. For example, it is less than two seconds in the figure shown.

From Figs. 4 and 5, another important observation can also be made. It can be seen that surface quenching can occur at relatively high wall temperatures (mid-side and top), and the surface temperature at quenching can be very different along the channel at the bottom. This is contrary to the mechanism generally accepted for conduction-controlled models of surface rewetting (Yamanouchi [6] and Duffey and Porthouse [7]). The conduction-controlled model assumes a well-defined surface temperature, the rewetting or Leidenfrost temperature, such that rewetting can occur only when the surface temperature falls below it. This temperature has been postulated to range from 160 to 260°C for water at atmospheric pressure (Godleski and Bell [1], Gottfried, et al. [2], Patel and Bell [3], Berenson [8], Hosler and Westwater [9] and others).

In the present study, no well-defined rewetting temperature was found. This suggests that the conduction-controlled model is not applicable in general to the system under investigation. Instead, the propagation of the quench front appears to be largely controlled by hydrodynamic mechanisms. The initiation of a Kelvin-Helmholtz type of interfacial instability in film boiling is later proposed as the governing mechanism that leads to surface rewetting. This model leads to reasonable predictions of the experimentally-observed rewetting conditions (including temperatures) and, therefore, data on rewetting temperatures is not needed to interpret the experiments. Details are discussed in Chan and Banerjee [4].

Rewetting Velocities

Since the quench front appears to be stratified (Fig. 1) and the stratified length is not constant, the rewetting velocity cannot be uniquely defined. From the experimental results obtained, we defined three rewetting velocities with respect to the quenching of the top, mid-side and bottom of the channel. In general, they are not equal. The rewetting velocities can be obtained locally or averaged over the length of the test section.

Local Rewetting Velocities

The local rewetting velocities are obtained by taking the time difference between the quenching of adjacent thermocouples along the channel. The top, mid-side, and bottom thermocouples are used to obtain the local rewetting velocities at these locations. From Figs. 4 and 5, it can be seen that these quench time differences can vary. That is, the local rewetting velocities can change significantly along the channel. Some typical results are shown in Fig. 6. Plotted in the figure are the ratios of the local and the corresponding average velocities along the channel. The mid-side velocities are shown for various initial wall temperatures. The large variations of the local velocities are apparent from the figure.

In general, the local rewetting velocities tend to be more uniform along the channel for high initial wall temperatures and/or high inlet flows. Since local rewetting velocities are complicated functions of the local flow situation, local heat transfer coefficients and local heater surface conditions, the results are hard to generalize. In order to compare the results when different initial and boundary conditions are used, average rewetting velocities are more useful. By ignoring the local variations and taking the average velocities over the whole test section, most of the experimental data can be summarized by the rewetting velocity versus inlet flow curves. This is discussed below.

Average Rewetting Velocities

Three average rewetting velocities were defined, $\overline{V}_T$, $\overline{V}_S$ and $\overline{V}_B$. They are, in general, not equal, but close to each other. An example is given in Fig. 7. Plotted in the figure are the three average rewetting velocities as a function of inlet flow rates. It can be seen that the average velocities tend to deviate more from each other at high inlet flows. $\overline{V}_B$ and $\overline{V}_S$ are very close to each other in most cases.

Effects of different parameters on the average rewetting velocities will now be discussed. The data will be compared with existing experimental and theoretical results.

Effect of Initial Wall Temperature. The effect of initial wall temperature is clearly illustrated in Fig. 8 which summarizes the Group I experimental results. The average rewetting velocity ($\overline{V}_S$) is plotted as a function of inlet flows for different initial wall temperatures. Results from other experimental groups (II to VI) also exhibit similar trends.

It can be seen that the rewetting velocity decreases as the initial dry wall temperature increases. This is in agreement with all existing investigations, both for vertical channel flooding (Thompson [10], Yamanouchi [6], Bennett, et al. [11] and Groeneveld and Young [12]) and horizontal channel rewetting (Lee, et al. [13]).

If the inverse rewetting velocity is plotted against the initial dry wall temperature, a linear relationship is obtained as shown in Fig. 9. Since such a linear relationship is predicted using a conduction controlled rewetting model, this suggests that this model which is widely used in correlating data in vertical channel rewetting may also have a role in the phenomena observed in horizontal systems. However, it should be noted that the applicability will be very limited because it ignores the thermohydraulic aspects of the problem which are particularly important in horizontal systems. In fact, the limitations of the conduction controlled model are evident when results in Fig. 9 are studied. First of all, the results are strongly dependent on inlet flow rates which is not expected explicitly in the conduction controlled model. Secondly, the rewetting temperature cannot be obtained by extrapolating the $1/\overline{V}$ curve to the X-intercept as suggested by the model. This, together with the fact that no well defined rewetting temperature was found as discussed previously, leads to the conclusion that the conduction controlled rewetting model, when applied to horizontal systems only gives qualitative trends with regard to the wall temperature dependence. Effects of other thermohydraulic parameters cannot be predicted. Hence, a more sophisticated model has to be used (Chan and Banerjee [4, 14]).

Effect of Inlet Flow Rate. For a given initial wall temperature, it can be seen that the rewetting velocity increases as inlet flow increases (Figure 8). This is true for all cases and is in agreement with other experiments (Yamanouchi [6], Shires, et al. [15] and Duffey and Porthouse [7]). In vertical systems, the reasons for the observed effect are not clear. Duffey and Porthouse [7] suggested that the flow rate effect results from increasing the wet side heat transfer coefficient with higher inlet flows. This improves the rate of axial heat conduction and hence leads to a faster rewetting rate. Thompson [16] on the other hand, suggested that the inlet flow rate affects precooling on the dry side rather than the heat transfer in the wet side. In the case of horizontal channels, with the rewetting processes as shown in Fig. 1, it is obvious that an increase in inlet flow rate increases the amount of water entrained in the liquid tongue and hence increases the region of film boiling heat transfer. In other words, precooling also plays a significant role in horizontal systems.

An interesting phenomenon that can be seen in Figure 8 is that under certain conditions the rewetting velocity can actually be higher than the inlet flow velocity. The inlet flow velocity is shown as broken line in the figure. This rather surprising result occurs when both inlet flow rate and initial wall temperature are low. We offer a possible

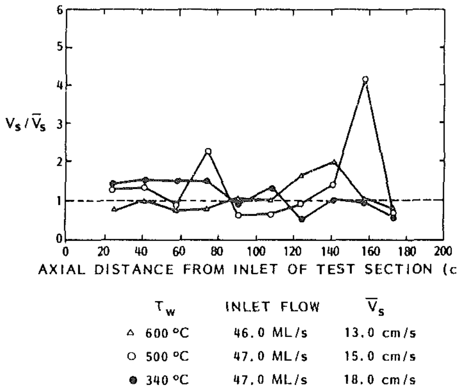

Fig. 6 Local rewetting velocity—mid-side of test section

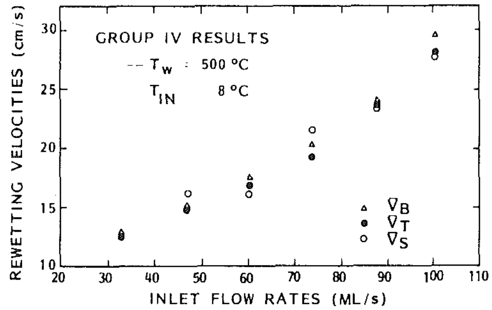

Fig. 7 Average rewetting velocities versus inlet flow rates

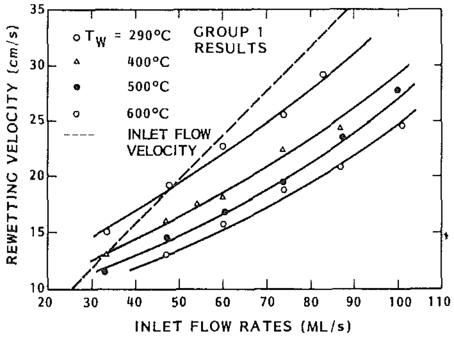

Fig. 8 Average rewetting velocity ($\overline{V}_s$) versus inlet flow rate for different wall temperatures

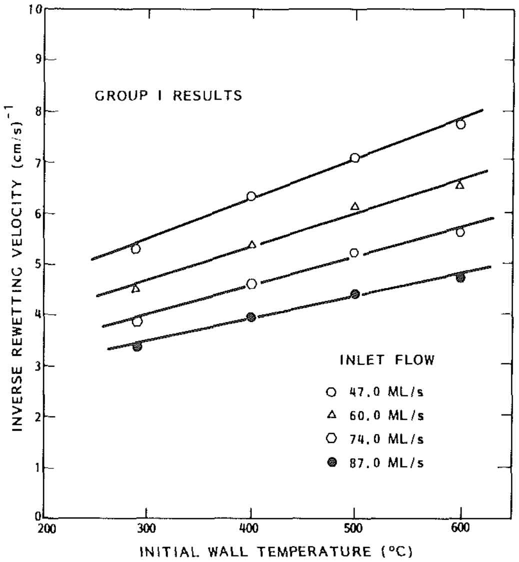

Fig. 9 Inverse rewetting velocity ($1/\overline{V}_s$) versus wall temperature—group I results

explanation. At the start of the transients, water is directed into the heated section with a constant flow rate. Since the channel is dry, the flow is stratified and the leading edge can acquire a velocity considerably higher than the inlet flow velocity. The process is analogous to the dam break problem (Streeter [17]). This problem will not be discussed here. It will suffice to say that the velocity of the leading edge can be much higher than the inlet flow velocity for low inlet flows. This high leading edge velocity, together with low wall temperature can result in rewetting velocities higher than the inlet flow velocity. On the other hand, if the wall temperature is high, the quenching process will be retarded and a "normal" rewetting velocity lower than the inlet flow velocity will be obtained.

Effect of Inlet Water Subcooling. In all the vertical channel experiments, it was observed that the quench rate increases as the inlet water subcooling increases. It was suggested by Piggot and Porthouse [18] that the observed effect results from an increase in heat transfer coefficient with subcooling behind the quench front. Thompson [16] however, argued that the effect is due to an increase in the rewetting temperature with water subcooling at the quench front.

In the present experiment, using horizontal channels, somewhat different effects of inlet water subcooling were found. This is shown in Fig. 10 which compares the rewetting velocities for two different inlet water temperatures (Groups I and II results). It can be seen that the effect of inlet water subcooling is not the same depending on the initial wall temperature. For high wall temperatures ($T_W \gtrsim 400°C$), the rewetting velocities are lower for lower inlet water subcooling. The opposite is true for lower wall temperatures ($T_W < 40°C$). The reasons for this observed effect are not clear. The stratification of the flow and the existence of an unstable stratified interface may be part of the reason.

Effect of Power Input. The effect of the power input during the transients can be obtained by comparing the groups I and III results. As is expected, with residual power input (Group I experiments), the rewetting velocities are lower than without power input during the transient (Group III experiments). The power input appears to retard quench front propagation and thus results in lower rewetting velocities.

Effect of Flow Boundary Conditions. The effect of constant flow and constant pressure boundary conditions can be assessed by comparing the Groups III and IV results. It was found that, in general, the effect is not very strong. The rewetting velocities tend to be slightly higher in the constant flow cases.

Effect of Insulation. When the test section is insulated, heat losses to the surroundings by natural convection and radiation are close to zero. More heat thus has to be removed by the quench front before it can advance. Therefore, a lower rewetting velocity is expected. This is indeed the case as was found by comparing the group VI results with groups IV and I data.

Effect of Inlet Water. Building tap water was used in most of the experiments. Effects of dissolved air and minerals in tap water were investigated by using de-aerated and de-ionized water in some cases (Group V experiments). Results are shown in Fig. 11. No significant difference in the average rewetting velocity was observed.

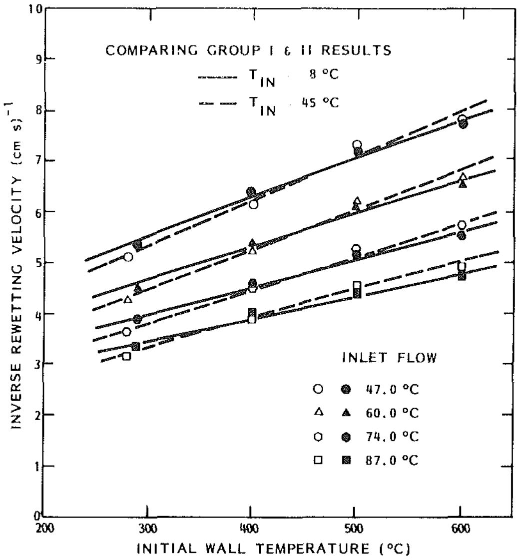

Fig. 10 Inverse rewetting velocity ($1/\bar{V}_s$) versus wall temperature—comparing group I and II results

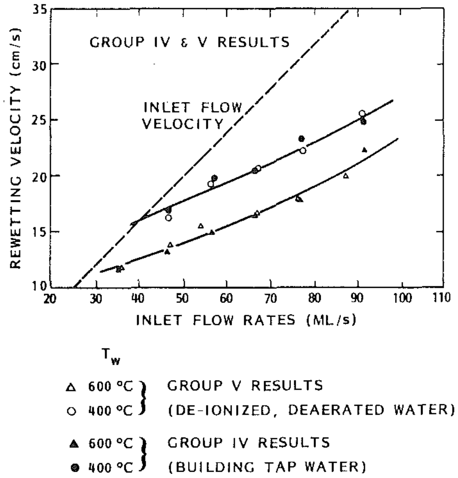

Fig. 11 Average rewetting velocity ($\bar{V}_s$) versus inlet flow rates—groups IV and V results

Table 2 Parametric effects on the average rewetting velocity ($\bar{V}_s$)

Experimental Group	T_w = 600°C		T_w = 400°C	
	QV = 40 ml/s	QV = 90 ml/s	QV = 40 ml/s	QV = 90 ml/s
I	12.0 cm/s	21.5 cm/s	14.2 cm/s	26.0 cm/s
II	11.8	20.8	14.6	26.4
III	12.5	23.8	14.8	28.0
IV	12.6	22.5	16.6	26.5
V	12.6	21.5	16.0	25.1
VI	11.1	19.0	—	—

Conclusions

The refilling and rewetting of a directly heated horizontal channel has been investigated experimentally. Considerable data have been taken for tests under different initial and boundary conditions. The data obtained are of interest in developing models for reactor LOCA analysis. They are of particular interest for heavy water reactors because the system used was horizontal, as in PHR fuel channels.

The experiments were done with well defined initial and boundary conditions. Although they were performed in a simple geometry—a thin walled tube—they contained many of the phenomena important in thermal and hydraulic aspects of the emergency cooling phase of LOCA in heavy water reactors. The experiments thus provide data for benchmark problems against which existing thermalhydraulics codes can be compared and assessed. The data and physical insight gained in doing these experiments are also valuable in testing and further developing thermalhydraulic analysis based on more advanced fluid flow models.

To summarize, some important parametric effects obtained under the experimental program are drawn in Table 2 for average rewetting velocities for each group in Table 1. In addition, the main flow patterns were inferred, at least qualitatively, and this will prove to be of help in analysing the results.

References

1 Godleski, E. S., and Bell, K. J., "The Leidenfrost Phenomenon for Binary Liquid Solution," *Proceedings of 3rd International Heat Transfer Conference*, Chicago, 1966, vol. IV, pp. 51–58.

2 Gottfried, B. S., Lee, C. J., and Bell, K. J., "The Leidenfrost Phenomenon: Film Boiling of Liquid Droplets on a Flat Plate," Paper presented at AIChE National Meeting, Minneapolis, 1965.

3 Patel, B. M., and Bell, K. J., "The Leidenfrost Phenomenon for Extended Liquid Masses," Paper presented at the Eighth National Heat Transfer Conference, Los Angeles, 1965.

4 Chan, A. M. C., and Banerjee, S., "Refilling and Rewetting of a Hot Horizontal Tube—Part III: Application of a Two-Fluid Model to Analyze Rewetting," ASME JOURNAL OF HEAT TRANSFER.

5 Chan, A. M. C., "Transient Two Phase Flows: Refilling and Rewetting of a Hot Horizontal Systems," Ph.D. Thesis, Department of Engineering Physics, McMaster University, 1980.

6 Yamanouchi, A., "Effect of Core Spray Cooling in Transient State After Loss of Coolant Accident," *Journal of Nuclear Science Technology.*, Vol. 5, 1968, pp. 547–558.

7 Duffey, R. B., and Porthouse, D. T. C., "The Physics of Rewetting in Water Reactor Emergency Core Cooling," *Nuclear Engineering and Design*, Vol. 25 (1973), pp. 379–394.

8 Berenson, P. J., "Film Boiling Heat Transfer from a Horizontal Plate," ASME JOURNAL OF HEAT TRANSFER Vol. 83, 1961, pp. 351–358.

9 Hosler, E. R., and Westwater, J. W., "Film Boiling on a Horizontal Plate," *ARS Journal*, Vol. 32, 1962, pp. 553–558.

10 Thompson, T. S., "Simulated Bottom-Flooding Emergency Core Cooling of a Close-spaced Rod Bundle," European Two-Phase Flow Group Meeting, Casaccia, June, 1972.

11 Bennett, A. W., Hewitt, G. F., Kearsey, H. A., and Keeys, R. K. F., "The Wetting of Hot Surfaces by Water in a Steam Environment at High Pressures," UKAEA Report, AERE-5146, 1966.

12 Groeneveld D. C., and Young, J. M., "Film Boiling and Rewetting Heat Transfer During Bottom Flooding of a Hot Tube," Sixth International Heat Transfer Conference, Toronto, 1978, Vol. 5, pp. 89–94.

13 Lee, Y., Chen, W. J., and Groeneveld, D. C., "Rewetting of Very Hot Vertical and Horizontal Channel by Flooding," Sixth International Heat Transfer Conference, Toronto, 1978, Vol. 5, pp. 95–100.

14 Chan, A. M. C., and Banerjee, S., "Refilling and Rewetting of a Hot Horizontal Tube—Part II: Structure of a Two-Fluid Model," ASME JOURNAL OF HEAT TRANSFER.

15 Shires, G. L., Pickering, A. R., and Blacker, P. T., "Film Cooling of Vertical Fuel Rod," UKAEA Report, AEEW-R343 (1964).

16 Thompson, T. S., "Rewetting of a Hot Surface," AECL-5060, 1975.

17 Streeter, V. L., *Fluid Mechanics*, 2nd Edition, McGraw Hill, 1958, pp. 408–409.

18 Piggott, B. D. G., and Porthouse, D. T. C., "Water Reactor Emergency Core Cooling: The Effect of Pressure, Subcooling and Surface Condition of the Rewetting of Hot Surfaces," CEGB Report RD/B/N2692, June, 1973.

A. M. C. Chan
S. Banerjee[2]
Mem. ASME

Department of Engineering Physics
McMaster University
Hamilton, Ontario L8S 4M1

Refilling and Rewetting of a Hot Horizontal Tube

Part II: Structure of a Two-Fluid Model

This is the second paper in a series of three papers reporting on a study on refilling and rewetting of horizontal tubes. The experimental work has been reported in a previous paper (Chan and Banerjee [1]). This paper concentrates on development of a mathematical model for analysis of the main thermal-hydraulic processes. The resulting set of equations are solved numerically. An explicit finite difference characteristics technique is used to solve the hydraulic equations. To assess the model and the accuracy of the numerical technique used, a relatively simple problem, refilling of a dry horizontal tube with no heat transfer, is investigated. Experimental and calculated results are compared. This problem highlights the hydraulic aspects of the more complicated refilling and rewetting problem which is analyzed in a subsequent paper (Chan and Banerjee [2]).

Introduction

From a macroscopic point of view, there are basically two possible mechanisms involved in the rewetting processes. The first mechanism is the conduction controlled advance of the quench front. The second mechanism involves the thermalhydraulic aspects of the processes which can also determine quench front propagation. For vertical systems, the first mechanism may dominate. Thus the conduction controlled rewetting model has been used with some success in correlating experimental data and predicting parametric trends (Yu et al. [3]). However, percursor cooling effects can be important and for horizontal channels, the hydraulic aspects of the processes are also very important, especially the gravitational effects leading to flow stratification. It has been found that the conduction controlled model does not appear to explain the experimental results for horizontal systems (Chan and Banerjee [1]). Therefore, a two-fluid model approach has been adopted here. A simplified two-fluid model has been developed with most of the important thermalhydraulic aspects incorporated into the model. The wall effects and transient wall temperature distribution appear as boundary conditions and through the use of appropriate heat transfer coefficients. The formulation of the model and comparison of its hydraulic aspects with experiments, i.e. performance in the absence of heat transfer, will be presented in this paper.

Mathematical Formulation

A considerable literature exists on two-fluid models and we will not review it here, but start with the general one-dimensional two-fluid model (Chan [4]), and obtain a simplified version by making certain assumptions. The assumptions must, of course, be consistent with the physical process under investigation. The set of generalized space/time averaged conservation equations is reproduced from Agee et al. [5].

Mass Conservation

$$\frac{\partial}{\partial t}\alpha_k\langle\rho_k\rangle+\frac{\partial}{\partial z}\alpha_k\langle\rho_k U_k\rangle=-\langle\dot{m}_k\rangle_i \tag{1}$$

Momentum Conservation

$$\frac{\partial}{\partial t}\alpha_k\langle\rho_k U_k\rangle+\frac{\partial}{\partial z}\alpha_k\langle\rho_k U_k{}^2\rangle+\alpha_k\frac{\partial\langle P_k\rangle}{\partial z}-\frac{\partial}{\partial z}\alpha_k\langle\tau_{zz,k}\rangle$$
$$-\Delta P_{ki}\frac{\partial\alpha_k}{\partial z}=\alpha_k\langle\rho_k F_{z,\,k}\rangle-\langle\dot{m}_k U_k\rangle_i-\langle\Delta P'_{ki}\rangle\, i$$
$$+\langle\hat{\mathbf{n}}_k\cdot\bar{\tau}_z\rangle_i+\langle\hat{\mathbf{n}}_{kw}\cdot\bar{\tau}_z\rangle_w \tag{2}$$

Energy Conservation

$$\frac{\partial}{\partial t}\alpha_k\left\langle\rho_k\left(h_k+\frac{U_k{}^2}{2}\right)\right\rangle+\frac{\partial}{\partial z}\alpha_k\left\langle\rho_k U_k\left(h_k+\frac{U_k{}^2}{2}\right)\right\rangle$$
$$-\alpha_k\frac{\partial\langle P_k\rangle}{\partial t}+\Delta P_{ki}\frac{\partial\alpha_k}{\partial t}+\frac{\partial}{\partial z}\alpha_k\langle q_{z,k}\rangle$$
$$-\frac{\partial}{\partial z}\alpha_k\langle\hat{\mathbf{n}}_z\cdot(\bar{\tau}_k\cdot\bar{v}_k)\rangle$$
$$=-\left\langle\dot{m}_k\left(h_k+\frac{U_k{}^2}{2}\right)+\hat{\mathbf{n}}_k\cdot\bar{v}_i\Delta P'_{ki}+\hat{\mathbf{n}}_k\cdot\bar{q}_k-\hat{\mathbf{n}}_k\cdot\bar{v}_k\cdot\bar{\bar{\tau}}_k\right\rangle i$$
$$-\langle\hat{\mathbf{n}}_{kw}\cdot\bar{q}_k\rangle_w+\alpha_k\langle\rho_k\bar{\mathbf{v}}_k\cdot\bar{F}_k+Q_k\rangle \tag{3}$$

The equations can be simplified if we assume constant liquid and vapor densities, and can be written as shown in the next section. It should be noted that the constant vapor density assumption implies that the vapor is treated as essentially incompressible. This is valid only when the vapor velocity is much less than the sonic velocity.

Conservation Equations

The equations are first presented for the liquid phase and then for the gas or vapor phase.

Liquid Phase:

$$\rho_L\frac{\partial\alpha_L}{\partial t}+\rho_L\frac{\partial}{\partial z}(\alpha_L U_L)=-\dot{m}_L \tag{4}$$

$$\rho_L\frac{\partial}{\partial t}(\alpha_L U_L)+\rho_L\frac{\partial}{\partial z}(\alpha_L U_L{}^2)=-\tau_L a_L+\tau_i a_i$$
$$-\alpha_L\frac{\partial P_L}{\partial z}+\Delta P_{Li}\frac{\partial\alpha_L}{\partial z}-\dot{m}_L u_i \tag{5}$$

where the variables are as defined in Fig. 1 for a horizontal circular channel and $\Delta P_{Li}=P_L-P_i$.

In equation (5), the fluctuating part of the pressure term, $\langle\Delta P'_{ki}\rangle_i$ is assumed to be zero. This is true only for stratified flow with no waves. The space/time averaging symbols for the dependent variables are omitted in the equations for simplicity. However, they should be understood to be space and time or ensemble averaged.

Since α_L and ΔP_{Li} are functions of h_L, the liquid level, we can write

$$\partial\alpha_L=\alpha_L'\partial h_L \tag{6}$$

and

$$\partial\Delta P_{Li}=(\Delta P_{Li})'\partial h_L \tag{7}$$

Expressions for α_L, ΔP_{Li} and their derivatives for a circular channel with given h_L are complicated and given in Chan [4].

With equations (6) and (7), equations (4) and (5) can be expressed

---

[1] Present address: Mechanical Research Department, Ontario Hydro, 800 Kipling Avenue, Toronto, Ontario M8Z 5S4 Canada

[2] Present Address—Department of Chemical and Nuclear Engineering, University of California, Santa Barbara, Calif. 93106

Contributed by the Heat Transfer Division for publication in THE JOURNAL OF HEAT TRANSFER. Manuscript received by the Heat Transfer Division June 12, 1980.

in terms of h_L as

$$\frac{\partial h_L}{\partial t} + U_L \frac{\partial h_L}{\partial z} + \frac{\alpha_L}{\alpha_L{}'} \frac{\partial U_L}{\partial z} = -\frac{\dot{m}_L}{\rho_L \alpha_L{}'} = E_1 \quad (8)$$

and

$$\frac{\partial U_L}{\partial t} + U_L \frac{\partial U_L}{\partial z} + \frac{1}{\rho_L \alpha_L} [\alpha_L (\Delta P_{Li})' + \Delta P_{Li} \alpha_L{}'] \frac{\partial h_L}{\partial z}$$
$$= -\frac{\tau_L a_L}{\rho_L \alpha_L} + \frac{\tau_i a_i}{\rho_L \alpha_L} - \frac{1}{\rho_L} \frac{\partial P_i}{\partial z} + \frac{\dot{m}_L}{\rho_L \alpha_L} (U_L - U_i) \quad (9)$$

Vapor Phase:

$$\rho_G \frac{\partial \alpha_G}{\partial t} + \rho_G \frac{\partial}{\partial z} (\alpha_G U_G) = \dot{m}_L \quad (10)$$

$$\rho_G \frac{\partial}{\partial t} (\alpha_G U_G) + \rho_G \frac{\partial}{\partial z} (\alpha_G U_G{}^2) = -\tau_G a_G - \tau_i a_i$$
$$- \alpha_G \frac{\partial P_G}{\partial z} + \Delta P_{Gi} \frac{\partial \alpha_G}{\partial z} + \dot{m}_L U_i \quad (11)$$

Where $\Delta P_{Gi} = P_G - P_i$

Assuming $P_G = P_i$, that is the vapor phase density contributes negligibly to gravity head terms, equation (11) can be reduced to

$$- \alpha_G \frac{\partial P_i}{\partial z} = \rho_G \alpha_G \left[\frac{\partial U_G}{\partial t} + U_G \frac{\partial U_G}{\partial z}\right] + \tau_G a_G$$
$$+ \tau_i a_i + \dot{m}_L (U_G - U_i) \quad (12)$$

Where equation (10) has been used in obtaining equation (12).

It should be noted that the energy equations have been left out in both phases. This is to decouple them from the mass and momentum equations in our numerical solutions. The energy equation can be solved afterwards. This procedure is acceptable if the kinetic energy terms are small in the energy equations.

Substituting equation (12) into (9), we obtain

$$\frac{\partial U_L}{\partial t} + U_L \frac{\partial U_L}{\partial z} + \frac{1}{\rho_L \alpha_L} [\alpha_L (\Delta P_{Li})' + \Delta P_{Li} \alpha_L{}'] \frac{\partial h_L}{\partial z}$$
$$= -\frac{\tau_L a_L}{\rho_L \alpha_L} + \frac{\tau_i a_i}{\rho_L} \left[\frac{1}{\alpha_L} + \frac{1}{\alpha_G}\right] + \frac{\dot{m}_L}{\rho_L} \left[\frac{U_L - U_i}{\alpha_L} + \frac{U_G - U_i}{\alpha_G}\right]$$
$$+ \frac{\rho_G}{\rho_L} \left[\frac{\partial U_G}{\partial t} + U_G \frac{\partial U_G}{\partial z}\right] + \frac{\tau_G a_G}{\rho_L \alpha_G} = E_2 \quad (13)$$

Since $\alpha_G = (1 - \alpha_L)$, therefore, if $\dot{m}_L$ is known, equations (8), (10) and (13) can be used to obtain U_L and h_L values along the channel. These values are directly comparable to the experimental data. Hence, the validity of the model or individual assumptions can be checked in a straightforward manner.

To solve the set of equations (18), (10), and (13), however, can be complicated. The equations can be greatly simplified if we make a physically realistic assumption: that the time derivative in equation (10) is small compared to the other terms in the equation. This is true for "slow" transients when the water level at a given location does not change rapidly. For the case of refilling and rewetting of hot horizontal channels, this assumption can be shown to hold well in general. The $\partial U_G / \partial t$ term on the right hand side of equation (13) can likewise be ignored.

With the above assumption, equation (10) can be integrated to give U_G. Knowing U_G, equations (8) and (13) can then be solved for U_L and h_L. The equations can be written as

$$\frac{\partial h_L}{\partial t} + U_L \frac{\partial h_L}{\partial z} + A \frac{\partial U_L}{\partial z} = E_1 \quad (14)$$

and

$$\frac{\partial U_L}{\partial t} + U_L \frac{\partial U_L}{\partial z} + B \frac{\partial h_L}{\partial z} = E_2 \quad (15)$$

Where

$$A = \alpha_L / \alpha_L{}' = y_h$$

$$B = \frac{1}{\rho_L \alpha_L} \left[\Delta P_{Li} \frac{\partial \alpha_L}{\partial h_L} + \alpha_L \frac{\partial \Delta P_{Li}}{\partial h_L}\right] = g$$

It is interesting to note that B can be simplified and reduces to the gravitational constant g for both rectangular and circular ducts. A is the ratio of flow area and free surface width. It is commonly defined as the hydraulic depth (y_h) in open channel flows (Sissom and Pitts [16]). E_1 and E_2 are defined as the right-hand side of equations (8) and (13), respectively.

Equations (14) and (15) can be reduced to the following form (Street [7] and Courant and Friedrichs [8]),

$$\frac{\partial \tilde{U}}{\partial t} + \tilde{A} \frac{\partial \tilde{U}}{\partial z} = \tilde{E} \quad (16)$$

with

$$\tilde{U} = \begin{bmatrix} h_L \\ U_L \end{bmatrix}; \tilde{A} = \begin{bmatrix} U_L & y_h \\ g & U_L \end{bmatrix}; \tilde{E} = \begin{bmatrix} E_1 \\ E_2 \end{bmatrix}$$

The characteristic directions are given by

$$\frac{dz}{dt} = U_L \pm \sqrt{g y_h} \quad (17)$$

They are the slopes of the forward and backward characteristics in the z-t plane respectively.

The characteristic equations are obtained by multiplying equation (14) by $\sqrt{g/y_h}$ and adding and subtracting the resulting equation from equation (15),

$$\left[\frac{\partial U_L}{\partial t} + (U_L + c) \frac{\partial U_L}{\partial z}\right] + \left[\frac{\partial \omega}{\partial t} + (U_L + c) \frac{\partial \omega}{\partial z}\right]$$
$$= E_2 + \sqrt{g/y_h}\, E_1 \quad (18)$$

and

$$\left[\frac{\partial U_L}{\partial t} + (U_L - c) \frac{\partial U_L}{\partial z}\right] - \left[\frac{\partial \omega}{\partial t} + (U_L - c) \frac{\partial \omega}{\partial z}\right]$$

Nomenclature

a = interfacial area
A = area
c = gravity wave velocity
C_p = heat capacity
D = diameter of tube
F = external forces
g = gravitational acceleration
h = enthalpy, heat transfer coefficient
h_L = liquid level
k = thermal conductivity
$\dot{m}$ = rate of interfacial mass transfer
M = total mass of liquid inflow
$\hat{\mathbf{n}}$ = normal unit vector
P = pressure
q = surface flux
Q = source term
AV = liquid volumetric flow rate
r = radial direction
t = time
T = temperature
U = velocity
$\bar{\mathbf{v}}$ = velocity vector
V = volume, flow velocity, rewetting velocity
y_h = hydraulic depth
z = axial direction
α = void fraction, thermal diffusivity
β = fraction of energy input used for evaporation
ΔM = mass difference
Δt = time step size
Δz = mesh size
θ = angular position
ρ = density
τ = shear stress
ω = Escoffier stage variable

Subscripts

F = fluid
G = vapor phase
i = interface
k = phase k
L = liquid phase
z = axial direction
w = channel wall

$$= E_2 - \sqrt{g/y_h}\, E_1 \quad (19)$$

where the equations have been further simplified by introducing the Escoffier stage variable, ω, defined as (Henderson [9])

$$\omega = \int_{h_L{}^0}^{h_L} \sqrt{g/y_h}\, dh_L \quad (20)$$

where $h_L{}^0 = 0$ for rectangular channels. However, for circular ducts, $y_h \rightarrow 0$ as $h_L \rightarrow 0$; therefore, a small but nonzero $h_L{}^0$ value should be used to prevent the integrand from going to infinity in numerical calculations. This is done for mathematical convenience and will not affect the calculated results.

In the above equations, c is the gravity wave velocity and is defined by

$$c = \sqrt{g y_h} \quad (21)$$

in open channel flow. This is the velocity with which a disturbance will move over the water surface.

It should be noted that y_h, and consequently c goes to infinity when the duct is completely filled (i.e. $h_L = D$ for a circular duct). The equations are thus no longer applicable in this situation. Instead, the single phase flow equations are used.

Thermal Equations

In order to solve the hydraulic equations (equations (18) and (19)), E_1 and E_2 which involve the interfacial mass and momentum transfer, vapor inertia as well as phase to wall viscous terms have to be known explicitly. This, in turn, requires that the channel wall and fluid temperature be known.

The channel wall temperature (T_w) can be obtained using the three-dimensional transient heat conduction equation in cylindrical coordinates (Eckert and Drake [10])

$$\frac{1}{\alpha_w}\frac{\partial T_w}{\partial t} = \frac{1}{r}\frac{\partial}{\partial r}\left(r\frac{\partial T_w}{\partial r}\right) + \frac{1}{r^2}\frac{\partial^2 T_w}{\partial \theta^2} + \frac{\partial^2 T_w}{\partial z^2} + \frac{Q'}{k_w} \quad (22)$$

with the convective thermal boundary condition at the inner surface,

$$k_w \frac{\partial T_w}{\partial r}\bigg|_{r_i} = \bar{h}(T_w - T_F) \quad (23)$$

where $\bar{h}$ is an appropriate effective heat transfer coefficient that is a function of T_W, θ, and z. T_F is the temperature of the fluid in contact with the surface. The contacting fluid can be liquid, vapor, or air. The thermal boundary condition at the outer surface can be adiabatic or convective depending on whether the test section is insulated or not.

The bulk liquid temperature (T_L) is given by the one-dimensional space/time averaged energy equation shown in equation (3). This equation can be simplified to

$$\frac{\partial}{\partial t}(\alpha_L T_L) + \frac{\partial}{\partial z}(\alpha_L U_L T_L) = \left(\frac{1}{\rho C_p}\right)_L \left[k_L \frac{\partial}{\partial z}\left(\alpha_L \frac{\partial T_L}{\partial z}\right) + (1-\beta)q'''\right] \quad (24)$$

where q''' is the heat flux per unit volume and is given by

$$q''' = \frac{1}{V}\int_0^{2\pi} \bar{h}(\theta, z)A(\theta)(T_W(\theta, z) - T_F(\theta, z))d\theta \quad (25)$$

q''' depends on the mode of heat transfer, e.g. for a refilling and rewetting problem it may assume different values for precursor cooling and/or film boiling in the dry wall region, and for nucleate boiling and liquid forced convection in the rewet region. As shown in Part III, transition between the rewet and dry regions can be related to the liquid depth in the tube, h_L, which is one of the variables calculated from the set of conservation equations.

(1-β) is the fraction of energy input that goes into heating the liquid phase. The vapor temperature (T_G) is taken to be the saturation temperature. That is, no vapor superheating is assumed.

It should be noted that the thermal equations (equations (22) and (24)) are coupled to the hydraulic equations (equations (18) and (19)). In principle, the two sets of equations have to be solved simultaneously. However, in order to simplify the problem and to reduce the complexity of the solution scheme, the two sets of equations can be solved numerically assuming explicit coupling, i.e. one set of equations (hydraulic or thermal) is solved first using previous time-step values for the coupling terms. The coupling terms that appear in the other set are then evaluated from these solutions. Solutions to the second set of equations are then obtained. The procedure is then repeated for another time step. A time lag is therefore introduced but may not be significant if the time steps are small. For larger time steps, iterations are required.

Refilling With no Heat Transfer

Before applying the two-fluid model approach to the rather complicated refilling and rewetting situation, the model was used to consider a relatively simple problem: the refilling of a dry horizontal channel with no heat transfer. This case highlights the hydraulic aspects of the problem. We will also take this opportunity to describe the numerical technique.

In this simple case, we do not have to consider the thermal equations, the vapor phase and mass and momentum transfer terms are also insignificant so the set of hydraulic equations (equations (18) and (19)) need to be solved. E_1 and E_2 in the equations reduce respectively to zero and—$\tau_L a_L/\rho_L \alpha_L$.

Numerical Solution—The Method of Characteristics

The hydraulic equations are solved numerically using an explicit finite difference characteristics method. The method of characteristics (Abbot [11]) is chosen because it has low numerical diffusion. An explicit scheme is used because it is easier to program and because implicit schemes present difficulties in calculating supercritical flow, so that when U_L becomes greater than c during computations, the results may be unstable (Liggett and Cunge [12]). The other reason for choosing an explicit scheme is because pressure waves are not considered in the present situation, i.e. the time-step size is not limited by the very high sonic speed. Therefore, there is no real advantage in having an implicit scheme.

The time-step size will, of course, be still limited by the gravity wave speed,

$$\Delta t \leq \min\left\{\frac{\Delta z}{|u_L + c|}, \frac{\Delta z}{|u_L - c|}\right\} \quad (26)$$

which is the Courant consideration as given by Isaacson and Keller [13] and Δz is the mesh size.

Since c can be large in closed conduit flows, small time steps may have to be used when the conduit is nearly full. Typical time-step sizes used in the present case is about 0.05. This value is acceptable because the experiments last less than 20 s in general.

The method characteristics is a semigraphical method. Its basic principle is to fill the (z, t)-plane with characteristics so that the dependent variables are defined at the intersections. The method is accurate but formulation and programming can be difficult and tedious. Simpler methods have thus been developed, notably the Hartree method (Fox [14]) and the method used by Stoker [15]. Stoker's method is particularly simple, the characteristic equations are solved explicitly using a fixed grid. The explicit finite difference characteristic method used here is based on the Stoker's method, though some modifications have been made. The formulation is extended to include supercritical flows and other changes made as described later.

The fixed finite differences grid used in the computation is shown in Fig. 2. The time-step size, Δt, must be chosen small enough in relation to Δz (equation (26)) so that the points such as P will fall within the appropriate domains of determinacy relative to the points used (L, M, R) in calculating the solution at P (Stoker [15]). The domain of determinacy is the region included within the forward characteristic from L and the backward characteristics from R. That is, points outside the range L-R (the domain of dependency of P) will have no influence on the solution at P.

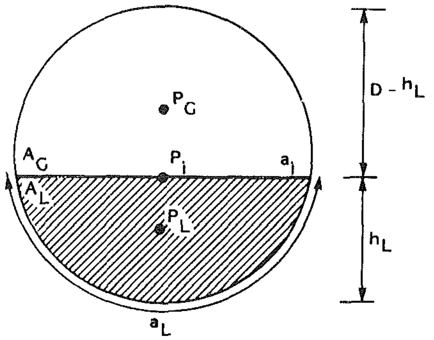

Fig. 1 **Definition of variables in the simplified two fluid model formulation**

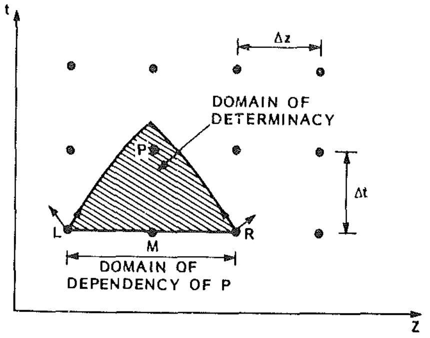

Fig. 2 **Finite difference grid used**

With the dependent variables known at points L, M, and R, values at points P can be calculated by replacing the time and space derivatives in equations (18) and (19) by the following difference quotients

$$\frac{\partial U}{\partial t} = \frac{U_p - U_M}{\Delta t}; \frac{\partial \omega}{\partial t} = \frac{\omega_P - \omega_M}{\Delta t} \tag{27}$$

$$\frac{\partial U}{\partial z} = \frac{U_M - U_L}{\partial z}; \frac{\partial \omega}{\partial z} = \frac{\omega_M - \omega_L}{\Delta z} \tag{28}$$

in equation (18) and

$$\frac{\partial U}{\partial z} = \frac{U_R - U_M}{\Delta z}; \frac{\partial \omega}{\partial z} = \frac{\omega_R - \omega_M}{\partial z} \tag{29}$$

in equation (19). The reason for using different difference quotients for equations (18) and (19) is because (18) is associated with the forward characteristics whereas (19) with the backward characteristic. The coefficients of the derivatives, $(u \pm c)$ and the function E are evaluated at the point M by Stoker. However, it was found that very poor mass conservation results. In the present numerical scheme, $(u_L \pm c)$ are evaluated at the points where the characteristics originate, i.e. an upwind characteristic finite difference scheme. For example, $(U + c)_L$ is used in equation (18) and $(U - c)_R$ in equation (19) for subcritical flows. E is always evaluated at point M. With this modification, mass can be conserved to within 3 percent using 30 nodes. The convergence of the numerical scheme will be discussed later.

Substituting equations (27) to (29) into (18) and (19), and solving for U_p and ω_p, we have for subcritical flows, i.e. $(U + c)_L > 0$ and $(U - c)_R < 0$

$$\omega_p = -\frac{\Delta t}{\Delta z}[(U + c)_L(U_M - U_L) - (U - c)_R(U_R - U_M) + (U + c)_L(\omega_M - \omega_L) + (U - c)_R(\omega_R - \omega_M)] + \omega_M \tag{30}$$

and

$$U_p = -\frac{\Delta t}{\Delta z}[-E_M \Delta z + (U + c)_L(\omega_M - \omega_L) - (U - c)_R(\omega_R - \omega_M) + (U + c)_L(U_M - U_L) + (U - c)_R(U_R - U_M)] + U_M \tag{31}$$

For supercritical flows, i.e. $(U - c_R) > 0$, no backward characteristic exists at point R, the other characteristic will have to come from M or M'. Two cases have to be distinguished as shown in Fig. 3.

(*a*) If flow at M is subcritical, i.e. $(U - c)_M < 0$, a point $M'(z_M < z_{M'} < z_R)$ will be chosen such that $(U - c)_{M'} < 0$ constitutes the backward characteristic and P is included in the domain of determinacy defined by the range $L - M'$. The dependent variables at M' can be obtained by interpolation between M and R. We define

$$D\omega = (U - c)_{M'}(\omega_R - \omega_{M'})$$

$$DU = (U - c)_{M'}(U_R - U_{M'}) \tag{32}$$

(*b*) If flow at M is supercritical, $(U - c)_M > 0$ constitutes the other characteristic and we define

$$D\omega = (U - c)_M(\omega_M - \omega_L)$$

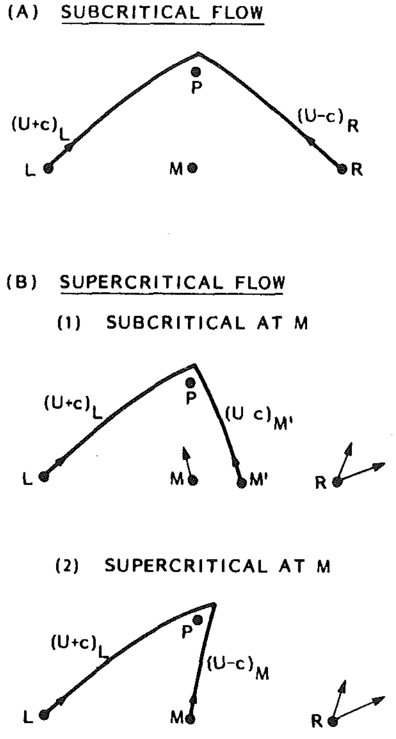

Fig. 3 **Forward and backward characteristics**

$$DU = (U - c)_M(U_M - U_L) \tag{33}$$

ω_p and U_p will then be given by

$$\omega_p = -\frac{\Delta t}{z}[(U + c)_L(U_M - U_L) - DU + (U + c)_L(\omega_M - \omega_L) + D\omega] + \omega_M \tag{34}$$

$$U_P = -\frac{\Delta t}{\Delta z}[-E_M \Delta x + (U + c)_L(\omega_M - \omega_L) - D\omega + (U + c)_L(U_M - U_L) + DU] + U_M \tag{35}$$

It should be noted that the technique is approximately first order accurate (Liggett and Cunge [12]), and care must be taken to ensure that P always lies within the domain of determinacy for a given range L-R so that the convergence condition is satisfied.

In general, the technique works as follows. Starting at $t = 0$ with the dependent variables U, ω, and c defined at all the grid points, U and ω at the next time step can be calculated using equations (20) and (31) or equations (34) and (35). The c values at each grid point are then obtained using the equation $c = \sqrt{gy_h}$ where y_h is related to ω through equation (20). The new U, ω, and c values are then used as starting values for the next time step computation.

The treatment of boundary conditions will now be described (see also Liggett and Cunge [12]). The number of conditions specified on a boundary must equal the number of characteristics originating at that boundary. Some possible situations are shown in Fig. 4. In cases (*a*) and (*b*), one boundary condition is required. At the upstream boundary (case (*a*)), the condition is used with the equation along the backward characteristic (R-Q) to obtain the other dependent variable at Q. At the downstream boundary, (case (*b*)), it is used with the equation along the forward characteristic (L-Q). In case (*c*), both dependent variables must be specified at the boundary and in case (*d*), no boundary condition is needed. The dependent variables at Q' for case (*d*) are given by equations (33), (34), and (35). That is, Q' can be treated as an interior point. The dependent variables at the boundary can be obtained by interpolating between L-Q'. In case (*a*), the equation along the backward characteristic is used (equation (13)), that is

$$\left[\frac{U_Q - U_M}{\Delta t} + (U - c)_R \frac{U_R - U_M}{\Delta z}\right] - \left[\frac{\omega_Q - \omega_M}{\Delta t} + (U - c)_R \frac{\omega_R - \omega_M}{\Delta z}\right] = E_M \quad (36)$$

If ω_Q is specified, U_Q will be given by

$$U_Q = \Delta t \left[E_M + \frac{\omega_Q - \omega_M}{\Delta t} + (U - c)_R \frac{\omega_R - \omega_M}{\Delta z} - (U - c)_R \frac{U_R - U_M}{\Delta x}\right] + U_m \quad (37)$$

Likewise, if U_Q is given as the boundary condition, ω_Q can be obtained from equation (36). Other boundary conditions can also be applied, for example, given inlet flow rates.

In case (*b*), the equation along the forward characteristic will be used (equation (18)),

$$\left[\frac{U_Q - U_M}{\Delta t} + (U + c)_L \frac{U_M - U_L}{\Delta z}\right] + \left[\frac{\omega_Q - \omega_M}{\Delta t} + (U + c)_L \frac{\omega_M - \omega_L}{\Delta z}\right] = E_M \quad (38)$$

Again, ω_Q (or U_Q) can be obtained if U_Q (or ω_Q) is given as a boundary condition.

A computer code called WAVEST has been developed. It solves the relatively simple problem of refilling with no heat transfer using the explicit finite difference characteristic method described above. Frictional relationships for developing open channel flow are needed to close the mathematical problem, and are discussed in Chan [4]. The results are relatively insensitive to the friction factors so they are not discussed here, but to some extent in Part III. Numerical and experimental results are compared later. First we will briefly describe the experimental procedure.

Experimental Setup

A simple experiment has been done to study the refilling characteristics of a dry horizontal duct with no heat transfer. The setup is shown schematically in Fig. 5. A glass tube was used so that the movement of the refilling front could be observed visually. The water injection system is the same as in the refilling and rewetting experiments (Chan and Banerjee [1]). QAV1 is closed and QAV2 opened when the tube is blown dry by compressed air. To initiate the experiment, QAV1 is opened and QAV2 closed at the same time, injecting water into the channel. The velocities of the leading and trailing edges of the refilling front were measured during refilling for different inlet flows.

Results and Discussion

The velocities of the leading and trailing edges along the tube are shown in Figs. 6 to 8 for different inlet flow rates. The numerical results obtained using the computer code WAVEST are also shown. It can be seen that the results compare very well. The leading edge has a high initial velocity and approaches the steady inlet flow velocity as the front moves downstream. The trailing edge velocity is close to the inlet flow velocity at all times.

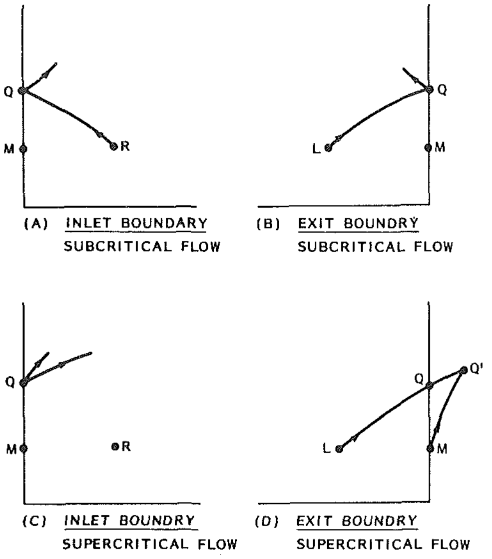

Fig. 4 Possible boundary conditions

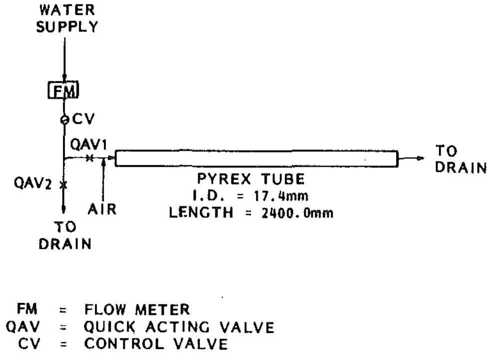

Fig. 5 Schematic of refilling setup with no heat transfer

Convergence of the numerical results have been tested with respect to mesh and time step sizes. The results for spatial convergence tests are shown in Table 1. Thirty, 60, and 100 nodes were used. ΔM is the difference of the liquid inventory in the system and the total mass of liquid inflow from the inlet. M is the total mass of liquid inflow, $\Delta M/M$ is a measure of mass conservation. It can be seen that, in general, the numerical scheme conserves mass reasonably well for all cases. Also, the average refilling velocity does not change significantly for the mesh sizes used. Therefore, we may conclude that the numerical results are converged if the number of nodes used are 30 or more. The time-step size used is determined by equation (26). However, reducing Δt to half of that given by equation (26) does not affect the refilling results.

The propagation and shape of the refilling front are obtained numerically. An example is shown in Fig. 9. Plotted in the figure is the level of refilling water along the channel at different times. The shape of the refilling front is in agreement with visual observation and is similar to the water wave profile following a dam-break as reported by Dressler [16]. It can be seen that the flow is highly stratified and because the movement of the leading edge is impeded by the viscous forces, a steep front results. It is also evident that before steady state is achieved, the leading edge moves much faster than the trailing edge and the stratified length (which may be defined as the projection of the refilling front onto the flow direction) increases as the front travels downstream.

Conclusion

A mathematical model has been developed to analyze the refilling and rewetting processes in a hot horizontal tube. The model was derived from the generalized one-dimensional two-fluid model. ΔP_{Li}

which is a function of liquid level is retained in the simplified model. It incorporates the necessary gravitational force effects that are responsible for flow stratification in horizontal channels. The resulting governing equations are the hydraulic equations for the liquid phase, and the thermal equations for the liquid phase and the channel wall. The vapor phase is assumed to be at saturation temperature.

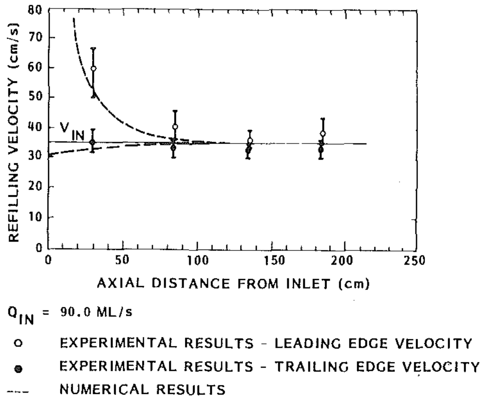

Fig. 6 Refilling velocities—*Q*in = 90.0 ml/s

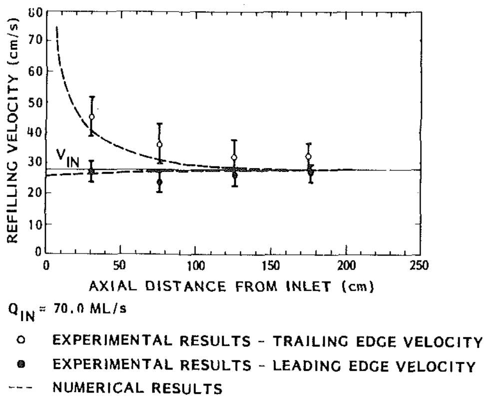

Fig. 7 Refilling velocities—*Q*in = 70.0 ml/s

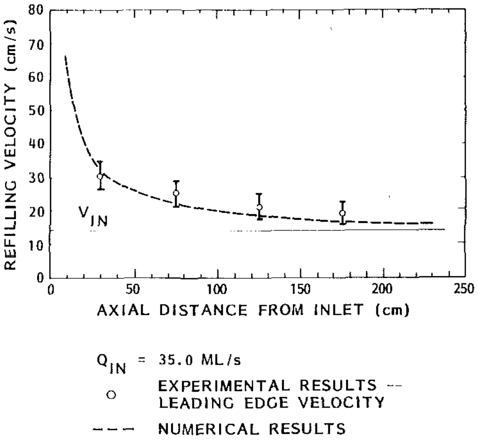

Fig. 8 Refilling velocities—*Q*in = 35.0 ml/s

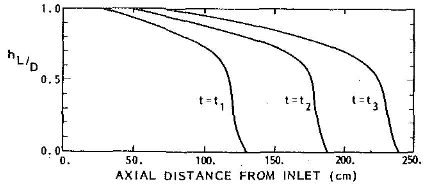

Fig. 9 Propagation of refilling front

As a first step in the model development effort, the model was used to predict the refilling of a cold tube. It was solved numerically using an upwind characteristic finite difference method. Some aspects of the method are novel and have been presented. The same scheme is used for analysis of the rewetting problem presented in Part III.

A simple experiment was done on refilling of a cold tube. Data compare quite well with numerical results. The shape of the refilling front obtained numerically also agrees with visual observations and other studies.

The good agreement between numerical and experimental results in the present case is encouraging. This suggests that the simplified one-dimensional two-fluid model may be adequate in predicting the hydraulic behavior, at least for the refilling of a cold horizontal tube. It also suggests that the numerical technique used to solve the hydraulic equations gives good results. The model and solution technique can then be used to interpret the refilling and rewetting experiments. In this more complicated case, the thermal equations and the liquid-vapor interfacial transfer terms (especially vapor generation term) must be taken into account. The set of equations thus becomes somewhat more complex. This case is analyzed in Part III (Chan and Banerjee [2]).

References

1 Chan, A. M. C., and Banerjee, S., "Refilling and Rewetting of a Hot Horizontal Tube. Part I: Experiments," Submitted to ASME JOURNAL OF HEAT TRANSFER.

2 Chan, A. M. C., and Banerjee, S., "Refilling and Rewetting of a Hot Horizontal Tube. Part III: Application of a Two-Fluid Model to Analyze Rewetting," Submitted to AMSE JOURNAL OF HEAT TRANSFER.

3 Yu, S. K. W., Farmer P. R., and Coney, M. W. E., "Methods of Correlations for the Prediction of Quenching Rates on Hot Surfaces," *Int. Journal Multiphase Flow,* Vol. 3, 1977, pp. 415–443.

4 Chan, A. M. C., "Transient Two Phase Flows: Refilling and Rewetting of Hot Horizontal System," Ph.D thesis, Department of Engineering Physics, McMaster University, 1980.

5 Agee, L. J., Duffey, R. B., and Banerjee, S., "Multi-Fluid Models for Transient Two-Phase Flow Analysis," EPRI NP-618-Sr, Nov. 1977.

6 Sissom, L. E., and Pitts, D. R., "Elements of Transport Phenomena," McGraw-Hill, 1972.

7 Street, R. L., "The Analysis and Solution of Partial Differential Equations," Brooks/Cole Publishing Co., 1973, Chapter 9.

8 Courant, R., and Friedrichs, K. O., "Supersonic Flow and Shock Waves," Interscience Publishers, 1948, Chapter 2.

9 Henderson, F. M., "Open Channel Flow," MacMillan Co., 1966, Chapter 8.

10 Eckert, E. R. G., and Drake Jr. R. M., "Analysis of Heat and Mass Transfer," McGraw-Hill, 1972, Chapter 4.

11 Abbott, M. B., "Method of Characteristics," *Unsteady Flow in Open Channels,* Edited by K. Mahmood and V. Yevjevich, Water Resources Publications, 1975, Vol. 1, pp. 63–68.

12 Liggett, J. A., and Cunge, J. A., "Numerical Methods of Solution of the Unsteady Flow Equations," *Unsteady Flow in Open Channels,* Edited by K. Mahmood and V. Yevjevich, Water Resources Publications, 1975, Vol. 1. pp. 89–179.

13 Isaacson, E., and Keller, H. B., "Analysis of Numerical Methods," Wiley, 1966, pp. 485–489.

14 Fox, L., "Numerical Solution of Ordinary and Partial Differential Equations," Pergamon, 1962.

15 Stoker, J. J., "Water Waves: The Mathematical Theory and Applications," Interscience Publishers, 1957, Chapters 10 and 11.

16 Dressler, R. F., "Comparison of Theories and Experiments for the Hydraulic Dam-Break Wave," International Assoc. of Hydrology, Assemblee Generale de Rome, Vol. III, 1954, p. 319.

Table 1 Convergence studies for the case of refilling with no heat transfer

	No. of Nodes Used					
	Q = 70 ml/s			Q = 90 ml/s		
	30	60	100	30	60	100
$\frac{\lvert\Delta M\rvert}{M}$	2.3%	2.5%	2.1%	4.5%	4.4%	—
$\overline{V}_B$(cm/s)	28.3	28.0	28.5	35.1	34.7	—

Quenching Studies on a Zircaloy Rod Bundle

V. K. Dhir
R. B. Duffey[1]
I. Catton
School of Engineering and Applied Science,
University of California, Los Angeles,
Los Angeles, Calif. 90024

Quenching data are presented for reflooding by cold water of zircaloy and stainless steel clad rod bundles. In particular a filling material (Al_2O_3) with thermophysical properties similar to UO_2 is used. The rods which are 1.1 mm in outside diameter and are 1.2 m high are arranged in a square lattice and are inductively heated. The experiments have been performed with initial rod surface temperatures up to 1400 K and flooding velocity varying over the range 1–30 cm/s. The subcooling of water at inlet was either 75 K or 50 K. Under identical flow conditions zircaloy is observed to quench faster than stainless steel. The quenching temperature and quench front velocity are found to increase with liquid subcooling and flooding velocity. The present data have been correlated and compared with existing models and correlations.

Introduction

In BWR's and PWR's, the ultimate cooling of the fuel rods following a loss of normal reactor coolant is by quenching the core with a reflooding water. Maintaining the integrity of the fuel rods until they are quenched is a major safety constraint. At present: knowledge of film and transition boiling heat fluxes during quenching of rod bundles is limited and a better understanding of the transient boiling process needs to be gained, particularly for Zircaloy clad bundles. The objective of this study is to help develop such an understanding.

Elliott and Rose [1] were the first to perform falling water film experiments on stainless steel, inconel 600 and Zircaloy tubes. They observed that due to its lower thermal capacity, Zircaloy quenched at about twice the quenching velocity for stainless steel. Rewetting experiments on single stainless steel and Zircaloy tubes and filled rods subjected to falling water film and bottom flooding were also performed by Piggott and Duffey [2]. The experiments were conducted at one atmosphere pressure and with water subcooling of 80 K. From their work, it was also shown that Zircaloy quenched faster than stainless steel. A conduction controlled analysis of rewetting has been developed [3–5] and later improved [6] to consider the heat transfer phenomenon in three distinct regions—film boiling, rewetting or sputtering region and a fully wet region. It is generally accepted that quenching data from simple geometries can be correlated assuming local conduction control of the quenching process. However, there is considerable disagreement over the quenching heat fluxes and whether a unique rewetting temperature exists [7, 8]. In the literature at least four definitions of rewetting temperature have been reported—Leidenfrost temperature, minimum film boiling temperature, quenching temperature from thermocouple observations and the temperature at which critical heat flux occurs. Data for the minimum tube temperature to accomplish re-wetting and the transient heat fluxes in film, transition and nucleate boiling have been reported for forced flow in steel tubes at both high [9] and low [10] pressures.

The only available rod bundle experiments with zircaloy are the FLECHT [11] experiments. Unfortunately, the high conductivity filling material used in the heaters for the FLECHT experiments dominates the heat released during quenching and is atypical of the low thermal conductivity of the reactor fuel rods. Furthermore, the gap conductance was not properly simulated. Pearson et al. [12] have shown that filler properties can also affect the quenching behavior by acting as a partial thermal barrier.

One of the major objectives of this work was to study quenching of zircaloy rods during reflooding and to compare it with stainless steel rods including data at very high temperatures. The experiments were conducted in a four-rod bundle to obtain data for quench front velocity, with additional information on film boiling heat transfer. How the quenching rate depends on variables such as high surface temperature, thermal capacity and oxidation of the surface of the rod was investigated for a prescribed liquid subcooling at inlet, flow velocity and initial temperature of the rod. The filler material in the tubes was chosen to be representative of the thermophysical properties of UO_2 relevant to the quenching process.

Experimental Apparatus and Procedure

A schematic diagram of the experimental apparatus used in the quenching tests is shown in Fig. 1. The experimental setup was designed to investigate the thermal-hydraulic phenomena associated with quenching of rods bundles, using rods arranged in a square lattice and housed in a vertical 5.5 cm o.d., 0.1 cm thick quartz tube. Tubes 120 cm long and 1.1 cm o.d. and of about 0.88 mm wall thickness filled with 0.91 cm dia Al_2O_3 pellets (i.e., identical to UO_2 pellets) were used. The tubes were heated inductively with a power supply from a 450 kHz, 25 kW induction heater. The equipment consisted of an induction coil, a pneumatic cylinder to move the induction coil in the vertical direction, a nitrogen or argon gas supply system to purge the test section and a flow loop. The flow loop includes the piping and a centrifugal pump placed between the solenoid valve and the reservoir. In these forced flow flooding tests, the flow rate through the pump was controlled by a metering globe valve and was measured with a magnetic flow sensor.

Figure 2 shows the test section and details of how the thermocouples are mounted in the tubes. Chromel-alumel, 26 gage thermocouples were spot welded 15 cm apart in the mid portion of the tube. The bare thermocouple wires were carried through six holes in the stacked alumina insulators (fillers). To measure the representative temperature of alumina, in one of the rods the top thermocouple was fixed to the insulator with adhesive cement. The thermocouple data were measured on X-Y strip chart recorders. The rods were held in a square grid with multi-hole orifice plates which also serve to provide flow of coolant through the test section. To avoid bowing of the rods due to uneven thermal expansion and contraction during preheating and quenching, pieces of 1.5 mm dia tantalum wire were welded to each rod at 22.5 and 38 cm from the lower and upper ends of the bundle, respectively.

The experiments were conducted by initially inductively heating the rods in an inert atmosphere. When the rod temperature reached a predetermined value, the induction heater was switched off and water was allowed to flood the test section at a controlled flow rate. During reflood period, the temperature time histories were obtained on the recorders while the quench phenomena on the rod bundle were captured on TRI-X film at 100 frames/s.

Results

A total of 70 experiments for the quenching of a four rod bundle containing all stainless steel, all zircaloy and two stainless steel and

---

[1] Safety and Analysis Department, Electric Power Research Institute, Palo Alto, CA.

Contributed by the Heat Transfer Division for publication in the JOURNAL OF HEAT TRANSFER. Manuscript received by the Heat Transfer Division July 21, 1980.

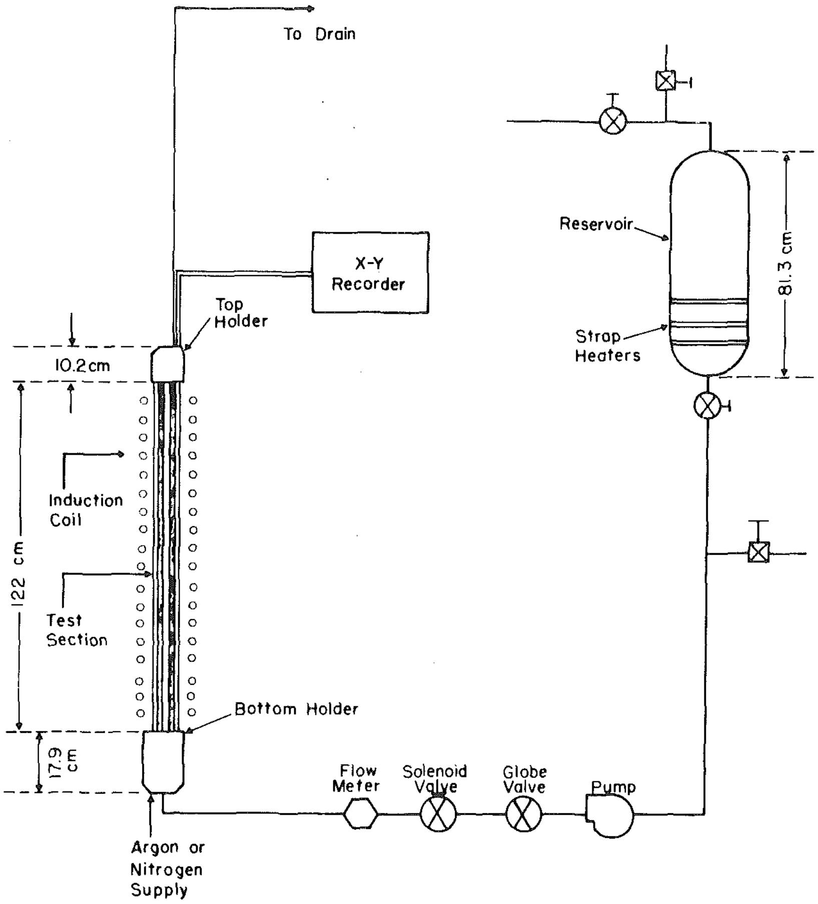

Fig. 1 Schematic diagram of the test section and flow loop

two zircaloy rods were made in order to determine the material property effects in pure and mixed bundles. In these experiments initial rod temperatures were varied up to 1400 K and the flooding velocities were varied from 1 to 30 cm/s. The uncertainty in flooding velocities is expected to be less than ±5 percent. For all of the experimental runs: water subcooling at inlet was 78 ± 2 or 50 ± 5 K. Complete details of the data and the information needed to model the tests are given in references [13, 14]. Usually at least two experiments were conducted at a given flooding velocity and initial rod temperature. The main output of a quenching experiment was the temperature time traces of the inner surface of zircaloy or stainless steel cladding. The temperature at which the slope of the temperature time trace began to increase rapidly was taken as the quenching temperature, T_0. This procedure was confirmed by visual observation of the location of quench front on the surface of the rods. As the film boiling Biot number for the zircaloy and stainless steel cladding is very small (<0.06), little error is made in assuming T_0 as the surface temperature.

The quenching temperature is generally highest near the inlet of the rod bundle where liquid is at its coldest and decreases in the vertical direction as liquid enthalpy increases. The wall temperature ahead of the quench front strongly affects the quench front velocity. In the experiments this temperature varied both with time and axial position. The temperature history when precursory cooling is important (presumably as a result of droplets hitting the surface) showed no clearly defined quenching temperature.

Discussion

In the following paragraphs the inferences drawn from these data are discussed in order of the role of such variables as:

i liquid subcooling
ii flooding velocity and initial rod temperature
iii rod materials properties
iv oxidation, especially in the case of zircaloy on the quenching behavior of the rod bundle.

(i) Liquid Subcooling. The quenching temperatures (temperatures at which a rapid increase in the slope of the temperature time trace was observed) as obtained from the temperature time traces were found to decrease with axial height before reaching an asymptotic value in the upper middle region of the rod bundle. The decrease

Nomenclature

Bi = Biot number, $h\delta/k$
C = circumference of a rod, cm
D_h = hydraulic diameter
G = mass flow rate per rod, gm/s
h = heat transfer coefficient, W/cm^2 K
k = thermal conductivity of cladding material, W/cm K
Re = Reynolds number, UD_h/ν
T_{CHF} = temperature of occurrence of critical heat flux
T_0 = quenching temperature
T_{sat} = saturation temperature at one atmosphere pressure
T_w = surface temperature
T^* = dimensionless temperature, $(T_0 - T_{\mathrm{sat}})/(T_w - T_0)$
U = flooding velocity
u = quenching velocity
u^* = dimensionless quenching velocity, $u\delta/\alpha$
α = thermal diffusivity of cladding material
δ = cladding thickness
ν = kinematic viscosity of water

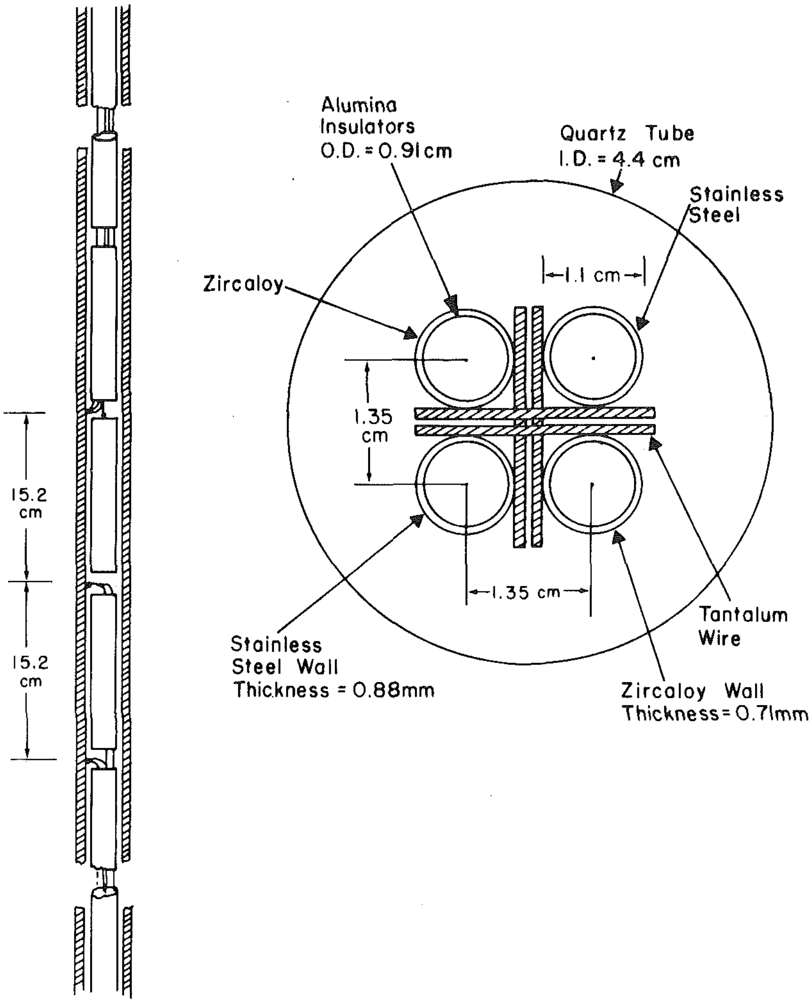

Fig. 2 Detailed view of thermocouple location and test section

in quenching temperature is presumably associated with increase in the enthalpy of the liquid as it moves upwards. Figure 3 shows an average quenching temperature of the four rods as a function of local liquid subcooling on an all zircaloy rod bundle for flooding velocities of 2, 5 and 30 cm/s. Local water subcooling was measured by thermocouples installed in the space between the rods. These water thermocouples were located at the same vertical locations as the thermocouples in the rods and generally gave average temperature of the core of the inverted annular film boiling flow. The data plotted in Fig. 3 are for the lower half of the rod bundle as in the upper region, the precursory cooling dominated the quenching process and a well defined quenching temperature could not be obtained from the temperature time traces. It is noted that the quenching temperature increases both with liquid subcooling and flooding velocity. The average quenching temperatures obtained by drawing mean lines through the data can be correlated to within ±50 K with the following equation:

$$T_q = 550 + 50\sqrt{U} + 3\Delta T_{\mathrm{sub}}\,\mathrm{K} \qquad (1)$$

In equation (1), U is the flooding velocity in cm/s. The square root dependence of the quenching temperature on the flooding velocity is indicative of the fact that heat transfer in the film boiling region downstream of the quench front affects the quenching temperature. It was shown in reference [15] that during forced flow film boiling on spheres the heat transfer coefficient increased as the square root of flow velocity. Interestingly, in dispersed flow Iloeje, et al. observed a similar dependence of quenching temperature on the mass flow rate through the tube.

The quenching temperature increases linearly with liquid subcooling; however, the dependence of quenching temperature on liquid subcooling is much smaller than that reported in reference [15] for minimum film boiling temperature on spheres. This is plausible since the length over which film boiling exists is much longer in rods than it was on spheres. This results in a thicker average thermal layer in the liquid, and in turn a smaller local liquid subcooling effect. Equation (1) does not contain a product term of flooding velocity and liquid subcooling. No appreciable interacting effect of ΔT_{sub} or U could be discerned from the existing data.

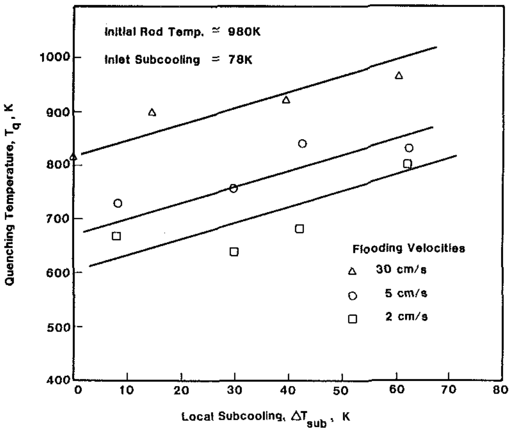

Fig. 3 Variation of quenching temperature with local subcooling and flow velocity

It should be pointed out that the data plotted in Fig. 3 are for oxidized zircaloy rod bundles. A comparison of the quenching temperature data obtained on fresh and oxidized rod surfaces showed that quenching temperatures on oxidized surfaces were 50 to 80 K higher than on fresh surfaces. The quenching temperature given by equation (1) for no flow and zero subcooling is about 100 K higher than Berenson's prediction for clean horizontal surfaces.

Quench front velocities in the lower half region of the zircaloy rod bundle are plotted in Fig. 4 for inlet water subcooling of 78 K. The quench front velocities are obtained by taking local slopes of the curves representing location of quench front as a function of time [13]. Though quench front velocities in a particular rod bundle vary from one rod to another, the quenching velocities decrease with distance from the inlet as does the liquid subcooling, until the liquid becomes nearly saturated. Thereafter, the quench front velocities increase again because of the strong influence of the precursory cooling.

(ii) Flooding Velocities and Initial Rod Temperature. Inspection of the quench front location data indicates that the quenching of different rods at the same vertical location may differ by a few seconds; however, the difference in quenching time is observed to decrease with flooding velocity. Generally the quench front velocities in the lowermost and uppermost parts of the rod bundle are higher than in the middle portion. As discussed earlier, higher quench front velocity in the lower region of the rod bundle is due to larger water subcoolings. In the upper region, the quench front velocity is increased because of precursory cooling. In the middle portion, liquid is nearly saturated and inverse annular type flow conditions exist with film boiling on the rod surface. The quench front velocity in the middle portion of the rod bundle where the liquid was slightly subcooled ($\Delta T_{\text{sub}} \approx 0$) is plotted in Fig. 5, as a function of flooding velocity for initial zircaloy rod temperatures of 1000 and 1380 K. The data plotted in Fig. 5 represents observations from different rods in a given experiment and several repeat experiments performed at the same flooding velocity and nearly the same initial temperature. It is noted that for a flooding velocity of 1 cm/s, the quench front velocity is about the same as the flooding velocity. For higher flooding rates, quench front velocity increases approximately as the square root of flooding velocity and is consistent with the observations reported in reference [1] and with the one-dimensional analysis of reference [5].

The effect of higher initial rod temperature is to reduce the quench front velocity. The zircaloy rod bundles quenched at a temperature of about 1400 K were found to degrade very rapidly because of uneven thermal stresses in the axial direction and formation of brittle oxide layers as a result of increased zircaloy-water reaction. After about four runs at the elevated temperatures, the rods were badly distorted and the oxide layers readily peeled off from the surface. In certain instances the zircaloy tubes were cracked at several places and the cracks generally ran in the longitudinal direction [13], giving rise to local tube failures.

(iii) Rod Material Properties. Several quenching runs made with two zircaloy and two stainless steel rods placed alternately in a square grid showed that in general zircaloy quenched faster than stainless steel. Figure 6 shows the quench front location data on stainless steel and zircaloy rods as obtained from one of the movies. In this figure, the quench front locations as interpreted from the temperature-time traces of the thermocouple output are also plotted. The thermocouple observations are found to agree with the data from the movies during early periods of quenching. However, at higher elevations when precursory cooling becomes important, thermocouple observations can be misleading. This is mainly because of difficulty in prescribing a quenching temperature on the temperature-time traces. In many instances the agitation or the flow by-pass resulting from the faster moving quench front was observed to cause a local breakup of the vapor film on the rod with the slower moving quench front. This in turn led to a step process during which a slower moving quench front caught up with the faster moving quench front. Such a step process can also be seen in the data plotted in Fig. 6. The faster quenching of zircaloy thus helps to improve the quenching of stainless steel also. It is suspected that a role similar to the zircaloy rod in the mixed rod bundle may be played by control rod tubes present in an array of fuel rods. Figure 7 shows a photograph of the quench front location on stainless steel and zircaloy rods. The quench front on the zircaloy rod is well ahead of that on the stainless steel rod. Nucleate boiling upstream of the quench front can be seen on both rods.

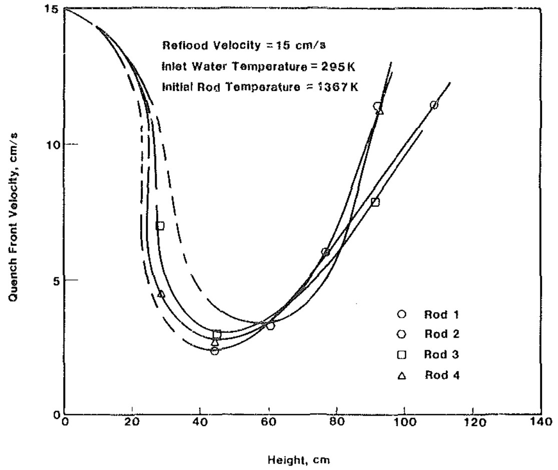

Fig. 4 Variation of quench front velocities in the axial direction of the all zircaloy rod bundle

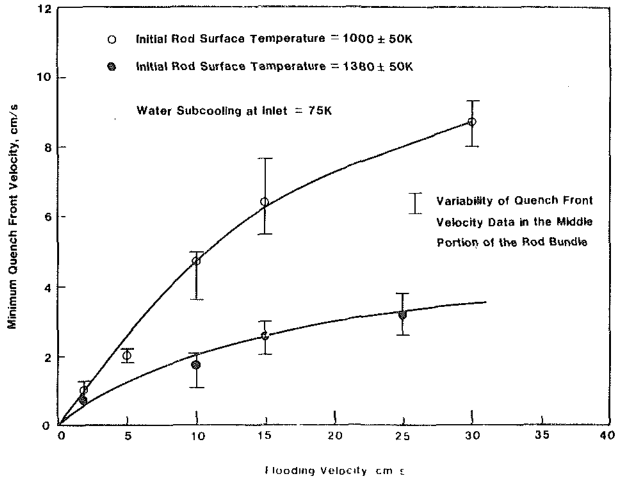

Fig. 5 The effect of flow velocity and initial rod temperature on quench front velocity in the middle portion of the all zircaloy rod bundle

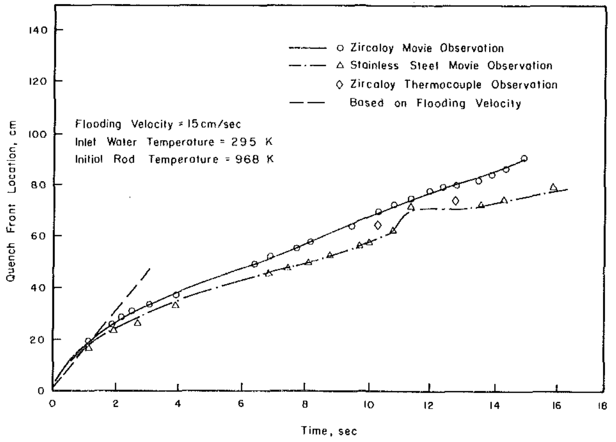

Fig. 6 Quench front location as a function of time on zircaloy and steel rods in a mixed bundle

The quench front velocities in the middle portion of the rod bundle where liquid was slightly subcooled and inverse annular flow conditions existed are plotted in Fig. 8 for all zircaloy and all stainless steel bundles, and for a mixed bundle containing two zircaloy and two stainless steel rods. The data plotted in Fig. 8 are for initial rod temperature of about 1000 K and inlet water subcooling of about 75 K.

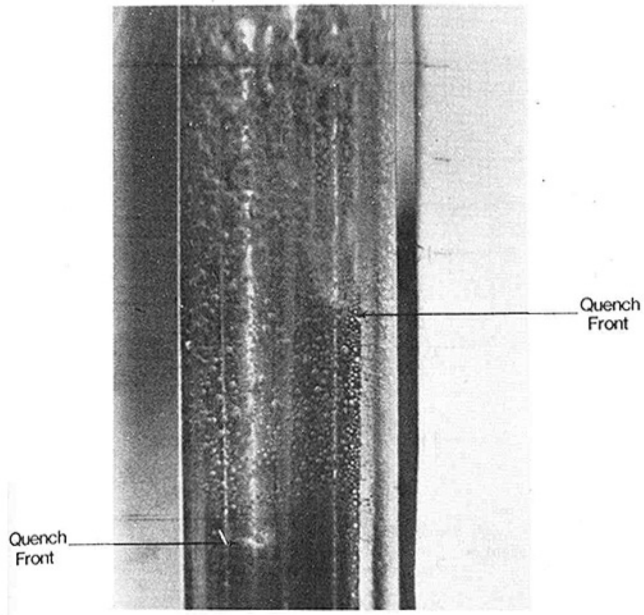

Fig. 7 Relative quench front locations on zircaloy (right) and steel (left) rods in a mixed zircaloy-stainless steel rod bundle

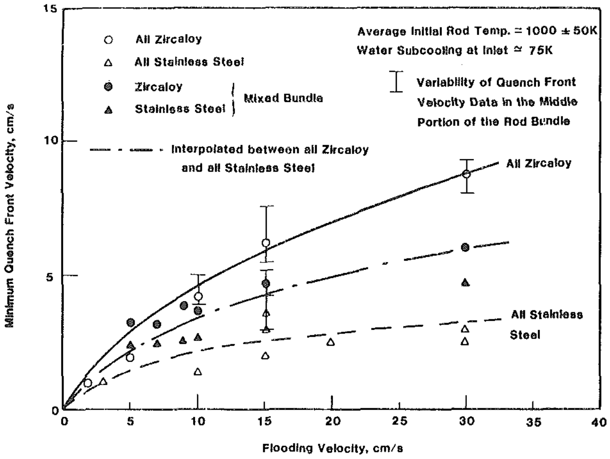

Fig. 8 Quench front velocities in all zircaloy, mixed, and all stainless steel rod bundles

The upper and lower bounds in the data represent variability of data obtained from several experiments. For a flooding velocity of about 2 cm/s, the quench front velocity on all rod bundles is about the same. However, as flooding velocity increases, the all zircaloy rod bundle is observed to quench about two times faster than the all stainless steel rod bundle. Faster quenching of zircaloy occurs because the density and specific heat of zircaloy are less than that of stainless steel. Also, in the present experiments the zircaloy cladding was about 20 percent thinner than the stainless steel cladding. Piggott and Duffey [2], in their single rod tests, noted that with filler the quenching rate of zircaloy was about 20–25 percent faster than stainless steel. However, when the filler was removed, zircaloy tended to quench at about twice the velocity of stainless steel. Here two distinct roles played by the filler with a proper gap conductance should be distinguished. In the film boiling region downstream of the quench front, the heat transfer process is quasistatic and the filler acts as an integral part of the cladding. At the quench front, very high transient heat fluxes for flooding velocities greater than 2 cm/s are achieved and the gap between the filler and the cladding acts to isolate the clad from the filler as long as filler temperature is not very high. Pearson, et al. [12], while analyzing the effect of filler properties on quench front velocity have also suggested that the effect of filler may be ignored when quench front velocity u, is greater than α/δ. As expected, the present data match closely with the observations of Piggott and Duffey on a hollow rod.

It is interesting to note that the minimum quench front velocity on the mixed rod bundle (observed to occur near the mid plane) is about the mean of the quench front velocities observed on all stainless steel and all zircaloy bundles. Or, in a mixed bundle the quench front on zircaloy tends to slow down while that on stainless steel tends to accelerate. Qualitatively it can be argued that reduction in local fluid velocity as a result of the absence of film boiling on the quenched region of zircaloy acts to reduce the heat transfer at the quench front which in turn slows down the quench front. The acceleration of the quench front on stainless steel is a manifestation of the local vapor film collapse initiated by the liquid trying to bypass the restriction caused by the presence of vapor film on the zircaloy rod also. As discussed above, the cross flow effect became prominent when the quench fronts on zircaloy and stainless steel were separated by about 10–15 cm.

(iv) Oxidation. The effect of oxidation on quenching behavior is most difficult to quantify. Thus, in an attempt to know the precise amount of oxidation of zircaloy during each run, a 45 cm long zircaloy tube cut as a half cylinder was placed in the test section along with an all zircaloy bundle. The half cut tube which served as the test specimen was placed in the test section such that it preserved the square grid spacing of the rods. Also, the exposure of both sides of the test specimen to the test section environment resulted in the same surface area as for a rod of the same length. The experiments were conducted by heating the rods as well as the specimen to about 1000 K and quenching the rod bundle at a flooding velocity of 2 cm/s. After each test run, the specimen was weighed. It was noted that the amount of oxide deposited [13] on the test specimen decreased with each subsequent run and the oxidation was complete after about two runs. Evaluation of the quench front velocities on the fresh and fully oxidized rod bundles showed that in the lower half region, the quench front moved at about the same rate on both the bundles. However, in the upper half region, the quench front velocity on the oxidized rod bundle was higher than on the fresh (presumably nonoxidized) bundle. Higher quenching velocity is thought to be due to increased wettability of the oxidized surface which allows for longer periods of good heat transfer during each contact of precursory cooling droplets. As pointed out earlier, examination of the quenching temperatures showed that oxidized rods quenched at temperatures aout 50–80 K higher than fresh rods. Similar observations have been made earlier by Iloeje, et al. [9].

Boiling Curve

The boiling curves as deduced from the temperature-time traces for a single stainless steel rod when the quench front was well defined, and when cooling of the rod bundle mainly occurred by precursory cooling droplets are compared in Fig. 9. The dependence of heat flux on temperature was obtained by solving the one-dimensional inverse transient conduction equation in the classing as well as in the insulators. The boiling curve obtained with the assumption of no filler but an insulated cladding inner surface was not much different except in the lower end of the nucleate boiling region. Slight modifications in the boiling curves, however, may occur if the two-dimensional inverse transient conduction equation is solved.

The transition boiling region in the boiling curve corresponding to a well defined quench front is extremely narrow. In fact, it suggests that the boiling process rapidly goes from film to nucleate boiling and that in the quenching models, heat transfer just behind the quench front should be evaluated from peak heat flux rather than from the average of minimum and maximum heat fluxes. The observed shape of the boiling curve confirms the assumption made by Murao [16] in his recent work on quenching. The transition boiling data obtained by Cheng, et al. [17] on an inconel tube embedded in a copper block and also plotted in Fig. 9 show a much different dependence of heat flux on wall superheat. It is possible that in their experiments, the copper block acted to flatten out any large temperature gradients and thus caused the tube wall temperature to vary slowly with time.

The heat transfer associated with precursory cooling is significantly higher than for film boiling ahead of the well defined quench front. The advantage becomes more clear if one integrates the heat flux over the time for which precursory cooling prevails on the rod surface instead of classical film boiling. It is interesting to note that maximum heat flux achieved with precursory cooling is much less than that at a well defined quench front. This is most probably due to lower rod temperature at the time of complete wetting.

Correlation of Quenching Data. Figure 10 shows the dimensionless inverse quench front velocity as a function of the Reynolds number based on the flooding velocity. The data plotted in Fig. 10 are for the lower middle portion of the rod bundle where inverse annular flow with film boiling on the rod surface existed. The average of several data points obtained at a given flooding velocity are correlated within ±30 percent as

$$\frac{T^*}{u^*} = 12\,\mathrm{Re}^{-1/2} \tag{2}$$

where Re is the Reynolds number based on the coolant inlet velocity. The one dimensional correlation of Duffey and Porthouse [5],

$$\frac{T^*}{u^*} = \frac{1}{3}\left(\frac{k}{\delta}\right)^{1/2}\left(\frac{C}{G}\right)^{1/2}, \tag{3}$$

is also seen to compare quite favorably with the data. The two dimensional solution for the quench front velocity on a cylinder has been given by Blair [18] and Duffey and Porthouse [5] as

$$\frac{T^*}{u^*} = \frac{\pi}{2}\frac{1}{\mathrm{Bi}} \tag{4}$$

The flooding velocity dependence in equation (4) is carried through the Biot number. If it is assumed that the Biot number would be a function of the Reynolds number, equations (2) and (4) can be equated to yield

$$\mathrm{Bi} = 0.14\,\mathrm{Re}^{1/2} \tag{5}$$

This translates to heat transfer coefficients of 5.7 and 31.2 W/cm^2 K for flooding velocities of 1 and 30 cm/s, respectively. Corresponding values obtained by using Yamanouchi's [4] correlation would be 44.8 and 245.4 W/cm^2 K. Very high heat transfer coefficients given by Yamanouchi's correlation are probably due to their use of a simplistic model for the quenching process.

Conclusions

1 Under similar flooding conditions, zircaloy has been observed to quench faster than stainless steel. The average quench front velocity on a mixed rod bundle is about half of that on all zircaloy and all stainless steel rod bundles.

2 For a given rod surface temperature, the quenching temperature increases with liquid subcooling and flooding velocity. A correlation for quench front temperature as a function of liquid subcooling and flooding velocity has been suggested for zircaloy.

3 Quench front velocity under inverse annular flow conditions has been found to increase as the square root of flooding velocity. For a given flooding velocity, the effect of increased initial rod temperature is to reduce the quench front velocity.

4 At a given rod temperature of about 1000 K, the oxidation of zircaloy has been observed to reach an asymptotic state after about two runs. During quenching, oxidized rods behave somewhat differently than fresh rods.

5 Transient boiling curves obtained under a well defined quench front show a very narrow region of transition boiling.

Acknowledgment

Financial support was provided by the Electric Power Research Institute under Contract No. RP1118-1 and is gratefully acknowledged.

References

1 Elliot, D. F., and Rose, P. W., "The Quenching of a Heated Zircaloy Surface by a Film of Water in a Steam Environment at Pressures up to 53 Bars," Report AEEW-M-1027, United Kingdom Atomic Energy Authority, 1971.

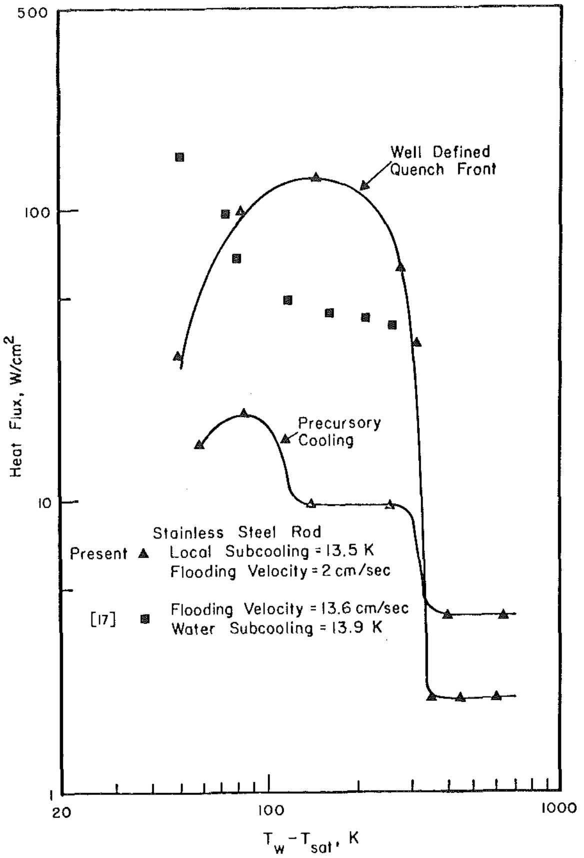

Fig. 9 Boiling curves obtained during quenching of stainless steel rods

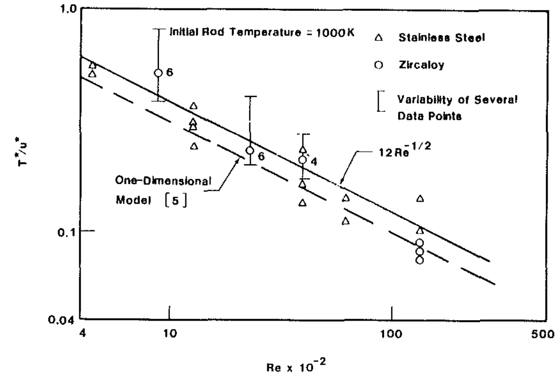

Fig. 10 Correlation of quenching data obtained under inverse annular flow conditions on stainless steel and zircaloy rod bundles

2 Piggott, B. D. G., and Duffey, R. B., "The Quenching of Irradiated Fuel Pins," *Nuclear Engineering and Design*, Vol. 32, 1975.

3 Semeria, R., and Martinet, B., "Calefaction Spots on a Heating Wall: Temperature Distribution and Resorption," Proceedings of the Institute of Mechanical Engineering, 1980, Part 3C, 1966.

4 Yamanouchi, A., "Effect of Core Spray Cooling in Transient State After Loss of Coolant Accident," *Journal of Nuclear Science and Technology*, Vol. 5, 1968.

5 Duffey, R. B., and Porthouse, D. T. C., "The Physics of Rewetting in Water Reactor Emergency Core Cooling," *Nuclear Engineering and Design*, Vol. 25, 1973.

6 Sun, K. H., Dix: G. E., and Tien, C. L., "Cooling of a Very Hot Vertical Surface by a Falling Liquid Film," ASME JOURNAL OF HEAT TRANSFER, Vol. 96, 1974.

7 Piggott, B. D. G. and Porthouse, D. T. C., "A Correlation of Rewetting Data," *Nuclear Engineering and Design*, Vol. 32, 1975.

8 Farmer, P. R., and Coney, M. W. E., "The Rewetting of Hot Surfaces by Bottom Flooding—The Effect of Water Flow Rate and Temperature," Paper presented at European Two Phase Flow Meeting, Haifa, Israel, June 1978.

9 Iloeje, O. C., Plummer, D. N., Griffith, P., and Rohsenow, W. M., "An Investigation of the Collapse and Surface Rewet in Film Boiling in Forced Vertical Flow," ASME Paper No. 73-WA/HT-20. Presented at the ASME Winter Annual Meeting, Detroit, Mich., Nov. 1973.

10 Seban, R., et al., "UC-B Reflood Program: Experimental Data Report," EPRI NP-643, Apr. 1978.

11 Blaisdell, J. A., Hochreiter, L. E., and Waring, J. D., "PWR FLECHT-SET Phase BI Data Report," USAEC Report WCAP-8238, Westinghouse Electric Corp., NTIS, 1973.

12 Pearson, D. K., Piggott, B. D. G., and Duffey, R. B., "The Effect of Thermal Diffusion from Fuel Pellets on Rewetting of Overheated Water Reactor Pins," *Nuclear Engineering and Design*, Vol. 41, 1977.

13 Dhir, V. K., and Catton, I., "Zircaloy Rod Bundle Thermal-Hydraulics," EPRI Report NP-1277, Dec. 1979.

14 Dhir, V. K., et al., "Zircaloy Rod Bundle Thermal-Hydraulics," EPRI Report to be published, 1980.

15 Dhir, V. K., and Purohit, G. P., "Subcooled Film Boiling Heat Transfer from Spheres," *Nuclear Engineering and Design*, Vol. 47, 1978.

16 Murao, Y., "Correlation of Quench Phenomena for Bottom Flooding During Loss of Coolant Accidents," *Journal of Nuclear Science and Technology*, Vol. 15, No. 12, 1978.

17 Cheng, S. C. and Ragheb, H., "Transition Effect of Heated Surface Thermal Properties on Transition Boiling," International Multiphase Symposium, Miami, Apr. 1979.

18 Blair, J. M., "An Analytical Solution to a Two Dimensional Model of the Rewetting of a Hot Dry Rod," *Nuclear Engineering and Design*, Vol. 32, 1975.

K. Mastanaiah
Research Assistant.

E. N. Ganić
Associate Professor.

Department of Energy Engineering,
University of Illinois at Chicago Circle,
Chicago, Ill. 60680

Heat Transfer in Two-Component Dispersed Flow

Measurements have been made of heat transfer near atmospheric pressure in the post dryout region of air-water dispersed flow in an electrically heated 12.95 mm i.d. vertical stainless steel tube with a length of 889 mm. The mass velocity ranges from 30 to 83 kg/m^2*·s, and the average wall heat flux is varied from 6.4 to 36.2 kW/*m^2 *in the experiments. Correlation of a theoretical analysis with the measured wall temperatures suggests that the effectiveness of wall-to-drop heat transfer depends mainly on the wall superheat for surface temperatures below the minimum film boiling temperature. The local two-phase heat transfer coefficient decreases with increasing wall temperature. It is also found that the thermal entrance length for two-phase dispersed flow exceeds that of the single-phase gas flow, and that it decreases with an increase in wall temperature.*

1 Introduction

The study of heat transfer characteristics in the turbulent two-phase two-component dispersed flow is of interest in spray cooling and in many chemical engineering applications, yet it has received much less attention than the corresponding one-component system. To the authors' knowledge, the only data on turbulent binary dispersed flow are those reported by Takagi and Ogasawara [1] for an air-water system in a vertical channel.

One major uncertainty in the analysis of dispersed flow heat transfer pertains to the effectiveness of heat exchange, ϵ, between the wall and the droplets that come in contact with the wall due to the deposition process. In general ϵ depends on a number of variables including wall temperature, drop impact velocity, nature of the fluid, nature of the heating wall and coupling of fluid and wall, drop temperature and surface state of heating wall (oxidation, surface roughness, etc.), the wall temperature being the most important variable [2]. The data for ϵ under stationary vapor conditions exhibit large scatter with the wall temperature [3–5] as shown in [2], but suggest the decreasing trend of ϵ with wall temperature in excess of the saturation temperature T_s. At surface temperatures in excess of the Leidenfrost temperature, a vapor film will be formed between the wall and the droplet (spheroidal state), thereby preventing the droplets from wetting the heat transfer surface. The heat transfer characteristics of droplets on heated surfaces have also been recently studied [6, 7].

The nature of the wall-to-drop heat transport appears to be further complicated in the presence of flowing vapor conditions [2]. Koizumi, et al. [8] recently correlated a theoretical analysis with the data on R-113 fluid flowing in a vertical tube. Their analysis assumes constant value of ϵ independent of the wall temperature. It is shown that a value of ϵ in the range 0–0.2 predicts well the measured wall temperatures, implying that the heat from the tube wall is principally transferred to the vapor. Takagi and Ogasawara [1] assume a constant value of $\epsilon = 1$ in their analysis. On the other hand, Ganic and Rohsenow [2] and Chiang, et al. [9] have considered an exponential decay of ϵ with the wall temperature in describing their experimental data on dispersed flow.

The purpose of the present work is to study experimentally and theoretically the two-component (air-water) dispersed flow in a uniformly heated vertical tube. The wall temperatures are maintained below the minimum film boiling temperature for water, which is about 557 K for water at atmospheric pressure [10]. This serves to insure the existence of significant wall-to-drop heat transfer. The present experimental data are limited to low pressure and low mass velocity. The results are expected to be useful in the development of improved correlations for steam-water mixtures [11], since the properties of steam and air at low pressure are not quite different, and the dynamics of droplet deposition in a two-component system is similar to that in a one-component system. In fact it has been shown that [11] the two recent nonequilibrium correlations of Groeneveld and Delorme [12] and of Chen, et al. [13] for a one-component flows, which are satisfactorily correlated with the data at high pressures, are quite unsuccessful in predicting the few available low pressure data of Nijhawan, et al. [11].

2 Experimental Apparatus and Procedure

A schematic of the experimental setup used for the heat transfer studies is illustrated in Fig. 1. Details of the experiment are given in [14]. In the experiments, compressed air passes first through a refrigerated air dryer to remove moisture, and later through an oil filter to eliminate oil content. The clean dry air is then metered through calibrated variable-area rotometers before entering the test section. Distilled water from a water tank is circulated by a variable-speed pump through a calibrated flow meter. A flow integrator is incorporated at the discharge end of the water pump to minimize any flow pulsations.

The liquid droplets are generated by an atomizer with a sharp-edged air orifice and a cylindrical liquid nozzle, and by using secondary air stream. The primary air stream is used to vary the bulk flow rate in the test section. The major dimensions of the atomizer are similar to those employed by Nukiyama and Tanasawa [15] in some

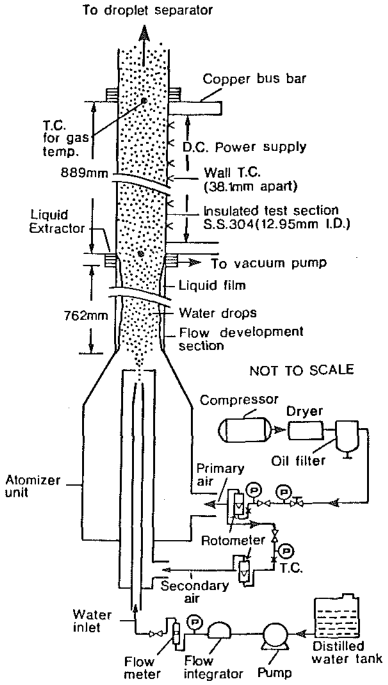

Fig. 1 Schematic of experimental set-up

Contributed by the Heat Transfer Division for publication in the JOURNAL OF HEAT TRANSFER. Manuscript received by the Heat Transfer Division, April 16, 1980.

of their experiments. The Sauter mean diameter d_{32} of the droplet size at the inlet of the test section is computed from the well-known correlation of Nukiyama and Tanasawa [15, 16]. An entrance section having 12.95 mm i.d. and a length of 59 diameters is employed to insure that the flow is fully developed at the inlet of the test section.

The heat transfer test section is a smooth commercially drawn stainless steel type—304 circular tube, 12.95 mm i.d., 3.048 mm thick and 889 mm long. The electrical power is supplied by a d-c rectifier with an a-c input of 220V, 3ϕ, 60 c/s and an output range of 0–15V and 0–2000 A. The output voltage from the rectifier can be varied in twenty-four steps by means of knife switches. Copper bus bars 6.35 mm × 101.6 mm cross-section are silver soldered to each end of the test section. The inlet and outlet lines connecting the test section to the rest of the flow system are insulated electrically from the test section with asbestos washers. In order to limit the power level to the test section, a load bank comprising 16 resistors in parallel, each resistor having 0.285 Ω resistance, is connected in series with the test section, and mounted on the rectifier unit.

The liquid film formed at the outlet of the entrance section is removed through an extraction unit (50.8 mm long) placed at the inlet of the test section, and connected to a vacuum pump. The speed of the vacuum pump is adjusted so that the liquid film at the inlet of the test section is completely removed. The extractor unit has a unique design, and is described in [14].

The outer wall temperature distribution of the test section is measured by 29 chromel-alumel thermocouples of 24 gauge spot-welded to the outer surface. The thermocouples are spaced 38.1 mm apart longitudinally in a zig-zag manner displaced 120 deg apart circumferentially. Thermocouple #1 is fixed at 12.7 mm from the inlet, while thermocouple #29 is attached at 38.1 mm below the outlet of the test section. At three locations along the test section (z/D = 9.8, 36.27 and 62.74), three thermocouples are fixed equidistant around the circumference to check the circumferential nonuniformity of the surface temperature. To minimize the conduction errors, the thermocouple lead wires are wound around the tube for two turns before leaving the test section through 44 mm thick zirconia insulation. The error in the thermocouple output due to d-c interference caused by the existence of a very small gap between the thermocouple wires fixed on the surface has been calibrated by the current shut-off method first suggested in [17].

The thermocouple output is measured by a Hewlett Packard digital multimeter (Model 3465-B) having 1.0 μv sensitivity and 0.03 percent accuracy in the 0–20 mV range. The inside wall temperatures are estimated from the measured outer surface temperatures from the steady-state heat conduction solution for a hollow cylinder with uniform internal heat generation and insulated outer wall [18]. Thermocouples are placed at the center-line at the inlet and the outlet of the test section to estimate the bulk fluid temperature. At the inlet the bulk temperature is taken equal to the center-line temperature. No special provision is made for the measurement of bulk gas temperature at the outlet of the test section, which becomes difficult due to the impact of the droplets on the thermocouple probe. An improved design of the probe for measuring vapor superheat in dispersed flow systems has been recently reported by Nijhawan, et al. [11]. An attempt is however made to approximately estimate the bulk temperature at the exit from the measured center-line temperature and the measured surface temperature, assuming one-seventh power law for the temperature profile in the turbulent boundary layer. A pressure measurement is made at the inlet of the test section, and the pressure drop across the test section is measured by a water manometer. Other necessary pressure and temperature measurements in the loop are made.

The electrical power input to the test section is determined from the measured voltage drop across the test section, and the resistivity of the test section material corresponding to the measured average wall temperature of the test section. Resistivity values measured in a temperature range of 323–373 K using a standard resistor in the circuit are found to be within one percent of the literature value for

Nomenclature

$\bar{c}$ = bulk concentration, $W_d/(W_g/\rho_g + W_d/\rho_d)$, kg/m^3
c_p = specific heat, J/(kg·K)
C = mass concentration of vapor, kg/m^3
C_d = drag coefficient
d_{10}, d_{20}, d_{30}, d_{32} = characteristic mean droplet diameters, m; arithmetic, surface, volume and Sauter mean, respectively
d_{mn} = generalized characteristic drop size,

$$\int_0^\infty d_p^n P(d_p) d(d_p)$$

(m, n = 1, 2, or 3)
d_p = drop diameter, m
D = test section inner diameter, m
D_m = mass diffusivity of the vaporizing liquid, m^2/s
f_s = friction factor, $2\,\tau_w/\rho_g V_g{}^2$
G = mass velocity, kg/(m^2·s)
h = local heat transfer coefficient, W/(m^2·K)
h_{fg} = latent heat of vaporization, J/kg
h_m = mass transfer coefficient, m/s
k = thermal conductivity, W/(m·K)
k_d = drop deposition velocity, m/s
L = test section length, m
M = molecular weight, kg/kg mole
$\dot{m}$ = droplet evaporation rate, kg/s
N = droplet number density, droplets/m^3
N_0 = mass rate of deposition of droplets, kg/(m^2·s)
Nu = Nusselt number, hD/k_g
P = static pressure, bar
$P(d_p)$ = probability distribution of droplets
P_d = saturation pressure at T_d, bar
P_v = vapor pressure in the gas, bar
Pr = Prandtl number, $c_p\mu_g/k_g$
q = heat flux, W/m^2
r_0 = tube inner radius, m
$r_0{}^+ = u^* r_0/\nu_g$
R = universal gas constant, bar·m^3/(kg mole·K)
Re = Reynolds number, $V_g D/\nu_g$
Re$_d$ = drop Reynolds number, $|V_g - V_d|d_{20}/\nu_g$
S = slip ratio, V_g/V_d
Sc = Schmidt number, ν_g/D_m
Sh = Sherwood number, $h_m d_{20}/D_m$
T = temperature, K
T_s = saturation temperature at P, K
$T_s{}'$ = saturation temperature at P_v, K
$\overline{T} = (T_g + T_d)/2$
u^* = friction velocity, $V_g\sqrt{f_s/2}$, m/s
V_d = drop axial velocity, m/s
V_{dn} = drop impact velocity normal to the wall, m/s
V_g = superficial gas velocity, m/s
W = mass flow rate, kg/s
We = drop Weber number, $\rho_g(V_g - V_d)^2 \cdot d_{20}/\sigma$
We$_w$ = drop Weber number, $\rho_d V_{dn}{}^2\, d_{10}/\sigma$
X_A = actual quality, W_g/W
y = radial distance from the wall, m
y^+ = dimensionless radial distance, $u^* y/\nu_g$
z = axial distance from inlet, m
ϵ = effectiveness of wall-to-drop heat exchange, $q_{wd}/\{N_0[h_{fg}(T_e) + c_{pd}(T_e - T_d)]\}$
ρ = density, kg/m^3
μ = dynamic viscosity, N·s/m^2
ν = kinematic viscosity, m^2/s
τ = drop relaxation time based on Stokes drag, $d_{10}{}^2\,\rho_d/18\mu_g$, s
τ_w = wall shear stress, N/m^2
τ^+ = dimensionless drop relaxation time, $\tau\, u^{*2}/\nu_g$
ΔT_s = wall superheat, $(T_w - T_s)$, K

Subscripts

1 = single phase flow of gas
2 = two-phase
∞ = fully developed
b = bulk
c = center-line
d = droplet
e = evaporation
f = liquid, film
g = gas phase, bulk, air-water vapor mixture
in = inlet
n = normal to the wall
s = saturation
t = total mass flow of gas
v = vaporizing liquid vapor
w = wall
wd = wall-to-drop

Superscripts

$-$ = average sign

similar material [19], and therefore the literature values have been used in the present work for the entire temperature range. The temperature-dependent thermal conductivity data for the test section material are also taken from the literature [19] for similar material. Heat loss by natural convection from the test section insulation is evaluated using the measured outer surface temperature of the insulation and the room temperature, and employing a standard correlation. The heat loss from the insulation is found to be less than 4 percent of the total power input in the present experiments, and is taken into account in computing the average wall heat flux in the test section. Local heat flux is obtained from the average heat flux and a correction factor accounting for the variation of tube metal resistivity from end to end in conjunction with the calculated local wall temperature. In the present experiments, the local wall heat flux for $3 < z/D < 60$ (ignoring the region of end heat loss due to wall conduction) is found to vary within 3 to 9 percent about the average wall heat flux $\bar{q}_w$, and can be considered nearly uniform. All measurements are made after steady state is established as indicated by the thermocouple output. The measured wall temperature is believed to be accurate within ±3 K.

In order to check the system reliability, tests are initially conducted using single phase turbulent flow of air. The measured fully developed Nusselt numbers $\mathrm{Nu}_{1\infty}$ which are estimated to be accurate within 5 percent, are plotted in Fig. 2 over a range of Re from 13,500 to 70,000, and compared with the correlation recommended by Kays [20] for turbulent pipe flow of gases in the range $0.5 < \mathrm{Pr} < 1.0$ under a uniform wall heat flux boundary condition as given by

$$\mathrm{Nu}_{1\infty} = 0.022\,\mathrm{Re}_b{}^{0.8}\,\mathrm{Pr}_b{}^{0.6}\,(T_w/T_b)^{-0.5} \tag{1}$$

Since the results are in satisfactory agreement with the accepted correlation, the test set up is considered reliable and the accuracy of the results adequate. The measured entrance region Nusselt numbers in single phase flow are also satisfactorily compared with the data of Depew [21] for turbulent flow of air in a uniformly heated tube, which are approximated by [8]

$$\mathrm{Nu}_1(z) = \mathrm{Nu}_{1\infty}[1 + 1.25/(z/D)^{1.34}] \tag{2}$$

3 Analysis

The present analysis is similar to that of Koizumi et al. [8], but accounts for the temperature dependence of ϵ and the binary diffusion due to the presence of two components. The present analysis is more general in that it considers a two-component system, while only a one-component system is analyzed in [8]. As done in most of the previous models [2] superposition of the heat flux has been assumed. The total heat flux consists of wall-to-gas heat transfer and wall-to-droplet heat transfer. If the wall temperature is not high, as is the case in the present study, radiation can be neglected. Thus we have

$$q_w = q_{wg} + q_{wd} \tag{3}$$

The heat flux q_{wg} is calculated as

$$q_{wg} = h_1(T_w - T_g) \tag{4}$$

with h_1 determined locally from equations (1) and (2).

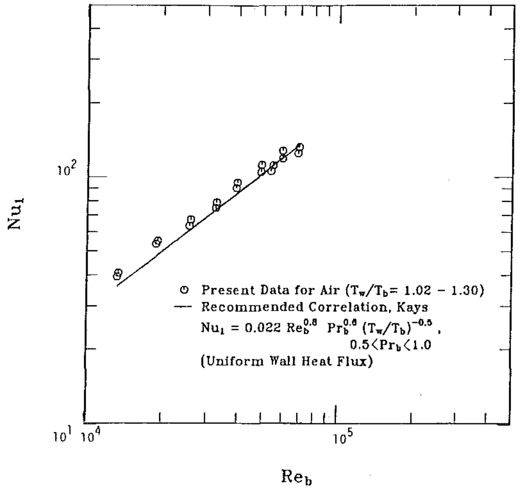

Fig. 2 Comparison of heat transfer data for single-phase turbulent flow of air

3.1 Wall-to-Droplet Heat Transfer.

The mass flux of droplets that deposit on the wall can be expressed as

$$N_0 = k_d \bar{c} f \tag{5}$$

where the deposition velocity k_d and the deposition factor f [2] are determined by the dynamics of drop deposition. Note that f represents the fraction of the drops entering the boundary layer which reach the wall. For large particles having dimensionless relaxation time $\tau^+ > 40$, the authors have recently obtained an expression for k_d [14], which describes the existing deposition data for a wide range of Re from 6000 to 2×10^5. The results of [14] show that k_d/u^* depends on Re and τ^+. The deposition factor f as obtained in [22] is equal to unity as the drop sizes in this study are large enough (i.e., $\tau^+ > 40$, see Table 1) to traverse the boundary layer.

The wall-to-drop heat transfer rate is given by

$$q_{wd} = \epsilon N_0[h_{fg}(T_e) + c_{pd}(T_e - T_d)] \tag{6}$$

where ϵ represents the effectiveness of heat exchange between the wall and the droplet. The evaporation temperature T_e in equation (6) is taken as

$$T_e = T_w, \quad \text{if } T_s' < T_w < T_s \tag{7}$$

$$T_e = T_s, \quad \text{if } T_w > T_s \tag{8}$$

Equation (7) is based on the consideration that for an air-water system when the wall temperature is less than the saturation temperature corresponding to the test section pressure, i.e., $T_w < T_s$, the deposited droplets, which are initially at T_d, approach and are maintained at T_w by absorbing energy from the tube wall, and evaporate at T_w due to diffusion, if T_w is greater than the saturation temperature T_s' corresponding to the partial vapor pressure in the air P_v; i.e., if $T_w > T_s'(P_v)$. The condition that $T_w > T_s'$ is satisfied in the present work since $T_w > T_g$, and $T_g \geq T_s'$. However in a steam/water droplet system, the droplets remain and evaporate at T_s, so that in equation (6) $T_e = T_s$, regardless of T_w.

Kendall and Rohsenow [23] report that in the surface wetting region total evaporation of drops has been observed. The recent experimental data of Styrikovich, et al. [7] for drop-wall contact time show the trend of an exponential decay with the wall superheat. In view of this information, the effectiveness ϵ for the air-water droplet system is modelled in the present work as follows:

$$\epsilon = 0, \quad T_w < T_s' \tag{9a}$$

$$= 1, \quad T_s' < T_w < T_s \tag{9b}$$

$$= \exp\,[1 - (T_w/T_s)^n], \quad T_w > T_s \tag{9c}$$

The form of equation (9c) is first introduced in reference [2]. For a steam/droplet system, $T_s' = T_s$, and we will have

$$\begin{aligned} \epsilon &= 0, \quad \text{for } T_w < T_s \\ &= \exp[1 - (T_w/T_s)^n], \quad \text{for } T_w > T_s \end{aligned}$$

3.2 Vapor-to-Droplet Heat Transfer.

The droplet Nusselt number in the presence of evaporation is given by

$$\mathrm{Nu}_d = \mathrm{Nu}_{d0} \ln(1 + B)/B \tag{10a}$$

where B is the Spalding transport number defined as

$$B = c_{pgf}(T_g - T_d)/[h_{fg}(T_d) - q_r/\dot{m}] \tag{10b}$$

with q_r, the radiation transfer to droplet, taken as zero in the present experiments. The Nusselt number for a single non-evaporating droplet moving in a gas stream Nu_{d0} is given by [24]:

$$\mathrm{Nu}_{d0} = 2 + 0.6\,\mathrm{Re}_d{}^{1/2}\,\mathrm{Pr}^{1/3} \tag{10c}$$

where the drop Reynolds number Re_d is defined as

$$\mathrm{Re}_d = |V_g - V_d| d_{20}/\nu_g \tag{10d}$$

The droplet axial velocity V_d is determined from the equation of the motion of the droplet [8]:

$$\frac{dV_d}{dz} = \frac{1}{V_d}\left[\frac{3}{4} C_D \frac{\rho_{gf}}{\rho_d} \frac{{d_{20}}^2}{{d_{30}}^3}(V_g - V_d)^2 - g - \frac{1}{\rho_d}\frac{dP}{dz}\right] \tag{11a}$$

The drag coefficient C_D in the presence of evaporation is taken as [25]:

$$C_D = C_{D0}/(1 + B) \tag{11b}$$

where C_{D0} is the drag coefficient for a nonevaporating droplet. The heat transfer rate from the gas per unit surface area of the droplet is given by

$$q_{gds} = h_d(T_g - T_d) \tag{12}$$

where $h_d = \mathrm{Nu}_d k_{gf}/d_{20,}$ and Nu_d is given by equation (10a).

Assuming uniform temperature in the droplet, the droplet temperature is given by the energy transport relation involving heat and mass transfer as [14, 34]:

$$V_d\left(\frac{\pi}{6} {d_{30}}^3 \rho_d c_{pd}\right)\frac{dT_d}{d\,z} = q_{gd} - \dot{m}\, h_{fg}(T_d) \tag{13a}$$

In equation (13a), the gas-to-droplet heat transfer q_{gd} is given by

$$q_{gd} = q_{gds} \cdot \pi\, d^{202} \tag{13b}$$

The mass transfer rate from the droplet $\dot{m}$ is given by:

$$\dot{m} = (\pi\, {d_{20}}^2)\, h_m[C(T_d) - C_\infty] \tag{13c}$$

where

$C(T_d)$ = mass concentration of vapor at the droplet surface

$$= \frac{P_d M_v}{RT_d},$$

C_∞ = mass concentration of vapor in the air $= \dfrac{P_v M_v}{RT_g}$

$$\mathrm{Sh} = h_m d_{20}/D = 2 + 0.6\,(\mathrm{Sc})^{1/3}\,{\mathrm{Re}_d}^{1/2} \tag{13d}$$

3.3 Heat Transfer Relations. The total heat transferred to the droplets per unit surface area of droplets is written as [8]

$$q_{ds} = q_{gds} + \frac{4\, q_{wd}}{\pi D {d_{20}}^2 N} \tag{14a}$$

where N is the local number density of droplets (per unit volume of gas) and given by

$$N = \frac{W(1 - X_A)}{\left(\frac{\pi}{6} {d_{30}}^3\right) \rho_d \frac{\pi}{4} D^2\, V_d} \tag{14b}$$

It is assumed in the analysis that the droplets do not break up. This assumption is justified in the present experiments, as will be mentioned later in the text. The axial change of the drop diameter d_{30}, the actual quality X_A and the gas temperature T_g are given by [8]:

$$\frac{d}{dz}(d_{30}) = \frac{2\, q_{ds}}{V_d \rho_d h_{fg}(T_d)} \frac{{d_{20}}^2}{{d_{30}}^2} \tag{15}$$

$$\frac{dX_A}{dz} = \frac{\pi^2 D^2 {d_{20}}^2 N q_{ds}}{4\, W h_{fg}(T_d)} \tag{16}$$

$$\frac{dT_g}{dz} = \frac{1}{X_A c_{pg}}\left[\frac{\pi D q_w}{W} - \{h_{fg}(T_d) + c_{pg}(T_g - T_d)\}\frac{dX_A}{dz}\right] \tag{17}$$

The local two-phase heat transfer coefficient, h_2, is defined as

$$h_2 = q_w/(T_w - T_g) \tag{18}$$

3.4 Solution Procedure. The characteristic drop diameters d_{10}, d_{20} and d_{30} are estimated from the drop size relations developed by Tatterson, et al. [26] using the drop size measurements of many investigators. Their relations are

$$d_{32}/d_{10} = 4.667, \quad d_{32}/d_{20} = 2.917, \quad d_{32}/d_{30} = 2.059 \tag{19}$$

The calculations have been performed using a finite difference explicit method with an axial interval $\Delta z = 0.01$ m. At the inlet of the test section $z = 0$, the slip ratio S is taken as 1·1. The solution is relatively insensitive to the initial value of S. The experimental value of the local wall heat flux is determined from the measured average wall heat flux and the local resistivity of the test section corresponding to the local calculated wall temperature obtained by solving equations (1–19). The initial values of T_g and T_d are taken from the output of the thermocouples at the inlet. The term dP/dz in equation (11a) is obtained from the measured pressure drop along the test section, and assuming linear variation of pressure along the test section. The mass fraction of water vapor at the inlet is taken as zero. Using the information regarding the various quantities at station i, the values of V_d, T_d, d, X_A, T_g, T_w and h_2 at station $i + 1$ are calculated by solving equations (1–19). The calculation proceeds up to the end of the test section $z = L$, and is repeated using the improved wall temperature to obtain the improved local wall heat flux. The interval $\Delta z = 0.01$ m and three iterations are found to be sufficient to insure convergence of solution for T_w. The property data for pure air, pure water vapor and air-water vapor mixtures are taken from [27].

4 Results and Discussion

The test conditions for the dispersed flow heat transfer are displayed in Table 1, showing the mass velocity, average wall heat flux, inlet pressure, droplet concentration, drop size and drop impact velocity. The values of k_d calculated from the theory of [14] are also shown in Table 1. The analysis is correlated with the measurements of wall temperatures assuming different values for the free parameter n in equation (9c), and it is found that a value of $n = 1$ is able to satisfactorily describe the experimental system response at all the mass velocities used in this study. This leads to the present relation for ϵ as

$$\epsilon = 0, \quad T_s' < T_w < T_s \tag{20a}$$

$$= 1, \quad T_w < T_s \tag{20b}$$

$$= \exp\,[-\Delta T_s/T_s], \quad T_w > T_s \tag{20c}$$

Experiments of Koizumi, et al. [8], who obtains a constant value of $\epsilon = 0$ or $\epsilon = 0.2$ independent of T_w, involve a maximum wall superheat in the range of 40–100 K. Obviously a value of $\epsilon = 0$ at these

Table 1 Test conditions for dispersed flow heat transfer

Run #,	P_{in} bar	G kg/m²·s	$\bar{c}_{\mathrm{in}}$ kg/m³	$\bar{q}_w$ kW/m²	$W_g \times 10^3$ kg/s	$d_{10,\mathrm{in}}$ μm	${\tau_{\mathrm{in}}}^+$	ΔP bar	$V_{dn,\mathrm{in}}$ m/s	$k_{d,\mathrm{in}}$ m/s
1	1.23	82.73	0.0207	23.69	10.75	8.6	139	.045	1.38	0.29
2	1.22	82.76	0.0207	29.59	10.76	8.6	139	.050	1.39	0.29
3	1.22	82.82	0.0207	36.20	10.77	8.6	140	.055	1.39	0.29
4	1.10	52.30	0.0197	14.06	6.79	13.8	176	.023	0.98	0.21
5	1.12	52.26	0.0197	18.87	6.79	13.7	172	.024	0.96	0.21
6	1.10	51.93	0.0197	24.20	6.79	13.9	176	.027	0.96	0.21
7	1.07	30.36	0.0107	6.40	3.97	23.6	208	.0093	0.51	0.12
8	1.07	30.75	0.0107	8.34	4.02	23.4	210	.0093	0.52	0.12
9	1.07	30.36	0.0107	14.54	3.97	23.6	208	.00114	0.51	0.12

low wall superheats is in contrast with the trend of data shown in [2]. The difference between the present model ($n = 1$, in equation (9c)) and the model of [2] suggesting $n = 2$, may be attributed to the fact that a more precise value of k_d is employed in the present work. Interestingly, a value of $n = 1$ as proposed here agrees with the form of the correlation suggested by Tong, et al. [28] for the transition boiling region.

Figures 3(a)–3(c) show the measured and the calculated wall temperature distributions in air-water dispersed flow at $G = 82.8$, 52.2 and 30.5 kg/m²·s, respectively, with $\bar{q}_w$ as a parameter. It is seen that near the inlet of the test section the measured wall temperatures show an increasing trend with axial distance implying the existence of dryout conditions. The absence of a liquid film on the wall is attributed to the fact that the liquid droplet evaporation at the wall dominates the inadequate liquid supply by deposition on the wall [29]. It is interesting that the dryout occurs even before the surface reaches T_s corresponding to the test section pressure, because of the mass transfer as indicated by equation (9b). The negative slope in the measured T_w near the exit of the test section is due to longitudinal heat loss, which is found to be less than 0.3 percent of the total heat input, and is considered negligible.

It is seen from Figs. 3(a)–3(c) that the calculated wall temperatures are in fair agreement with the measurements over most of the portion of the tube length except near the entrance. Near the entrance, the calculated wall temperatures are found to be higher than the measured wall temperatures. This is mainly ascribed to the entrance effects on deposition, as analogous to heat and mass transfer in single phase flows, while the theory of [14] used here for obtaining k_d assumes a fully developed concentration profile. For instance, it is shown by the deposition data of Cousins and Hewitt [30] that the value of k_d near the entrance is about 60 percent higher than the corresponding fully developed value. It can be seen from equations (3–6) that for a prescribed q_w, consideration of a higher value of k_d near the entrance than that given by [14] would cause an increase in q_{wd} and therefore a decrease in q_{wg}, resulting in lower calculated T_w which is closer to the measured wall temperature. However, no satisfactory deposition theory now presently exists to account for the entrance effects showing the dependence of k_d on z/D. The results seem to suggest that the entrance effects of deposition probably persist up to about 10 to 20 tube diameters in the present experiments.

The measured wall temperatures in the present experiments are below about 540 K, which is less than the minimum film boiling temperature of water at atmospheric pressure [10]. Therefore, the proposed correlation for the effectiveness ϵ given by equation (20c) is applicable primarily in the nucleate and the transition boiling region. Extrapolation of equation (20c) to the film boiling region should however be viewed with caution, since the vapor film formed will influence ϵ through the fluid properties. In such cases, the magnitude of ϵ is itself rather small, as evidenced by the data shown in [2], and therefore becomes less important.

The comparisons also reveal that ϵ is primarily dependent on T_w, but essentially independent of G which controls the drop impact velocity V_{dn} normal to the wall. The values of V_{dn} at the inlet calculated from the deposition model [14] are shown in Table 1, and vary from 0.5 m/s to 1.4 m/s as G increases from 30 to 83 kg/m²·s. The present result showing the weak dependence of n on V_{dn} is in qualitative agreement with the data of Corman [5], and also with the recent observation of Styrikovich, et al. [7] for water droplets in air using a photographic method. The latter reports that the main heat transfer (conduction followed by boiling) takes place during the contact between the wall and the droplet. They mention that while the electrical contact time of the superheated surface temperature is significant, the effect of drop normal velocity on the electrical contact time is insignificant if the deposited drop does not break out, which is the case in our present experiments, since $\mathrm{We}_w \ll 70$ [31]. In the present experiments, the maximum value of We_w (based on drop density ρ_d and drop velocity normal to the wall V_{dn}) varies from 0.33 at $G = 83$ kg/m²·s to 0.13 at $G = 30$ kg/m²·s. The drop velocity V_{dn} is varied from 0 to 1.5 m/s in their experiments, and is comparable to that employed in the present study.

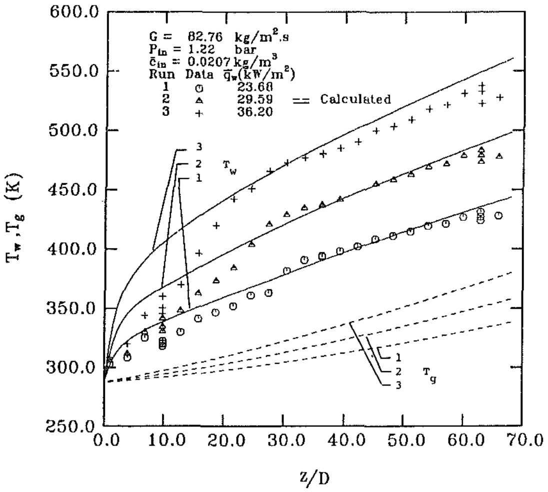

Fig. 3(a) Comparison of calculated and experimental wall temperature distributions in air-water dispersed flow

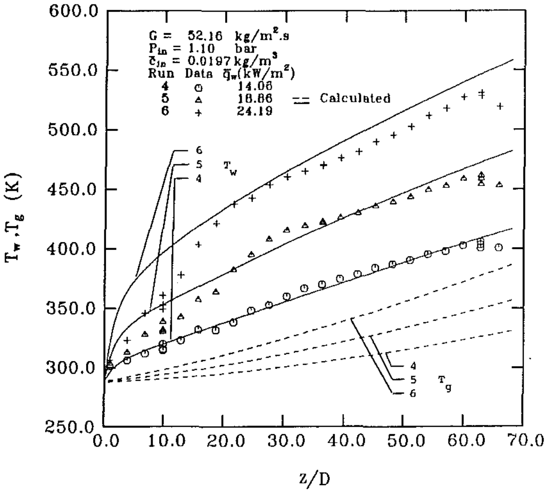

Fig. 3(b) Comparison of calculated and experimental wall temperature distributions in air-water dispersed flow

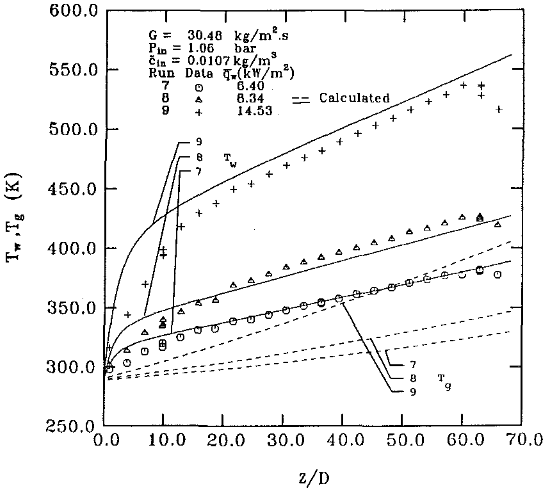

Fig. 3(c) Comparison of calculated and experimental wall temperature distributions in air-water dispersed flow

The droplet break-up in the gas stream is assessed by the Weber number We, based on gas density ρ_g, and the relative axial velocity between the drop and the gas. It is found that for all the test conditions of the present study, the value of We based on d_{20} is less than 0.01. The corresponding value of We based on d_{30} is less than 0.014. This value is much less than the critical Weber number, We_c of 6.5 for water droplets in an accelerating gas stream, according to the experiments of Isshiki [32], and We_c of close to 7 as used by Plummer [33]. It is therefore considered that the droplets do not break up in the gas stream, as assumed in the analysis.

The calculated droplet temperatures T_d are found to be nearly constant along the test section and range from 284–316 K in all the experiments, while the maximum calculated gas temperature is about 405 K for run #9 of the present data. This shows that there is significant thermal nonequilibrium present between the two-phases [29].

The distribution of calculated gas temperature T_g are also shown in Figs. 3(*a*)–3(*c*). The calculations have shown that the estimated bulk temperatures at the exit are always lower than those predicted by the analysis. As mentioned earlier, this discrepancy is due to the fact that the droplets can hit the thermocouple probe, thus making accurate measurement of T_g quite difficult.

The measured and predicted heat transfer enhancement factor h_2/h_{1t} are also shown in Figs. 4(*a*)–4(*c*), where h_{1t} corresponds to the same total mass velocity with gas only flowing in the tube. It is observed that the measured h_2/h_{1t} decreases with an increase in wall heat flux. Since an increase in wall heat flux is accompanied by an increase in wall temperature, it can be interpreted that h_2/h_{1t} decreases with increase in wall temperature, while h_{1t} is nearly independent of T_w, except for a property dependence as shown by equation (1). The dependence of h_2 on T_w is attributed to the presence of droplets in the gas, and the effect of T_w on ϵ. Similar dependence of h_2 on T_w has also been observed by Takagi, et al. [1] in their study on binary mist flow.

Very little is known about the behavior of the thermal entrance lengths for droplet flow. The present data shown in Figs. 4(*a*)–4(*c*) suggest that the two-phase thermal entrance length decreases with increase in wall temperature, and is higher than the entrance lengths for single phase gas flow, which are about 10–15 tube diameters. The results show that the theory represents the trends of the observed data for h_2/h_{1t}. However, in the region of 15 diameters downstream of the inlet, the theory underpredicts the measured h_2/h_{1t}. This is to be expected due to the possible entrance effects on drop deposition as explained earlier in the text. For z/D in excess of about 15, the theory fairly agrees with the experimental data.

Figure 5 shows the ratio q_{wd}/q_w as a function of axial length for a particular mass velocity. It is seen that at lower heat flux, q_{wd} is as high as 60 percent of q_w near the entrance, and decreases downstream due to increase in wall temperature, becoming about 10 percent of q_w at the exit. With an increase in wall heat flux, q_{wd}/q_w decreases, as is to be expected.

5 Conclusion

Experiments have been performed on heat transfer in the post dryout region in a two-phase two-component air-water dispersed system in a vertical tube at low pressure and low mass velocities. A theoretical analysis has also been carried out in conjunction with the experimental data, and the following conclusions can be drawn.

1 The effectiveness of wall-to-drop heat transfer ϵ is found to be primarily dependent on wall temperature, but independent of the mass velocity, for surface temperatures below the minimum film

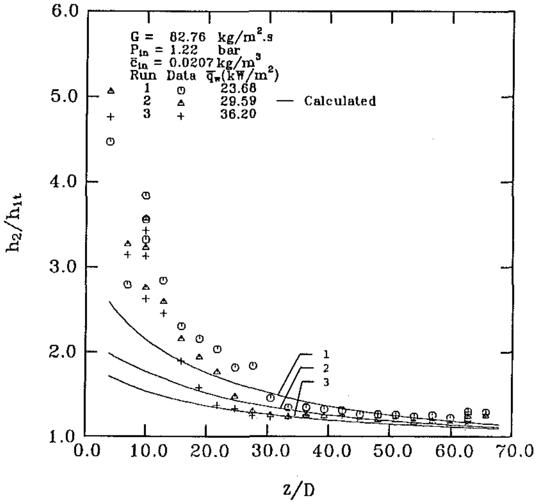

Fig. 4(*a*) Comparison of calculated and measured ratio of two-phase to single-phase heat transfer coefficient in air-water dispersed flow

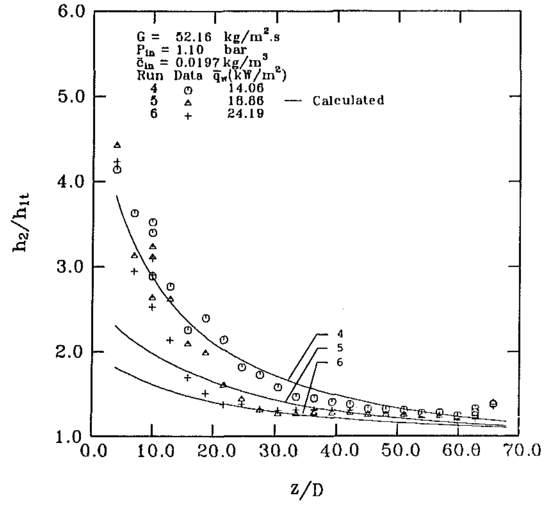

Fig. 4(*b*) Comparison of calculated and measured ratio of two-phase to single-phase heat transfer coefficient in air-water dispersed flow

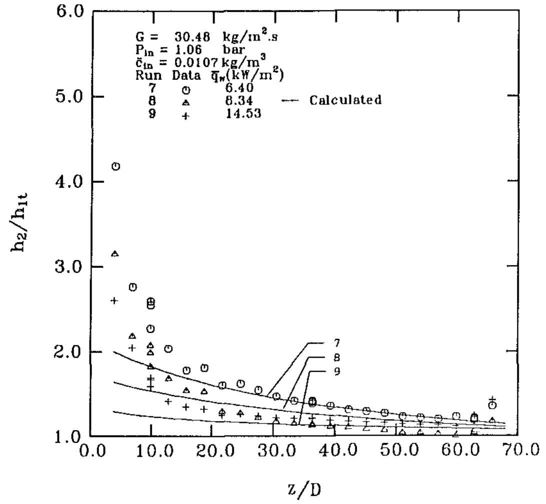

Fig. 4(*c*) Comparison of calculated and measured ratio of two-phase to single-phase heat transfer coefficient in air-water dispersed flow

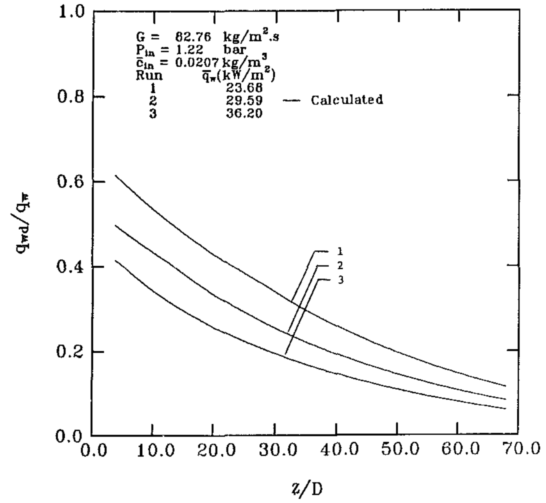

Fig. 5 Distribution of wall-to-drop heat flux along the test section

boiling temperature.

2 The two-phase heat transfer coefficient h_2 decreases with an increase in wall temperature.

3 The two-phase thermal entrance length is larger than that for single phase flow, and decreases with an increase in wall temperature.

Acknowledgment

This work was supported by a National Science Foundation Grant ENG 78-06211.

References

1 Takagi, T., and Ogasawara, M., "Some Characteristics of Heat and Mass Transfer in Binary Mist Flow," *Proceedings of the Fifth International Heat Transfer Conference*, Tokyo, 1974.

2 Ganic, E. N., and Rohsenow, "Dispersed Flow Heat Transfer," *International Journal Heat and Mass Transfer*, Vol. 20, 1977, pp. 855–866.

3 Pederson, C. O., "The Dynamics and Heat Transfer Characteristics of Water Droplets upon a Heated Surface," Ph.D. Thesis, Carnegie Institute of Technology, 1967.

4 Wachters, L. H. J., and Westerling, N. A. J., "The Heat Transfer from a Hot Wall to Impinging Water Drops in the Spheroidal State," *Chemical Engineering Science*, Vol. 21, 1966, pp. 1047–1056.

5 Corman, J. C., "Water Cooling of a Thin, High Temperature Metal Strip," Ph.D. Thesis, Carnegie Institute of Technology, 1966.

6 Itaru Michiyoshi and Kunihide Makino, "Heat Transfer Characteristics of Evaporation of a Liquid Droplet on Heated Surfaces," *International Journal of Heat and Mass Transfer*, Vol. 21, 1978, pp. 605–613.

7 Styricovich, M. A., Baryshev, Yu. V., Tsiklauri, G. V., and Grigorieva, M. E., "The Mechanism of Heat and Mass Transfer between a Water Drop and a Heated Surface" *Proceedings of the Sixth International Heat Transfer Conference*, Toronto, 1978, pp. 239–243.

8 Koizumi, Y., Ueda, T., and Tanaka, H., "Post Dryout Heat Transfer to R-113 Upward Flow in a Vertical Tube," *International Journal of Heat and Mass Transfer*, Vol. 22, 1979, pp. 669–678.

9 Chiang, T., France, D. M., and Carlson, R. D., "Post-CHF Heat Transfer and Transition Boiling Characteristics in an LMFBR Steam Generator Tube," ANL-CT-79-14, 1978.

10 Berenson, P. J., "Film Boiling Heat Transfer from a Horizontal Surface," ASME JOURNAL OF HEAT TRANSFER, Vol. 83, Aug. 1961, pp. 351–358.

11 Nijhawan, S., Chen, J. C., Sundaram, R. K., and London, E. J., "Measurement of Vapor Superheat in Post-Critical-Heat-Flux Boiling," in *Nonequilibrium Interfacial Transport Processes* (eds. J. C. Chen and S. G. Bankoff), ASME-AIChE, Aug. 1979, pp. 45–51.

12 Groeneveld, D. C., and Delorme, G. G. J., "Prediction of Thermal Nonequilibrium in the Post-Dryout Regime," *Nuclear Engineering and Design*, Vol. 51, 1976, pp. 143–155.

13 Chen, J. C., Sundaram, R. K., and Ozkaynak, F. T., "A Phenomenological Correlation for Post-CHF Heat Transfer," USNRC Report NUREG-0237, June 1977.

14 Mastanaiah, K., "Experimental and Theoretical Investigation of Droplet Deposition and Heat Transfer in Air-Water Dispersed Flow," Ph.D. Thesis, Dept. of Energy Engng., University of Illinois at Chicago Circle, 1980.

15 Nukiyama, S., and Tanasawa, Y., "An Experiment on the Atomization of Liquid by Means of an Air Stream," Reports 1 and 4, *Trans. JSME*, Vol. 4, 1938, p. 86 and Vol. 5, 1939, p. 68.

16 Wallis, G. B., *One-Dimensional Two-Phase Flow*, McGraw-Hill, New York, 1969.

17 Davenport, M. E., Magee, P. M., and Leppert, G., "Thermocouple Attachment to a Direct-Current Heater," ASME JOURNAL OF HEAT TRANSFER, Vol. 84, May 1962, pp. 187–188.

18 Hynek, S. J., Rohsenow, W. M., and Bergles, A. E., "Forced Convection, Dispersed-Flow Film Boiling," M.I.T. Report No. 72718-91, 1974.

19 Dickinson, N. L., and Welch, C. P., "Heat Transfer to Supercritical Water," *Trans. ASME*, Apr. 1958, pp. 746–752.

20 Kays, W. M., *Convective Heat and Mass Transfer*, McGraw-Hill, New York, 1966.

21 Depew, C. A., "Heat Transfer to Air in a Circular Tube Having Uniform Heat Flux," ASME JOURNAL OF HEAT TRANSFER, Vol. 84, May 1962, pp. 186–187.

22 Ganic, E. N., and Rohsenow, W. M., "On the Mechanism of Liquid Drop Deposition in Two-Phase Dispersed Flow," ASME JOURNAL OF HEAT TRANSFER, Vol. 101, May 1979, pp. 288–294.

23 Kendall, G. E., and Rohsenow, W. M., "Heat Transfer to Dispersed Flows and Sprays: The Liquid Contribution," *Proceedings of Second Multi-Phase Flow and Heat Transfer Symposium-Workshop*, Miami Beach, Florida, 1979.

24 Rane, Anil, and Yao, S. C., "Heat Transfer of Evaporating Droplet Flow in Low Pressure Systems," ASME Paper No. 79-WA/HT-10, 1979.

25 Eisenklam, P., Arunachalam, S. A., and Weston, J. A. "Evaporation Rates and Drag Resistance of Burning Drops," in *11th Symposium (International) on Combustion*, 1967, pp. 715–728.

26 Tatterson, D. F., Dallman, J. C., and Hanratty, T. J., "Drop Size in Annular Gas-Liquid Flows," *AIChE Journal*, Vol. 23, 1977, pp. 68–76.

27 Harpole, G. M., "Water Droplet Evaporation in High Temperature Surrounds," ASME Paper No. 79-WA/HT-6, 1979.

28 Tong, L. S., "Heat Transfer Mechanisms in Nucleate and Film Boiling," *Nuclear Engineering and Design*, Vol. 21, 1972, pp. 1–25.

29 Collier, J. G., *Convective Boiling and Condensation*, McGraw-Hill, 1972.

30 Cousins, L. B., and Hewitt, G. F., "Liquid Phase Mass Transfer in Annular Two-Phase Flow: Droplet Deposition and Liquid Entrainment," AERE-R 5657, 1968.

31 Ueda, T., Enomoto, T., and Kanetsuki, M., "Heat Transfer Characteristics and Dynamic Behavior of Saturated Droplets Impinging on a Heated Vertical Surface," In *Proceedings of the 15th Japan National Heat Transfer Symposium*, 1978, pp. 283–285.

32 Isshiki, N., "Theoretical and Experimental Study on Atomization of Liquid Drop in High Speed Gas Stream," Report No. 35, Transportation Technical Research Institute, Tokyo, Japan, 1959.

33 Plummer, D. N., "Post Critical Heat Transfer to Flowing Liquid in a Vertical Tube," Ph.D. Thesis, Mech. Engng. Dept., M.I.T., 1976.

34 Habib, I. S., "Spray Quenching in a Ventilated Duct Fire," ASME JOURNAL OF HEAT TRANSFER, Vol. 102, Feb. 1980, pp. 110–114.

A. Segev
L. J. Flanigan
R. E. Kurth
R. P. Collier
Battelle Columbus Laboratories,
505 King Avenue,
Columbus, Ohio 43201

Experimental Study of Countercurrent Steam Condensation

An experimental study of steam condensation on subcooled liquid films in countercurrent flow has been conducted in a small inclined test apparatus having a rectangular cross-section. Condensation heat transfer coefficients were determined and the dependence on steam and water flow rates, the degree of subcooling, and test section inclination were all studied. The results were correlated in terms of local parameters for the complete penetration and bypass regions. It was found that the local Nusselt number increases with steam and liquid Reynolds numbers and liquid Prandtl number when no bypass occurs. In the bypass region the Nusselt number drops sharply due to the strong effects of the reduced liquid film flow rate. It is shown that the local heat transfer coefficient may be related to the turbulence intensity in the liquid film which suggests that a general turbulence-centered model can be constructed.

Introduction

During a postulated loss-of-coolant accident (LOCA) due to a break in a cold leg pipe in a pressurized water reactor (PWR), emergency core cooling (ECC) water would be injected to provide cooling for the reactor core. The depressurization during the blowdown phase of the LOCA would result in reverse core steam flow through the downcomer annulus, with the potential to retard or even to prevent liquid penetration to the lower plenum.

Extensive experimental studies of the liquid behavior in the downcomer and the resultant penetration has been conducted with steam-water flows in 1/15- and 2/15-scale models of a PWR at Battelle's Columbus Laboratories [1, 2] and in 1/30- and 1/15-scale models at Creare, Inc. [3, 4]. It was shown that in these scaled models the penetration of liquid into the lower plenum of the pressure vessel is highly dependent on the condensation rate of core steam on the subcooled ECC water. However, the processes which control the condensation mechanism in countercurrent flow are not well understood.

Condensation rates in a direct-contact mode have been studied in a variety of flow configurations and geometries. Apparent heat transfer coefficients may vary by several orders of magnitude from less than 1 kW/m^2°C in stratified open channel flow [5] to 1700 kW/m^2°C obtained from an oscillating bubble in a cold water jet [6], making it difficult to predict a condensing heat transfer coefficient in general.

One of the flow configurations which suffers from lack of experimental data is the configuration pertinent for ECC penetration, namely, countercurrent flow. Most of the studies on direct contact condensation of steam on subcooled water films in countercurrent flows involve flows in small-scaled models of PWR's. Due to the highly agitated steam-water interactions in this geometry, the effects of condensation on the flow behavior in the downcomer can only be estimated. This is done by defining an overall condensation efficiency parameter (f) which reflects the average degree of thermal nonequilibrium in the system. It is defined so that $f = 1$ when the two counter-current phases mix perfectly and achieve thermal equilibrium. This bypasses the problem of determining surface areas and heat transfer coefficients, relying instead on evaluating the dependency of f on flow conditions by correlating liquid penetration data.

To further the understanding of condensation effects on ECC penetration, an experimental study has been conducted in a small inclined test apparatus having a rectangular cross-section. The main objective of the experimental study was to evaluate the condensation heat transfer of saturated steam in direct contact with subcooled water in countercurrent flow. The dependence on steam and water flow rates, the degree of subcooling, and test section inclination angle were all studied.

Experiment

A schematic diagram of the experimental test section is shown in Fig. 1. Saturated steam and subcooled liquid flow in opposite directions through a rectangular cross-section, 106.6 cm long and 15.2 cm wide. The channel height may be adjusted by moving the top plate, allowing operation at any desired gap height up to 15.2 cm. Preliminary experiments with 2.5 cm gap height resulted in severe liquid oscillations due to liquid bridging over the gap at relatively low steam flow rates. Thus, the gap height in the present experiments was set at 5.1 cm which is large enough to eliminate any liquid bridging.

The test section is constructed of aluminum except for the sides which are formed from polished Pyrex glass to allow visual observation and photography of flow behavior. The bottom plate is 1.3 cm thick with a 45.7-cm long, 7.6-cm thick section, which may be utilized for heat storage in nonadiabatic studies.

To provide a uniform flow of steam into the test section, steam is supplied through an inlet plenum chamber and a perforated plate as shown in Fig. 1. A second plenum chamber is fitted to the test section at the steam outlet region and serves as an expansion chamber to minimize condensation on the bypassed water. Inlet and outlet volumetric steam flow rates are measured with turbine flow meters.

Liquid flow is introduced to the test section through an adjustable inlet port which spans the test section width. The height of the port above the plate is adjustable to provide a smooth liquid film at the entrance region. The volumetric flow rate of the inlet liquid is measured with a turbine flow meter. Liquid exits the test section through a similar adjustable outlet port and is collected in a tank. The weight of the tank is monitored by a load cell, from which the outlet liquid mass flow rate is determined. The height of the outlet port is adjusted to minimize interference with the inlet steam flow.

The test section is mounted such that it can be positioned at any inclination from horizontal to vertical. Three inclinations were

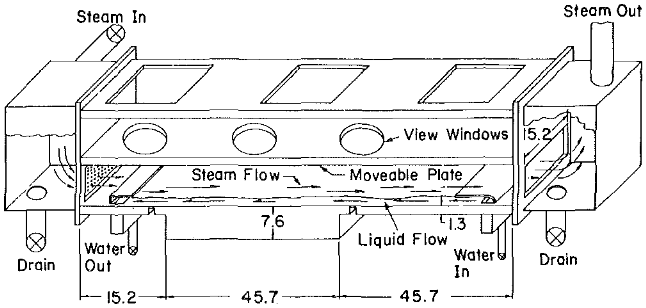

Fig. 1 Schematic sketch of experimental test section (all dimensions are in cm)

Contributed by the Heat Transfer Division for publication in the JOURNAL OF HEAT TRANSFER. Manuscript received by the Heat Transfer Division, June 20, 1980.

studied: 0.5, 17, and 45 deg from the horizontal. It was found that the results with 0.5 deg inclination were different in comparison with the 17 and 45 deg positions. Since the inclined positions (17 and 45 deg) represent the pertinent configuration more closely, the results obtained with the 0.5 deg inclination will not be discussed here but can be found in reference [7].

Twelve thermocouples are used to monitor the liquid and solid temperatures inside the test section. A schematic sketch of their location along the centerline is shown in Fig. 2. Six thermocouples are imbedded in the solid surface at various axial locations, 1.6 mm ($^1/_{16}$ in.) from the solid-liquid interface. Liquid temperatures are measured along the test section by six thermocouples, four of which are mounted in the top plate and two in the bottom plate. Wall surface temperatures were found to represent the film temperatures quite well. When no significant bypass occurs, the temperatures measured by thermocouples situated in the liquid film are within about ±2°C of the surface temperatures. However, when large waves are generated at the interface or when significant reduction in film thickness occurs, liquid temperature measurements are not reliable since the liquid thermocouples are situated occasionally in the steam, resulting in temperature readings that are higher than the wall surface temperatures. Measurements also have shown that the local temperature gradient in the direction normal to the flow is almost zero, except near the steam-water interface where temperatures drop from saturation to the average film temperature over a thin layer.

Liquid film thickness is measured with micrometer-mounted conductivity probes located immediately upstream and downstream of the thick section. These measurements were conducted at the beginning of each test when only liquid was flowing in the test section. The average thickness along the film was correlated as a function of liquid flow rate. As one may expect, the film thickness correlations for the inclined positions are approximated quite well by the Nusselt equation.

All measurements, other than film thickness, are recorded on magnetic tape every 20 ms by a minicomputer-based data acquisition system. The data are further processed on the in-house CDC computer.

Tests were conducted at atmospheric pressure. Each test was conducted as follows: A predetermined liquid flow to the test section was initiated. Inlet and outlet port heights were adjusted to produce a smooth liquid film. Film thicknesses were measured and recorded. Steam flow to the test section was begun, increasing in small increments. For each steam flow rate the liquid drain valve, which is situated between the outlet port and the weigh tank, was adjusted to minimize the escape of steam through the liquid drain line. When liquid and adjacent wall thermocouples indicated a steady-state situation, measurements were recorded for 30 s. The ranges of water and steam flow rates were limited by the desire to maintain less than total condensation on the film to avoid uncertainties related to temperature profile evaluation.

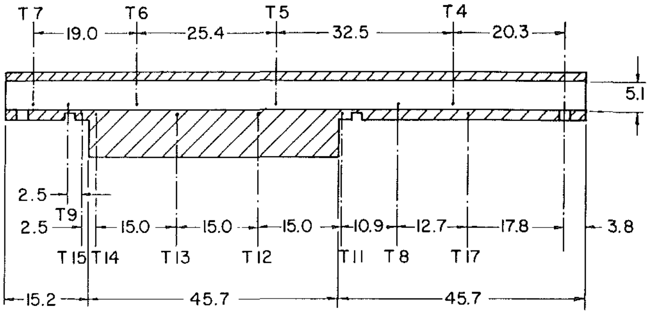

Fig. 2 Schematic sketch of thermocouple location (all dimensions are in cm)

Experimental Results

Visual observations of the flow pattern in the test section revealed that the interface between the steam and the countercurrent liquid film is characterized by the presence of wavelike disturbances. Depending mainly on the inlet steam flow rate, different interfacial conditions may be observed. At very low steam flow rates the interface remains smooth, corresponding to complete steam condensation on the lower portion of the liquid film. An increase of steam flow results in the appearance of two-dimensional waves which extend over the entire channel width. This range of steam flow is defined as Region A. Three-dimensional waves are generated for higher inlet steam flows, giving the surface a pebbled appearance.

At the high range of inlet steam flow rates, large amplitude roll waves are formed, traveling upstream on the liquid film interface. As the waves move upstream, their amplitude and intensity decay until they disappear. The distance of travel depends on the steam flow rate. We define the range of steam flows which resulted in three-dimen-

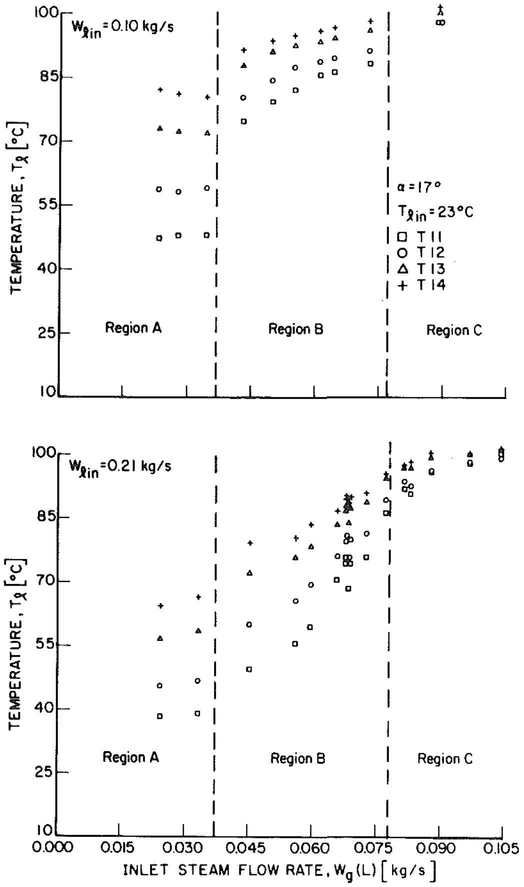

Fig. 3 Liquid film temperatures as functions of inlet steam flow rate

Nomenclature

b = width of channel
C = constant
c_p = specific heat of liquid
f = condensation efficiency
h = heat transfer coefficient
h_{fg} = heat of vaporization
k = thermal conductivity
L = length of channel

n_1, n_2, n_3 = exponents
Nu = Nusselt number
Pr = Prandtl number
Re = Reynolds number
T = temperature
T_s = saturation temperature
t = film thickness
W = mass flow rate
z = coordinate

α = inclination angle
μ = viscosity

Subscripts

g = vapor
in = inlet conditions
ℓ = liquid
x = phase x

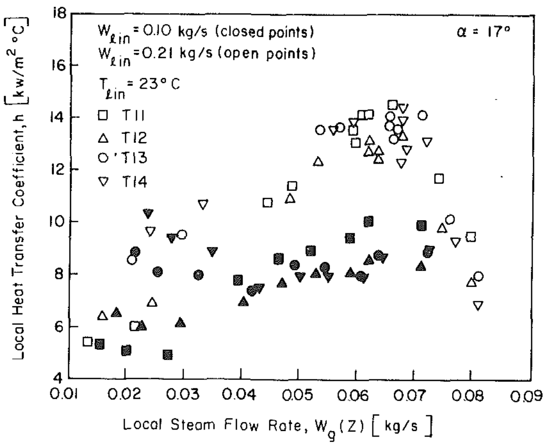

Fig. 4 Local heat transfer coefficient for α = 17 deg and low liquid flow rates

sional waves or roll waves with complete penetration as Region B. As the waves reach the liquid inlet injector, partial bypass occurs (Region C). When steam flows are high enough to cause a complete bypass situation, the lower part of the channel dries out and liquid is circulated from the liquid injector toward the steam outlet region by flowing over the liquid injector. It is interesting to note that even with these high steam flow rates no significant entrainment of droplets is observed.

In most cases the liquid temperatures are well correlated with the interfacial structure. An example is shown in Fig. 3, where temperature measurements at four stations along the plate (T11–T14) are described as a function of inlet steam flow rate for 17 deg inclination, inlet liquid temperature of 23°C and two inlet liquid flow rates. For steam flow rates less than 0.037 kg/s we notice that the temperature at each station is almost constant indicating that condensation in this region (Region A) is independent of steam flow. This is probably because the two-dimensional waves which are generated in this region do not significantly affect the turbulence intensity of the liquid film. Note that the temperature level is inversely proportional to the inlet liquid flow rate, i.e., lower temperatures are measured for higher liquid flow rates, due to better transport processes in the liquid film and shorter residence time.

For steam flow rates above ~0.077 kg/s partial bypass occurs, corresponding to roll waves with large amplitude. Comparing the temperatures in this bypass region (Region C) to the temperatures in Region B, which covers the range $0.037 < W_g(L) < 0.077$ kg/s, we find that the bypass results in higher liquid temperatures which approach the saturation temperature. Also, the temperature gradients along the film become very small in Region C due to the intense turbulence in this liquid film. In Region B, we see that the temperatures and the temperature gradients depend on liquid and steam flow rates and they correspond to the appearance of pebbled surface and roll waves.

Interfacial structure and its effect on liquid temperature can also be well correlated with the local condensation heat transfer coefficient. It seems that the most reliable method to determine the local condensation rate, and consequently the heat transfer coefficient, is to evaluate it from measured liquid temperatures. Thus,

$$h(z) = \frac{c_p W_\ell(z)}{b(T_s - T)} \frac{dT}{dz} \qquad (1)$$

where b is the channel width and $W_\ell(z)$ is the local liquid flow rate calculated from the measured penetration rate at the bottom of the channel ($z = L$), according to

$$W_\ell(z) = W_\ell(L) \frac{h_{fg} + c_p[T_s - T(L)]}{h_{fg} + c_p[T_s - T(z)]}. \qquad (2)$$

Equation (1) arises from an energy balance on the water film, taking into account condensation at the water-steam interface (assumed to be smooth) and assuming that the temperature profile across the liquid film is uniform. To calculate the heat transfer coefficient, local temperature gradients were evaluated for each test by fitting a second

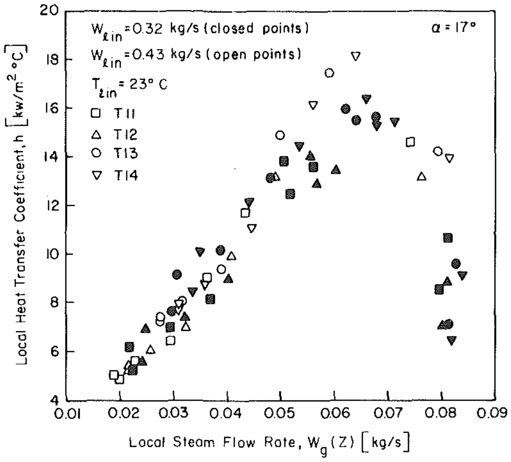

Fig. 5 Local heat transfer coefficient for α = 17 deg and high liquid flow rates

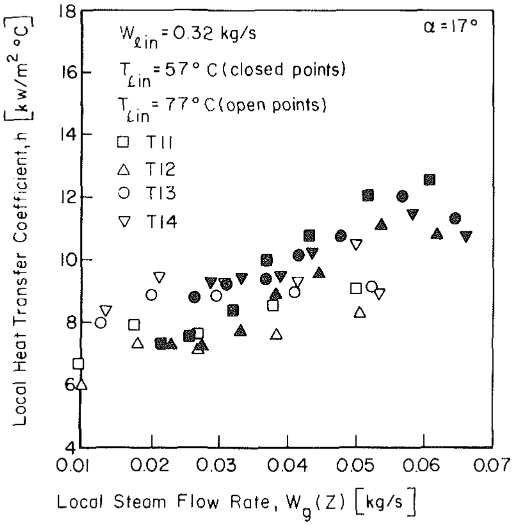

Fig. 6 Local heat transfer coefficient for $T_{\ell in}$ = 57°C and 77°C

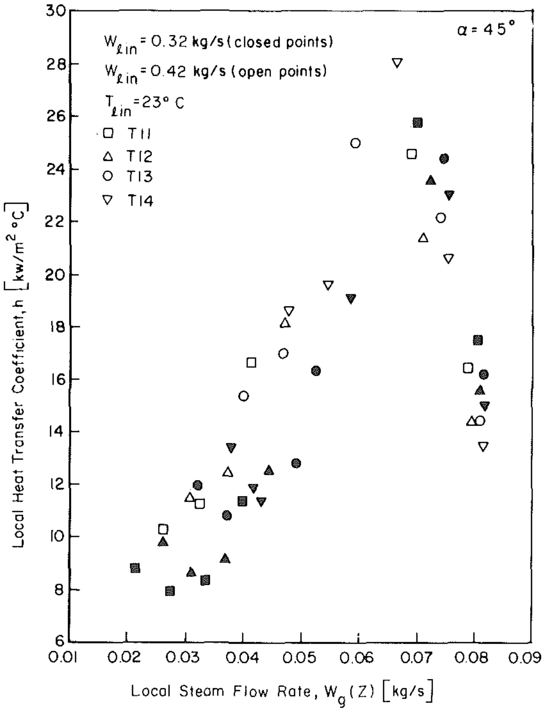

Fig. 7 Local heat transfer coefficient for α = 45 deg

order polynomial through the measured temperatures along the plate. Runs in which the liquid film became saturated were deleted. The criterion for a saturated film was a temperature difference between the upper and lower thermocouples that was less than 5°C. In general, the experimental data indicate that the local condensing heat transfer coefficient increases with the increasing steam flow rate, water flow rate, degree of subcooling, and inclination angle.

Figures 4 and 5 show the local heat transfer coefficient dependence on local steam flow rate as a function of inlet liquid flow rate for the 17 deg inclination. In general, heat transfer coefficients vary from about 4 $kW/m^2{}^\circ C$ to about 18 $kW/m^2{}^\circ C$, which is of the same order as the values obtained by Linehan, et al. [8] (6–28 $kW/m^2{}^\circ C$), and Lee, et al. [9] (6–13 $kW/m^2{}^\circ C$), for stratified, cocurrent steam-water flows in a horizontal channel.

We postulate that the critical factor that governs the condensation process is related to the intensity of turbulent interactions at the interface between the countercurrent streams. It depends on the liquid and steam flow rates, as well as liquid temperature in the same manner that the heat transfer coefficient does. When liquid flow rate is increasing, turbulence intensity increases, resulting in higher values for h, as shown in Figs. 4 and 5. The increased transport process in the liquid film is responsible not only for the decrease in temperature level shown in Fig. 3, but also contributes to enhanced condensation. The role of heat transport in the liquid film is especially important when partial bypass occurs. Liquid bypass results in a significant reduction of liquid flow rate, which in turn reduces the heat transfer coefficient, even though the changes in steam flow are relatively small. This significant reduction of h in the partial bypass region is the major difference between condensation in cocurrent and countercurrent flow configurations. Figures 4–7 show that when steam flow rate increases in Region B, higher values for h are obtained. Increases in the turbulence intensity and the turbulent mixing at the interface result in an equivalent increase in mass and heat exchange.

A significant change was observed when the inlet liquid temperature was varied. Experimentally we found that, for low subcooling tests, the wave characteristics were much less distinct than they were with high subcooling. The most pronounced difference was in the bypass mechanism. For highly subcooled inlet water, the bypass is controlled by waves which are initiated near the liquid outlet. For low inlet water subcooling, bypass is controlled by liquid sweep-out occuring near the liquid injector. A general decrease of the heat transfer coefficient is observed when the liquid inlet temperature is increased. Similarly, the dependence of h on the local steam flow rate is reduced as inlet liquid temperature increases. Figure 6 shows that for inlet liquid temperature of 57°C the dependence of h on the local steam flow rate is still noticeable, with a slight reduction of h at the higher steam flow rate. However, this dependence is diminished when the inlet liquid temperature is increased to 77°C. The effects of temperature are probably related to the turbulence intensity as the shear stresses at the interface are reduced with an increase in liquid temperature. Also, the heat transport potential in the liquid film is reduced when liquid temperature increases.

Figure 7 describes the heat transfer coefficient behavior for a 45 deg inclination for the same inlet liquid flow rates as in Fig. 5. As shown, the behavior of the heat transfer coefficient for the 45 deg inclination is similar to that exhibited for the 17 deg inclination. However, it may be noticed that an increase in inclination results in an increase of h for the same local steam and liquid flow rates. This suggests that the liquid velocity, or alternatively the liquid film thickness, is an important scaling parameter. As will be shown later, fairly good results were obtained when using the film thickness as a characteristic dimension.

The heat transfer coefficient data can be correlated by defining a local Nusselt number as a function of local liquid Reynolds and Prandtl numbers, as is usually done for turbulent forced convection. In addition to those parameters, the steam Reynolds number should also be included since it affects the available heat transfer areas and the turbulence intensity in the liquid through the shear at the interface. Thus, the following interfacial heat transfer correlation will be sought:

$$\mathrm{Nu} = C\,\mathrm{Re}_g^{\,n_1}\,\mathrm{Re}_\ell^{\,n_2}\,\mathrm{Pr}^{n_3} \tag{3}$$

where the local Reynolds number of phase x is defined by

$$\mathrm{Re}_x \equiv \frac{W_x(z)}{b\mu_x(z)}, \tag{4}$$

and the local Nusselt number is defined by

$$\mathrm{Nu} \equiv \frac{ht}{k_\ell}, \tag{5}$$

where t is the local film thickness, evaluated according to experimental measurements described before.

The local liquid flow rate is given by equation (2) and the local steam flow rate is evaluated according to

$$W_g(z) = W_g(L) - [W_l(L) - W_\ell(z)]. \tag{6}$$

Neglecting the small number of points in Region A, the data from both inclinations were separated according to the regions observed experimentally. For a given inlet liquid temperature of 23°C a least-square fit of the data in these regions yields:

Region B:

$$\mathrm{Nu} = 1.16 \times 10^{-3}\mathrm{Re}_g^{\,0.28}\mathrm{Re}_\ell^{\,0.87}\mathrm{Pr}^{0.05} \tag{7}$$

Region C:

$$\mathrm{Nu} = 5.79 \times 10^{-4}\mathrm{Re}_g^{\,0.016}\mathrm{Re}_\ell^{\,1.08}\mathrm{Pr}^{2.0} \tag{8}$$

Comparing the correlations for the two regions reveals the relative effects of the different parameters. In Region B, equation (7) indicates that steam and liquid Reynolds numbers have a significant effect on Nu whereas the local Pr is insignificant, evidently because of the relatively low liquid temperatures. Equation (7) also describes the effect of inclination on the heat transfer coefficient in Region B. For given conditions, h increases as film thickness decreases ($h \sim 1/t$), or alternatively, h increases as inclination increases. In Region C, where bypass occurs, equation (8) indicates that the effect of Re_g diminishes and Nu drops sharply due to the strong effects of the reduced liquid film flow rate, and subsequently, the high liquid temperatures, described by Re_ℓ and Pr, respectively. In this region the heat transfer coefficient dependent on tube inclination is not as clear as in Region B since the film thickness in Region C does not correspond to the channel inclination (as it does in Region B), but is related to the bypass mechanism by the reduced liquid film flow rate. These observations are in full accordance with the experimental results.

The effects of varying inlet liquid subcooling on Nu are shown when the data in Region B for both 17 and 45 deg inclinations are correlated together (data for different subcoolings are not available in Region C):

$$\mathrm{Nu} = 8.5 \times 10^{-4}\mathrm{Re}_g^{\,0.25}\mathrm{Re}_\ell^{\,0.85}\mathrm{Pr}^{0.5} \tag{9}$$

As expected, the only significant change is in the dependence on Pr.

Discussion

The process of steam condensation on countercurrent flow of liquid film has been investigated in a simple flow geometry. This study was conducted in an inclined test section to minimize the complications involved in verticle tubes studies such as unstable wave growth, existence of several flow regimes and end effects [10]. This allowed us to examine more effectively the relationship between the different physical processes that affect the condensation rate.

Experimental results show that the values of the heat transfer coefficient and its dependence on flow parameters in countercurrent flow with no bypass do not differ significantly from those in cocurrent flow. This is probably because the interfacial shear effects in both configurations are similar when relatively low steam flow rates in the countercurrent flow are considered. A significant difference between the two configurations would be expected for high steam flow rates which may induce a highly agitated and turbulent liquid film. But, at these high steam flow rates, liquid bypass occurs and the countercurrent flow configuration changes, acquiring concurrent flow characteristics. Thus, it is not surprising that even in this region, the heat transfer coefficients are of the same order at both configurations. However, the dependence on flow parameters is different in this region as an increase in steam flow in the countercurrent flow configuration results in reduction of liquid film flow rate and a consequent reduction of h, whereas in the cocurrent flow configuration, such an increase results in an equivalent increase in liquid turbulence and consequently an increase in h. It is interesting to note that the general behavior observed in the 17 and 45 deg inclination was similar to the behavior in the 0.5 deg inclination (horizontal) even though the films in the latter were much thicker. However, the results in the horizontal position were more sensitive to variations in steam flow rate since wave action was propagated further along the horizontal films compared to the inclined films. More information about the horizontal results can be found in reference [7].

The results of this study were applied successfully in a mechanistic model which describes ECC penetration behavior [11, 12] by using an empirical relation for the film thickness. This application is still open to question since flows in vertical channels are more complicated due to inherent instabilities (which may enhance condensation rates) and end effects. More experiments are required to resolve this question. However, it seems that some degree of empiricism will be needed in any case, since the flow patterns in a PWR are even more complex than these in simple vertical tubes.

This study has also shown that the local heat transfer coefficient may be related to the turbulence intensity in the liquid film which suggests that a general turbulence-centered model for steam-water condensation can be constructed. However, for a complete formulation, many more data on local condensation rates in a variety of flow configurations are needed along with a better fundamental understanding of the relevant turbulence properties such as turbulence intensity and transport processes.

Acknowledgment

This research was sponsored by the U.S. Nuclear Regulatory Commission under Contract NRC-04-76-293-04.

References

1 Collier, R. P., et al., "Status Report on ECC Penetration Scaling Research," NUREG/CR-0651, BMI-2019, Feb. 1979. Available from National Technical Information Service (NTIS), Springfield, Va. 22161.

2 Cudnik, R. A., et al., "Topical Report on Baseline Plenum Filling Behavior in a 2/15-Scale Model of a Four-Loop Pressurized Water Reactor," NUREG/CR-0069, BMI-1997, Apr. 1978. Available from National Technical Information Service (NTIS), Springfield, Va. 22161.

3 Crowley, C. J., and Rothe, P. H., "Analysis of Superheated Wall Effects During Refill at Small Scale," NUREG/CR-0599, Creare TN-287, Mar. 1979. Available from National Technical Information Service (NTIS), Springfield, Va. 22161.

4 Crowley, C. J., Block, J. A., and Cary, C. N., "Downcomer Effects in a 1/15-Scale PWR Geometry-Experimental Data Report," NUREG-0281, Creare TN-252, Feb. 1977. Available from National Technical Information Service (NTIS), Springfield, Va. 22161.

5 Thomas, R. M., "Condensation of Steam on Water in Turbulent Motion," *International Journal of Multiphase Flow*, Vol. 5, 1979, pp. 1–15.

6 Bankoff, S. G., and Mason, J. P., "Heat Transfer from the Surface of a Steam Bubble in Turbulent Subcooled Liquid Stream," *AIChE Journal*, Vol. 8, 1962, pp. 30–33.

7 Segev, A., and Collier, R. P., "Turbulent Steam Condensation in a Horizontal Channel," in *Cavitation and Polyphase Flow Forum—1980*, J. W. Hoyt, ed., ASME, New York, 1980, pp. 45–46.

8 Linehan, J. H., Petrick, M., and El-Wakil, M. M., "The Condensation of a Saturated Vapor on a Subcooled Film During Stratified Flow," *AIChE Progress Symposium Series*, Vol. 66, No. 102, 1970, pp. 11–20.

9 Lee, L., et al., "Local Condensation Rates in Horizontal Cocurrent Steam-Water Flow," in *Nonequilibrium Interfacial Transport Processes*, J. C. Chen, and S. G. Bankoff, eds., ASME, New York, 1979, pp. 79–83.

10 Wallis, G. B., et al., "Countercurrent Annular Flow Regimes for Steam and Subcooled Water in a Vertical Tube," EPRI NP-1336, Jan. 1980.

11 Segev, A., et al., "Countercurrent Steam Condensation and Its Application to ECC Penetration," in *Experimental and Analytical Modeling of LWR Safety Experiments*, L. E. Hochreiter and G. L. Sozzi, eds., ASME, New York, 1980, pp. 101–108.

12 Segev, A., and Collier, R. P., "Momentum and Mass Exchange in Countercurrent Flow in PWR Geometries," 1980 ANS-ENS Mtg. on Thermal Reactor Safety, Knoxville, Tenn., Apr. 7–11, 1980.

Dynamic Simulation of LMFBR Plant under Natural Circulation[3]

A. K. Agrawal
Mem. ASME

I. K. Madni[1]
Mem. ASME

J. G. Guppy
W. L. Weaver III[2]

Department of Nuclear Energy,
Brookhaven National Laboratory,
Upton, New York 11973

Dynamic simulation of the entire LMFBR plant is needed to determine after-heat dissipation capability of the plant via natural circulation. Models required to accomplish this task are briefly described. The resulting computer code, Super System Code-Loop (SSC-L), is then applied to a loop-type fast reactor design to illustrate the system response for a loss-of-electric-power event. Where possible, the Clinch River Breeder Reactor Plant (CRBRP) specifications are used. Entire simulation is performed for up to 1800 seconds of the transient time. Even with rather detailed modeling of essential components, the computing time required on the CDC-7600 machine was slightly less than the real time. For the assumed plant conditions, it is found that the decay heat is adequately removed via natural circulation. The effect of advanced modeling on system performance is also demonstrated. Finally, a scenario of an event that could impose more stringent testing of the plant's capability for adequate dissipation of decay heat is described.

Introduction

An adequate demonstration of after-heat dissipation via natural circulation is of great significance [1–3] in the design and safety evaluation of liquid metal fast breeder reactors (LMFBR). Such a demonstration could best be made by performing an actual test with the plant under investigation. This is clearly not possible, however, because sufficient demonstration must be made prior to the building of the plants. A two-pronged approach, therefore, is generally taken: (1) analytical simulation, and (2) small-scale laboratory experiments. The latter approach can lead to a more qualified simulation model. This paper deals with an analytical simulation of system dynamics of the entire plant, with particular emphasis for those phenomena that may be encountered under natural circulation conditions. An application of this simulation model will be shown for the Clinch River Breeder Reactor Plant (CRBRP).

The complexity of the system required for thermohydraulic simulation of the whole plant is shown in Fig. 1. This schematic is typical of loop-type designs. Although a plant may have two or more such parallel loops coupled through the inlet and outlet plena of the reactor vessel, most of the transients may be simulated by considering only one set of loops. In situations where only a set of loops may be subjected to perturbations, the system can be simulated by two sets of equivalent loops. Inherent in this statement is the assumption that all loops are physically identical to each other and that multi-dimensional effects in the common regions are negligible.

A number of physical processes may be encountered in the off-normal transient simulation of whole plant events such as decay heat removal by natural convection, pipe rupture and operational transients. Some of the major processes are:

- dynamic flow redistribution in the reactor vessel,
- heat conduction in the reactor core,
- coolant mixing in plena,
- thermohydraulics of pipings, heat exchangers, and
- two-phase flow in the steam generator.

Restricted analytical models and associated computer codes, such as IANUS for the Fast Flux Test Facility [4], DEMO for CRBRP [5], have been developed and are in use. More sophisticated and general models for these processes have been developed and reported elsewhere [6, 7]. A brief description of these models is noted. The numerical integration methodology is then discussed. The resulting code, SSC-L, is then applied to simulate the flow coastdown transient to natural circulation in a loop-type LMFBR. The CRBRP design and operating data were used, where available. The ongoing effort to study decay heat removal under natural circulation from near-isothermal plant conditions is then described. Finally, major conclusions of this study are noted.

Models

All of the processes of interest are modeled in one spatial dimension. For example, fluid flow is modeled in one-spatial dimension in the direction of flow. Heat conduction in the fuel rods is treated in the radial direction only. In regions where multi-dimensional effects are considered important, an approximate allowance is made.

Power Generation. The primary source of energy is due to fission reactions that take place in the reactor. Heat is also produced when the fission products and transuranic elements decay via emission of β- and γ-rays. The rate of heat generation depends on their characteristic half-lives. Yet another source of heating is by absorption of γ-rays in coolant and the structural materials. During normal power operation, the relative split between fission and decay heating is approximately in the ratio of 9 to 1. For scram-initiated transients, this relative split quickly becomes one-to-one in a few seconds. For longer times (greater than a minute), essentially all of the heating is from decay of the radioactive nuclides. This split of power production depends upon a number of factors, including fuel composition and irradiation history.

The entire reactor core consists of a collection of fuel, blanket, control and shielding assemblies. The amount of heat generation can vary drastically from one assembly to another. In order to predict accurately the temperature distribution in the core, the reactor core is represented by a number of parallel channels. Power generation due to fission is computed via a point kinetics model, while that due to fission products is allowed to vary from one channel to another [7].

For the transient under investigation the reactor is scrammed at 0.75 s. The resulting normalized power generation in either the fuel

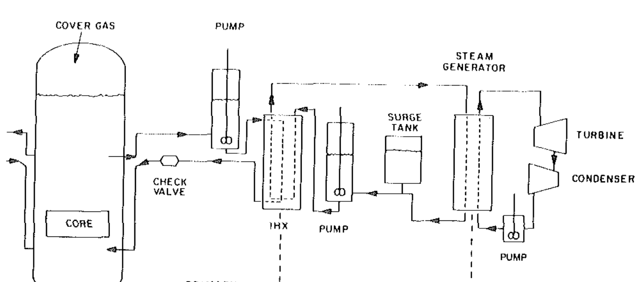

Fig. 1 A schematic of one set of loops in a loop-type LMFBR

---

[1] Present Address: Department of Mechanical Engineering, University of Petroleum and Minerals, Dhahran, Saudi Arabia.

[2] Present Address: EG&G Idaho, Inc., Idaho Falls, Idaho 83415.

[3] Work performed under the auspices of the U. S. Nuclear Regulatory Commission.

Contributed by the Heat Transfer Division for publication in the JOURNAL OF HEAT TRANSFER. Manuscript received by the Heat Transfer Division February 29, 1980.

or blanket assemblies as a function of time after scram is shown in Fig. 2. For times beyond 100 s, essentially all of the heat generation is due to the decay of the radioactive nuclides. The normalized values for heating rates in blanket assemblies is seen to be roughly 50 percent more than that in the fuel assemblies.

Core Thermohydraulics. The heat generation rate and coolant flow across the core varies over a wide range of values resulting in a nonuniform radial temperature profile. During flow coastdown transients, heat generation rates in these assemblies do not necessarily drop by the same fraction. Furthermore, the coolant flows through these assemblies drop to laminar flow regime (not necessarily at the same time during a flow coastdown transient), and buoyancy effects begin to be a dominant factor. These factors lead to the consideration of the following:

- dynamic inter-assembly flow redistribution,
- inter-assembly heat transfer,
- intra-assembly dynamics,
- intra-assembly heat transfer, and
- partial flow reversal.

The inter-assembly flow redistribution results from a delicate balance of the frictional pressure losses and buoyancy forces in an assembly and its relationship with the rest of the assemblies. The inter-assembly heat transfer arises from a nonuniform radial temperature profile across the reactor core. The intra-assembly flow and heat transfer dynamics refer to the consideration of non-uniform flow and power profiles in a single assembly. Such nonuniformity in sodium temperature is a consequence of rod bundle packing in a hexagonal can and variation in power generation within the assembly and flow field. Since our interest is in predicting the overall system response, the effect of intra-assembly dynamics can be, and is, ignored [8]. Such an effect can, however, be estimated adequately by using a more detailed, single assembly modeling code.

The effect of inter-assembly heat transfer can be significant in influencing the system behavior. Its magnitude depends upon several factors, including the extent of radial power variation within an assembly as well as across the reactor core, the power-to-flow ratios for different assemblies, and the geometric characterization. Singer, et al. [9] have argued that the inter-assembly heat transfer is important in the natural circulation simulation experiments in EBR-II. It appears that because of more pronounced radial power variation and other characteristics of EBR-II, the inter-assembly heat transfer is accentuated. In large power reactors, on the other hand, the magnitude of the inter-assembly heat transfer is expected to be less pronounced since the radial temperature variation across the reactor core is minimized by design. In any case, this effect should be included in more detailed thermal analysis of the reactor core. At present, the SSC-L code ignores the inter-assembly heat transfer effects.

Out of the above mentioned inter- and intra-effects, the SSC-L code accounts for the inter-assembly flow redistribution effect only. This appears to be the most significant contributor, particularly for the inner core assemblies. Coffield, et al. [10] have recently confirmed so in a recent paper. For certain assemblies, some of the other factors could be significant. In such cases these contributions can be calculated outside of the whole plant simulation code, like SSC-L, in a manner similar to the one outlined by Coffield, et al. It should be added here that there is no intrinsic reason preventing us from adding the neglected contributors if one is willing to pay for the added computational effort. We feel that, at least for certain conditions, these factors can be evaluated outside the whole plant simulation work.

A partial and/or complete reversal of coolant flow may be possible in certain transient events, such as a pipe rupture accident in the cold leg. There also exists a possibility of upward flow through some of the assemblies and downward flow through others. In other words, there could be, through various assemblies, an internal circulation in the reactor core between the lower and upper reactor plenum regions. Because of the importance and possibility for reverse flow through the core, an allowance is made in the SSC-L code such that one or more than one channel can undergo flow reversal.

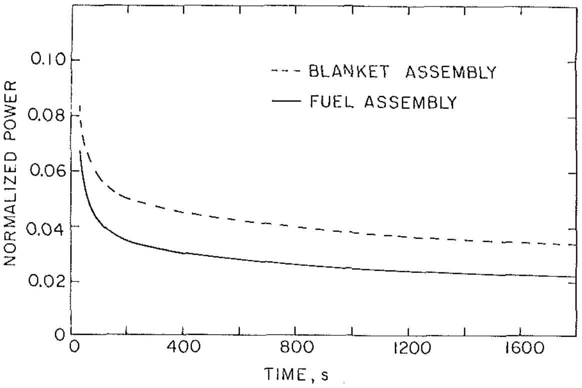

Fig. 2 Normalized power in fuel and blanket assemblies

In SSC-L, a channel represents, at a minimum, one assembly; it can also represent a group of assemblies with similar power and/or flow characteristics. These channels are coupled hydraulically through common pressure points in the lower and upper plena of the reactor vessel. They are also coupled neutronically.

It should be noted that the level of natural convection flow through the reactor core is based on small differences between the overall pressure head due to buoyancy forces and the frictional pressure losses. Fluid flow through wire-wrapped rod bundles does not appear to show the classical transition that is observed for flow in pipings between the turbulent and laminar flow regimes. Recent data obtained at HEDL [3] indicate a smooth transition in friction factor for rod bundles. Similar results are also reported by Rehme [11] and Chiu, et al. [12]. Another important observation is that for the laminar flow region, the friction factor varies as 84/Re instead of the 64/Re observed for smooth pipes. Very recently, Engel, et al. [13] have published a new pressure drop correlation for flow in a wire-wrapped rod bundle. Accordingly, the friction factor is found to vary as 110/Re for Reynolds number below 400. Current analysis utilizes the HEDL correlation.

Flow Stratification. Flow stratification can occur when cooler sodium enters a large body filled with hotter fluid. There exists a possibility of stratification in many parts of the plant. These include (1) upper mixing region in the reactor vessel, (2) pipings, and (3) the intermediate heat exchanger plenum. Perhaps the most significant impact is due to stratification in the upper plenum in the reactor vessel.

In the SSC-L code, use is made of a two-zone mixing model [14]. Here, the core exit temperature and flow are calculated by using a flow-weighted condition from all reactor channels to form a single equivalent jet. This single jet then penetrates the mixing region. The jet penetration height is then used to divide the plenum region into two zones. In each of the zones, perfect coolant mixing is assumed.

The above described coolant mixing model has been applied to simulate the $^1/_{15}$-scale test performed at the Argonne National Laboratory. The effective mixing volumes as calculated by the SSC-L model, agree well with the test data [15]. However, the effect of transport delay on the sodium temperature at the vessel outlet is included only approximately. Perhaps addition of smaller mixing zones will more properly account for the transport delay.

Thermohydraulics of Pipings. A detailed model for thermohydraulics in sodium carrying pipings is formulated by writing down the appropriately averaged conservation equations in one spatial dimension [16]. This model permits discrete representation of the entire piping networks. This treatment is preferable to a simple transport time-delay model, as often used, for two reasons. Firstly,

Nomenclature

A = heat transfer area (m^2), or flow area (m^2)
D = hydraulic diameter (m)
D_e = equivalent diameter of the pipe (m)
ϵ = pipe roughness (m)
K = loss coefficient due to bends, fittings, etc.
ρ = density (kg/m^3)
W = coolant flow rate (kg/s)

the temperature signal is not only delayed in its passage from inlet to outlet of a pipe run, but also altered. Secondly, a detailed temperature distribution will result in a more accurate determination of the gravitational heads. It is noted that the current version of Westinghouse's DEMO code, subsequent to writing of this paper, now incorporates the piping heat transport model as opposed to the time-delay model used in the earlier version.

Key assumptions made in developing this model are (1) one-dimensional flow, i.e., uniform velocity and temperature profiles normal to the flow direction for all flow regimes; (2) incompressible, single-phase liquid; (3) single mass flow rate, i.e., at any instant of time the mass flow rate would be uniform everywhere in the circuit, except at a free surface; (4) no axial heat conduction in the walls, and (5) perfect insulation on the wall surface.

The energy equations for coolant and pipe wall are formulated using the nodal heat balance method. The overall heat transfer coefficient is obtained by combining the film and wall resistances.

The hydraulic model essentially calculates the pressure losses in the pipe section as

$$(\Delta P_{f,g})_{\text{pipe}} = \text{acceleration loss} + \text{frictional loss} + \text{gravity loss} + \text{other losses.}$$

$$= \frac{W^2}{A^2}\left(\frac{1}{\rho_N} - \frac{1}{\rho_1}\right) + \frac{1}{2}\frac{W|W|}{DA^2}\int_0^L \frac{f}{\rho}\,dx + g\int_0^L \rho \sin\theta\,dx + K\frac{W|W|}{\bar{\rho}A^2}, \quad (1)$$

where f is a flow-dependent friction factor and K is a user-specified loss coefficient to account for losses due to bends, fittings, etc.

The friction factor, f, can change by as much as a factor of two from its nominal value to that applicable for very low flow conditions, prevalent at natural circulation. Hence, flow-dependent friction factor in the following form [17] is used:

$$f = 0.0050\left\{1 + \left[20000\frac{\epsilon}{D_e} + \frac{10^6}{\text{Re}}\right]^{1/3}\right\}. \quad (2)$$

This correlation is accurate within ±5. For laminar flows, i.e., $\text{Re} \leq 2000$, $f = 64/\text{Re}$. A linear interpolation for f is used for the transition regions.

Pumps. Liquid metal pumps used in LMFBRs are free-surface, variable speed, centrifugal units. The impeller behavior is characterized in the model by homologous head and torque relations encompassing all regions of operation, including the locked rotor condition. The homologous characteristics were derived by Madni, et al. [18] from independent model test results with a centrifugal pump of specific speed (N_s) equal to 35 (SI units), and are applicable to many pumps such as the ones used in the Fast Flux Test Facility ($N_s \simeq 27.2$), CRBRP ($N_s \simeq 42.8$), PHENIX ($N_s \simeq 36.9$), SNR ($N_s \simeq 40.8$), and others. The transient speed and discharge that influence the pump head are evaluated from impeller and coolant dynamic equations. In particular, the effect of friction torque which begins to dominate pump motion at low speeds is included in the code, as more fully discussed in reference [18].

Intermediate Heat Exchangers. The intermediate heat exchanger (IHX) serves to physically separate the radioactive primary coolant from the nonradioactive intermediate coolant, while thermally connecting them in order to transfer the reactor-generated heat to the steam generator. Since the IHX is the primary heat sink, an adequate characterization is needed.

There generally is some flow maldistribution present in the IHX. Taking credit for the presence of devices to promote radial mixing, e.g., baffles in the CRBRP IHX, the effect of this flow maldistribution is considered small, and hence neglected [19]. This permits us to model the IHX tube bundle by a single equivalent tube.

The axial temperature distribution in the IHX and heat transfer from primary to secondary coolant, is predicted by discretizing the entire heat transfer region into several sections, and then applying energy balance over each section. A section consists of tube-side coolant, tube wall, shell-side sodium and structure associated with the shell. The overall heat transfer coefficients include the film resistance, wall resistance, and the fouling resistance. The hydraulic response is obtained in terms of pressure drop characteristics on both primary and secondary sides of the IHX. The model includes variable friction factor in the heat transfer region, gravity head, and losses due to contraction, expansion, etc. The code lumps these factors into an uncertainty loss term of the form KW|W|/R. The loss coefficient, K, in this term remains constant during transient, thereby enabling a dynamic evaluation of pressure losses in the IHX.

Steam Generating System. The steam generating system consists of five basic elements—evaporator, superheater, feedwater circuit, turbine (pressure sink) and condenser (temperature sink). There can be, and indeed are, various design options such as once-through or recirculation type systems. The SSC-L code model is designed to be flexible to accommodate either of these designs.

The thermohydraulics of the system is modeled in terms of a few-pressure model [20]. Basically, the entire system is divided into flow-path and plenum cells. Flow-path cells are connected together to form flow paths that begin and end at plenum cells. A momentum-integral flow model, in which fluid compressibility effects are included, is applied to each flow path where conservation of mass and energy is applied to each cell in the flow path, while momentum conservation is applied to the flow path as a whole. In plenum cells only conservation of mass and energy are applied since the fluid is assumed to be stagnant. A reference pressure for each flow path is defined as the average of the pressures at the two ends of the flow path. Thus, for a system containing a few flow paths, a few-pressure model is generated.

The multi-tube evaporator and superheater bundles are each represented by a single equivalent heat transfer tube. The tube is divided into a number of axial sections. Each section consists of a tube-side steam/water node, the tube wall node and one shell-side sodium node. The overall heat transfer coefficient between sodium and steam/water includes film resistance, wall resistance and fouling factor. The film coefficients for the steam/water side are calculated from the Dittus-Boelter correlation [21] for the forced convection; Chen's correlation [22] for subcooled and saturated nucleate boiling; saturated film boiling by Bishop [23], and forced convection to superheated steam by Heineman [24]. The location of the DNB point is calculated by using an Atomics International correlation [25].

An adequate simulation of the overall plant transients requires proper representation of the auxiliary feedwater system, recirculation pumps and associated hardware, as well as the superheater steam flow following a plant trip. These are modeled through the overall plant protection and control systems, as described in reference [26].

Numerical Considerations

Physically, an LMFBR plant consists of many systems and subsystems which are interconnected by various processes and/or components. Mathematically, each subsystem is represented by a set of first-order, nonlinear, ordinary differential equations. The total number of such equations depends, of course, on the level of nodalization in the entire plant. Typically, one may have 1000 state variables. It is, therefore, desirable to ascertain that the numerical integration method employed does not require excessive computing time. For computing machines, such as CDC-7600, the ratio of the computing time to simulation time should be no greater than a factor of two to four. A preliminary analysis of the characteristic response times for processes in various subsystems indicated [27] that the timestep size could vary from 10^{-6} second to 1 s. It seems evident that the most direct method of integration, which will have to use the smallest timestep size allowed anywhere in the system, would not be efficient.

One integration strategy which can efficiently accommodate these varying timesteps is the multiple timestep scheme (MTS). In this method, various portions of the overall system are advanced at different timesteps, all being controlled by a master clock, however. In other words, there are many sub-timesteps within a master timestep. The level of nesting or sub-timesteps depends upon the number of locations in the system where subsystems could be conveniently uncoupled. From the logistics point of view, this splitting should not be excessive. In the SSC-L code, the components/processes are partitioned into five major computational blocks. The five resultant timesteps are forced to adhere to a rigid timestep hierarchy.

The integration methods used in SSC-L are implicit or semi-implicit everywhere except for the loop hydraulics equations. The latter are solved by a fifth-order predictor-corrector scheme. To provide for automatic control of sub-timesteps, criteria for accuracy, numerical stability, and interface conditions are applied. Experience to date has shown savings in computing time, using the MTS method, of as much as a factor of five over that required for the single timestep scheme.

Natural Circulation Simulation

To demonstrate some of the features of the SSC-L code, it was applied to simulate a flow coastdown transient to natural circulation. An attempt was made to utilize the CRBRP thermohydraulic design data [28] as much as possible. The natural circulation transient was simulated from nominal power at turbine of 975 MW with all three loops in operation. A total loss of electric power was assumed to have occurred at time zero. The reactor was scrammed at 0.75 s as a result of the loss-of-electric power signal. In the SSC-L simulation, the shutdown reactivity of $6.00 was inserted linearly in two second intervals. The response of the entire system was calculated up to 1800 s (½ hr) after the initiation of the event.

Pre-Transient Calculations. Figure 1 shows a schematic of one of the three parallel loops of CRBRP. All three sets of loops were simulated by one equivalent set of the primary, intermediate and steam/water heat transport loops. A close agreement between the steady-state operating profile, as noted in CRBRP PSAR [28], and the values used in the current simulation is shown for major global variables in Table 1. These results were generated by the steady state part of the SSC-L code.

The CRBRP reactor core consists of 198 fuel and 150 blanket assemblies arranged in a homogeneous configuration, i.e., all fuel (inner and outer core zones) assemblies are surrounded by blanket assemblies. The fuel assemblies are serviced by four orifice zones. For an SSC-L simulation, assemblies are grouped together into channels by their hydraulic characteristics.

Figure 3 shows various orifice zones and the SSC-L channel number for a 30 deg sector of the CRBRP core. The power and flow fractions assigned to the twelve-channel model are noted in Table 2. It should be pointed out that only one fuel assembly in the entire core was used to represent the hot fuel channel. The location of this assembly is shown in Fig. 3 at the interface of the inner and outer core zones. Other assemblies (eleven of them) in this location are grouped with Channel 2. Similarly, the hot blanket channel represents only one blanket assembly in the core (Row 11 in Fig. 3). The remaining 11 assemblies in the location are grouped with Channel 10. Note that the power fraction values are expressed in terms of fraction of core-generated heat of 967. 4 MW. When heat generated by sodium pumps is included, the total power becomes 975 MW. Heat losses through insulation and other components are small and, hence, neglected. Total in-vessel flow of coolant is 5224 kg/s. A steady-state plant characterization is done by the code from the above information and other design information, including power shapes. All of the conditions used here are representative of the end-of-life equilibrium cycle. This condition was chosen so that the blanket assemblies will have maximum power generation. The decay heat values were taken to be 125 percent of the nominal values for the fission product heating and 110 percent of the nominal values for decay of the transuranic elements. The peak axial power in hot fuel and blanket channels are 39.7 kW/m and 29.9 kW/m, respectively. It should be noted that there are 217 pins and 61 pins in each of the fuel and blanket assemblies, respectively.

The term "hot channel" used in this paper includes both systematic variation within the assembly as well as appropriate statistical variations. The selection of the hot channel parameters was based upon the available information on CRBRP. Therefore, a complete accord between the hot channel factors used in the present analysis and the

Table 1 Pretransient CRBRP global variables

Parameter		FSAR [28]	SSC-L
Total Plant Duty	MW	975.0	975.0
Reactor Power	MW	967.4	967.4
Number of Loops	--	3	3
Primary Heat Transport System			
Sodium Flow per Loop	kg/s	1741.3	1741.3
Reactor Inlet Temperature	K	661.1	662.9
Reactor Outlet Temperature	K	808.3	808.8
Reactor Temperature Rise	K	147.2	145.9
Intermediate Heat Exchanger Temperatures			
Primary Sodium Inlet	K	808.9	809.4
Primary Sodium Outlet	K	661.1	662.9
Intermediate Sodium Inlet	K	617.2	618.6
Intermediate Sodium Outlet	K	767.8	767.9
Log-mean ΔT	K	42.5	42.9
Intermediate Heat Transport System			
Sodium Flow per Loop	kg/s	1699.7	1699.7
Superheater Temperatures			
Sodium Hot Leg	K	767.8	767.9
Sodium Cold Leg	K	725.0	725.3
Saturated Steam	K	604.4	601.1
Evaporator			
Sodium Hot Leg Temperature	K	725.0	725.3
Sodium Cold Leg Temperature	K	617.0	618.0
Evaporator Inlet Temperature	K	560.0	556.5
Steam Drum Temperature	K	604.4	601.1
Quality	--	0.50	0.50
Feedwater			
Flow per Loop	kg/s	139.9	139.7
Temperature	K	515.6	505.0
Steam Header			
Flow (total)	kg/s	419.6	419.0
Temperature	K	758.9	754.7
Pressure	$10^7 N/m^2$	1.069	1.062

Table 2 Steady-state power and flow fractions in SSC-L

Channel Number	Assembly Type	No. of Assemblies	Power Fraction	Power Per Pin KW	Flow Fraction	Flow Per Pin kg/s	Coolant Temp. Rise K
1	Fuel	1	0.0067	29.87	0.0033	0.0794	297.8
2		65	0.30916	21.20	0.2994	0.1109	150.8
3		78	0.34651	19.80	0.30842	0.0952	164.1
4		36	0.14894	18.44	0.12308	0.0823	176.9
5		12	0.04459	16.57	0.03902	0.0783	167.0
6		6	0.01939	14.41	0.01651	0.0662	171.6
7	Blanket	1	0.001644	26.07	0.00073	0.0625	330.5
8		24	0.02961	19.57	0.03414	0.1218	126.5
9		30	0.03259	17.23	0.03966	0.1132	119.8
10		53	0.035346	10.58	0.04275	0.0691	120.5
11		42	0.018760	7.08	0.01772	0.0361	154.6
12	Control	19	0.00676	--	0.0600	--	16.3
Bypass	Bypass	--	0	--	0.01527	--	0

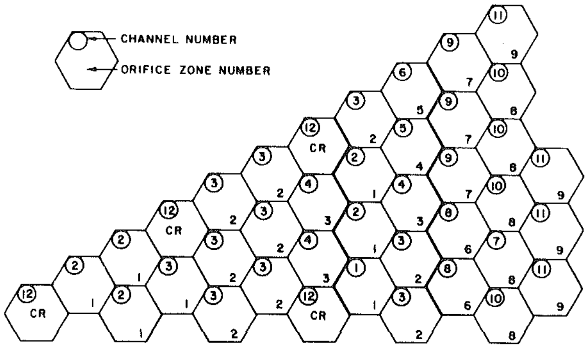

Fig. 3 Orificing scheme and SSC-L channels for the CRBRP core

CRBRP data may not be seen. The core-wide average coolant temperature rise is predicted to be 161.9 K and that for the blanket region is 127.4 K. The coolant enthalpy rise hot channel factor is defined as the ratio of the temperature rise in the hot channel to that in the average channel of the region. Accordingly, the coolant enthalpy rise hot channel factors for fuel and blanket assemblies used in the present analysis are 1.839 and 2.594, respectively. The SSC-L predicted hot channel coolant temperatures for the equilibrium end-of-life core with design plant parameters for the fuel and blanket assemblies are 960.7 K and 993.4 K, respectively. Because of the lack of detailed data from the CRBR Project, only an indirect comparison could be made for the hot blanket channel. For the "expected" operating conditions (reactor inlet temperature of 653.3 K instead of 662.9 K and the total coolant flow rate of 5549.4 kg/s instead of 5224 kg/s), the hot channel blanket temperature for the coolant is about 972.2 K [29]. After accounting for the differences in coolant inlet temperature and the flow rate, this temperature would be 1001.7 K. Thus, it is seen that the conditions used in the SSC-L code lead to slightly lower (by about 8 K) hot channel blanket temperature.

It is important to note that, contrary to the blanket assemblies, the maximum hot channel sodium temperature in the fuel assembly will occur for the beginning-of-life equilibrium core and not for the end-of-life conditions. No comparison for this channel with CRBRP data was made due to the lack of complete data.

Transient Calculations. Figures 4 and 5 show the temporal plots of the hot channel sodium temperatures in the fuel and blanket assemblies, respectively. The coolant temperatures are displayed at two axial locations for two cases—with and without interassembly transient flow redistribution. Also, the maximum coolant temperatures are shown by the dashed curves in these figures. In the case of the fuel, the two locations are the top of the active core and top of the fission gas plenum. For the blanket channel, the two locations are the top of the blanket region and top of the fission gas plenum. Note that a key effect of the flow redistribution is to lower the maximum temperature from about 1100 K to 1030 K in the hot fuel channel, and from 1180 K to 1065 K in the hot blanket channel. The sodium saturation temperature at these locations is about 1200 K. The sodium temperature remains near the high value for about 80 to 100 in the fuel assembly and about 200 s in the blanket assembly. It might be noted that the maximum temperatures occur about 120 s after the transient begins. Any small differences in the scram delay time, such as 0.75 s versus 0.5 s, would not cause any significant difference in the maximum sodium temperatures.

The predicted temperature responses in the fuel and blanket assemblies can be explained as follows: In Fig. 4, the coolant temperature is seen to increase initially due to the 0.75 s delay in the insertion of control rods. The sharp drop in sodium temperature is due to more rapid decay of heat generation than the flow rate. The power-to-flow ratio then begins to rise around ten seconds into the transient since the power generation rate becomes essentially constant (almost all of it is due to decay heating which itself shows a very slow decrease), but the sodium flow rate continues to drop according to the pump coatdown characteristics. The coolant temperature, therefore, rises until it reaches a peak value when the natural circulation in the primary circuit is established. Finally, the sodium temperature shows a more gradual decrease due to slight increase in the coolant flow and slow decrease in heat generation. The hot blanket channel (Fig. 5), on the other hand, behaves differently from that in the fuel channel in the first few seconds of the transient. This is largely due to the fact that blanket channels do not see the same degree of drop in power generation.

The effect of interchannel flow redistribution is displayed more clearly in Fig. 6. Here, the normalized coolant flow fractions, $f_i(t)/f_i(0)$, are shown as a function of time for various channels. The quantity $f_i(t)$ is the fraction of total in-vessel flow in the i-th channel at time t. The hot channels are seen to draw coolant from other cooler channels (including the bypass channel). This effect begins to be pronounced around 60 to 70 s after scram. Another interesting point to note is that for very long times, the relative amount of sodium flow in different channels will approach their pretransient levels. If the flow redistri-

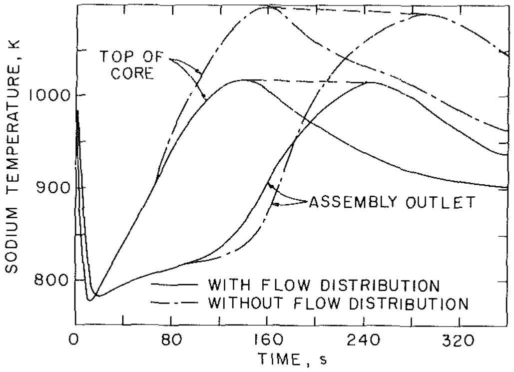

Fig. 4 Coolant temperature in a hot fuel channel

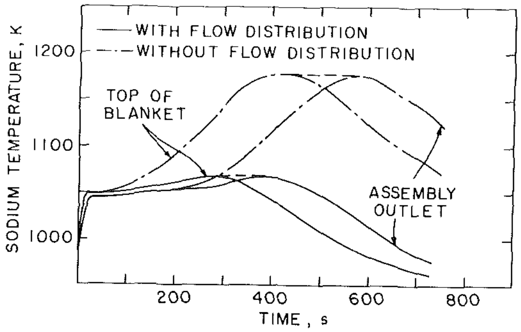

Fig. 5 Coolant temperatures in a hot blanket channel

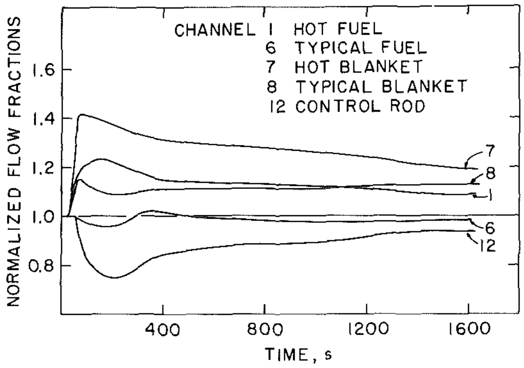

Fig. 6 Normalized flow fractions in various channels

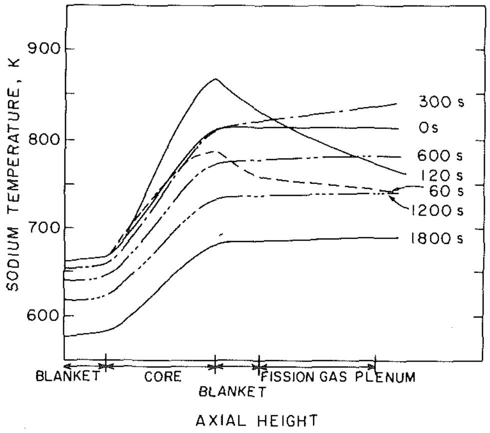

Fig. 7 Axial coolant temperature profiles in a fuel assembly (Channel 2)

bution were not included in the analysis, which is unrealistic, the normalized flow fractions would be identical to one at all times for all channels.

The axial temperature profiles of sodium in a fuel assembly are shown in Fig. 7 for a number of transient times. It is seen that the maximum coolant temperature gradually passes from the active fuel region to the fission-gas plenum region and eventually out of the assembly into the reactor outlet plenum.

Figure 8 shows the normalized sodium flow rates in the primary and intermediate heat transport loops. It is seen that the primary loop flow reaches its lowest value around 80 to 100 s, and, as the natural circulation builds up, it shows a slight increase. For long times, it begins to taper off since the buoyancy head begins to diminish as the rate of heat generation decreases. A similar phenomenon is observed for the intermediate loop sodium flow. It should be added that almost all of the design data used in the heat transport loop were taken to be their nominal values and not the "worst" case values.

The IHX serves as the heat sink for the primary sodium. The temperature distributions in the primary side are shown in Fig. 9. Note that most of the heat is transferred in the top section of the IHX. Therefore, a sufficient number of nodes should be allowed here, otherwise unrealistic temperatures will result. In our analysis, a total of 40 equi-distant nodes were used.

For very long times, the system response will depend upon the conditions in the steam generator where the reactor-generated decay heat is ultimately rejected. In the present analysis, the steam generating system operates as if the reactor were in the normal, power producing mode. The only exception is that the recirculation pump in the evaporator loop has been shut down so that the evaporator is operated as a natural circulation boiler. The consequences of operating the steam generator in this mode rather than the normal shutdown mode is to continue to remove heat using the superheater as well as the evaporator. Under normal decay heat removal conditions, the superheater is isolated so that no heat is rejected through this module. The sodium temperature distribution in the cold side of the intermediate circuit is altered, resulting in a different natural convection flow rate in the intermediate sodium loop. However, this difference is believed to have only a small effect on the temperatures and flow rates in the primary heat transport system.

Finally, a word on the computational efficiency. For the transient under discussion and for the geometric details noted above, it took 1,785 CPU s on a CDC-7600 machine for a simulation time of 1800 s. In other words, for this case the computational time was slightly less than the simulation time.

Further Studies. Further studies are being conducted to calculate the entire system response for a variety of other transients. These include starting from pre-transient conditions at less than and greater than nominal power levels, the effect of the number of heat transfer loops, and delayed loss of power to pony motors. In the last case, the system will attempt to establish natural circulation from nearly isothermal conditions.

In the present analysis, most of the plant parameters used represented their nominal values. An estimate of the sensitivity of the pressure drop across the check valve was made. When this pressure drop was considered to be at its maximum value, the primary sodium flow was found to drop to 2.9 percent from 3.05 percent of the nominal rate. This resulted in an increase by 16 K in the fuel hot channel sodium temperature. A "worst" case study, such as the one reported in reference [30], was not performed. The effect of selecting most conservative parameters will also be examined.

Conclusions

A brief description of the models that are required for simulation of the loop-type LMFBR plant, particularly for the natural circulation transients, was presented. These models were programmed on a CDC-7600 digital machine. The computer program is labeled as SSC-L. In this code, numerical integration of the governing equations was performed by using a multiple timestep scheme. The most commonly used single timestep scheme would have required up to twice the computing time as the MTS method even for an extended simulation time, such as 1800 seconds. The MTS method is even more efficient for short simulation times.

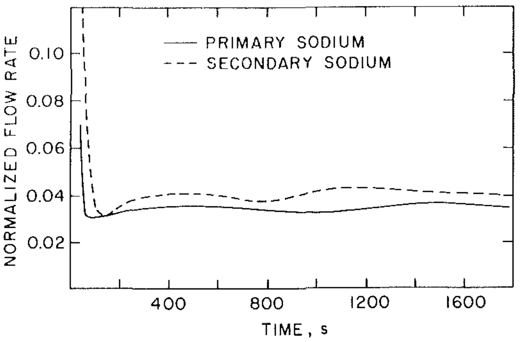

Fig. 8 Normalized primary and secondary loop sodium flow rates

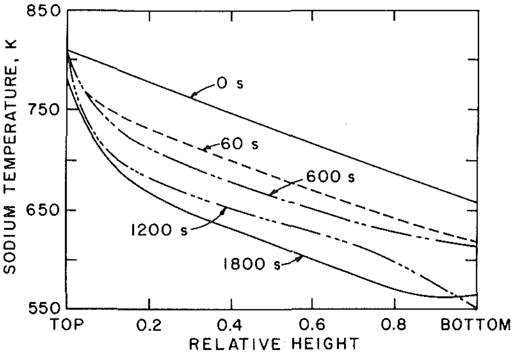

Fig. 9 Primary sodium temperature profiles in the IHX

From the results presented, the following conclusions may be drawn:

1 The interassembly flow redistribution in the reactor core is significant.

2 The hot channel sodium temperatures for both the fuel and blanket assemblies are considerably lower than those obtained by scaling of the corresponding average channel temperatures by appropriate time-invariant hot channel factors. This reduction was about 100 K (180 F) for the hot fuel channel, and 120 K (215 F) for the blanket hot channel.

3 The maximum temperatures as computed here do not allow for interassembly heat transfer. This effect may lead to further decrease in the hot channel temperatures.

4 The intra-assembly flow redistribution and heat conduction effects were not modeled. If these effects were to be included, the maximum temperatures would be further reduced.

5 Response of the balance-of-plant is not very sensitive to the details of in-vessel treatment for this transient.

6 For the design parameters used, the decay heat is seen to be adequately removed via natural circulation. This finding, of course, is based upon the availability of the ultimate heat sink.

Acknowledgment

The authors would like to thank M. Khatib-Rahbar for many discussions on this paper.

This work was performed under the auspices of the U. S. Nuclear Regulatory Commission.

References

1 *Decay Heat Removal and Natural Convection in Fast Breeder Reactors*, edited by Agrawal, A. K., and Guppy, J. G., Hemisphere Publishing, New York (in press).

2 Singer, R. M., Grand, D., and Martin, R., "Natural Circulation Heat Transfer in Pool-Type LMFBRs," in *Symposium on the Thermal and Hydraulic Aspects of Nuclear Reactor Safety, Vol. 2: Liquid Metal Fast Breeder Reactors*, edited by Jones, O. C. and Bankoff, S. G., ASME, 1977.

3 Additon, S. L., and Parziale, E. A., "Natural Circulation in FFTF, a Loop-Type LMFBR," in *Symposium on the Thermal and Hydraulic Aspects*

of Nuclear Reactor Safety, Vol. 2: Liquid Metal Fast Breeder Reactors, edited by Jones, O. C. and Bankoff, S. G., ASME, 1977.

4 Additon, S. L., McCall, T. B., and Wolfe, C. F., "Simulation of the Overall FFTF Plant Performance," HEDL-TC-556, Hanford Engineering Development Laboratories, 1976.

5 "LMFBR Demonstration Plant Simulation Model, DEMO," Westinghouse Advanced Reactor Division, Waltz Mill, Pennsylvania, WARD-D-0005 (Rev. 3), 1975.

6 Agrawal, A. K., et al., "An Advanced Thermohydraulic Simulation Code for Transients in LMFBRs (SSC-L Code)," Brookhaven National Laboratory, BNL-NUREG-50773, 1978.

7 Agrawal, A. K., Guppy, J. G., Madni, I. K., Quan, V., Weaver III, W., and Yang, J. W., "Simulation of Transients in Liquid-Metal Fast Breeder Reactor Systems," *Nuclear Science Engineering*, Vol. 64, 1977, p. 480.

8 Guppy, J. G. and Agrawal, A. K., "System and In-Core Interactions for Thermohydraulic Transients," *Transactions of the American Nuclear Society*, Vol. 31, June 1979.

9 Singer, R. M. et al., *Transactions of the American Nuclear Society*, Vol. 30, 1978, p. 412.

10 Coffield, Jr., R. C. et al., "Buoyancy Induced Flow and Heat Redistribution During LMFBR Core Decay Heat Removal," in *Decay Heat Removal and Natural Convection in Fast Breeder Reactors*, edited by Agrawal, A. K. and Guppy, J. G., Hemisphere Publishing, New York (in press).

11 Rehme, K., "Pressure Drop Correlation for Fuel Element Spacers," *Nuclear Technology*, Vol. 17, 1973, p. 15.

12 Chiu, C., Todreas, N. E., and Rohsenow, W. M., "Pressure Drop Measurements in LMFBR Wire-Wrapped Blanket Bundles," *Transactions of the American Nuclear Society*, Vol. 30, 1978, p. 541.

13 Engel, F. C., Markley, R. A., and Bishop, A. A., "Laminar Transition, and Turbulent Parallel Flow Pressure Drop Across Wire-Wrap Spaced Rod Bundles," *Nuclear Science Engineering*, Vol. 69, 1979, p. 290.

14 Yang, J. W., and Agrawal, A. K., "An Analytical Model for Transient Fluid Mixing in Upper Outlet Plenum of an LMFBR," in *Proceedings of International Conference on Fast Reactor Safety and Related Physics*, Chicago, Illinois, Oct. 5–8, 1975, CONF-761001, 1977, p. 1448.

15 Yang, J. W., "Comparative Studies of FFTF Upper Plenum Mixing and Stratification," *Transactions of the American Nuclear Society*, Vol. 30, 1978, p. 535.

16 Madni, I. K., "Transient Analysis of Coolant Flow and Heat Transfer in LMFBR Piping Systems," Brookhaven National Laboratory, NUREG-CR-1404, 1980.

17 Levy, S., "Fluid Flow," in *The Technology of Nuclear Reactor Safety, Vol. 2*, edited by Thompson, T. J. and Beckerly, J. G., Chapter 15, The MIT Press, Cambridge, 1973.

18 Madni, I. K., Cazzoli, E. G., and Agrawal, A. K., "A Single-Phase Sodium Pump Model for LMFBR Thermal-Hydraulic Analysis," in *Proceedings of International Meeting on Fast Reactor Safety Technology*, Seattle, Washington, American Nuclear Society, 1979, p. 1273.

19 Aburomia, M. M., Chu, A. W., and Cho, S. M., "Heat Transfer in Tube Bundles of Heat Exchangers with Flow Baffles Induced Forced Mixing," Paper No. 76-WA/HT-73, presented at the ASME Winter Annual Meeting, New York, N. Y., Dec. 5, 1976.

20 Weaver III, W. L., Meyer, J. E., and Agrawal, A. K., "A Few-Pressure Model for Transient Two-Phase Flows in Networks," *Transactions of the American Nuclear Society*, Vol. 28, 1978, p. 273.

21 Dittus, F. W., and Boelter, L. K., *University of California Publication in Engineering*, Vol. 2, 1930, p. 433.

22 Thom, J. R. S., Clark, J. A., Lady, E. R., and Merte, H., "Boiling Heat Transfer at Low Heat Flux," ASME JOURNAL OF HEAT TRANSFER, Vol. 89, 1967, p. 235.

23 Bishop, A. A., Sandberg, R. I., and Tong, L. S., "Forced Convection Heat Transfer at High Pressure after Critical Heat Flux," ASME Paper No. 65-HT-31, 1965.

24 Heineman, J. B., "An Experimental Investigation of Heat Transfer to Superheated Steam in Round and Rectangular Channels," Argonne National Laboratory, ANL-6213, 1960.

25 Harty, R. B., "Modular Steam Generator Final Project Report," Atomics International, Canoga Park, Calif. TR-097-330-010, 1974.

26 Khatib-Rahbar, M., Agrawal, A. K., and Srinivasan, E. S., "Feedback Control Systems for Non-Linear Simulation of Operational Transients in LMFBRs," *Proceedings of International Meeting on Fast Reactor Safety Technology*, Seattle, Washington, American Nuclear Society, 1979, p. 1316.

27 Agrawal, A. K., "Numerical Considerations in LMFBR Advanced Thermal Transient Code SSC," *Transactions of the American Nuclear Society*, Vol. 21, p. 219.

28 "Clinch River Breeder Reactor Project Preliminary Safety Analysis Report," Project Management Corporation, with amendments through 40, July 1977.

29 Lowrie, R. R., and Severson, W. J., "A Preliminary Evaluation of the CRBRP Natural Circulation Decay Heat Removal Capability," Westinghouse Advanced Reactors Division, CRBRP-ARD-0132, 1977.

30 Perkins, K. R., Bari, R. A. and Albright, D. C., "Natural Circulation Decay Heat Removal in an LMFBR," *Transactions of the American Nuclear Society*, Vol. 27, 1977, p. 542.

S. Banerjee[1]
Mem. ASME

A. Khachadour
**Department of Engineering Physics,
McMaster University,
Hamilton, Ontario,
Canada L8S 4M1**

A Radioisotope Method for Interfacial Area Measurements in Two-Component Systems

A technique for measuring interfacial area in two-component two-phase flows, based on the transmission of short-range beta or alpha particles across interfaces is proposed. One of the phases contains the radioisotope source, whereas the other contains scintillating material. For short-range particles, it was hypothesized that the number crossing interfaces would originate from very thin layers that are immediately adjacent, and therefore, would lead to a scintillation rate directly proportional to the interfacial area and radioisotope concentration. A series of experiments to check this hypothesis was done with solid-liquid and liquid-liquid systems of known interfacial area. It was found that the scintillation count rate was independent of the orientation of the interfaces and directly proportional to their area. The count rate was also essentially independent of thicknesses of the radioisotope-bearing fluid and the solid scintillating material. However, when a liquid scintillator was used the count rate was found to increase slowly with the scintillator thickness. If this problem can be resolved, it should be possible to measure interfacial area in two-phase systems by this method.

Introduction

In a two-phase system such as when a gas forms a dispersion in a liquid, a knowledge of the interfacial area is often required for a prediction of system behavior. For example, in the analysis of mass transfer between two phases, if the interfacial area can be estimated, then the corresponding mass transfer rate can be predicted with greater confidence. Interphase mass transfer is of great importance in many industrial operations, such as organic oxidations, chlorinations and other fast reactions. Interfacial areas are also of importance in determining the interphase transfer of mass, momentum and energy in steady and transient two-phase flow. Therefore, the objective of this work is to develop a technique for measuring interfacial area that is relatively independent of flow regime. The principle used will be discussed later. First we present a brief survey of the methods currently available.

Several investigations to determine interfacial areas in bubble columns and stirred vessels have been reported in the chemical engineering literature. These have led to correlations relating interfacial area to system variables such as flow rates, densities, etc. Due to the lack of good hydrodynamic models, the relevant variables are not completely identified and their effect is not well understood. The various factors affecting overall transfer in fluid-fluid dispersions have been reviewed by Sideman, et al. [1] and Valentin [2].

Various methods are available for measuring interfacial areas in gas-liquid and liquid-liquid systems. The most widely-used methods are either chemically-based or optically-based.

In the chemical method, interfacial areas are determined by measuring the rates of absorption of a gas that undergoes chemical reaction with a component in the liquid phase. The reaction kinetics must be well understood. The theory of the available methods for the measurement of interfacial area, gas and liquid side mass transfer coefficient have been discussed in a survey by Sharma and Danckwerts [3]. In their paper they also discussed the types of chemical systems useful for such measurement in gas-liquid and liquid-liquid systems. Shilimkan and Stepanek [4] have measured the interfacial area for the case of cocurrent gas-liquid upward flow in tubes, 10, 15 and 20 mm in inside diameter, using the technique of absorption with fast chemical reaction of carbon dioxide into 1 N aqueous solution of sodium hydroxide. The technique is similar to that originally used by Banerjee, et al. [5] for cocurrent gas-liquid flow in helically-coiled tubes. Kasturi and Stepanek [6] also investigated the interfacial area, and liquid and gas side mass transfer coefficients in a smaller diameter tube. Their work was carried out for cocurrent gas-liquid flow through a vertical tube 6 mm i.d., by absorbing sulphur dioxide into sodium hydroxide solution and sulphur dioxide into sodium carbonate-sodium bicarbonate solution respectively. Other gas-liquid systems for use in determining interfacial area have been discussed by Sridharan and Sharma [7], Mehta and Sharma [8], Westertep, et al. [9], and Linek and Mayrhoferova [10].

Although the chemical method is an elegant one for determining interfacial areas, it has the disadvantage that a systematic investigation of liquid phase properties, such as viscosity and interfacial tension, on interfacial area is very difficult, since the addition of surface active or viscous components would make a new and time-consuming investigation of the kinetics of the chemical reaction necessary.

In optically-based methods, three techniques have been used to measure interfacial areas, namely; light scattering or transmission, light reflection and photography.

Light scattering is the most widely-used technique in this category. It is based on the light scattering properties of gas bubbles in liquids. The principle is that a parallel light beam is passed through the dispersion and a photocell is placed some distance from it. Only the part of the beam which does not meet any obstacle, e.g. a gas bubble, is detected by the photocell. The technique has been used by Vermeulen, et al. [11], Calderbank [12] and McLaughlin and Rushton [13]. Calderbank [12] has investigated the attenuation of a light beam passing through a dispersion and derived the relationship

$$\ln I_0/I = SL/4 \tag{1}$$

This formula has been used by many other workers. McLaughlin and Rushton [13] and Curl [14] have shown that the bubble size distribution does not affect the fraction of light transmitted by a dispersion and that the fraction of light transmitted is directly related only to the interfacial area and the path length. This statement also leads to equation (1) above.

Lee and Meyrick [15] found that the maximum value of (I_0/I), the ratio of incident to transmitted light intensity, which can be used with reasonable accuracy and reliability is about 100. This means that the above relationship holds up to $SL < 20$. Above this value multiple scattering becomes important. Assuming a minimum path length of 0.03m, which seems to be a reasonable requirement, it follows that the maximum interfacial area which can be measured with this

---

[1] Present address: Professor of Chemical and Nuclear Engineering, University of California, Santa Barbara, Calif. 93106.

Contributed by the Heat Transfer Division for publication in the JOURNAL OF HEAT TRANSFER. Manuscript received by the Heat Transfer Division July 7, 1980.

Table 1 Properties of some scintillators

Scintillator	Type	Specific Density	Wavelength of max. emission, nm	Refractive Index	Light yield percent anthracene	Decay time constant, ns
Anthracene	Crystal	1.25	447	1.62	100	30
Stilbene	Crystal	1.16	410	1.626	50	4.5
NaI (Tl)	Crystal	3.67	413	1.775	230	230
Pilot B	Plastic	1.032	408	1.58	68	1.8
NE-224	Liquid	0.877	425	1.505	80	2.6
NE-213	Liquid	0.874	425	1.508	78	3.7

method is about 700m^2/m^3. They have also found that this technique could be used with confidence for bubbles down to 100 μm diameter. Recent improvements by Landau, et al. [16] may allow the technique to be used for $SL > 20$. It is still limited to applications in bubbly flow only.

The second technique in this category is light reflection. It is not widely used because it is only suitable for measurements of interfacial area near vessel walls and, therefore, is not applicable for the measurements of integral values of interfacial area in vessels with large local variations of interfacial areas as discussed by Calderbank, et al. [17].

Photographic techniques have been used by several workers taking photographs of the liquid contents of the reactor through a transparent vessel wall or with an endoscope in the interior of the reactor, see Van Dierendonck, et al. [18] and Towell, et al. [19]. In another experiment, Kawecki et al. [20] extracted bubbles from the reactor by means of a tube connected to a small, square-section column. The bubbles in the column were photographed. This technique was also used by Brown and Craddock [21]. The specific interfacial area, S, was calculated from the following relationship.

$$S = 6(1 - \epsilon)/d \tag{2}$$

There are two serious limitations to both photographic measuring techniques. The first is that only local samples can be taken, and second that the hydrodynamic behavior of the dispersion at the sampling point is disturbed. Again the techniques are not suitable for flow regimes other than bubbly.

It has been observed that the chemical and physical methods yield different values of interfacial area measured under identical geometrical, physical and operational conditions. Only in a very few cases were the same values of interfacial area measured in identical systems with different measuring techniques. An exception was the comparison by Reith and Beek [22] of the chemical method and the photographic method in bubble columns. Excellent agreement was obtained, probably because there were no relatively stagnant (nonrenewed) portions of the interface. A comparison between these techniques for determining interfacial areas in gas-liquid dispersions in stirred tanks and bubble columns reported by several authors is given in Reith [23]. Sridhar and Potter [24] also compared the light transmission and chemical methods for measuring interfacial areas in agitated vessels. They have found that the latter yields consistently higher values of interfacial area. They suggest that the criteria for the absorption rate with chemical reactions to be independent of hydrodynamics may fail when the mass transfer coefficients vary widely, and that while the chemical method gives a measure of the geometric interfacial area for bubble columns, it is unreliable when applied to contactors where surface renewal rates are not relatively constant.

Both the chemically and optically-based methods have limitations and are not reliable in all flow regimes. It was, therefore, of interest to investigate a more direct method of measuring interfacial area. The basic principle is simple. If a radioisotope with very short-range radiation is present in one phase, and a scintillating material in the other, then the number of radiation particles crossing the interface will be dependent on a very thin region near the interface. Furthermore, the radiation will be absorbed within a very short distance in the scintillating phase. Thus, the number of scintillations can be expected to be proportional to the volume of the fluid very near the interface and hence, to the interfacial area. The work reported in this paper tests this hypothesis.

Details of the experiments and analysis may be found in [25]. The thesis also contains a discussion of scintillating materials and their properties as related to the technique. Table 1 lists properties of some scintillators for reference, but is by no mean complete.

Experimental Aspects

As mentioned earlier, the technique proposed in this paper depends on the short range of alpha or low-energy beta particles in liquids. For example, tritium particles have a stopping distance of 6 μm in materials of about the density of room-temperature water. Therefore, tritium beta particles crossing the interface can be expected to originate from a layer about 6 μm thick near the interface. If the other phase contains a uniformly-distributed scintillating material, then the number of scintillation events can be expected to be proportional to the number of betas crossing the interface, and hence, the interfacial area. This assumes, of course, that the betas are completely absorbed in the other phase. Since the absorption distance is proportional to density, quite reasonable absorption distances can be obtained even if the other phase is an order or two of magnitude less dense than water. The absorption distance for brehmstrahlung due to beta stoppings must also be calculated if the scintillator is sensitive to gamma rays.

The basic principle is plausible if the light collected by the system is not sensitive to where the scintillations are produced within the volume of interest i.e. the photonic flux measured is proportional to the number of scintillations. However, the hypothesis requires testing. Therefore, a series of experiments were first done with solid scintillators of known interfacial area. The interfacial area per unit volume and the orientation of the interfacial area were varied. The experiments were then repeated with a liquid scintillator.

Experimental Equipment and Procedure. Most of the work done in these tests was with commercial plastic scintillator (Pilot B obtained from Nuclear Enterprises, San Carlos), which is a polyvinyl-toluene host containing polyterphenyl and diphenyl-stilbene. Some tests with liquid scintillators (with the commercial names NE225 and NE213) were also carried out. The source of radiation was aqueous tritium solution which emits weak β-particles with a maximum energy of 18 keV [25].

Disks of 2 to 3 mm thickness were cut from a plastic scintillator rod 25 mm in diameter and prepared for the experiments. Manufacturer's recommendations for preparing these disks were followed closely and details may be found in [25].

The liquid β-source and the scintillator disk were placed together in a cylindrical container made of plexiglas. This in turn was placed in a light-tight aluminum housing where the counting was done as shown in Fig. 1.

Nomenclature

d = bubble diameter
I_0 = incident light intensity
I = transmitted light intensity
L = optical path length
S = interfacial area per unit volume
ϵ = liquid volume fraction

The general procedure for the tests was as follows. Samples of aqueous tritium solution and one or more scintillators were placed in the plexiglas container, and then positioned in the chamber well of the aluminum housing. The surface area of scintillators was varied by fixing aluminum disks on the surfaces. The aluminum disks had different diameter holes in their centers. After each sample was counted, the aluminum disk was replaced and the counting procedure was repeated. Each sample was counted for 60 s, and at least five readings were taken for each sample. After each sample count was completed, it was necessary to disconnect the aluminum housing for the next sample. Therefore, precautions were taken not to expose the photocathode to direct light as this could cause a large dark current.

The inside of the housing was painted flat black except the well portion in order to eliminate reflection. A block diagram of the system used in these tests is also shown in Fig. 1. The PMT was supplied with a voltage of 1200 V. The pulses from the PMT were fed to a preamplifier, amplifier and then to a Tracor Northern multi-channel analyzer, type TN-1705.

Test Matrix. Tests were first carried out with the plastic scintillator. The radioisotope was tritium contained in water. The tests reported in this paper are outlined below.

Test Series 1. This test was run to determine the variation of counting rate with specific activity of tritium at constant volume. Ten samples of different activities ranging from 0.5 mCi/ml to 20 mCi/ml were prepared for this purpose. A single plastic scintillator disc was used in this test. Readings of count rate were taken for each sample.

Test Series 2. In this test a single plastic scintillator disc was also used with various source activities. Three different activities viz. 0.5, 6 and 8 mCi per ml were used. The interfacial area of the scintillator was varied by changing the aluminum disk.

Test Series 3. In this test readings were taken with more than one plastic scintillator. With the housing in a vertical position, the plastic scintillator disks were placed one on top of each other, so that several disks were stacked on top of each other with a small space in between. The plastic scintillator disks were held on thin plexiglas rings, about 3 mm thick, which kept them apart. A maximum of four such disks were used, and the count rates were recorded for 1, 2, 3 and 4 disks. To see if the orientation of the disks affected the counting rate, the test was repeated with the disks rotated 90 deg from their previous position, i.e. with their faces vertical instead of horizontal.

Test Series 4. A test with two plastic scintillator disks was carried out by varying the distance between the disks, to see whether the separation distance had any effect on count rate. The separation was varied from 0.5 mm to 3 mm.

Test Series 5. Some tests with liquid scintillators were also carried out. First, a single plexiglas container was used with 2 ml of tritium solution of specific activity 5 miCi/ml, covered with 1 ml of liquid scintillator, NE224. The same procedure used for the plastic scintillator was used here. Then, four cylindrical plexiglas containers were machined. These had approximately equal volumes (4.5 ml), but different diameters, with very thin walls. Each of these containers was filled with 2 ml of tritium solution with a specific activity 2 mCi/ml. On top of the tritium-bearing solution, an equal thickness (3mm) of the liquid scintillator was added. Readings were taken for each container in two positions, first with the axes of container and PMT in the same line, and then with these axes at right angles to each other.

Test Series 6. A series of tests with liquid scintillators and plastic scintillator were carried out to observe the effect of scintillator thickness on count rate. The first run was done with the plastic scintillator. A constant volume of tritium solution with a specific activity of 3 mCi/ml was used in one of the plexiglas containers. The thickness of the scintillator was varied from 2 mm to 10.5 mm, and the count rate in each case was recorded. Similar tests were carried out with the two available liquid scintillators. Results were recorded for four different thicknesses in each case. Another run was done with the liquid scintillator, NE224, using inactive distilled water. Count

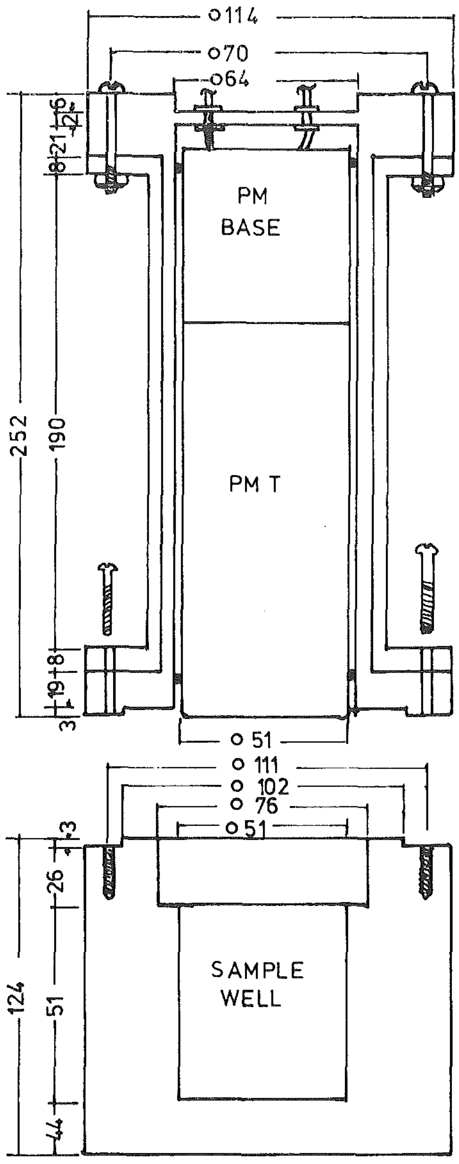

Fig. 1(*a*)

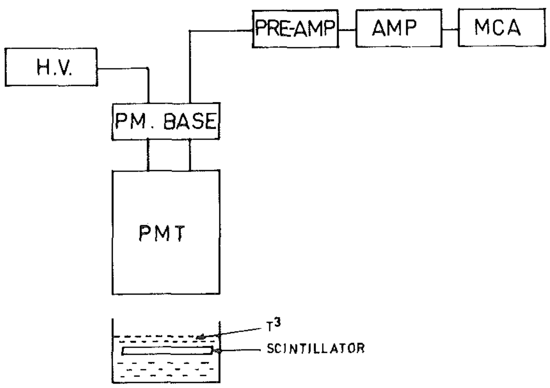

Fig. 1(*b*)

Fig. 1 Details of the test facility

rates for three different thicknesses of the scintillator were recorded.

Test Series 7. This test was carried out to see the time effect on a liquid scintillator sample. Two milliliter of inactive distilled water was introduced in a container (25.4 mm i.d.) and a small amount of liquid scintillator, NE224, was added on top of it, so that the thickness of the scintillator was 3 mm. The sample was counted every hour. Seven sets of readings were taken. The same test was repeated with tritium solution replacing the inactive distilled water.

Experimental Results and Discussions

Solid Scintillations. The variation of light intensity (count rate) from the scintillator disk as a function of specific activity for a constant volume of tritium-bearing liquid, scintillator and constant interfacial area is shown in Fig. 2. It can be seen that a linear relationship exists between the two parameters. This graph was used afterwards to make the necessary corrections, when the specific activity varied from one test to another.

Figure 3 shows typical variations in count rate versus interfacial area of the plastic scintillator. It was observed that a slight deviation from linearity exists at small surface areas when the activity was low, namely 0.5 mCi/2ml. However, in the other cases, this phenomenon was not noticed (see Khachadour [25]).

Figure 4 shows a set of count rates as a function of interfacial area, when more than one plastic scintillator was used. In this test a larger volume container was used so that it could accommodate four scintillator disks. As can be seen from the graph, linearity was not affected when more than one scintillator disk was used. The above arrangement of the disks is analogous to the case of parallel water layers in a two-phase flow, when several of these layers are in the same line.

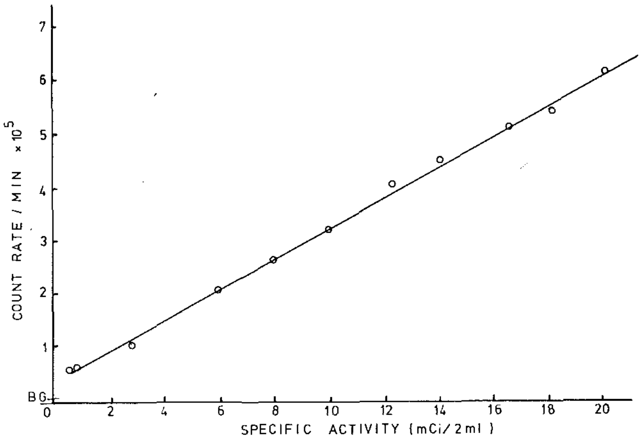

Fig. 2 Variation of count rate with specific activity of tritium

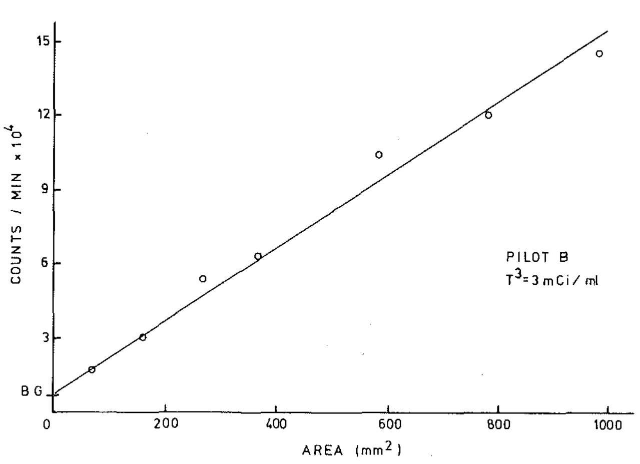

Fig. 3 Response of count rate to interfacial area (T^3 = 2mCi/ml. (Note T^3 denotes tritium.)

Table 2 Effect of separation between two scintillator disks on count rate

Pilot B—2 disks Sample activity = 8 mCi	Sample volume = 12 ml Counting time = 1 min.				
	Back-ground	Distance between the two scintillators (mm) 0.5	1	2	3
Counts/min	7004	82718	85140	83857	88553
	7009	84967	85700	87050	86762
	7359	82611	86466	88621	86593
	9243	82186	86962	86376	87902
	8806	83305	87300	87712	87362
Average Counts	7684	83157	86314	86723	87435

Results of these multiple-disk tests are summarized on a single graph as shown in Fig. 5 which indicates the linear character of the relationship between interfacial area and count rate, irrespective of the number of plastic scintillators.

It was observed that a variation in the distance separating scintillator disks did not affect the results. Table 2 shows the results of such tests, where the distance was varied from 0.5 to 3 mm. This indicates that the count rate is independent of the separation distance between two or more disks, at least over the range studied, and the only thing that matters is the total interfacial area.

The disks could also be arranged with their faces vertical as shown

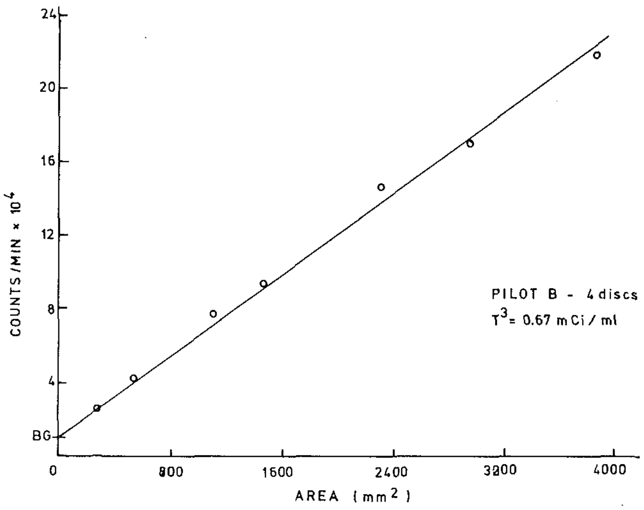

Fig. 4 Response from four horizontal disks

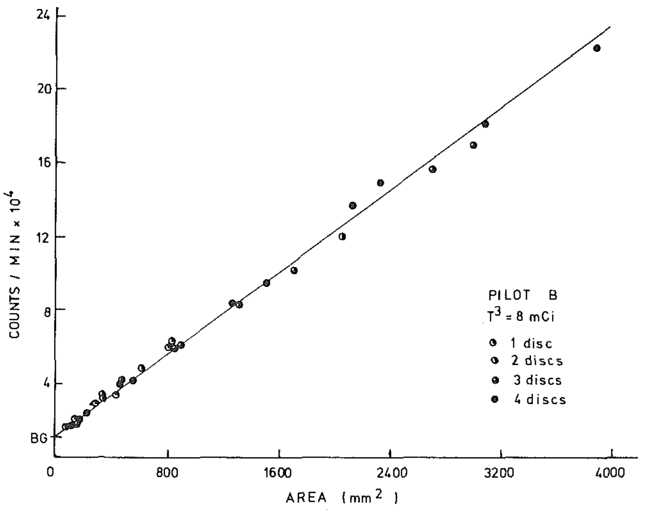

Fig. 5 Response from horizontal disks for tests with one to four scintillators

in the insert to Fig. 6. Experiments were done with one to four disks in the vertical arrangement and the results are summarized in Fig. 6. It is again evident that the count rate only depends on the interfacial area and not on the number of disks.

Several points from the graphs of the multiple disk tests were redrawn on a single graph in Fig. 7. Activity corrections (using Fig. 4) were necessary since the two tests had different tritium activities. It can be deduced that the orientation of the plastic scintillator, whether vertical or horizontal with respect to the PMT, is not significant, and the only thing that should be taken into account is the total interfacial areas.

Liquid Scintillator. Results of tests with liquid scintillator, NE 224, are shown in Fig. 8. The results are for four different diameter containers used in two orientations; axes parallel and perpendicular. These graphs show that a linear relationship between interfacial area and count rate also exists in the case of the liquid scintillator. However, as mentioned before, all the containers had an equal thickness of scintillator on top of the tritium.

It was observed that the count rate was related to liquid scintillator thickness. So when the thickness was increased, the count rate also increased as shown in Fig. 9. Similar behavior was also noticed when using the other liquid scintillator, NE213.

A similar test was arranged with the plastic scintillator disks, using either a single or multiple disks. Results of these tests indicated that variations in readings from the plastic scintillator are well within statistical error and do not show any trends with thickness.

An investigation was carried out to determine the cause for the anomalous behavior of the liquid scintillators. The absorption distance of the β-rays is so small that the thickness should have no effect. Therefore, it was thought that the increase in count rate would be due to self-fluorescence in the liquid scintillators i.e. through no effect of β-particles crossing the interface. To check this, a control test was run using distilled water (containing no tritium) and liquid scintillator only. The thickness of scintillator was varied, but the count rate remained constant within the experimental error. Therefore, the increase in count rate with scintillator thickness shown in Fig. 9 could not be due to self-fluorescence.

Another test was run with liquid scintillator and distilled water, to see the effect of time elapsed on the count rate. The sample was kept inside the light-tight housing for six hours, and readings were taken every hour interval. No change in the count rate was observed. A similar effect was noticed with a tritium sample. Therefore, the increase in count rate with scintillator thickness was not due to slow diffusion of tritium into the scintillator. However, it has been pointed out that isotopic equilibration between the scintillator and the tritium bearing solution may be rapid and would explain the behavior in Fig. 9 quantitatively assuming a 0.05 percent water solubility. This was not verified directly because the apparatus had been dismantled by the time this idea was presented. If this did occur, the volume fraction of the scintillating phase would have to be measured within the volume of interest and the background counts subtracted. The method could still be used but would lack sensitivity if the volume fraction of the scintillating phase was large relative to the specific interfacial area.

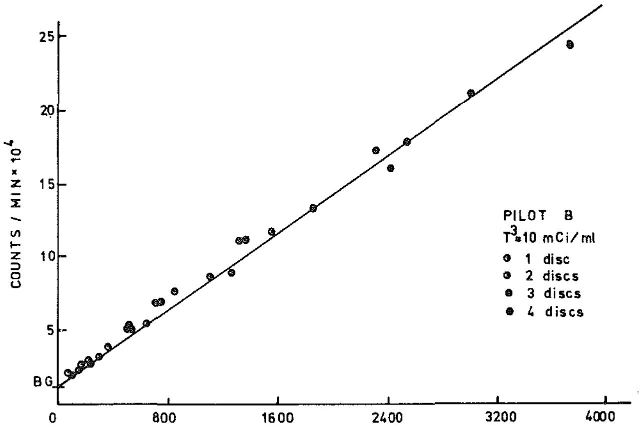

Fig. 6 Response from vertical disks for tests with one to four scintillator disks

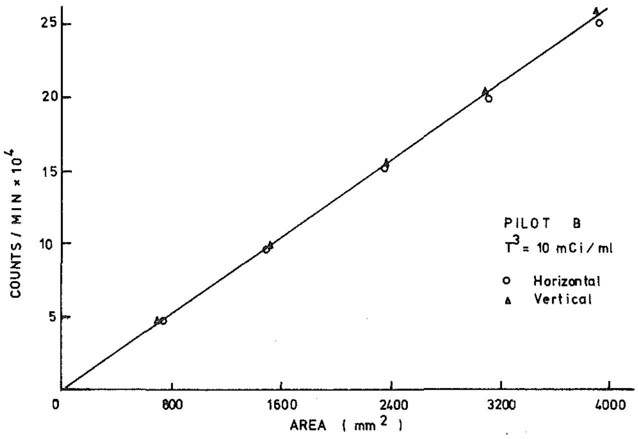

Fig. 7 Response from horizontal and vertical counting arrangements

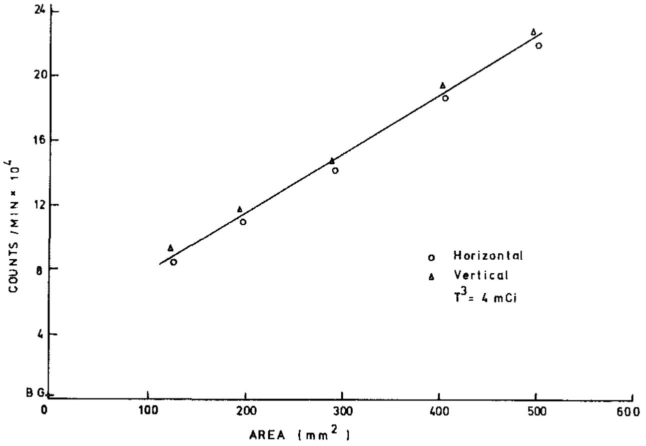

Fig. 8 Response to liquid scintillator from several containers

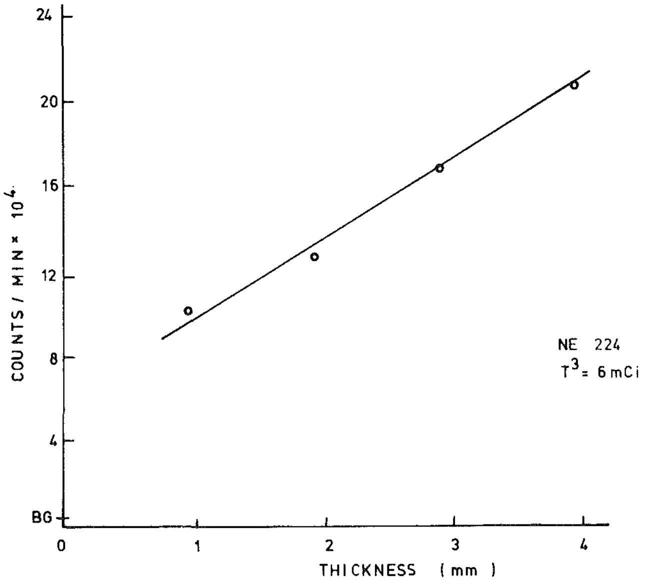

Fig. 9 Effect of scintillator thickness on count rate

Conclusions

A radioisotope-based method to estimate interfacial areas in two-phase flow has been investigated. Experimental results have been obtained to check the method for solid-liquid and liquid-liquid systems. The method should also be applicable to gas-liquid systems, where the gas density is one or two orders of magnitude less than that of water. For example, the β-emitter could be present in the gas. However, the stopping distance would vary from 60 to 600 μm so bubbles of this size would act as volume sources of β-particles rather than surface sources. Therefore, the technique would be limited to resolving the surface area of bubbles larger than 60-600 μm for gas-liquid systems. β-particles from tritium, and plastic and liquid scintillators were used in experiments reported. It was found that a linear relationship exists between interfacial area and count rate, except at very low tritium concentrations, independent of the orientation of the discontinuous phase (in this case scintillators) with respect to PMT position. However, anomalous behavior of the liquid scintillators was observed when the scintillator thickness was varied. The count rate varied with thickness for a fixed interfacial area, although the maximum range of β-particles from tritium is much less than the thickness under investigation. The effect could be due to rapid isotopic equilibration between the tritium bearing liquid and liquid scintillator. The effect can be compensated for if the volume fraction of the scintillator is known, but will reduce sensitivity in certain situations.

The technique could be used to study interfacial areas in two-phase flow, once the anomalous behavior of the liquid scintillator is fully explained, because of the high sensitivity that the method generally offers. One of the phases could be labeled with tritium and liquid scintillator could be used in the second phase. Several PMT s may be employed if necessary. Scattering of photons from scintillating bubbles or drops should not be a serious problem, provided there is negligible light attenuation and an adequate light collection system. This paper provides a status report of the pilot experiments completed. More work is needed to demonstrate applicability to two-phase flows.

Acknowledgment

The idea for these experiments originated in a conversation with Dr. W. G. Mathers of Atomic Energy of Canada Ltd. We are also grateful to Dr. John Harvey of McMaster University for many illuminating discussions.

References

1 Sideman, S., Hortascu, O., and Fulton, J. W., "Mass Transfer in Gas-Liquid Contacting Systems," *Industrial and Engineering Chemistry*, Vol. 58, 1966, pp. 32–47.

2 Valentin, F. H. H., "Absorption in Gas-Liquid Dispersions: Some Aspects of Bubble Technology," *E. and F. N. Spon Ltd.*, London, 1967.

3 Sharma, M. M., and Danckwerts, P. V., "Chemical Methods of Measuring Interfacial Area and Mass Transfer Coefficients in Two-Fluid Systems," *British Chemical Engineering*, Vol. 15, pp. 522–528, 1970.

4 Shilimkan, R. V., and Stepanek, J. B., "Interfacial Area in Cocurrent Gas-Liquid Upward Flow in Tubes of Various Sizes," *Chemical Engineering Science*, Vol. 32, 1977, pp. 149–153.

5 Banerjee, S., Scott, D. S., Rhodes, E., "Studies on Cocurrent Gas-Liquid Flow in Helically Coiled Tubes II: Theory and Experiments on Turbulent Mass Transfer with and without Chemical Reaction," *Canadian Journal of Chemical Engineering*, Vol. 48, 1970, pp. 542–551.

6 Kasturi, G., and Stepanek, J. B., "Two Phase Flow—IV: Gas and Liquid Side Mass Transfer Coefficients," *Chemical Engineering Science*, Vol. 29, 1974, pp. 1849–1856.

7 Sridharan, K. and Sharma, M. M., "New Systems and Methods for the Measurement of Effective Interfacial Area and Mass Transfer Coefficients in Gas-Liquid Contactors," *Chemical Engineering Science*, Vol. 31, 1976, pp. 767–77.

8 Mehta, V. D., and Sharma, M. M., "Mass Transfer in Mechanically Agitated Gas-Liquid Contactors," *Chemical Engineering Science*, Vol. 26, 1971, pp. 461–479.

9 Westerterp, K. R., Van Dierendonck, L. L. and deKraa, J. A., "Interfacial Areas in Agitated Gas-Liquid Contactors," *Chemical Engineering Science*, Vol. 18, 1963, pp. 157–176.

10 Linek, V. and Mayrhoferova, J., "The Chemical Method for the Determination of the Interfacial Area: Influence of Absorption Rate on the Hold-up and on the Interfacial Area in a Heterogeneous Gas-Liquid System," *Chemical Engineering Science*, Vol. 24, 1969, pp. 481–496.

11 Vermeulen, T., Williams, G. M., and Langlois, G. E., "Interfacial Area in Liquid-Liquid and Gas-Liquid Agitation," *Chemical Engineering Progress*, Vol. 51, 1955, pp. 85F-94F.

12 Calderbank, P. H., "Physical Rate Processes in Industrial Fermentation Part I: The Interfacial Area in Gas-Liquid Contacting with Mechanical Agitation," *Transactions of the Institute of Chemical Engineers*, Vol. 36, 1958, pp. 443–463.

13 McLaughlin, C. M., and Rushton, J. H., "Interfacial Areas of Liquid-Liquid Dispersions from Light Transmission Measurements," *American Institute of Chemical Engineering Journal,"* Vol. 19, 1973, pp. 819–827.

14 Curl, R. L., "Note on Light Transmission through a Polydisperse Dispersion," *American Institute of Chemical Engineering Journal*, Vol. 20, 1974, pp. 184–188.

15 Lee, J. C., and Meyrick, D. L., paper presented at the Symposium on Gas-Liquid Reactions, Institute of Chemical Engineers, Manchster, Jan 1969.

16 Landau, J., Boyle, J., Gomaa, H. G. "Comparison of Methods for Measuring Interfacial Areas in Gas-Liquid Dispersions," *Canadian Journal of Chemical Engineering*, Vol. 55, 1977, pp. 13–18.

17 Calderbank, P. H., Evans, F. and Rennie, J., "Mass Transfer Coefficients in Gas-Liquid Contacting with and without Mechanical Agitation," *Proceedings of 1960 International Symposium*, Institute of Chemical Engineers, London.

18 VanDierendonck, L. L., Fortuin, J. M. H., and Venderbos, D., paper presented at the Fourth European Symposium on Chemical Reaction Engineering, Brussels, 1968.

19 Towell, G. D., Strand, C. P., and Ackerman, G. H., "Rotating Disk Contactor Performance," *American Institute of Chemical Engineering, Symposium Series No. 10*, Institute of Chemical Engineers, London, 1965.

20 Kawecki, W., Reith, T., Van Heuven, J. W., et al. "Bubble Size Distribution in the Impeller Region of a Stirred Vessel," *Chemical Engineering Science*, Vol. 22, 1967, pp. 1519–1523.

21 Brown, D. E., and Craddock, J., paper presented at the Symposium on Mixing, Institute of Chemical Engineers, Leeds, Sept. 1969.

22 Reith, T., and Beek, W. J. paper presented at the Fourth European Symposium on Chemical Reaction Engineering, Brussels, 1968.

23 Reith, T., "Interfacial Area and Scaling-Up of Gas-Liquid Contractors," *British Chemical Engineering*, Vol. 15, 1970, pp. 1559–1563.

24 Sridhar, T., and Potter, O. E., "Interfacial Area Measurements in Gas-Liquid Agitated Vessels," *Chemical Engineering Science*, Vol. 33, 1978, pp. 1347–1353.

25 Khachadour, A., "Interfacial Area Measurement using a Radioisotope Technique," M. Eng. Thesis is Engineering Physics, McMaster University, 1979.

R. Cook
C. Y. Tung
P. C. Wayner, Jr.
Department of Chemical Engineering,
Rensselaer Polytechnic Institute,
Troy, N. Y. 12181

Use of Scanning Microphotometer to Determine the Evaporative Heat Transfer Characteristics of the Contact Line Region

A scanning microphotometer was used to measure in situ the profile of an evaporating decane meniscus in the contact line region on a smooth inclined silicon substrate as a function of the evaporative heat flux. The use of this new experimental design to determine the effect of heat flux on the profile in the contact line region is discussed. The results support the hypothesis that fluid flow in the contact line region of an evaporating thin film results from a change in the thin film thickness profile.

Introduction

It is evident that improved understanding of the effect of interfacial phenomena on change of phase heat transfer would lead to enhanced efficiencies in many engineering devices. Within this broad research area, evaporation and fluid flow in an extended meniscus is particularly important. As a result of observations made during our past work [1–4], we feel that, in general, the contact line region looks like an extended meniscus. The extended meniscus is defined to include both the intrinsic meniscus (section where fluid flow is controlled by capillarity) and the adjacent very thin film region (section where fluid flow is controlled by the liquid-solid interfacial forces). In addition to its importance to the classical regimes of heat transfer like boiling and the rewetting of a hot spot, various engineering devices are being developed which capitalize on the potentially large and efficient heat sink capability of an extended meniscus (e.g. grooved evaporators and the inverted meniscus heat pipe). Herein we are concerned with determining the heat transfer characteristics of the contact line region of an evaporating extended meniscus. It has been proposed that, since the local chemical potential of the liquid in an evaporating meniscus is a function of its temperature, thickness and curvature, the meniscus shape and temperature can be used to describe the evaporative heat transfer characteristics [1–4]. This paper concerns the use of a scanning microphotometer to measure in situ the thickness profile of an evaporating thin film in the form of an extended meniscus and the analyses of the measurements to obtain the heat transfer characteristics.

Various different experimental techniques to determine the heat transfer characteristics of a stationary evaporating meniscus have been discussed in the literature. Renk and Wayner used interferometry to measure the microscopic thickness profile of a steady state evaporating ethanol meniscus on a glass substrate [2, 3]. This use of an interference technique to measure the liquid profile has much in common with studies of the transient microlayer evaporation phenomenon at the base of a growing bubble in nucleate boiling [5–9]. The steady-state evaporating meniscus has also been experimentally studied from a more macroscopic point of view. For example, Schultz, et al. measured the steady-state evaporative heat transfer coefficient for water evaporating from the grooves of a horizontal threaded tube [10]. Saaski and Hamasaki analyzed the details of the evaporating meniscus in their experimental heat pipe studies [11]. Preiss and Wayner photographed as a function of the heat flux the cross section of an evaporating meniscus formed at the exit of a capillary tube [12]. Orell and Bankoff measured the apparent contact angle of an evaporating ethanol film [13]. In contrast with these macroscopic studies, the current paper is microscopic in nature and is primarily concerned with the details of the transport processes.

Herein, we report on the use of a scanning microphotometer to measure in situ the evaporating meniscus profile. This improved experimental design significantly enhances the accuracy, ease and speed of the data acquisition techniques discussed in [2, 3] because the steps associated with taking, developing, and printing photographs have been eliminated. The necessary information is recorded directly on a strip chart. In addition, the use of a silicon-decane system allows a more fundamental interfacial characterization of the experimental system. For example, because the surface characteristics of silicon have been extensively studied, the solid-liquid interfacial force constant for this system can be theoretically calculated from the dielectric constants of the liquid and solid. Further, numerous papers concerning the Hamaker constants for the alkanes have been presented in the literature [14–17]. Although the experimental portion of the paper is primarily concerned with the region of curvature control, the thin film portion is included for completeness. We note that the contact angle for the silicon-decane system is zero whereas it was greater than zero in [2, 3].

Theoretical Model

In Fig. 1, an isothermal extended meniscus formed on an inclined flat plate is shown along with an imaginary extension of the meniscus formed in contact with an imaginary vertical plate (vertical dashed line). The imaginary extension of the meniscus is included for the purpose of discussion. A comparison between our results for an inclined flat plate and the frequently studied isothermal vertical flat plate (herein, called imaginary) is instructive. For the equilibrium isothermal extended meniscus, the sum of the gravitational potential energy and the chemical potential per unit volume (effective pressure) relative to the flat surface of the liquid pool is given by equation (1).

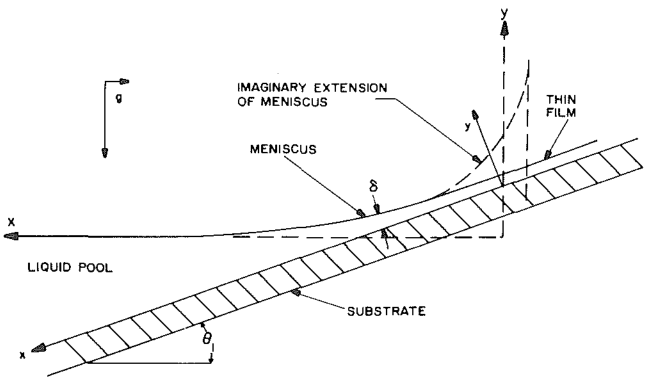

Fig. 1 Isothermal meniscus—thin film system

Contributed by the Heat Transfer Division for publication in the JOURNAL OF HEAT TRANSFER. Manuscript received by the Heat Transfer Division September 8, 1980.

$$\mu + \rho g Y = 0 \tag{1}$$

The chemical potential in the liquid at the liquid-vapor interface can be given in terms of the interfacial curvature, K, and the film thickness, δ, [1, 18–21]

$$\mu = -\gamma K - a\delta^{-n} \tag{2}$$

where

$$K = \frac{\delta''}{[1 + (\delta')^2]^{3/2}} \tag{3}$$

and $' = d/dx$.

Except for extremely thin films, the surface tension is not a function of film thickness. For film thicknesses $\delta < 100 - 150$Å, the thin film approximation for the reduction in chemical potential due to van der Waals forces gives $n = 3$ and $a = A/6\pi$, where A is the Hamaker constant [17]. The thick layer approximation for $\delta > 300 - 400$Å gives $n = 4$ and

$$a = \frac{-3\hbar c(\epsilon_{30} - \epsilon_{10})(\epsilon_{30} - \epsilon_{20})}{16\pi^2\sqrt{\epsilon_{30}}(\epsilon_{30} + \epsilon_{10})(\epsilon_{30} + \epsilon_{20})} \tag{4}$$

in which ϵ_{10}, ϵ_{20}, and ϵ_{30} are the static dielectric constants of the vapor, solid and liquid, [17]. Equation (2) has been solved for the meniscus profile where $a\delta^{-n} \rightarrow 0$ [e.g., 22]:

$$X = B^{0.5}\, ln \left\{\frac{2B^{0.5}}{Y}\left(1 + \left[1 - \frac{Y^2}{4B}\right]^{0.5}\right)\right\} - 2\left[B - \frac{Y^2}{4}\right]^{0.5} + C \tag{5}$$

in which C is a constant of integration which fixes the location of the Y axis and $B = \gamma/\rho g$. Equation (5) describes the imaginary meniscus and that portion of the experimental extended meniscus formed on the inclined flat plate which is locally not effected by the liquid-solid interfacial forces, $a\delta^{-n} \rightarrow 0$. For the liquid-solid system of interest herein, this occurs when $\delta \gtrsim 5 \times 10^{-7}$ m. In addition, the following equation was given for the height of the liquid-vapor interface as a function of the angle of the tangent at the interface, θ:

$$Y^2 = 2B(1 - \cos\theta) \tag{6}$$

These equations are used below to evaluate our isothermal experimental results.

Using an external heat source on the upper portion of the plate, the liquid can be evaporated. It has been proposed that the change in the extended meniscus profile with evaporation causes fluid to flow up the plate to replenish the evaporating fluid [1–4]. The lubrication approximation for steady flow in a thin film leads to the following model for fluid flow in the meniscus [23]:

$$\Gamma = -\frac{\delta^3}{3\nu}\frac{d}{dx}[\mu_\ell + \rho g Y] \tag{7}$$

Using equations (7) and (2) with $P_\ell = \mu_\ell$ gives

$$\Gamma = -\frac{\delta^3}{3\nu}\left[\frac{dP_\ell}{dx} + \rho g\frac{dY}{dx}\right] \tag{8}$$

$$= -\frac{\delta^3}{3\nu}\left[-\gamma\frac{dK}{dx} + an\delta^{-(n+1)}\frac{d\delta}{dx} - \rho g \tan\theta\cos\theta_1\right] \tag{9}$$

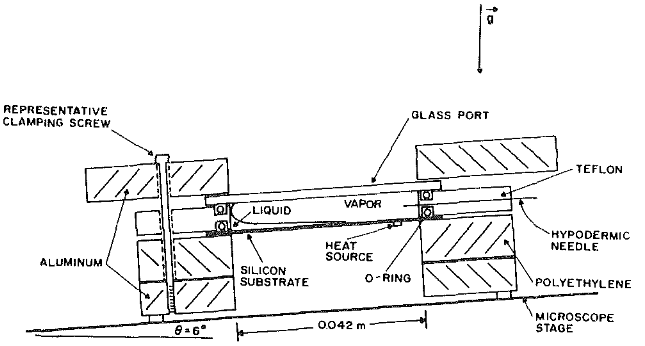

Fig. 2 Cross section of heat transfer cell along centerline, thermocouples not shown

Thus, the change in the meniscus profile can be used to calculate the local fluid flow rate and therefore the heat flux distribution if the temperature effects on the fluid properties and the chemical potential are neglected.

Herein, the interference phenomena associated with light reflected from a tapered film was used to determine the thickness profile of the meniscus as a function of heating. Alternating constructive and destructive interference occur when coherent light is reflected from the two interfaces of the thin film and recombine. Destructive interference occurs when the optical paths of the two reflected beams is such that they are out of phase by π. In our case $n_v < n_\ell < n_s$, therefore, there is a phase shift equal to π at each interface. The relevant equation for the film thickness associated with the minima is

$$\delta = \frac{(2L + 1)\lambda}{4n_\ell \cos\phi_r} \quad L = 0,1,2,3\ldots \tag{10}$$

In the reported data, cos ϕ_r monotonously decreased with an increase in thickness, had a minimum value of approximately 0.998 and was neglected. Equation (10) was used with the measured values of the relative locations of the minima and known values of L, n_ℓ, and λ to determine the profile ($\delta = f(x)$).

Experimental Design and Procedure

A cross section of the test cell is presented in Fig. 2. A horizontal meniscus was formed on an inclined flat plate by injecting a small amount of decane (98 percent by GC) through a hypodermic needle into a cell which was closed to the atmosphere except through the needle opening. The substrate was a 3.55×10^{-4} m thick, 0.059 m × 0.050 m rectangular plate cut from a single crystal silicon wafer (N-type, phosphorous dopent) which had been lapped and chemically polished to a mirror finish. This is a standard electronics material which is used for making solid state devices. For uniformity, the wafers were initially cleaned and dipped in hydrofluoric acid to remove the original oxide surface layer. It is known that a passivating layer of SiO_2 approximately 3–4 × 10^{-9} m thick grows on a silicon surface in the atmosphere at room temperature. Further growth at an appreciable rate is severely limited below 600 C by the slow diffusion of oxygen through the SiO_2 film. Therefore, our "silicon surfaces" were in fact

Nomenclature

A = Hamaker constant
a = constant, equation (2)
$B = \gamma/\rho g$
c = speed of light
g = acceleration due to gravity
$\hbar$ = Planck's constant
K = curvature
P = pressure
p = power input
Q = heat flow rate per unit length of contact line
q = heat flux
$\bar{q}$ = average heat flux for $0 \lesssim \delta(x) \lesssim \delta$
n = exponent equation (2) index of refraction
$\bar{x}$ = X axis with $X = 6 \times 10^{-4}$ m at $\delta = 9 \times 10^{-6}$ m
x = axis, see Fig. (1)
X = axis, see Fig. (1)
Y = axis, see Fig. (1)
γ = surface tension
Γ = local mass flow rate per unit length of contact line
ΔH = heat of vaporization
δ = film thickness
ϵ = dielectric constant
θ = inclination angle of plate, tangent angle of liquid-vapor interface
λ = wave length of light in air
μ = chemical potential
ν = kinematic viscosity
ρ = density
ϕ = angle of refraction

Subscripts

ℓ = liquid
r = refraction
s = solid
v = vapor
10 = vapor static dielectric constant
20 = solid static dielectric constant
30 = liquid static dielectric constant

a silicon base with a 3–4 × 10^{-9} m coating of SiO_2. The rectangular side of the (100) surface oriented silicon substrate was cut parallel to the [110] direction in its face centered cubic lattice.

The plate was inclined relative to gravity at an angle of approximately 6° by placing it on the scanning stage of a tilted Leitz MPV-2 microscope/photometer. An optical interference pattern representing the thickness profile was readily observed through the microscope using monochromatic light. The MPV-2 microphotometer has a variable speed automatic scanning stage and a variable diaphram which allowed the reflectivity of a small rectangular area set parallel to the fringes to be measured using green light (548 nm) and recorded on a strip chart recorder. Using a 20 × objective, the average reflectivity from an area approximately 2 × 10^{-6} m × 2 × 10^{-5} m was recorded. Since the output was continuous, the locations of the maximum and minimum reflectivity could be accurately determined as the plate moved relative to the photometer.

A platinum electrical resistance heat source was positioned parallel to the z axis on the elevated end of the substrate. The platinum film was brushed on the underneath surface and baked at 600°C for 10 min and connected to a d-c power supply. The system was first washed with soap and rinsed in deionized water. Then it was cleaned with reagent grade acetone and alcohol and finally dried at 90°C. The cell was charged with sufficient decane to form a meniscus approximately half way up the plate, placed on the microscope stage, and left to equilibrate with the surroundings for 1–2 days before taking the isothermal data.

The speeds of the scanning stage and strip chart recorder were calibrated using the calibrated graduations on a microscope slide. The photometer was calibrated using a reflectivity standard. The reflectivity of our clean silicon substrate was found to be 33 percent which agrees with the theoretical reflectivity of a silicon substrate with a thin oxide coating. In order to measure the temperature gradient in the x-direction, twelve chromel-alumel thermocouples (wire diameter = 1.3 × 10^{-4} m) were attached to the underneath side of the silicon substrate at intervals of 1.5 × 10^{-3} m along the centerline. Except in the immediate vicinity of the contact line, the large value of the width to thickness ratio, and the substantial value of the thermal conductivity of silicon (k = 120 w/m-K) allows us to use this temperature gradient to calculate the local heat flux in the x-direction. However, due to the relatively short distance over which high rates of evaporation occur (1 − 6 × 10^{-4} m) these temperature sensors can only give the integral value of the meniscus heat sink for a microscopic heat balance.

Using the above system, the relative location of approximately 50 destructive interference fringes were recorded. It was also necessary to determine the absolute order of the interference at some point in the destructive interference pattern. This was done using a video system to display the fringe pattern on a CRT. With the microscope stage fixed, the relative location of the first 15 fringes of the fringe pattern for three different wavelengths (434, 548 and 634 nm) were marked on the face of the CRT itself. Since the stage was stationary the film thickness at a given position on the CRT was constant. However, the fringe locations varied with wavelength. Thus, the order of a particular fringe could be determined by comparing the three patterns. In this way, the thickness at the first *straight* dark fringe using green light in the isothermal system was found to be $\delta = 2.91 \times 10^{-7}$ m (second interference fringe in green light, $L = 1$ in equation (10)). At a very low heat flux setting the first straight dark fringe had a thickness of 0.971 × 10^{-7} m (first interference fringe, $L = 0$ in equation (10)). Following the isothermal meniscus measurements, the current source was turned on and a series of profile measurements were made at progressively increasing power inputs. At least four hours were allowed for equilibration between the setting of a new power level and the recording of data. Additional information concerning the above experiments can be found in reference [24].

Experimental Results

Photographs of the observed interference patterns are presented in Fig. 3. The spacing between the locations of the minimum reflectivity in the first two wide fringes in the photograph on the left for a low heat flux is 4 × 10^{-5} m. The adjacent photograph at the same magnification is for a much higher heat flux. We believe that the decrease in spacing between the fringes in the photographs is due to the increased liquid flow rate associated with an increase in the power input. Additional discussion concerning the photographs is given below.

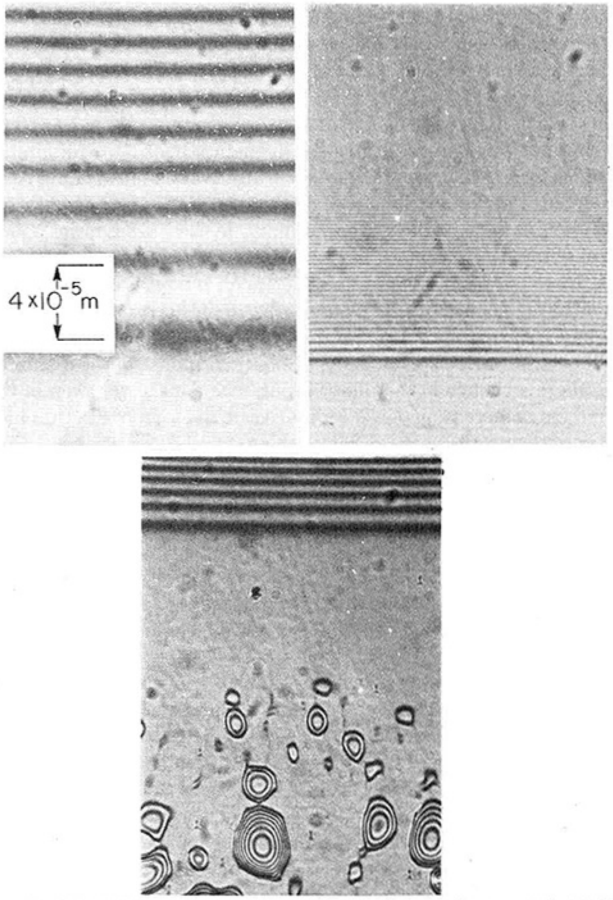

Fig. 3 Microphotographs of evaporating meniscus using monochromatic green light. The upper left hand photograph is of a meniscus with a low evaporation rate. The scale which is given in this photograph is the same for all three photographs. The upper right hand photograph is of a high evaporation rate process. The lower photograph shows evaporating lenses which moved up the plate.

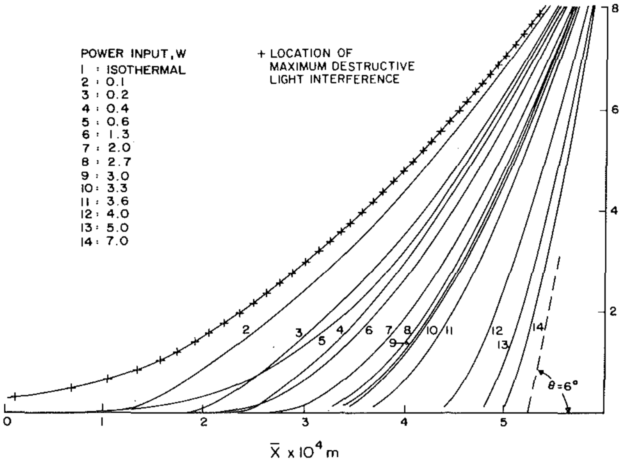

Fig. 4 Meniscus profiles for various power inputs: film thickness versus distance along silicon substrate

The measured profiles of the meniscus for various power inputs, p, are presented in Fig. 4. Since the slopes are small, the horizontal and vertical scales are different. In order to separate the details near the interline, the liquid thickness at the 50th dark fringe, $\delta = 9.617 \times 10^{-6}$ m, is arbitrarily located at $\bar{x} = 6 \times 10^{-4}$ m for all the profiles.

Each of the curves for $0 \leq p \leq 4w$ represent 50 dark fringe data points. For all practical purposes most of the data points fall very close to the smoothed curves. A deviation of the measured thickness from the smoothed curve of greater than 100Å was obviously inconsistent. These deviations were usually due to the scanning stage gear. The isothermal data points are given in the figure. In order to obtain the profiles for $p > 4w$, the interference fringes were photographed and analyzed. This was necessitated by the vibration of the evaporating meniscus at higher values of power input. In these cases fewer points were obtainable. We note that the slope of the meniscus interface relative to the flat plate at $\delta = 8 \times 10^{-6}$ m for $p = 5w$ is approximately equal to the slope of the flat plate relative to the horizontal. Therefore, we have reached the surface of the pool in this region at $5w$.

The most obvious result is the dramatic response of the meniscus profile to a change in the power input. The data were taken in the direction of increasing power inputs. An obvious change in the character of the profile near the contact line occurs after $p = 0.4w$. This change in the profile was readily observable and repeatable. It appeared to represent a change in the wetting characteristics of the thin film in the immediate region of the contact line. This allowed the film to stretch out with an increase in heat flux. It is useful to note the following *approximate* slopes of the liquid-vapor interface at $\delta = 4.8 \times 10^{-8}$ m which were obtained by taking the ratio of this thickness to the distance from the *apparent* (as viewed) contact line: $p = 0$, $\tan\theta = 0$; $p = 0.1$, $\tan\theta = 0.0030$; $p = 0.4w$, $\tan\theta = 0.0031$; $p = 0.6w$, $\tan\theta = 0.00086$. The real profile for $p > 0$ below this line is not readily obtainable with our current procedures. We also note that although these effects are easily viewed through the microscope the exact cause of the process at the contact line is more difficult to determine.

The accuracy of the experimental *isothermal* thickness profile for the decane extended meniscus on the silicon substrate was evaluated as follows. Since the interference fringes were found to be parallel and straight for film thicknesses greater than or equal to the second dark fringe, $\delta \geq 0.291 \times 10^{-6}$ m, the measured profile was compared with equation (5) in the thickness range $0.291 \times 10^{-6} \leq \delta \leq 9.617 \times 10^{-6}$ m. First, the horizontal location of the Y axis is fixed by selecting a value of the meniscus height $Y = Y_0$ for $X = 0$. This Y_0 is calculated using equation (6) with $\theta = \theta_1$, the inclination of the experimental flat plate. The X axis is then shifted to a plane $\delta = 0.291 \times 10^{-6}$ m below the height Y_0 and rotated θ_1 deg so that it represents the inclined experimental substrate. Various values of θ were tried numerically at $\delta = 0.291 \times 10^{-6}$ m until a best fit to the experimental data was obtained. The angle was found to be $\theta = 5.918$ deg which was well within the accuracy of our anticipated liquid-vapor interfacial tangent angle at $\delta = 0.291 \times 10^{-6}$ m for an inclination angle of approximately 6 deg. In the thickness range $0.7 \times 10^{-6}\text{ m} < \delta < 9.6 \times 10^{-6}$ m, the theoretical and experimental results were found to agree within 1 percent. In the thickness range $0.291 \times 10^{-6}\text{ m} < \delta < 0.7 \times 10^{-6}$ m, the disagreement was found to be as large as 4 percent. We presume that this is caused by the effect of van der Walls forces which are not included in equation (5). These results were taken to indicate that we could accurately measure the meniscus profile over the whole range. It is noted that with a heated substrate, the first dark fringe ($\delta = 0.097 \times 10^{-6}$ m) is straight and parallel to the other fringes. For the isothermal case, the film thickness below $\delta = 0.291 \times 10^{-6}$ m was not uniform at a given value of Y. Instead, small specks of dirt and other unknown surface nonuniformities gave various irregular fringe contours. We further note that the terms γK and $a\delta^{-n}$ in equation (2) are comparable at approximately the thickness of the first dark fringe. Therefore, we would expect the thickness to be very sensitive in this region to indeterminate variations in the interfacial forces represented by $a\delta^{-n}$. The analysis of experimental results for the region were $a\delta^{-n} \gtrsim 1$ percent γK was beyond the scope of this study. Theoretically, if the substrate is pure silicon, the region is represented by $a \approx 1 \times 10^{-28}$ $N - \text{m}^2$, which was obtained using equation (4), $\delta \lesssim 3 \times 10^{-7}$ m ($a\delta^{-4} \approx 0.01\gamma K$) and $\delta' \lesssim 4.5 \times 10^{-3}$ from Fig. 6. For pure SiO_2, $a \approx 8.6 \times 10^{-30}$ $N - \text{m}^2$, $\delta \lesssim 10^{-7}$ m, $\delta' \lesssim 2 \times 10^{-3}$.

In order to evaluate the hypothesis that flow of the evaporating fluid results from a change in the meniscus-thin film profile, the data were fitted with polynominals of the mth degree, $2 \leq \text{m} \leq 7$. The degree was varied to obtain a best fit to the data using a least squares criterion. In general, the data could be fitted with a polynomial to within 0.1 percent. For the isothermal case with m = 2 (the constant curvature model is a good approximation for a short distance), the experimental curvature, equation (3'), was found to be equal to at one point and within 15 percent of the theoretical prediction obtained using equations (5) and (6) with $\theta = 5.918$. Since it was possible to also fit the isothermal data with a polynomial of degree $m > 2$, a negligible flow rate towards the contact line could be calculated using equation (9). This flow was at least an order of magnitude less than the flow rates associated with the $p = 0.6w$ case. In Figs. 5 and 6, the curvatures obtained using the polynomial representation of the data are presented as functions of δ and δ', respectively. These results demonstrate

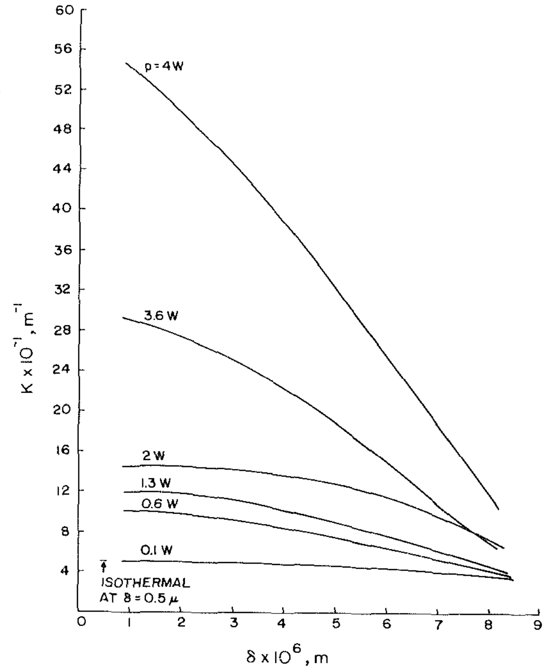

Fig. 5 Local curvature versus film thickness for various power inputs

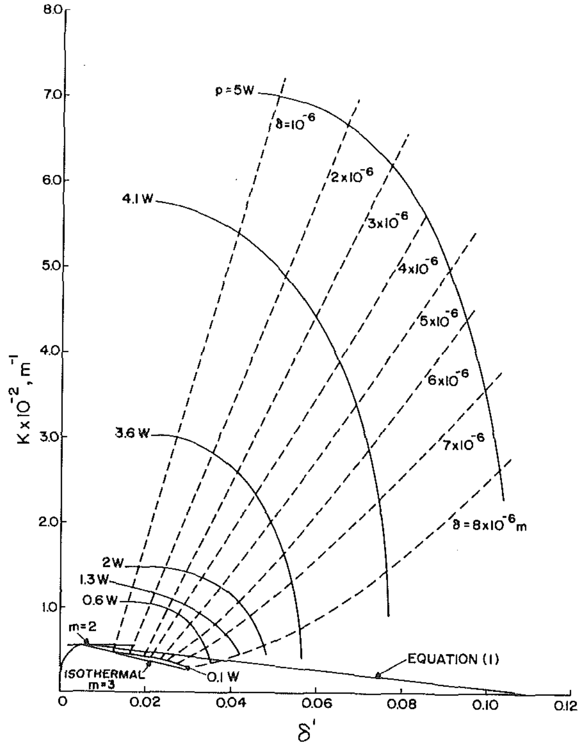

Fig. 6 Local curvature versus liquid-vapor interfacial slope relative to silicon surface

that there is a significant curvature gradient for fluid flow. In Fig. 6 the isothermal curvature obtained experimentally is compared with the theoretical curvature obtained using equation (1). The theoretical curvature varies between zero at the surface of the pool where $\delta' = 0.105$ to a maximum value of approximately 56.6 m^{-1} at $\delta = 0.29 \times 10^{-6}$ m and $\delta' = 0.0014$. For completeness, the curve for constant $\gamma K + a\delta^{-n}$ is also given for $0 \leq \delta' \leq 0.005$ with $a = 10^{-28} N - \mathrm{m}^2$ and $n = 4$. A second degree polynomial representation of the data gives $K = 56.8\ \mathrm{m}^{-1}$ for the region $0 \leq \delta' \leq 0.014$. A third degree fit to the isothermal data is also shown in the figure. Noting that the second derivative of a polynomial representation of the data is required for the curvature, these results represent adequate agreement between theory and experiment for us to proceed and gives us an estimate of the accuracy of the procedure using a polynomial fit.

In Fig. 6 each of the parametric curves for a particular heat flux setting start at a thickness of $\delta \approx 0.3 \times 10^{-6}$ m and extend to $\delta \approx 9 \times 10^{-6}$ m. The curvatures at various values of the thickness are indicated. The results demonstrate that the curvature starts at a maximum value in the contact line region and decreases to zero as the slope or thickness increases. Although not demonstrated by the data, we hypothesize that the curvature starts at zero at $\delta' = 0$ (for a zero contact angle system) and increases in the region where the solid-liquid interfacial forces predominate to a maximum value before decreasing as shown in Figs. 5 and 6 [1, 25]. Alternatively, the curvature for a finite contact angle system starts with maximum value at the contact line [19]. Although the results in Fig. 6 are slightly skewed relative to the isothermal theoretical results, the analyses of the data clearly demonstrate the presence of substantial changes in the curvature with heat flux and position. We note that the data for $p > 0.6w$ could not be adequately fitted with a constant curvature model.

The local mass flow rate in the liquid film at a given thickness was obtained using the polynomial equation for the data and equation (9). Assuming complete evaporation, the product of the local mass flow rate, Γ, at "x" and the heat of vaporization gives the evaporative heat flow rate for the region between a given position "x" and the interline, $Q(x) = \Gamma \Delta H$. The results of these calculations are given in Fig. 7. For comparison, the evaporative heat flow rate based on the temperature distribution was also calculated. The temperature distributions measured using the thermocouples attached to the bottom surface of the substrate are given in Fig. 8 for various power settings. All thermocouples read identically 22.1°C for the isothermal case. The approximate locations of the first dark fringe for the different power settings are given. We note that the thermocouples were slightly larger than the squares in the figure. The temperature profile above the contact line is linear and was used with a one dimensional heat conduction model based on Fourier's law to obtain the heat flow rate into the zone of evaporation. Temperature variations in the y and z directions were neglected in this analysis. A drop in temperature occurs at approximately the location of some of the lenses which are discussed below. The temperature profile below the contact line region is not as linear because of the larger heat transfer coefficient in the pool. However, the approximate integral heat loss due to evaporation in the meniscus region can be obtained by taking the difference between the heat flow rates based on the temperature gradients above and just below the location of the lenses. These results are also given in Fig. 7 and are found to be close to the evaporative heat flow rates calculated using the thickness profiles around $\delta = 8 - 9 \times 10^{-6}$ m. As indicated by the results in Fig. 6, this is close to the end of the capillary driven flow region because the residual curvature or slope available to pump fluid in the region $\delta > 8 - 9 \times 10^{-6}$ m is small. In addition, the thickness across which conduction and/or convection occurs is getting relatively large. At the higher fluxes, the heat sink predicted by the fluid flow model is larger. This is possibly due to the presence of thermocapillary shear at the liquid-vapor interface which is not included in the model. Considering the approximations associated with the above procedures, we feel that the consistency of these results and the favorable comparison between the heat flow rates based on two different sets of measurements strongly support the hypotheses associated with the model represented by equation (9). We hasten to note that the term associated with the London-van der Waals dispersion force, $a\delta^{-n}$, was not adequately tested and that large errors are possible in the region where $K \rightarrow 0$ and the thickness becomes large. We also note that thermocapillarity was not included in our model and our results indicate that it was not the dominant driving force for flow. Finally, we calculate the average heat flux for the region between a given value of δ and the contact line by dividing the results given in Fig. 7 by the length $\bar{x} - \bar{x}_0$. These results are given in Fig. 9.

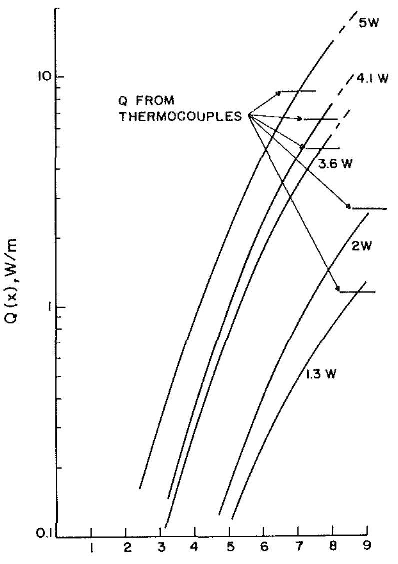

Fig. 7 Evaporative heat flow rate per unit length of contact line based on equation (9) for the region $0 \lesssim \delta(x) \leq \delta$ versus film thickness, δ

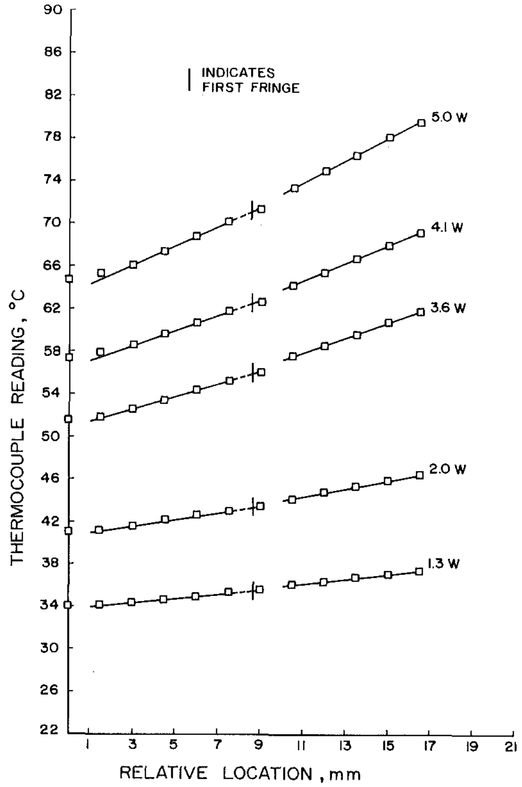

Fig. 8 Temperature distribution on underside of substrate

Additional insight concerning the evaporation process can be obtained from the photographs of the observed interference patterns presented in Fig. 3. The top left photograph is for a low heat flux and the top right is for a high heat flux. In one of the photographs small lenses of liquid can be seen beyond the first dark fringe. Lenses of

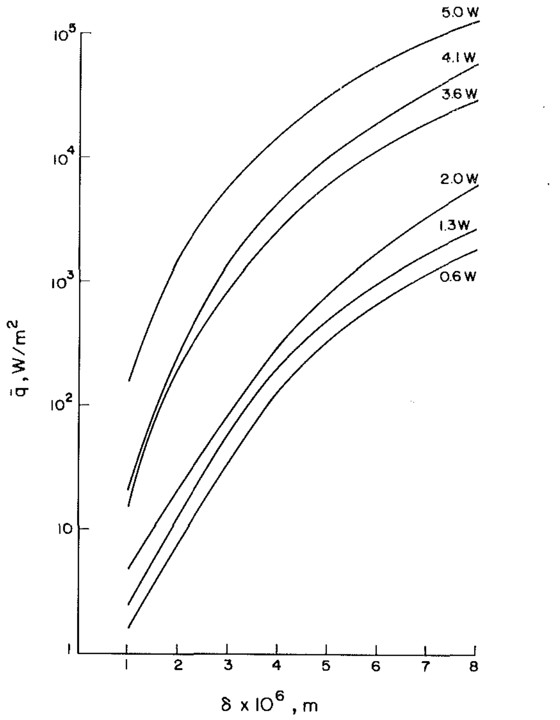

Fig. 9 Average evaporative heat flux for the region $0 \le \delta(x) \le \delta$

various sizes were present at all the power levels. Although not observable in the photographs, there was a variation in the reflectivity between the lenses and the first dark fringe. In addition, the lenses changed in size and moved towards the heat source. At low evaporation rates, the lenses grew in size, coalesced and moved slowly out of view. At higher heat fluxes, small evaporating lenses could be seen moving a short distance up the plate. This significant observation confirms the presence of fluid motion even at those fluxes where the meniscus has a steady state shape with no apparent motion. Since our fluid was only 98 percent pure, the combination of the moving lenses and the above analyses indicate the presence of a steady-state distillation process in the contact line region. We note that a mixture with a higher boiling point would have a higher surface tension. This could lead to lens formation because a nonuniform surface tension causes a surface shear stress towards the point of higher surface tension. This tendency for additional fluid flow could cause dry patches to form because of insufficient fluid flow into the region from below. The effect of composition on the surface tension appears to offset the temperature effect on surface tension in this region and with this fluid. We note that the varying composition associated with distillation would tend to stabilize the interline because of its effect on the vapor pressure and the evaporation rate.

A direct comparison of the results presented herein with those presented in [3, 26] is beyond the scope of this paper because the systems are significantly different. The ethanol-glass system used in [3, 26] was a nonspreading system with an apparent contact angle equal to 0.022 radians. Whereas, the system used herein was a spreading system with a contact angle equal to zero. The isothermal curvature at the contact line in [3, 26] was equal to 1630 m^{-1}, whereas, herein it is equal to 56.6 m^{-1}. This dramatic difference between the isothermal curvatures is a result of the current experimental design which allowed a small hydrostatic head difference to be easily used. An adequate polynomial representation of the nonisothermal data presented in [3, 26] was not found. On the other hand, the extensive computational effort associated with the nonlinear model used in [26] was avoided herein because a good polynomial fit to the nonisothermal spreading data was obtained. As discussed above, the polynomial representation of the isothermal data ($m = 2$) was used to obtain good agreement between the theoretical and experimental curvatures. Using the same approach with the isothermal data given in [3], the difference between the theoretical and experimental curvatures was found to be 10 percent.

The above results demonstrate that significant information concerning evaporating thin films in the contact line region can be obtained with relative ease using a scanning microphotometer.

Acknowledgment

The paper is based on work supported by the National Science Foundation Grant No. CME78-28039. Any opinions, findings and conclusions or recommendations expressed in this publication are those of the authors and do not necessarily reflect the views of the National Science Foundation.

References

1 Potash, M. L. Jr., and Wayner, P. C., Jr., "Evaporation from a Two-Dimensional Extended Meniscus," *International Journal of Heat Mass Transfer*, Vol. 15, 1972, pp. 1851–1863.

2 Renk, F., and Wayner, P. C. Jr., "The Measurement of Fluid Flow and Heat Transfer in an Evaporating Meniscus," *Proceedings of the Fifth International Heat Transfer Conference*, Vol. 5, 1974, pp. 252–256.

3 Renk, F., and Wayner, P. C. Jr., "An Evaporating Ethanol Meniscus, Part I: Experimental Studies," ASME JOURNAL OF HEAT TRANSFER, Vol. 98, 1976, pp. 178–181.

4 Wayner, P. C. Jr., "The effect of the London-van der Waals Dispersion Force on Interline Heat Transfer," ASME JOURNAL OF HEAT TRANSFER, Vol. 100, 1978, pp. 155–159.

5 Hendricks, R. C., and Sharp, R. R., "Initiation of Cooling Due to Bubble Growth on a Heating Surface," NASA TN D2290, 1964.

6 Sharp, R. R., "The Nature of Liquid Film Evaporation During Nucleate Boiling," NASA TN D1997, 1964.

7 Jawurek, H. H., "Simultaneous Determination of Microlayer Geometry and Bubble Growth in Nucleate Boiling," *International Journal of Heat Mass Transfer*, Vol. 12, 1969, pp. 843–848.

8 Voutsinos, C. M., and Judd, R. L., "Laser Interferometric Investigation of the Microlayer Evaporation Phenomenon," ASME JOURNAL OF HEAT TRANSFER, Vol. 97, 1975, pp. 88–92.

9 Judd, R. L., and Hwang, K. S., "A Comprehensive Model for Nucleate Pool Boiling Heat Transfer Including Microlayer Evaporation," ASME JOURNAL OF HEAT TRANSFER, Vol. 98, 1976, pp. 623–629.

10 Schultz, V. N., Edwards, D. K., and Catton, I., "Experimental Determination of Evaporative Heat Transfer Coefficients on Horizontal, Threaded Tubes," 1976 National Heat Transfer Conf., St. Louis, MO, Aug. 1976.

11 Saaski, E. W., and Hamasaki, R. H., "Study of a High Performance Evaporative Heat Transfer Surface," NASA Report CR-152, 008, May 1977.

12 Preiss, G., and Wayner, P. C. Jr., "Evaporation From a Capillary Tube," ASME JOURNAL OF HEAT TRANSFER, Vol. 98, 1976, pp. 178–181.

13 Orell, A., and Bankoff, S. G., "Formation of a Dry Spot in a Horizontal Liquid Film Heated From Below," *International Journal of Heat Mass Transfer*, Vol. 14, 1971, pp. 1835–1842.

14 Blake, T. K., "Investigation of Equilibrium Wetting Films of n-Alkanes on α-Alumina," *Journal of the Chemical Society, Faraday Transactions I*, Vol. 71, 1975, pp. 192–208.

15 Ingram, B. T., "Wetting of Silica by n-Alkanes," *Journal of the Chemical Society, Faraday Transactions I*, Vol. 70, 1974, pp. 868–876.

16 Churaev, N. V., "Molecular Forces in Wetting Films of Non-Polar Liquids," *Kolloidnyi Zhurnal* (*English Translation*), Vol. 36, 1974, pp. 287–290.

17 Churaev, N. V., "Calculation of Dispersion Forces in the Translational Region of Interbody Distances," *Kolloidnyi Zhuranl* (English Translation), Vol. 37, 1975, pp. 656–660.

18 Deryagin, B. V., "Definition of the Concept of and Magnitude of the Disjoining Pressure and Its Role in the Statics and Kinetics of Thin Layers of Liquid," *Kolloidnyi Zhurnal* (English Translation), Vol. 17, 1955, pp. 191–197.

19 Wayner, P. C. Jr., "Interfacial Profile in the Contact Line Region of a Finite Contact Angle System," *Journal of Colloid Interface Science*, Vol. 77, 1980, pp. 495–500.

20 Zheleznyi, B. V., "Form of the Equilibrium Contact Angle," Dokl. Akad. Nauk. SSSR (English Translation), Vol. 206, 1972, pp. 775–778.

21 Mohanty, K. K., Davis, H. T., and Scriven, L. E., "Thin Films and Fluid Distributions in Porous Media," 3rd International Conference on Surface and Colloid Science," Stockholm, Sweden, Aug. 20–25, 1979.

22 Bankoff, S. G., "The Contortional Energy Requirement in the Spreading of Large Drops," *Journal of Physical Chemistry*, Vol. 60, 1956, pp. 952–955.

23 Wayner, P. C., Jr., Kao, Y. K., and LaCroix, L. V., "The Interline Heat Transfer Coefficient of an Evaporating Wetting Film," *International Journal of Heat Mass Transfer*, Vol. 19, 1976, pp. 487–491.

24 Cook, R., "Experimental Study of Evaporative Heat Transfer in the Interline Region and Adjacent Meniscus," M.S. Thesis, Rensselaer Polytechnic Institute, Troy, N. Y., 1981.

25 Moosman, S., and Homsy, G. M., "Evaporating Menisci of Wetting Fluids," *Journal of Colloid Interface Science*, Vol. 73, 1980, pp. 212–223.

26 Renk, F. J., and Wayner, P. C., Jr., "An Evaporating Ethanol Meniscus, Part II: Analytical Studies," ASME JOURNAL OF HEAT TRANSFER, Vol. 101, 1979, pp. 59–62.

J. Hoch
Engineer,
Pope, Evans and Robbins, Inc.,
Consulting Engineers,
New York, N. Y. 10004
Assoc. Mem. ASME

L. M. Jiji
Professor,
Department of Mechanical Engineering,
The City College of the City University
of New York
New York, N. Y. 10031
Mem. ASME

Theoretical and Experimental Temperature Distribution in Two-Dimensional Turbulent Jet-Boundary Interaction

A theoretical and experimental study of the temperature characteristics of two-dimensional heated turbulent jets discharging parallel to and in the vicinity of a solid boundary is presented. The model is based on an integral formulation of the basic conservation laws and uses the flow field solutions of corresponding nonbuoyant jets. The theory takes into consideration the effects of free-stream motion and jet offset distance. Theoretical predictions of temperature were found to be in good agreement with experimental data.

Introduction

Concern over thermal pollution during the past decade has motivated numerous theoretical and experimental investigations on heated turbulent jets. Much of the work has been limited to free jets discharging in an unbounded ambient. Few attempts have been made to study the interaction between a turbulent heated jet and an adjacent solid boundary and to define the characteristics of jet-boundary interaction.

This paper deals with a theoretical and experimental study of a heated two-dimensional, nonbuoyant turbulent jet discharging parallel to and offset from an adiabatic solid boundary. The effects of ambient fluid motion and discharge offset parameter on the thermal characteristics of the jet are examined. Predictions of the maximum axial temperature variation along the jet axis as well as the temperature in the recirculation region are compared with experimental data.

The proximity of a solid boundary to a two-dimensional offset jet significantly affects jet behavior. Reduced entrainment from the boundary side of the jet results in a low pressure between the jet and the boundary, causing the jet to bend towards the boundary and eventually be attached to it.

In the flow regime prior to jet attachment, known as the preattachment region (see Fig. 1), pressures are generally lower than hydrostatic levels. As the jet approaches the boundary, pressure levels inside the jet increase, causing the jet to decelerate, eventually reaching a maximum as the jet is attached. A recirculation region is thus set up which is bounded by the discharge plane, the solid boundary and the dividing or reattaching streamline. Fluid entrained by the jet from the recirculation region is returned to it resulting in no net mass exchange.

The fluid above the dividing streamline is accelerated along the boundary following jet reattachment due to the jet's positive pressure. In the second or impingement region, the pressure decreases eventually reaching hydrostatic levels, and the acceleration ceases. In the third zone, the jet undergoes turbulent diffusion analagous to that of a wall jet in what is known as the wall jet region.

Previous Studies

Numerous models which predict the velocity and temperature behavior of submerged heated free jets have been presented. These include studies that account for such factors as ambient fluid motion, buoyancy, free-surface interaction and discharge geometry and orientation. A detailed review of these studies can be found in Jirka and Harleman [1]. Corresponding studies on the temperature distribution in offset jets have not been carried out. However, the limiting case of a heated wall jet has been treated in film cooling investigations.

The temperature field of a heated turbulent two-dimensional wall jet with an adiabatic wall boundary condition was investigated by Seban and Back [2]. Their solution for the temperature is based on Glauert's [3] corresponding similarity solution of the velocity distribution. Assuming a linear temperature profile, a semi-empirical formula for the adiabatic wall temperature is presented. Although this formula does not account for free stream velocity effects, it was compared to experimental data compiled in the presence of a free stream. Agreement with experimental data is fair. It should be noted however that their assumed linear temperature profile does not satisfy the adiabatic wall boundary condition.

Other empirical solutions that yield the adiabatic wall temperature as a function of discharge orientation are reviewed by Rohsenow and Hartnett [4].

To theoretically analyze the temperature distribution in offset jets, an analytical description of the velocity field is needed. The velocity and pressure behavior of an incompressible, two-dimensional offset jet was first investigated by Bourque and Newman [5]. The problem was greatly simplified by assuming that the presence of the boundary has no effect on the velocity distribution of the jet. Thus, the velocity field is taken from the solution of the two-dimensional, free-turbulent jet. This can only be accomplished by assuming a constant jet trajectory and radius of curvature, and a zero pressure gradient along the jet. The model, which is limited to the preattachment region, gives reasonable closed form predictions of the reattachment point. However, the assumption of constant radius of curvature and base pressure and the use of the free jet velocity distribution are not borne out by their experimental data. The model also fails to account for the rise in pressure and deceleration of the jet as it approaches the point of reattachment.

The constant radius of curvature and base pressure assumption was also used by Sawyer [6, 7] in his studies of the preattachment region. Detailed measurements of the velocity field, wall pressure, and shear stress for an offset jet are presented for small values of the offset parameter by Rajaratnam and Subramanya [8].

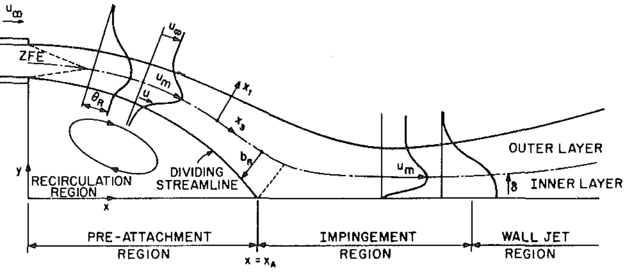

Fig. 1 Schematic of the two-dimensional offset jet

Contributed by the Heat Transfer Division for publication in the JOURNAL OF HEAT TRANSFER. Manuscript received by the Heat Transfer Division, April 16, 1980.

The constant radius of curvature restriction was eliminated by Hoch and Jiji [9] in their investigation of the two-dimensional turbulent offset jet. In a theoretical and experimental study that includes effects of free stream motion, the classical jet-integral solution was extended to account for variations of pressure in both the preattachment and impingement regions of the jet. Predictions of axial velocity, jet-trajectory, reattachment length, maximum wall pressure, and jet width agree very well with experimental data.

The flow field solution of Hoch and Jiji [9] is used here to obtain theoretical solutions to the temperature distribution in offset jets.

Since the flow field solutions of Hoch and Jiji [9] require numerical integration of ordinary differential equations, a simplified model which yields a closed-form solution is also presented. This model is used to generate analytic solutions for the temperature distribution.

Theoretical Analysis

(i) Formulation. In the preattachment region the jet interchanges energy with both the ambient fluid and the recirculation region. To simplify the analysis the fluid temperature in the recirculation region, which is bounded by the dividing streamline, is assumed to be uniform. This approximation is valid because of the efficient mixing in this region. Using the coordinate system shown in Fig. 1, the dimensionless integral form of the conservation of energy is

$$\frac{d}{dx_3}\int_{-w}^{w} u\Theta dx_1 - \Theta_R \frac{d}{dx_3}\int_{-w}^{0} u dx_1 = 0,\ x < x_A \tag{1}$$

where u is the axial velocity, Θ the jet temperature, Θ_R the temperature inside the recirculation region, w the jet's outer limit, and x_1 and x_3 are the transverse and axial directions, respectively.

For an adiabatic wall condition, the dimensionless integral form of the conservation of energy in the impingement and wall jet regions using the rectangular coordinate system in Fig. 1 gives:

$$\frac{d}{dx_3}\int_{0}^{w} u\Theta dy = 0,\ x > x_A \tag{2}$$

The integrals in equations (1) and (2) are evaluated using appropriate velocity and temperature profiles in each region. In the preattachment region a Gaussian-shaped velocity profile is used:

$$u = u_\infty + (u_m - u_\infty)\, e^{-(x_1/b)^2},\ x_1 > 0 \tag{3}$$

$$u = u_m\, e^{-(x_1/b)^2},\ x_1 < 0 \tag{4}$$

where u_m is the maximum axial velocity, u_∞ the free steam velocity, and b a measure of jet spread. Here the variables $u_m(x_3)$ and $b(x_3)$ are obtained from the nonbuoyant flow field solution. Implicit in equations (3) and (4) is the assumption that jet velocity within the recirculation region is small compared to the maximum axial velocity u_m.

Because of the difference in temperature between the ambient and recirculation region, the jet temperature profile is asymmetrical given by:

$$\Theta = \Theta_m\, e^{-(x_1/b_T)^2},\ x_1 > 0 \tag{5}$$

$$\Theta = (\Theta_m - \Theta_R)\, e^{-(x_1/b_T)^2},\ x_1 < 0 \tag{6}$$

where Θ_m is the temperature along the jet axis and b_T is a measure of the thermal jet spread.

In the impingement and wall jet regions the flow is assumed parallel to the boundary. The assumed velocity profile in these regions is described by:

$$u = u_m(y/\delta)^{1/7},\ 0 \le y \le \delta,\ x > x_A \tag{7}$$

$$u = (u_m - u_\infty)e^{-(y-\delta/b)^2} + u_\infty,\ y > \delta,\ x > x_A \tag{8}$$

where δ is the vertical distance measured from the solid boundary to the point of maximum axial velocity and x_A is the reattachment length. Again, x_A and the variables $u_m(x)$, $b(x)$ and $\delta(x)$ are taken from the velocity solution of the corresponding nonbuoyant jet.

For an adiabatic wall boundary condition, the temperature profile may be assumed as:

$$\Theta = \Theta_m e^{-(y/b_T)^2},\ y > 0,\ x > x_A \tag{9}$$

Unlike the linear temperature profile used by Seban and Back [2], the above does satisfy the adiabatic wall boundary condition.

The only remaining unknown is the thermal jet width b_T. In free jet studies the thermal half-width, $b_{T1/2}$, is related to the velocity half width, $b_{1/2}$, by [1]:

$$b_{T1/2} = \lambda b_{1/2} \tag{10}$$

where $b_{1/2}$ and $b_{T1/2}$ are measured from the jet axis to the point at which velocity and temperature are one-half their maximum value, respectively. The dispersion coefficient, λ, is the ratio of thermal to momentum diffusion coefficients for turbulent flow, and is also referred to as the turbulent Prandtl number.

In the preattachment region, using Gaussian profiles, equation (10) reduces to:

$$b_T(x_3) = \lambda b(x_3) \tag{11}$$

where $b(x_3)$ is obtained from the velocity solution and λ is empirically established.

In the impingement and wall jet regions equation (10) is modified to:

Nomenclature

b = measure of jet spread, b^*/d^*

b_R = distance from dividing streamline to jet axis, b_R^*/d^*

b_T = measure of thermal jet spread, b_T^*/d^*

d^* = discharge height

h = offset height, h^*/d^*

T^* = temperature

u = axial velocity, u^*/u_d^*

u_m = maximum axial velocity, u_m^*/u_d^*

w = jet width, w^*/d^*

x = horizontal coordinate, x^*/d^*, (see Fig. 1)

x_A = horizontal distance along x between discharge and reattachment point

x_{3A} = distance along jet coordinate axis x_3 between discharge and the reattachment position (see Fig. A-1)

x_1, x_3 = jet coordinates in the preattachment region (see Fig. 1)

x_i = virtual origin of wall jet

y = vertical coordinate, y^*/d^* (see Fig. 1)

$y_{1/2}$ = value of y at which $(u - u_\infty)/(u_m - u_\infty) = 1/2$

$y_{T_{1/2}}$ = value of y at which $(T^* - T_\infty^*)/(T_m^* - T_\infty^*) = 1/2$

γ = angle hetween the tangent to x_3 and x (see Fig. A-1)

γ_A = jet angle near the reattachment point (see Fig. A-1)

δ = thickness of inner layer for a wall jet, δ^*/d^*

η_A = ratio of b_R to b, evaluated at reattachment point A

Θ = dimensionless temperature, $(T^* - T_\infty^*)/(T_d^* - T_\infty^*)$

Θ_m = dimensionless maximum temperature, $(T_m^* - T_\infty^*)/(T_d^* - T_\infty^*)$

λ = turbulent Schmidt number

Superscripts

$*$ = dimensional quantity

Subscripts

A = reattachment point

d = discharge

m = maximum

R = recirculation

T = thermal

$1/2$ = location where velocity or temperature is one-half the maximum value

∞ = ambient condition

$$b_T(x) = \lambda[b(x) + \delta(x)/.83] \qquad (12)$$

where $\delta(x)$ and $b(x)$ are obtained from the flow field solution.

(ii) Solutions for uniform discharge conditions, $u(0) = 1$, $\Theta(0) = 1$ and $w(0) = \frac{1}{2}$, integration of equations (1) and (2) along the jet axis gives:

$$\int_{-w}^{w} u\Theta dx_1 - \Theta_R \int_{-w}^{o} u dx_1 = 1 - \Theta_R/2, x < x_A \qquad (13)$$

and

$$\int_{o}^{w} u\Theta dx_1 = 1, x > x_A \qquad (14)$$

Substituting profiles (3)–(6) into (13), we obtain the following relationship for the maximum axial temperature distribution in the preattachment region:

$$\Theta_m(x_3) = \frac{1 + \dfrac{\Theta_R}{2}\left[u_m b_T \sqrt{\dfrac{\pi}{1 + (b_T/b)^2}} - 1\right]}{\dfrac{b_T}{2}\sqrt{\dfrac{\pi}{1 + (b_T/b)^2}}\,(2u_m - u_\infty) + \dfrac{\sqrt{\pi}}{2} u_\infty b_T} \qquad (15)$$

Similarly, the maximum axial temperature distribution in the impingement and wall jet regions is obtained by substituting profiles (7)–(9) into equation (14) to give:

$$\Theta_m(x) = \frac{1}{u_m \displaystyle\int_o^\delta (y/\delta) e^{1/7 - (y/b_T)^2} dy + (u_m - u_\infty) \int_\delta^\infty e^{-(y-\delta/b)^2 - (y/b_T)^2} dy + u_\infty \int_\delta^\infty e^{-(y/b_T)^2} dy} \qquad (16)$$

The recirculation temperature Θ_R is determined by evaluating equation (16) at the point of reattachment, $x = x_A$, where $\Theta_R = \Theta_m(x_A)$. This follows from the assumption that the temperature in the recirculation region is uniform.

To determine the temperature distribution Θ_m from equations (15) and (16), jet flow characteristics such as trajectory, point of reattachment and the variables b, u_m, and δ must first be established. Two flow field models are used to obtain these flow characteristics. One model gives the flow field in numerical form while the other, which is more simplified, provides closed-form solutions for the required jet characteristics.

(*a*) *Solutions Based on the Numerical Flow Field Solution.* Hoch and Jiji [9] used the integral form of the basic conservation equations and obtained a set of ordinary differential equations. Pressure and the local radius of curvature in the preattachment region were considered as variables to be determined by the solution. By allowing the pressure to vary, the model resulted in an axial velocity distribution distinctly different from that of a free jet. The entrainment assumption used was essentially the same as the one advanced by Morton, et al. [10]. The favorable agreement between theoretical predictions and experimental data supports the hypothesis that the entrainment mechanism in an offset jet is not affected by the pressure field.

Except for the pressure terms, the governing conservation equations are similar to their free jet counterparts. However, because jet pressure and radius of curvature were treated as variables, the conventional jet integral solutions are not applicable. The integral method was therefore modified by specifying a polynomial profile for the jet trajectory. The polynomial coefficients were determined in an iterative procedure from boundary conditions, geometric considerations, and two approximate momentum relationships, the first introduced by Bourque and Newman [1], and Sawyer [3], and the second, conservation of horizontal momentum for a control volume covering the reattached portion of the jet. The resulting jet trajectory, axial velocity distribution, and reattachment pressure compare well with experimental data. The wall pressure in the impingement zone was found to be similar with respect to offset height. The resulting pressure variation automatically accounts for the flow deceleration and subsequent acceleration.

The flow field results thus determined are substituted in equations (15) and (16) to determine the maximum temperature distribution Θ_m and the recirculation temperature Θ_R. The integrals in equation (16) are evaluated numerically.

(*b*) *Solutions Based on Simplified Closed-Form Flow Field Results.* A simplified model which is based on Bourque and Newman's [5] approximations is used to generate closed-form solutions for the flow field characteristics. In the preattachment region the radius of curvature is assumed constant and the decay of the maximum velocity, u_m, and the growth of the jet width b are approximated by those of a free jet. Appendix A outlines the formulation of this model and gives closed-form solutions for the jet trajectory and the variables u_m, b, and δ. While the solutions presented in Appendix A are for an offset jet discharging in a quiescent ambient, the analysis can be easily extended to take into consideration free-stream motion.

Experimental Setup

An experimental investigation of the two-dimensional jet-boundary interaction problem was conducted in the low speed wind tunnel facility of the Mechanical Engineering Laboratory of the City College of the City University of New York. The tunnel has a test section measuring 42 in. (1.07m) wide by 30 in. (0.75m) high by 90 in. (2.3m) long. The working section is enclosed in a large pressure-tight chamber. Air flow through the wind tunnel, which was used to simulate free-stream motion, was produced by a centrifugal blower which exhausts air from the observation chamber. The maximum velocity obtained under this arrangement was approximately 13 ft/s (4m/s). Lower velocities were produced by adjusting the blower's exhaust baffles. A detailed description of the wind tunnel is found in reference [12].

Observations and measurements on two-dimensional jet-boundary interaction were made in the wind tunnel test section. The free-stream velocity through the test section was designed to be steady and uniform with recorded turbulence intensity levels below 0.1 percent. The primary air was heated by a thermostatically controlled electric heater and supplied to the test section through a rectangular inlet duct which was connected to a horizontally oriented rectangular nozzle. Two different nozzles were used, one with a height d^* of 0.26 in. (0.66cm) and another of 0.46 in. (1.17cm). Both nozzles had a width of approximately $4\frac{7}{8}$ in. (12.4cm). Average jet discharge velocities were varied from approximately 10 to 120 ft/s (3 to 36 m/s), depending on nozzle height. Maximum discharge temperatures up to 250°F were obtained to ±1°F. Discharge Reynolds numbers were well within the turbulent range and discharge velocity and temperature profiles were observed to be nearly top-hat.

In order to ensure that the jet remains two-dimensional, two plexiglass plates were placed vertically on each side of the jet nozzle, forming a channel with a spacing equal to the nozzle width. The upstream leading edge was tapered to prevent any separation of the free stream. Flow measurements revealed that boundary layer buildup was not a problem. A horizontal plate was inserted at the bottom of the channel with which jet interaction took place.

The offset distance h^* between the jet and the bottom plate was varied using removable connecting ducts of different dimensions. The offset parameter, h, was also varied using different values of d^* at a fixed nozzle location.

Mean velocities were measured using a constant temperature hot wire anemometer system. RMS turbulence measurements were also used to locate the position of the dividing streamline, which may be characterized by peak RMS values [12]. Copper-constantan thermocouples were used to measure temperatures.

Wall pressure distribution was determined by the use of pressure taps on the bottom surface. A micromomometer was used to measure pressure.

Results

The maximum axial temperature distribution as given by either equation (15) or (16) is dependent on the value chosen for the turbulent Prandtl number λ. Reported values of λ for two-dimensional free jets vary from 1.12 to 1.41 [1, 11]. Although the value of λ in the preattachment region will be close to that of a free jet, it is difficult to verify this experimentally from measurements of velocity and temperature half-widths. The difficulty is due to jet curvature, asymmetry of temperature profiles and the steep transverse temperature gradients near the discharge. However, experimental determination of jet velocity and temperature half-widths is more feasible in the impingement and wall jet regions. Fig. 2 gives the variations of the velocity and temperature half-widths along x in these regions for two values of the offset parameter h. A least square of the experimental data gives $\lambda = 1.15$ for $h = 0$ (wall jet) and $\lambda = 1.18$ for $h = 5.6$. The closeness of these values of λ to that of the two-dimensional free jet justifies using $\lambda = 1.15$ in predicting Θ_m throughout the offset jet. The validity of our assumed Gaussian temperature profile is demonstrated in Fig. 3. Temperature profile data taken at various axial distances in the impingement and wall jet regions for three values of the offset distance h are plotted and compared with a Gaussian profile. As shown in Fig. 3, the distribution of data does follow a Gaussian shape.

A basic assumption in the derivation of equation (15) is that due to efficient mixing, the temperature inside the recirculation region is uniform. A temperature map of the preattachment region, which includes the recirculation region, is shown in Fig. 4 for $u_\infty = 0$, for $h = 8.7$. The relative uniformity of temperature in the recirculation region is demonstrated. Theoretical predictions of the jet axis and the dividing streamline are compared with experimental data. Jet axis is determined from hot wire velocity measurements and is defined as the locus of maximum axial velocities. The dividing streamline is established from RMS readings. Reasonable agreement between theory and experiment is obtained.

Theoretical results, based on the flow field theory of Hoch and Jiji [9], for the axial temperature decay are compared with experimental data for offset parameters of 3.0 and 8.7 in Fig. 5. Agreement between theory and experiment is good. The effects of the offset parameter h are most noticeable in the preattachment region but diminish downstream where both theory and experimental data tend to coalesce into a single curve.

Ambient velocity effects on the maximum temperature decay, Θ_m, for $h = 5.7$ are shown in Fig. 6. As in Fig. 5, the required flow field characteristics are taken from the numerical results of [9]. Figure 7 shows the effect of offset distance on Θ_R. Both theory and experimental data show that Θ_R is significantly affected by changes in the

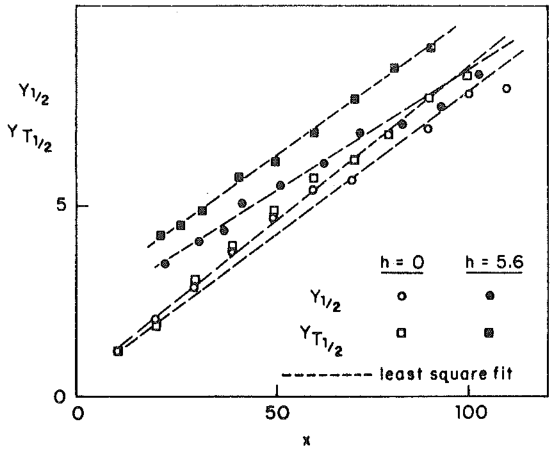

Fig. 2 Velocity and temperature half-width in the impingement and wall jet regions

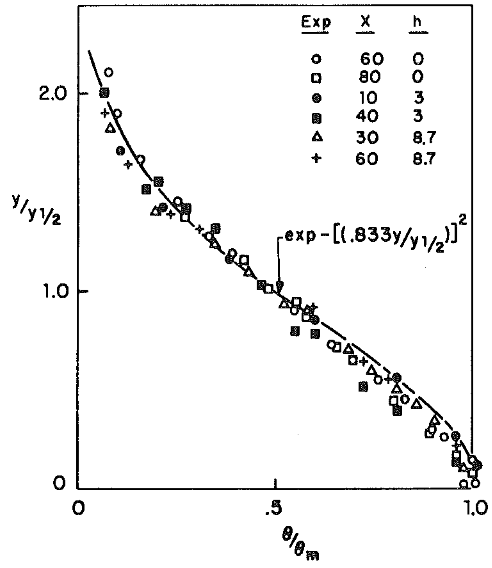

Fig. 3 Temperature profiles in the impingement and wall jet regions

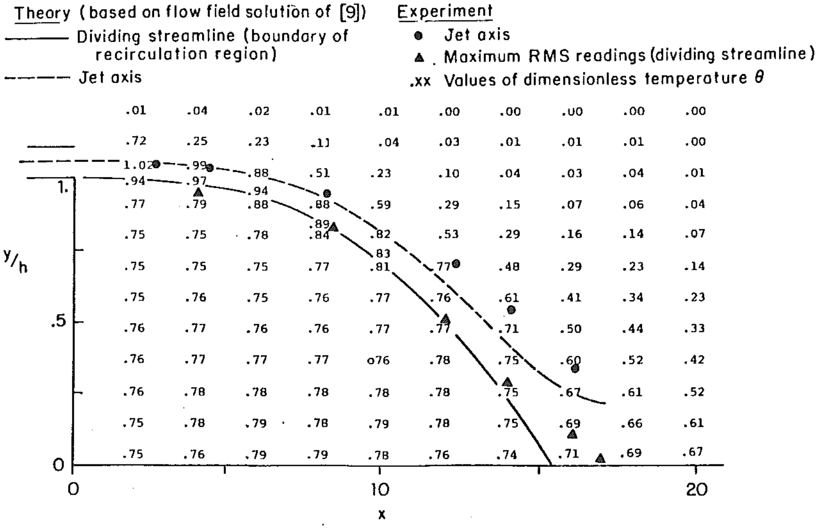

Fig. 4 Temperature map of the preattachment region ($u_\infty = 0$, $h = 8.7$)

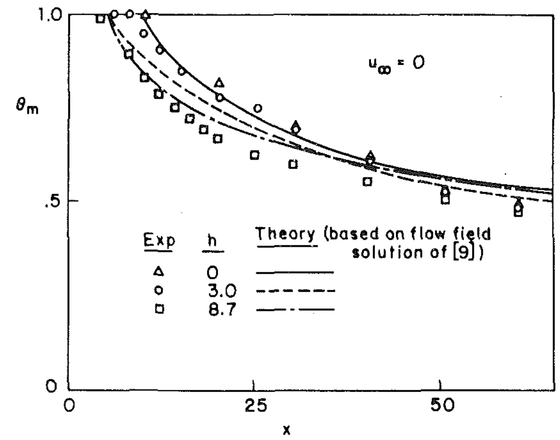

Fig. 5 Effect of offset parameter *h* on the maximum axial temperature decay ($u_\infty = 0$)

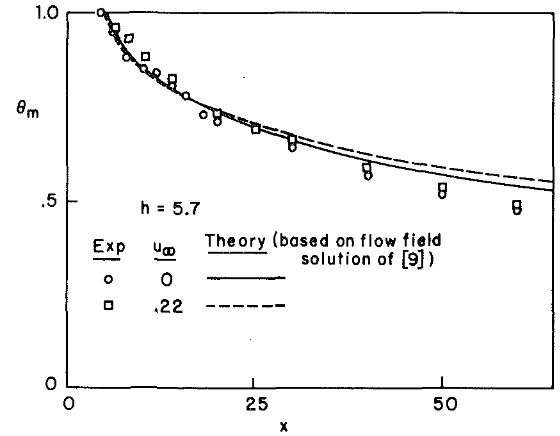

Fig. 6 Effect of free stream velocity on the maximum axial temperature decay ($h = 5.7$)

offset distance h, decreasing as h is increased. However, an increase in the free stream velocity u_∞ results in a small decrease in Θ_R.

Since the simplified flow field model yields convenient closed form solutions for the jet characteristics which are used directly to determine the temperature distribution, it is useful to examine the accuracy with which the simplified flow model predicts Θ_m and Θ_R. Figure 8 compares the theoretical temperature distribution $\Theta_m(x)$ of Fig. 5, which is based on the flow field results of [9], with that using the closed-form flow solution of Appendix A. Excellent agreement is noted for two offset distances $h = 3$ and $h = 8.7$. Theoretical predictions of the recirculation region temperature Θ_R for the two theories are also shown in Fig. 8. It is noted that agreement between the two theories is fair at low values of h but improve as h is increased.

Conclusions

The Gaussian nature of temperature profiles in the reattached portion of the jet and the uniformity of temperature in the recirculation region were substantiated experimentally. Measurements of jet velocity and temperature half-widths in this region gave a turbulent Prandtl number of 1.15, which is within the range of values reported for turbulent free jets.

Free stream velocity, within the range of our experimental data ($u_\infty = 0$ to $u_\infty = 0.22$), was found to have a minor effect on the maximum axial temperature distribution. Variations in the offset distance between 0 and 8.7 were found to have noticeable influence on the maximum axial temperature in the preattachment region, diminishing progressively downstream.

In general, our theoretical solutions for temperature distribution were found to be in good agreement with experimental data. Temperature solutions using the simplified closed-form flow field results outlined in Appendix A compares well with those based on the results of [9]. While the closed-form flow solution is convenient to use for

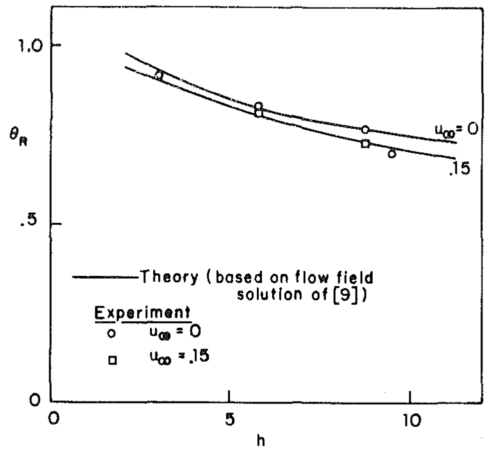

Fig. 7 Effect of offset distance on the recirculation region temperature

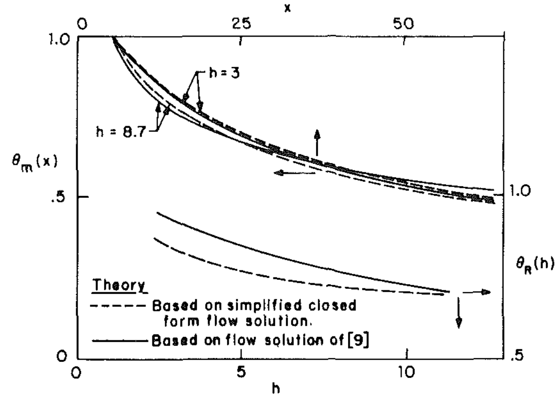

Fig. 8 Comparison of temperature predictions using closed-form flow solutions and that of [9]

temperature predictions, it may not adequately describe jet flow characteristics. However, due to the nature of integral solutions, temperature predictions are not adversely affected.

Acknowledgment

This study was sponsored by the National Science Foundation under Grant No. ENG-78-10004.

References

1 Jirka, G., and Harleman, D. R. F., "Heat Dissipation from Power Plants," MIT Parsons Laboratory for Water Resources and Hydrodynamics, Technical Report No. 206, 1975.

2 Seban, R. A., and Back, L. H., "Velocity and Temperature Profiles in a Wall Jet," Vol. 3, No. 4, 1961, pp. 255–265.

3 Glauert, M. B., "The Wall Jet," *Journal of Fluid Mechanics*, Vol. 1, 1956, pp. 625–643.

4 Rohsenow, W. M., and Hartnett, J. P., *Handbook of Heat Transfer*, McGraw-Hill, New York, 1973.

5 Borque, C., and Newman, B. G., "Reattachment of a Two-Dimensional Incompressible Jet to an Adjacent Flat Plate," *Aeronautical Quarterly*, Vol. 11, 1960, pp. 201–232.

6 Sawyer, R. A., "The Flow Due to a Two-Dimensional Jet Issuing Parallel to a Flat Plate," *Journal of Fluid Mechanics*, Vol. 9, 1960, pp. 543–560.

7 Sawyer, R. A., "Two-Dimensional Reattaching Jet Flows Including the Effect of Curvature on Entrainment," *Journal of Fluid Mechanics*, Vol. 17, 1963, pp. 481–498.

8 Rajaratnam, N., and Subramanya, N., "Plane Turbulent Reattached Wall Jets," *ASCE Journal of Hydraulics Division*, 94, HY1, 1968.

9 Hoch, J., and Jiji, L. M., "Two-Dimensional Turbulent Offset Jet-Boundary Interaction," ASME *Journal of Fluids Engineering*, Vol. 103, 1981.

10 Morton, B. R., Taylor, G. I., and Turner, J. S., "Turbulent Gravitational Convection from Maintained and Instantaneous Sources," *Proceedings Royal Society, London*, Series A234, 1956, pp. 1–23.

11 Davies, A. E., Keffer, J. F., and Baines, W. D., "Spread of a Heated Plane Turbulent Jet," Vol. 18, No. 7, 1975, pp. 770–775.

12 Tandowski, B., "Near Field Pollution Due to Emissions from Short Stacks on Buildings," Ph.D. dissertation, Mechanical Engineering Department, The City College of the City University of New York, 1977.

APPENDIX A

Simplified Flow Field Model-Closed Form Solution

This section presents closed-form solutions for the jet trajectory and variables u_m, b, and δ for use in the temperature solutions (15) and (16). The solutions are based on Bourque and Newman's [5] approximations for two-dimensional offset jets. While this approach is applied to jets in a quiescent ambient, the analysis can be easily extended to include the effects of free stream motion.

Consideration is given to the two main regions of the jet: the preattachment region and wall jet region. Here we ignore the impingement region and assume that immediately after the jet reattaches it behaves like a wall jet.

(i) Preattachment Region. Following Bourque and Newman we assume that the variation of the jet maximum axial velocity u_m and width b along the curved axis x_3 is the same as the variation of these variables along the axis of a free jet. Thus, replacing x by x_3, the solution for two-dimensional free jets gives [1]

$$u_m = \sqrt{\frac{5.2}{x_3}} \tag{A-1}$$

and

$$b = 0.154 x_3 \tag{A-2}$$

To complete the solution in this region the jet trajectory must be determined. Assuming constant radius of curvature r, the trajectory coordinates x, y are given by (see Fig. A-1):

$$x = r \sin \gamma \tag{A-3}$$

and

$$y = (h + 1/2) - r(1 - \cos \gamma) \tag{A-4}$$

where h is the offset distance and γ is the angle between the tangent to x_3 and the horizontal axis (see Fig. A-1). The radius of curvature r is determined from (A-4) by setting $y = 0$:

$$r = \frac{h + 1/2}{1 - \cos \gamma_A} \tag{A-5}$$

where γ_A is the jet angle near the reattachment point.

The distance along the jet axis x_3 is given by

$$x_3 = \frac{(h + 1/2)\gamma}{1 - \cos \gamma_A} \tag{A-6}$$

Geometric consideration of Fig. A-1 gives the point of reattachment x_A:

$$x_A = \frac{(h + 1/2)}{(1 - \cos \gamma_A)} \sin \gamma_A - \frac{b_R(x_{3A})}{\sin \gamma_A} \tag{A-7}$$

where $b_R(x_{3A})$ is the distance between the dividing streamline and the jet axis evaluated at $x_3 = x_{3A}$. Here x_{3A} is the distance along x_3 measured from the discharge to the reattachment position (see Fig. A-1).

To determine the two unknowns b_R and γ_A use is made of laws of conservation of momentum and mass. Neglecting local pressure variations, conservation of horizontal momentum for the control volume shown in Fig. A-1 gives [5, 6]:

$$\cos \gamma_A \int_{-w}^{w} u^2 dx_1 = \int_{-b_R}^{w} u^2 dx_1 - \int_{-w}^{b_R} u^2 dx_1 \tag{A-8}$$

The variable b_R is determined by observing that the dividing streamline extends from the edge of the discharge to the point of reattachment. Thus all the mass entrained in the inner part of the jet is returned to the recirculation region at impingement. The equation for the dividing streamline is therefore given by

$$\int_{-b_R}^{o} u dx_1 = 1/2 \tag{A-9}$$

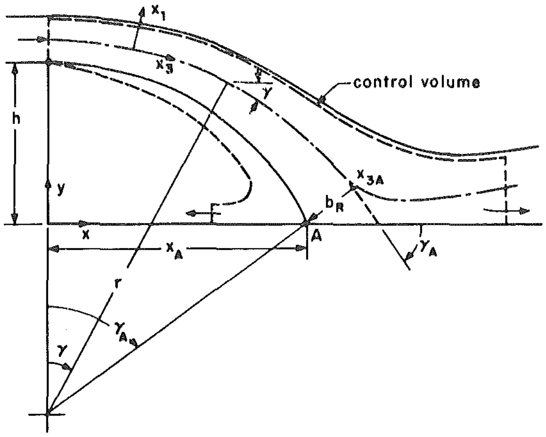

Fig. A-1 Schematic of the two-dimensional offset jet for the simplified flow model

Substituting the assumed velocity profiles (3) and (4), with $u_\infty = 0$, into (A-8) and (A-9), evaluating the integrals at $x_3 = x_{3A}$, we obtain:

$$\cos \gamma_A = \text{erf}\,(\sqrt{2}\,\eta_A) \tag{A-10}$$

and

$$\text{erf}\,\eta_A = \frac{1.61}{\sqrt{x_{3A}}} \tag{A-11}$$

where

$$\eta_A = \frac{b_R(x_{3A})}{b(x_{3A})} \tag{A-12}$$

Equations (A-10) and (A-11) contain two unknowns γ_A and η_A. Once η_A is determined, (A-12) gives $b_R(x_{3A})$ since $b(x_{3A})$ is given by (A-2). Solving (A-10) for γ_A, evaluating (A-6) at $\gamma = \gamma_A$ and substituting into (A-11) we obtain a single equation for η_A:

$$\cos^{-1} [\text{erf}\,(\sqrt{2}\,\eta_A)] = \frac{1 - \text{erf}\,(\sqrt{2}\,\eta_A)}{(h + 1/2)(\text{erf}\,\eta_A)^2} \tag{A-13}$$

Once η_A is determined, equation (A-10) gives γ_A.

(ii) Wall Jet Region. The jet in this region is assumed to behave like a wall jet. For a wall jet it has been found that [8]:

$$u_m = \frac{3.5}{\sqrt{x}} \tag{A-14}$$

$$b \sim x \tag{A-15}$$

$$\delta \sim x \tag{A-16}$$

We now assume that the jet behaves as if it is issued from an imaginary or virtual origin located at $x = x_i$ with respect to our coordinate system. The virtual origin is determined by matching the velocity of equation (A-14) with that of equation (A-1) at the reattachment position. This yields:

$$x_i = x_A - 2.36 x_{3A} \tag{A-17}$$

The velocity field is thus described by

$$u_m(x) = \frac{3.5}{\sqrt{x - x_i}} \tag{A-18}$$

$$b(x) = \frac{(x - x_i)}{(x_A - x_i)} b(x_{3A}) \tag{A-19}$$

and

$$\delta(x) = \frac{(x - x_i)}{(x_A - x_i)} \delta(x_{3A}) \tag{A-20}$$

where $\delta(x_{3A})$ is determined from conservation of mass for the flow between the jet axis and the wall at $x_3 = x_{3A}$:

$$\delta(x_{3A}) = \frac{4}{7} \sqrt{\pi}\, b(x_{3A})\, \text{erf}\, \eta_A \tag{A-21}$$

Streamwise Flow and Heat Transfer Distributions for Jet Array Impingement with Crossflow

L. W. Florschuetz
Professor,
Mem. ASME

C. R. Truman
Graduate Student,
Student Mem. ASME

D. E. Metzger
Professor,
Mem. ASME

Department of Mechanical Engineering,
Arizona State University,
Tempe, Ariz

Two-dimensional arrays of circular jets of air impinging on a heat transfer surface parallel to the jet orifice plate are considered. The air, after impingement, is constrained to exit in a single direction along the channel formed by the surface and the jet plate. The downstream jets are subjected to a crossflow originating from the upstream jets. Experimental and theoretical results obtained for streamwise distributions of jet and crossflow velocities are presented and compared. Measured Nusselt numbers resolved to one streamwise hole spacing are correlated with individual spanwise row jet Reynolds numbers and crossflow-to-jet velocity ratios. Correlations are presented for both inline and staggered hole patterns including effects of geometric parameters: streamwise hole spacing, spanwise hole spacing, and channel height, normalized by hole diameter. The physical mechanisms influencing heat transfer coefficients as a function of flow distribution and geometric parameters are also discussed.

Introduction

Impingement with high velocity gas jets has become an established method of convectively cooling or heating surfaces in a wide variety of process and thermal control applications. Examples include cooling of gas turbine airfoils and electronic equipment, drying of paper and textiles or other thin layers or films, annealing of metals, and glass tempering operations.

For gas turbine airfoils a significant application utilizing a two-dimensional array of jets is the cooling of the midchord region with a trailing edge discharge. The jet air, after impingement, is constrained to flow toward the rear of the airfoil along the channel formed between the jet orifice plate and the inner surface of the airfoil envelope. Thus, in this configuration, exhaust from the upstream jets imposes a confined crossflow on the downstream jets.

An investigation, supported by the National Aeronautics and Space Administration, was initiated with the primary objective of determining heat transfer behavior for a variety of uniformly spaced impingement array configurations which model those of interest in current and contemplated gas turbine airfoil cooling applications. Earlier publications based on this project presented results for both array mean Nusselt numbers and spanwise averaged, streamwise resolved Nusselt number profiles for arrays having ten spanwise rows of holes [1, 2, 3]. These results were for streamwise resolutions from one-third to twice the streamwise hole spacing, and were presented in terms of array mean jet Reynolds numbers and geometric parameters. Results for arrays with both inline and staggered hole patterns were included.

Subsequently, the use of a simple one-dimensional momentum flux model was found to quite accurately predict the row-by-row streamwise flow distributions. In this paper both development of the model and experimental determination of the flow distributions are presented and the results compared. These flow distributions then provide the means by which the spanwise averaged, streamwise resolved Nusselt numbers are examined as a function of the individually associated spanwise row jet Reynolds numbers and crossflow-to-jet velocity ratios. Correlations are presented for both inline and staggered hole patterns for Nusselt numbers resolved to one streamwise hole spacing. Specifically, these Nusselt numbers are correlated in terms of the individual spanwise row jet Reynolds number (Re_j) and crossflow-to-jet velocity ratio (G_c/G_j); and in terms of three geometric parameters: the streamwise hole spacing, the spanwise hole spacing, and the channel height each normalized by hole diameter (x_n/d, y_n/d, and z/d). The overall ranges of these variables are Re_j, 2.5×10^3 to 7×10^4; G_c/G_j, zero to 0.8; x_n/d, 5 to 15 for inline hole patterns and 5 to 10 for staggered patterns; y_n/d, 4 to 8; and z/d, 1 to 3. The aspect ratios, x_n/y_n, for the jet plates ranged form 0.625 to 3.75.

Experimental Facility

Only a brief description of the test facility is given here, though a summary of the significant characteristics of the jet array geometries tested is included. Additional details may be found in [1] and [2], with complete details available in [3].

The basic test geometry and nomenclature are shown schematically in Fig. 1 for the case of an inline hole pattern. In the test facility the region between the jet plate and the heat transfer test surface was enclosed on three sides. This constrained the exhaust air from the jets to exit in a single direction along the channel thus formed.

The channel height was set by the thickness of interchangeable spacers which formed the side walls. Other variations in geometric scale and geometric parameters were obtained via interchangeable air supply plenums each with matching interchangeable jet plates. Streamwise resolution of heat transfer coefficients was achieved by the design of the single test surface, which was segmented in the streamwise direction. The basic geometric characteristics of the configurations tested and the maximum resolution for each plenum size are summarized in Table 1. The smallest jet hole diameter is near prototype size for the gas turbine application, while the larger sizes provided for improved streamwise resolution of heat transfer coefficients. Emphasis in this paper is placed on results from the B, C, and D sizes since, for these, heat transfer coefficients can be resolved to at least one streamwise hole spacing. Note that the number of spanwise (transverse) rows of holes was fixed at 10 for all jet plates. The first row (counting from upstream) was always displaced $x_n/2$ from the upstream end of the channel (Fig. 1). Each jet plate with a staggered hole pattern was identical to its inline counterpart, except that alternating spanwise rows were offset by one-half the spanwise hole spacing. Each individual configuration tested can be uniquely identified by specifying a size designation (A, B, C, or D), a set of geometric parameters ($x_n/d, y_n/d, z/d$), and a hole pattern (I or S). For brevity, specific configurations will be referred to by designations such as B(5,8,2)I; or when it is unnecessary to indicate in this way a specific size, hole pattern, and/or geometric parameter value, obvious notations such as B(5,8)I, B(5,8), or simply (5,8) will be used. Attention is called to the fact that a number of the configurations of different sizes listed in Table 1 are geometrically similar. Considering sizes B, C, and D the maximum length scale factor is 3; including A-size, the maximum factor is 6. Discharge coefficients for each jet plate tested

---

Contributed by the Gas Turbine Division and presented at the International Gas Turbine Conference and Products Show, Houston, Texas, March 9–12, 1981 of THE AMERICAN SOCIETY OF MECHANICAL ENGINEERS. Manuscript received by the Heat Transfer Division December 10, 1980. Paper No. 81-GT-77.

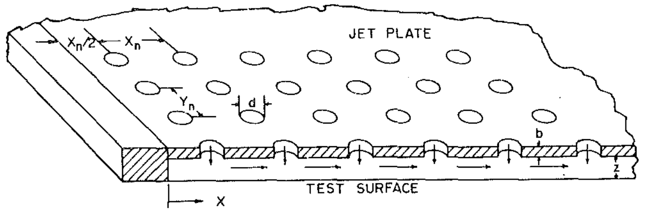

Fig. 1 Basic test model geometry and nomenclature

are also summarized in Table 1, with the single exception of jet plate A(10,6)I which was included in the heat transfer test program, although the discharge coefficient was not determined.

Flow Distribution

The determination of the distribution of the jet flow among the individual spanwise rows was an essential step prior to attempting correlation of the streamwise resolved heat transfer coefficients with the individual row jet and crossflow rates. Streamwise channel pressure traverses were accomplished with static pressure probes inserted from the downstream end of the channel. Jet plate discharge coefficients were measured over a range of Re_j spanning that for which data was obtained in the heat transfer tests. The C_D values were essentially independent of Re_j over this range. The mean values of C_D, as listed in Table 1, were used in determining the flow distributions. Additional details regarding the experimental procedures, pressure profile results, and discharge coefficients may be found in [4].

Results. The distribution of the jet flow as calculated from the pressure traverse and discharge coefficient results is illustrated by the data points in Fig. 2. These points were drawn from the results for the B and C-size configurations, and represent the jet mass velocity for the individual spanwise rows normalized by the mean of the individual values over all ten rows. The sum of the flow rates over all rows closed to within 3 percent or better of the total flow rate measured upstream of the plenum for all these cases, except one which closed to within 6 percent. The vertical arrows along the abscissa indicate the row locations. The corresponding points for the crossflow parameter, G_c/G_j, are shown in Fig. 3 (excepting the C(5,6,1)I case, omitted for clarity).

The curves in both figures are based on the one-dimensional model outlined below. The agreement is quite satisfactory. The model leads to the result that the flow distribution is independent of the streamwise hole spacing and hole pattern, depending, for a given discharge coefficient and number of rows, only on the geometric parameter $(y_n/d)(z/d)$. Data for $x_n/d = 10$ and 15 and for staggered patterns (not shown in Figs. 2 and 3) verify this result [4]. The range of this parameter covered in Figs. 2 and 3 matches that for the heat transfer

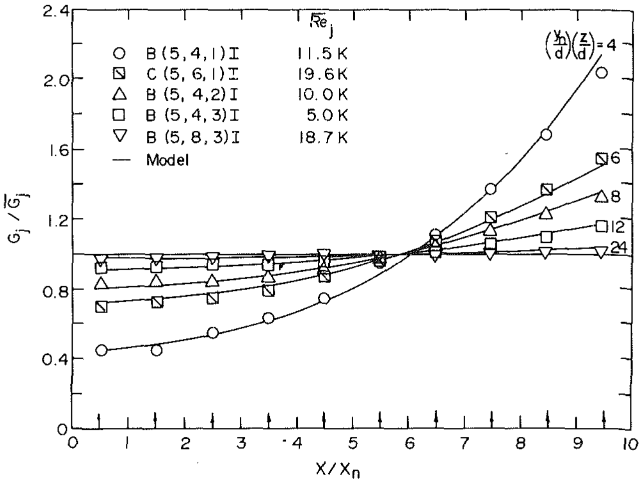

Fig. 2 Streamwise distribution of jet velocities—comparison between measured values and model, equation (7)

Table 1 Geometric characteristics of configurations tested

					$\overline{C}_D$		Maximum
Plenum Size	L (cm)	d & b (cm)	x_n/d	y_n/d	I	S	Streamwise Resolution
A	6.35	0.0635	10	6	—	0.80	$2x_n$
				8	0.83	—	
B	12.7	0.254	5	4	0.85	0.85	x_n
				8	0.80	0.79	
		0.127	10	4	0.76	0.73	
				8	0.76	0.74	
C	25.4	0.508	5	4	0.81	—	$x_n/2$
				6	0.77	—	
				8	0.78	0.78	
		0.254	10	4	0.82	0.83	
				6	0.79	—	
				8	0.79	0.80	
D	38.1	0.762	5	4	0.81	0.79	$x_n/3$
		0.381	10	4	0.80	—	
				8	0.78	—	
		0.254	15	4	0.83	—	
				6	0.80	—	
				8	0.79	—	

Notes: Channel heights (z/d) fixed at 1, 2, and 3. Number of spanwise (transverse) rows of holes (L/x_n) fixed at 10 for all tests. Channel span fixed; number of holes across span varied, depending on y_n, from 4 to 48. I denotes in line, S denotes staggered hole pattern.

Nomenclature

A = coefficient of Reynolds number in power function fit or correlation equations
A_0^* = ratio of jet hole area to opposing heat transfer surface area (open area ratio)
b = thickness of jet plate
B = coefficient in crossflow function of correlation equation
β = flow distribution parameter introduced following equation (7), $C_D\sqrt{2}\ (\pi/4)/[(y_n/d)(z/d)]$
C = constant appearing in correlation equation
C_D = jet plate discharge coefficient
d = jet hole diameter
G_c = channel crossflow mass velocity based on channel cross-sectional area
G_j = jet mass velocity based on jet hole area
G_j^* = superficial jet mass velocity based on jet plate or equivalent opposing heat transfer surface area
h = convective heat transfer coefficient resolved in streamwise direction, averaged across span
i = spanwise hole row number
k = thermal conductivity of fluid
L = streamwise length of heat transfer surface
m = Reynolds number exponent in power function fit or correlation equation
M = flow distribution parameter introduced at equation (4), $\sqrt{2}\,A_0^*C_D/z$
μ = dynamic viscosity
n = exponent in crossflow function of correlation equation
n_x, n_y, n_z = constants appearing in correlation equation
N_c = number of spanwise rows in streamwise direction
Nu = Nusselt number resolved in streamwise direction, averaged across span, hd/k
Nu_1 = value of Nu at first upstream spanwise row of holes where $G_c/G_j = 0$
P = channel pressure
P_0 = plenum pressure
Pr = Prandtl number
Re_j = jet Reynolds number, G_jd/μ
ρ = fluid density
x = streamwise location along heat transfer surface measured from upstream end of channel
x_n = streamwise jet hole spacing
y_n = spanwise jet hole spacing
z = channel height (jet plate-to-impingement surface spacing)

Superscripts

$\overline{(\ )}$ = overbar refers to mean value

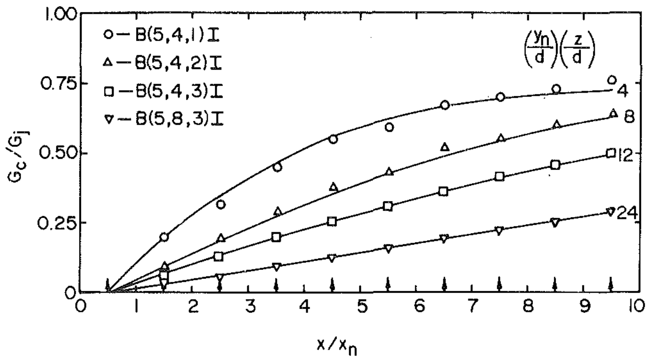

Fig. 3 Streamwise distribution of crossflow-to-jet velocity ratio—comparison between measured values and model, equation (8)

tests. For the largest value, 24, the distribution is essentially uniform with a corresponding linear increase in the crossflow parameter, G_c/G_j. For the smallest value, 4, the distribution is highly nonuniform with the jet velocity as small as one-half the mean at the first row, and as large as twice the mean at the tenth row; G_c/G_j increases linearly upstream but levels off quickly downstream to a maximum value of about 0.75.

Model. The discrete hole array is imagined to be replaced by a surface over which the injection is continuously distributed (Fig. 4). The jet velocity G_j is related to the continuously distributed injection velocity G_j^* through the open area ratio, $G_j^* = G_j A_0^*$. Thus, assuming incompressible flow, the distributed injection velocity may be written in terms of the discrete hole discharge coefficient as

$$G_j^* = A_0^* C_D [2\rho(P_0 - P)]^{1/2} \tag{1}$$

The streamwise pressure gradient in the channel is assumed to be primarily due to the acceleration of the flow caused by the injected fluid, with negligible influence of the wall shear. Accordingly, a force-momentum balance on the control volume indicated in Fig. 4(*a*) results in

$$dP = -\frac{2G_c dG_c}{\rho} \tag{2}$$

A mass balance leads to

$$G_j^* = z\frac{dG_c}{dx} \tag{3}$$

For constant C_D and P_0, the elimination of G_j^* and P from (1), (2), and (3) in favor of G_c yields

$$\frac{d^2G_c}{dx^2} - M^2 G_c = 0 \tag{4}$$

where $M = \sqrt{2}\, A_0^* C_D/z$. The upstream boundary condition is $G_c = 0$ at $x = 0$. A second boundary condition results from an overall mass balance for a channel length L written in terms of the overall mean injection velocity; i.e., $G_c = \overline{G}_j^* L/z$ at $x = L$. Integration of (4) then gives

$$\frac{G_c}{\overline{G}_j^*} = \frac{L \sinh Mx}{z \sinh ML} \tag{5}$$

for the crossflow distribution. The corresponding injected flow distribution obtained from (3) with the aid of (5) is given by

$$\frac{G_j^*}{\overline{G}_j^*} = \frac{ML \cosh Mx}{\sinh ML} \tag{6}$$

The discrete hole array jet velocity distribution is determined from (6) by assuming that the value of G_j for a given spanwise row of holes is that corresponding to $G_j^*(x)$ with x evaluated at the centerline of the row. For the uniform rectangular arrays of interest here $A_0^* = (\pi/4)/[(x_n/d)(y_n/d)]$, $L = x_n N_c$, and the first row is at $x = x_n/2$. Noting also that $\overline{G}_j^* = \overline{G}_j A_0^*$, the jet velocity distribution based on (6), may be written as

$$\frac{G_j}{\overline{G}_j} = \frac{\beta N_c \cosh \beta(x/x_n)}{\sinh \beta N_c} \tag{7}$$

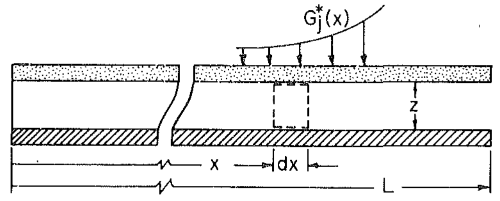

Fig. 4(*a*) Continuous injection model

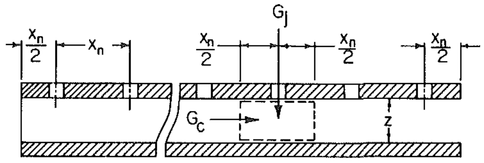

Fig. 4(*b*) Discrete hole injection model

where $\beta = C_D\sqrt{2}(\pi/4)/[(y_n/d)(z/d)]$ and $x = x_n(i - 1/2), i = 1, 2, 3 \ldots N_c$.

Besides the jet array velocity distribution given by (7), an additional flow parameter relevant to the correlation of the streamwise resolved heat transfer coefficients is the ratio of the crossflow velocity immediately upstream of a given spanwise row to the jet velocity of that row. This may be satisfactorily approximated utilizing G_c from (5) evaluated one-half a hole spacing upstream of the given row (Fig. 4(*b*)), divided by G_j from (7). This results in

$$\frac{G_c}{G_j} = \frac{1}{\sqrt{2}\, C_D} \frac{\sinh \beta(x/x_n - 1/2)}{\cosh \beta(x/x_n)} \tag{8}$$

where the spanwise hole row locations are the same as previously indicated following (7). The curves shown in Figs. 2 and 3, previously discussed, are based on (7) and (8), respectively.

The one-dimensional model developed above is similar to that presented by Martin [5] for an array of slot nozzles in which the outlet flow is constrained to exit in a single direction parallel to the slots, resulting in continuous injection in the flow direction. The present results indicate the applicability of a one-dimensional model for discrete hole arrays as well.

Heat Transfer Coefficients

Both mean and streamwise resolved heat transfer coefficients for jet plate configurations summarized in Table 1 were previously presented and discussed as a function of mean jet Reynolds number and geometric parameters [1, 2, 3]. Heat transfer coefficients resolved to one or two streamwise hole spacings [1, 3] and to one-third the hole spacing [2, 3] were considered. The experimental procedures and data reduction techniques were outlined in [1] and are further detailed in [3], which includes a complete tabulation of mean and resolved Nusselt numbers. The heat transfer coefficients were determined for an isothermal test surface. The experimental uncertainty for the Nusselt numbers was estimated to be ±5 percent for a confidence level of 95 percent [3].

The present objectives are to examine the heat transfer coefficients resolved to one streamwise hole spacing as a function of the associated spanwise row jet velocity, crossflow velocity, and geometric parameters; and to achieve a correlation in terms of these quantities. Thus, we consider

$$h = f(G_j, G_c, x_n, y_n, z, d)$$

or in dimensionless form, taking account also of relevant fluid properties,

$$\text{Nu} = f(\text{Re}_j, G_c/G_j, \text{Pr}, x_n/d, y_n/d, z/d) \tag{9}$$

Since the flow distribution model presented in the previous section was well supported by the flow distribution data, this model was used for determination of Re_j and G_c/G_j. It should be emphasized, however, that only the *distribution* of Re_j relative to the mean, i.e., $\text{Re}_j/\overline{\text{Re}}_j = G_j/\overline{G}_j$ was determined from (7). The mean values were taken from the square-edged orifice total flow rate measurements upstream of the plenum since they are more accurate than the sum of the individual row flow rate measurements.

The maximum nominal range of $\overline{\mathrm{Re}}_j$ for which heat transfer data were obtained was 5×10^3 to 5×10^4, though the full range was not covered for every individual geometry. Considering the geometries with the most highly nonuniform flow distribution, $(y_n/d)(z/d) = 4$, the maximum nominal range of Re_j was 2.5×10^3 to 1.75×10^4 for Row 1 ($G_c/G_j = 0$) and 10^4 to 7×10^4 for Row 10 ($G_c/G_j \cong 0.75$). For the most nearly uniform flow conditions, $(y_n/d)(z/d) = 24$, the Re_j range for all rows ($0 \leq G_c/G_j \leq 0.28$) was essentially the same as the range for $\overline{\mathrm{Re}}_j$. The effects of both geometric and crossflow parameters on Nu resolved to one streamwise hole spacing, at constant Re_j, are discussed in the following paragraphs.

Examination of Fig. 5[1] indicates that Nu_I, for which $G_c/G_j = 0$, decreases significantly with both x_n/d and y_n/d for fixed Re_j. The points shown are for $\mathrm{Re}_j = 10^4$; however, the trend with geometric parameters is similar over the Re_j range of the tests. The sensitivity to z/d is quite small except for the highest hole density configuration, $(x_n/d, y_n/d) = (5,4)$, where Nu_I for $z/d = 1$ is significantly larger than the values for $z/d = 2$ and 3. This is not a spurious data point because the data for the corresponding geometrically similar sizes corroborate this behavior. The trend of Nu_I with z/d is decreasing for small values of x_n/d and y_n/d, but increasing for large values. This type of behavior tends to work against development of a tight correlation of simple form.

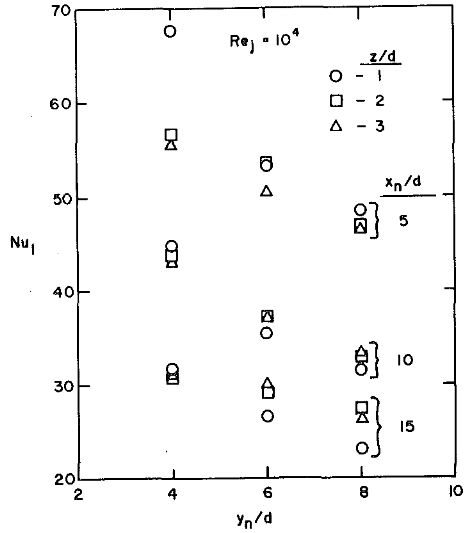

Fig. 5 Effect of geometric parameters on Nusselt number for initial upstream row of array. Inline hole pattern

Effect of Crossflow. The matrix of plots in Fig. 6 shows the effect of the crossflow parameter, G_c/G_j, on Nu where Nu is normalized by Nu_I. Each plot presents results for $z/d = 1$, 2, and 3 for a single hole spacing combination $(x_n/d, y_n/d)$. The data shown are for the smallest geometric size tested for that combination (excluding A-size for which Nu could not be resolved to one streamwise spacing). All points are for $\mathrm{Re}_j = 10^4$ but in this normalized form are representative of the general trends over the full Re_j range.

The trend of $\mathrm{Nu}/\mathrm{Nu}_I$ with G_c/G_j shifts from a monotonic decreasing function to a form which exhibits a broad minimum as x_n/d and y_n/d increase, and as z/d decreases. Thus, for $x_n/d \geq 10$, $y_n/d \geq 6$, $z/d = 1$, and $G_c/G_j \gtrsim 0.4$, $\mathrm{Nu}/\mathrm{Nu}_I$ increases slowly. A plausible explanation for this behavior, consistent with the fact that it occurs for large hole spacings and small channel heights, is that the crossflow provides an increasingly significant direct contribution to the heat transfer rate but does not cause a large degradation in the direct contribution from jet impingement. It may be remarked that results for heat transfer coefficients resolved to better than one streamwise hole spacing indicate that for these geometries the jets at the final downstream row still impinge on the surface; and, indeed, the impingement point is deflected downstream only a small fraction of the hole spacing [2, 3]. This inference is further corroborated by observations of discoloration patterns on the copper heat transfer surface subsequent to these test runs, which clearly indicate impingement of all jets with only slight deflection even at the final downstream row. In contrast, for smaller hole spacings and/or larger channel heights the jets are deflected and diffused more by the crossflow, and though they still impinge on the heat transfer surface, their cooling effectiveness is more significantly reduced. At the same time there is less surface area available for direct cooling by the crossflow.

The effect of increasing z/d, where significant, is to decrease $\mathrm{Nu}/\mathrm{Nu}_I$ at fixed G_c/G_j. This latter trend is consistent with the results of Metzger and Korstad [6] for a single row of jets transverse to a crossflow. The sensitivity of $\mathrm{Nu}/\mathrm{Nu}_I$ versus G_c/G_j to z/d increases with x_n/d but decreases with y_n/d. Thus, the effect of z/d is significant for $(x_n/d, y_n/d) = (15,4)$, the lower left plot, but essentially disappears for (5,8), the upper right plot. Or, stated another way the sensitivity of the crossflow effect to z/d appears to increase as the aspect ratio x_n/y_n increases. The complexity of the interacting jet/crossflow phenomena in the two-dimensional array precludes arriving with high confidence at a particular explanation, at least on the basis of currently available information. However, it may be appropriate to note several factors which contribute to the complexity, and may be involved in potential explanations.

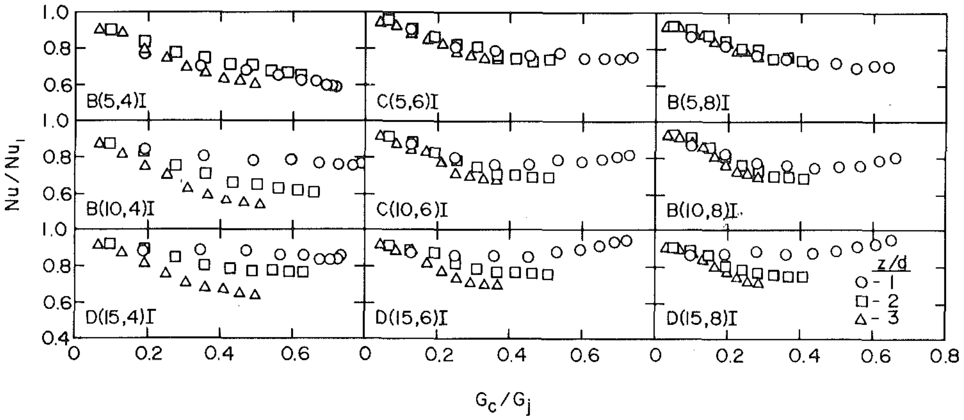

Fig. 6 Effect of crossflow and geometric parameters on streamwise resolved Nusselt numbers. Inline hole pattern

First, the crossflow velocity appearing in the crossflow parameter G_c/G_j as used in characterizing the present results is a mean value over the channel cross-section. Consider the distribution across the channel span of the crossflow velocity averaged over the channel

---

[1] The points for each specific hole spacing combination $(x_n/d, y_n/d)$ are drawn from the same geometric sizes (B, C, or D) identified in Fig. 6.

height. There is some evidence, e.g., flow visualization, indicating that for the inline arrays the crossflow tends to become channelized between adjacent streamwise jet rows. Thus, the spanwise flow distribution would be nonuniform with velocities between jets larger than those directly approaching the next downstream jet. The degree of nonuniformity would vary with array geometric parameters. Thus, the crossflow velocity seen by a single jet in an array would be smaller than the mean velocity over the cross-section by differing amounts depending on array geometry. Heat transfer coefficients obtained during preliminary tests with a spanwise uniform initial crossflow approaching the array were smaller than those measured at a downstream row of the array without initial crossflow, but total upstream jet flow rate adjusted to provide the same value of G_c/G_j at the downstream row.

Second, the values of Nu being compared for various $(x_n/d, y_n/d)$ combinations are averages over rectangles of widely varying aspect ratios, from $x_n/y_n = 0.625$ for the (5,8) case where no z/d effect is apparent to 3.75 for the (15,4) case where the effect is significant.

Third, results for potential core length obtained by Stoy and Ben-Haim [7] for a single jet in a confined crossflow indicate that for the present range of z/d, impingement may occur for certain jets before they are developed, and for others (even in the same array) after they are developed.

Effect of Hole Pattern. This effect is illustrated in Fig. 7 where Nusselt numbers for staggered hold patterns normalized by those for their counterpart inline patterns are plotted against the crossflow parameter. The effect is not significant for the largest hole spacing, $(x_n/d, y_n/d) = (10,8)$. However, as x_n/d and y_n/d decrease, and as z/d increases, the staggered pattern results in increasingly reduced heat transfer coefficients relative to the inline values for increasing crossflow.

This behavior is thought to be associated with differences in spanwise distribution of the crossflow in the two cases [2, 3]. The tendency of the crossflow to become channelized between adjacent streamwise rows of the inline pattern reduces the direct influence it can exert on each downstream jet. In contrast, the spanwise crossflow distribution presumably remains more nearly uniform for the staggered patterns; hence the crossflow approach velocity directly upstream of each jet is somewhat larger than for the matching inline case.

Correlation

Correlation attempts were carried out primarily in terms of the variables indicated in equation (9). Consideration of the number of these variables (six in all, excluding Prandtl number) coupled with close examination of the data indicated the improbability of achieving a really tight correlation of simple form. After a number of attempts utilizing forms of varying complexity, the following form was finally adopted:

$$\mathrm{Nu} = A\,\mathrm{Re}_j^m\,\{1 - B[(z/d)(G_c/G_j)]^n\}\mathrm{Pr}^{1/3} \qquad (10a)$$

where the coefficients A and B, and the exponents m and n are each permitted to depend on the geometric parameters in the form of simple power functions. That is,

$$A, m, B, \text{and } n = C(x_n/d)^{n_x}(y_n/d)^{n_y}(z/d)^{n_z} \qquad (10b)$$

The form (10) was applied separately to the inline and staggered hole pattern data for B, C, and D sizes. The analyses were carried out using a multivariable nonlinear regression routine with a least squares objective function [8]. The objective function was based on the logarithm of the dependent variable (Nu). In this way, the relative deviations rather than the absolute magnitudes were minimized. The resulting best fit values for the coefficients and exponents are summarized in Table 2 for both inline and staggered hole patterns.

The inline correlation, based on a total of 1400 data points, produced a standard error of the deviations of 5.6 percent. By actual count 95 percent of the points fall within 11 percent of the fit line, while 99 percent fall within 16 percent. All the points fall within 19 percent, save one which deviated by 26 percent. The staggered correlation, based on a total of 680 points, produced a standard error of 6.1 percent. Ninety-five percent of these points were within 12 percent of the fit line, 99 percent were within 16 percent, and all the points fell within 18 percent, save one which again deviated by 26 percent. The bulk of the points having the larger deviations tended to occur for upstream rows for small Re_j at $z/d = 1$.

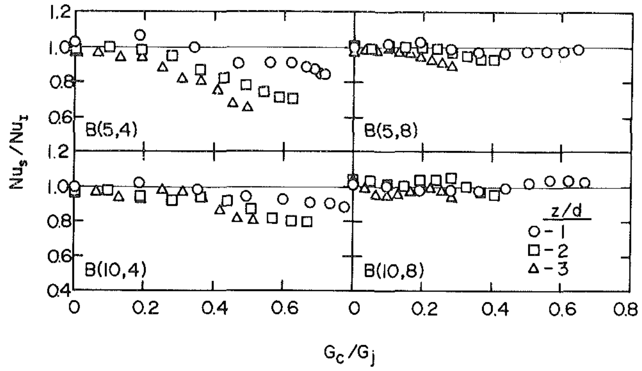

Fig. 7 Effect of hole pattern (staggered versus inline) on streamwise resolved Nusselt numbers as function of crossflow and geometric parameters

Table 2 Constants for use in correlation, equation (10)

	Inline Pattern				Staggered Pattern			
	C	n_x	n_y	n_z	C	n_x	n_y	n_z
A	1.18	−0.944	−0.642	0.169	1.87	−0.771	−0.999	−0.257
m	0.612	0.059	0.032	−0.022	0.571	0.028	0.092	0.039
B	0.437	−0.095	−0.219	0.275	1.03	−0.243	−0.307	0.059
n	0.092	−0.005	0.599	1.04	0.442	0.098	−0.003	0.304

In an earlier report [3], the degree of consistency of the results obtained for geometrically similar configurations was assessed in detail. Least squares fits in the form $\mathrm{Nu} = A\,\mathrm{Re}_j^m$ were carried out for the combined data of the several sizes for each set of geometrically similar configurations. In effect, A and m were permitted to be adjustable constants taking different best fit values for each parameter set $(x_n/d, y_n/d, z/d)$ and each spanwise row number (i.e., each value of G_c/G_j). Ninety-five percent of the points were within 7 percent of the respective fit lines, 99 percent were within 10 percent, and all were within 14 percent. These percentages give some indication of the best that might be done if the optimum functional form were to be found. Viewed in this context the proposed correlations appear to be quite acceptable.

The data for the A-size geometries listed in Table 1 were excluded from the data sets relied on for correlation for two reasons. First, the maximum heat transfer coefficient resolution for these data was two rather than one streamwise hole spacing. Second, as previously pointed out [1, 3], compressibility effects were present for these cases at the higher Reynolds numbers. It is of interest, nevertheless, to compare the A-size data with the correlation. This was done for Nu resolved to $2x_n$. Despite the Mach numbers for some of these cases approaching or equal to unity, 95 percent of the points still fall within 16 percent of the correlation, with only one of 140 points deviating by more than 20 percent to a value of 27 percent. (The data used for the A(10,8,1)I case are a revised set, recently obtained, which is more consistent with the corresponding B, C, and D size data than the original set documented in [3] and reported in [1]. The reasons for this are explained in [4].)

Prior heat transfer measurements involving two-dimensional arrays of circular orifices in which the orifice plate and the heat transfer surface form a channel of uniform height with flow constrained to exit in a single direction parallel to jet hole rows were reported by Friedman and Mueller [9], Huang [10], Kercher and Tabakoff [11], and Chance [12]. These studies reported mean heat transfer coefficients for the entire surface opposite the array [9], or values for spatial resolutions greater than or equal to one streamwise hole spacing [10, 11, 12]. Only Kercher and Tabakoff, and Chance measured streamwise flow distributions and suggested correlations for streamwise resolved heat transfer coefficients in terms of individual spanwise row jet and crossflow velocities. Kercher and Tabakoff's study included measurements for 16 different combinations of hole spacing and channel height. Only two of these combinations provided streamwise resolutions down to one streamwise hole spacing, and these had just four rows of holes. All were inline arrays with an aspect ratio (x_n/y_n) of unity. Their correlation requires use of three graphical presentations. Chance tested square, equilateral triangular, and rectangular arrays, but did not report specific hole spacings or numbers of holes for his jet plates.

Values of Nu_1 based on the present correlation are compared with those based on the Kercher and Tabakoff correlation in Fig. 8. The comparison is for square, inline arrays at the extreme values of the geometric parameters which fall within the ranges covered by both investigations. Results based on the correlation of Chance are also shown for cooling of the surface by the jets, which is the same condition under which Kercher and Tabakoff's and the present data were obtained. Chance's correlation for data with heating of the surface fall 10 percent above that shown in the figure. The effect of crossflow as calculated from these same correlations is compared in Fig. 9 for the same geometries as Fig. 8.

Permitting both the coefficients and exponents in equation (10a) to depend on the geometric parameters provided the flexibility to achieve a reasonably tight overall correlation. This correlation is recommended for detailed analysis and design calculations, particularly when incorporated in computer programs where the larger number of specified constants is not a disadvantage.

An alternate correlation, more convenient for hand computation or examination of trends, is presented below. This correlation is of the same form as (10a), but with exponents m and n not permitted to depend on geometric parameters:

$$Nu/Nu_1 = 1 - C(x_n/d)^{n_x}(y_n/d)^{n_y}(z/d)^{n_z}(G_c/G_j)^n \qquad (11a)$$

where

$$Nu_1 = 0.363(x_n/d)^{-0.554}(y_n/d)^{-0.422}(z/d)^{0.068}Re_j{}^{0.727}Pr^{1/3} \qquad (11b)$$

and the constants in (11a) take the following values:

	C	n_x	n_y	n_z	n
Inline	0.596	−0.103	−0.380	0.803	0.561
Staggered	1.07	−0.198	−0.406	0.788	0.660

This correlation is essentially as good as that of equation (10) in terms of standard error and 95 percent confidence levels, but is not as tight overall.

Concluding Remarks

Results appropriate for use in analyzing circular jet array impingement systems in which the jet flow is constrained to exit in a single direction along the channel formed by the jet plate and the impingement surface have been developed and presented.

Specifically, row-by-row jet and crossflow velocity distributions may be calculated from equations (7) and (8), which have been verified by experimental results. Knowledge of the jet plate discharge coefficient is required. In the absence of specific values for the particular plates of interest, for jet plates similar to those utilized here a value of 0.79 is recommended.

Heat transfer coefficients resolved to one streamwise hole spacing may be computed from the correlations of either equation (10) or (11), for both inline and staggered hole patterns. Knowledge of jet and crossflow velocities at the spanwise row of interest, as well as geometric parameters is required. The heat transfer coefficients on which the correlations are based were measured for a uniform impingement surface temperature.

The parameter ranges on which the results are based are specified in the paper. Caution should be exercised in extrapolating the results beyond those ranges.

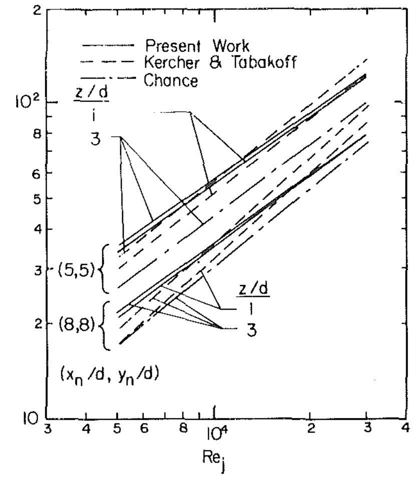

Fig. 8 Nusselt number for initial upstream row of array—correlations compared

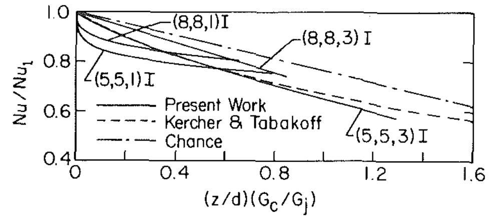

Fig. 9 Effect of crossflow on streamwise resolved Nusselt numbers—correlations compared

Acknowledgment

The support of the National Aeronautics and Space Administration, Lewis Research Center, under Grant NSG3075 is hereby gratefully acknowledged.

References

1 Metzger, D. E., Florschuetz, L. W., Takeuchi, D. I., Behee, R. D., and Berry, R. A., "Heat Transfer Characteristics for Inline and Staggered Arrays of Circular Jets with Crossflow of Spent Air," ASME JOURNAL OF HEAT TRANSFER, Vol. 101, 1979, pp. 526–531.

2 Florschuetz, L. W., Berry R. A., and Metzger, D. E., "Periodic Streamwise Variations of Heat Transfer Coefficients for Inline and Staggered Arrays of Circular Jets with Crossflow of Spent Air," ASME JOURNAL OF HEAT TRANSFER, Vol. 102, 1980, pp 132–137.

3 Florschuetz, L. W., Metzger, D. E., Takeuchi, D. I., and Berry, R. A., *Multiple Jet Impingement Heat Transfer Characteristics—Experimental Investigation of Inline and Staggered Arrays with Crossflow*, NASA-CR-3217, Department of Mechanical Engineering, Arizona State University, Tempe, Jan. 1980.

4 Florschuetz, L. W., Metzger, D. E., and Truman, C. R., "Jet Array Impingement with Crossflow—Correlation of Streamwise Resolved Flow and Heat Transfer Distributions," NASA-CR-3373, Department of Mechanical Engineering, Arizona State University, Tempe, Jan. 1981.

5 Martin, H., "Heat and Mass Transfer Between Impinging Gas Jets and Solid Surfaces," *Advances in Heat Transfer*, Vol. 13, Academic Press, New York, 1977, pp 1–60.

6 Metzger, D. E., and Korstad, R. J., "Effects of Cross Flow in Impingement Heat Transfer," ASME *Journal of Engineering for Power*, Vol. 94, 1972, pp. 35–41.

7 Stoy, R. L., and Ben-Haim, Y., "Turbulent Jets in a Confined Crossflow," ASME *Journal of Fluids Engineering*, Vol. 95, 1973, pp. 551–556.

8 Kuester, J. L., and Mize, J. H., *Optimization Techniques with Fortran*, McGraw-Hill, New York, 1973, pp. 240–250.

9 Friedman, S. J., and Mueller, A. C., "Heat Transfer to Flat Surfaces," *Proceedings, General Discussion on Heat Transfer*, The Institute of Mechanical Engineers, London, England, 1951, pp. 138–142.

10 Huang, G. C., "Investigations of Heat Transfer Coefficients for Air Flow Through Round Jets Impinging Normal to a Heat Transfer Surface," ASME JOURNAL OF HEAT TRANSFER, Vol. 85, 1963, pp. 237–243.

11 Kercher, D. M., and Tabakoff, W., "Heat Transfer by a Square Array of Round Air Jets Impinging Perpendicular to a Flat Surface Including the Effect of Spent Air," ASME *Journal of Engineering for Power*, Vol. 92, 1970, pp. 73–82.

12 Chance, J. L., "Experimental Investigation of Air Impingement Heat Transfer Under an Array of Round Jets," *Tappi*, Vol. 57, No. 6, 1974, pp. 108–112.

Prediction of Horizontal and Vertical Turbulent Buoyant Wall Jets

M. Ljuboja[1]
W. Rodi

Sonderforschungsbereich 80,
University of Karlsruhe,
Karlsruhe, West Germany

A buoyancy-extended version of the $k - \epsilon$ turbulence model is described which predicts well the main features of turbulent buoyant wall jets. The model relates the turbulent shear stress and heat flux to the mean velocity and temperature gradients respectively and to the turbulent kinetic energy k and the dissipation rate ϵ by way of the Kolmogorov-Prandtl eddy viscosity/diffusivity relation and determines k and ϵ from semi-empirical transport equations. The empirical constant c_μ in the Komogorov-Prandtl expression and the usually constant turbulent Prandtl number σ_t are replaced by functions which are derived by reducing model forms of the Reynolds-stress and heat-flux transport equations to algebraic expressions, retaining the buoyancy terms and the wall-damping correction to the pressure-strain/scrambling model in these equations. The extended $k - \epsilon$ model is applied to buoyant wall jets along a horizontal wall and to a plume developing along a vertical wall. The predictions are compared with experimental data whenever possible and are found to be in good agreement with the data.

1 Introduction

Turbulent buoyant wall jets arise when fluid is discharged from a slot tangentially to a wall with a density that is different from the density of the ambient. In general the wall may form any angle with the gravity vector, but here attention is restricted to the two limiting cases of horizontal and vertical walls, and these situations are sketched in Fig. 1. Buoyant wall jets along veritcal walls are sometimes also called wall plumes. In this paper only two-dimensional situations are considered, that is wall jets originating from long slots. Further, the walls are considered adiabatic so that there is no heat transfer to or from the walls. As indicated in Fig. 1 the general case of moving ambient is considered for the horizontal wall jet, but in the vertical wall jet situation only the case with stagnant ambient.

The special features of turbulent buoyant wall jets will now be discussed briefly. Compared with free jets and plumes, wall jets spread significantly less, and the reduction in spreading rate is due mainly to the damping of lateral velocity fluctuations by the wall, a mechanism that also reduces the lateral momentum transfer. The second important feature is the influence of buoyancy on the jet development. This influence depends on the direction of the flow (and thus of the orientation of the wall) relative to the gravity vector. In horizontal wall jets, gravity has no direct influence on the mean flow as the gravity vector is perpendicular to the mean-flow direction. In this case the only influence is on the turbulence behavior; for example when heavier fluid is discharged, a stable stratification is set-up and the turbulent motion (in particular the vertical fluctuations) are damped, and as a consequence entrainment of ambient fluid into the jet is reduced, leading to a reduction in jet growth. Under these conditions the turbulence may collapse completely and the jet may cease to grow altogether. In the case of a vertical buoyant jet, buoyancy affects the mean flow directly; for example when the discharged fluid is heated as in the example of Fig. 1 it is accelerated by upward buoyancy forces. In the vertical jet situation the turbulence is also influenced by buoyancy, but now the turbulent motion is enhanced by the gravitational effects.

Turbulent buoyant wall jets or closely related flows occur in many practical flow situations. Horizontal buoyant wall jets behave in many respects like density currents (at least behind the head of the current), although the driving mechanism is different in the two flows. Density currents are frequently found in the atmosphere, and examples are Katabatic winds, cold air fronts or, when the density difference is caused by suspended particles, snow powder avalanches and dust storms. In oceans and lakes, natural density currents may also exist, for example due to cold water from artic regions flowing along the bottom underneath warmer water, or due to suspended particles leading to turbity currents. Density currents due to outfalls are also of considerable importance, for example those due to the discharge of brine into the ocean. Vertical buoyant jets or plumes are of great practical relevance in fire problems and in the general area of air conditioning.

Because of the great practical significance of turbulent buoyant wall-jet flows, there is substantial need for calculation procedures for these flows. In particular, procedures are required that have a large degree of universality so that the methods do not have to be adjusted and empirical input added for each new application. The main problem in developing such a general method is the mathematical description of turbulent transport processes, that is the determination of turbulent stresses and heat fluxes. Commonly used eddy-viscosity turbulence models, like the mixing-length hypothesis, do not simulate the special buoyant-wall-jet features mentioned above, unless they are modified empirically. However, no generally valid empirical modification is available. The widely used standard $k - \epsilon$ turbulence model as described by Launder and Spalding [1] is also not directly applicable because it does not account for the wall damping due to the lateral fluctuations and also not properly for buoyancy effects. On the other hand, second-order closure schemes are available which solve transport equations for the individual turbulent stresses and heat fluxes, and these schemes have the potential of describing the special features occuring in buoyant wall jets. However, their use in practical applications is not desirable because they are rather complex and uneconomical. In this paper therefore a truncated form of a second-order model is presented in which the differential transport equations are reduced to algebraic expressions, leading to an extended version of the $k - \epsilon$ model. It will be shown that the wall-damping and buoyancy effects can be accounted for with sufficient accuracy by this simpler algebraic model. Separately, this has been shown for non-

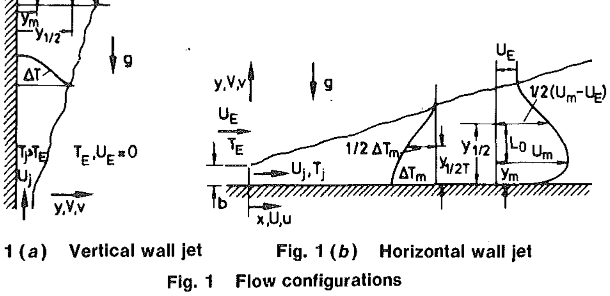

Fig. 1 (*a*) Vertical wall jet

Fig. 1 (*b*) Horizontal wall jet

Fig. 1 Flow configurations

---

[1] On leave from Unis, Sarajewo, Yugoslavia

Contributed by The Heat Transfer Division for publication in the JOURNAL OF HEAT TRANSFER. Manuscript received by the Heat Transfer Division June 27, 1980.

buoyant wall jets already by Ljuboja and Rodi [2] and for buoyant jets remote from walls by Hossain and Rodi [3–5]. The present contribution is to combine the features of the wall-damping and buoyancy model extensions described in these papers to form a more general model applicable to buoyant flows near walls. This combination can be obtained only by deriving the model from the original Reynolds stress and heat-flux equations. The derivation is given in the following section, where these equations, as modelled in [6], are reduced to algebraic expressions by introducing simplifying assumptions about the convection and diffusion terms. The resulting shear-stress and heat-flux expressions are of the form of the Kolmogorov-Prandtl eddy viscosity/diffusivity relation, but with the empirical constant c_μ and the turbulent Prandtl number σ_t now replaced by functions of the wall influence and the buoyancy. The kinetic energy k of the turbulent motion and the rate of its dissipation ϵ appearing in the algebraic expressions are determined from differential transport equations. The model is applied to horizontal wall jets in stagnant and moving surroundings and to a vertical wall jet in stagnant surroundings, and the predictions are compared with experiments whenever possible.

2 Mathematical Model

2.1 Mean-Flow Equations. The distribution of velocity and temperature (or other scalar quantities causing a density difference) in two-dimensional wall jets is governed by the following equations:

continuity equation:

$$\frac{\partial U}{\partial x} + \frac{\partial V}{\partial y} = 0 \tag{1}$$

x-momentum equation:

$$\frac{DU}{Dt} = -\frac{\partial \overline{uv}}{\partial y} \left(+ g\,\frac{\rho_E - \rho}{\rho_E} \right) \tag{2}$$

temperature equation:

$$\frac{DT}{Dt} = -\frac{\partial \overline{vT'}}{\partial y} \tag{3}$$

equation of state:

$$\rho = \rho(T) \tag{4}$$

where the symbols are defined in Fig. 1 and in the Nomenclature. As is usual for thin shear layers, the normal stress term was neglected in the momentum equation (2) and the longitudinal heat-flux term in the temperature equation (3). Further, molecular transport terms have been neglected so that the equations are not valid in the viscous sublayer very near the wall. In this layer the equations will not be integrated; rather this layer will be bridged by so-called wall functions as explained in the section on boundary conditions below. The buoyancy term in dotted parentheses in the momentum equation (2) is present only in the vertical buoyant jet case. A turbulence model is necessary to determine the turbulent shear stress $\overline{uv}$ and the turbulent heat flux $\overline{vT'}$ in order to close the system of equations, and such a model will be introduced in the following subsection.

2.2 Turbulence Model. The development of the turbulence model presented here starts from the modelled forms of the transport equations for the Reynolds stresses $\overline{u_i u_j}$, turbulent heat fluxes $\overline{u_i T'}$ and temperature fluctuations $\overline{T'^2}$. Exact transport equations for these quantities can be derived which contain automatically buoyancy terms. However, in order to obtain a closed scheme, model assumptions had to be introduced into the exact equations about the diffusion, viscous destruction and pressure strain/scrambling terms. The latter terms represent correlations between the fluctuating pressure and fluctuating velocity and temperature gradients and are of particular importance in the transport equations. Here the second-order closure model of Gibson and Launder [6] is adopted, which is an extension of the work of Launder, Reece and Rodi [7]. A useful discussion of the model assumptions, which are based on a mixture of analysis and empirical information, is also given in Launder [8]. The most important aspect of the Gibson-Launder model is the suggestion for the pressure-strain/scrambling term, which involves a wall correction leading to the desired wall damping of the lateral fluctuations [9] and also a buoyancy contribution to the pressure-strain term. For the turbulent stresses and fluxes relevant in two-dimensional buoyant wall-jet flows, special forms of the equations applicable to horizontal and vertical wall jets are compiled in Table 1. The equations are again thin-shear-layer forms of the full equations. As buoyancy acts differently in the vertical and in the horizontal wall jet case, the buoyancy terms in the equations are different and are given in two separate columns, one applicable to the horizontal jet and the other to the vertical jet. Equations for the turbulent kinetic energy k and the rate of its dissipation ϵ are also needed in the model and are included in Table 1. The diffusion model is not given explicitly, as further simplifying assumptions are introduced for the diffusion later. The convection and the mean-field production as well as the buoyancy-production/destruction terms are exact. The terms involving f in the pressure-strain/scrambling model are the wall-proximity corrections and account for the influence of a wall on the turbulence structure. Exact analysis [8] has shown that such additional terms are necessary near walls. f is an empirical damping function which is to reduce the effect of the wall correction with increasing distance from the wall; it is assumed proportional to L/y, where $L \propto k^{3/2}/\epsilon$ is the length scale of the turbulent motion and y the distance from the wall so that [6]:

$$f = \frac{k^{3/2}}{c_w y \epsilon}. \tag{12}$$

The empirical coefficients c_w, c_1' and c_2' in the wall-proximity correction were taken over from [2], where c_w was adjusted such that $f = 1$ near the wall.

Nomenclature

B = buoyancy flux = $\int_0^\infty U \Delta\gamma dy$, buoyancy parameter defined in equations (18) and (21)
b = width of jet nozzle
c's = constants in the turbulence model
c_f = friction coefficient = $\tau_w / \frac{1}{2}\rho U_m{}^2$
E = roughness parameter in log-law (24), rate of entrainment defined in Fig. 3
F = densimetric Froude number = $U_j/\sqrt{bg\Delta\rho_j/\rho_E}$
f = wall damping function, equation (12)
G = rate of buoyancy production of turbulent kinetic energy, defined in equation (10)
g = gravitational acceleration
k = turbulent kinetic energy = $\frac{1}{2}(\overline{u^2} + \overline{v^2} + \overline{w^2})$
L_0 = width of outer free mixing layer = $y_{1/2} - y_m$
P = rate of shear production of turbulent kinetic energy, defined in equation (10)
R = ratio of time scales of temperature and velocity fluctuations
R_f = flux Richardson number based on buoyancy production of $\overline{v^2}$
Ri = Richardson number defined in Fig. 3
T = mean temperature
ΔT = excess/defect temperature
T' = fluctuating temperature
U, V = mean velocity components
U_τ = friction velocity = $\sqrt{\tau_w/\rho}$
u, v = fluctuating velocity components
x, y = co-ordinates (see Fig. 1)
x_0 = virtual origin of jet
y^+ = dimensionless wall distance = $U_\tau y/\nu$
α = coefficient defined in equation (18)
β = volumetric expansion coefficient
$\Delta\gamma$ = weight density defect = $g(\rho_E - \rho)$
ϵ = rate of dissipation of turbulent kinetic energy
$\varkappa$ = von Karman constant
ν = kinematic molecular viscosity
ν_t = turbulent viscosity = $-\overline{uv}/\partial U/\partial y$
ω = coefficient in equation (15)
ρ = fluid density
σ_t = turbulent Prandtl number
$\sigma_{k,\epsilon}$ = constants in turbulence model

Subscripts

c = value at point just outside viscous sublayer
E = external (ambient)
j = jet exit conditions
m = maximum
$\frac{1}{2}$ = value at location where ΔU or ΔT is half of its maximum value

Table 1 Transport equations for turbulence correlations in horizonal and vertical buoyant wall jets

Variable	Convection	Diffusion	Mean-field production	Buoyancy production/ destruction		viscous destr.	Pressure-strain/scrambling			Eq. No.
				vertical	horizontal		non-buoyant	buoyant contribution		
								vertical	horizontal	
$\overline{uv}$	$\frac{D\overline{uv}}{Dt} =$	$\mathrm{Diff}\ \overline{uv}$	$-\overline{v^2}\frac{\partial U}{\partial y}$	$+\beta g\overline{vT'}$	$+\beta g\overline{uT'}$		$-c_1\frac{\varepsilon}{k}\overline{uv}\left(1+\frac{3}{2}\frac{c_1'}{c_1}f\right)$ $+c_2\left(1-\frac{3}{2}c_2'f\right)\overline{v^2}\frac{\partial U}{\partial y}$	$-c_3\beta g\overline{vT'}$	$-c_3\beta g\overline{uT'}$	(5)
$\overline{v^2}$	$\frac{D\overline{v^2}}{Dt} =$	$\mathrm{Diff}_{\overline{v^2}}$			$+2\beta g\overline{vT'}$	$-\frac{2}{3}\varepsilon$	$-c_1\frac{\varepsilon}{k}\left[\left(1+2\frac{c_1'}{c_1}f\right)\overline{v^2}-\frac{2}{3}k\right]$ $-\frac{2}{3}c_2\left(1-2c_2'f\right)\overline{uv}\frac{\partial U}{\partial y}$		$-\frac{4}{3}c_3\beta g\overline{vT'}$	(6)
$\overline{uT'}$	$\frac{D\overline{uT'}}{Dt} =$	$\mathrm{Diff}_{\overline{uT'}}$	$-\overline{uv}\frac{\partial T}{\partial y}-\overline{vT'}\frac{\partial U}{\partial y}$	$+\beta g\overline{T'^2}$			$-c_{1T}\frac{\varepsilon}{k}\overline{uT'}+c_{2T}\overline{vT'}\frac{\partial U}{\partial y}$	$-c_{3T}\beta g\overline{T'^2}$		(7)
$\overline{vT'}$	$\frac{D\overline{vT'}}{Dt} =$	$\mathrm{Diff}_{\overline{vT'}}$	$-\overline{v^2}\frac{\partial T}{\partial y}$		$+\beta g\overline{T'^2}$		$-(c_{1T}+c_{1T}'f)\frac{\varepsilon}{k}\overline{vT'}$		$-c_{3T}\beta g\overline{T'^2}$	(8)
$\overline{T'^2}$	$\frac{D\overline{T'^2}}{Dt} =$	$\mathrm{Diff}_{\overline{T'^2}}$	$-2\overline{vT'}\frac{\partial T}{\partial y}$			$-\frac{\overline{T'^2}}{kR}\varepsilon$				(9)
k	$\frac{Dk}{Dy} =$	$\frac{\partial}{\partial y}\left(\frac{\nu_t}{\sigma_k}\frac{\partial k}{\partial y}\right)$	$\underbrace{-\overline{uv}\frac{\partial U}{\partial y}}_{P}$	$\underbrace{+\beta g\overline{uT'}}_{G}$	$\underbrace{+\beta g\overline{vT'}}_{G}$	$-\varepsilon$				(10)
ε	$\frac{D\varepsilon}{Dy} =$	$\frac{\partial}{\partial y}\left(\frac{\nu_t}{\sigma_\varepsilon}\frac{\partial \varepsilon}{\partial y}\right)$	$-c_{\varepsilon 1}\frac{\varepsilon}{k}\overline{uv}\frac{\partial U}{\partial y}$	$+c_{\varepsilon 1}\frac{\varepsilon}{k}\beta g\overline{uT'}$	$+c_{\varepsilon 1}\frac{\varepsilon}{k}\left(1-c_{\varepsilon 3}\right)\beta g\overline{vT'}$	$-c_{\varepsilon 2}\frac{\varepsilon^2}{k}$				(11)

Together with the k- and ϵ-equations also given in Table 1 and an explicit model for the diffusion terms, the equations for the individual stresses and fluxes in Table 1 would form a second-order closure scheme for turbulent buoyant wall jets. However, because of the many differential equations involved, further model assumptions are introduced in order to simplify the model. It is however important to retain the wall damping effect and the buoyancy influence in the simplified model. The differential equations can be reduced to algebraic expressions by making suitable assumptions about the convective and diffusive transport. As $\overline{v^2}$ is a component of the total energy k, its transport is assumed proportional to the transport of k [10], which according to (10) is $P + G - \epsilon$:

$$(\text{Conv.-Diff.})_{\overline{v^2}} = \frac{\overline{v^2}}{k}(\text{Conv.-Diff.})_k = \frac{\overline{v^2}}{k}(P + G - \epsilon) \qquad (13)$$

while convection and diffusion of the other quantities are neglected *on the assumption that the turbulence is nearly in local equilibrium*. With these assumptions, the differential equations (5) to (9) can be reduced to algebraic expressions, which for the shear stress $\overline{uv}$ and the lateral heat flux $\overline{vT'}$ can be written in the form of the eddy viscosity/diffusivity relation (14), with the eddy diffusivity and viscosity related to k and ϵ by the so-called Kolmogorov-Prandtl expression:

$$\overline{uv} = -\nu_t\frac{\partial U}{\partial y}, \quad \overline{vT'} = -\frac{\nu_t}{\sigma_t}\frac{\partial T}{\partial y} \qquad (14)$$

with

$$\nu_t = c_\mu\frac{k^2}{\epsilon} \quad \text{and} \quad c_\mu = \frac{\overline{v^2}}{k}\omega \qquad (15)$$

In these equations, c_μ and the turbulent Prandtl number σ_t are not constants as for example in the standard $k - \epsilon$ model but they depend on the wall-damping function f and on the buoyancy influence. Of course these functions are different for horizontal and vertical buoyant wall jets, and the individual expressions are now presented.

Horizontal buoyant jet:

$$c_\mu = \omega\frac{\overline{v^2}}{k} \quad \text{with} \quad \omega = \frac{1 - c_2 + \frac{3}{2}c_2c_2'f}{c_1 + \frac{3}{2}c_1'f}$$

$$\times\frac{1 - \dfrac{1 - c_3}{1 - c_2 + \frac{3}{2}c_2c_2'f}\,\dfrac{1 - c_{2T}}{c_{1T}}\alpha B}{1 + \dfrac{1 - c_3}{c_1 + \frac{3}{2}c_1'f}\cdot\dfrac{1}{c_{1T}}B} \qquad (16)$$

$$\frac{\overline{v^2}}{k} = \frac{2}{3}$$

$$\times\frac{c_1 - 1 + \dfrac{P + G}{\epsilon}(c_2 - 2c_2c_2f) + \dfrac{G}{\epsilon}(3 - c_2 - 2c_3 + 2c_2c_2'f)}{c_1 + 2c_1'f + \dfrac{P + G}{\epsilon} - 1} \qquad (17)$$

$$\sigma_t = \frac{\omega}{\alpha}, \alpha = \frac{1}{c_{1T} + c_{1T}'f + 2(1 - c_{3T})RB}, \quad B = \beta g\frac{k^2}{\epsilon^2}\frac{\partial T}{\partial y} \qquad (18)$$

Vertical buoyant jet:

$$\omega = \frac{1 - c_2 + \frac{3}{2}c_2c_2'f}{c_1 + \frac{3}{2}c_1'f}\left[1 + \frac{(1 - c_3)B}{(c_{1T} + c_{1T}'f)(1 - c_2 + \frac{3}{2}c_2c_2'f)}\right] \qquad (19)$$

$$\frac{\overline{v^2}}{k} = \frac{2}{3}\,\frac{c_1 - 1 + \dfrac{P + G}{\epsilon}(c_2 - c_2c_2'f) + \dfrac{G}{\epsilon}(c_3 - c_2 + 2c_2c_2'f)}{c_1 + \dfrac{P + G}{\epsilon} - 1 + 2c_1'f} \qquad (20)$$

$$\sigma_t = \omega(c_{1T} + c_{1T}'f), \quad B = \beta g\frac{k}{\epsilon}\frac{\partial T/\partial y}{\partial U/\partial y} \qquad (21)$$

$$\overline{uT'} = \frac{1}{c_{1T}}\frac{k}{\epsilon}\left[\overline{uv}\frac{\partial T}{\partial y} + (1 - c_{2T})\,\overline{vT'}\frac{\partial U}{\partial y} - \beta g(1 - c_{3T})\,\overline{T'^2}\right] \qquad (22)$$

with

$$\overline{T'^2} = -2R\frac{k}{\epsilon}\overline{vT'}\frac{\partial T}{\partial y} \qquad (23)$$

The correlations $\overline{uT'}$ and $\overline{T'^2}$ originally appearing in the set of algebraic expressions for the horizontal buoyant jet have been eliminated with the aid of the truncated forms of (6) and (8). They are not further needed in this model. In the case of the vertical buoyant jet however, the correlation $\overline{uT'}$ appears in the buoyancy source term of the k-equation and is therefore presented in (22). Since $\overline{T'^2}$ appears in this equation, an algebraic expression for $\overline{T'^2}$ is also needed and is given in (23).

Table 2 Constants in the turbulence model

$c_{\epsilon 1}$	$c_{\epsilon 2}$	$c_{\epsilon 3}$	σ_k	σ_ϵ	c_1	c_2	c_3	c_w	c_1'	c_2'	c_{1T}	c_{2T}	c_{3T}	c_{1T}	R
1.44	1.92	0.8	1.	1.3	1.8	0.6	0.6	3.72	.6	.3	3.	.5	.5	.5	.8

For nonbuoyant free shear layers ($f = 0, B = 0, G = 0$) with $P \simeq \epsilon$ there results $c_\mu = 0.108$ when c_1 and c_2 are given the values listed in Table 2 below. When this value of c_μ is used instead of the usual value of 0.09 [1] in the standard $k - \epsilon$ model, the growth of free shear layers is overpredicted. Therefore, the c_μ expressions given above for both vertical and horizontal buoyant wall jets are not used directly but are multiplied by

$$0.09/\left(\frac{1-c_2}{c_1}\frac{2}{3}\frac{c_1 - 1 + c_2\dfrac{P+G}{\epsilon}}{c_1 + \dfrac{P+G}{\epsilon} - 1}\right)$$

so that in the limiting case of nonbuoyant free shear layers a value of c_μ of 0.09 will result and the model reduces exactly to the standard $k - \epsilon$ model.

k and ϵ appearing in the above algebraic expressions are determined from the transport equations (10) and (11). The buoyancy production/destruction term in the k-equation is a direct consequence of the derivation of this equation, while the buoyancy term in the ϵ-equation is a model assumption. The two variants of the ϵ-equation given for vertical and horizontal buoyant jets are special forms of a general ϵ-equation suggested by Rodi [11] which has as source term the expression:

$$c_{1\epsilon}\frac{\epsilon}{k}(P + G)(1 + c_{3\epsilon}\mathrm{R}_f) - c_{2\epsilon}\frac{\epsilon^2}{k}$$

in which R_f is the flux Richardson number based on the buoyancy production of the lateral fluctuations $\overline{v^2}$, i.e. $\mathrm{R}_f = -\frac{1}{2}\,\mathrm{Prod}_{\overline{v^2}}/(P + G)$. In horizontal wall jets, where v is the direction of gravity, all buoyancy production goes into the component $\overline{v^2}$ so that $\mathrm{Prod}_{\overline{v^2}} = 2G$ and $\mathrm{R}_f = -G/(G + P)$. In vertical wall jets however the lateral component is perpendicular to the gravity vector and receives no buoyancy contribution so that $\mathrm{R}_f = 0$. With these values for R_f for the vertical and horizontal jets, the production terms given in equation (11) follow. It is only through the use of this empirical flux-Richardson-number term that the same ϵ-equation can be used for horizontal and vertical buoyant shear layers, as is discussed in greater detail in Rodi [11].

The values of the empirical constants are taken mainly from Gibson and Launder [6] and, were applicable, from Launder and Spalding [1]. As suggested by Ljuboja and Rodi [2], the wall correction constant c_1' is somewhat different from the value suggested by Gibson and Launder. The values of all the constants are listed in Table 2.

2.3 Boundary Conditions. The mean-flow equations (2) and (3) and the turbulence model introduced above are valid only for fully turbulent flow at high Reynolds numbers so that they do not apply to the viscous sublayer very close to solid walls. Here the wall function approach outlined in [1] is adopted which allows the equations to be integrated outside the viscous sublayer only. This approach is based on the assumption that just outside this sublayer there is a region where the velocity follows the logarithmic law of the wall, the turbulent shear stress $-\rho\,\overline{uv}$ is approximately equal to the wall shear stress τ_w, and production P and dissipation ϵ of the turbulent kinetic energy are approximately in balance. The first assumption implies that the velocity at a point in this region with wall distance y_c can be related to the wall shear stress by:

$$\frac{U_c}{U_\tau} = \frac{1}{\varkappa}\ln\,(y_c{}^+E) \tag{24}$$

where $U_\tau = \sqrt{\tau_w/\rho}$ is the friction velocity, $y_c{}^+ = U_\tau y_c/\nu$ is a dimensionless wall distance, $\varkappa$ is the von Kármán constant and E is a roughness parameter. $\varkappa$ was taken as 0.435 and E as 9.0 for smooth walls. These values were suggested by Patankar and Spalding [12] and were used in many previous $k - \epsilon$ model calculations. A recent review of experimental wall-jet data [13] has shown that the usual logarithmic velocity law holds also in wall jets but extends up to much smaller y^+-values than in boundary layers. The assumptions made above also imply that the values of k and ϵ at the point y_c are [1]:

$$k_c = \frac{U_\tau{}^2}{\sqrt{c_\mu}}, \quad \epsilon_c = \frac{U_\tau{}^3}{\varkappa y_c} \tag{25}$$

These are the boundary conditions for k and ϵ applied at point y_c in the present calculations, the value of c_μ being determined from the c_μ-relations given above at y_c. In order for the above assumptions to be approximately valid, point y_c should lie in the range $30 \leq y_c{}^+ \leq 50$. Condition (25) also implies that c_w has to have the value $\varkappa/c_\mu{}^{3/4}$ if the wall damping function f according to (13) is to have a value of 1 at the near-wall point y_c.

As the wall is assumed to be adiabatic, the appropriate wall boundary condition for temperature is a zero gradient $\partial T/\partial y$. This condition was applied right at the wall and no wall function was used for the temperature. At the free boundary of the wall jet, velocity and temperature are given their free-stream values while the turbulence quantities k and ϵ are set to zero so that the ambient is assumed to be free of turbulence.

3 Application of the Model

This section describes the application of the mathematical model introduced above to various horizontal buoyant wall jets and to self-similar vertical buoyant wall jets in stagnant surroundings. The mean-flow equations (1) to (3), together with the k- and ϵ-equations (10) and (11), were solved numerically with the marching-forward procedure which Patankar and Spalding [12] developed for two-dimensional boundary layers. Forty grid nodes were used across the wall jet, and the forward step was typically 0.015 times the total jet width.

3.1 Horizontal Buoyant Jets. First calculations were carried out for horizontal buoyant wall jets in stagnant surroundings. The purpose of these calculations was to study the influence of stable stratification on jet spreading and entrainment. Unfortunately, there are no measurements available for comparison in this case, but the limiting case of a nonbuoyant wall jet has been shown to be described well by the model [2]. The calculations were started at the jet exit with uniform velocity and temperature profiles and low values for the turbulent quantities k and ϵ. The development of the jet was then calculated up to an axial station of $x/b = 300$. The effect of buoyancy is characterized here by the exit densimetric Froude number $\mathrm{F} = U_j/\sqrt{gb\Delta\rho_j/\rho_E}$. For the case of the nonbuoyant jet ($\mathrm{F} = \infty$) and for three buoyant cases with lower Froude numbers, Fig. 2 shows the development of the half-widths of the velocity field $y_{1/2}$ and of the temperature field $y_{1/2T}$ (for a definition see Fig. 1) and the decay of the maximum velocity U_m. It can be seen that the jet spreading and the decay of U_m are reduced significantly by the stable stratification prevailing in the buoyant situations, that is when the Froude number F is decreased. For the lowest value of F, the jet spreads very little at the furthest downstream station of $x/b = 300$. It is of interest here also that the temperature field spreads faster than the velocity field for the nonbuoyant wall jet, which reflects the fact that the turbulent Prandtl number is smaller than unity. However, when the Froude number is reduced, the temperature field spreads increasingly less than the velocity field. This implies that the turbulence model (i.e. equation (18)) predicts $\sigma_t > 1$ for stable stratification which is in agreement with experimental observations of Young [14] in a nearly-homogeneous stratified shear layer.

The reduction in jet growth is a consequence of the reduced entrainment of ambient fluid into the jet. The entrainment is shown in Fig. 3, where the entrainment rate E, nondimensionalized with its

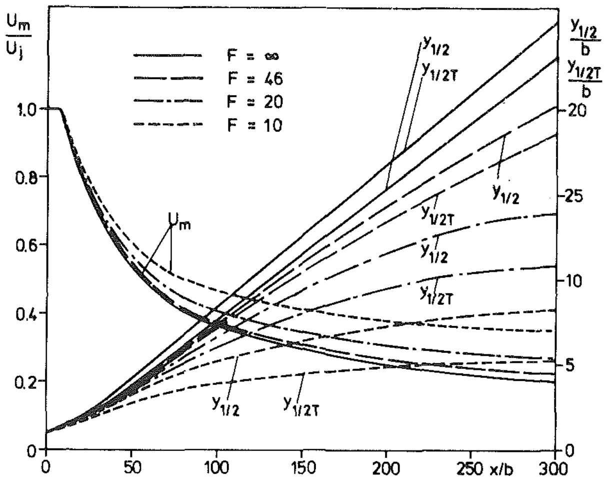

Fig. 2 Variation of maximum velocity U_m, velocity half width $y_{1/2}$ and temperature half width $y_{1/2T}$ in horizontal wall jets in stagnant surroundings

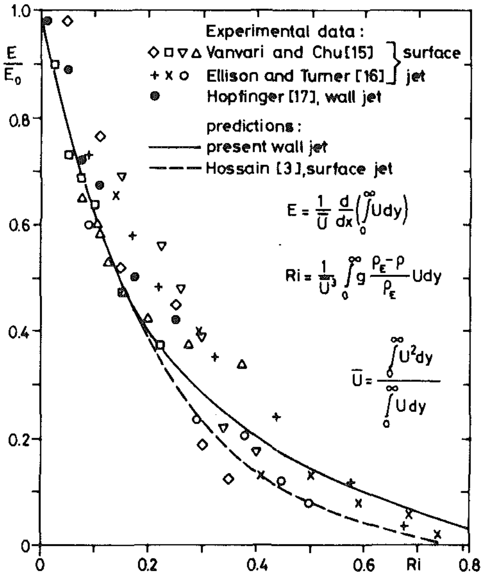

Fig. 3 Reduction of entrainment rate due to buoyancy for horizontal wall jet

value for the nonbuoyant wall jet E_0 (which is independent of x), is plotted versus the Richardson number, Ri, characterizing the buoyancy influence at each cross section of the jet. E and Ri are defined in Fig. 3, and Ri increases from an initial exit value in the downstream direction, indicating that buoyancy effects get stronger as the wall jet develops. When E/E_0 is plotted versus Ri, the results for the calculation of the three F-values collapse on a single curve, except for the developing region near the exit (this development is excluded from Fig. 3). This single curve is compared with experimental data obtained in the closely related flow situation of a two-dimensional heated surface jet and also with a few data from Hopfinger's [17] study of a buoyant wall jet with finite free-stream velocity (U_E/U_j = 0.375). The predicted entrainment curve agrees with the data within the experimental scatter. Hossain [3] used a similar model to predict the heated-surface-jet situation and his results are also included. Similar results were obtained for the heated surface jet with a somewhat different model by Gibson and Launder [18].

The only experiments on horizontal buoyant wall jets known to the authors are those of Hopfinger [17] who studied wall jets for the two velocity ratios U_E/U_j of 0.375 and 0.625 with and without buoyancy. The case with the lower velocity ratio is chosen here for simulation with the mathematical model, as the review study [13] has shown that two-dimensionality is easier to achieve at lower velocity ratios. Calculations were carried out both for the non-buoyant case (F = ∞) and for the buoyant case where the Froude number was F = 17.9. Hopfinger [17] plotted the measured development of the flow against the non-dimensional distance from the exit, $(x + x_0)/b$, where x_0 is the virtual origin of the wall jet ($x_0/b = -12.5$ for the velocity ratio of 0.375). The calculations were started at $(x + x_0)/b = 40$ from measured profiles of U and T in the outer free mixing region ($y > y_m$); in the near wall region ($y \leq y_m$) a $\frac{1}{7}$th power law was used for the velocity, and very near the wall the log-law (24) is adopted with U_τ from a friction coefficient $c_f = \tau_w/\frac{1}{2}\rho U_m{}^2 = 0.005$, which is a good average value for wall jets [13]. The temperature in the near wall region was assumed to be constant for purposes of specifying the initial profiles. In the free mixing region the kinetic energy was assumed proportional to the shear stress ($k = \overline{uv}/0.24$) and $\overline{uv}$ was determined from $\nu_t \partial U/\partial y$ with the velocity gradient from the measured profile and ν_t adjusted to give initially the correct growth of the free-mixing-layer width $L_0 = y_{1/2} - y_m$. The choice of ν_t was found to have an influence only on the initial development of L_0. The initial profile of ϵ in the free mixing layer was then calculated from $\epsilon = c_\mu k^2/\nu_t$ according to (15). At the near-wall point y_c, the values of k and ϵ are fixed by relation (25). A connection between these values and the free-mixing-layer distribution was drawn that appeared plausible.

With these initial conditions and the model described above, the distribution of width of the outer layer could be predicted well, but not the growth of y_m characterizing the width of the inner layer and also not the decay of the velocity maximum U_m. Attempts to obtain a better behavior of these quantities by changing the initial conditions did not prove fruitful. Whatever initial conditions were chosen, y_m soon approached a curve which Kruka and Eskinazi [19] found to be a good correlation of many wall-jet experiments, and it is somewhat strange that in Hopfinger's experiment y_m grows nearly twice as fast as in other experiments. A check on the momentum balance [13] revealed that there is a momentum loss of about 40 percent between the first and the last measurement station. The reasons for this considerable momentum loss are not clear; nevertheless Hopfinger's experiments were taken as test case for the present model since they are the only ones on horizontal buoyant wall jets. In order to allow a comparison between predictions and experiments, the momentum loss in the experiment was simulated by a large wall roughness, which was certainly not present in the experiments. When the wall roughness parameter E in the log-law (24) is given a value of 0.5, the correct development of y_m and also of U_m is predicted as shown respectively in Figs. 4 and 5. L_0 is hardly affected at all by a change of E from 9 to 0.5. With the measured behaviour of Hopfinger's nonbuoyant wall jet well described by the mathematical model, this was then applied to the buoyant situation with F = 17.9. Fig. 4 shows that the spread of the outer free mixing zone, whose width is L_0, is reduced and that there is good agreement with the experiments. The width of the inner layer is virtually unaffected by buoyancy in the predictions. In the experiments y_m also grows slower in the buoyant situation, but Hopfinger [20] now believes that these results for y_m are not so reliable as to reach any conclusions on the influence of buoyancy on y_m. Fig. 5 shows that the decay of U_m is also reduced by the stable stratification, in good agreement with the experiments. This figure also includes the variation of the maximum deficit temperature, which is again in good accord with the data.

3.2 Vertical Buoyant Jets. Grella and Faeth [21] have carried out experiments in a plume above a line heat source at the base of a vertical adiabatic wall. They have also carried out a similarity analysis for this flow which, when a constant friction coefficient c_f is assumed, yields the same behavior as obtained for free line plumes, that is a linear growth of the plume width, constant maximum velocity U_m and a variation of the maximum weight density defect $\Delta\gamma_m = g(\rho_E - \rho)_m$ as x^{-1}. It follows also from the similarity theory that when $U/(B/\rho)^{1/3}$ and $\Delta\gamma/(\rho B^2/x^3)^{1/3}$ are plotted versus y/x they should result in a single curve for various distances from the origin and also for various initial conditions. Here B is the buoyancy flux $B = \int_0^\infty U\Delta\gamma dy$. With this scaling, the experimental data do indeed fall approximately on a single curve, as can be seen in Fig. 6. There is considerable experimental scatter, but this is not larger than in the free-plume experiments of Rouse, et al. [22].

The calculations were started with uniform velocity and temperature profiles at a discharge slot and were carried out until similarity of the profiles was achieved. As these similarity profiles are independent of the initial conditions, the exact details of these conditions are not of interest here. The predicted similarity profiles are compared in Fig. 6 with the measured ones for the velocity and the weight density defect $\Delta\gamma$ which is basically the temperature profile. The agreement with the experiments is fairly good, especially when one takes the asterisk symbols resulting from measurements at the largest x-distance from the source and also for the highest Reynolds number experiment. The predicted velocity maximum is however somewhat too close to the wall. This discrepancy is also present in the nonbuoyant wall jet calculations of [2] and is caused by the use of the eddy viscosity concept. The spreading of the plume on the other hand is rather well predicted by the model.

The similarity curves for free-line plumes are also included in Fig. 6 (they originate from the measurements of Rouse, et al. [22]), and it can be seen that free plumes spread much faster than wall plumes and also have a much stronger dilution. This behaviour was predicted correctly with the free-flow version of the model by Hossain [3].

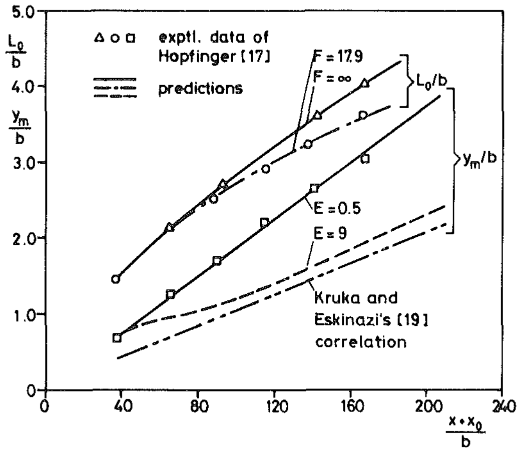

Fig. 4 Development of L_0 and y_m in Hopfinger's [17] wall jet in a moving stream

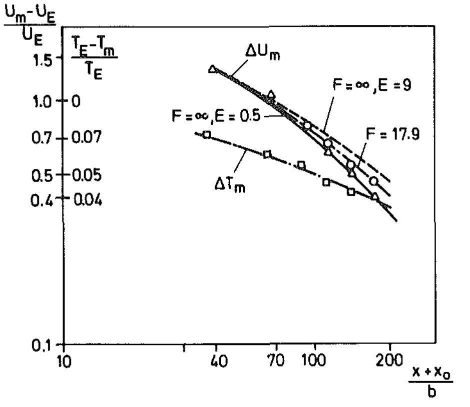

Fig. 5 Decay of U_m and T_m in wall jet in a moving stream, lines are predictions and symbols Hopfinger's [17] data

4 Concluding Remarks

A modified version of the $k - \epsilon$ turbulence model was presented which accounts for buoyancy effects on the turbulence and also for the wall damping of lateral fluctuations and the resulting reduction of shear stress experienced in wall jets. The modifications were derived by simplifying the modelled forms of the transport equations for the Reynolds stresses, the turbulent heat fluxes and the temperature fluctuations given in [6]. These equations contain buoyancy terms partly because of their derivation from the Navier-Stokes equations and the instantaneous temperature equation and partly due to model assumptions for the pressure-strain/scrambling term. The wall-damping effect is also due to the modelled form of the pressure-strain/scrambling term. The main assumption introduced in this paper is that turbulence is nearly in local equilibrium so that the differential transport terms can be eliminated and the equations reduce to algebraic expressions. The modified version of the $k - \epsilon$-model was applied to two limiting cases of turbulent buoyant wall jets, namely to a jet along a horizontal wall and to a jet along a vertical wall. The model was shown to predict these limiting cases with an accuracy sufficient for practical purposes. In particular the reduction of jet spreading and entrainment in the horizontal case under stably stratified conditions was predicted correctly, and in the vertical situation the considerably smaller spreading and dilution compared with the case of a free vertical buoyant jet (or plume) was reproduced. It would have been desirable to compare the present predictions with results obtained with different models, but such results are not available. It is clear, however, from [2] that the wall-damping correction is needed to obtain the slower spreading of the wall jet compared with that of the free jet and from [3] that the buoyancy extension is also necessary. Finally, it is important to note that the empirical constants in the model were not adjusted to suit the problems considered but were taken from the literature where they were determined by reference to experiments in quite different flows. Therefore, the new model is considered a step forward in the search for a generally applicable turbulence model.

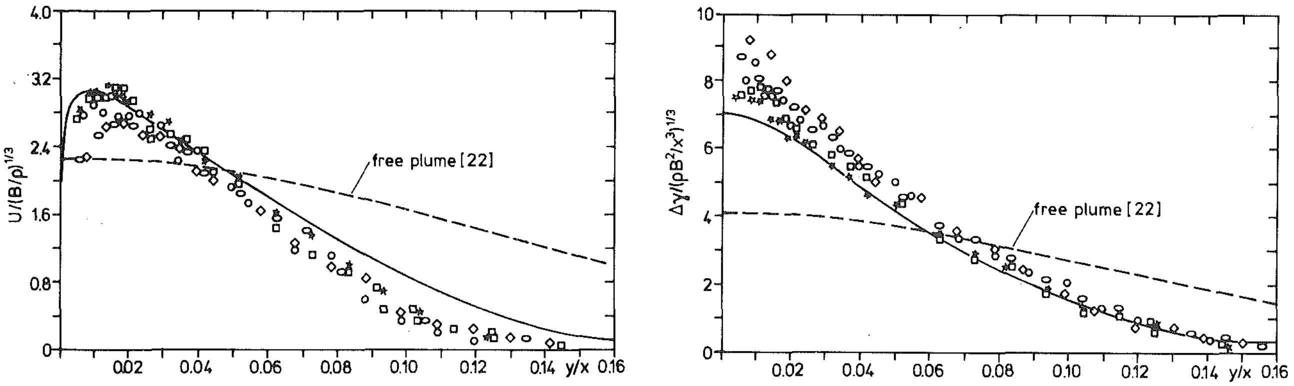

Fig. 6 (a) Velocity profile

Fig. 6 (b) Weight defect profile

Fig. 6 Self-similar velocity and weight defect profiles in vertical wall plume; solid lines are present predictions and symbols measurements [21] for various Reynolds numbers and distances from the source (see key in [21])

Acknowledgments

The first author acknowledges financial support from the Deutsche Akademische Austauschdienst. The calculations were carried out on the BORROUGHS B 7700 computer of the University of Karlsruhe.

References

1 Launder, B. E., and Spalding, D. B., "The Numerical Computation of Turbulent Flow," *Computer Methods in Applied Mechanics and Engineering*, Vol. 3, 1974, pp. 269–289.

2 Ljuboja, M., and Rodi, W., "Calculation of Turbulent Wall Jets with an Algebraic Reynolds Stress Model," ASME *Journal of Fluids Engineering*, Vol. 102, 1980, pp. 350–356.

3 Hossain, M. S., "Mathematische Modellierung von turbulenten Auftriebsströmungen," Ph.D. Thesis, University of Karlsruhe, 1980.

4 Hossain, M. S. and Rodi, W., "Influence of Buoyancy on the Turbulence Intensities in Horizontal and Vertical Jets," in *Heat Transfer and Turbulent Buoyant Convection, Studies and Applications for Natural Environment, Buildings and Engineering Systems*, Spalding, D. B. and Afgan, N., eds. Hemisphere Publishing Corporation, Washington, D. C., 1977.

5 Hossain, M. S. and Rodi, W., "Mathematical Modelling of Vertical Mixing in Stratified Channel Flow," *Proceedings 2nd International Symposium on Stratified Flows*, Trondheim, Norway, 1980.

6 Gibson, M. M. and Launder, B. E., "Ground Effects on Pressure Fluctuations in the Atmospheric Boundary Layer," *Journal of Fluid Mechanics*, Vol. 86, 1978, pp. 491–511.

7 Launder, B. E., Reece, G. J. and Rodi, W., "Progress in the Development of a Reynolds Stress Turbulence Closure," *Journal of Fluid Mechanics*, Vol. 68, 1975, pp. 537–566.

8 Launder, B. E., "Heat and Mass Transport," Chapter 6 in *Turbulence*, ed. by P. Bradshaw, Topics in Applied Physics, Vol. 12, Springer Verlag, 1976.

9 Shir, C. C., "A Preliminary Numerical Study of Atmospheric Turbulent Flow in the Idealized Planetary Boundary Layer," *Journal of Atmospheric Sciences*, Vol. 30, 1973, pp. 1327–1339.

10. Rodi, W., "A New Algebraic Relation For Calculating the Reynolds Stresses," *Zeitschrift für Angewandte Mathematik und Mechanik*, Vol. 56, 1976, pp. T219–T221.

11 Rodi, W., "Influence of Buoyancy and Rotation on Equations for the Turbulent Length Sclae," Paper at *2nd Symposium on Turbulent Shear Flows*, London, 1979.

12 Patankar, S. V., and Spalding, D. B., "*Heat and Mass Transfer in Boundary Layers*," 2nd ed., Intertext, London, 1970.

13 Launder, B. E. and Rodi, W., "Review of Turbulent Wall Jet Data," *Progress in Aerospace Sciences*, in press.

14 Young, S. T. B., "Turbulence Measurements in a Stably Stratified Turbulent Shear Flow," Queen Mary College London, Report QMC-EP 6018, 1975.

15 Chu, V. H. and Vanvari, M. R., "Experimental Study of Turbulent Stratified Shearing Flow," ASCE *Journal of the Hydraulics Division*, HY6, 1976, pp. 691–706.

16 Ellison, T. H. and Turner, J. S., "Turbulent Entrainment in Stratified Flows," *Journal of Fluid Mechanics*, Vol. 6, 1959, pp. 423–448.

17 Hopfinger, J. E., "Development of a Stratified Turbulent Shear Flow," *International Symposium in Stratified Flows*, Novosibirsk, 1972.

18 Gibson, M. M. and Launder, B. E., "On the Calculation of Horizontal Turbulent Free Shear Flow under Gravitational Influence," ASME JOURNAL OF HEAT TRANSFER, Vol. 98C, 1976, pp. 81–87.

19 Kruka, V. and Eskinazi, S., "The Wall Jet in a Moving Stream," *Journal of Fluid Mechanics*, Vol. 20, 1964, pp. 555–579.

20 Hopfinger, E. J., private communications, 1978.

21 Grella, J. J. and Faeth, G. M., "Measurements in a Two-Dimensional Thermal Plume along a Vertical Adiabatic Wall," *Journal of Fluid Mechanics*, Vol. 71, 1975, pp. 701–710.

22 Rouse, H., Yih, C. S. and Humphreys, H. W., "Gravitational Convection from a Boundary Source," *Tellus*, Vol. 4, 1952, pp. 201–210.

F. H. Azad
Student Member, ASME

M. F. Modest[1]
Mem. ASME

Department of Mechanical Engineering,
Aeronautical Engineering & Mechanics
Rensselaer Polytechnic Institute
Troy, N. Y. 12181

Evaluation of the Radiative Heat Flux in Absorbing, Emitting and Linear-Anisotropically Scattering Cylindrical Media

The contribution of thermal radiation to heat transfer in an emitting, absorbing and linear-anisotropically scattering medium of one-dimensional cylindrical geometry is investigated. It is assumed that the radial temperature distribution in the medium is known or is found in conjunction with overall conservation of energy. The exact solution results in a first-order integral equation in the radial coordinate which is a substantial improvement over previous formulations developed for nonscattering media. Also, two approximate methods are established and tested for their accuracy. The first method is the differential approximation modified to accommodate linear-anisotropic scattering. The second method consists of an exponential kernel approximation in which the geometric integrand functions are replaced by simple exponential functions. The results presented indicate that in engineering applications either approximate method may be used to accurately model the radiative contribution to overall heat transfer rates, reducing the nonlinear integrodifferential energy conservation equation to a nonlinear differential equation.

Introduction

In recent years considerable attention has been given to the study of radiative transfer in cylindrical media. Some practical applications for such analyses include high temperature flows of gas-particulate suspensions in cylindrical furnaces, exhaust plumes of solid propellant rockets, etc.

Many of the previous investigations which have considered the scattering of radiation have been limited to planar geometry. These studies range from the investigation of the simple case of isotropic scattering, e.g. [1–2], to dealing with realistic scattering phase functions. Dayan and Tien [3] obtained numerical and exponential-kernel solutions for linear-anisotropic scattering in a gray slab at radiative equilibrium. Buckius and Tseng [4] investigated the effect of Fresnel reflection from the boundary of an isothermal gray slab. Buckius and King [5] used the exponential kernel method combined with linear anisotropic scattering to predict diffuse solar radiation.

In an effort to deal with more realistic scattering phase functions, Bergquam and Seban [6] employed a two-flux method, a modified version of which was later used by Domoto and Wang [7]. Chin and Churchill [8] used the more accurate six-flux method in their study of scattering.

A number of papers deal also with exact solutions to higher-order anisotropic scattering. Hottel et al. [9] used a four-term phase function. Love and Grosh [10] employed the full Mie equations and presented a numerical solution of the resulting integro-differential equations for an isothermal slab. Viskanta and Toor [11] studied solar transmission in semi-infinite water bodies using isotropic, Rayleigh, and experimental scattering phase functions. In an effort to establish the accuracy of linear anisotropic scattering for collimated solar radiation in atmospheric applications, Potter [12] used an experimental phase function and showed that removal of the sharp forward-scattering peak results in negligible error.

Publications dealing with radiative transfer in cylindrical media, however, have been relatively few in number and have dealt mostly with nonscattering materials. Kesten [13] presented equations for the spectral radiant heat flux distribution in an absorbing, emitting, nonisothermal gas contained in a long cylinder with black walls. In this analysis the radiative heat flux was expressed in terms of a second-order integral equation. His results are presented in two different forms, the latter of which appears to be incorrect due to an integral-transformation error. Later Habib and Greif [14], in presenting an analysis on nongray gas effects, used the erroneous equation of Kesten [13] in their calculations and reported a discrepancy between their results and Kesten's. They also developed a kernel approximation which used a total band absorptance model for radiation. This model was in a later work [15] applied to the study of turbulent flow in a black cylindrical pipe. Greif [16] subsequently also included the influence of natural convection on laminar flow in a vertical tube.

The problem of nongray radiative transfer in cylinders was further studied by Wassel and Edwards [17–19]. In their first paper [17] they formulated the radial radiative heat flux in terms of a modified band absorptance tailored to the cylindrical geometry. They then applied the model to thermally developed laminar and turbulent flow with constant wall temperature [18] and constant wall flux [19]. The equation for the heat flux used by Wassel and Edwards [17–19] was the correct version of Kesten's [13] analysis. Nakra and Smith [20] studied the interaction of radiative transfer with convection for slug flow in an absorbing-emitting gas in a circular tube with an isothermal black wall. They used the zone method for their numerical calculations.

Heaslet and Warming [21] developed analytical and numerical methods for predicting radiative transfer for a homogeneous medium of one-dimensional cylindrical geometry. Although their formulation accounted for isotropic scattering, they did not present any exact results for scattering media. Echigo et al. [22, 23] used Heaslet and Warming's [21] radiation model to study the effect of radiative transfer in laminar and turbulent flow of gas particulate suspensions in circular tubes. In their analysis, the medium was assumed to be gray and non-scattering. Adzerikho et al. [24, 25] investigated the luminescence of an isotropically scattering cylinder, using the differential approximation [24] and numerical quadrature [25]. Bayazitoglu and Higenyi [26] introduced a higher-order differential approximation, applying it to concentric cylinders. Their work is, however, limited to nonscattering media.

The present paper deals with the problem of radiative transfer in an absorbing, emitting and linear-anisotropically scattering medium of one-dimensional cylindrical geometry. Its purpose is two-fold: 1) to show that exact solutions can be found with relative ease for such applications where high accuracy is of the essence, and 2) to supply very simple, yet accurate approximate models that are useful in the

---

[1] Current address: Department of Mechanical Engineering, University of Southern California, Los Angeles, Calif. 90007

Contributed by The Heat Transfer Division for publication in the JOURNAL OF HEAT TRANSFER. Manuscript received by The Heat Transfer Division November 24, 1980

solution of nonlinear combined-heat-transfer-modes problems, where large numbers of iterations may be necessary.

There are two reasons for limiting the discussion to linear-anisotropic scattering: 1) Exact analytical solutions are practically impossible to obtain for higher-order scattering phase functions. This is due to the fact that the azimuthal direction cannot be eliminated by integration as in the planar case, resulting in higher-order integral equations in the radial and local direction coordinates. 2) The accuracy of a linear-anisotropic approximation to realistic scattering phase functions in heat transfer applications without collimated irradiation was established in a previous paper [27]. There any forward-scattering peak was removed from the phase function and treated as transmitted. Backward-scattering peaks were removed in a similar fashion, while the remnant of the scattering phase function was approximated by linear-anisotropic scattering. Using the resulting modified scattering coefficient and modified phase function gave excellent prediction of radiative transfer rates as long as the phase function was relatively smooth and had insignificant back-scattering.

The exact solution presented here results in a first-order integral equation which is a substantial improvement over previous works. Also two approximate methods, viz. differential approximation [28], and a kernel approximation are presented which reduce the problem to a solution of a differential rather than an integral equation. The results presented demonstrate the accuracy and applicability of both approximate methods.

Analysis

Exact Solution. The equation of radiative transfer for an emitting, absorbing and anisotropically scattering medium is given by [27]:

$$\mathbf{s}\cdot\nabla I_\lambda(\mathbf{r},\mathbf{s}) = \kappa_\lambda I_{b\lambda}(\mathbf{r}) - \beta_\lambda I_\lambda(\mathbf{r},\mathbf{s}) + \frac{\sigma_\lambda}{4\pi}\int_{4\pi} I_\lambda(\mathbf{r},\mathbf{s}')\Phi_\lambda(\mathbf{s}\cdot\mathbf{s}')d\omega' \quad (1)$$

where I_λ is the spectral intensity, $I_{b\lambda}$ is the black-body intensity, κ_λ, σ_λ, and $\beta_\lambda = \kappa_\lambda + \sigma_\lambda$ are wavelength-dependent absorption, scattering and extinction coefficients, respectively, and Φ_λ is the scattering phase function.

In a previous paper [27] it was shown that for typical applications, such as radiative transfer in particulate-suspensions with a distribution of particle size, a linear-anisotropic scattering model represents any actual situation with sufficient accuracy if the scattering coefficient is suitably modified to account for forward and backward scattering peaks. Using this model the scattering phase function may be expressed as:

$$\Phi_\lambda(\mathbf{s}\cdot\mathbf{s}') = 1 + a_{1\lambda}\mathbf{s}\cdot\mathbf{s}' \quad (2)$$

Also, for the aforementioned applications where the absorption and scattering coefficients do not have a strong wavelength dependence, the gray medium assumption may be adopted. For the gray case, considered in the following, equations (1) and (2) remain valid with subscripts λ dropped.

Before integrating equation (1), it is useful to introduce the following definitions using the coordinate system shown in Fig. 1:

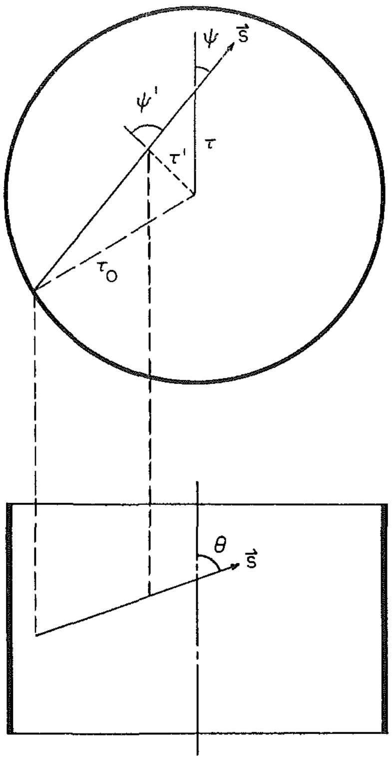

Fig. 1 Coordinate systems for cylindrical geometry

$$I_0(\tau_s) \equiv \int_0^\pi \int_0^{2\pi} I(\tau_s,\psi,\theta)\sin\theta d\psi d\theta, \quad (3)$$

and

$$q(\tau_s) \equiv \int_0^\pi \int_0^{2\pi} I(\tau_s,\psi,\theta)\cos\psi\sin^2\theta\, d\psi d\theta, \quad (4)$$

where I_0 is the integrated intensity, q is the radial radiative heat flux and τ_s defined by $d\tau_s = \beta ds$ is the optical distance along a path **s**.

Now equation (1) may be integrated along path s to yield

$$I(\tau_s,\mathbf{s}) = I_w e^{-\tau_s} + \int_0^{\tau_s} S(\tau'_s,\mathbf{s})\exp[-(\tau_s-\tau'_s)]\,d\tau'_s, \quad (5)$$

where

$$S(\tau_s,\mathbf{s}) \equiv (1-\omega)I_b(\tau_s) + \frac{\omega}{4\pi}[I_0(\tau_s) + a_1\sin\theta\cos\psi q(\tau_s)]. \quad (6)$$

In the above equations I_w is the intensity emanating from the wall, ω is the single scattering albedo and a_1 is the coefficient in the scattering phase function and represents the degree of anisotropy.

In the present analysis for the cylindrical geometry it is assumed that the medium temperature varies only radially. With this assumption, equation (5) may conveniently be transformed to the conventional one-dimensional cylindrical coordinate system. In doing so, the problem must be considered separately in two regions, namely

Nomenclature

a_1 = degree of anisotropy, equation (2)
B = Planck function, $\sigma T^4/\pi$
B_w = Planck function evaluated at wall temperature
F, G, G^*, g = geometric functions
I_λ, I = monochromatic or gray medium intensity
I_0 = integrated intensity
I_w = intensity emanating from cylinder wall
q = radiative heat flux
R_w = surface radiosity given by equation (9a)
r = position vector
r = radial distance
s = unit direction vector
S = source function defined by equation (6)
S^* = modified source function defined by equation (15b)
T, T_w, $T_{\text{℄}}$ = medium, wall, and center-line temperatures, respectively
β = extinction coefficient, $\kappa + \sigma$
ϵ = surface emissivity
θ = polar angle (Fig. 1)
κ = absorption coefficient
σ = Stefan-Boltzmann constant, or scattering coefficient
τ = optical radial coordinate, βr
ψ = azimuthal angle (Fig. 1)
ω = single scattering albedo, σ/β

where $\psi \le \pi/2$ and where $\psi \ge \pi/2$ (see Fig. 1). Using simple trigonometric relations the intensity in the two regions may be expressed as:

$\psi \le \pi/2$:

$$I(\tau,\psi,\theta) = I_w \exp\left\{-\frac{\tau}{\sin\theta}\left[\cos\psi + \sqrt{\left(\frac{\tau_0}{\tau}\right)^2 - \sin^2\psi}\right]\right\}$$
$$+ \int_{\tau|\sin\psi|}^{\tau_0}\left(\left[(1-\omega)I_b(\tau') + \frac{\omega}{4\pi}I_0(\tau')\right]\frac{(\tau'/\tau)}{\sin\theta\sqrt{\left(\frac{\tau'}{\tau}\right)^2 - \sin^2\psi}}\right.$$
$$\left. - \frac{a_1\omega}{4\pi}q(\tau')\right)\exp\left\{-\frac{\tau}{\sin\theta}\left[\cos\psi + \sqrt{\left(\frac{\tau'}{\tau}\right)^2 - \sin^2\psi}\right]\right\}d\tau'$$
$$+ \int_{\tau|\sin\psi|}^{\tau}\left(\left[(1-\omega)I_b(\tau') + \frac{\omega}{4\pi}I_0(\tau')\right]\frac{(\tau'/\tau)}{\sin\theta\sqrt{\left(\frac{\tau'}{\tau}\right)^2 - \sin^2\psi}}\right.$$
$$\left. + \frac{a_1\omega}{4\pi}q(\tau')\right)\exp\left\{-\frac{\tau}{\sin\theta}\left\{\cos\psi - \sqrt{\left(\frac{\tau'}{\tau}\right)^2 - \sin^2\psi}\right]\right\}d\tau', \quad (7a)$$

$\psi \ge \pi/2$:

$$I(\tau,\psi,\theta) = I_w \exp\left\{-\frac{\tau}{\sin\theta}\left[\cos\psi + \sqrt{\left(\frac{\tau_0}{\tau}\right)^2 - \sin^2\psi}\right]\right\}$$
$$+ \int_{\tau}^{\tau_0}\left(\left[(1-\omega)I_b(\tau') + \frac{\omega}{4\pi}I_0(\tau')\right]\frac{(\tau'/\tau)}{\sin\theta\sqrt{\left(\frac{\tau'}{\tau}\right)^2 - \sin^2\psi}}\right.$$
$$\left. - \frac{a_1\omega}{4\pi}q(\tau')\right)\exp\left\{-\frac{\tau}{\sin\theta}\left[\cos\psi + \sqrt{\left(\frac{\tau'}{\tau}\right)^2 - \sin^2\psi}\right]\right\}d\tau', \quad (7b)$$

where $\tau = \beta r$ is the optical distance along the cylinder radius and τ_0 is the total optical distance from center to wall. Using the definition for q (i.e., equation (4) with τ_s replaced by τ), equation (7) can be integrated over all directions to yield

$$q(\tau) = 4R_w F(\tau,\tau_0) + \int_{\tau}^{\tau_0}\left(a_1\omega q(\tau')F(\tau,\tau')\right.$$
$$\left. + [4\pi(1-\omega)B(\tau') + \omega I_0(\tau')]\frac{dF(\tau,\tau')}{d\tau'}\right)d\tau'$$
$$+ \int_0^{\pi/2}\left\{\int_{\tau\sin\psi}^{\tau}\left(a_1\omega q(\tau')G(\tau,\tau',\psi) + [4\pi(1-\omega)B(\tau')\right.\right.$$
$$\left.\left. + \omega I_0(\tau')]\frac{dG(\tau,\tau',\psi)}{d\tau'}\right)d\tau'\right\}d\psi, \quad (8)$$

where R_w is the surface radiosity [29],

$$R_w = \sigma T_w{}^4 + \frac{1-\epsilon}{\epsilon}q(\tau_0), \quad (9a)$$

and B is the Planck function,

$$B \equiv \sigma T^4/\pi, \quad (9b)$$

and

$$F(\tau,\tau') \equiv -\frac{1}{\pi}\int_0^{\pi}\int_0^{\pi/2}\exp\left[-\frac{\tau}{\sin\theta}\left(\cos\psi + \sqrt{\left(\frac{\tau'}{\tau}\right)^2 - \sin^2\psi}\right)\right]$$
$$\times \sin^2\theta\cos\psi\, d\theta\, d\psi, \quad (10)$$

$$G(\tau,\tau',\psi) \equiv \frac{1}{\pi}\int_0^{\pi/2}\left\{\exp\left[-\frac{\tau}{\sin\theta}\left(\cos\psi - \sqrt{\left(\frac{\tau'}{\tau}\right)^2 - \sin^2\psi}\right)\right]\right.$$
$$\left. - \exp\left[-\frac{\tau}{\sin\theta}\left(\cos\psi + \sqrt{\left(\frac{\tau'}{\tau}\right)^2 - \sin^2\psi}\right)\right]\right\}\sin^2\theta\cos\psi\, d\theta. \quad (11)$$

Equation (8) still involves an integration over the angle ψ and is, thus, a second-order integral equation. In order to reduce equation (8) to a first-order integral equation, a new function is defined:

$$G^*(\tau,\tau',\psi) \equiv \begin{cases} G(\tau,\tau',\psi) & \tau' \ge \tau\sin\psi, \\ 0. & \tau' \le \tau\sin\psi. \end{cases} \quad (12)$$

With this definition it can be shown that

$$\int_0^{\pi/2} G^*(\tau,\tau',\psi)d\psi = \int_0^{\sin^{-1}(\tau'/\tau)} G^*(\tau,\tau',\psi)d\psi$$
$$+ \int_{\sin^{-1}(\tau'/\tau)}^{\pi/2} G^*(\tau,\tau',\psi)d\psi = \frac{\tau'}{\tau}F(\tau',\tau). \quad (13)$$

Using equation (12) and also integrating by parts to eliminate derivatives of F and G, equation (8) becomes, after some manipulation

$$q(\tau) = [-4R_w + 4\pi(1-\omega)B(\tau_0) + \omega I_0(\tau_0)]F(\tau,\tau_0)$$
$$+ \int_0^{\tau} S^*(\tau')F(\tau',\tau)\left(\frac{\tau'}{\tau}\right)d\tau' + \int_{\tau}^{\tau_0} S^*(\tau')F(\tau,\tau')d\tau', \quad (14a)$$

where

$$S^*(\tau) \equiv -4\pi(1-\omega)\frac{dB}{d\tau} - \omega\frac{dI_0}{d\tau} + a_1\omega q(\tau). \quad (15a)$$

Finally, I_0 may be eliminated from equations (14a) and (15a) by using the direction-integrated form of equation (1), i.e.:

$$\nabla_\tau \cdot \mathbf{q} = \frac{1}{\tau}\frac{d}{d\tau}(\tau q) = (1-\omega)[4\pi B(\tau) - I_0(\tau)] \quad (16)$$

to yield

$$q(\tau) = \left\{4[\pi B(\tau_0) - R_w] - \frac{\omega}{1-\omega}\left[\frac{1}{\tau}\frac{d}{d\tau}(\tau q)\right]_{\tau_0}\right\}F(\tau,\tau_0)$$
$$+ \int_0^{\tau} S^*(\tau')F(\tau',\tau)\frac{\tau'}{\tau}d\tau' + \int_{\tau}^{\tau_0} S^*(\tau')F(\tau,\tau')d\tau', \quad (14b)$$

and

$$S^*(\tau) \equiv a_1\omega q(\tau) + \frac{\omega}{1-\omega}\frac{d}{d\tau}\left(\frac{1}{\tau}\frac{d}{d\tau}(\tau q)\right) - 4\pi\frac{dB}{d\tau}. \quad (15b)$$

It is, therefore, seen that by introducing the geometric function $F(\tau, \tau')$, the equation for the radiative heat flux is reduced to a first-order integro-differential equation.

Note that the F-functions can be evaluated numerically once and for all. The complexity of the problem has now been basically reduced to that of the planar case, with the exception that the relatively simple exponential integrals have been replaced by the more complicated and untabulated F-functions. In order to facilitate the use of numerical quadrature for calculation of F's, the limits of integration in equation (10) are transformed to yield:

$$F(\tau,\tau') = \frac{1}{\pi}\int_0^1\int_0^1\{\exp[-\tau(\sqrt{x^2-\eta^2} - \sqrt{1-\eta^2})/\sqrt{1-\xi^2}]$$
$$- \exp[-\tau(\sqrt{x^2-\eta^2} + \sqrt{1-\eta^2})/\sqrt{1-\xi^2}]\}\sqrt{1-\xi^2}\,d\xi\, d\eta, \quad (17)$$

where

$$x = \tau'/\tau. \quad (18)$$

Equation (17) was used for the numerical evaluation of F. Use of 41 nodes for each variable (i.e., ξ and η) yielded three significant-figure accuracy. Figures 2 and 3 show the typical behavior of the F-function for several values of τ. The numerical solution of equation (14b) was also performed by expanding the integrals and the derivatives into quadratures and then solving a system of simultaneous equations for the unknown heat flux. In order to achieve additional numerical accuracy, the integrations in equation (14b) were performed outward

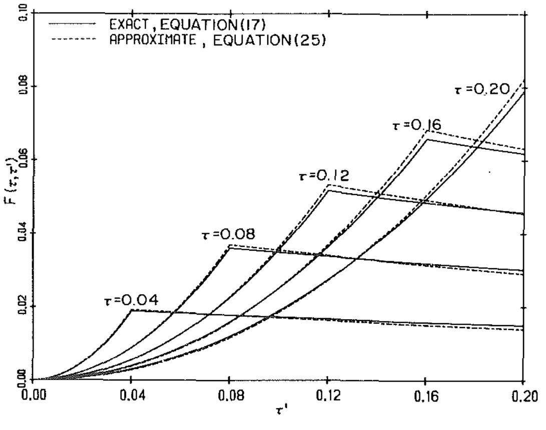

Fig. 2 Comparison of exact and approximate kernels for small values of optical thickness, (τ, $\tau' \leq 0.2$, $a = 2.0$, $b = 2.0$)

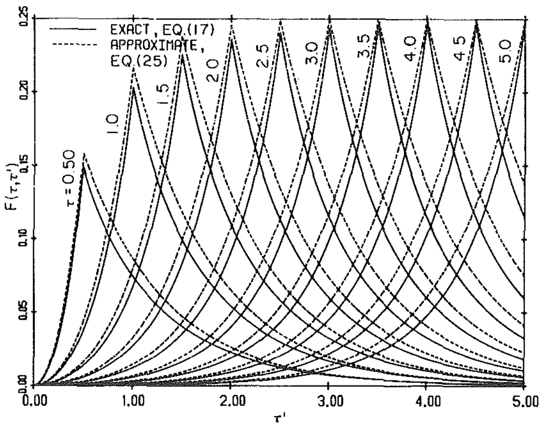

Fig. 3 Comparison of exact and approximate kernels for large values of optical thickness, ($a = 1.2$, $b = 2.0$)

from the point under consideration. A combination of Newton-Cotes quadratures was used such that integration near the point under consideration was approximated by higher order quadratures and only in the outermost subinterval a quadrature of lower order was used to accommodate the variable limits of integration. This method assured accurate integration at or near the point under consideration, where the integrands are substantially larger than near the outer limit. The derivatives appearing in equation (15b) were also discretized using second-order finite-difference formulae. The resulting N linear, simultaneous, algebraic equations for the unknowns q_j ($j = 1, \cdots, N$) at the N spatial nodes were solved by L-U decomposition utilizing Gaussian elimination with partial pivoting. For the systems considered in this paper, the above method proved to be quite accurate. For larger systems of linear equations, however, a matrix iteration type method may be preferable.

Approximate Methods. Although it is possible to obtain the exact numerical solution for equation (14b) without the use of extensive computer time, the task can be simplified considerably if the radiative heat flux can be obtained by solving a differential equation. This simplification would be of great value in cases where the divergence of the radiative heat flux appears as a part of the more complicated general energy equation, which is nonlinear, making it necessary to evaluate heat transfer rates and temperature profiles by iteration. One such convenient method is the differential approximation.

In a previous publication [28], the validity of the differential approximation for calculation of the radiative heat flux in a gray, emitting, absorbing and linear-anisotropically scattering planar medium was established. For an optically thick medium, for which this approximation is valid, the intensity can only deviate slightly from an isotropic distribution and may be approximated by [28]:

$$I \cong \frac{1}{4\pi}(I_0 + 3\mathbf{q}\cdot\mathbf{s}). \tag{19}$$

Using equation (19) and multiplying equation (1) by $\mathbf{s}$ and integrating over all solid angles one obtains:

$$\nabla_\tau I_0 = -3(1 - a_1\omega/3)\mathbf{q}. \tag{20}$$

Expressing equation (20) in a one-dimensional cylindrical coordinate system and combining with equation (16) to eliminate I_0 yields:

$$\frac{d^2q}{d\tau^2} + \frac{1}{\tau}\frac{dq}{d\tau} - \left(\gamma^2 + \frac{1}{\tau^2}\right)q = 4\pi(1-\omega)\frac{dB}{d\tau}, \tag{21}$$

where

$$\gamma^2 = 3(1-\omega)(1 - a_1\omega/3). \tag{22}$$

For the case of isotropic scattering ($a_1 = 0$), the present formulation reduces to the moment method introduced by Heaslet and Warming [21]. The first boundary condition for equation (20) is obtained from the condition of symmetry:

$$q(0) = 0. \tag{23}$$

The second boundary condition is the customary jump boundary condition [28] which expressed in terms of q becomes:

$$\left[\frac{1}{1-\omega}\frac{1}{\tau}\frac{d}{d\tau}(\tau q)\right]_{\tau_0} + 2\left(\frac{2-\epsilon}{\epsilon}\right)q(\tau_0) = 4\pi[B(\tau_0) - B_w]. \tag{24}$$

Equation (21) together with its boundary conditions constitute the differential approximation for the cylindrical geometry and can be solved by a simple finite difference scheme for any given medium temperature distribution. It should be noted here that, although the differential approximation is valid for optically thick media, in the case of a one-dimensional hollow cylinder it also reduces to the correct optically thin limit.

An alternative method which also reduces the problem to solving a linear differential equation can be developed by finding a simple exponential function to approximate the F-function which appears as the kernel of the integrands in equation (14). One such approximation is

$$F(\tau, \tau') \cong \frac{1}{4}e^{-a(\tau'-\tau)}[1 - e^{-b\tau}], \tag{25}$$

where a and b are constants. The choice of $a = b = 2$ yields excellent accuracy for small values of τ (Fig. 2), owing to the fact that it constitutes the exact optically thin limit. For larger values of τ, however, the choice of a smaller value for a results in a better approximation. Figure 3 shows the comparison between exact and approximate kernels F which were used in the calculation of heat fluxes for the case of $\tau_0 = 5$. For the approximate curves of Fig. 3 a value of $a = 1.2$ was used.

Substituting equation (25) into equation (14), differentiating and eliminating the integrals one gets, after some manipulation:

$$\left[\frac{(\tau q(\tau)e^{a\tau})'}{(g(\tau)e^{a\tau})'}\right]' + S^*(\tau)e^{-a\tau} = 0, \tag{26}$$

where primes denote differentiation with respect to τ and

$$g(\tau) \equiv \frac{\tau}{4}e^{a\tau}(1 - e^{-b\tau}), \tag{27}$$

and $S^*(\tau)$ is given by equation (15b).

The boundary conditions for equation (26) are:

$$q(0) = 0, \tag{28a}$$

$$q(\tau_0) = \left[\frac{g(\tau_0)}{\tau_0}\left\{4[\pi B(\tau_0) - R_w] - \frac{\omega}{1-\omega}\left[\frac{1}{\tau}\frac{d}{d\tau}(\tau q)\right]_{\tau_0}\right\} + \int_0^{\tau_0} S^*(\tau')g(\tau')d\tau'\right]e^{-a\tau_0} \tag{28b}$$

Equation (26), despite its apparent complexity, can be solved as a boundary-value problem in the following fashion: a solution to the homogeneous equation, $q_H(\tau)$, is found, subject to boundary conditions $q_H(0) = 0$ and, say, $q'_H(0) = 1$, noting that the second boundary condition is arbitrary. A particular solution to equation (26) is then found by setting

$$q_p(\tau) = \phi(\tau) q_H(\tau), \tag{29}$$

subject to arbitrary boundary conditions, say $\phi(0) = \phi'(0) = 0$. The complete solution is then determined from

$$q(\tau) = C q_H(\tau) + q_p(\tau) = q_H(\tau)[C + \phi(\tau)], \tag{30}$$

where the constant C is determined by plugging equation (30) into the second boundary condition, equation (28*b*).

Results and Discussion

To the extent possible the present results were compared with others in the literature [13, 21]. Comparison with Kesten's [13] results is somewhat problematic as (1) one of his two relations appears to be incorrect and it is not known which one was used for generating results, and (2) the boundary temperature used for his results is not stated. Comparison with his (non-scattering) results shows good agreement inside the cylinder but disagreement close to the boundary. Heaslet and Warming [21] present only some approximate wall fluxes for an isothermal cylinder with isotropic scattering, using a method identical to the present differential approximation.

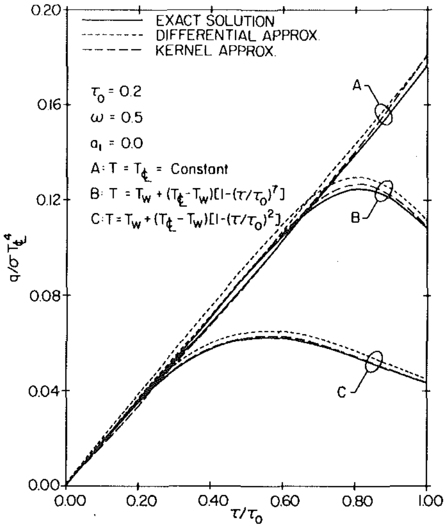

Fig. 4 Variation of nondimensional heat flux with medium temperature distribution, (isotropic scattering, $\omega = 0.5$, $\tau_0 = 0.2$)

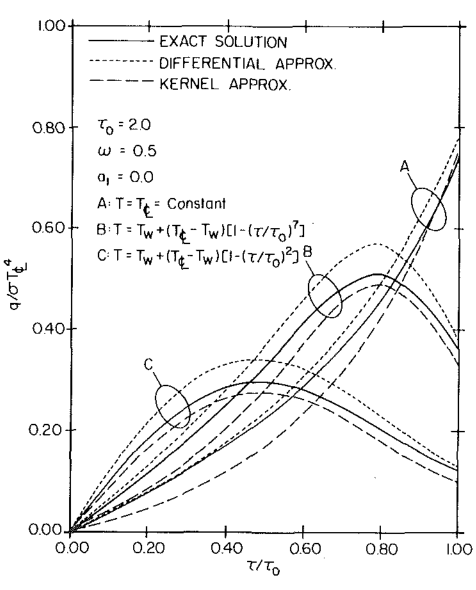

Fig. 5 Variation of nondimensional heat flux with medium temperature distribution, (isotropic scattering, $\omega = 0.5$, $\tau_0 = 2.0$)

The three methods of solution are compared for various combinations of the four governing parameters, viz., optical thickness τ_0, medium temperature distribution $T(r)$, degree of anisotropy a_1, and scattering albedo ω. In all cases considered here, the cylinder wall is assumed to be black.

In order to compare the three solution methods without crowding the graphs, Figs. 4–7 are limited to the representative case of isotropic scattering ($a_1 = 0$) with an albedo of $\omega = .5$. Deviations from those results for different values of a_1 and ω may be estimated from Figs. 8–10.

Figure 4 shows the nondimensional radiative heat flux as a function of radial distance for three different temperature profiles. Profile A represents a constant temperature medium with the tube wall at a different temperature T_w. Profiles B and C simulate turbulent and laminar flows, respectively. For all numerical calculations a value of $T_{℄}/T_w = 5$ was used. The results of Fig. 4 are for an optical thickness of $\tau_0 = 0.2$ which is a suitable choice for the demonstration of the behavior of the three methods of solution for optically thin media. It is seen that the kernel approximation with $a = b = 2.0$ yields excellent predictions of heat flux for all temperature profiles. The differential approximation, although generally only valid for optically thick media, reduces to the proper optically thin limit in the hollow cylindrical

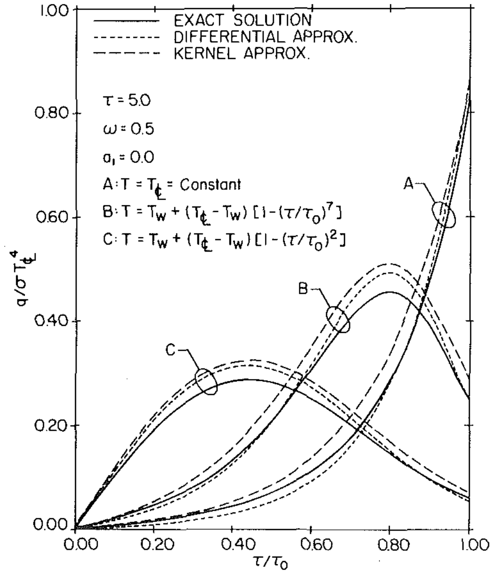

Fig. 6 Variation of nondimensional heat flux with medium temperature distribution, (isotropic scattering, $\omega = 0.5$, $\tau_0 = 5.0$)

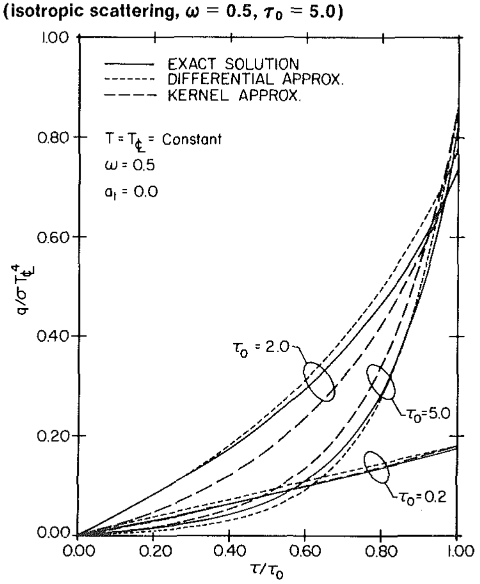

Fig. 7 Effect of optical thickness on radiative heat flux in an isothermal medium with temperature jump at the boundary, (isotropic scattering, $\omega = 0.5$)

geometry, thus also resulting in a good approximation of the heat flux for all three cases. It must be emphasized that this holds true only for the case of radiative interchange between a participating medium and an isothermal enclosure, as the one considered in this paper.

Figure 5 depicts a similar comparison for optical thickness of $\tau_0 = 2.0$. This value is considered to be a typical intermediate optical thickness and, as expected, the differential-approximation prediction of heat fluxes for profiles B and C, which have large temperature gradients, become less accurate, resulting in a maximum error of about 10 percent. The predictions obtained from the kernel approximation depend on the choice of the two constants a and b (equation (25)). For $\tau_0 = 2.0$ the heat flux variations obtained from the choice of $a = b = 2.0$ underpredict the exact results, suggesting that with increasing optical thickness, the value of a should be decreased.

Figure 6 shows the results for a medium of relatively high optical thickness ($\tau_0 = 5$). As expected, the differential approximation yields good results with its maximum deviation being at regions of large temperature gradients. For the kernel approximation, values of $a = 1.2$ and $b = 2.0$ are used in this case which result in heat fluxes that overpredict the exact values slightly. A comparison of Figs. 2 and 3 demonstrates the effect of decreasing the value of the constant a on the behavior of the approximate kernel, indicating that it would be possible to establish a suitable set of values for the constants a and b to produce reasonable approximations for the F-functions in different ranges of optical thickness.

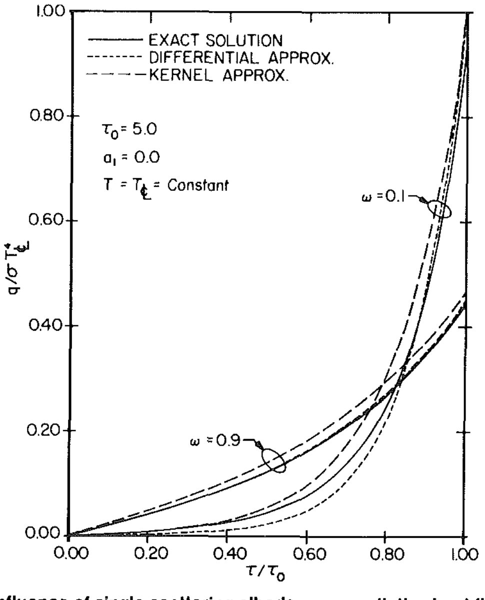

Fig. 8 Influence of single scattering albedo, ω, on radiative heat flux distribution in a constant temperature medium with isotropic scattering

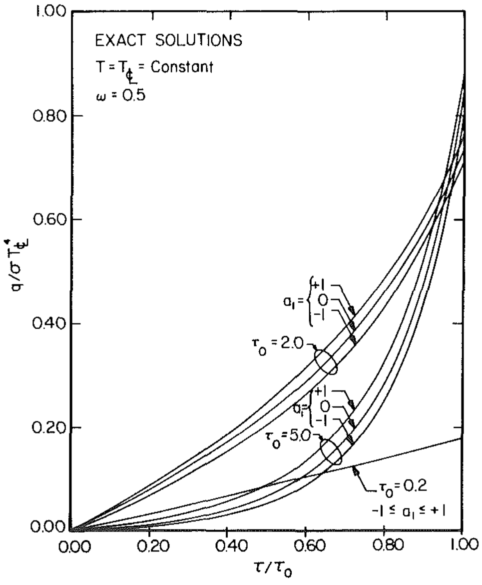

Fig. 9 Effect of degree of anisotropy, a_1, on radiative heat flux at various optical thicknesses, ($\omega = 0.5$, $T(r)$ = constant)

A comparison of Figs. 4, 5, and 6 provides a good insight into the effect of temperature profile on the radiative heat flux distribution for different values of optical thickness: In an optically thin medium (Fig. 4), energy absorption is quite uniform over the radial coordinate, while emission of energy depends on the local temperature. For all three temperature profiles considered here, the center-line temperature is the same and the heat fluxes obtained for all three profiles overlap near the center. While the wall temperature is the same for all three profiles, for profile A the medium temperature at the wall is not the same as the wall temperature, while profile B and C contain no such jump. This difference accounts for the decrease near the wall of heat fluxes for profiles B and C. With increasing optical thickness, both emission and absorption increase, but large absorption prevents the process of direct energy exchange between the core and the tube wall, thus accounting for the flattening of the heat flux profiles near the tube center.

Since the radiative heat flux must vanish in both limits of zero and infinite optical thickness, one would expect the heat flux to increase with increasing optical thickness until a critical value of τ_0 is reached and to diminish beyond that point. The results obtained for profiles B and C which have no temperature jump at the wall, demonstrate this trend clearly (Figs. 4, 5, and 6). With a temperature jump at the boundary, however, the behavior is slightly different: Figure 7 depicts the variation of the radiative heat flux with optical thickness for profile A and shows that the heat flux at the wall increases with increasing optical thickness while becoming smaller near the core, due to strong absorption.

Figure 8 demonstrates the effect of changing the scattering albedo ω on the radiative heat flux for a medium at constant temperature and optical thickness of $\tau_0 = 5.0$. Small values of ω (e.g., $\omega = 0.1$) indicate that emission and absorption of energy within the medium dominate over scattering. This, together with the large value of optical thickness, account for the relatively large heat flux near the wall and its rapid decay towards the center. For large ω, however, scattering dominates and causes a more isotropic intensity distribution, which is the reason for the excellent prediction obtained from the differential approximation.

The effect of the degree of anisotropy a_1, is depicted in Fig. 9. To avoid crowding of the graph, only the exact solutions are depicted here. The approximate solutions follow the same trends as demonstrated in Figs. 4–7. A value of $a_1 = +1$ indicates strong forward scattering, while $a = -1$ represents strong backscattering of radiation. Forward scattering enhances the energy transfer from the core towards the tube wall, thus increasing the radiative heat flux, while backscattering has the opposite effect and causes a decrease in the heat flux.

To further demonstrate the influence of the single-scattering albedo and the degree of anisotropy on heat transfer rates, Fig. 10 shows the case of an isothermal cylinder which, for all cases considered, has an identical optical thickness based on absorption coefficient, $\kappa R = 1.0$. Thus different optical thicknesses are entirely due to different scattering coefficients (or albedo) through the relation $\tau_0 = \kappa R/(1 - \omega)$. Again, to avoid crowding, only one method of solution is shown in Fig. 10, in this case the differential approximation. It is seen that for an albedo below a relatively large value like $\omega = 0.5$ the heat flux rates remain relatively unaffected (the wall flux diminishes compared to the nonscattering case by ~13 percent for $\omega = 0.5$ and strong backscattering, $a_1 = -1$). Only for very large values of ω is the heat transfer diminished significantly. As $\omega \rightarrow 1$, of course, the heat transfer rate must go to zero (pure scattering).

All of the above figures show that the inaccuracy of the approximate methods is never more than ~10 percent of maximum flux. In view of the fact that radiative properties are rarely known accurately, and

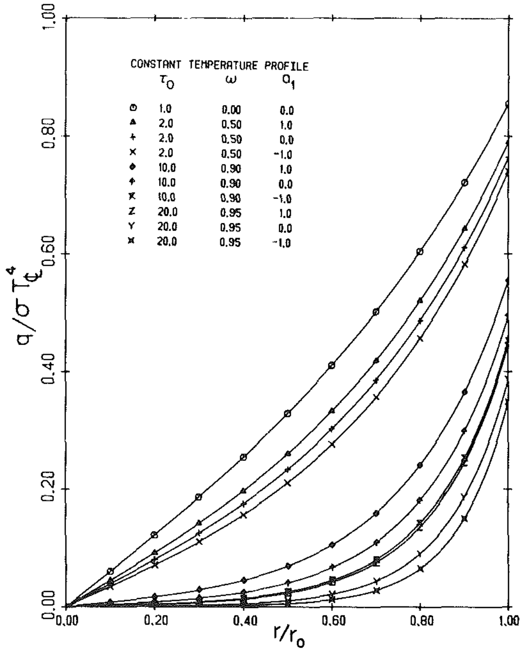

Fig. 10 Effect of scattering albedo, ω, and anisotropy, a_1, on radiative heat flux (T = constant, κR = 1.0)

that nongray effects have been neglected, the approximate methods should prove sufficient for the vast majority of applications.

Summary and Conclusion

An exact solution for radiative transfer in a gray, emitting, absorbing and linear-anisotropically scattering medium of one-dimensional cylindrical geometry has been developed. The solution results in a first-order integral equation in the radial coordinate. The exact results are compared with two approximate models, viz. (1) the differential approximation, (2) a kernel approximation. The first model reduces to the correct optically thick and thin limits and also yields reasonable results in the optically intermediate range. The second model produces excellent results for the optically thin regions and by appropriate choice of two constants it can also yield good approximations for the radiative heat flux at larger values of optical thickness. Both approximate methods involve the solution of differential rather than integral equations, offering a valuable simplification for applications in which the radiative heat flux is only a part of the more complex general energy equation. In addition, the results show that scattering is of importance only for large values of the albedo. Thus, in many engineering applications scattering may be neglected without significant loss of accuracy.

References

1 Edwards, R. H., and Bobco, R. P., "Radiant Heat Transfer from Isothermal Dispersions with Isotropic Scattering," ASME JOURNAL OF HEAT TRANSFER, Vol. 89, pp. 300–308, 1967.

2 Armaly, B. F., and El-Baz, H. S., "Influence of the Refractive Index on the Radiative Source Functions of an Isotropically Scattering Medium," *Journal of Quant. Spectrosc. Radiat. Transfer*, Vol. 18, pp. 419–424, 1977.

3 Dayan, A., and Tien, C. L., "Heat Transfer in Gray Medium with Linear Anisotropic Scattering," ASME JOURNAL OF HEAT TRANSFER, Vol. 97, pp. 391–396, 1975.

4 Buckius, R. O., and Tseng, M. M., "Radiative Heat Transfer in a Planar Medium with Anisotropic Scattering and Directional Boundaries, *Journal of Quant. Spectrosc. Radiat. Transfer*, Vol. 20, pp. 385–402, 1978.

5 Buckius, R. O., and King, R., "Diffuse Solar Radiation on a Horizontal Surface for a Clear Sky," *Solar Energy*, Vol. 21, pp. 503–509, 1978.

6 Bergquam, J. B., and Seban, R. A., "Heat Transfer by Conduction and Radiation in Absorbing and Scattering Materials," ASME JOURNAL OF HEAT TRANSFER, Vol. 93, pp. 236–239, 1971.

7 Domoto, G. A., and Wang, W. C., "Radiative Transfer in Homogeneous Nongray Gases with Nonisotropic Particle Scattering," ASME JOURNAL OF HEAT TRANSFER, Vol. 96, pp. 385–390, 1974.

8 Chin, J. H., and Churchill, S. W., "Anisotropic, Multiple Scattered Radiation from an Arbitrary, Cylindrical Source in an Infinite Slab," ASME JOURNAL OF HEAT TRANSFER, Vol. 89, pp. 167–172, 1967.

9 Hottel, H. C., Sarofim, A. F., Evans, L. B., and Vasalos, I. A., "Radiative Transfer in Anisotropically Scattering Media: Allowance for Fresnel Reflection at the Boundaries," ASME JOURNAL OF HEAT TRANSFER, Vol. 90, pp. 56–62, 1968.

10 Love, T. J., and Grosh, R. J., "Radiative Heat Transfer in Absorbing, Emitting and Scattering Media," ASME JOURNAL OF HEAT TRANSFER, Vol. 87, pp. 161–166, 1965.

11 Viskanta, R., and Toor, J. S., "Effect of Multiple Scattering on Radiant Energy Transfer in Waters," *Journal Geophysical Res.*, Vol. 78, No. 18, pp. 3538–3551, 1973.

12 Potter, J. F., "The Delta Function Approximation in Radiative Transfer Theory," *Journal of Atmospheric Science*, Vol. 27, pp. 943–949, 1970.

13 Kesten, A. S., "Radiant Heat Flux Distribution in a Cylindrically-Symmetric Nonisothermal Gas with Temperature-Dependent Absorption Coefficient," *Journal of Quant. Spectrosc. Radiat. Transfer*, Vol. 8, pp. 419–433, 1968.

14 Habib, I. S. and Greif, R., "Nongray Radiative Transport in Cylindrical Media," ASME JOURNAL OF HEAT TRANSFER, pp. 29–32, 1970.

15 Landram, C. S., Greif, R., and Habib, I. S., "Heat Transfer in Turbulent Pipe Flow with Optically Thin Radiation," ASME JOURNAL OF HEAT TRANSFER, Vol. 91, pp. 330–336, 1969.

16 Greif, R., "Laminar Convection with Radiation: Experimental and Theoretical Results," *Int. Journal of Heat Mass Transfer*, Vol. 21, pp. 477–480, 1978.

17 Wassel, A. T., and Edwards, D. K., "Molecular Gas Band Radiation in Cylinders," ASME JOURNAL OF HEAT TRANSFER, Vol. 96, pp. 21–26, 1974.

18 Wassel, A. T., Edwards, D. K., and Catton, I., "Molecular Gas Radiation and Laminar or Turbulent Heat Diffusion in a Cylinder with Internal Heat Generation," *Int. Journal of Heat Mass Transfer*, Vol. 18, pp. 1267–1276, 1975.

19 Wassel, A. T., and Edwards, D. K., "Molecular Gas Radiation in a Laminar or Turbulent Pipe Flow," ASME JOURNAL OF HEAT TRANSFER, Vol. 98, pp. 101–107, 1976.

20 Nakra, N. K. and Smith, T. F., "Combined Radiation-Convection for a Real Gas," ASME JOURNAL OF HEAT TRANSFER, Vol. 99, pp. 60–65, 1977.

21 Heaslet M. A., and Warming, R. F., "Theoretical Predictions of Radiative Transfer in a Homogeneous Cylindrical Medium" *J. Quant. Spectrosc. Radiat. Transfer*, Vol. 6, pp. 751–774, 1966.

22 Echigo, R., Hasegawa, S., and Tamehiro, H., "Radiative Heat Transfer by Flowing Multiphase Medium—Part II. An Analysis on Heat Transfer of Laminar Flow in an Entrance Region of a Circular Tube," *Int. Journal of Heat Mass Transfer*, Vol. 15, pp. 2595–2610, 1972.

23 Tamehiro, H., Echigo, R., and Hasegawa, S., "Radiative Transfer by Flowing Multiphase Medium—Part III. An Analysis on Heat Transfer of Turbulent Flow in a Circular Tube," *Int. Journal of Heat Mass Transfer*, Vol. 16, pp. 1199–1213, 1973.

24. Adzerikho, K. S., and Nekrasov, V. P., "Luminescence Characteristics of Cylindrical and Spherical Light-Scattering Media," *Int. Journal of Heat Mass Transfer*, Vol. 18, pp. 1131–1138, 1975.

25 Adzerikho, K. S., and Antsulevich, V. I., Lapko, Ya. K., and Nekrasov, V. P., "Luminescence of Two-Phase Inhomogeneous Media of Cylindrical Geometry," *Int. Journal of Heat Mass Transfer*, Vol. 22, pp. 131–136, 1979.

26. Bayazitoglu, Y., and Higenyi, J., "Higher Order Differential Equations of Radiative Transfer: P_3 Approximation," *AIAA Journal*, Vol. 17, No. 4, pp. 424-431, 1979.

27 Modest, M. F., and Azad, F. H., "The Influence and Treatment of Mie-Anisotropic Scattering in Radiative Heat Transfer," ASME JOURNAL OF HEAT TRANSFER, Vol. 102, 1980, pp. 92–98.

28 Modest, M. F., and Azad, F. H., "The Differential Approximation for Radiative Transfer in an Emitting, Absorbing and Anisotropically Scattering Medium," *J. Quant. Spectrosc. Radiat. Transfer*, Vol. 23, 1980, pp. 117–120.

29 Sparrow, E. M., and Cess, R. D., "Radiation Heat Transfer," McGraw-Hill, New York, 1978.

Carbon Particulate in Small Pool Fire Flames

S. Bard[1]
P. J. Pagni

Mechanical Engineering Department and
Lawrence Berkeley Laboratory,
University of California, Berkeley, CA. 94720

Flame radiation, the dominant heat transfer mechanism in many combustion and fire safety related problems, is primarily controlled by the fraction of flame volume occupied by solid carbon particulate. A multi-wavelength laser transmission technique is used here to measure carbon particulate volume fractions and approximate particle size distributions in ten common solid, cellular and liquid fueled small scale, 0 (10 cm dia), pool fire diffusion flames. The most probable particle radius, r_{max}, and concentration, N_0, are two parameters in the assumed gamma function size distribution form which are determined for each fuel by simultaneously measuring light transmission of two superimposed laser wavelengths. The resulting soot volume fractions range from $f_v \sim 4 \times 10^{-6}$ for cellular polystyrene to $f_v \sim 7 \times 10^{-8}$ for alcohol. Cellular polystyrene has the largest particles, $r_{max} \sim 60$ nm while wood has the smallest, $r_{max} \sim 20$ nm. The carbon particulate optical properties used in the analysis are shown to be representative of actual flame soot and are more accurate than the soot refractive index usually assumed in the literature. Finally, mean particle sizes obtained for all fuels indicate that the small particle absorption limit assumption is a reasonable approximation for infrared flame radiation calculations.

Introduction

Flame radiation, the dominant heat transfer mode in many combustion problems [1], is strongly influenced by the fraction of flame volume occupied by solid carbon particulate. Carbon particulate formation processes have been studied for many years but it is not yet possible to predict flame particle size distributions and concentrations. Thus, experimental methods for characterizing flame soot are necessary and important. A multi-wavelength laser transmission technique is reported here to determine "in situ" carbon particulate volume fractions and size distributions. Ten common solid, cellular, and liquid hydrocarbon fueled, small scale 0 (10 cm) buoyant diffusion flames are studied.

Optical techniques for characterizing particulates are attractive due to their nonintrusive nature. However, accurate soot refractive indices as a function of wavelength are required in any light scattering [2–8] transmission [9, 10] or radiance [11, 12] experiment from which particulate volume fractions and size distributions are to be deduced. There has existed some uncertainty regarding the soot refractive index, $m = n(1 - ik)$. Diffusion flame soot volume fractions and size distributions previously published [3, 8, 10, 12] incorporated the refractive indices reported by Dalzell and Sarofim [13] based on reflectance measurements from compressed soot samples, (e.g., $m = 1.57 - 0.56\,i$ at 488nm). However, the reference [13] values may be in error due to the presence of unavoidable voids in the compressed soot. Medalia and Richards [14] estimate from compressibility data that the compressed soot of reference [13] is actually 1/3 air by volume. Based on this void volume fraction, Graham [15] estimates that Dalzell and Sarofim's n and nk may be 20 percent low. Also, Chippet and Gray [16] combined electronmicrographic particle size analysis and spectral transmission measurements to obtain an average m = 1.9–0.35i in the visible wavelength range. Absorption of incident radiation by gaseous molecules or radicals may have slightly affected the results obtained from their premixed acetylene flames [8, 17]. Recently, in situ soot optical properties, improved over reference [13] in the direction suggested above [14–16], have been reported by Lee and Tien [18]. They propose a dispersion model based on a rigorous consideration of carbon particle electron band structure. Dispersion constants are determined from independent transmission measurements in polymethylmethacrylate and polystyrene fueled flames at visible [10] and infrared wavelengths [12]. Their soot optical properties, reflecting values of actual flame soot, are summarized in Table 1 for several wavelengths.

There is good agreement of the Table 1 optical properties with the Chippet and Gray [16] results and with the corrections to reference [13] indicated by Graham [15]. The soot refractive index was shown in reference [18] to be rather insensitive to fuel hydrogen/carbon ratio and to temperature, in the range of typical flame temperatures. The multiwavelength laser transmission techniqued developed here determines particulate volume fractions and size distributions from the ratios of experimentally measured extinction coefficients at several different wavelengths. This technique is used to demonstrate that the reference [13] optical properties produce particle sizes and volume fractions which are not consistent at different wavelength combinations. In some cases the extinction coefficient ratios actually exceed the theoretical limit. However, when Lee and Tien's optical properties (Table 1) are used, the resulting volume fractions and size distributions are consistent at every extinction coefficient ratio. The previous arguments lead to the conclusion that the Table 1 soot optical properties are valid as mean values representative of the full range of fuels studied here.

The experiments to measure extinction coefficients are described in the next section. Use of these data in the analysis described in the following section enables accurate determination of soot volume fractions. Finally, the use of the soot volume fractions to make infrared flame radiation calculations is discussed.

Experiment

Multiwavelength laser transmission experiments are performed with the apparatus shown schematically in Fig. 1. A CW Coherent (model CR-MG) argon/krypton laser operating at either λ = 0.4579 μm, 0.488 μm, or 0.5145 μ with ~250 mW output and a Spectra-

Table 1 Soot optical properties, $m(\lambda) = n(\lambda)\,[1 - ik(\lambda)]$

Wavelength, (μm)	$n(\lambda)$	$nk(\lambda)$	$F_a(\lambda)$
0.4579	1.94	0.58	0.033
0.4880	1.94	0.54	0.031
0.5145	1.93	0.52	0.030
0.6328	1.89	0.48	0.029
1.6	1.9	0.80	0.045
2.5	2.1	1.1	0.048
3.0	2.3	1.3	0.046
4.0	2.5	1.5	0.040
5.0	2.7	1.6	0.035

[a] Lee, D. and Tien, C. L.: to be published in the *Eighteenth Symposium (International) on Combustion*, 1980.

---

[1] Current address: Thermal Science and Engineering Group, Jet Propulsion Laboratory, 4800 Oak Grove Drive, Pasadena, CA 91103

Contributed by The Heat Transfer Division for publication in the JOURNAL OF HEAT TRANSFER. Manuscript received by The Heat Transfer Division May 29, 1980.

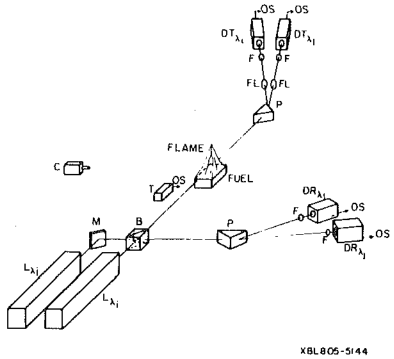

Fig. 1 Schematic of apparatus for simultaneous multiwavelength laser transmission measurements.

L_{λ_i}, L_{λ_j} —Laser at λ_i or λ_j
M —Mirror
B —Beamsplitter
P —Prism
T —Digital timer
C —Video camera
FL —Focusing lens (f = 147 mm)
F —Bandpass filter (30 Å bandwidth)
DT_{λ_i}, DT_{λ_j} —Detector for transmitted intensity
DR_{λ_i}, DR_{λ_j} —Detector for reference intensity
OS —Output signal to amplifier and computer

Physics (model 125) helium/neon laser emitting at $\lambda = 0.6328\ \mu$m and ~50 mW are used. The beams from each laser are superimposed with a beam splitter cube and occupy the same physical path through the flame. After traveling through the flame, the two wavelengths are separated with an equilateral prism. Each beam is then passed through a narrow band pass filter at its own wavelength (0.003 μm bandwidth) to eliminate noise and stray light from the other beam. The beams are each focused with an f = 147 mm lens onto two photodiode detectors (Newport Research Co., model 820 power meter). A reference intensity from each laser is also monitored. The output signals from the detectors are sent through a d-c amplifier and input to a (Digital Equipment Corp.) AR11 16-channel, 10-bit A/D converter and stored in a PDP-11/34 minicomputer. Data are read from the detectors when triggered by a clock tick from the variable frequency timer. The digital display of the timer and the flame are filmed with an RCA (model CC002) color video camera connected to a Sanyo (model VTC 8200) video tape recorder.

For each fuel 100 instantaneous stored intensity measurements at each wavelength are correlated with the simultaneous laser pathlengths measured separately for each data point. The laser beam pathlength, L, is taken as the width of the continuous luminosity on a videotape frame. It will be shown in the next section that superposition of the two beams enables determination of mean particle sizes without knowing L, therefore reducing the experimental error.

Analysis

Extinction Coefficient. When a monochromatic beam passes through a homogeneous polydisperse aerosol, the transmitted intensity, I, is related to the initial intensity, I_0, by

$$I(\lambda)/I_0(\lambda) = \exp(-\tau(\lambda)L) \qquad (1)$$

The intensity and pathlength data I, I_0, and L are used to calculate instantaneous extinction coefficients at each wavelength, $\tau(\lambda)$, which are then averaged. Results at each of two wavelengths give two independent values for the extinction coefficient, τ. These two values are used to find the two parameters in the size distribution, $N(r)$, as explained below. Physically, one would not expect τ to be homogeneously distributed along the pathlength. Thus, it is the average extinction coefficient and average soot volume fraction, along a line of sight which is actually obtained here. From the viewpoint of calculating flame radiation, these averages are precisely the information required.

The extinction coefficient is related to the extinction efficiency, $Q(\lambda, m, r)$, of each individual particle of radius r, and to the particle concentration, $N(r)dr$, by

$$\tau(\lambda, m, r) = \int_0^\infty N(r)Q(\lambda, m, r)\pi r^2 dr. \qquad (2)$$

If spherical particles are assumed, then $Q(\lambda, m, r)$ is well known from Mie scattering theory [10, 19, 20]. A randomly oriented aerosol of chain-like particles, which is probably the situation in turbulent buoyant plumes above pool fires, is not expected to give transmission measurements significantly different from a spherical particle aerosol [10, 21].

Size Distribution. No previous in situ carbon particulate detailed size distribution measurements in diffusion flames are known. Most studies use a monodisperse particulate [4, 7, 9, 22]. Size measurements in premixed flames [23] and previous studies here [10] suggest a Gamma distribution [24] with the constraint of a specified ratio of standard deviation to mean particle radius, $\sigma/r_m = 1/2$, as a reasonable functional form. In terms of the most probable radius, $r_{\max}$, and the total particle concentration, N_0, the distribution form is

$$N(r)/N_0 = (27r^3/2r_{\max}^4)\exp(-3r/r_{\max}) \qquad (3)$$

Note this is a general two parameter distribution. For each fuel, the two extinction coefficients independently measured at separate wavelengths provide two equations for the two unknown size distribution parameters, N_0 and $r_{\max}$.

The soot volume fraction is

$$f_v \equiv \frac{4}{3}\pi \int_0^\infty N(r)r^3 dr. \qquad (4)$$

Substituting equation (3) into equation (4) yields

$$f_v = \frac{54\pi}{38}\Gamma(7)N_0 r_{\max}^3 \approx 18.62\ N_0 r_{\max}^3 \qquad (5)$$

The width choosen for the distribution does not strongly affect f_v. For example, choosing $\sigma/r_m = 1/5$ instead of 1/2 would cause only ~15 percent change in f_v [21].

Normalized Extinction Coefficient Ratio. The Mie theory extinction coefficient [10, 19, 20] and the size distribution of equation (3) are substituted into equation (5) which is then integrated numerically. The result is shown in Fig. 2 in terms of a nondimensional extinction coefficient,

$$\tau'(\alpha_{\max}, \lambda, m) = \tau/N_0 r_{\max}^2, \qquad (6)$$

Nomenclature

c_0 = speed of propagation of electromagnetic radiation in vacuum
c_2 = Planck's second radiation constant, 1.4388 cm K
f_v = carbon particulate volume/flame volume
$F(\lambda)$ = optical properties function
H_b = height above fuel surface
I = radiant intensity
K = Boltzmann constant
L = mean beam length or length
m = complex index of refraction
n = real index of refraction
nk = imaginary index of refraction
N = particle concentration
Q = extinction efficiency
r = particle radius
s = experimental standard deviation
T = temperature
$\alpha = 2\pi r/\lambda$
ϵ = emissivity
κ = soot emission parameter
λ = wavelength
τ = extinction coefficient
χ_{ij} = normalized extinction coefficient ratio, equation (9)

Subscript

a = absorption
b = beam
fl = flame
i = first wavelength
j = second wavelength
m = mean
max = most probable

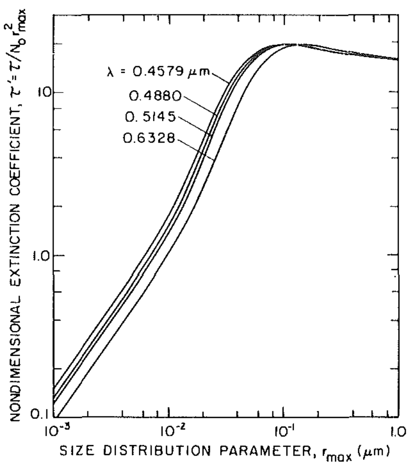

XBL 805-5143

Fig. 2 Nondimensional extinction coefficient, $\tau' = \tau/N_0\, r_{max}^2$, versus the most probable particle radius, parameterized in wavelength, with the soot optical properties listed in Table 1

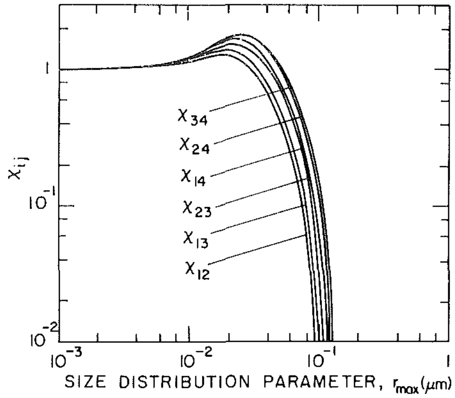

XBL 805-5140

Fig. 3 Normalized extinction coefficient ratio, $\chi_{ij} = [\tau_i/\tau_j - 1]/[\tau_i/\tau_j - 1]_{abs}$, versus the most probable particle radius with $\lambda_1 = 0.4579$ μm, $\lambda_2 = 0.4880$ μm, $\lambda_3 = 0.5145$ μm, and $\lambda_4 = 0.6328$ μm, using the soot optical properties of reference [18] listed in Table 1

Table 2 Measured extinction coefficients, τ_i, and extinction coefficient ratios, τ_i/τ_j, with their experimental standard deviations, s

	Fuel length L_o cm	Beam ht. H_b cm	Wave-length^a i	τ_i cm^{-1}	Experimental Standard Deviation $s\tau_i$ cm^{-1}	Wave-length Pair^a i- j	τ_i/τ_j	Experimental Standard Deviation $s\tau_i/\tau_j$
Solids								
Polystyrene	7.5	2	1	0.60	0.034	1- 3	1.15^b	0.08^b
$(C_8H_8)_n$				0.52	0.028	1- 4	1.50^b	0.12^b
				0.40	0.044	3- 4	1.30^b	0.16^b
Wood, ASTM Class B	15.0	4	1	0.044	0.012	1- 4	2.00	0.26
Fire Brand, (CH_2O)			4	0.023	0.007			
Polypropylene	7.5	2	1	0.036	0.010	2- 4	1.71	0.29
$(C_3H_6)_n$			2	0.0355	0.009	3- 4	1.53	0.30
			3	0.032	0.008	1- 2	1.01^b	0.42^b
			4	0.021	0.005	1- 3	1.13^b	0.43^b
						1- 4	1.71^b	0.63^b
						2- 3	1.11^b	0.40^b
Polymethylmethacrylate	7.5	2	1	0.040	0.007	1- 3	1.18^b	0.33^b
$(C_5H_8O_2)_n$, PMMA			3	0.034	0.010	1- 4	1.54^b	0.23^b
			4	0.026	0.004	3- 4	1.29^b	0.32^b
Foams								
Polystyrene, GM-48	15.0	2	1	0.594	0.060	1- 3	1.03^b	0.11^b
$(C_8H_8)_n$			3	0.576	0.027	1- 4	1.28	0.10
			4	0.464	0.040	3- 4	1.24^b	0.10^b
Polyurethane, Mattress	15.0	2	1	0.097	0.009	1- 3	1.12	0.13
$(C_{3.2}H_{5.3}ON_{0.23})_n$			3	0.087	0.008	1- 4	1.43	0.11
			4	0.068	0.004	3- 4	1.28	0.11
Polyurethane, GM-21	15.0	2	2	0.083	0.020	2- 4	1.36	0.19
$(C_{3.4}H_{6.1}ON_{0.16})_n$			4	0.061	0.015			
Liquids								
Iso Octane	15.0	4	1	0.083	0.004	1- 3	1.15^b	0.06^b
(C_8H_{18})			3	0.072	0.003	1- 4	1.51^b	0.09^b
			4	0.055	0.004	3- 4	1.31^b	0.08^b
Acetone	15.0	4	2	0.017	0.004	2- 4	1.54	0.32
(C_3H_6O)			3	0.016	0.004	3- 4	1.46	0.16
			4	0.011	0.003	2- 3	1.05	0.36
Alcohol	15.0	4	2	0.010	0.002	2- 4	1.73	0.30
(C_2H_6O)			3	0.009	0.002	3- 4	1.50	0.18
			4	0.006	0.001	2- 3	1.15	0.34

a = i refers to λ_i (λ_1 = 0.4579 μm, λ_2 = 0.4880 μm, λ_3 = 0.5145 μm, λ_4 = 0.6328 μm).

b = computed with separate paths for each wavelength.

for the four wavelengths used in the experiment. The parameter $\alpha = 2\pi r/\lambda$ describes the interaction of radiation at wavelength λ with a particle of radius r. In the small particle absorption limit, $\alpha \ll 1$, τ is independent of the size distribution and the ratio of two different wavelength τ's becomes

$$[\tau_i/\tau_{j\ \text{absorption}} = \lambda_j F_a(\lambda_i)/\lambda_i F_a(\lambda_j), \tag{7}$$

where the optical properties information is all contained in

$$F_a(\lambda) = \frac{n^2 k}{[n^2 - (nk)^2 + 2]^2 + 4n^4k^2}. \tag{8}$$

In the large particle limit, $\alpha \gg 1$, $Q \rightarrow 2$ and $\tau_i/\tau_j \rightarrow 1$. Thus, the normalized extinction coefficient ratio [10],

$$\chi_{ij} = [\tau_i/\tau_j - 1]/[\tau_i/\tau_j - 1]_{\text{absorption}}, \tag{9}$$

is adopted as being most convenient for extracting size distribution information from experimental extinction coefficients. Figure 3 shows χ_{ij} as a function of most probable radius, $r_{\max}$, for the six different possible wavelength combinations used here.

Using the measured τ_i and τ_j's, the experimental χ_{ij} is obtained from equations (1, 7, 8, and 9). The experimental χ_{ij} is used to extract $r_{\max}$ from Fig. 3. Note that since the τ's were superimposed, $r_{\max}$ is known independent from L, thereby eliminating a large source of possible error (~10 percent). τ' is then determined from $r_{\max}$ and Fig. 2. N_0 is obtained from equation (6) and one of the experimental extinction coefficients. Knowing $r_{\max}$ and N_0 gives f_v from equation (5). Note that since L must be known to obtain τ, the error in measurement of L does affect the accuracy of N_0 and f_v.

Results

Experimental Summary. Table 2 presents the measured extinction coefficients and extinction coefficient ratios at several wavelengths for the ten fuels examined. The sample diameter or length in the beam direction, L_0, and laser beam height above each fuel surface, H_b, is also given. The GM designation refers to the well described [25] Products Research Committee cellular plastics material bank. More than one wavelength pair was run when it was necessary to isolate the correct $r_{\max}$ in the double valued region of the χ_{ij} versus $r_{\max}$ curves. The experimental standard deviations are shown, calculated from $\gtrsim$100 data points for each fuel. Table 2 thus gives the useful raw data needed in the multiwavelength technique.

Table 3 applies the data in Table 2 and shows the resulting calculatons of χ_{ij}, the most probable radius, the total particle concentration and the soot volume fraction obtained from each wavelength pair run for every fuel. Table 3 demonstrates the consistency of the results among different wavelength pairs run for each fuel. No common pathlength experimental value lies above the theoretical limit for χ_{ij}. This is in contrast to the reference [10] results based on the soot optical properties of Dalzell and Sarofim [13] (see Table 3 of reference [18]). The I/I_0 and L data from separate single wavelength experiments previously reported [10] are reinterpreted using Table 1 and are included in Table 3 for comparison with the new common pathlength multiwavelength data for polystyrene foam, polypropylene, acetone and alcohol. The discrepency between the seperate pathlength and common pathlength experiments for polypropylene is due to the low laser light attenuation in this relatively clean flame. The new simultaneous wavelength pair results, which contain less error from pathlength uncertainty, agree very well for different wavelength combinations. The separate pathlength polystyrene foam results are quite compatible with the new common path values, but only the more accurate simultaneous multiwavelength data are included in averages reported for these fuels in Table 4. Note the consistency of the f_v values among different, common path wavelength pairs for all fuels.

Of the fuels which reside in the double valued region of Fig. 3 (i.e., $\chi_{ij} \gtrsim 1$), all except acetone and alcohol lie in the single valued region for at least one alternate wavelength pair. The correct $r_{\max}$ for the double valued case is chosen as closest to the single valued result. For acetone and alcohol, the correct $r_{\max}$ is resolved as previously described [10], i.e., by choosing that $r_{\max}$ of the double value which is most common among the results from different wavelength pairs.

Table 3 Experimental flame soot volume fractions and size distributions from multiwavelength experiments

	Wave-length Pair[a] i–j	χ_{ij}	$r_{\max}$ $\times 10^2$ μm	$N_0 X$ 10^{-9} cm^{-3}	$f_v \times 10^6$
Solids					
Polystyrene	1–3	0.647[b]	4.4	2.1	3.3
	1–4	0.864[b]	4.7	1.7	3.3
	3–4	1.08[b]	5.0	1.4	3.3
Wood	1–4	1.72	2.3	1.3	0.29
Polypropylene	2–4	1.82	2.4	1.0	0.27
	3–4	1.88	2.5	0.90	0.26
	1–4	1.23[b]	3.7	0.21	0.20
Polymethyl-methacrylate	1–3	0.758[b]	4.0	0.18	0.22
	1–4	0.928[b]	4.5	0.13	0.22
	3–4	1.09[b]	5.0	0.09	0.23
Foams					
Polystyrene, GM-48	1–3	0.231[b]	6.6	0.75	4.0
	1–4	0.486	6.2	0.85	3.8
	3–4	0.851[b]	5.7	1.1	3.8
Polyurethane	1–3	0.494[b]	5.0	0.24	0.55
	1–4	0.735[b]	5.2	0.21	0.56
	3–4	0.991[b]	5.3	0.20	0.56
Polyurethane, GM-21	2–4	0.938	5.2	0.19	0.51
Liquids					
Iso Octane	1–3	0.656[b]	4.4	0.29	0.46
	1–4	0.877[b]	4.7	0.24	0.46
	3–4	1.10[b]	4.9	0.21	0.46
Acetone	2–4	1.40	3.9	0.09	0.10
	3–4	1.62	3.5	0.14	0.11
Alcohol	2–4	1.87	2.4	0.30	0.077
	3–4	1.77	3.0	0.13	0.065

[a] i refers to same λ_i as Table 2.
[b] computed with separate paths for each wavelength.

Table 4 Summary of soot volume fractions and size distributions

Fuel	$r_{\max}$ $\times 10^2$ μm	$N_0 \times$ 10^{-9} cm^{-3}	$f_v \times$ 10^6	percent carbon converted to soot
Solids				
Polystyrene	4.7	1.7	3.3	15.
Wood	2.3	1.3	0.29	1.4
Polypropylene	2.5	0.93	0.27	0.7
Polymethylmethacrylate	4.5	0.13	0.22	1.2
Foams				
Polystyrene, GM-48	6.2	0.85	3.8	15.
Polyurethane	5.2	0.21	0.56	3.1
Polyurethane, GM-21	5.2	0.19	0.51	3.1
Liquids				
Iso Octane	4.7	0.24	0.46	3.1
Acetone	3.7	0.12	0.11	0.7
Alcohol	2.7	0.19	0.071	0.5

Discussion

The averages over the wavelength pair results for each fuel in Table 3 are summarized in Table 4. The primary output of this study are the soot volume fractions in the fourth column for the fuels in the first column. The most probable radius and total particle concentration obtained from the multiwavelength technique are listed in the second and third columns, respectively. This table replaces previously reported results [10]. The volume fraction ranking within each fuel type

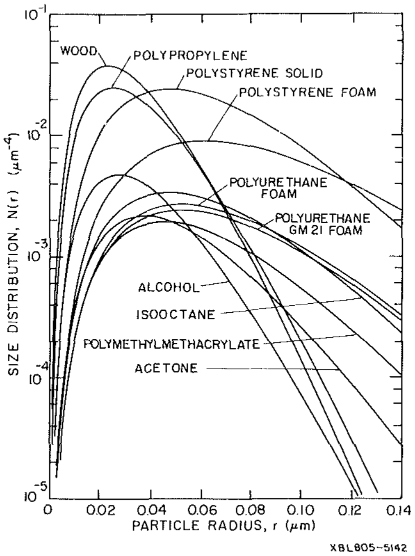

Fig. 4 Approximate particulate size distribution, *N*(*r*), versus particle radius for several fuels

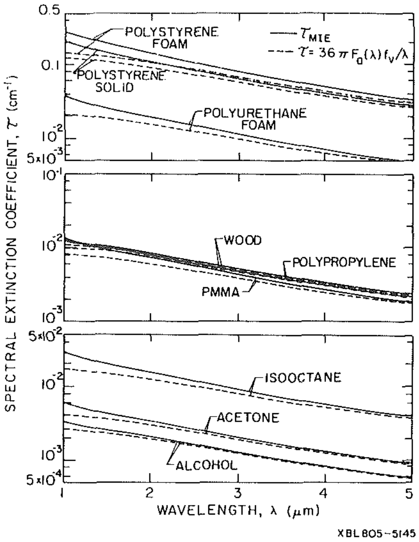

Fig. 5 Mie theory and Rayleigh small particle limit extinction coefficient as a function of wavelength with the particulate size distributions and soot volume fractions in Table 4

remains unchanged and is consistent with observations of flame luminosity and smokiness. The newly tested wood sample has an f_v and $r_{\max}$ very close to that of polypropylene. A detailed uncertainty analysis shows that the experimental error in f_v is ± ~10 percent [24, 21].

In the final column of Table 4 are estimates of the fraction of fuel carbon converted to soot (see reference [21] for calculation details). A large fraction of the carbon in polystyrene, ~15 percent, is converted to soot. The respective values for polyurethane and isooctane are ~3 percent and the remaining fuels result in $\lesssim$0(1 percent) fuel carbon conversion to solid particulate. There is reasonable agreement with de Ris [1] who estimated carbon to soot conversion of 18 percent for polystyrene, 1.9 percent for PMMA and 5.5 percent for polypropylene, with a high uncertainty in the latter value. Good quantitative agreement is obtained with the infrared transmittance and radiance results reported by Buckius and Tien [12] when the more accurate Lee and Tien [18] optical properties are used. Agreement is also achieved with Markstein's soot volume fractions [11] if the larger size of his flames is taken into account. This scaling effect is addressed in a seperate experiment performed here and the results are reported elsewhere [26].

Figure 4 shows detailed size distributions given by equation (3), using the experimentally measured parameters in Table 4 for the ten fuels considered. Note that the semi-log plot broadens the actually rather narrow distributions. No fuel was observed to have average particle sizes within the Rayleigh absorption limit for visible radiation. The most probable particle radii are generally twice as large as those calculated in reference [10] due to using the revised optical properties in Table 1 instead of the usually [8–12] assumed refractive index from reference [13]. Only the anamolous foam polystyrene $r_{\max}$ has not been substantially altered. The foam samples interestingly have the largest $r_{\max}$, with the two polyurethanes not found to be significantly different.

Infrared Extinction Coefficient. The ability to predict flame radiation from the soot volume fraction results is of primary interest here. In most flames of practical scale soot emission dominates gas species emission [27]. The nongray soot emissivity can often be represented [28] within 10 percent by the simple gray expression,

$$\epsilon = 1 - \exp(-\kappa L) \tag{10}$$

where L is the pathlength or mean beam length and κ is the absorption coefficient or soot emission parameter, defined as

$$\kappa = \tau(\bar{\lambda}) = 36\pi F_a(\bar{\lambda}) f_v/\bar{\lambda} \tag{11}$$

$$\bar{\lambda} T_{fl} \cong c_2/3.6 = 0.40 \text{ cm K} \tag{12}$$

T_{fl} is an equivalent homogeneous flame temperature and $c_2 = hc_0/k = 1.44$ cm-K is Planck's second constant.

The derivation of equation (10) is based on an empirical fit to the Rayleigh limit nongray emissivity [28, 27] which assumes that the spectral extinction coefficient varies as $1/\lambda$ [1, 27, 29]. This is valid as long as $\alpha \ll 1$ in the infrared spectral region where most of the flame emission occurs. The Mie theory spectral extinction coefficient based on equation (2), the experimental size distributions, and f_v for each fuel, is compared in Fig. 5 to the small particle limit extinction coefficient approximation of equation (11). Only the foam mattrees result is shown for the two polyurethanes since they are so similar. For fuels with $r_{\max} \lesssim 0.04$ μm, the approximation is reasonable from $\lambda = 2$ μm to $\lambda = 3$ μm, where the flame emission spectra peak. The approximation underpredicts the Mie theory τ by ~20 percent for polystyrene foam, by ~15 percent for polyurethane foam, and by $\lesssim$0 (10 percent) for the remaining fuels. However, the effect of this error on the flame emissivity may be small. For polystyrene foam with a pathlength of 30 cm and a soot emission temperature of 1200 K, equations (10) and (11) give a soot absorption-emission coefficient of $\kappa = 0.05$ cm^{-1} and a soot emissivity of $\epsilon = 0.78$. If actually $\kappa = 0.06$ cm^{-1} (20 percent higher) then $\epsilon = 0.83$, i.e., a 20 percent underestimate of κ causes only ~6 percent underestimate of ϵ. Because emissivity determines flame emission, it is significant that propagation of soot emission coefficient error into ϵ is small. It is also important to note that the Mie theory τ is dependent on the size distribution. If the actual size distribution differed, and was narrower than the assumed form in equation (3), then the Mie theory τ would be closer to the approximate τ. The volume fraction results are not strongly dependent on the assumed form of the size distribution and use of the approximate expression for τ, which depends on f_v and not on the size distribution, may be even more accurate than it seems from Fig. 5. Within the assumptions and experimental uncertainties, it is reasonable for typical engineering applications to consider all the fuels examined here to generate soot particles which are within the small particle absorption limit for infrared flame radiation calculations and thus permit use of equations (10–11).

Conclusions

Table 4 presents carbon particulate volume fractions of $0(10^{-6})$ and approximate size distributions measured in situ for ten common solid, cellular, and liquid fueled, small scale buoyant diffusion flames. A multiwavelength laser transmission technique [10] has been refined so that beams of two wavelengths from seperate lasers now occupy the same physical path through the flames, thereby reducing experimental errors.

The analysis uses the soot optical properties obtained by Lee and

Tien [18] (see Table 1). They were determined from a rigorous consideration of electron band structure and the dispersion constants, in conjunction with independent transmission measurements at visible [10] and infrared [12] wavelengths, and are thus considered to be representative of actual flame soot. These soot refractive indices are shown here to yield theoretical extinction coefficient ratios as large as experimental values and give consistent results for different wavelength pairs for each fuel. This is in contrast to previous results based on the usually assumed [3, 8, 10, 12] soot refractive indices measured by Dalzell and Sarofim [13] in collected and compressed soot samples.

Polystyrene flames have the largest soot volume fraction ($f_v \sim 3.5 \times 10^{-6}$) and the largest estimate of fuel carbon converted to soot ($\sim$15 percent). The cellular foam fuels, polystyrene and two polyurethanes, are observed to have the largest size particles of all the fuels studies ($r_{\max}$ = 62 nm and 52 nm, respectively). The ranked order of the f_v values is consistent with observed flame luminosity and is in agreement with literature data [11, 12], including results obtained here previously [10]. However, due to use of the new optical properties of Table 1, the values for most probable particulate radii have increased at least twofold and the soot volume fractions have decreased significantly from the original results [10] for all the fuels except the foam polystyrene.

Finally, the mean particle sizes obtained for all fuels indicate that the small particle absorption limit assumption may cause only slight underestimates ($\lesssim$20 percent for polystyrene, $\lesssim$15 percent for polyurethane, and $\lesssim$0 (10 percent) for the remaining fuels) of infrared flame absorption-emission coefficients, but is a reasonable approximaton for flame radiation calculations.

Acknowledgment

The authors are grateful for support from the Center for Fire Research of the National Bureau of Standards.

References

1 de Ris, J., "Fire Radiation—A Review," *Seventeenth Symposium (International) on Combustion.*, The Combustion Institute, 1979, pp. 1003–1016.

2 Erickson , W. D., Williams, G. C., and Hottel, H. C., "Light Scattering Measurements on Soot in a Benzene-Air Flame," *Combustion and Flame*, Vol. 8, 1964, p. 127.

3 Dalzell, W. H., Williams, G. C., and Hottel, H. C., *Combustion and Flame*, Vol. 14, 1970, p. 161.

4 Kunugi, M., and Jinno, J., "Determination of Size and Concentration of Particles in Diffusion Flames by a Light Scattering Technique," *Eleventh Symposium (International) on Combustion*, The Combustion Institute, 1967, pp. 257.

5 Mori, Y., and Makino, K., *Bulletin of JSME*, Vol. 12, 1951, p. 1448.

6 D'Alessio, A., Beretta, F., and Venitozzi, C., *Combustion Science and Technology*, Vol. 5, 1972, p. 263.

7 D'Alessio, A., Di Lorenzo, A., Sarofim, A. F., Beretta, F., Masi, S., and Venitozzi, C., "Soot Formation in Methane-Oxygen Flames," *Fifteenth Symposium (International) on Combustion*, The Combustion Institute, 1974, p. 1427.

8 Muller-Dethlefs, K., "Optical Studies of Soot Formation and the Addition of Organic Peroxides to Flames," Ph.D. Dissertation, Dept. of Chemical Engineering and Chemical Technology, Imperial College, London, 1979.

9 Kent, J. H., and Wagner, H. G., "Soot Formation in a Laminar Diffusion Flame," presented at the *Eighteenth Symposium (International) on Combustion*, Ontario, Canada, August 1980.

10 Pagni, P. J., and Bard, S., "Particulate Volume Fractions in Diffusion Flames," *Seventeenth Symposium (International) on Combustion*, The Combustion Institute, 1970, pp. 1017–1028.

11 Markstein, G. H., "Radiative Properties of Plastic Fires," *Seventeenth Symposium (International) on Combustion*, The Combustion Institute, 1979, p. 1053.

12 Buckius, R. O. and Tien, C. L., *International Journal of Heat Mass Transfer*, Vol. 20, 1977, p. 93.

13 Dalzell, W. H., and Sarofim, A. F., ASME JOURNAL OF HEAT TRANSFER, Vol. 91, 1969, p. 100.

14 Medalia, A. I. and Richards, L. W., *Journal Colloid Interface Science*, Vol. 40, 1972, p. 233.

15 Graham, S. C., *Combustion Science and Technology*, Vol. 9, 1974, p. 159.

16 Chippet, S., and Gray, W. A., *Combustion and Flame*, Vol. 31, 1978, p. 149.

17 Bard, S. and Pagni, P. J., "Comparison of Laser Induced Fluorescence and Scattering in Pool Fire Diffusion Flames," *Journal of Quantative Spectroscopy Radiative Transfer*, in press, 1980.

18 Lee, S. C. and Tien, C. L., "Optical Constants of Soot in Hydrocarbon Flames," presented at the *Eighteenth Symposium (International) on Combustion*, Ontario, Canada, August 1980.

19 Mie, G., *Ann. Physik*, Series 4, 25, 377, 1908.

20 Kerker, M., *The Scattering of Light and Other Electromagnetic Radiation*, Academic Press, New York, 1969.

21 Bard, S., "Diffusion Flame Particulate Volume Fractions," Ph.D. Dissertation, Dept. of Mechanical Engineering, University of California, Berkeley, 1980.

22 Haynes, B. S., Jander, H., and Wagner, H. Gg., "Optical Studies of Soot-Formation Processes in Premixed Flames," presented at the *Eighteenth Symposium (International) on Combustion*, Ontario, Canada, August 1980.

23 Wersborg, B. L., Howard, J. B., and Williams, G. L., *Fourteenth Symposium (International) on Combustion*, The Combustion Institute, 1973, p. 929.

24 Hahn, G. H., and Shapiro, S. S., *Statistical Models in Engineering*, John Wiley and Sons, New York 1968.

25 Tewarson, A., and Pon, R. F., "A Laboratory-Scale Test Method for the Measurement of Flammability Parameters," FMRC Serial No. 22524 Report, Factory Mutual Research Corp., Norwood, Ma., Oct. 1977.

26 Bard, S., and Pagni, P. J., "Spatial Variation of Soot Volume Fractions in Pool Fire Diffusion Flames," *Combustion and Flame*, in press, 1980.

27 Felske, J. D., and Tien, C. L., *Combustion Science and Technology*, Vol. 7, 1973, p. 25.

28 Yuen, W. W., and Tien, C. L., *Sixteenth Symposium (International) on Combustion*, The Combustion Institute, 1974, p. 1481.

29 Hottel, H. C., and Sarofim, A. F., *Radiative Transfer*, McGraw-Hill Book, New York, 1967.

Ice Formation in a Pipe Containing Flows in the Transition and Turbulent Regimes

R. R. Gilpin
Department of Mechanical Engineering,
University of Alberta,
Edmonton, Alberta, Canada

The form of the ice growth that occurs in a pipe containing flows which are initially in the transition and turbulent regimes was investigated. The ice-band structure reported previously [1] for Reynolds numbers near transition was observed to be of steady state ice structure formed in a pipe for flows with Reynolds numbers over the entire range of the present investigation (up to $Re_D = 1.4 \times 10^4$). Difference were, however, observed in the nature of the transient approach to this steady state ice structure. The influence of the ice-band structure on pressure drop and on pipe freeze-off were also investigated.

Introduction

In reference [1] a study was reported of visual observations of the form of the ice growth in a pipe containing a flow near transition Reynolds numbers. For the entire range of the Reynolds numbers that could be obtained in that experiment (370 to 3025) it was observed that the final steady-state ice profile did not produce a uniformly tapered flow passage as has been predicted by most previous theories [2–4]. Instead, a flow passage with a dramatic cyclic variation in cross-section along the length of the pipe was observed. This ice structure was called an 'ice-band' structure. In this paper the morphology of the ice bands is studied over a larger range of parameters and the results are related to freeze-off conditions in a pipe.

Experiment

Visual observations of the ice forming in a pipe were made possible by the apparatus shown in Fig. 1. Test section of this apparatus was constructed of two concentric glass tubes surrounded by a square acrylic plastic box. The water in which freezing occurred was pumped through the center tube which had a 33 mm i.d. was 1.5 m long and had a 1 mm wall thickness. The coolant (methonal and water) was circulated at high velocity through a 3 mm wide annulus between the two tubes. The outer box was filled with ethylene glycol-water mixture and was intended to minimize the optical distortion caused by the curved walls of the glass pipes. To minimize the additional complications caused by secondary free convection at low velocity flows the tests reported in this paper were conducted with the pipe in the vertical position.

In the present experiment Reynolds numbers (based on pipe i.d.) up to 1.4×10^4 could be obtained. To obtain a significant amount of ice formation in the pipe at this Reynolds number coolant temperatures, T_c, as low as $-10°C$ and inlet water temperatures, T_w, as low as 0.3°C had to be used. This combination of temperatures gave the maximum value of the freezing parameter, $\theta = (T_f - T_c)/(T_w - T_f)$ which was used ($\theta_{\max} = 30$). Because of the high flow velocities and the relatively short length of the test section temperatures drops that occurred along the length of the water pipe and the coolant channels were small and the variation in θ between the inlet and outlet were usually less than 20 percent.

It should be noted that the experimental configuration described does not produce a constant wall temperature condition for the freezing pipe. The thermal resistance of the glass wall of the inner pipe plus the convective resistance between the pipe and the coolant fluid is equivalent to an overall heat transfer coefficient of about 300 W/(m^2 × °C) or a Biot number

$$\mathrm{Bi} = \frac{h_{\mathrm{eff}} D}{2\, k_i} = 2.5.$$

The fact that a convective boundary condition exists makes the theoretical prediction of the ice profile shape more difficult; however, it is closer to a situation of more practical interest than a constant wall temperature condition would be.

Observations on the Transient and Steady-State Ice Morphology in a Pipe

It was found that the nature of the transient development of ice structure in a pipe depends on whether a laminar or turbulent flow existed in the pipe prior to ice nucleation. In the case of a laminar initial flow the photographs in Fig. 2 show the sequence of development that was normally observed. In these photographs the dark horizontal lines are the flow passages in the center pipe at various times. The water was colored with a small amount of dye to make it distinguishable from the ice.

At $t = 0$ ice growth was initiated. In reference [5] the normal ice nucleation temperature for quiescent tap water was found to be in the range −5 to −7°C. The flowing water in the present experiment was found not to nucleate until the pipe wall was cooled to below −3 to −4°C. To initiate ice growth it was sometimes necessary to momentarily lower the coolant temperature or introduce a nucleant such as silver iodide into the water stream. After ice nucleates and up until $t = 2$ hrs. The ice growth proceeds as would be expected. The water passage formed tapers uniformly from inlet to exist. At $t = 2$ hrs. this ice profile appears to have reached almost a "steady state" as the diameter of the flow passage at the exit is changing only very slowly with time. Continued observation of this ice profile shows, however, that

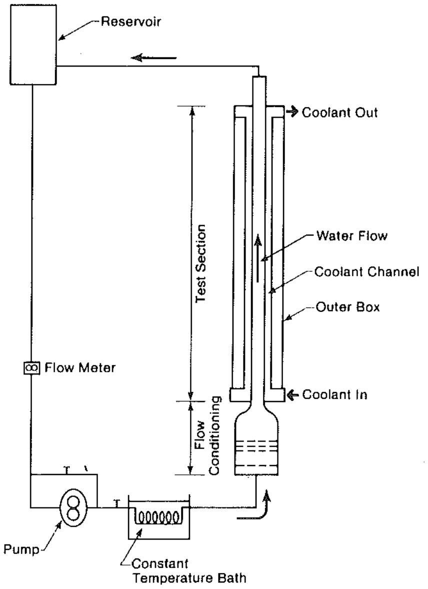

Fig. 1 Apparatus for observing ice growth in a pipe

Contributed by the Heat Transfer for publication in the JOURNAL OF HEAT TRANSFER. Manuscript received at ASME Headquarters September 8, 1980.

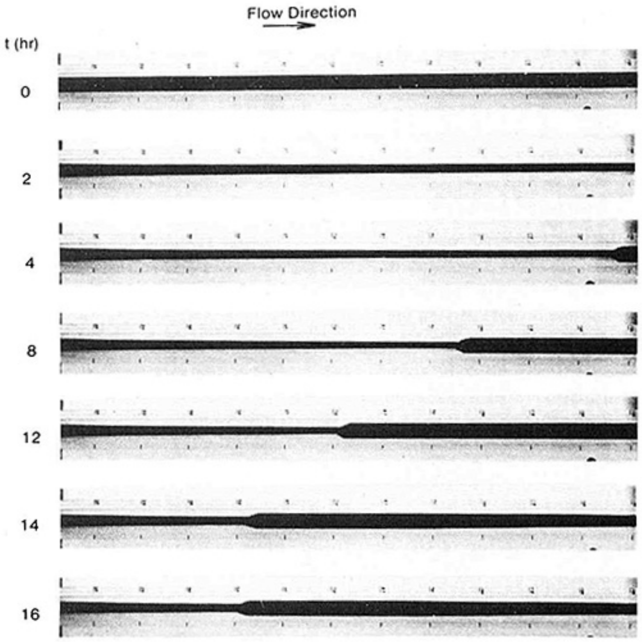

Fig. 2 **Transient development of the ice structure in a pipe when the initial flow is laminar. $\theta = 2.6$, $Re_D = 3025$**

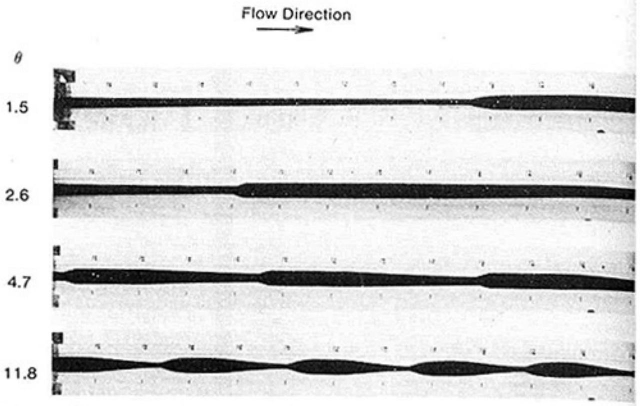

Fig. 3 **Steady-state ice profiles for successively lower temperatures (that is larger values of θ). $Re_D = 3025$**

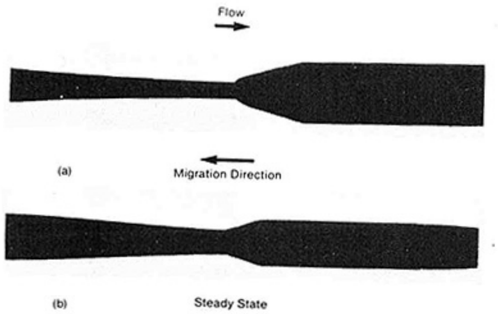

Fig. 4 **Shapes of the expansion section of an ice band (*a*) for a separation point migrating upstream (*b*) for a separation point at its equilibrium position**

this is not the ultimate steady state. Near the exit of the cooling section a sharp expansion of the flow passage forms (t = 4 hrs.). The position of this expansion point then migrates slowly upstream (t = 4 to 14 hrs.). Downstream of this sharp change in cross-section of the flow passage the ice is completely melted away. As the first expansion migrates further upstream a new ice growth may form, provided nucleation occurs, near the pipe exit. In Fig. 2 the second ice growth nucleated at t = 14 hrs. As time proceeds the sequence of events described results in the development of a series of ice-bands interspersed with ice-free zones. Each point at which an expansion occurs migrates upstream until it reaches some equilibrium point at which time further changes in the ice morphology cease. This is considered to be the ultimate steady state ice growth for the given conditions of temperature and flow. For the conditions in Fig. 2 this steady state has only one expansion point located at 45 cm from the inlet (t = 16 hrs.).

Decreasing the temperatures of the coolant or water flows, that is increasing the temperature ratio, causes an increase in the number of cycles of expansion and contraction of the flow passage along the length of the test section. Figure 3 shows the sequence of development that results if the temperatures are lowered in incremental steps and after each step change in temperature the ice structure is allowed to develop to its new steady state. For the lowest temperatures used here for which $\theta = 11.8$ there are 6 cycles of expansion and contraction of the flow passage along the length of the test section.

There are two criterion necessary for the development of the ice profiles seen in Figs. 2 and 3. First, the monotonically thickening ice layer seen at t = 1 hr in Fig. 2 is unstable with respect to large disturbances. If the flow passage undergoes a rapid expansion at some point a flow separation will result generating a region of intense turbulence downstream. This turbulence results in a greatly enhanced heat transfer rate from the water to the ice thus insuring that once produced the large disturbance is self-perpetuating. In the present study this large disturbance was automatically supplied by the expansion of the flow passage at the exit from the cooled section of pipe. In some tests, however, a disturbance was produced by introducing a partial blockage of the pipe part way along the test section. This obstruction produced a series of disturbances which also migrated upstream with the result that the ultimate steady state profile was the same as that observed in Fig. 3.

The second important feature of these disturbances is their upstream migration. This appears to occur because the turbulent heat transfer downstream of the separation point melts away the ice on the downstream face of the ice-band. Figure 4 shows the typical shapes of two ice bands—one for which the conditions are such that the separation point is migrating upstream and one for which the separation point is at its ultimate steady-state position. For each case, a close examination of the ice surface reveals that a distinct line, that is a change in slope of the ice layer, exists near the position of the minimum low passage diameter. This line indicates the position of the flow separation on the ice surface. For a separation point that was migrating the change in slope at the separation point was near to 90 deg, that is the ice was being "under-cut." At the steady-state condition the ice surface downstream of the separation point formed a

Nomenclature

Bi = Biot number
C = pressure loss coefficient
d = minimum diameter of flow passage (neck diameter) at an ice-band
D = diameter of pipe (i.d.)
f = effective friction factor of a pipe containing ice-bands
G = ice growth parameter
h_{eff} = overall heat transfer coefficient between inside wall of pipe and coolant fluid
k_i = thermal conductivity of ice
K = flow acceleration parameter
n = number of ice-bands in the pipe
Re_D = Reynolds number based on inside diameter of pipe
S = spacing between ice-bands
t = time
T_c, T_f, T_w = temperatures of the coolant, freezing point, and the water
v = mean velocity of water in flow passage
v_0 = mean velocity of water in pipe without ice
x = distance along pipe
ν = kinematic viscosity of water
δ = ratio d/D
ρ = density of water
θ = cooling temperature ratio $(T_f - T_c)/(T_w - T_f)$

smooth cone with an expansion angle of approximately 20 to 30 deg.

The changes in geometry of the ice at the separation point are caused by the fact that as it migrates upstream it is passing into regions of thinner ice layer and thus a stronger temperature gradient. This means that for a given change in heat transfer coefficient caused by the separation point a smaller change in ice thickness results. Presumably then upstream migrate stops when a local heat balance can be achieved at all points on the ice surface as in Fig. 4(*b*).

It should be pointed out that it is the development of flow separation points that can migrate upstream that is the physical aspect of the problem not considered in most theories. These theories assume that the flow passage cross-section varies slowly with position along the pipe. The equations developed are then parabolic and thus do not allow for any upstream migration of disturbances.

The behavior of the separation points in a pipe is very similar to the behavior of the laminar to turbulent transition observed during ice growth on a flat plate [6]. In that study it was found that the flow transition on an ice layer could occur by a step change in the ice thickness with an associated flow separation. When a flow separation occurred the step in the ice layer thickness migrated upstream to a point where the Reynolds number was as much as an order of magnitude less than the Reynolds number normally associated with transition on a flat plate. This is consistent with the observation in reference [1] that the ice-band structure could occur in the test section for Reynolds number down to the lowest value tested, that is 370.

At high Reynolds numbers where the initial flow in the pipe was turbulent transient development of the ice structure was quite different. Figure 5 shows the sequence of ice profile development for a Reynolds number, $\mathrm{Re}_D = 9100$. In this case the ice bands and their associated separation points develop along the length of the pipe. Each band appears to grow spontaneously from very small undulations in the flow passage diameter to its final steady-state size. The initial spacing of the bands appears to be quite irregular (times 2 hours and less in Fig. 5). It is not until the fully developed, steady-state is approached that the regular spacing appears. In general the initial spacing was greater than that in the steady state thus the number of bands increased with time. Occasionally, however, when two of the initial separation points were very close together one may disappear during the transient period. In Fig. 5 it can be seen that the third separation from the left very nearly disappears at about $t = 1{:}30$.

Even though the transient growth phase is quite different the final steady state ice-band structure is very similar in form to that observed at lower Reynolds' numbers. This is perhaps not unreasonable since once the ice-band structure had developed the original Reynolds' number based on the inside diameter of the pipe may lose much of its significance. This would be so because separated flows such as those that occur downstream from each ice-band are generally found to be largely Reynolds' number independent and also in the ice-band necks themselves the flow experiences rapid accelerations so that the Reynolds' number based on flow passage diameter may vary by an order of magnitude over one ice-band.

The development of the ice-band structure in a pipe has a number of similarities to the phenomenon of "ice-waves" development. It has been observed that when an initially flat ice-water interface is melted by a turbulent water stream, a large amplitude "sand dune" like wave pattern develops at the interface. This ice-wave phenomenon has been observed in the case of a fully developed turbulent channel flow [7] and in the case of a developing turbulent boundary layer [8]. The ice-band structure reported in this paper is undoubtedly the manifestation of the same phenomenon in the case of pipe flow. An examination of the known facts about the ice wave phenomenon on a flat ice surface may, therefore, shed some light on the causes of and conditions for the ice-band structure in a pipe.

Thorsness and Hanratty [9] have developed a theoretical model of the stability of a wavy ice surface in the presence of a turbulent flow. Their predictions of the wave velocity and the most unstable wave length agree very favorably with measured values [8]. The essential mechanism of the instability as proposed by this theory involves the effects of flow acceleration on turbulence properties and thus on heat transfer rates at the ice water interface. The inverse relationship between flow acceleration and heat transfer rates means that in regions of accelerating flow heat transfer is suppressed causing a thickening of the ice layer which reinforces the flow acceleration. Likewise in a deaccelerating flow turbulence and heat transfer are enhanced causing a thinning of the ice. In the case of pipe flow the accelerations and decelerations of the flow may be expected to be stronger than they would be in planer geometry, thus making the ice surface in a pipe even more unstable. In the coverging flow-passage on the upstream of each ice-band the flow acceleration appears to be strong enough to relaminarize the flow. The accleration parameter K, given by

$$K = \frac{\nu}{\upsilon^2}\frac{d\upsilon}{dx} \tag{1}$$

was estimated to have a value of the order of 10 to 50×10^{-6} in these flow regions. Moretti and Kays [10] suggest that a value of $K = 3.3 \times 10^{-6}$ is sufficient to relaminarize a turbulent flow.

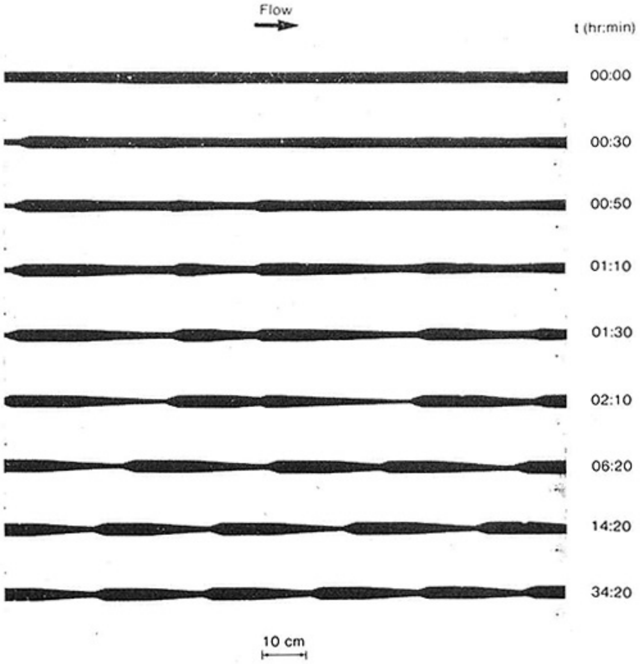

Fig. 5 Transient development of the ice structure in a pipe when the initial flow is turbulent. $\theta = 13.3$, $\mathrm{Re}_D = 13{,}500$

In [8] it was shown that the main damping factor for the ice-wave instability is heat conduction in the ice. The instability parameter defining this effect was the growth parameter, G which is the ratio of the conducted heat flux away from the interface in the ice to the convected heat flux from the water to the ice. A planer ice surface shows it greatest instability for values of $G < 1$, that is for a melting ice surface; however, the instability also exists at steady-state conditions, $G = 1$, and it was predicted [8] that the instability would also exist for a growing interface for values of G up to 2.3. For growing ice interfaces with values of G greater than this value the ice wave would be expected to be damped out. A similar damping of the ice-band structure in a pipe may be expected to occur for a very rapidly thickening ice layer; however, the exact conditions required for this dampening to occur in a pipe flow are at present unknown.

Geometry of the Steady State Ice Band Structure

The two aspects of the ice band structure that are most important in determining pressure drop and freeze-off conditions in a pipe are the spacing of the ice-bands and the extent of the flow blockage they cause. The relationship of these two parameters to the flow conditions and temperatures in a pipe will now be examined.

In Fig. 6 the distance, S, between separation points on consecutive ice-bands has been normalized by the pipe diameter D and is plotted as a function of the temperature ratio parameter θ. It can be seen that the ice-band spacing, that is their wavelength, decreases rapidly with θ for small values of θ. This behavior was also observed in the photographs in Fig. 3. For $\theta > 10$ the ratio S/D has an approximately constant value of 6. This dependence of S/D on θ appears to be largely independent of Reynolds number. It should be pointed out, however, that at any given value of θ one can only have a limited range of Reynolds number for which ice exists in the pipe but does not freeze it off.

The independence of ice-band spacing of Reynolds' number is quite different than the behavior observed for ice-waves on a flat plate. There the wave length is significantly effected by Reynolds' number [9]. This difference may be related to the fact that, as stated earlier, the Reynolds' number of the flow loses importance in the highly accelerating and decelerating flow through a fully developed ice-band structure. Tests in which the temperatures were held approximately constant and the flow rate (Reynolds' number) was suddenly changed showed that the ice-band spacing stayed essentially constant while the flow passage diameter changed.

The property of the ice band structure of most interest is perhaps the diameter of the water passage (the "neck diameter") immediately upstream of the separation point. This is the amount of flow blockage caused by the ice. In Fig. 7 the diameter of the minimum flow passage normalized again by the pipe diameter is correlated with the pipe Reynolds number and the temperature ratio parameter θ. For a value of θ less than about 5 the ratio d/D appears to depend only on Reynolds number. That is, for values of θ below 5 increasing θ, lowering the pipe temperature, does not result in an increased ice thickness as might at first be expected. Instead the separation points move closer together, thus maintaining a constant neck diameter. For larger values of θ and at higher Reynolds number the neck diameter shows a dependence on both these parameters.

Pressure Drop in a Partially Frozen Pipe

The most important consequence of ice formation in a pipe is its effect on pressure drop. The pressure drop caused by the steady state ice band structure observed in the previous section will now be calculated.

For a pipe with ice in it there are two components of the pressure drop that must be considered. The first is due to viscous drag at the ice-water interface. This component is most important for a long pipe section with a smooth, slowly tapering flow passage and is the pressure drop which has normally been calculated for freezing pipes [2–4]. However, when an ice band structure exists in a pipe the greatest pressure losses occur in the sudden expansions downstream of each separation point. This pressure drop will be approximated by assuming that each ice-band acts as a nozzle constriction in the flow with a diameter ratio $d/D = \delta$.

In that case the pressure drop caused by each ice-band will be

$$\Delta P = C \frac{1}{2} \rho v^2 \tag{2}$$

where the velocity, v at the neck of the nozzle is v_0/δ^2 and the pressure loss coefficient is approximately given by $1 - \delta^4$. The normalized loss in a pipe with n ice bands is then

$$\frac{\Delta P}{\frac{1}{2} \rho v_0^2} = n \frac{1 - \delta^4}{\delta^4} . \tag{3}$$

The number of ice-bands predicted for a pipe length L is the integer value of L divided by the ice-band spacing S. The pressure drop then is expected to occur in integral steps; however, as a rough approximation for the case $L > S$ one could write a approximate friction factor, f, for a pipe containing an ice band structure as

$$f = \frac{\Delta P}{\frac{1}{2} \rho v_0^2 L/D} = \frac{1}{S/D} \frac{1 - \delta^4}{\delta^4} . \tag{4}$$

Using Figs. 6 and 7 to relate δ and S/D to the temperature and flow conditions Figure 8 was prepared for the friction factor of a partially frozen pipe. Decreasing Reynolds number for a given value of θ it can be seen that the friction factor rises abruptly from the Moody value for a smooth pipe towards values several orders of magnitude greater as blockage of the pipe proceeds.

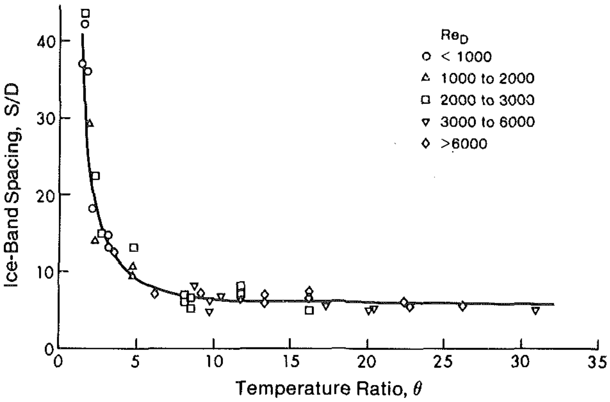

Fig. 6 The steady-state ice band spacing in a pipe

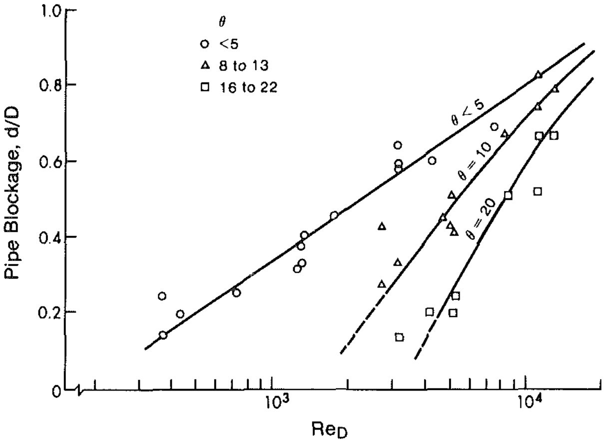

Fig. 7 Normalized flow passage diameter for various flow and temperature conditions

Some values of pressure drop (expressed as a friction factor) measured in the present and other studies, [13] and [14], are shown for comparison on this figure. At the higher values of θ (8 to 20) used in the present experiment there is general agreement between the predicted and measured values. For these values of θ there were five to seven separation points along the test pipe thus the assumption of $L > S$ is reasonable. Most of the pipe freezing experiments in which pressure drops have been measured [2, 11, 12] were done for values of θ of 0.5 and less. At these values of θ an extrapolation of Fig. 6 would suggest that the equilibrium spacing between separation points would be very large and in fact larger than the L/D ratio for most of the experiments. In these experiments the measured pressure drop would be due to the viscous drag component and generally as would be expected in that case reasonable agreement has been obtained between theory and experiment. The two other experiments [13, 14] which were done with the highest values of θ and the largest L/D ratio are shown on Fig. 8. In these experiments it is, however, still not clear whether or not one would have a ice-band structure.

Prediction of Pipe Freeze-Off

The ultimate objective of the study of ice formation in a pipe is to predict conditions under which a pipe will freeze off. Unfortunately this is not a simple matter. Firstly, as has been pointed out in this paper the freezing phenomena occuring in a pipe are complex and secondly the freeze-off is not just the function of the ice growth behavior in a pipe but is a function of the pressure-discharge characteristic of the water source [11,12].

To define the problem of pipe freeze-off more accurately it is best to look at those design applications in which the question of freeze-off may arise. One case would be that of a water piping system for use in a cold environment in which freeze-off and possible breakage of the pipe would be catastrophic. In this case one may choose a very conservative design approach which would ensure that the pipe wall was always maintained above the freezing point. This may involve some or all of the following measures—heating the water before it enters the pipe, application of heat tracer elements to the pipe, and pipe insulation. Due to economic considerations one would often like to design somewhat less conservatively thus allowing some ice formation to occur in the pipe. This would be particularly true for temporary piping installations. In other applications freeze-off of the pipe may be the desired consequence as for example when freezing is used as a temporary valve to plug a pipe during a repair operation. In these latter two design situations a more accuate prediction of the conditions under which a pipe will freeze-off is required. Ideally one would like to have two bounds on these conditions—one for which blockage could possibly occur and one for which blockage is highly probable. A prediction of the conditions under which the steady-state ice-band structure will cause a blockage can be obtained using the friction factor data in Fig. 8. This, it will be explained later, gives an estimate of when blockage is highly probably to occur.

As mentioned previously ice blockage is a system problem and therefore is difficult to represent in a totally general way. In this paper freeze-off will be examined by comparing predicted conditions and actual conditions of freeze-off for the particular experimental apparatus used in these tests.

Rewriting equation (3) gives

$$\frac{\Delta P}{\frac{1}{2}\rho\left(\frac{\nu}{D}\right)^2} = \left\{\frac{L/D}{S/D}\right\}_I \mathrm{Re}_D{}^2 \frac{1-\delta^4}{\delta^4} \tag{5}$$

where the operation $\{\ \}_I$ implies taking the integral value of the operant. Using equation (5) and the data in Figs. 6 and 7 the normalized pressure drop can then be plotted as a function of Re and θ for the particular value of L/D, 45, appropriate to the present experiment. This result is shown in Fig. 9. Also indicated on this figure are some conditions of θ and Re at which freeze-off occurred in the pipe and the approximate pressure—flow rate characteristics that existed for the pump at the freeze-off conditions. To obtain the range of flows used in this experiment both the pump speed and the amount of by-pass were varied. At higher flow rates no by-pass was required and the gear pump approaches a constant flow rate source up until the available pump motor power is reached (curve A, Fig. 9). To obtain lower flow rates the amount of by-pass is increased producing a pressure-flow rate characteristic in which the flow is a stronger function of pressure drop (curves B and C in Fig. 9). It can be seen that in the four cases where freeze-off occurred the pipe pressure-flow curve was close to being tangent to the pressure-flow characteristic for the pump. As has been pointed out [11] the system is unstable at this point. Any further decrease in flow results in a pressure drop in the pipe that is greater than the pump can supply.

In the present experiment freeze-off usually occurred during tests designed to measure the dependence of d/D on θ for values of d/D approaching zero. In these tests temperature conditions would be lowered while attempting to maintain a constant flow. As can be seen in Fig. 7 the smallest values of d/D that were measured were about 0.2. It was usually at about this point that sporadic fluctuations in flow coupled with similar fluctuations in the flow passage diameter were observed. When freeze-off occurred it would occur rapidly and sometimes occurred unexpectedly at conditions for which the system had operated for many hours.

As an aside it is important to note that freeze-off of a pipe containing an ice-band structure is particularly destructive. If a pipe with a monotonically tapered flow passage freezes off it is quite likely that breakage of the pipe will not occur as excess water volume generated by the freezing process has a passage to escape the freezing zone. Alternatively when an ice-band structure exists freeze-off occurs first at each neck in the band with the result that a series of pockets of water are trapped along the freezing pipe. Subsequent freezing of these water pockets results in a pipe rupture at each band.

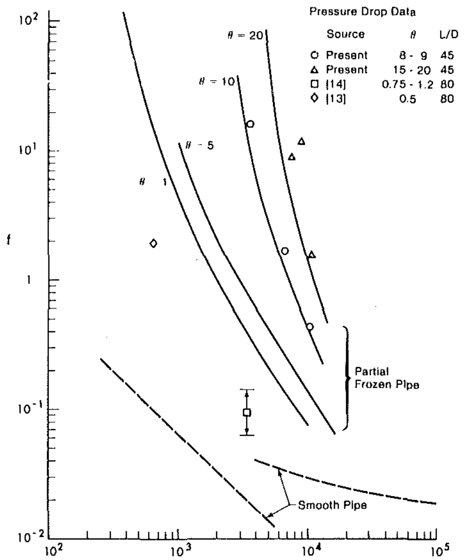

Fig. 8 **Friction factor for a pipe containing a steady state ice band structure**

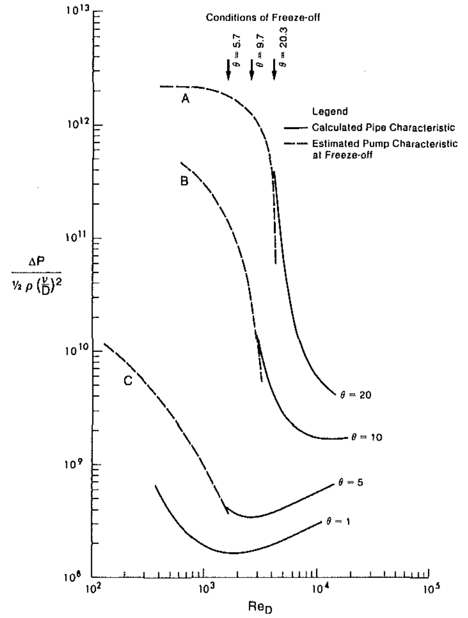

Fig. 9 **Pressure-flow characteristics for the partially frozen pipe and the pump in the present experiment. Experimental conditions at which freeze-off occurred are also shown**

The main difference between this study and other pipe freezing studies that have not observed any anomolous effects that might be attributed to the formation of ice-bands, is the value of θ used. In most of the other tests constant head tanks capable of generating relatively small pressure differences along the pipe were used. As can be seen from Fig. 9 the values of θ required to cause a pipe freeze-off is then very small. Also for small values of θ the spacing between separation points becomes very large and thus the previously developed theories based on a uniformly tapered flow passage [2,3] are appropriate.

As mentioned earlier the use of steady state conditions provides an estimate of the conditions at which freeze-off is highly probable. That is, it would be very unlikely to have a pipe with an open flow passage at temperature conditions colder than or at Reynolds numbers less than those predicted. It is, however, possible that freeze-off could occur at warmer temperatures or at higher flows during the transient cooling process. In Figs. 2 and 5 it can be seen that the greatest restriction in the flow pasage occurs during the transient cooling process. Since the pressure drop depends on the fourth power of the neck diameter at the separation point substantially larger pressure drops may occur during the transient phase than exists in the steady state. For example, in one test on the present apparatus with $\mathrm{Re}_D = 3025$ the temperature of the coolant was inadvertently decreased suddenly so that θ changed from 0 to 3.5 in a very short time. The pipe froze off and was destroyed whereas if temperature had decreased slowly or in small steps as was normally done freeze-off at this Reynolds number would not be expected to occur until θ was approximately 10.

Whether or not the pipe freezes off during the transient cooling period depends on the rate of cooling relative to the rate at which the steady state ice-band structure develops. For an initially laminar flow where the separation points form at the pipe exit and migrate upstream the approach to steady state is very slow. Typical velocities of migration of the separation points is in the range 40 to 120 mm/hrs so that for the 1.5 m long test section used in the present experiment the time required to reach steady state in the laminar case was of the order of 12 to 36 hrs. A rate of change of θ of the order of one per day or less is therefore required before it can be assumed that steady-state conditions are maintained. In the case of an initially turbulent flow where separation points develop all along the pipe approach to equilibrium takes considerably less time. For example, in Fig. 5 the steady state has been essentially reached in 1 to 2 hrs. One would therefore expect that the steady state ice band structure would be an accurate assumption for many practical situations where a high Reynolds number normally exists and particularily in underground water piping where cooling proceeds slowly through the winter season.

Conclusions

It appears that a common morphology of the steady state ice structure inside a cooled pipe containing flowing water will be one that produces a flow passage with a cyclic pattern of contractions and expansions along the length of the pipe. This ice form, called the 'ice-band' structure, was observed to occur for the entire Reynolds number range thus far investigated -3.7×10^2 to 1.4×10^4. The behavior of the transient approach to steady state was found to depend on whether the initial flow in the pipe was laminar or turbulent; however, the qualitative appearance of the steady state ice-band structure was very similar over the entire range of Reynolds numbers studied. The quantitative aspects of the ice-band structure, the spacing between bands and the minimum flow passage diameter at the necks in the ice-bands, was found to correlate with the Reynolds' number, Re_D, and the cooling temperature ration, θ. It was found that the ice-band structure is a feature that occurs predominately at value of θ greater than one. For values of θ less than one uniformly tapered flow passage is likely to be the more common ice configuration.

One of the main consequences of the ice-band structure in a pipe is that it is a large scale roughness and thus greatly enhances the pressure drop. Treating each ice-band as a nozzle obstruction in the pipe gave a good prediction of the pressure-drop observed. For a long pipe with many ice-bands their effect can be incorporated in an enhanced friction factor for the pipe. Combining a knowledge of how this friction factor varies with Reynolds' number and specification of the pressure-discharge characteristics of the water source a prediction can then be made of the temperature condition, θ, at which the system will freeze-off. This prediction agreed satisfactorily with observed freeze-off condition in the present experiment. It must be remembered, however, that the use of an average friction factor for the pipe is somewhat artificial in that the pressure-drop will occur in discrete steps as the number of ice bands along the pipe changes. Also, it is important to note that the greatest flow restriction thus the highest pressure drops and the greatest likelyhood of freezing generally occurs during a period of rapid cooling and not at the steady-state conditions.

Acknowledgment

This work was supported by the Nature Sciences and Engineering Research Council of Canada.

References

1 Gilpin, R. R., "The Morphology of Ice Structure in a Pipe At or Near Transient Reynolds Numbers," Heat Transfer—San Diego 1979, *AIChE Symposium Series 189,* Vol. 75, pp. 89–94

2 Zerkle, R. D., and Sunderland, J. E., "The Effect of Liquid Solidification in a Tube Upon Laminar-Flow Heat Transfer and Pressure Drop," ASME JOURNAL OF HEAT TRANSFER, Vol. 90, 1968, pp. 183–190.

3 Ozisik, M. N., and Mulligan, J. C., "Transient Freezing of Liquids in Forced Flow Inside Circular Tubes," ASME JOURNAL OF HEAT TRANSFER, Vol. 91, 1969, pp. 385–389.

4 Stephan, K., "Influence of Heat Transfer on Melting and Solidification in Forced Flow," *International Journal of Heat Mass Transfer,* Vol. 12, 1969, pp. 199–214.

5. Gilpin, R. R., "A Study of Factors Affecting the Ice Nucleation Temperature in a Domestic Water Supply," *Canadian Journal of Chemical Engineering,* Vol. 56, 466, 1978.

6 Hirata, T., Gilpin, R. R., and Cheng, K. C., "The Steady State Ice Layer Profile on a Constant Temperature Plate in a Forced Convection Flow—II. The Transition and Turbulent Regimens," *International Journal of Heat Mass Transfer,* Vol. 22, 1979, pp. 1435–1443.

7 Ashton, G. D. and Kennedy, J. F., "Ripples on Underside of River Ice Covers," *J. Hydraulic Div.* ASCE 98, 1972, pp. 1603–1624.

8 Gilpin, R. R., Hirta, T., and Cheng, K. C., "Wave Formation and Heat Transfer at an Ice-Water Interface in the Presence of a Turbulent Flow," *Journal Fluid Mechanics*, Vol. 99, 1980, pp. 619–640.

9 Thorsness, C. B., and Hanratty, T. J., "Stability of Dissolving or Depositing Surfaces," *AIChE Journal 25,* 1979, pp. 697–701.

10 Moretti, P. M. and Kays, W. M., "Heat Transfer to a Turbulent Boundary Layer with Varying Free-Stream Velocity and Varying Surface Temperature—An Experimental Study," *International Journal of Heat Mass Transfer,* Vol. 8, 1965, pp. 1187–1202.

11 Des Ruisseax, N., and Zerkle, R. D., "Freezing of Hydraulic Systems," *Canadian Journal of Chemical Engineering,* Vol. 47, 1969, pp. 233–237.

12 Depew, C. A. and Zenter, R. C., "Laminar Flow Heat Transfer and Pressure Drop with Freezing at the Wall," *International Journal Heat Mass Transfer,* Vol. 12, 1969, pp. 1710–1714.

13 Mulligan, J. C., and Jones, D. D., "Experiments on Heat Transfer and Pressure Drop in a Horizontal Tube with Internal Solidification," *International Journal Heat Mass Transfer,* Vol. 19, 1976, pp. 213–219.

14 Thomason, S. B., Mulligan, J. C., and Everhart, J., "The Effect of Internal Solidification on Turbulent Flow Heat Transfer and Pressure Drop in a Horizontal Pipe," ASME JOURNAL OF HEAT TRANSFER, Vol. 100, 1978, pp. 387–394.

15 Mortinez, E. P., and Beaubouef, R. T., "Transient Freezing in Laminar Tube-Flow," *Canadian Journal of Chemical Engineering,* Vol. 50, 1972, pp. 445–449.

Periodic Growth and Decay of a Frozen Crust over a Heat Generating Liquid Layer

F. B. Cheung
Reactor Analysis and Safety Division,
Argonne National Laboratory,
9700 South Cass Avenue,
Argonne, IL 60439

A theoretical investigation is made of thermal oscillations in a horizontal layer of liquid heated at high Rayleigh number from within and cooled to freezing from above. The processes of turbulent thermal convection in the liquid layer and transient heat conduction in the solidified layer are modeled and the conditions leading to periodic self-sustained oscillations are identified. The results of this study indicate that there are five independent parameters that control the oscillatory behavior of the system. Effects of these parameters on the behavior of the transient liquid temperature and the instantaneous crust thickness are obtained and discussed. Validity of the present approach is justified based upon the higher-order solutions.

1 Introduction

When a heat-generating liquid layer, insulated at the bottom, is cooled from above by contact with a cold environment maintained at a fixed subfreezing temperature, a layer of frozen "crust" may form at the top. Previous studies of heat transfer in such a system have assumed that the crust is thermally stable to allow a steady state to attain in the liquid layer [1]. This assumption appears to be physically realistic when there is sufficient cooling of the layer at the surface to remove all the heat generated from within. However, if the top cooling is not strong enough, a situation may arise where no steady state exists in the system. The crust simply grows and decays periodically, disappears in one time and reappears in another time.

It is of interest to examine this phenomenon by first considering the case in which the crust is present in the system. If there is insufficient cooling at the top, the liquid temperature may rise substantially above its freezing point due to over-heating of the liquid layer from within. As a result, a strongly unstable temperature gradient may be developed which induces turbulent thermal convection in the layer. This in turn greatly enhances the rate of heat transfer from the liquid to the crust. Consequently, remelting of the crust may occur until it finally disappears. Once the crust is gone, however, there is a step increase in the rate of top cooling, mainly because of the fact that the effective conductivity of the turbulent fluid is much higher than the conductivity of the crust. This causes the liquid temperature to drop again, eventually leading to the formation of a new crust layer. Thus a new cycle of thermal oscillation commences in the system. The purposes of this study are to identify the conditions for the occurrence of thermal oscillations and to examine the effects of various parameters that control the oscillatory behavior of the system.

Laboratory observation of periodic crust growth and decay has been performed by Welander for a water-ice-air system [2]. In his experiment, a body of water was heated internally at a constant rate while it was cooled at its free surface to freezing by contact with air kept at a fixed subzero temperature. For large internal heating and negative air temperature, the water temperature with ice was found to be too high and the water temperature without ice too low to allow any steady state to exist physically. The data indicated that there were self-sustained oscillations in the system with ice forming and disappearing periodically.

Based upon a simple mechanistic model, Welander has also given a theoretical discussion of the temperature transients and thermal oscillations in the system [3]. He considers that there are ice-free and ice-covered states following each other in an infinite sequence. He further assumes that the water and the air are well mixed except in thin boundary layers near the interface and that the ice is very thin compared to the water layer as a whole. Thus the temperature profile through the ice is linearly approximated and the heat content variations of the ice are neglected. The coefficients of heat transfer across all boundaries are treated to be constant so that the heat transfer rate is proportional to the momentary difference in temperature on both sides. This simple analysis leads to the conclusion that the oscillation between an ice-free and an ice-covered regime is of a single-period self-sustained form. Unfortunately, effects of various controlling parameters cannot be assessed by the model.

In this study, some generalization of Welander's theory is made to better describe the physical process. It is known that, for a liquid layer heated internally at high Rayleigh number, the rate of heat transfer in the layer is not simply proportional to the momentary temperature drop across the thermal boundary layer but is a strong function of the instantaneous Rayleigh number [4]. Here, the correlation equation for turbulent thermal convection in a heat-generating fluid layer [5] is employed to model the Rayleigh number effect on the surface heat transfer of the layer. This is coupled with the process of transient heat conduction in the crust through proper formulations about interfacial conditions. The M. E. Shvets method [6, 7] is adopted to determine the transient crust temperature. In so doing, the heat capacity of the crust and the nonlinearity in the crust temperature profile, which have been neglected in the Welander's model [3], are fully taken into account in the present case. The effects of various controlling parameters on the oscillatory behavior of the system, in particular the maximum crust thickness and the durations of the crust-covered and crust-free periods, are obtained and discussed.

2 Mathematical Formulation

The system under consideration is depicted in Fig. 1. A horizontal layer of liquid, insulated at the bottom, is heated at high Rayleigh number from within and cooled to freezing from above. The layer is assumed to be infinite in extent so that heat transfer in the system is one-dimensional. The rate of internal heating of the layer and the exterior temperature, T_o, are assumed to be constant. The liquid layer is considered to be in turbulent thermal convection, with the liquid temperature, T_ℓ, being uniform throughout the layer except in a region near the liquid-crust interface. For the purpose of simplicity, we shall assume that all properties are constant and that there are no variations of properties upon phase transition.[1] If, in addition, the crust is assumed to be mechanically stable regardless its thickness [8], then the crust temperature, T_s, may be described by

$$\partial T_s/\partial t = \alpha \partial^2 T_s/\partial x^2, \; 0 \leq x \leq \delta(t), \tag{1}$$

$$x = 0: T_s = T_i(t), k\partial T_s/\partial x = h(T_i - T_o), \tag{2}$$

Contributed by the Heat Transfer Division for publication in the JOURNAL OF HEAT TRANSFER. Manuscript August 29, 1980.

---

[1] This is merely to minimize the number of independent parameters of the system and is not the limitation of the present approach. The assumption can be relaxed with little difficulty.

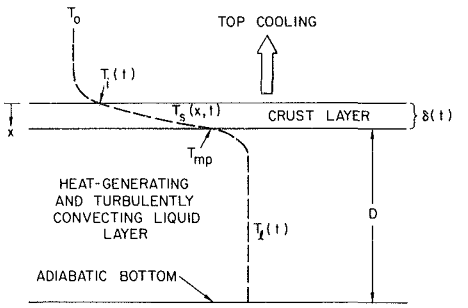

Fig. 1 Schematic of the liquid-crust system, indicating nomenclature

$$x = \delta\text{: } T_s = T_{mp},\ \rho\lambda d\delta/dt = k\partial T_s/\partial x - Q, \tag{3}$$

where x is the vertical co-ordinate measured downward from the surface, δ, the instantaneous crust thickness, T_i, the unknown surface temperature, h, the heat transfer coefficient for top cooling, and Q, the convective heat flux from the liquid to the crust. In writing equation (1), we have assumed that there is no heat generation in the crust layer. The coefficient, h, which is likely to be a complicated function of temperature in many physically realistic cases, shall be assumed constant in the subsequent analysis. This assumption shall be examined later (see the section on Validity of the Present Approach).

To complete the formulation, an expression for the convective heat flux, Q, must be obtained from considerations of heat transfer in the liquid layer. Previous studies of turbulent thermal convection in a heat-generating layer with an adiabatic bottom indicate that the overall resistance of the layer to heat transfer lies within a boundary layer region at the upper wall where heat transfer is controlled principally by molecular diffusion [4]. If ℓ denotes the instantaneous boundary layer thickness, then Q may be written as

$$Q = k(T_\ell - T_{mp})/\ell, \tag{4}$$

where $(T_\ell - T_{mp})$ is the momentary temperature drop across the boundary layer. For high Rayleigh number flows, the experimental data of internally heated layers suggest that ℓ is related to $(T_\ell - T_{mp})$ by [5]

$$g\beta(T_\ell - T_{mp})\ell^3/\alpha\nu = 106.2(\ell/D)^{-0.391}, \tag{5}$$

where D is the depth of the liquid layer. The above correlation has been demonstrated to be representative for transient turbulent flow situations [9]. In particular, Kulacki, et al. have found the correlation to be in excellent agreement with their earlier experimental results [10] and with their recent turbulent-to-turbulent transition data [11]. In what follows, we shall assume the liquid layer to be very thick compared to the crust, so that D may be treated as a constant during the transients. The validity of this assumption is to be justified later. Finally, an overall energy balance on the liquid layer leads to

$$\rho C_p D dT_\ell/dt = qD - k(T_\ell - T_{mp})/\ell, \tag{6}$$

where the variation of temperature within the thin boundary layer has been neglected. This may result in an error of the order $\ell/D (\ll 1)$. Equations (4–6) have been used successfully in predicting the results of a series of transient turbulent convection experiments [11].

Thus far, we have considered the situation in which a solidified layer exists in the system, i.e., $\delta > 0$. If, however, the system is free of crust, i.e., $\delta = 0$, then the governing equations are of different forms. These are

$$\rho C_p D dT_\ell/dt = qD - k(T_\ell - T_i)/\tilde{\ell}, \tag{7}$$

$$k(T_\ell - T_i)/\tilde{\ell} = h'(T_i - T_o), \tag{8}$$

where $\tilde{\ell}$ is the boundary layer thickness at the free surface and h' is a new coefficient describing the heat transfer directly from the liquid to the upper environment. Combining equations (7) and (8) and eliminating the unknown T_i, we obtain

$$\rho C_p D dT_\ell/dt = qD - \tilde{h}(T_\ell - T_o), \tag{9}$$

where $\tilde{h} = h'/(1 + h'\tilde{\ell}/k)$ is now a new coefficient of heat transfer.[2] As in the crust-covered case, we shall assume $\tilde{h}$ to be a constant, with the understanding that $\tilde{h}$ is likely to be a complicated function of temperature in many physically realistic cases. This assumption will be further discussed in the later section. Note that equation (9) applies if and only if $\delta = 0$ and $T_\ell > T_{mp}$.

3 Occurrence of Thermal Oscillations

To determine the conditions leading to periodic crust growth and decay, we must first identify the various controlling parameters. Dimensional considerations of equations (1–6) and of equation (9) indicate that the behavior of the system is dependent upon the values of the following dimensionless groups:

$$M = \alpha\rho\lambda/qD^2, \qquad N = hD/k, \quad S = h/\tilde{h}, \tag{10}$$

---

[2] Generally, the main change in temperature occurs in the upper environment, viz., $(T_i - T_o) \gg (T_\ell - T_i)$, so that we have $h'\tilde{\ell}/k \ll 1$. Hence we may assume $h \sim h'$ or $h'(T_i - T_o) \sim h'(T_\ell - T_o)$, as a first approximation.

Nomenclature

C_p = specific heat
D = depth of the liquid layer
g = acceleration due to gravity
h = heat transfer coefficient for top cooling in the crust-covered regime
$\tilde{h}$ = heat transfer coefficient for top cooling in the crust-free regime
k = thermal conductivity
ℓ = thermal boundary layer thickness
M = dimensionless ratio of the rate of latent heat production to the rate of internal heat generation, equation (10)
N = surface Nusselt number, equation (10)
P = dimensionless temperature difference between the melting point of the crust and the environment, equation (10)
q = volumetric rate of heat generation
Q = surface heat flux, equation (4)
Q_r = radiative heat flux, equation (31)
R = Rayleigh number of the liquid layer, equation (10)
S = ratio of the heat transfer coefficients, h and $\tilde{h}$, equation (10)
t = time
T_o = temperature of the environment
T_i = temperature at the crust surface
T_ℓ = liquid temperature
T_{mp} = melting point of the crust
T_s = crust temperature
V = radiation parameter, equation (36)
x = vertical coordinate measured downward from the surface
η = dimensionless distance, equation (11)
τ = dimensionless time, equation (11)
δ = crust thickness
Δ = dimensionless crust thickness, equation (11)
β = isobaric coefficient of thermal expansion
ρ = density
λ = latent heat of fusion
α = thermal diffusivity
ν = kinematic viscosity
ϵ = surface emissivity
σ = Stefan-Boltzmann constant
θ_i = dimensionless temperature at the crust surface, equation (11)
θ_ℓ = dimensionless liquid temperature, equation (11)
$\theta_{\ell 0}$ = initial value of θ_ℓ
θ_s = dimensionless crust temperature, equation (11)

Subscripts

o = initial condition or environmental condition
i = surface condition
ℓ = liquid condition
s = crust condition

$$P = k(T_{mp} - T_o)/qD^2, \qquad R = g\beta qD^5/k\alpha\nu.$$

The physical significance associated with each of these parameters will be discussed. For later convenience, the following dimensionless variables are also introduced:

$$\begin{aligned} &\tau = \alpha h^2 t/k^2, && \eta = hx/k, \\ &\theta_s = k(T_s - T_o)/qD^2, && \theta_\ell = k(T_\ell - T_{mp})/qD^2, \\ &\theta_i = k(T_i - T_o)/qD^2, && \Delta = h\delta/k. \end{aligned} \tag{11}$$

The governing equations for the case of crust-covered (i.e., $\Delta > 0$) become

$$\partial\theta_s/\partial\tau = \partial^2\theta_s/\partial\eta^2, \qquad 0 \leq \eta \leq \Delta(\tau) \tag{12}$$

$$\theta_s(\tau, 0) = \partial\theta_s/\partial\eta|_{\eta=0} = \theta_i(\tau), \theta_s(\tau, \Delta) = P, \tag{13}$$

$$Md\Delta/d\tau = \partial\theta_s/\partial\eta|_{\eta=\Delta} - 0.253R^{0.295}\theta_\ell{}^{1.295}/N, \tag{14}$$

$$N^2 d\theta_\ell/d\tau = 1 - 0.253\mathrm{R}^{0.295}\theta_\ell{}^{1.295}. \tag{15}$$

However, for the case of crust-free (i.e., $\Delta = 0$, $\theta_\ell > 0$), we have

$$N^2 d\theta_\ell/d\tau = 1 - N(\theta_\ell + P)/S. \tag{16}$$

If steady-state exists in the crust-covered regime, we must have $\partial\theta_s/\partial\tau = d\Delta/d\tau = d\theta_\ell/d\tau = 0$. Solutions of equations (12–15) lead to

$$\theta_s(\infty, \eta) = P(1 + \eta)/(1 + \Delta), \qquad \Delta(\infty) = NP - 1, \tag{17}$$

which is physically realistic if and only if $NP \geq 1$. For the case of large internal heat generation, viz., $qD > h(T_{mp} - T_o)$, or $NP < 1$, no steady-state crust formation is possible in the system. Similarly, if steady-state exists in the crust-free regime, we must have $d\theta_\ell/d\tau = 0$. Equation (16) gives

$$\theta_\ell(\infty) = (S - NP)/N, \tag{18}$$

which is physically realistic if and only if $S \geq NP$. For the case of strong top cooling, viz., $\bar{h}(T_{mp} - T_o) > qD$, or $S < NP$, no steady-state crust-free regime is possible in the system. Obviously, for $S < NP < 1$, the system is inherently unstable and must oscillate forever between the crust-covered and the crust-free regime.

It is of interest to note that $\bar{h} > h$ is a necessary condition for the occurrence of thermal oscillations. Physically, this requires that heat transfer directly from the liquid layer to the upper environment be more effective than heat transfer from the crust to the environment. If, in addition, the internal heat sources are strong enough, crust oscillations may occur. This phenomenon, which has been observed in laboratory experiments [2], is believed to exist in some geophysical and nuclear reactor systems.[3]

4 Approximate Transient Solutions

We shall now determine the oscillatory behavior of the system under the conditions of $S < NP < 1$. If, initially, the system is free of crust and the liquid temperature is at $\theta_\ell(0) = \theta_{\ell 0} > 0$, then by integration of equation (16), we get[4]

$$\theta_\ell = \theta_{\ell 0} e^{-\tau/SN} - (P - S/N)(1 - e^{-\tau/SN}). \tag{19}$$

Since we are interested in the case of $S < NP$ or $P > S/N$, we may expect the liquid temperature to decrease monotonically with time from its initial value of $\theta_{\ell 0}$. Freezing commences when $\theta_\ell(\omega) = 0$, where

$$\omega = SN[\ln(\theta_{\ell 0} + P - S/N) - \ln(P - S/N)]. \tag{20}$$

Beyond this time, a frozen crust is present (periodically) in the system and we must seek solutions from equations (12–15). Here we employ the M. E. Shvets method [6, 7] to obtain the transient behavior of the crust.[5] In the first approximation, the transient term on the left-hand side of equation (12) is neglected. This results in a crust temperature that depends linearly upon the vertical coordinate. However, in contrast to the model with a linear temperature profile, this is valid only for the first approximation. In the second and the higher approximations, the lower-order solutions are introduced into the left-hand side of equation (12) and the higher-order solutions are found by integrating the resultant equation along with equation (13). The final expression for the temperature gradient at the liquid-crust interface, i.e., $\partial\theta_s/\partial\eta|_{\eta=\Delta}$, is then introduced into equation (14) and the ordinary differential equation so obtained is integrated together with equation (15) to determine the time variations of the crust thickness and the liquid temperature. Following the examples of [6, 7], we shall limit ourselves to a second approximation. However, a third approximation will also be considered at the end of the paper to justify the present approach.

The first-order solution is given by equation (17). If both θ_s and Δ are treated to be time-dependent, then by introducing this solution into the left-hand side of equation (12), we get

$$\partial^2\theta_s/\partial\eta^2 = -P(1 + \eta)(1 + \Delta)^{-2} d\Delta/d\tau. \tag{21}$$

Using the boundary conditions of equation (13), the above equation may be integrated twice with respect to η to yield

$$\theta_s = \frac{P}{1 + \Delta}\left\{\left[1 + \frac{\Delta^2 d\Delta/d\tau}{2(1 + \Delta)^2}(1 + \Delta/3)\right](1 + \eta) - \frac{d\Delta/d\tau}{2(1 + \Delta)}(1 + \eta/3)\eta^2\right\}. \tag{22}$$

Hence the temperature gradient at the lower boundary of the crust is

$$\left.\frac{\partial\theta_s}{\partial\eta}\right|_{\eta=\Delta} = \frac{P}{1 + \Delta}\left[1 - \frac{\Delta d\Delta/d\tau}{(1 + \Delta)^2}(1 + \Delta + \Delta^2/3)\right]. \tag{23}$$

From equations (14–15), and (23), together with the results of the crust-free solutions, we obtain a system of governing equations describing the characteristics of the crust-covered regime:

$$\frac{d\Delta}{d\tau} = \frac{P/(1 + \Delta) - 0.253R^{0.295}\theta_\ell{}^{1.295}/N}{M + P\Delta(1 + \Delta + \Delta^2/3)/(1 + \Delta)^3}, \tag{24}$$

$$\frac{d\theta_\ell}{d\tau} = \frac{1}{N^2}(1 - 0.253R^{0.295}\theta_\ell{}^{1.295}), \tag{25}$$

$$\Delta(\omega) = \theta_\ell(\omega) = 0, \tag{26}$$

where ω is given by equation (20). For prescribed values of M, N, P, and R, the above equations may be solved numerically using the Runge-Kutta method to obtain the time dependence of $\Delta(\tau)$ and $\theta_\ell(\tau)$.

It can be seen from equation (25) that the liquid temperature, θ_ℓ is a monotonically increasing function of time during the entire crust-covered stage.[6] On the other hand, we may expect from equation (24) that the value of $d\Delta/d\tau$ changes from positive to negative within the same period. Physically, the curst must grow at first, reaching a maximum size, and starts to decay therafter. If τ_{crust} denotes the lifetime of the crust, then we must have $\Delta = 0$ and $\theta_\ell > 0$ at $\tau = \omega + \tau_{\text{crust}}$. Beyond this time, the system is temporarily free of crust again. To continue the solution, equations (19) and (20) must be applied, with the initial liquid temperature being taken to be the value of θ_ℓ at $\tau = \omega + \tau_{\text{crust}}$. This leads us to a new cycle.

---

[3] In nuclear reactor safety studies, we are concerned with the behavior of a frozen crust over a molten UO_2 layer with decay heating at a very high Rayleigh number. The layer is cooled from above by radiative and convective heat transfer to a cold environment at a temperature far below the freezing point of UO_2.

[4] It will be shown that the oscillatory behavior of the system does not depend on the initial conditions (see Fig. 2). Hence it is not important whether we assume the system to be initially crust free or be initially crust-covered.

[5] The M. E. Shvets method has been used successfully in the calculation of ice accretion [7]. Since we are concerned principally with the crust thickness-time history, not with the detailed crust temperature profile, the method appears to be quite adequate for our use.

[6] Owing to the fact that $d^2\theta_\ell/d\tau^2 < 0$, the speed of rise of the liquid temperature must get smaller and smaller as time proceeds.

5 Results and Discussion

Within the framework of the present model, there are five independent parameters, namely, M, N, P, R, and S, which control the oscillatory behavior of the system. Obviously, it is not possible to present the combined effect of all of these parameters in a simple manner. For this reason, results are obtained for a base case and are later used as standard references. The base case is chosen such that it represents the conditions commonly encountered in a physically realistic system (see next paragraph). Deviations from the base case are then studied to examine the individual effect of each parameter.

For turbulent thermal convection in a layer of nuclear reactor core melt [1, 4], the Rayleigh number, R, is of the order of 10^{10}. The corresponding Nusselt number, N, is about 50.[7] The parameter P, which represents the dimensionless temperature difference between the melting point of the crust and the environment, is in many cases of the same order as the dimensionless liquid temperature. At $R = 10^{10}$, the steady-state liquid temperature, when exists, is equal to 0.015 [4, 9]. Since we require $NP < 1$ and since $N \sim 50$, a value of $P \sim 0.01$ is chosen for the base case. With this choice of (N, P), the value of S is required to be less than 0.5. Physically, the parameter S represents the ratio of the heat transfer coefficients, h and $\bar{h}$, and is not likely to be much smaller than unity. Thus a value of $S = 0.25$ is assumed for the base case. Finally, based on the estimated value for a core melt [1], the parameter M which represents the ratio of the rate of latent heat production to the rate of internal heat generation, is taken to be 0.1.

Results obtained for the base case are shown graphically in Fig. 2. The solid lines represent the situation in which the initial conditions are $\Delta(0) = 0$ and $\theta_\ell(0) = 0.015$; whereas the dashed lines represent the situation in which the initial conditions are $\Delta(0) = 0$ and $\theta_\ell(0) = 0.006$. Apparently, the solid lines are identical to the dashed lines except they are out of phase. The oscillatory behavior of the system is in fact independent of the initial conditions. More importantly, the transient liquid temperature and the crust thickness in a given cycle of oscillation[8] are found to be the same as those in other cycles. Thus the computational process may be terminated at the end of the first complete cycle. During the crust-covered period, the liquid temperature is found to rise continuously in time to a peak value smaller than the steady-state liquid temperature.[9] At the same time the crust grows to a maximum and then decays to zero. In the crust-free period where $\Delta = 0$, the liquid temperature is found to be a monotonically decreasing function of time. The observed liquid-temperature transients for the crust-covered and the crust-free regimes are in good qualitative[10] agreement with those measured by Welander for a water-ice-air system [2].

We have remarked that $NP < 1$ is a necessary condition for the occurrence of thermal oscillations. This criterion is illustrated in Fig. 3. In this figure, time variations of the crust thickness are presented for three different values of N and P. The parameters M, R, and S are kept constant having the same values as those in the base case. For $N = 90$ and $P = 0.01$ (viz., $NP = 0.9$), the oscillatory behavior of the system is quite similar to the one observed in the base case, except that the maximum crust thickness is larger and the crust lifetime is longer in the present case. For $N = 50$ and $P = 0.02$ (viz., $NP = 1$), however, the behavior is quite different. The system ceases to oscillate. Instead, it reaches a steady state after an initial transient, with the final crust thickness being zero.[11] For $N = 50$ and $P = 0.03$ (viz., $NP = 1.5$), no oscillation is observed but the crust is at all time thicker than the crust in the previous case. The final system is crust-covered and, again, at a steady state.

The effects of the parameters M and R are shown in Fig. 4. The dashed lines represent the results for the base case ($M = 0.1$ and $R = 10^{10}$) whereas the solid lines represent the results for two other cases ($M = 1$, $R = 10^{10}$; and $M = 0.1$, $R = 10^{12}$; respectively). The parameters N, P, and S are the same in all cases. Obviously, as the value of M is increased, the maximum crust thickness decreases while the crust lifetime increases. This is due to the fact that the latent heat effect is stronger for a larger value of M. On the other hand, there is no effect of M on the system during the crust-free periods. A substantially different behavior of the system is obtained in the situation when R increases from 10^{10} to 10^{12}. The maximum crust thickness, the crust lifetime, and the crust-free period for $R = 10^{12}$ are all smaller than those for $R = 10^{10}$. Physically, the system tends to oscillate faster at higher Rayleigh numbers because of larger heat transfer rate and turbulent mixing in the liquid layer.

The combined effects of M and R on the maximum crust thickness and the crust lifetime are further illustrated in Fig. 5. Although these two parameters do not have any influence on the conditions for the occurrence of thermal oscillations, the oscillatory behavior of the system (when exists) does depend heavily on their values. Clearly, the important effects of M and R, which were totally neglected in Welander's model [3], must be fully considered in describing the actual physical process. The values of $\Delta_{\max}$ and τ_{crust} calculated from the first-order solution are also shown in Fig. 5 by the circles for the case of $R = 10^{10}$ and for three different values of $M = 0.01, 0.1$, and 1. Assuming a linear temperature profile in the crust, namely, $\theta_s = P(1 + \eta)/(1 + \Delta)$, equation (14) becomes

$$\frac{d\Delta}{d\tau} = \frac{1}{M}\left[P/(1 + \Delta) - 0.253\, R^{0.294}\theta_\ell^{1.295}/N\right]. \qquad (27)$$

Based upon the second order solution, which is governed by equation (24), the first-order, linear-temperature-profile approximation is found to be valid only if

$$M \gg P\Delta(1 + \Delta + \Delta^2/3)/(1 + \Delta)^3. \qquad (28)$$

Inspection of the figure indicates that there are marked errors involved in the first order-solution when the condition of $P/M \ll 1$ or $C_p(T_{mp} - T_o)/\lambda \ll 1$ is not met.[12] For the case of a molten UO_2 layer, for example, we have $C_p \sim 0.12$ cal/g = K, $(T_{mp} - T_o) \sim 2750$ K, and $\lambda \sim 67$ cal/g. This gives $P/M \sim 5$, which precludes the possible use of the linear profile approximation. This justifies the necessity of going to a second-order solution over the first-order in the prediction of core melt behavior.

Unlike the crust-covered regime which is independent of the parameter S, the crust-free regime[13] is a strong function of S. Figure 6 displays the effect of S on the lifetime of the crust-free regime. Three different initial liquid temperatures are considered, namely, $\theta_\ell(0) = 0.1, 0.01$, and 0.001. The solid lines represent the results for the case of $N = 50$ and $P = 0.01$ (viz., $NP = 0.5$) whereas the dashed lines represent the results for the case of N = 50 and $P = 0.05$ (viz., $NP = 0.25$). As expected, a longer crust-free period is obtained at a higher initial liquid temperature. On the other hand, a shorter period is obtained at a larger value of NP. In all cases, τ_{free} is found to vary sharply with S and becomes infinite as the value of S approaches the value of NP. For $S > NP$, the system ceases to oscillate and is in a steady-state crust-free regime.

---

[7] Under post-accident heat removal conditions, the level of decay heating is of the order $q \sim 5$ cal/cm^3-s. The depth of a typical molten fuel layer is about $D \sim 10$ cm. Near the melting point of UO_2, namely, at $T_{mp} = 3150$K, the values of various properties of the fuel are: $k = 0.0062$ cal/cm-s-K, $\alpha = 0.0067$ cm^2/s, $\nu = 0.005$ cm^2/s, and $\beta = 4 \times 10^{-5}$K^{-1}. With these values, the Rayleigh number is $R \sim 4 \times 10^{10}$. Using the heat transfer correlation of Kulacki and Emara [10] the surface Nusselt number is estimated to be $N = 0.21R^{0.226} \simeq 52$.

[8] Each cycle of thermal oscillation consists of a crust-covered stage and a crust-free stage. In general, the two stages have different lifetimes (see Figs. 5 and 6).

[9] At $R = 10^{10}$, the steady-state liquid temperature, when exists, is equal to 0.015.

[10] In Welander's work [2], a magnetic stirrer was used to enhance mixing in the volumetrically heated water layer. No measurements of heat flux nor of the ice-layer thickness were made in the experiment. Only the water temperature in the middle of the water body was recorded as a function of time. The study was largely qualitative in nature with the sole purpose of observing the occurrence of thermal oscillation in a water-ice-air system.

[11] Whether the final system is crust-free or crust-covered (with an infinitesimal crust thickness) is uncertain. The case of $NP = 1$ represents a singularity point of the system.

[12] In Fig. 5, the value of P is fixed at 0.01. Significant differences between the first-order and the second-order predictions are observed for $M < 0.1$.

[13] Note that the crust-free regime does not depend on the parameter M.

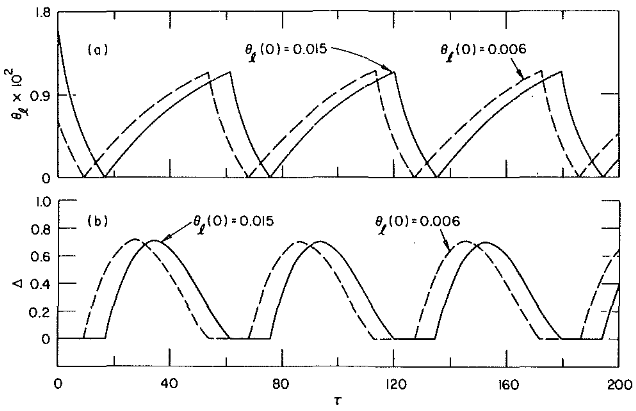

Fig. 2 Transient liquid temperature and crust thickness in the base case

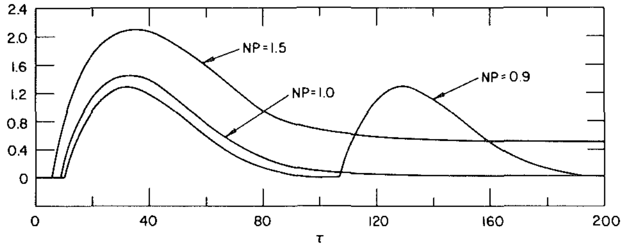

Fig. 3 Effects of *N* and *P* on the oscillatory behavior of the system: transient crust thickness

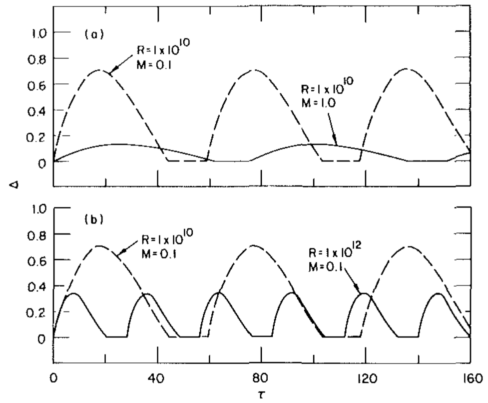

Fig. 4 Effects of *M* and *R* on the oscillatory behavior of the system: transient crust thickness

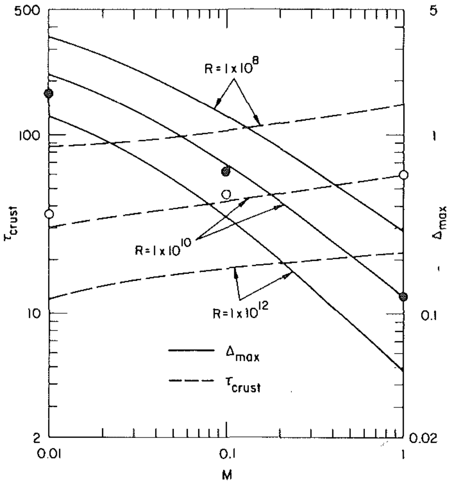

Fig. 5 Dependence of the maximum crust thickness and crust lifetime on *M* and *R*

6 Validity of the Present Approach

Thus far, we have limited ourselves to a second approximation. It is necessary to justify the present results based on the higher-order solutions. To do this, equation (22) is introduced into the left-hand side of equation (12) to yield

$$\partial^2\theta_s/\partial\eta^2 = -\frac{P}{(1+\Delta)^2}\Bigg\{(1+\eta)\left[\frac{d\Delta}{d\tau} - \frac{\Delta}{(1+\Delta)^2}\left(\frac{d\Delta}{d\tau}\right)^2 - \frac{\Delta^2(1+\Delta/3)}{2(1+\Delta)}\frac{d^2\Delta}{d\tau^2}\right] + \eta^2\left(1+\frac{1}{3}\eta\right)\left[\frac{1}{2}\frac{d^2\Delta}{d\tau^2} - \frac{1}{1+\Delta}\left(\frac{d\Delta}{d\tau}\right)^2\right]\Bigg\}. \quad (29)$$

Integration of the above equation using the boundary conditions of equation (13) gives

$$\theta_s = \frac{P}{1+\Delta}\Bigg\{(1+\eta)\Bigg(1+\frac{\Delta^2(1+\Delta/3)}{2(1+\Delta)^2}\left[\frac{d\Delta}{d\tau} - \frac{\Delta}{(1+\Delta)^2}\left(\frac{d\Delta}{d\tau}\right)^2 - \frac{\Delta^2(1+\Delta/3)}{2(1+\Delta)}\frac{d^2\Delta}{d\tau^2}\right] + \frac{\Delta^4(1+\Delta/5)}{12(1+\Delta)^2}\left[\frac{1}{2}\frac{d^2\Delta}{d\tau^2} - \frac{1}{1+\Delta}\left(\frac{d\Delta^2}{d\tau}\right)\right]\Bigg) - \frac{\eta^2}{2(1+\Delta)}\Bigg(\frac{1}{6}\eta^2\left(1+\frac{1}{5}\eta\right)\left[\frac{1}{2}\frac{d^2\Delta}{d\tau^2} - \frac{1}{1+\Delta}\left(\frac{d\Delta}{d\tau}\right)^2\right] + \left(1+\frac{1}{3}\eta\right)\left[\frac{d\Delta}{d\tau} - \frac{\Delta}{(1+\Delta)^2}\left(\frac{d\Delta}{d\tau}\right)^2 - \frac{\Delta^2(1+\Delta/3)}{2(1+\Delta)}\frac{d^2\Delta}{d\tau^2}\right]\Bigg)\Bigg\}, \quad (30)$$

where the values of $\Delta(\tau)$ may be obtained from equations (13–15).[14]

The calculated profiles of $\theta_s(\eta)$ at three different times, namely, $\tau/\tau_{crust} = 0.1, 0.2$, and 0.4 are shown in Fig. 7. The values of M, N, P, R, and S are the same as those chosen for the base case. As expected, the second-order solutions (which are represented by the dashed lines) are only slightly different from the corresponding third-order solutions (which are given by the solid lines). Hence there is no need to go beyond the second approximation. For $\tau < 0.4\ \tau_{crust}$ the temperature profiles are found to be higher nonlinear. This indicates that the linear-temperature-profile approximation [3] is not a valid assump-

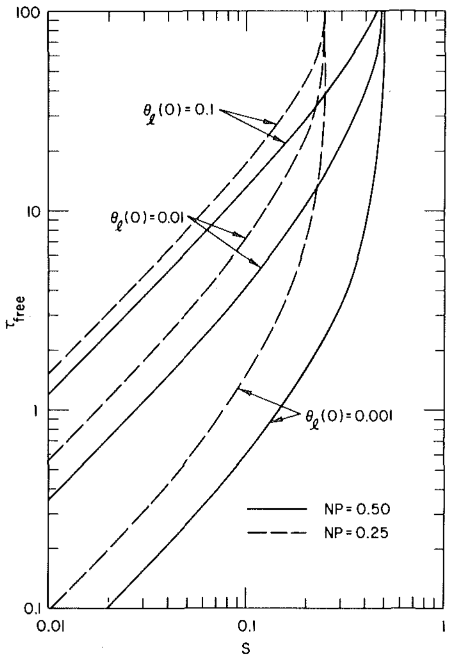

Fig. 6 The predicted lifetime for the crust-free regime

---

[14] Note that an initial condition is needed for $d\Delta/d\tau$ in the third approximation. This is obtained from equation (24) by setting $\Delta = \theta_\ell = 0$, which results in $d\Delta/d\tau = P/M$ at the beginning of crust formation.

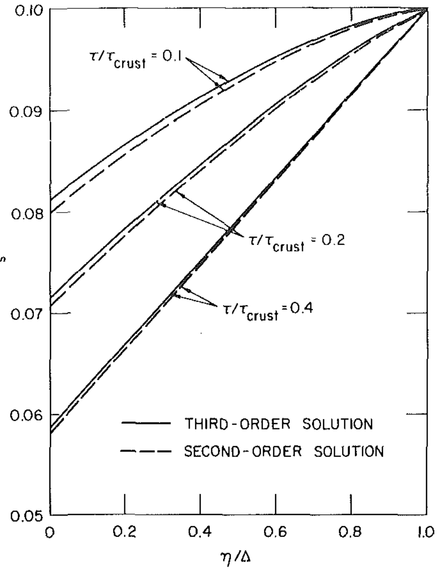

Fig. 7 Comparison of the second- and third-order solutions: transient crust temperature profile

tion. It should be pointed out that $0 < \tau < 0.4\ \tau_{\text{crust}}$ corresponds to the period in which the crust is growing, as can be seen in Fig. 2.

The use of equation (15) requires that the motion of the liquid be turbulent at all times. However, at the beginning of the crust-covered regime, we have $\theta_\ell(0) \sim 0$ so that there is not enough buoyancy to sustain the turbulent motion. Fortunately, for $R \geq 10^8$, the duration in which this occurs is found to be only one or two percents of the total crust lifetime. Thus there is practically negligible error involved in the use of equation (15). To further demonstrate this point, let us consider heat transfer of the layer at $R = 10^{10}$. If we define an instantaneous Rayleigh number for the layer as $g\beta(T_\ell - T_{mp})D^3/\alpha\nu$ which is equal to $R\theta_\ell$, then we require $R\theta_\ell > 10^6$ for the liquid layer to be in turbulent motion [4, 9]. From the results obtained for the base case (Fig. 2), we have $\theta_\ell \sim 10^{-4}$ or $R\theta_\ell \sim 10^6$ at $\tau \sim 0.5$. Hence turbulence may prevail in the layer as early as $\tau \sim 0.012\ \tau_{\text{crust}}$.

Another important limitation imposed on the present model is $\delta \ll D$ or $\Delta \ll N$. To seek the conditions under which this is valid, the results presented in Fig. 5 are employed. In this figure, N has a value of 50. For $M > 0.01$ and $R \geq 10^8$, it is quite obvious that $\Delta < 5$ or $\Delta/N < 0.1$. Hence $\delta \ll D$ is a reasonable assumption for large values of R and M. Significant errors, however, may be resulted from this approximation if M is much less than 0.01.

Finally, we should discuss the assumption of constant heat transfer coefficients for top cooling. In reality, the values of h and $\tilde{h}$ may vary from case to case and must be determined by considering the nature of top cooling in a given situation. It is recognized that h and $\tilde{h}$ may be temperature-dependent in a particular system. In such case, the oscillatory behavior of the system may depend on addition parameters other than those discussed in this study. The assessments of post-accident heat removal from a core melt [1], for example, have found the radiative loss at the upper surface of a molten UO_2 pool to represent a significant percentage of the upward heat flux. In that situation, combined convection and radiation must be considered to describe the rate of top cooling. For radiant heat exchange between infinitely wide parallel grey surfaces at temperature T_i and T_o (see Fig. 1), the radiative loss may be written as

$$Q_r = \bar{\epsilon}\sigma(T_i^4 - T_o^4) \tag{31}$$

with $\bar{\epsilon}$, an interchange factor, given by

$$\bar{\epsilon} = \epsilon_i\epsilon_o/(\epsilon_i + \epsilon_o - \epsilon_i\epsilon_o), \tag{32}$$

where ϵ_i and ϵ_o are the emissivities of the surfaces. An effective heat transfer coefficient may thus be introduced to describe the surface heat flux in the combined convection-radiation case. This is

$$h_{\text{eff}} = h_{\text{conv}} + \bar{\epsilon}\sigma(T_i^3 + T_i^2T_o + T_iT_o^2 + T_o^3)$$

or

$$h_{\text{eff}} = h_{\text{conv}} + \bar{\epsilon}\sigma T_{mp}^3[(T_i/T_{mp})^3 + (T_i/T_{mp})^2(T_o/T_{mp}) + (T_i/T_{mp})(T_o/T_{mp})^2 + (T_o/T_{mp})^3]. \tag{33}$$

In nuclear reactor safety studies, the cold environment is at a temperature far below the melting point of UO_2, viz, $T_o/T_{mp} \ll 1$. If we assume the crust layer to be very thin, which is true at least for the case of $M > 0.1$ and $R > 1 \times 10^{10}$ (see Fig. 5), we may approximate T_i by T_{mp}, i.e., we may expect $T_i/T_{mp} \sim 1$. This leads to

$$h_{\text{eff}} \simeq h_{\text{conv}} + \bar{\epsilon}\sigma T_{mp}^3 = h_{\text{ref}}, \tag{34}$$

which is essentially a constant. Thus for $M > 0.1$ and $R > 1 \times 10^{10}$ the present results may be applied directly to reactor safety analysis. For the case of $M < 0.1$ and $R < 1 \times 10^{10}$, however, there may be significant temperature drop across the crust layer so that T_i may be appreciably less than T_{mp}. Hence the variation of h_{eff} with T_i/T_{mp} must be taken into account in estimating the effect of radiative losses on the oscillatory behavior of the crust formation process. In this case, the reference value of h_{eff}, namely, h_{ref}, may be conveniently used in defining the parameter N as well as the various dimensionless variables given by equation (11). Also, an effective heat transfer coefficient may be introduced for the crust-free regime. This is

$$\tilde{h}_{\text{eff}} = \tilde{h}_{\text{conv}} + \bar{\epsilon}\sigma T_{mp}^3[(T_i/T_{mp})^3 + (T_i/T_{mp})^2(T_o/T_{mp}) + (T_i/T_{mp})(T_o/T_{mp})^2 + (T_o/T_{mp})^3]. \tag{35}$$

Note that in the crust-free case, the interface temperature must be larger than or equal to the melting temperature, i.e., $T_i/T_{mp} \geq 1$. Thus we have $\tilde{h}_{\text{eff}} \geq \tilde{h}_{\text{conv}} + \bar{\epsilon}\sigma T_{mp}^3$. This is in contrast to the crust-covered case where $T_i/T_{mp} \leq 1$ and $h_{\text{eff}} \leq h_{\text{conv}} + \bar{\epsilon}\sigma T_{mp}^3$. It follows that the condition, $\tilde{h}_{\text{eff}} > h_{\text{eff}}$, is satisfied automatically if $\tilde{h}_{\text{conv}} > h_{\text{conv}}$. Clearly, in the presence of surface radiation, the oscillatory behavior of the system is also a function of a radiation parameter defined by

$$V = \bar{\epsilon}\sigma T_{mp}^3/h_{\text{ref}}, \tag{36}$$

where h_{ref} is given by equation (34).

Numerical calculations have been made for the base case (i.e., $V = 0$) and for the case of $V = 0.5$.[15] The results are: $\Delta_{\max} \sim 11$, $\tau_{\text{crust}} \sim 64$, and $\tau_{\text{free}} \sim 8$ for the combined convection-radiation case. The results for the corresponding purely convection case are: $\Delta_{\max} \sim 7.2$, $\tau_{\text{crust}} \sim 43$, and $\tau_{\text{free}} \sim 14$. Obviously, radiative heat loss tends to increase the crust lifetime and the crust thickness whereas it tends to shorten the crust-free period. It should be noted that, for a large value of V, different conditions for the occurrence of thermal oscillations may be resulted over different temperature ranges.

7 Conclusions

An approximate theory has been developed to describe the transient behavior of a liquid layer heated internally at high Rayleigh number and cooled to freezing from above. It is demonstrated that for $S < NP < 1$, single-period self-sustained oscillations may occur in the system. The oscillatory behavior, when exists, is independent of the initial liquid temperature and crust conditions. Except for some limiting cases which meet the criterion given by equation (28), the first-order, linear-temperature-profile approximation is in general not valid. Hence a second-order solution is often required.

Within the framework of this study, the gross properties of the crust-covered and the crust-free regimes, namely, $\theta_{\max}$, $\Delta_{\max}$, τ_{crust}, and τ_{free} are functions of M and R as well as N, P, and S. The important effects of these five independent, controlling parameters have been illustrated. The case of combined convection and radiation heat transfer at the top surface has also been discussed. Although we have limited ourselves primarily to the case of constant heat transfer coefficients for top cooling, the present approach should apply to the

---

[15] This corresponds to the case in which the rate of radiative loss is about the same as the convective cooling rate, i.e., $\bar{\epsilon}\sigma\ T_{mp}^3 = h_{\text{conv}}$.

case of variable coefficients as well. Results of this study may prove valuable in providing useful guidance to future experimental developments in this area.

References

1 Baker, L., Cheung, F. B., et al., "Postaccident Heat Removal in Fast Reactors," ANL/RAS 75-44, Argonne National Laboratory, 1975.

2 Welander, P., "Observation of Oscillatory Ice States in a Simple Convection Experiment," *Journal Geophysical Research*, Vol. 82, 1977, pp. 2591–2592.

3 Welander, P., "Thermal Oscillations in a Fluid Heated from Below and Cooled to Freezing from Above," *Dynamics Atmospheres and Oceans*, Vol. 1, 1977, pp. 215–223.

4 Cheung, F. B., "Turbulent Natural Convection in a Horizontal Fluid Layer with Time Dependent Volumetric Energy Sources," AIAA/ASME Thermophysics and Heat Transfer Conf., Palo Alto, Paper No. 78-HT-6.

5 Cheung, F. B., "Correlation Equations for Turbulent Thermal Convection in a Horizontal Fluid Layer Heated Internally and from Within," ASME JOURNAL OF HEAT TRANSFER, Vol. 100, 1978, pp. 416–422.

6 Shvets, M. E., "Approximative Theory of Ice Accretion," *Meterologiya i gidrologiya*, No. 5, 1949, pp. 78–87.

7 Efroimson, V. O., "Calculation of Ice Accretion," *Meterologiya i gidrologiya*, No. 8, 1977, pp. 32–42.

8 Epstein, M., "Stability of a Submerged Frozen Crust," ASME JOURNAL OF HEAT TRANSFER, Vol. 99, 1977, pp. 527–532.

9 Cheung, F. B., "The Boundary Layer Behavior in Transient Turbulent Thermal Convection Flow," ASME JOURNAL OF HEAT TRANSFER, Vol. 102, 1980, pp. 373–375.

10 Kulacki, F. A., and Emara, A. A., "Steady and Transient Thermal Convection in a Fluid Layer with Uniform Volumetric Energy Sources," *Journal Fluid Mechanics*, Vol. 83, 1977, pp. 375–395.

11 Keyhani, M., and Kulacki, F. A., "An Experimental Study of Turbulent Thermal Convection with Time Dependent Volumetric Energy Sources," NUREG/CR-1173, U.S. Nuclear Regulatory Commission, 1979.

Transient Simultaneous Heat and Mass Transfer in Moist, Unsaturated Soils

J. G. Hartley
Assistant Professor.

W. Z. Black
Professor.

School of Mechanical Engineering,
Georgia Institute of Technology,
Atlanta, Ga. 30332

The transient heat and mass transfer in a moist porous medium adjacent to a cylindrical heat source is analyzed in order to characterize the thermal stability of the medium. In the context of this paper, thermal instability occurs in a moist porous medium as a result of significant drying due to excessive thermally induced moisture movement. A dry zone is created which propagates into the medium and thereby inhibits dissipation of heat from the source. The drying of the porous medium adjacent to the heat source is predicted to occur in two distinct stages. During the first stage the rate of moisture movement initially decreases until a "critical moisture content" is reached. Thereafter the drying rate generally increases until complete drying of the material in the vicinity of the heat source has occurred. The value of the critical moisture content is found to be essentially independent of the strength (heat transfer rate per unit length) of the heat source. The parameters which most significantly influence the transport processes are identified and correlated on the basis of numerical solutions of the governing equations. The critical moisture content and critical heat flux are defined and used to quantify thermal stability limits. The correlations are validated through comparison with experimental measurements made on a native soil. The thermal stability model developed in this work establishes the relationship between the thermal stability limits for large-diameter and small-diameter heat sources. From this relationship the thermal stability associated with large-diameter sources can be accurately predicted from experimental measurements using small-diameter sources and small samples.

Introduction

The process of simultaneous heat and mass transfer in soils is of practical interest in a variety of engineering applications. These include heat dissipation from underground electrical power cables, heat transfer to and from buried heat pump coils, recovery of geothermal energy, and waste heat rejection from power plant condenser water used to extend the growing season in cold regions, as well as important civil engineering and agricultural applications.

Heat transfer in soils is complicated by the presence of solid, liquid and gaseous phases. Thermal gradients in a moist soil can induce moisture movement which, in turn, can result in a decrease in the thermal conductivity of the soil in contact with the heat source. If the thermally induced moisutre movement is significant the development of a dry zone adjacent to the heat source creates an insulating layer which further inhibits dissipation of heat from the source. In underground electrical cable installations, this phenomenon can result in so-called "thermal instability." The ability to identify the precise conditions under which significant moisture migration will occur is extremely important, particularly when the heat source is required to transfer large amounts of heat, as in the case of underground electrical cables and buried heat pump coils.

Experimental and analytical studies have been conducted in the past in an effort to characterize moisture movement under thermal gradients. Important parameters identified in these studies which can result in significant moisture migration include the initial moisture content of the soil [1–6]; the surface temperature of the heat source [7]; the heat flux at the surface of the source [8, 9]; and soil properties such as grain size, size distribution and density. However, a comprehensive analysis of the parameters which influence thermal stability has yet to be developed.

This work is subdivided into two phases. The first phase consists of formulating the conservation equations for simultaneous heat and mass transfer in a homogeneous, isotropic porous medium. The governing equations are nondimensionalized, and an order-of-magnitude analysis is performed to determine those dimensionless groups which have the most significant effect on the heat transfer and moisture movement in the soil surrounding the heat source. An implicit, finite difference scheme is used to solve the governing equations for transient temperature and moisture content distributions. The second phase consists of correlating the results of the analysis so that the conditions which lead to significant moisture migration away from the heat source in soils can be predicted. The results of the analysis are compared with experimental measurements.

Although the results here are applied to simultaneous heat and mass transfer in a soil, the equations and technique of identifying critical or dominant parameters that limit the transport processes apply equally well to any moist, unsaturated porous medium.

Mathematical Model

The buried heat source is modeled by a constant heat flux cylindrical surface of finite diameter surrounded by an infinite, homogeneous, unsaturated porous medium. The transient mathematical formulation in cylindrical coordinates has rotational and axial symmetry since the effects of gravity, surface phenomena (e.g. heat flux and moisture movement at the earth's surface) and location of the water table are neglected in the analysis. In the formulation of the model it is assumed that, under the influence of the constant heat flux, monotonic drying of the soil predominates so that hysteretic characteristics of the soil are not significant.

These assumptions have been made in an effort to focus attention on the dominant characteristics of the heat source and the surrounding medium. One of the objectives of current research at Georgia Institute of Technology under the sponsorship of the Electric Power Research Institute is to assess the influence of surface phenomena and the presence of a water table on the model prediction presented here.

The analytical model of simultaneous heat and mass transfer in soil is based on the equations of conservation of mass and conservation of energy together with expressions for the mass and energy fluxes. Derivation of the governing and supporting equations is lengthy and only the major results are presented here. Details of the analysis can be found in [10].

Contributed by the Heat Transfer Division for publication in The JOURNAL OF HEAT TRANSFER. Manuscript received by the Heat Transfer Division September 22, 1980.

The equation of conservation of mass for the soil moisture is [11]

$$\frac{\partial \theta}{\partial t} = -\nabla \cdot \left(\frac{\mathbf{j}_m}{\rho_2}\right) \tag{1}$$

Similarly, the conservation of energy equation is [10]

$$\left[C + u_{21}(\epsilon - \theta)\frac{\partial \rho_1}{\partial T}\right]\frac{\partial T}{\partial t} + \left[u_{21}(\epsilon - \theta)\frac{\partial \rho_1}{\partial \theta} - \rho_1 u_1\right]\frac{\partial \theta}{\partial t} = \nabla \cdot (k\nabla T) - \nabla \cdot (h_{21}\mathbf{j}_1) - \mathbf{j}_m \cdot \nabla h_2 \tag{2}$$

Liquid Flux. The mass flux of liquid in an unsaturated porous medium is governed by the modified Darcy's law [12]

$$\mathbf{j}_2 = -\rho_2 K_2 \nabla \Phi \tag{3}$$

where K_2 is the unsaturated hydraulic conductivity and Φ is the total soil potential. The total soil potential reduces to $\Phi = \psi$ when the effects of gravity are neglected.

The hydraulic conductivity and the soil potential are functions of temperature and moisture content. Therefore it is desirable to rewrite equation (3) as the sum of fluxes due to gradients of temperature and moisture content.

The result, in the notation of Klute [13] and Philip [14], is

$$\frac{\mathbf{j}_2}{\rho_2} = -(D_{\theta l}\nabla \theta + D_{Tl}\nabla T) \tag{4}$$

Vapor Flux. The appropriate form of Fick's law which describes the mass flux of vapor in the porous medium is [15]

$$\mathbf{j}_1 = -\rho D_{13}\nabla(\rho_1/\rho) \tag{5}$$

Here D_{13} is the modified molecular diffusivity of water vapor in air

$$D_{13} = a(\epsilon - \theta_2)D_a$$

This represents the product of the molecular diffusivity of water vapor in air, D_a, the volumetric air content of the medium, $\epsilon - \theta_2$, and a tortuosity factor, a.

Assuming ideal gas behavior for the water vapor, air and water vapor-air mixture equation (5) can be written in terms of ρ_1 and T as

$$\mathbf{j}_1 = -\frac{\nu D_{13}}{T}\nabla(\rho_1 T)$$

where $\nu = M_3/M$.

The density of the water vapor may be written as

$$\rho_1 = h\rho_s \tag{6}$$

where ρ_s is the density of saturated water vapor, a function of temperature only, and h is the relative humidity of the porous medium which Philip and de Vries [16] have shown to be largely independent of temperature, being determined mainly by the moisture content.

With this result it is possible, as in the case of the liquid flux, to express the vapor flux as the sum of fluxes due to gradients of temperature and moisture content,

$$\mathbf{j}_1/\rho_2 = -(D_{\theta v}\nabla \theta + D_{Tv}\nabla T) \tag{7}$$

Thus the governing differential equations, in terms of the temperature and volumetric moisture content of the soil are

$$\frac{\partial \theta}{\partial t} = \nabla \cdot (D_\theta \nabla \theta + D_T \nabla T) \tag{8}$$

and

$$\left[C + u_{21}(\epsilon - \theta)h\frac{\partial \rho_s}{\partial T}\right]\frac{\partial T}{\partial t} + \left[u_{21}(\epsilon - \theta)\rho_s\frac{\partial h}{\partial \theta} - \rho_1 u_1\right]\frac{\partial \theta}{\partial t} = \nabla \cdot [(k + \rho_2 h_{21} D_{Tv})\nabla T] + \nabla \cdot (\rho_2 h_{21} D_{\theta v}\nabla \theta) + \rho_2 c_2(D_\theta \nabla \theta + D_T \nabla T)\cdot \nabla T \tag{9}$$

Boundary Conditions. The boundary conditions for the problem under consideration consist of the following:

1 The temperature and moisture content of the soil very far removed from the heat source are constant and equal to the initial values, or

$$T(r, t) = T_i \text{ as } r \rightarrow r_\infty \tag{10}$$

$$\theta(r, t) = \theta_i \text{ as } r \rightarrow r_\infty \tag{11}$$

2 The surface of the heat source is assumed to be impermeable to moisture so that the net flux of moisture at the surface, r_c, is zero.

$$\mathbf{j}_m = -\rho_2(D_\theta \nabla \theta + D_T \nabla T) = 0 \text{ at } r = r_c \tag{12}$$

3 The heat transfer rate per unit length of the heat source, q', is specified at the surface and is related to the heat flux at the surface by

$$q' = 2\pi r \mathbf{q}'' \text{ at } r = r_c \tag{13}$$

and $\mathbf{q}''$ is given by

$$\mathbf{q}'' = -k\nabla T + h_1\mathbf{j}_1 + h_2\mathbf{j}_2 = -k\nabla T + h_{21}\mathbf{j}_1 + h_2\mathbf{j}_m$$

At the surface, $r = r_c$, the last term in the above equation is zero as a result of equation (12). Substituting the definition of $\mathbf{j}_1$ from equation (7), the heat flux at the surface of the heat source can be expressed as

$$\mathbf{q}'' = -k_e\nabla T - \rho_2 h_{21} D_{\theta v}\nabla \theta$$

where $k_e = k + \rho_2 h_{21} D_{Tv}$ is an "effective" thermal conductivity which includes a contribution due to vapor movement. Therefore:

Nomenclature

a = tortuosity factor
c = specific heat, (J/kg K)
C = volumetric specific heat, (J/m^{3}K)
D_a = molecular diffusivity of water vapor in air = (2.17×10^{-5}) (P_0/P) $(T/T_0)^{1.25}$, (m^2/s)
D_T = thermal moisture diffusivity = $D_{Tl} + D_{Tv}$, (m^2/s K)
D_{Tl} = thermal liquid diffusivity $= K_2 \left.\frac{\partial \psi}{\partial T}\right)_\theta$, (m^2/s K)
D_{Tv} = thermal vapor diffusivity $= \frac{\nu h D_{13}}{\rho_2 T}\frac{d(\rho_s T)}{dT}$, (m^2/s K)
D_θ = isothermal moisture diffusivity $= D_{\theta l} + D_{\theta v}$, (m^2/s)
$D_{\theta l}$ = isothermal liquid diffusivity $= K_2 \left.\frac{\partial \psi}{\partial \theta}\right)_T$, (m^2/s)
$D_{\theta v}$ = isothermal vapor diffusivity $= \frac{\nu \rho_s D_{13}}{\rho_2}\frac{dh}{d\theta}$, (m^2/s)
D_{13} = modified molecular diffusivity of water vapor in air = $a(\epsilon - \theta_2)D_a$, (m^2/s)
Fo = Fourier number = $\frac{\alpha_d t}{r_c{}^2}$
h = enthalpy, with subscript, (J/kg)
h = relative humidity, without subscript
$\mathbf{j}$ = mass flux of moisture, (kg/m^{2}s)
k = thermal conductivity, (W/m K)
K = unsaturated hydraulic conductivity, (m/s)
Ko = Kossovich number = $2\pi u_{21}\rho_2 \epsilon \alpha_d/q'$
Le = Lewis number = α_d/D_θ
Le* = Lewis number based on vapor diffusivity = $\alpha_d/D_{\theta v}$
M = apparent molecular weight of air-water vapor mixture
M_3 = molecular weight of air
Pn = form of Posnov number = $q'D_T/(2\pi k_d \epsilon D_\theta)$
P_0 = reference pressure = 1 atm
q' = heat transfer rate per unit length, (W/m)
$\mathbf{q}''$ = heat flux, (W/m^2)
r = radial coordinate, (m)

$$q' = -2\pi r\left[k_e \frac{\partial T}{\partial r} + \rho_2 h_{21} D_{\theta v} \frac{\partial \theta}{\partial r}\right] \text{ at } r = r_c \tag{14}$$

In order to evaluate the significance of the individual terms in the governing equations, the equations are nondimensionalized and an order-of-magnitude analysis is performed. The moisture content is normalized with respect to the porosity, ϵ,

$$\Theta = \frac{\theta}{\epsilon}$$

and the temperature is nondimensionalized as

$$T^* = \frac{2\pi k_d}{q'}(T - T_i)$$

The radial coordinate, r, is nondimensionalized with respect to r_c,

$$R = \frac{r}{r_c}$$

and the time is nondimensionalized with a Fourier number defined as

$$\mathrm{Fo} = \frac{\alpha_d t}{{r_c}^2}$$

Since only radial variations are considered terms such as $\nabla\cdot(K\nabla(\,))$ reduce to

$$\nabla^* \cdot (K\nabla^*(\,)) = {r_c}^2/\nabla \cdot (K\nabla(\,)) = \frac{1}{R}\frac{\partial}{\partial R}\left(RK\frac{\partial(\,)}{\partial R}\right)$$

With these definitions, equations (8) and (9) can be written in dimensionless form as

$$\frac{\partial \Theta}{\partial \mathrm{Fo}} = \nabla^*\left(\frac{1}{\mathrm{Le}}\nabla^*\Theta + \frac{\mathrm{Pn}}{\mathrm{Le}}\nabla^* T^*\right) \tag{15}$$

and

$$\begin{aligned}\left(\frac{C}{C_d} + \frac{\mathrm{Ko}\beta}{\epsilon}\right)\frac{\partial T^*}{\partial \mathrm{Fo}} + \mathrm{Ko}\,\eta\,\frac{\partial \Theta}{\partial \mathrm{Fo}} \\ = \nabla^*\cdot\left(\frac{k_e}{k_d}\nabla^* T^*\right) + \nabla^*\cdot\left(\frac{\mathrm{Ko}}{\mathrm{Le}^*}\nabla^*\Theta\right) \\ + \delta\left(\frac{1}{\mathrm{Le}}\nabla^*\,\Theta + \frac{\mathrm{Pn}}{\mathrm{Le}}\nabla^* T^*\right)\cdot\nabla^* T^*\end{aligned} \tag{16}$$

Some of the dimensionless groups which appear in equations (15) and (16) are the Lewis number based on the isothermal moisture diffusivity, Le; the Lewis number based on the isothermal vapor diffusivity, Le*; the Kossovich number [11], Ko; and a form of the Posnov number [11] based on the thermal and isothermal moisture diffusivities, Pn (see nomenclature for definitions).

An in depth order-of-magnitude analysis applied to the energy equation (see reference [10] for details) leads to the following simplified forms of equations (15) and (16)

$$\begin{aligned}\frac{C}{C_d}\frac{\partial T^*}{\partial \mathrm{Fo}} = \nabla^*\cdot\left(\frac{k_e}{k_d}\nabla^* T^*\right) + \nabla^*\cdot\left(\frac{\mathrm{Ko}}{\mathrm{Le}^*}\nabla^*\Theta\right) \\ + \delta\left(\frac{1}{\mathrm{Le}}\nabla^*\,\Theta + \frac{\mathrm{Pn}}{\mathrm{Le}}\nabla^* T^*\right)\cdot\nabla^* T^*\end{aligned} \tag{17}$$

and

$$\frac{\partial \Theta}{\partial \mathrm{Fo}} = \nabla^*\left(\frac{1}{\mathrm{Le}}\nabla^*\Theta + \frac{\mathrm{Pn}}{\mathrm{Le}}\nabla^* T^*\right) \tag{18}$$

for the low moisture contents and

$$\frac{C}{C_d}\frac{\partial T^*}{\partial \mathrm{Fo}} = \nabla^*\cdot\left(\frac{k_e}{k_d}\nabla^* T^*\right) + \frac{\delta}{\mathrm{Le}}\nabla^*\Theta\cdot\nabla^* T^* \tag{19}$$

and

$$\frac{\partial \Theta}{\partial \mathrm{Fo}} = \nabla^*\cdot\left(\frac{1}{\mathrm{Le}}\nabla^*\Theta\right) \tag{20}$$

for the high moisture contents.

The dimensionless forms of the initial and boundary conditions are

$$T^* = 0 \text{ and } \Theta = \Theta_i \text{ at } \mathrm{Fo} = 0 \text{ for } R \geq 1$$

$$T^* = 0 \text{ and } \Theta = \Theta_i \text{ for } \mathrm{Fo} > 0 \text{ and } R \to \infty$$

$$(\nabla^*\Theta + \mathrm{Pn}\nabla^* T^*)\cdot\hat{n} = 0 \text{ at } R = 1$$

$$\left(\frac{k_e}{k_d}\nabla^* T^* + \frac{\mathrm{Ko}}{\mathrm{Le}^*}\nabla^*\,\Theta\right)\cdot\hat{n} = 1 \text{ at } R = 1$$

Therefore, in general, the functional dependence of the dimensionless temperature rise is primarily of the form

$$T^* = T^*\left(\mathrm{Fo}, R, \frac{C}{C_d}, \frac{k_e}{k_d}, \delta, \mathrm{Le}, \frac{\mathrm{Ko}}{\mathrm{Le}^*}, \mathrm{Pn}, \Theta_i\right)$$

and a similar functional expression exists for the dimensionless moisture content.

Experimental Apparatus and Techniques. Evaluation of the thermal and hydraulic properties appearing in equations (8) and (9) requires experimental determination of the thermal conductivity, the hydraulic conductivity and the soil moisture characteristic over the entire range of moisture contents. Two soils, Plainfield sand and a sandy silt soil commonly encountered in the southeastern United States, were chosen for this study. The values for Plainfield sand were available in the literature from Jury [17]. The properties of the sandy silt were measured by Bush [18] in an associated project. The properties for both soils are presented in graphical form in reference [10].

The soil moisture characteristic curve, ψ versus θ, was developed

Nomenclature Continued

R = dimensionless position variable = r/r_c
t = time, (s)
T = temperature, (K)
T^* = dimensionless temperature $= \dfrac{2\pi k_d(T - T_i)}{q'}$
T_0 = reference temperature = 273 K
u = internal energy, (J/kg)
α = thermal diffusivity, (m^2/s)
β = unnamed dimensionless group $= \dfrac{hq'\,(\epsilon - \theta)\,d\rho s}{2\pi K_d/dT}$
γ = Euler's constant = 0.5772 . . .
ϵ = porosity, (m^2/m^3)
η = unnamed dimensionless group $= \dfrac{(\epsilon - \theta)\,\rho_s\dfrac{dh}{d\theta} - \rho_1 u_1/u_{21}}{\rho_2}$
θ = volumetric moisture content = $\theta_1 + \theta_2$, (m^3/m^3)
θ_1 = volumetric vapor content = $\rho_1(\epsilon - \theta_2)/\rho_2$ (m^3/m^3)
θ_2 = volumetric liquid content
Θ = dimensionless moisture content = θ/ϵ
ν = ratio of molecular weight of air to apparent molecular weight of mixture
ρ = density, (kg/m^3)
ϕ = total soil moisture potential, (m of H_2O)
ψ = capillary moisture potential, (m of H_2O)

Subscripts

1 = vapor phase
2 = liquid phase
3 = air
a = atmosphere
c = surface of heat source or cable
crit = critical value
d = dry medium
e = effective value
i = initial value
m = moisture (liquid plus vapor)
o = reference value
p = probe
s = saturated water vapor
T = thermal
θ = moisture

from measurements of soil potential using a pressure membrane apparatus (ASTM D3152-72), a porous plate apparatus (ASTM D2325-68), and tensiometers. Saturated hydraulic conductivity was determined from constant head measurements (ASTM D2434-68), and unsaturated hydraulic conductivity was subsequently calculated using the modified Millington-Quirk method [19].

Thermal conductivity measurements and small-scale thermal stability tests are based on the transient response of a thermal probe [18]. The probe is composed of an 0.24 cm o.d. stainless steel tube (0.25 mm wall thickness, 10 cm long) into which a four-hole, 0.16 cm dia, alumina ceramic tube is inserted. A 20-cm length of Nichrome wire threaded through two holes of the ceramic tube forms the heating element. A precision thermistor is placed in the ceramic tube at the midpoint of the probe length for temperature measurement. All air spaces are filled by vacuum impregnating the interior of the probe with epoxy. The actual heated length of the probe is determined by calibration measurements of thermal conductivity on a standard specimen.

A regulated d-c power supply is used to heat the thermal probe and digital multimeters are used to accurately monitor the power dissipated. Temperature-time data acquisition is controlled by a microprocessor-based instrument developed at Georgia Institute of Technology. This instrument monitors the transient response of the thermal probe, records temperature-time data pairs at selected intervals, performs a straight-line least square fit of the data, calculates the thermal conductivity of the specimen, and evaluates the thermal stability criteria discussed in the next section.

Test specimens for small-scale tests are prepared in sample containers 10 cm in diameter and 15 cm long similar to those described in ASTM D698-70. Large-scale thermal stability tests were conducted by Bush [18] using a short length of full-sized underground power cable buried in a large soil tank (0.91 × 0.91 × 1.8 m).

The density selected for the sandy silt was 1280 kg/m^3. Undisturbed samples of this soil in the southeastern United States are typically 1250 to 1450 kg/m^3. The heat input levels chosen for the stability measurements are representative of heat generation rates experienced with underground electrical power cables. For example, heat generation rates of 50 to 120 W/m are typical for a 230 kV, 2500 kcmil copper pipe-type cable installation while rates of 20 to 60 W/m are typical for a 138 kV, 2000 kcmil aluminum extruded dielectric cable [20]. The highest rate in each of these ranges would correspond to emergency operating conditions. Furthermore, the thermal gradients in the soil surrounding a three-phase circuit using extruded dielectric cables can be as much as three times as high as those experienced with a single cable depending on the spacing between cables in the circuit [20]. Thus the practical range for thermal stability as applied to electrical power cables is 20 to 180 W/m.

Results and Discussion. Solutions to equation (15) and (16) were obtained with an implicit finite difference formulation. Due to the nonlinearity of the governing equations and the temperature and moisture content dependence of the property values, an iterative numerical scheme was employed. Details of the numerical technique are provided in reference [10].

Numerical simulations were conducted with the dimensionless form of the governing equations to determine the influence of the various coefficients and to verify the results of the order-of-magnitude analysis. This was done for the two soils investigated by first reducing the values of the coefficients to zero and then increasing them by an order of magnitude. The thermal and hydraulic property values for the sandy silt and Plainfield sand were used.

Various initial moisture contents and surface heat transfer rates were used in the numerical simulations. The results [10] showed that reducing Ko to zero in equation (16) had no significant effect on either the moisture content distribution or the temperature distribution. Likewise, reducing δ/Le, β or Pn to zero in the energy equation had no significant effect for any conditions tested for either soil. The maximum percent error encountered with the coefficients multiplied by a factor of ten was about ten percent. This is a qualitative measure of the effect of an error in property measurements and is seen to have minimal effect on calculated temperature and moisture content distributions for the conditions tested. These results confirm the major conclusions of the order-of-magnitude analysis.

It should be noted, however, that the calculated moisture content distribution is sensitive to changes in the values of the coefficients appearing in the conservation of mass equation. Numerical simulations indicate that the relative magnitudes of the two coefficients in equation (15) are quite important. The Posnov number, the dimensionless ratio of thermal diffusivity to liquid diffusivity, is a direct measure of the relative magnitudes of the coefficients. For the cylindrical heat source, temperature gradients are generally larger than gradients of moisture content, and a Posnov number near unity or larger results in net migration of moisture away from the heat source.

On the strength of these results the energy equation was simplified to the following form

$$\left(\frac{C}{C_d}\right)\frac{\partial T^*}{\partial \mathrm{Fo}} = \nabla^* \cdot \left(\frac{k_e}{k_d}\nabla^* T^*\right) \tag{21}$$

which is the conduction equation with an effective thermal conductivity that depends upon the moisture content of the soil. Therefore, the energy equation is essentially uncoupled from the conservation of mass equation except for the moisture dependence of the thermal properties. Furthermore, equation (21) and the accompanying boundary conditions indicate that the functional dependence of the dimensionless temperature rise can be approximated by

$$T^* = T^*\left(\mathrm{Fo}, R, \frac{C}{C_d}, \frac{k_e}{k_d}, \Theta_i\right)$$

and for a fixed porosity the dimensionless temperature rise at a fixed location (say $R = 1$) is

$$T^*|_{R=1} = T^*\,(\mathrm{Fo}, \Theta_i)$$

The temperature rise has been nondimensionalized with respect to the heat transfer rate. Thus the actual temperature rise and moisture content change at the surface of the heat source depend primarily on the heat transfer rate, q', the Fourier number, and the initial moisture content for a given soil of fixed porosity. The implication, then is that a common Fourier number exists at which particular temperature and moisture content conditions occur at the surface of heat sources of different radii in the same soil subject to an identical heat transfer rate and initial moisture. In other words, the same temperature and moisture content conditions exist at the actual times, t_c and t_p, corresponding to source radii of r_c and r_p, and these times should be related by the square of the ratio of the radii.

$$\frac{t_c}{t_p} = \left(\frac{r_c}{r_p}\right)^2. \tag{22}$$

The experimental verification of this conclusion is discussed later.

Since the temperature has been normalized with respect to the surface heat transfer rate, a plot of T^* versus ln Fo in a straight line and represents a universal curve for specified initial soil conditions in the absence of property variations caused by moisture movement. This, of course, is the same as the well-known long-time probe solution [21],

$$T - T_i = \frac{q'}{4\pi k}\left[\ln\left(\frac{4\alpha t}{r^2}\right) - \gamma\right] \tag{23}$$

Typical numerical simulations for sand are shown in Fig. 1. The slope of the straight-line portion of the curve is inversely proportional to thermal conductivity of the soil evaluated at the initial conditions. As the soil begins to dry next to the heat source, the curve deviates from this straight line. When the soil adjacent to the heat source is completely dry, a second straight-line portion with a steeper slope is achieved. The slope of the steeper line is inversely proportional to the thermal conductivity of the dry soil. In both instances, the thermal conductivity can be calculated by applying the simple probe solution.

Figure 1 shows that significant drying occurs at smaller values of the Fourier number as the surface heat transfer rate is increased. The

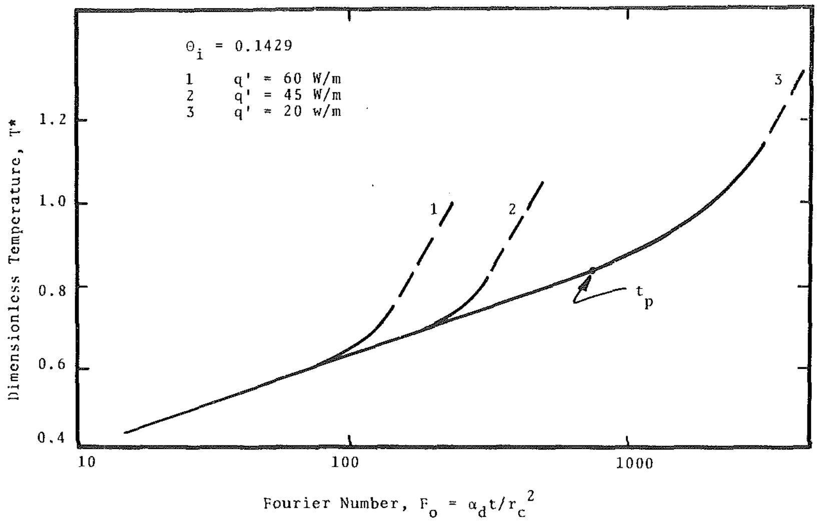

Fig. 1 Typical dimensionless temperature-time response for Plainfield sand

characteristic behavior shown in this figure makes it possible to identify the presence or absence of thermal instability. The onset of thermal instability for each heat transfer rate is coincident with the time at which the transient temperature rise at the surface of the heat source deviates significantly from the initial straight line response.

From the standpoint of drying of the medium, examination of the variation in the rate of moisture movement at the surface of the heat source reveals some distinguishing characteristics. Typical computer predictions for the sandy silt with different heat transfer rates are shown in Fig. 2. These results show that a distinct minimum rate of moisture movement was achieved for each value of the surface heat transfer rate. The magnitude of this minimum value decreases with decreasing surface heat transfer rate, but the minimum value occurs at essentially the same surface moisture content regardless of the heat transfer rate. Furthermore, the value of the moisture content, Θ_{crit}, at which the minimum rate of moisture movement occurs is a function of soil type and it shows a general decrease as the initial moisture content of the medium decreases as indicated in Fig. 3.

The behavior depicted in Fig. 2 can be explained qualitatively in the following manner. If one considers the simplified form of the governing equations (15) and (21), an exact solution can be obtained using the method of Smirnov [23] for the constant property case. From this solution the rate of change of moisture can be expressed as

$$\frac{\partial\Theta}{\partial\mathrm{Fo}} = -\frac{\mathrm{Pn}}{2(k_e/k_d)\mathrm{Fo}} \qquad (24)$$

for Fo ≫ 1. This indicates that the rate of moisture movement at the surface of the heat source would decrease continuously as time progressed provided that the property values remained constant. However, in soils and other porous media the thermal conductivity decreases gradually but the value of Pn changes approximately exponentially with moisture content as the soil dries out due to moisture content decreases for moisture contents above about $\Theta = 0.2$ for the sandy silt and about $\Theta = 0.05$ for the Plainfield sand. Below these values Pn begins to decrease exponentially as the moisture content decreases. The value of Pn is also directly proportional to the heat transfer rate q'. Thus, viewing equation (24) as a quasi-steady decription of the soil behavior, the rate of moisture movement should be expected to decrease initially as time progresses. As the soil dries out due to this moisture movement the increase in the value of Pn could eventually become large enough to overcome the tendency of the rate of moisture movement to decrease with time according to equation (24). Should this occur the rate of moisture movement would reach a minimum and subsequently begin to increase as depicted in Fig. 2, and the onset of thermal instability would be clearly evident. Two other possibilities also exist. First, if the heat flux is sufficiently high the rate of moisture movement could be rapid enough that the critical moisture content is reached almost immediately and the rate of moisture movement would continue to increase. Second, the heat flux could be sufficiently low that very small moisture movement rates would substantially lengthen the time to reach the critical moisture content.

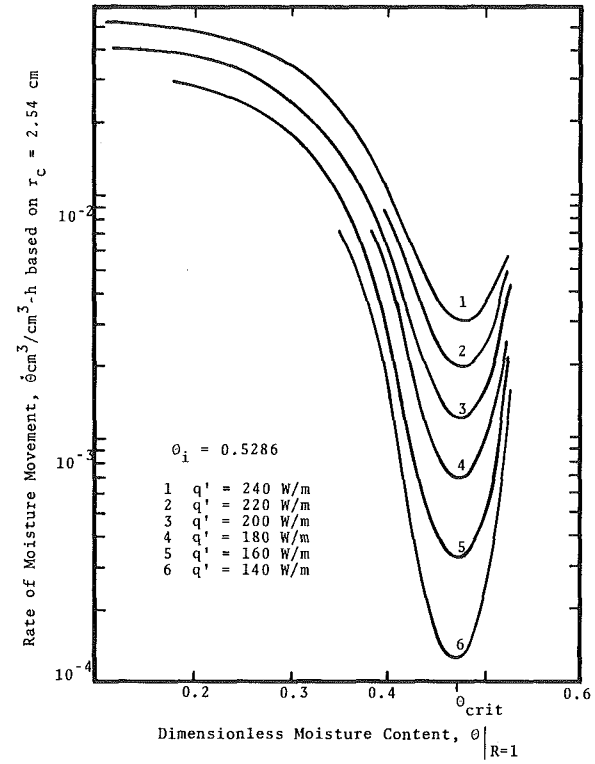

Fig. 2 Rate of moisture movement at heat source surface for sandy silt

This interpretation indicates that the thermal stability of a soil is strongly dependent on the behavior of Pn which includes the strength, q', of the heat source and the ratio of the thermal- and isothermal-moisture diffusivities.

Since the critical moisture content is essentially independent of the surface heat transfer rate, it is possible to determine the value of the Fourier number at which Θ_{crit} occurs for various surface heat transfer rates as shown in Fig. 4. This Fourier number increases as the surface heat transfer rate is decreased. The curves in Fig. 4 exhibit the same trend predicted by the quasi-steady analysis of the rate of moisture movement. That is, for a sufficiently low surface heat transfer rate the time to reach Θ_{crit} becomes very large. The limiting value is called the critical heat transfer rate, q'_{crit}, and it is a function of the initial moisture content for a given soil of specified porosity.

When the surface heat transfer rate is maintained above the value of q'_{crit} the rate of moisture movement continually decrease until Θ_{crit} is reached. Thereafter, the rate of moisture movement increases continuously until the soil adjacent to the source is completely dry, provided that a constant surface heat transfer rate is maintained. Under these conditions the soil is thermally unstable. If the surface heat transfer rate is maintained below the critical value, q'_{crit}, the rate of moisture movement decreases continuously and complete drying of the soil is not expected to occur for a very long time. In this case, the soil is thermally stable. Experimental verification of the computer generated initial drying times has been obtained by Drew [22] using the thermal probe.

With these results it is possible to predict when significant drying will commence if the surface heat transfer rate is specified. Or, alternately, for a given soil with known initial moisture content one could prescribe the surface heat transfer rate q'_{crit}, below which the soil will remain thermally stable. The surface temperatures calculated based on the moisture content Θ_{crit} would therefore predict conservative values which would not be exceeded during operation (e.g. an electrical cable) if the surface heat transfer rate is maintained below q'_{crit}.

The numerical results for the sand showed the same trends as those of the sandy silt. Experimental verification for the model predictions based on the sandy silt has been achieved with both large-scale and small-scale experiments. The large-scale experiment was conducted by Bush [24] using a 1.83 m length of heated cable (2.54 cm outside radius) buried in a large soil tank. The soil had a dry density of 1280 kg/m^3 (80 lb/ft^3) with an initial moisture content of about 21 percent by dry weight (Θ_i = 0.53), and two experiments were conducted. In the first, the surface heat transfer rate was maintained at approximately 43.3 W/m for about 400 hours (Fo = 1000). At the end of the test moisture measurements showed that no discernable moisture movement occurred at the cables surface. Figure 4 indicates that this heat transfer rate is well below q'_{crit} for the prevailing initial moisture content, so that significant differences in the surface moisture content should not be expected.

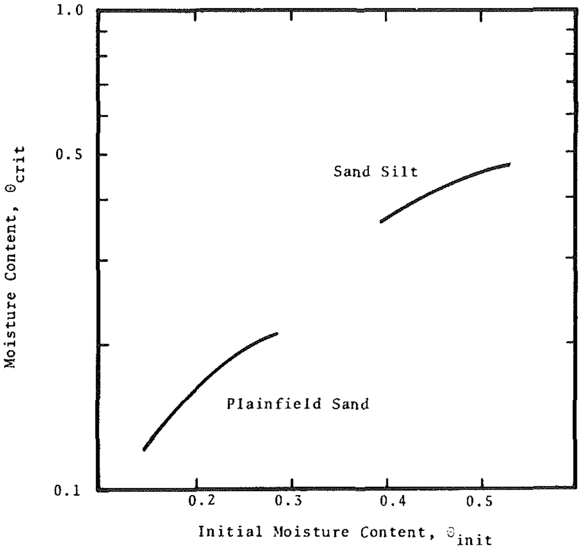

Fig. 3 Dependence of Θ_{crit} on initial moisture content

The surface heat transfer rate for the second test [24] was selected such that significant moisture movement would occur. Therefore, 177 W/m was used and was maintained constant for about 20 hours at which time it increased to an average value of 195 W/m. Fig. 4 shows that for a heat transfer rate of 195 W/m, q'_{crit} is exceeded and Θ_{crit} = 0.475 (19 percent moisture by dry weight) should be reached at a Fourier number of about 95 (37 hr). The moisture content near the cable surface measured by Bush [24] was 19.9 percent by dry weight at 33 hr and 18.3 percent at 53 hr. Additional information concerning the experimental verification can be found in reference [18].

Small scale experiments have also been used for thermal stability measurements on the sandy silt. These measurements were conducted by Drew [22] using a thermal probe (0.24 cm dia). Power inputs to the probe were selected such that drying would occur and drying of the specimen was visibly evident in each case. The results of several tests on the sandy silt with a dry density of 1280 kg/m^3 (80 lb/ft^3) are shown in Fig. 4. The experimental results agree remarkably well with the computer predictions.

As indicated previously, the thermal conductivity of the moist soil can be determined (using equation (23)) from the initial straight line portion of the temperature-time response of a thermal probe such as is shown in Fig. 1. If the power input to the probe is above q'_{crit} for the initial moisture content of the soil drying will occur and a second straight line will eventually be established. Since the thermal response of the cylindrical probe is most influenced by the soil adjacent to it, the second straight line portion of the probe response can be used to determine the thermal conductivity of the dry soil. For example, a thermal probe measurement [22] on a sample of the sandy silt at 1280 kg/m^3 with and initial moisture content of 15.9 percent by dry weight (Θ = 0.3984) indicated a thermal conductivity of the moist soil of 1.077 W m^{-1}K^{-1}. For this test the heat dissipation rate was selected such that drying of the soil would occur. Using the secondary straight line portion of the probe response, the thermal conductivity of the dry soil was calculated to be 0.422 W m^{-1} K^{-1}. Independent measurements

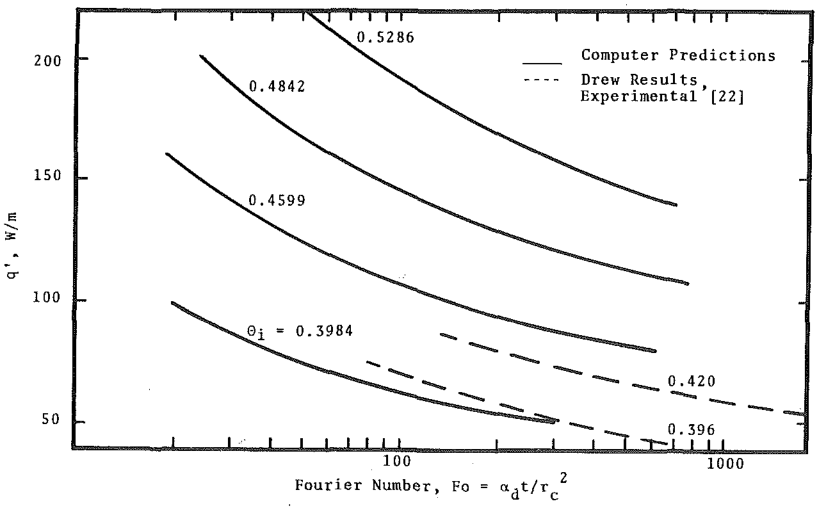

Fig. 4 Fourier number at attainment of Θ_{crit} for sandy silt

by Bush [24] on moist and dry samples of the same soil gave thermal conductivity values of 1.076 W m^{-1} K^{-1} and 0.425 W m^{-1} K^{-1}, respectively.

Thus the model predictions, as verified by these experiments, show that from a single thermal probe test it is possible to:

1 determine the thermal conductivity of the moist soil;

2 determine the thermal conductivity of the dry soil;

3 determine the approximate time for the onset of drying adjacent to the surface of the source; and

4 determine when drying is complete in the soil adjacent to the source;

5 predict the thermal and hydraulic response of soil surrounding a large diameter heat source.

As a practical application of these results one could, for example, survey the soil in a proposed cable route using a needle probe. By examining the temperature-time response of the probe of radius r_p for given heat dissipation rates, the time (e.g., t_p in Fig. 1) required for the onset of significant drying in the soil adjacent to the probe can be determined. The response of a cable with radius r_c buried in the same soil with the same heat dissipation rate would be related to the probe response through the Fourier number as indicated in equation (22). That is, significant drying at the cable would be expected to occur at the time $t_c = t_p(r_c/r_p)^2$. The validity and accuracy of this has been experimentally verified by Bush [18, 24]. If q' is fixed by cable design and the thermal response of the native soil proved unacceptable, the response of the soil at higher densities could be investigated. One could thus determine if proper compaction of the backfill would sufficiently enhance the thermal response of the soil. Otherwise, special backfills or soil additives should be considered. In this manner, thermal stability problems could be avoided.

Conclusions

This analysis of the transient, simultaneous heat transfer and moisture movement in the soil surrounding a cylindrical heat source has shown that:

1 The coupled equations used to describe the temperature and moisture distributions in the soil can be simplified considerably by determining the influence of the dimensionless coefficients. The conduction equation with moisture-dependent thermal conductivity is adequate to determine the temperature distribution.

2 The drying of the soil adjacent to the heat source is predicted to occur in two distinct stages for the conditions examined in this study. During the first stage the rate of moisture movement decreases until a moisture content, Θ_{crit}, is reached after which the rate generally increases until complete drying of the soil adjacent to the heat source has occurred.

3 The value of the moisture content Θ_{crit} is essentially independent of the surface heat transfer rate, and is a function of the initial moisture content of the soil for a given porosity. The magnitude of Θ_{crit} decreases as the initial moisture content decreases.

4 The attainment of Θ_{crit} and the point of accelerated drying predicted by the numerical model agree favorably with experimental observations for one soil.

5 For a given soil (specified porosity and initial moisture content) the model indicates that there is a surface heat transfer rate below which significant drying will be delayed considerably, possibly indefinitely. If the surface heat transfer rate is sufficiently high, a thermal-probe test of a soil sample can provide information concerning the thermal conductivity of the moist soil, the thermal conductivity of the dry soil, the onset of drying at the surface of the probe, and the time when drying at the surface of the probe is complete. From this information, it is possible to predict the behavior of the same soil in the vicinity of a larger buried source because the corresponding times are related through the Fourier number. Thus the results provided by a small diameter thermal-probe test could also be used to predict the thermal stability of the soil heated by a large diameter source.

6 Thermal stability limitations should be considered when the thermal probe method is used to measure the thermal conductivity of a moist sample. Whenever possible, the probe power input should be maintained below q'_{crit} to avoid erroneous results due to significant drying of the sample. With moderately moist samples it is possible that the soil adjacent to the probe can be completely dried before the initial probe transient has passed.

References

1 Adams, J. I., and Baljet, A. F., "Discussion on Influence of Moisture Content of Soil on Buried-Cable Ratings," *Proceedings of IEE*, Vol. iii, 1964, pp. 2081–2095.

2 Bauer, C. A., and Nease, R. J., "Soil Factors Affecting Buried-Pipe-Cable Temperatures," *AIEE Transactions*, pt, III, Vol. 76, 1957, pp. 257–268.

3 Hadley, W. A., and Elsenstadt, R., "A Critical Soil Moisture Condition Affecting Buried Transmission Cables," *Transactions. AIEE*, pt. III, Vol. 72, 1953, pp. 849–851.

4 Radhakrishna, H. A., Chu, F. Y., and Boggs, S. A., "Thermal Instability and Its Prediction in Cable Backfill Soils," *IEEE Transactions on Power Apparatus and Systems*, Vol. PAS-99, No. 3, May/June 1980, pp. 856–863.

5 Milne, A. G., and Mochlinski, K., "Characteristics of Soil Affecting Cable Ratings," *Proceedings of IEE*, Vol. 111, 1964, pp. 1017–1039.

6 Radhakrishna, H. S., "Heat Flow and Moisture Migration in Cable Backfills," *Ontario Hydro Research Quarterly*, Vol. 20, 1968, pp. 10–20.

7 Arman, A. N., Cherry, D. M., Gosland, L., Hollingsworth, P. M., "Influence of Soil-Moisture Migration on Power Rating of Cables in H.V. Transmission Systems," *Proceedings of IEE*, Vol. 111, No. 5, 1964, pp. 1000–1016.

8 Fink. L. H., "Control of the Thermal Environment of Buried Cable Systems," *AEEE Transactions*, 1954, pp. 406–412.

9 Schmill, J. V., "Discussion on Influence of Moisture Content of Soil on Buried-Cable Ratings," *Proceedings of IEE*, Vol. 111, No. 12, 1964, pp. 2081–2095.

10 Hartley, J., "An Analysis of the Thermal Stability of The Soil Environment of Underground Electrical Cables," Ph.D. Thesis, School of Mechanical Engineering, Georgia Institute of Technology, Atlanta, Ga., 1977.

11 Luikov, A. V., *Heat and Mass Transfer in Capillary-Porous Bodies*, Pergamon, Press, London, 1966.

12 Childs, E. C., and Collis-George, N., "The Permeability of Porous Materials," *Proceedings of the Royal Society*, Vol. A201, 1950, pp. 392–405.

13 Klute, A., "The Determination of the Hydraulic Conductivity and Diffusivity of Unsaturated Soils," *Soil Science*, Vol. 113, 1972, pp. 264–276.

14 Philip. J. R., "The Concept of Diffusion Applied to Soil Water," *Proceedings of the National Academy of Science, India*, Vol. 2A, 1955, pp. 93–104.

15 Bird, R. B., Stewart, W. E., and Lightfoot, E. N., *Transport Phenomena*, John Wiley and Sons, New York, 1960.

16 Philip, J. R., and de Vries, D. A., "Moisture Movement in Porous Materials Under Temperature Gradients," *Transactions of the American Geophysical Union*, Vol. 38, 1957, pp. 222–232.

17 Jury, W. A., "Simultaneous Transport of Heat the Moisture Through a Medium Sand," Ph.D. Thesis, Univ. of Wisconsin, 1973.

18 Bush R. A., Black, W. Z., and Martin, M. A., "Soil Thermal Properties and Their Effect on Thermal Stability and the Rating of Underground Power Cables," 7th IEEE/PES Transmission and Distribution Conference and Exposition, Atlanta, Ga. April, 1979.

19 Jackson, R. D., Reginato, R. J., and van Bavel, C. H. M., "Comparison of Measured and Calculated Hydraulic Conductivities of Unsaturated Soils," *Water Resources Research*, Vol. 1, 1965, pp. 375–380.

20 Martin, M. A., Black, W. Z. Bush, R. A. and Hartley, J. G., "Practical Aspects of Applying Soil Thermal Stability Measurements to the Ratings of Underground Power Cables," to be published in *IEEE Transactions on Power Apparatus and Systems*, 1981.

21 Carslaw, H. S., and Jaeger, J. C., *Conduction of Heat in Solids*, Oxford Press, Second Edition, 1959, pp. 261–262.

22 Drew, B. A., "Thermal Stability Measurements Using the Thermal Probe Method," proposed M.S. Thesis, School of Mechanical Engineering, Georgia Institute of Technology Atlanta, Ga., 1981.

23 Smirnov, M. S., "On a System of Differential Equations for Highly Intensive Heat and Mass Transfer," *International Journal of Heat and Mass Transfer*, Vol. 5, 1962, pp. 521–524.

24 Bush, R. A., "Experimental Prediction of Thermal Instability in the Soil Surrounding Underground Power Cables," proposed M.S. Thesis, School of Mechanical Engineering, Georgia Institute of Technology, Altanta, Ga., 1981.

Alon Gany[1]
Research Associate,
Mem. ASME

L. H. Caveny[2]
Senior Professional Staff Member,
Mem. ASME

Mechanical and Aerospace
Engineering Department,
Princeton University,
Princeton, N. J.

J. W. Johnson
Chemist,
Army Materials and Mechanics Research Center,
Watertown, Mass.

Water Vapor Contribution to the Erosion of Steel by High Temperature Flows

Experimental results on the role of water vapor in the mass loss mechanism of steel by hot, high pressure flows are described and interpreted in terms of a surface reaction model. Situations in which highly transient heat transfer and chemical interactions at the gas-metal interface produce erosion of the surface occur in a variety of systems, e.g., gun barrels, gas turbines, vents, nozzles, and furnaces. This research is directed at conditions in which the metal surface temperature remains below the melting point and mass loss is the result of chemical attack. The rate of reaction depends on the unsteady pressure and surface temperature. The study reveals that in high shearing flows, when the build-up of oxide protective layer is limited, surface chemical attack of the steel by water vapor can be the main erosion source in combustion gas atmospheres, and the process is controlled mainly by turbulent transport phenomena.

Introduction

Erosion (i.e., mass loss) and damage produced by high-pressure, hot reactive gases flowing over steel surfaces maintained below the melting point, occur in a variety of situations, e.g., gun barrels, gas turbines, vents, nozzles, and furnaces. Interpretations of the interactions of gas mixtures (in particular, combustion gases) are usually obscured by having to contend with a multitude of possible reactions. Previous studies [1] revealed that when the steel is subjected to heating cycles in which the metal surface achieves the melting point, mass loss is mainly the result of melt and wipe-off, and is dependent on heat transfer to the surface, either by convection or chemical reactions. Under such conditions the contribution of chemical reactions to the overall erosion is via enhancing the surface heating, hence increasing melting rate.

In most practical systems, the metal surface is maintained below the melting temperature. Thus, interest is centered at direct chemical attack as the mass loss mechanism.

Results for high temperature corrosion under low flow conditions or quiescent atmospheres do not apply when very high shearing flows sweep away protective oxide layers. In such cases the metal surface is exposed to heterogeneous chemical attack [1].

Both experimental and theoretical research has been performed to isolate these chemical species which have the potential of attacking steel. The experimental results were obtained using carefully controlled individual gases and gas mixtures in a ballistic compressor. The ballistic compressor increases the gas temperature and pressure (e.g., 3000 K and 350 MPa) and produces high shear flow across the steel specimens for several miliseconds. A detailed description of the apparatus and the experimental approach are given in reference [1]. Thermodynamic investigation based on the free energy and enthalpy changes classify the likelihood of heterogeneous reactions between steel and the various gases (over a range of temperatures) and the heat involved in those reactions. Heat and mass transfer analyses which consider a reacting turbulent boundary layer with surface reactions, indicate that turbulent transport controls the gas-metal interactions.

Both the analysis and the experiments indicate an important role of water vapor in steel erosion. In combustion gas systems, water vapor appears to be the dominant chemical erosion cause. This special role of water vapor in the chemical erosion of steel, subjected to high shearing hot flows of various gas mixtures, was not identified before. A knowledge of the role of water vapor is of considerable significance both in the understanding of the aerothermochemistry processes and in searching for ways to decrease and avoid erosion.

Physical Modeling and Formulation

As has been hypothesized elsewhere [1], under high-pressure, high-speed hot flows the build-up of protective oxide shells on the metal surface is limited and the metal is exposed to heterogeneous chemical attack by reactive species in the flow. The rate of the chemical reactions is dependent on both the transport processes of heat and mass to the surface and on the chemical kinetics of the heterogeneous reactions. Since the chemical kinetic constants depend on the surface temperature, the heat transfer processes both in the gas (boundary layer type) and in the condensed phase (conduction) are significant.

An ideal gas behavior was assumed in the calculations. Thus, some error is introduced when using the following equations. However, in the range of pressures and high temperature considered, deviation from the ideal state is less than 20 percent.

The convective transport rates of both heat and mass from the flow to the metal surface were calculated from boundary layer approximations assuming quasi-steady processes

$$q_g = h(T_r - T_s) \tag{1}$$

$$J_i = (h_m/R_u T)(p_{i,\infty} - p_{i,s}) \tag{2}$$

where the index i represents the ith chemical species. Heat flux inside the metal bulk was approximated by the one-dimensional heat conduction equation. Heating by surface reactions is proportional to the reaction rates which are relative to the reactive species fluxes to the surface,

$$q_{R,i} = J_i(-\Delta H_{R,i}) \tag{3}$$

where $H_{R,i}$ is the enthalpy of the specific reaction between gaseous species i and the metal per mole of reacting gas.

The reaction between water vapor and steel was represented by the reaction of water vapor with iron. This particular reaction in the high temperature range (above 1000 K) is

$$\mathrm{Fe} + \mathrm{H_2O} \underset{k_{\mathrm{rev}}}{\overset{k_f}{\rightleftharpoons}} \mathrm{FeO} + \mathrm{H_2} \tag{4}$$

Since iron and its oxide are condensed phases, the equilibrium constant can be expressed in terms of partial pressures of H_2O and H_2 as follows:

$$K_p \equiv k_f/k_{\mathrm{rev}} = p_{\mathrm{H_2}}/p_{\mathrm{H_2O}} \tag{5}$$

---

[1] Present address: Department of Aeronautical Engineering, Technion, Haifa, Israel.

[2] Present address: Air Force Office of Scientific Research, Bolling AFB, Washington, DC 20332.

Contributed by the Heat Transfer Division for publication in the JOURNAL OF HEAT TRANSFER. Manuscript received by the Heat Transfer Division December 26, 1979.

It can be related to the standard Gibbs free-energy change in this reaction via

$$\Delta G = -R_u T \ln K_p \qquad (6)$$

If all chemical constituents involved in equation (4) are present in sufficient amounts and close contact in the reaction zone (i.e., at the metal surface) the following description for the gas-metal chemical interactions may be suggested. Assuming forward and reverse reactions at the surface the water vapor mass flux balance is

$$J_{H_2O} = k_f p_{H_2O,s} - k_{rev} p_{H_2,s} \qquad (7)$$

where J_{H_2O} is the net mass flux of H_2O from the free stream to the wall. This does not imply that each water molecule arriving at the surface reacts to form oxide. Equations (2, 5) and (7) yield the water vapor concentration at the surface (in terms of partial pressures).

$$p_{H_2O,s} = (H_m/H_m + k_f)p_{H_2O,\infty} + [k_f/K_p(H_m + k_f)]p_{H_2,s} \qquad (8)$$

where $H_m = h_m/R_uT$.

The mass loss rate of the steel is a function of the net mass flux of H_2O, to the surface (see equation (4)) and can be expressed in terms of linear erosion rate:

$$r = J_{H_2O} M/\rho \qquad (9)$$

where M and ρ are the molecular weight and density of the steel (represented by those of iron).

Equations (2) and (8) indicate that the erosion rate is controlled by nonequilibrium processes (i.e., mass transport and chemical kinetics), as well as by concentrations of gaseous species involved in the surface reactions. It can be shown that for very fast chemical kinetics ($k_f \gg H_m$) chemical equilibrium will be approached at the metal surface. The erosion rate will then be the maximum for the given flow conditions and the process will be controlled by the mass transport phenomena. For $k_f \ll H_m$ the process will be chemical kinetic controlled, and the metal consumption rate will be low (as $J_{H_2O} \to 0$). However, not only slow chemical kinetics, but also the reactant concentration ratio can suppress the chemical attack. As indicated by equations (7) and (8), the heterogeneous reaction (equation (2)) will take place if

$$p_{H_2,s}/p_{H_2O,\infty} < K_p \qquad (10)$$

Depending on the shear force and other characteristics of the heating cycle, it is suspected that, under certain extreme conditions, the FeO formed is almost instantaneously wiped off from the metal surface; hence only forward chemical reaction rather than equilibrium process should take place. In such a case the net water vapor flux to the wall will be

$$J_{H_2O} = k_f p_{H_2O,s} \qquad (11)$$

and the water vapor concentration at the surface

$$p_{H_2O,s} = p_{H_2O,\infty}[H_m/(H_m + k_f)] \qquad (12)$$

The limiting cases of a mass transport controlled process (where $k_f \gg H_m$) and chemical kinetics controlled process (for $k_f \ll H_m$) can still apply. However, under such circumstances, the erosion rate as indicated by equation (9) is independent of the hydrogen concentration at the surface, and equation (10) is not valid.

While the chemical equilibrium state between water vapor and steel can be approximated by that of water vapor with iron, and is easily derived from known thermodynamic properties, no data were found on the reaction rates in such regimes where metal is continuously stripped of its oxide and exposed to reactive gas attack. Furthermore, the chemical kinetics may differ from one steel type to another depending on the surface treatment and alloying elements. Thus, under certain conditions, one steel may react vigorously with water vapor while the other resists the chemical attack. With the absence of chemical kinetic data, the equations included in this chapter cannot determine the rate of reaction. However, they do set the limits of the chemical erosion in given conditions.

Results and Discussion

Classification of gas species typical to combustion products according to their reactivity with iron is given in Fig. 1 and Table 1. Data are taken from references [2] and [3]. Figure 1 shows the changes of Gibbs free-energy in various reactions vs the temperature. Note that the tendency of the reaction to occur increases for higher negative values of ΔG. By tendency of reaction we mean the preference of the forward reaction and not the reaction rate which always increases with increasing temperature. Table 1 summarizes the enthalpy and Gibbs free energy changes of the various reactions at a typical high surface temperature (1400 K), as well as the equilibrium states for these reactions.

Oxygen was proven to be extremely reactive with steel under these conditions [1]. However, among the less reactive species available in combustion products mainly H_2O and CO_2 seem to be candidates for attacking the steel surface (see ΔG in Fig. 1 and Table 1), although only the reaction of iron with H_2O is exothermic.

The experiments used individual gases and well-controlled gas mixtures in a ballistic compressor which produced a pulse of high temperature (maximum about 3000 K) and high pressure (up to about 400 MPa). Figure 2(*a*) shows the gas temperature and pressure variations during a typical heating cycle. The compressed gas flowed through a choked cylindrical passage (0.66 mm diam and 2.5 mm long) in the steel specimen (most of the experiments were performed with AISI 4340 steel). The leading edge of the passage was streamlined (by machining a 0.38 mm radius) to reduce contracta effects. Mass loss (measured to 0.01 mg accuracy) by the steel specimen during the test yields the average eroded depth.

The experimental results show no erosion when using pure nitrogen and relatively little erosion for CO_2 and CO. The use of water vapor in various concentrations does, however, show evidence of erosion which systematically increases with increasing the H_2O concentration.

Theoretical calculations of the surface temperature resulting from the heating cycle of Fig. 2(*a*) are shown in Fig. 2(*b*). Metal properties were taken from reference [4]. Also shown in Fig. 2(*b*) is the calculated instantaneous erosion rate when employing an H_2O/N_2 gas mixture (containing 8 percent mole fraction of water vapor). The calculations were made by assuming very fast surface chemical kinetics and by considering a gas-phase mass transfer controlled process. In the calculation, it was hypothesized that significantly rapid reaction takes place above some critical threshold temperature. Experiments performed over a variety of conditions and different heating cycles (with corresponding changes in peak surface temperature) indicate that the calculated threshold temperature should be about 1100 K. Note that

Nomenclature

G = standard Gibbs free energy per kg mole of reacting gas, J
h = heat transfer coefficient, W/m^2 − K
h_m = mass transfer coefficient based on molar concentrations, m/s
H_m = mass transfer coefficient based on partial pressures, kg mol − m − K/J − s
ΔH_R = enthalpy of reaction, J/kg − mol − gas
J = mass flux on molar basis, kg − mol/m^2 − s
k = reaction rate constant
K_p = equilibrium constant based on partial pressures
M = molecular weight, kg/kg − mol
p = pressure, Pa
q = heat flux, W/m^2
r = linear erosion rate, m/s
R_u = universal gas constant, J/kg − mol − k
t = time, s
T = temperature, K
ρ = density, kg/m^3

Subscripts

f = forward chemical reaction
g = gas
i = gaseous chemical species i
r = gas recovery temperature
rev = reverse chemical reaction
R = chemical reaction
s = surface
∞ = free stream conditions

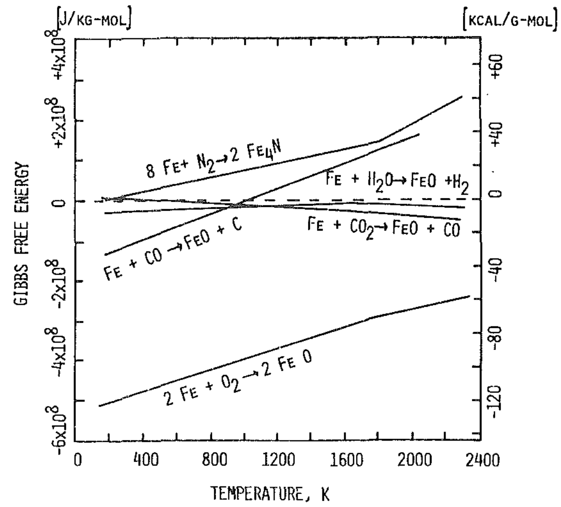

Fig. 1 Gibbs free energy versus temperature for the heterogeneous reactions of iron with various gases

Table 1 Heterogeneous reactions between iron and various gases at high temperature

Reaction	Enthalpy of Reaction ΔH_R [kJ/g-mole gas]	Standard Gibbs free energy at 1400 K ΔG [kJ/g-mole gas]	Theoretical equilibrium at 1400 K
$2\ Fe + O_2 \rightleftarrows 2FeO$	-533	-360	$P_{O_2} = 3.7\cdot10^{-15}$ MPa
$Fe + CO_2 \rightleftarrows FeO + CO$	+36	-20.9	$P_{CO}/P_{CO_2} = 6$
$Fe + CO \rightleftarrows FeO + C$	-143	+57.3	$P_{CO} = 13.9$ MPa
$Fe + H_2O \rightleftarrows FeO + H_2$	-11	-11.7	$P_{H_2}/P_{H_2O} = 2.7$
$8Fe + N_2 \rightleftarrows 2Fe_4N$	-9	+106	$P_{N_2} = 936$ MPa

the mass loss throughout a cycle is an integration of the instantaneous erosion rate with time.

The theoretical curve of the steel mass loss based on the above assumptions was used for comparison to experimental data of ballistic compressor tests over a range of water vapor concentrations (see Fig. 3). The good agreement indicates that the chemical attack of AISI 4340 steel by water vapor is, indeed, very fast, since the erosion obtained under these conditions should approach the theoretical maximum.

Indication of the chemical nature of the erosion can be seen in scanning electron microscope (SEM) photographs of the eroded surface after the test, showing evidence of iron oxide on the surface and no evidence of melting (or mechanical) erosion. However, to study whether quasi-equilibrium state exists at the surface (i.e., reverse reaction as in equation (4) takes place) or only forward reaction occurs, the following investigation was conducted. As indicated by equation (10), if both the forward and reverse surface reactions take place, the chemical attack of the metal should be suppressed when H_2 concentration at the surface is above the critical value determined by the equilibrium constant. Tests were made with AISI 4340 steel specimens exposed to flows composed of mixtures on N_2, H_2 and H_2O in different ratios of p_{H_2}/p_{H_2O}, below and above the critical value (which is approximately 3). Test results did not show distinct differences between the mass loss obtained by flows containing water vapor without hydrogen or those containing water vapor plus hydrogen, even in p_{H_2}/p_{H_2O} ratios of above 3. It is, therefore, concluded that in these special test conditions only the forward chemical reaction (see equation (4)) takes place. Apparently, the reason is the rapid wipe-off of the FeO formed. Indeed, SEM findings of the eroded surface (similar to reference [5]) do not show the existence of a continuous layer or heavy

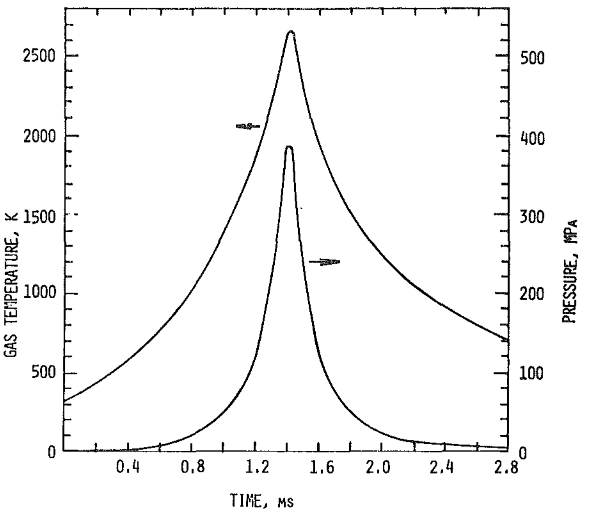

Fig. 2(*a*) A typical experimental heating cycle in the erosion research

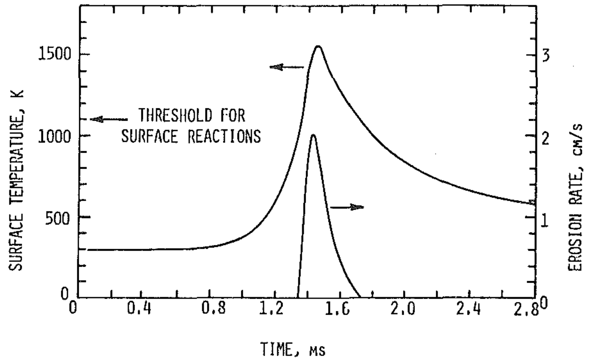

Fig. 2(*b*) Calculated surface temperature and erosion rate transients for the heating cycle of Fig. 2(*a*) employing 8 percent mole fraction of water vapor in H_2O/N_2 mixture

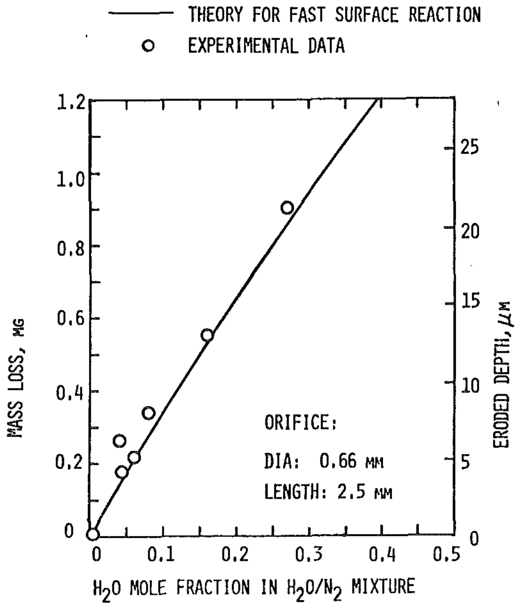

Fig. 3 Erosion of AISI 4340 steel by water vapor, showing good agreement between theory and experiment

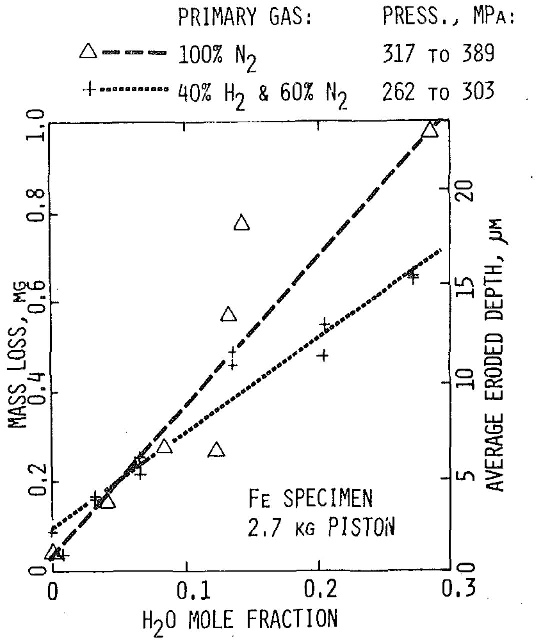

Fig. 4 **Addition of hydrogen tends to reduce the mass loss produced by the higher mole fractions of water vapor**

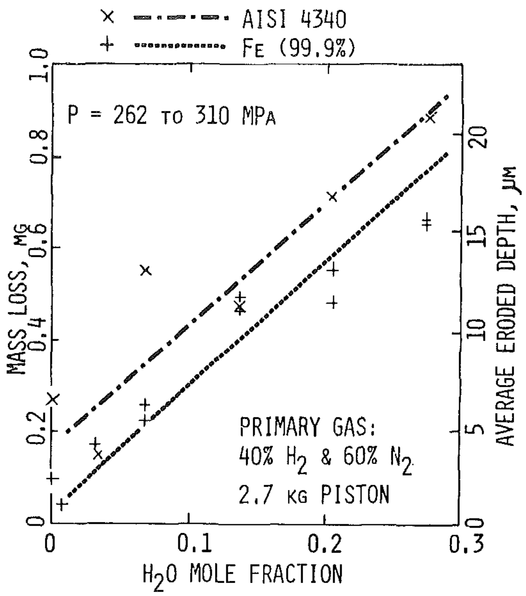

Fig. 5 **Iron tends to experience less mass less than AISI 4340**

deposits of iron oxide. The oxide layers that were observed probably formed during the end of the pressure cycle.

It is believed that suppression of H_2O attack on steel in the presence of H_2 above the critical value indicated by equation (10) may be found in experiments where well-controlled and less extreme shear flow conditions are maintained. Under such conditions, FeO remains in greater amounts on the surface during the reaction.

Adding H_2 to N_2 at the 40 percent level appreciably increases the thermal conductivity (about 160 percent at 2000 K) of the gases and as indicated by Fig. 4 tends to increase erosion at low concentrations of H_2O. Substitution of H_2 for N_2 does not appreciably alter the pressure vs time cycle since both are diatomic gases and respond similarly to compression. However the addition of H_2O, a triatomic gas, was accompanied by a higher driver gas pressure to achieve an equivalent peak pressure.

AISI 4340 tends to experience higher mass loss than Fe (see Fig. 5). The same trend was found for oxygen-containing flows reference [4]. This result is consistent with erosion produced using propellant combustion gases. The somewhat lower (about 30 K) solidus point of AISI 4340 does not account for all of the difference. However, based on the results of reference [6], the thermal diffusivities of AISI 4340 are expected to be significantly lower than that of Fe. Thus, the surface temperature of AISI 4340 will increase at a higher rate than that of Fe. Stainless steel AISI 304 exhibited no erosion under similar conditions. This result indicates that special properties of AISI 304 resist heterogeneous chemical reaction with water vapor even under extreme heating and shearing conditions. It is worth noting that both AISI 304 and AISI 4340 steels are attacked severely and to an approximate equal extent by oxygen-containing, high pressure hot flows.

Conclusions

Systematic classification, both theoretical and experimental, of the reactivity of various high temperature and high pressure gases flowing over steel surfaces revealed the erosion trends of steel in the submelting temperature range. In this range, the surface chemical attack of the steel is hypothesized to be the main erosion source. Various types of steel generally resist the attack of gases such as N_2, CO, and CO_2. However, water vapor can vigorously react with steel (e.g., AISI 4340, 1020, etc.) and produce erosion which is controlled by boundary layer transport processes. Thus, in practical systems employing hot flowing combustion gases under conditions favorable to surface chemical attack, the main cause of steel erosion is water vapor. To our knowledge, previous investigations did not identify the special role of water vapor in erosion of steel under high shearing flows.

The methodology used in this research can be applied to estimate erosion produced by specific steel and combustion gas interactions. Also, the thermochemical explanations suggest methods for reducing erosion.

Acknowledgment

This research was sponsored by the U. S. Army Materials and Mechanics Research Center under Contract DAAG46-76-C-0069. The reviewers interpretation of the experimental results added to the paper by pointing out that the reverse reaction is unlikely.

References

1 Gany, A., Caveny, L. H., and Summerfield, M., "Aerothermochemistry of Metal Erosion by Hot Reactive Gases," ASME JOURNAL OF HEAT TRANSFER, Vol. 100, No. 3, Aug 1978, pp. 531–536.

2 Fast, J. D., *Interaction of Metals and Gases, I: Thermodynamics and Phase Relations*, Academic Press, New York, 1965.

3 Muan, A., and Osborn, E. F., *Phase Equilibria Among Oxides in Steelmaking*, Addision-Wesley, Reading, MA, 1965.

4 *Thermophysical Properties of Matter, The TPRC Data Series*, Touloukian, Y. S., ed., IFI/Plenum, New York, 1970.

5 Alkidas, A. C., Christoe, C. W., Caveny, L. H., and Summerfield, M., "Erosive Effects of High Pressure and High Temperature Gases on Steel," *ASME Journal of Engineering Materials and Technology*, Vol. 99, No. 3, July 1977, pp. 239–243.

6 Butler, C. P., and Inn, E. C. Y., "Thermal Diffusivity of Metals at Elevated Temperatures," *ASME Symposium of Thermal Properties*, 1959, pp. 377–390.

Effective Thermal Conductivities of Fibrous Composites

L. S. Han
Professor

A. A. Cosner[1]
Graduate Research Associate.

Department of Mechanical Engineering
The Ohio State University
Columbus, Ohio

Most composite research to date has been concerned with mechanical properties. However, with anticipated use of composite materials in high temperature aero-space structures and other applications, thermal properties have become essential design information. This paper summarizes the results of a rigorous analysis to determine the steady-state effective thermal conductivities of fiber-matrix type of composites. A principal purpose of the present work is to investigate a class of heat conduction problems for which the proximity effects of the embedded fibers are significant. The fibers are considered dispersed uniformly in a matrix of resin. The dispersion patterns or configurations considered are: (1) uni-directional fibers in a matrix, as the simplest geometry, and (2) 0/90 configuration in which uni-directional tapes are overlaid at 90 deg to each other. The method of analysis is to solve a two-region steady-state heat conduction equation analytically or numerically. The analysis assumes prior knowledge of the geometry and the thermal conductivities of the composite constituents.

Introduction

A composite material is composed of two or more elemental materials joined together to form a new medium which is discontinuous in its microstructure but has its combined macroscopic properties superior to those of its individual constituents. It is for this reason intensive development efforts have been under way for the past decades to create literally a new class of materials for application heretofore deemed unlikely or impossible. The main competitive characteristics are of course: light weight, high strength and dimensional stability, to name a few.

Published literature abounds with investigations on mechanical properties of composites with emphasis on stiffness, elastic moduli, fatigue limit, etc. Far fewer accounts, however, are concerned with their thermo-physical properties, which are now beginning to receive attention with a view to extend the application of composites to severe environments with thermal and moisture gradients.

In the early seventies, there appeared a group of analyses by Horvay and his coworkers which dealt with transient temperature distributions in laminated composites with the principal heat propagation along the laminate plane. In their first paper, Horvay, et al. [1] analyzed for isotropic laminated composites with two different laminations alternately stacked to form a semi-infinite region. The problem was to determine the temperature response when an edge of the laminated stack was given a temperature variation periodic in time and space with the latter variation to coincide with the lamination stacking sequence. In a later publication, Manaker and Horvay [2], a similar problem was studied with the heat flux boundary condition replacing that for temperature. Even for this simple class of composites, there are quite a few parametric values involving the thermal properties, geometrical proportions etc. and the two subsequent publications by Horvay and Manaker [3] and Kaczenski and Horvay [4] were devoted to cover the temperature fluctuation frequency spectrum. For composites with three kinds of laminates, the corresponding problems were investigated by Horvay, Gold, and Kaczenski [5] and by Gold and Horvay [6] for high and low exciting frequencies respectively. The above group of analyses is characterized by the use of exact mathematical procedures, is conceptually complete and is self-contained.

With a view to render the classical approach more utilitarian, Hegemier and his colleagues demonstrated the conceptual advantage of a parametric expansion method by solving the laminate-composite heat transient problems. Their noteworthy contribution is the recognition of the small transverse dimension of a laminate or a fiber relative to the dimension in the propagation direction. In the "downstream" region where the ratio of these two dimensions is small, a "quasi steady state" temperature distribution is reached. Hence, the entire solution domain can be classified by different orders of the parameter (r/z). This parametric ordering of solutions in thermal analyses originated in their earlier work on stress propagation in laminated composites by Hegemier and Bache [7]. A distinct advantage lies in the fact that from a pragmatic viewpoint, fewer terms or simpler solutions would be adequate to achieve good engineering accuracy. This series of investigations is exemplified by Maewal, et al. [8] and Murakami, et al. [9].

Turning to transient problems with heat propagation perpendicular to laminations, the solution is not conceptually difficult, since for each layer the problem is one-dimensional, but is operationally tedious in joining the many single-layer solutions to form a compatible assembly. Typical of this class of investigations are the study by Schimmel, et al. [9] and that of Maewal, et al. [8]. Comparisons were made between the results of their exact analyses and those obtained by using effective thermal conductivities with the latter evaluated on the basis of conductances in series.

For composites with uni-directional fibers, heat conduction parallel to the fibers is in essence similar to that for laminates. Transverse to the fibers, however, significant differences emerge: that the dispersed fibers form individual inclusions in the bulk of the matrix and that the heat flow phenomenon involves a doubly-connected region. Physically speaking, the resulting heat flow pattern is comprised of a combination of series and parallel paths. This complexity precludes, in the authors' view, a case-by-case exact analysis of the heat conduction problems, and a viable approach from a practical viewpoint is the replacement of the discrete microstructure by a continuum model with an effective thermal conductivity. From such a zeroth-order model, subsequent refinements could be constructed by a parametric expansion method similar to that of Hegemier. Indeed, such a macroscopic replacement was investigated by Lee and Taylor [10]. They used dispersed copper spheres as inclusions in a composite and measured the transient responses from which thermal diffusionity values were inferred. The values thus obtained for media with up to 30 percent concentration by volume were found in fair agreement with a classical prediction by Maxwell [11]. Accurate prediction of effective thermal conductivities for composites is therefore not only useful in steady-state analyses but also essential as a first-order input for transient analyses.

To be sure, the topic of effective thermal conductivity is not new. Maxwell [11] and Lord Rayleigh [12] were the earlier ones to have studied the phenomena of electrical and magnetic properties in dispersed media. With the advent of composite media in engineering structure, interest in the effective conductivity was renewed. The investigations for fibrous composites have been along two parallel but

---

[1] Now with Detroit Diesel Allison Div., GMC. Indianapolis, Indiana.

Contributed by the Heat Transfer Division for publication in the JOURNAL OF HEAT TRANSFER. Manuscript received by the Heat Transfer Division February 19, 1980.

related approaches: one is to model the fiber-in-matrix orientations by simplified geometrical equivalent, and the second approach which relies on the results of the first for input information is to employ a statistical technique to determine upper and lower bounds of the effective thermal conductivity. Among those employing the model approach are the often-cited works of Springer and Tsai [13], and Behrens [14]. To the second approach, belong the publications of Hashin and Shtrikman [15], Berens and Silnutzer [16] and more recently Schulgasser [17]; the latter publication included a survey of the methodology and a list of related references.

Typically, results of the model approach are expressed as the ratio of an effective conductivity to the matrix conductivity, and characteristically this ratio is shown to depend on (1) a volume ratio, v = volume of fiber/total volume and (2) a conductivity ratio, β = fiber conductivity/matrix conductivity. Without going into the details of various model equations in use, which will be discussed elsewhere, a typical form is that by Behrens [14]:

$$(k_e/k_m) = [(\beta + 1) + v(\beta - 1)]/[(\beta + 1) - v(\beta - 1)] \qquad (1)$$

It is, of course, recognized that formulas of this type do not wholly consider the influence of the relative fiber position on heat conduction. Thus, they cannot be expected to yield quantitatively accurate results for the myriads of possible fiber geometrical patterns especially under conditions of high density packing currently in use. Furthermore, as the statistical approach relies on these model equations as guides, a more precise delineation of the effective conductivity is needed.

Accordingly the purpose of the present work is primarily to investigate a class of heat conduction problems in composites for which the proximity effects of the embedded fibers are significant. Secondly, the information on the effective conductivity thus generated would strengthen and enlarge the usefulness of the modeling approach by establishing accurate bounds through comparison with the presented results of analysis.

This paper addresses itself to the problem of transverse heat conduction in the steady state through composite materials, in particular those having isotropic fibers uniformly dispersed in an isotropic matrix. Specifically considered is a class of fiber-matrix composites having two geometrical arrangements for the fibers: (1) fibers in a uni-directional orientation, and (2) layered composites with fibers laid alternately along two mutually perpendicular directions—often referred to as the 0/90 arrangements. Results from these investigations are expressed in terms of an effective thermal conductivity which is useful in the following context: Fibers or bundles of fibers in a matrix are usually of such a small dimension that, for most engineering applications, the scale of desired resolution spans a number of fibers or bundles of fibers. A typical 0.5-inch thick graphite-fiber composite slab consists of 50 or more layers of graphite-tapes. Thus from a "macroscopic" viewpoint, an effective thermal conductivity reflecting the phenomenological aspect of the discrete fibers is a first and, in most instances, an adequate requirement to analyze the temperature gradients in such a composite body. This equivalence idea is not unlike the representation of a real gas by a continuum with phenomenological coefficients.

Unit-Cell Approach

Because of the disparity between the two scales—scale of resolution and scale of the fiber dimension—rigorous evaluation of effective thermal conductivity can be obtained only from consideration of a unit cell (Fig. 1(a)), of which the remainder of the composite is either a replica or a mirror-image. For uni-directional fibers, a regular dispersion pattern (with the fiber centers forming either a rectangle or a triangle) is assumed. Figure 1(a) depicts a unit-cell isolated from a fiber-composite with fibers forming a rectangular array. Such a unit-cell construction assumes a one-dimensional heat flow downward at its boundaries. Consequently, both the horizontal line midway between fibers and the one passing through the fiber centers are isotherms and the corresponding vertical lines are adiabats.

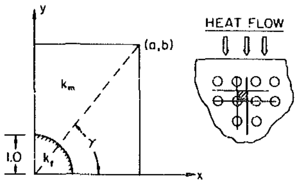

Fig. 1(*a*) Rectangular pattern

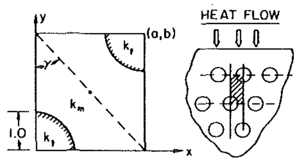

Fig. 1(*b*) Staggered pattern

Fig. 1 Unit cell of a uniformly dispersed fiber matrix

Figure 1(b) depicts a unit-cell constructed for fiber-composites with fiber-centers forming a triangular pattern. The insulated sides are $x = 0$, and $x = a$. The sides at a constant temperature are $y = 0$, and $y = b$. For both geometries, the fiber radius is set equal to one and the cell dimensions are ($x = 0, a$) and ($y = 0, b$).

For fiber-composites with the 0/90 arrangement, the unit cell is a box; it consists of two quarter-fibers located along two perpendicular but non-intersecting edges of the matrix box. Figure 2 depicts such a unit cell which is carved out of a 0/90 fiber-matrix composite, wherein layers are stacked uniformly in planes perpendicular to the y axis. The layer thickness is b and the tranverse fiber spacing within all layers is $2a$.

Principal Conductivities

There are three principal conductivities for the composites under consideration. For uni-directional fibers (Figs. 1(a) and 1(b)), the effective conductivity along the z axis, i.e. parallel to the fibers, can be simply obtained by a linear combination of the two constituent's thermal conductivities in proportion to their respective cross sections. Hence, the only ones which need to be analyzed are those along the x and y directions. Because of symmetry of the geometries involved, these two principal conductivities can be handled by a complementary-angle principle. In other words, solving for the effective conductivities for configurations of Figs. 1(a) and 1(b) with angles of γ and its complementary angle (90-γ), the values of the effective conductivities for these two angles constitutes an orthogonal pair, e.g. the value of k_e for $\gamma = 30$ deg corresponds to that along the y-direction and that for $\gamma = 60$ deg corresponds to that along the x-direction.

For the 0/90 arrangement, the orientation of the fibers in the unit cell, as depicted in Fig. 2, is such that the principal conductivities along the x and z directions must be equal. Hence, only two cases need to be dealt with; namely those along the x and y directions. For the former heat flow case, the heat path is transverse to one fiber and axial to another; the resulting effective conductivity is therefore termed in this paper as the "transverse-axial case." For the latter heat conduction analysis, i.e. along the y-direction, the term transverse-transverse case is used to denote its heat path.

Nomenclature

a = horizontal length of unit cell, see Figs. 1, 2
b = vertical length of unit cell, see Figs. 1, 2
k = thermal conductivity
T = temperature
v = volume ratio (fiber volume/total volume)
r = radial distance (polar coordinate)
x, y, z = Cartesian coördinates
γ = fiber packing angle, see Figs. 1(a), 1(b)
β = conductivity ratio (fiber conductivity/matrix conductivity)
θ = angular coördinate

Subscripts

e = effective value
f = fiber value
m = matrix value

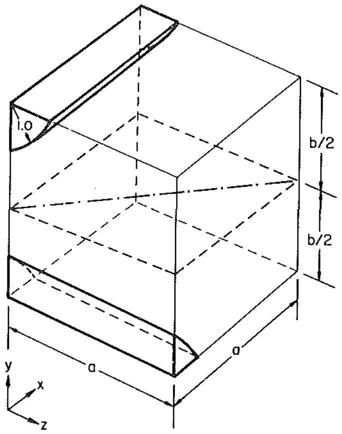

Fig. 2 Unit cell for (0/90) fiber composite

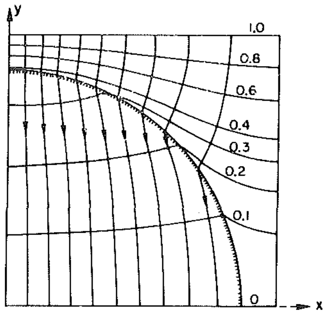

Fig. 3 Temperature field, rectangular array (β = 10, v = 0.6, γ = 45 deg)

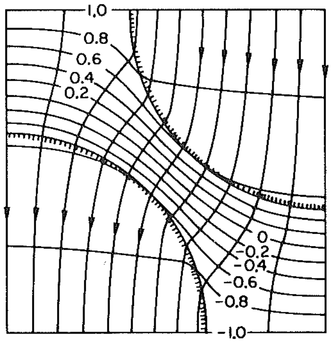

Fig. 4 Temperature field, staggered array (β = 10, v = 0.6, γ = 45 deg)

Method of Analysis

Uni-Directional Case, Rectangular Array (Fig. 1(*a*)). By considering a one-dimensional temperature field in the y-direction, the appropriate boundary conditions for the steady-state heat conduction equation are:

$$T(x,b) = 1,\ T(x,0) = 0,\ T_x(0,y) = 0,\ T_x(a,y) = 0 \qquad (2)$$

As discussed previously, a constant-temperature boundary condition is imposed at $y = 0$, and at $y = b$. On the sides, $x = 0$, and $x = a$, the lateral temperature gradient is taken to be zero to comply with the condition of symmetry or zero heat transfer.

The interface conditions at $r = 1$ are fulfilled by the equalities of the temperatures in these two regions and the normal heat fluxes. Symbolically, these are expressed as

$$T_f(1,\theta) = T_m(1,\theta)$$

$$k_f[\partial T_f/\partial r]_{r=1} = k_m[\partial T_m/\partial r]_{r=1} \qquad (3)$$

where a polar formulation is used for convenience; the subscripts f and m refer to fiber and matrix, respectively.

The solutions of the Laplace equation cast in cylindrical coordinates for this two-region problem are, respectively,

$$T_f = \sum E_n[2/(1+\beta)]r^n \sin n\theta$$

$$T_m = \sum E_n[r^n - r^{-n}(\beta - 1)/(\beta + 1)] \sin n\theta$$

$$n = \text{odd integers}$$

$$\beta = k_f/k_m \qquad (4)$$

where all boundary conditions have been satisfied except those for the two sides of the unit cell, $x = a$ and $y = b$. The coefficients E_n are to be determined accordingly.

The method employed for satisfying the conditions at these two sides is that of point-matching or boundary collocation, i.e. the boundary conditions are fulfilled at a selected number of points along these sides. The number of the points selected corresponds to the number of the undetermined coefficients E_n. By evenly spacing the points, the error is minimized. In practice, a total of 16 points excluding $(a,0)$ and $(0,b)$ appears an optimum choice. With the coefficients $E_1, E_3, \ldots$ determined the quality of the solution is judged (1) by calculating the temperature profile at the upper side $y = b$ where a maximum deviation of 0.1 per cent from the prescribed value of unity is permitted and (2) by calculating the x-gradient along the line $x = a$, where a maximum lateral heat flux, $k_m(\partial T_m/\partial x)_a$ is limited to 0.1 percent of the heat flux at the top surface $y = b$.

After defining the temperature distributions, equations [4], the heat flow from the top surface $y = b$ to the bottom surface $y = 0$ is calculated by summing up the y-gradients on these two surfaces separately. These two heat flows at the surface $y = 0$ and the surface $y = b$ are permitted to vary no more than 0.1 percent from one another, the difference representing, of course, the lateral heat flux at $x = a$. From these accuracy constraints and equations [4], an effective thermal conductivity k_e is deduced.

A qualitative display of the two-region isotherms and the resulting flux lines is presented in Fig. 3 for the conditions: fiber-to-matrix conductivity ratio $\beta = 10$, aspect ratio $(a/b) = 1$, and fiber volumetric content $v = 0.6$.

Uni-Directional Case, Staggered Array, (Fig. 1(*b*)). For the configuration depicted in Fig. 1(b), there are now three distinct regions in which the Laplace equation must be satisfied. Additionally, these solutions must join at the two interfaces where the fibers meet the matrix material. In order to adapt the two-region solution-technique developed for the preceding case to the current situation, consider the following arguments:

By imposing temperatures of +1 on the top surface and −1 at the bottom surface, the temperature distribution in the entire unit-cell of Fig. 1(b) possesses an odd-symmetry with respect to the central point $(a/2, b/2)$. Taking advantage of this fact it is apparent that any line passing through the central point has a temperature distribution such that the temperature on the right side of the central point is the negative of the temperature on the left side of it. Furthermore, on these conjugate sides, the y-gradients must be equal. With this simplification, the two-region matching technique is applied to the lower-left portion of Fig. 1(b), and the solutions for the fiber and the matrix regions are respectively

$$T_f = -1 + \sum E_n[2/(1+\beta)]r^n \sin n\theta$$

$$T_m = -1 + \sum E_n\ [r^n - r^{-n}(\beta - 1)/(\beta + 1)] \sin n\theta$$

$$n = \text{odd integers} \qquad (5)$$

where the boundary conditions at $y = 0$ $(T = -1)$ and at $x = 0$ are satisfied as well as those at the interface, $r = 1$. Along the diagonal from $(0,b)$ to $(a,0)$, anti-symmetry of the temperature and symmetry of the y-gradient with respect to the central point of the unit-cell serve to fix the undetermined coefficients E_n by a point-matching technique. A typical set of isotherms and heat flux lines is shown in Fig. 4 with the same parametric values as in Fig. 3.

Cross-Fiber Case, (0/90 Over-Lay, Fig. 2). For this configuration, a straight-forward finite difference approach is adopted. To determine the effective conductivity along the y-direction (transverse-transverse case), the faces $y = 0$, and $y = b$ are assumed to have temperatures of +1 and −1, respectively. With these specified temperatures and the fact that there is a quarter-fiber at both the top and the bottom surfaces, there ensues an odd-symmetry condition with respect to the diagonal line drawn through the mid-plane $y = b/2$, (see Fig. 2). In the midplane therefore, the temperature distribution on one side of the diagonal is the negative of the other side. Also, the y-gradient is symmetrical with reference to the diagonal bisector. In this way, the numerical work is much reduced. A grid of 20 to 30 divisions along each axis is used to balance numerical accuracy and computer time expenditure. A standard relaxation method for a seven-point cluster gives the temperatures at all interior points with three-place accuracy. The heat flow through the unit cell is calculated by a three-point formula.

Results

Uni-Directional Fiber Composites. Based on the analytical procedure described previously, the effective thermal conductivity ratio (k_e/k_m) is calculated for the two fiber-to-fiber arrangements. Figures 5, 6, and 7 show the data for fibers in rectangular array and for volume ratios of 0.5, 0.6, and 0.7, respectively. The angle γ is chosen so as to avoid fibers from overlapping each other.

Of particular importance are the principal conductivity data identified by the complementary directional angle γ. The curves for $\gamma = 30$ deg and $\gamma = 60$ deg form a set of principal effective thermal conductivities, and so forth. For $\gamma = 45$ deg, the two principal conductivities are of course equal and the conduction transverse to the fibers becomes isotropic.

Figure 8 portrays the three principal conductivities for the rectangular array arrangement and for the parametric values so identified. In all these figures the prediction through model equation (1) is also shown.

For filaments arranged in a staggered pattern, the corresponding data are displayed in Figs. 9–12.

Inspection of the general trend of the analytical results indicates a pattern of high degree of an-isotropy for $\beta \gg 1$, i.e. the fibers being much more conductive than the filler (typical of a graphite-fiber composite). To put it differently, the effective conductivity is quite sensitive to fiber orientation, other factors being unchanged. For this range of β, model equation (1) and its derivatives tend to yield inaccurate answers. For $\beta < 1$, i.e. the fibers are less conductive than the matrix, the effect of the fiber dispersion pattern on the effective conductivity is less pronounced.

Another interesting observation of the uni-directional analyses is the fact that for both fiber patterns, staggered array and rectangular array, the effective conductivity ratio (k_e/k_m) is principally governed by the distance between two adjacent fibers measured along the apparent heat flow line. As an example, the effective thermal conductivity for a rectangular fiber-array at $v = 0.6$ and $\gamma = 60$ deg is almost equal to that for a staggered fiber-array at $v = 0.6$ and at an angle γ such that in both cases the y-spacing b are equal. This is of significance in constructing an equivalent model for approximate heat conduction syntheses.

Also included in these figures for the effective transverse thermal conductivity ratios (k_e/k_m) are the values when the fiber conductivity becomes infinitely large. This situation is equivalent to that of conducting cables buried in an insulating material. Some data of an early vintage were reported in the *Heat Transfer Data Book* [15]; it appears that there are areas of agreement as well as divergence when compared with the accurate values reported here.

For the configuration of fibers in a square-pattern arrangement, the results were also obtained by Schneider and Romilly [16] using a finite-element method. Their results and those reported in this paper agreed to the third decimal place, thereby confirming the accuracy of both methods.

The (0/90) Layered Composites. Computations of the effective thermal conductivity are limited to two values of $(b/2a)$, namely 1 and 2. The volume ratio varies from 0.4–0.7. Figures 13–16 report the data from this investigation for the effective conductivity along the two principal directions. For $\beta \gg 1$, the large disparity between the two

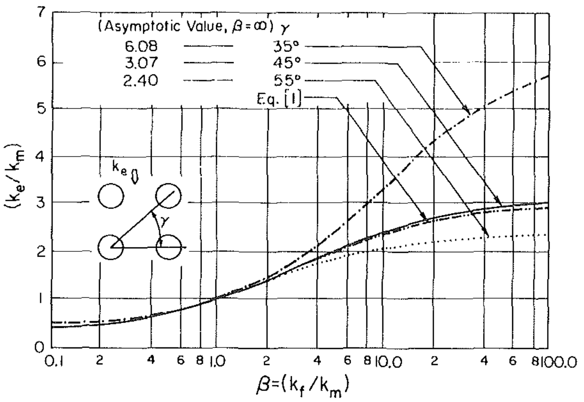

Fig. 5 Effective conductivities for unidirectional fiber composites (rectangular array, $v = 0.5$)

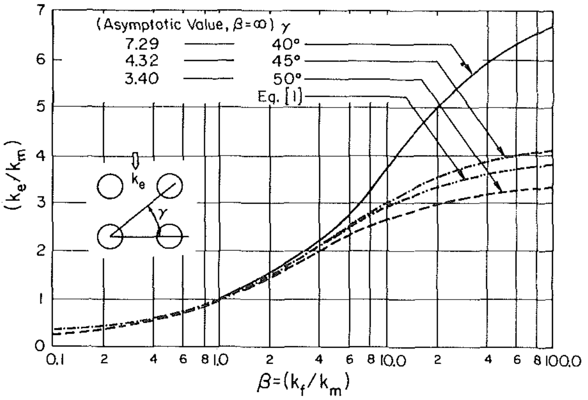

Fig. 6 Effective conductivities for unidirectional fiber composites (rectangular array, $v = 0.6$)

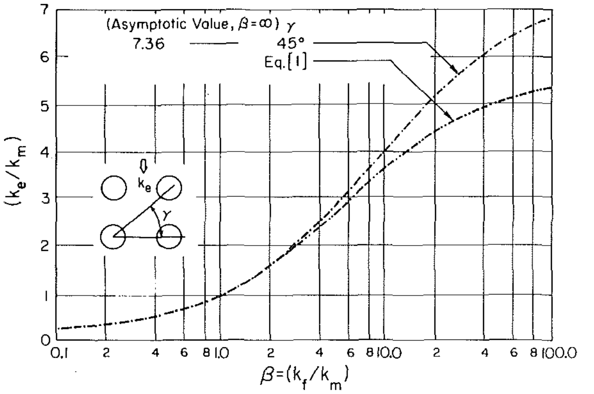

Fig. 7 Effective conductivities for unidirectional fiber composites (rectangular array, $v = 0.7$)

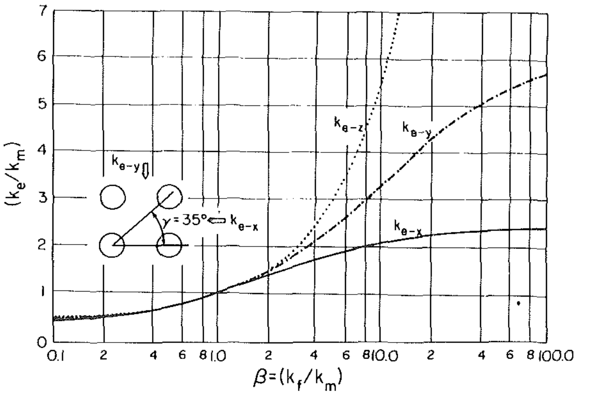

Fig. 8 Principal effective conductivities for unidirectional fiber composites (rectangular array, $v = 0.5$, $\gamma = 35$ deg)

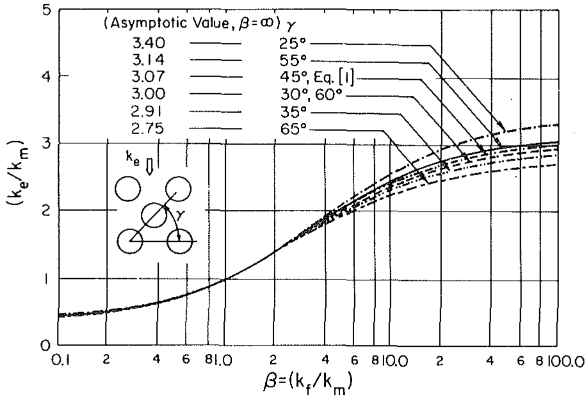

Fig. 9 Effective conductivities for unidirectional fiber composites (staggered array, $v = 0.5$)

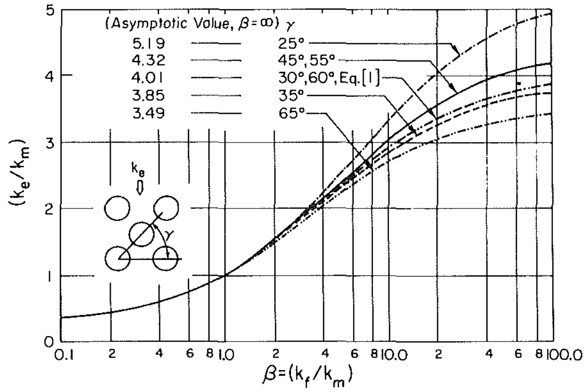

Fig. 10 Effective conductivities for unidirectional fiber composites (staggered array, $v = 0.6$)

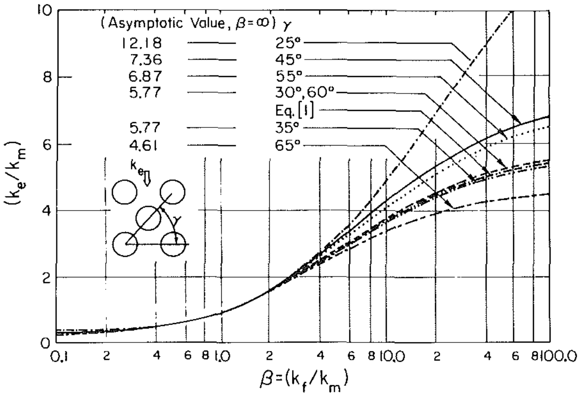

Fig. 11 Effective conductivities for unidirectional fiber composites (staggered array, $v = 0.7$)

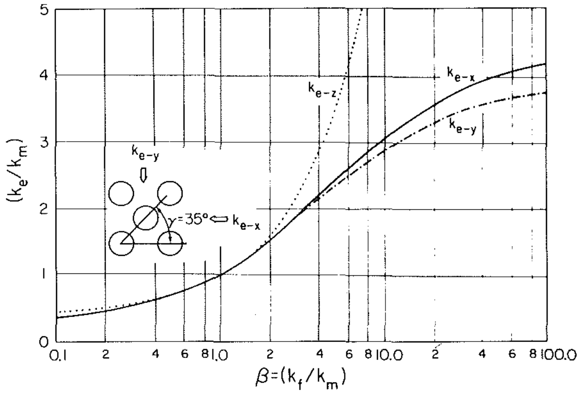

Fig. 12 Principal effective conductivities for unidirectional fiber composites (staggered array, $v = 0.6$, $\gamma = 35$ deg)

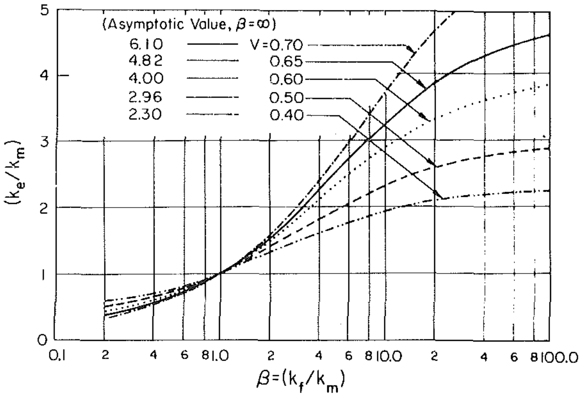

Fig. 13 Effective conductivities for (0/90) fiber composites (transverse-transverse direction, $b/2a = 1$)

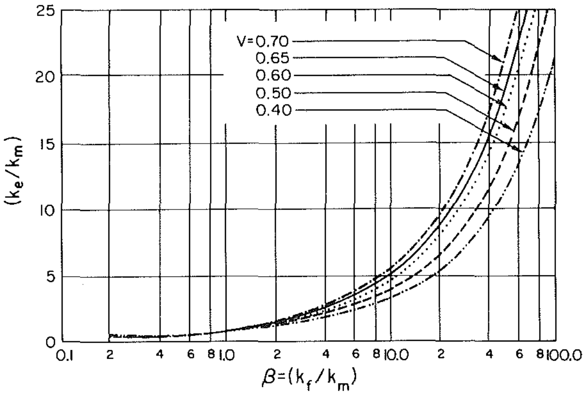

Fig. 14 Effective conductivities for (0/90) fiber composites (transverse-axial case, $b/2a = 1$)

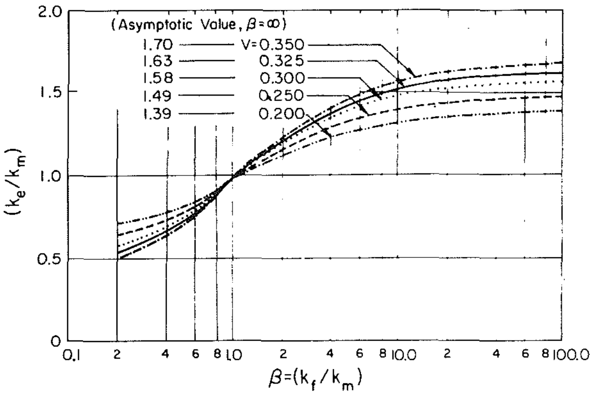

Fig. 15 Effective conductivities for (0/90) fiber composites (transverse-transverse case, $b/2a = 2$)

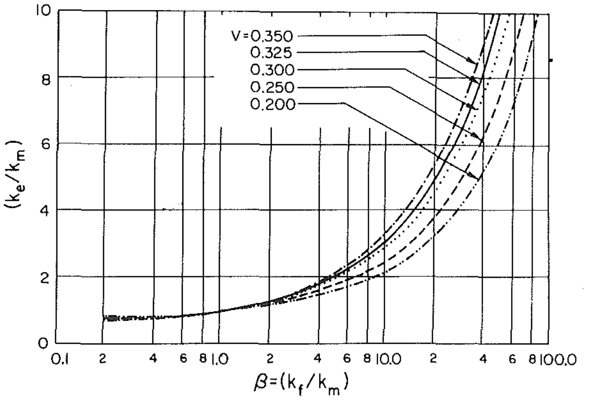

Fig. 16 Effective conductivities for (0/90) fiber composites (transverse-axial case, $b/2a = 2$)

principal conductivities is accentuated in Fig. 17. The fact that for the transverse-axial case, the effective thermal conductivity in the $\beta > 1$ range is much larger is due primarily to a direct flow path along the conductive fibers while for the transverse-transverse case the ineffective matrix region constitutes a heat conduction barrier. At large values of β, the ratio (k_e/k_m) for the transverse-axial case can be obtained from an elementary consideration of parallel heat flow. The resulting asymptotic equation is simply

$$(K_e/k_m) = \beta v/2 + (1 - v/2)$$

which can be used quite accurately for $\beta \geq 20$.

Acknowledgment

The authors are grateful for the financial support by the U.S. Air Force Office of Scientific Research through a grant to The Ohio State University, AFOSR-78-3640. The program is under the technical monitorship of Mr. Nelson Wolfe of AFFDL, Wright-Patterson Air Force Base. His help in shaping the manuscript for publication is appreciated. In addition, Miss L. Glower's graphical contribution enhances the readability of this paper.

Professor Richard H. Zimmerman's assistance in this part of the overall program is invaluable. Finally, the authors gratefully acknowledge the constructive comments and criticisms from our referees which give this paper a better prospective to the relevant literature.

References

1 Horvay, G., Mani, R., Veluswani, M. A., and Zinsmeister, G. E., "Transient Heat Conduction in Laminated Composites," ASME JOURNAL OF HEAT TRANSFER, Vol. 95, 1973, p. 309.

2 Manaker, A. M., and Horvay, G., "Thermal Response of Laminated Composites," *ZAMM*, Vol. 55, 1975, p. 503.

3 Horvay, G., and Manaker, A. M., "Heat Flow in Laminated Composites Parallel to the Layering When the Surface Heating is of High Frequency," *Proceedings of 1975 Boston AIME Conference on Composites*, Vol. 2, p. 527.

4 Kaczenski, E. S., and Horvay, G., "Thermal Response of Layered Composites," *Japan Society of Composite Materials*, Vol. 1, 1975, p. 1.

5 Horvay, G., Gold, B., and Kaczenski, E. S., "Longitudinal Heat Propagation in Three-Phase Laminated Composites at High Exciting Frequencies," ASME JOURNAL OF HEAT TRANSFER, Vol. 100, 1978, p. 281.

6 Gold, B., and Horvay, G., "Longitudinal Heat Propagation in Three-Phase Laminated Composites at Low Exciting Frequencies," *Journal of Applied Mechanics*, Vol. 46, 1979, p. 557.

7 Hegemier, G. A., and Bache, T. C., "A Continum Theory for Wave Propagation in Laminated Composites . . .," *Journal of Elasticity*, Vol. 3, 1973, p. 125.

8 Maewel, A., Bache, T. C., and Hegemier, G. A., "A Continum Model for Diffusion in Laminated Composite Media," ASME . JOURNAL OF HEAT TRANSFER, Vol. 98, 1976, p. 133.

9 Schimmel, W. P., Beck, J. V., and Donaldson, A. B., "Effective Thermal Diffusivity for a Multimaterial Composite Laminate," ASME JOURNAL OF HEAT TRANSFER, Vol. 99, 1977, p. 466.

10 Lee, H. J., and Taylor, R. E., "Thermal Diffusivity of Dispersed Composites," *Journal of Applied Physics*, Vol. 47, 1976, p. 148.

11 Maxwell, J. C., *A Treatise on Electricity and Magnetism*, Oxford University Press, 1904, Vol. 1, p. 440.

12 Rayleigh, Lord, "On the Influence of Obstacles . . .," *Philosophical Magazine*, Vol. 34, 1892, p. 481.

13 Springer, G. S., and Tsai, S. W., "Thermal Conductivities of Unidirectional Materials," *Journal of Composite Materials*, Vol. 1, 1967, p. 166.

14 Behrens, E., "Thermal Conductivities of Composite Materials," *Journal of Composite Materials*, Vol. 2, 1968. p. 2.

15 General Electric Co., *Heat Transfer Data Book*, Section G. 502.2.

16 Schneider, G. E., and Romilly, D., "The Apparent Thermal Conductivity of Long Cylindrical Fibers in a Matrix," ASME Paper No. 79-WA/HT-42.

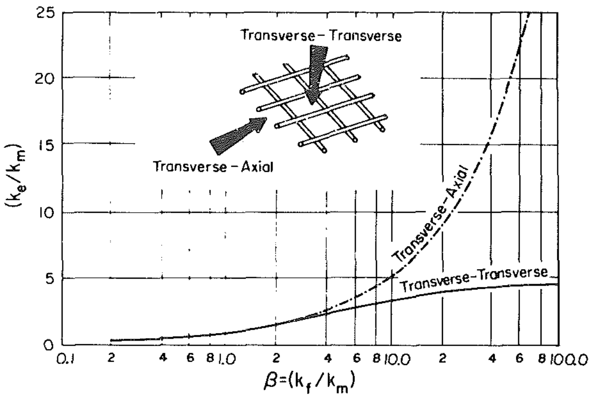

Fig. 17 Principal effective conductivities for (0/90) fiber composites (v = 0.65, $b/2a$ = 1)

Journal of Heat Transfer

Technical Notes

This section contains shorter technical papers. These shorter papers will be subjected to the same review process as that for full papers.

Pressure Drop Characteristics for a Shrouded Longitudinal-Fin Array with Tip Clearance

E. M. Sparrow[1] **and T. J. Beckey**[1]

Introduction

The design of energy-efficient heat exchange devices requires a knowledge of pressure drop (and/or pumping power) characteristics as well as of heat transfer characteristics. Presssure drop information is especially relevant in connection with enhanced heat transfer devices, since the heat transfer enhancement frequently gives rise to higher pressure losses. Among enhancement techniques, fins are, perhaps, the most prevalent and, therefore, their pressure drop characteristics are of practical relevance.

In this paper, pressure drop experiments are reported for airflow through an array of longitudinal fins attached to one of the principal walls of a flat rectangular duct. The other principal wall of the duct can be regarded as a shroud. In the absence of such a shroud, air would escape from the interfin spaces into the surroundings beyond the tips of the fins.

If the fin tips are in intimate contact with the shroud, then any pair of adjacent fins, together with the fin base surface and the shroud, forms a subchannel that is separate from the other similarly constituted subchannels. Each subchannel is, itself, a rectangular duct, and the pressure drop characteristics of rectangular ducts are sufficiently well studied so as not to require further elaboration.

If, on the other hand, a clearance gap is present between the tips of the fins and the shroud, there will be longitudinal flow through the gap as well as through the interfin spaces. The extent to which the flow subdivides itself between these parallel paths depends on the relative magnitude of the resistances encountered along the respective paths. In turn, the relative resistances depend on such geometrical parameters as the size of the clearance gap, the interfin spacing, and the height of the fins.

The research reported here is concerned with the fully developed pressure drop characteristics (i.e., friction factors) of an array of longitudinal fins in the presence of a clearance gap. The experimental apparatus was designed with a high degree of flexibility so that the key geometrical parameters could be varied without a major rebuilding of the system. All told, nine different geometrical configurations were investigated with the same apparatus, encompassing variations of interfin spacing, fin height, and fin-shroud clearance gap. For each configuration, the Reynolds number was varied over the full range permitted by the air supply and the instrumentation. Auxiliary experiments were carried out for rectangular ducts of various aspect ratios in order to confirm the experimental technique. Fully developed friction factors are presented for all cases.

A search of the literature failed to reveal any experimental work on the fin arrangement investigated here. The most closely related configuration for which experimental friction factors are reported is the longitudinally internally finned circular tube, for which [1] is a representative reference. Analytical results for the present fin arrangement have been reported in [2], but they are for laminar flow, while the experimental results obtained here are for turbulent and transitional flow.

The Experiments

A schematic cross-sectional view of the test section is shown in the upper part of Fig. 1. As seen there, the base plate, the upper wall, and the two side walls are made of heavy structural members (respectively 1.270-cm thick aluminum plate and 1.905-cm thick cold-rolled steel bars). On the base plate rest eleven spacer bars distributed across the span of the duct. Each bar is 0.635 cm thick and is made of cold-rolled steel. The spacer bars serve to support and position the fins, as can be seen from the enlarged view in the lower portion of Fig. 1. Each fin is held between the adjacent pair of spacer bars, with the lower part of the fin situated sandwich-style between the bars and the upper part jutting into the flow passage. Thus, the flow passage consists of the interfin space above the bars and the clearance gap between the fin tips and the upper wall.

The fins were fabricated from 0.0762-cm thick galvanized steel sheet selected specifically because of its surface smoothness. They were first cut to the approximate final height by a shear. The cut edges were finished to right angles with the aid of a large surface grinder, with a resulting tolerance of ±0.00127 cm on the fin height being maintained over the entire longitudinal extent of each fin.

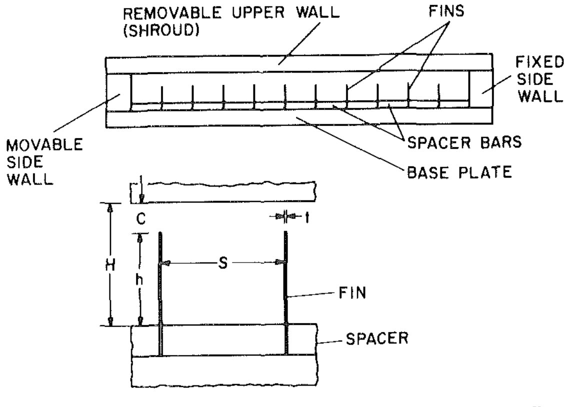

Fig. 1 *Schematic cross-sectional view of the test section (upper diagram) and detail of a subchannel (lower diagram)*

---

[1] Department of Mechanical Engineering, University of Minnesota, Minneapolis, Minn 55455

Contributed by the Heat Transfer Division for publication in the JOURNAL OF HEAT TRANSFER. Manuscript received by the Heat Transfer Division September 22, 1980.

The overall height H of the flow passage was maintained at 2.54 cm for all of the data runs; in addition, a fixed thickness $t = 0.0762$ cm was employed for all of the fins. The interfin spacing S and the fin height h were varied parametrically. Three interfin spacings were investigated, respectively characterized by $S/H = \frac{1}{4}, \frac{1}{2}$, and 1. For each fixed S/H, the fin height h/H was varied from $\frac{3}{8}$ to $\frac{5}{8}$ to $\frac{7}{8}$, with corresponding values of $C/H = \frac{5}{8}, \frac{3}{8}$, and $\frac{1}{8}$. The length of the test section in the flow direction is 121.9 cm.

The diagram in the upper part of Fig. 1 portrays the duct cross section with the widest spacer bars (i.e., $S = 2.54$ cm) in place. When the smaller spacers are installed, either $S = 1.27$ cm or 0.635 cm, the overall width of the flow cross section (equal to $11S + (10)(0.0762)$ cm) diminishes. This narrowing of the cross section was accommodated by the rightward repositioning of the left-hand wall of the test section. The installation or removal of the spacers and fins was accomplished by removal of the top wall of the test section.

For the measurement of the axial pressure distribution, twenty-one taps were distributed along the length of the test section. The taps were installed in the upper wall of the duct, along the centerline of the central subchannel. (Thus, a different set of taps was used for each of the three interfin spacings.) In addition, to check on the uniformity of the flow distribution among the various subchannels, auxiliary taps were installed along the centerline of the next-to-the-outermost channel adjacent to each sidewall. The pressure signals were conveyed via plastic tubing to a selector switch and thence to a Baratron solid-state capacitance-type pressure meter. Either of two pressure sensing heads were used depending on the flow rate. The heads could resolve pressure differences of 10^{-4} and 10^{-5} mm Hg respectively. The output of the Baratron was read with a digital voltmeter.

Air was drawn into the inlet of the test section from the laboratory room. After passing through the test section, the air discharged into a large plenum chamber, from which it was ducted to a rotameter and a control valve. One of three rotameters was used for flow metering depending on the flow rate.

Results and Discussion

Fully developed flow, as evidenced by the linear decrease of the pressure along the duct, was established after a short hydrodynamic development length. The linear region typically encompassed ten or more pressure taps. Figure 2 shows the axial pressure distribution for a representative data run.

A least-squares straight-line fit was employed to determine the pressure gradient $(-dp/dx)$ for each case. Then, the fully developed friction factor was evaluated from its definition

$$f = (-dp/dx)D_h/\tfrac{1}{2}\rho\bar{V}^2 \tag{1}$$

The hydraulic diameter D_h appearing in equation (1) corresponds to a subchannel bounded by the upper and lower walls of the flow passage and by the vertical symmetry lines passing through the half thickness of each fin. Thus, with A and P respectively designating the cross-sectional area and the wetted perimeter,

$$D_h = 4A/P,\ 3\ A = SH + 2(t/2)C \tag{2}$$

$$P = S + 2h + 2(t/2) + S + 2(t/2) \tag{3}$$

The mean velocity appearing in equation (1) was evaluated by prorating the measured mass flow uniformly among the eleven subchannels. The friction factors will be plotted as a function of the Reynolds number Re

$$\mathrm{Re} = \rho\bar{V}D/\mu,\ 3\ \rho\bar{V} = \dot{m}/A \tag{4}$$

where $\dot{m}$ is the subchannel mass flow.

The first set of results to be reported are those for the rectangular ducts which correspond to operation of the test section without the spacer bars and fins in place. These ducts will be designated by their aspect ratios 2.44, 4.64, and 9.04. The rectangular-duct friction factors are plotted as a function of the Reynolds number in the upper graph of Fig. 3. Also plotted there is the Prandtl equation

$$f^{-1/2} = 2\log(\mathrm{Re}f^{1/2}) - 0.8 \tag{5}$$

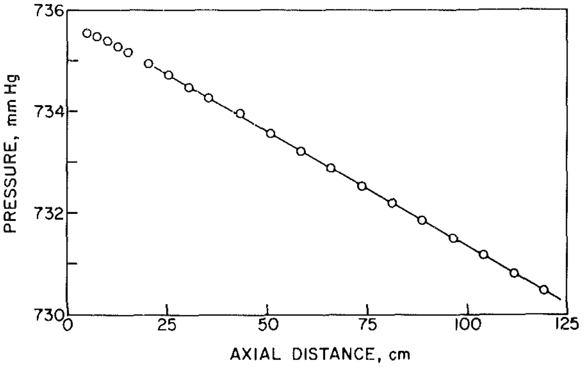

Fig. 2 Representative axial pressure distribution; the data are for $S/H = \frac{1}{4}$, $h/H = \frac{7}{8}$, and volume flow = 74 scfm

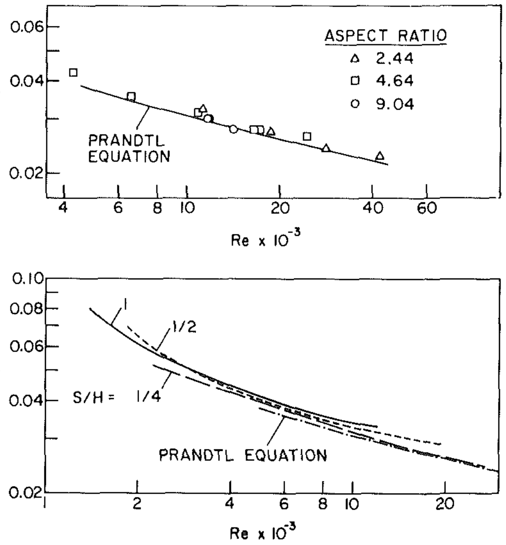

Fig. 3 Upper graph: rectangular-duct friction factors. Lower graph: comparison of friction factor results for various longitudinally finned ducts

which is the best established circular-tube friction factor correlation. It is frequently applied to noncircular ducts by substituting the hydraulic diameter D_h in place of the tube diameter.

Examination of the figure shows that the data for the three aspect ratios are in generally good agreement with each other. Furthermore, the trend of the data follows that of the Prandtl equation, with a mean deviation of the data from the Prandtl line of about four percent. Such a deviation is entirely acceptable, since it is well established in the literature that the hydraulic diameter does not precisely adapt circular-tube friction factors to rectangular ducts [3]. In general, the comparison shown in the upper part of Fig. 3 lends support to the experimental technique.

The friction factor results for the longitudinal fin arrays are presented in Fig. 4, with the lower, middle, and upper graphs corresponding respectively to fixed interfin spacings $S/H = \frac{1}{4}, \frac{1}{2}$, and 1. In each graph, the data for the various fin heights h/H and clearance gaps C/H are identified by different symbols. Curves have been faired through the data to provide continuity.

From an examination of Fig. 4, it is seen that in each graph (that is, at a fixed interfin spacing S/H), the data for the various fin heights and clearance gaps fall together, so that the friction factors are independent of h/H or C/H. This finding indicates that the use of the hydraulic diameter is effective in eliminating the tip-to-shroud clearance as an independent parameter in the friction factor—Reynolds number relationship. The fact that the f,Re correlation is independent of the clearance gap is an important design simplification.

Further inspection of Fig. 4 suggests that there are differences in the slopes of the f,Re distributions for the various interfin spacings S/H. To address this issue more directly, the faired curves from the

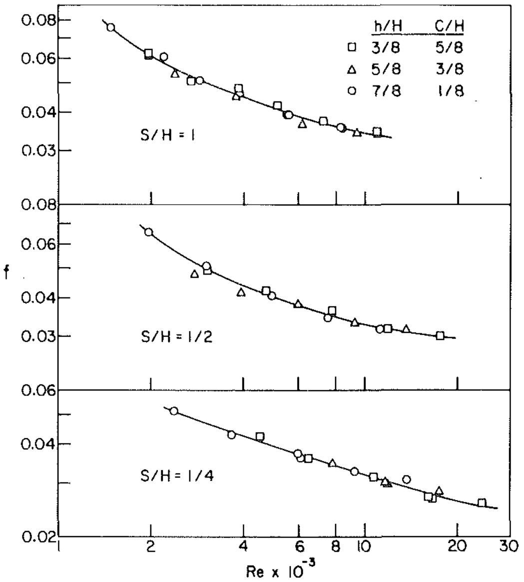

Fig. 4 Friction factor results for logitudinally finned ducts

three graphs of Fig. 4 have been brought together in the lower portion of Fig. 3, where the Prandtl equation is also plotted. From this comparison, it is seen that the spread among the experimental results is no greater than ten percent. At the high Reynolds number end of the range, however, there appears to be a tendency for the friction factors for the $S/H = \frac{1}{2}$ and 1 spacings to decrease more slowly than do the f values for the $S/H = 1/4$ spacing and from the Prandtl equation.

The fact that there is a spread of the experimental results with S/H indicates that the use of the hydraulic diameter is not fully able to eliminate the effects of interfin spacing. On the other hand, the relatively slower decrease of the larger-spacing friction factors at the higher Reynolds numbers is suggestive of possible fluid flow complexities. In this connection, it may be noted that a slowly decreasing friction factor with Reynolds number has been encountered in duct flows where there are significant inertial losses (e.g., roughness). It may be conjectured that in the present flow configuration, inertial-type losses may be induced by secondary flows (i.e., corkscrew-like flows). Such flows are known to exist in rectangular ducts under turbulent conditions. It is to be expected that the more vigorous the secondary flow, the greater the inertial losses. Thus, it would appear that the secondary flows are more constrained when the interfin spacing is small and are more vigorous for larger interfin spacings.

Acknowledgment

This research was performed under the auspices of the Office of Naval Research (contract no. N00014-79-C-0621).

References

1 Carnavos, T. C., "Heat Transfer Performance of Internally Finned Tubes in Turbulent Flow," in *Advances in Enhanced Heat Transfer*, American Society of Mechanical Engineers, New York, 1979, pp. 61–67.

2 Sparrow, E. M., Baliga, B. R., and Patankar, S. V., "Forced Convection Heat Transfer from a Shrouded Fin Array With and Without Tip Clearance," ASME JOURNAL OF HEAT TRANSFER, Vol. 100, 1978, pp. 572–579.

3 Jones, O. C., Jr., "An Improvement in the Calculation of Turbulent Friction in Rectangular Ducts," ASME *Journal of Fluids Engineering*, Vol. 98, 1976, pp. 173–181.

An Approximate Formula for Gas Convection Dominant Heat Transfer in Large-Particle Fluidized Beds

R. L. Adams[1]

Nomenclature

Ar = Archimedes number, $\frac{d_p^3 g}{\nu^2}\left(\frac{\rho_p}{\rho_g} - 1\right)$

D = tube diameter

d_p = particle diameter

k_g = gas thermal conductivity at bed temperature

Nu = Nusselt number, $\frac{\dot{q}'' L}{k_g(T_B - T_w)}$

Nu_p = Nusselt number based upon particle diameter

Nu_{p0} = stokes region contribution to average Nusselt number

$(\mathrm{Nu})_{2D}$ = two-dimensional Nusselt number

$(\mathrm{Nu}_p)_{\mathrm{Total}}$ = total Nusselt number for tube

Q_g^+ = dimensionless average interstitial gas velocity, Q_g/U_{mf}

Re_p = Reynolds number, $\frac{U_{mf} d_p}{\nu}$

r_p = particle radius

s_p = half of particle spacing at wall

T_B = bed temperature

T_w = wall temperature

U_{mf} = minimum fluidizing velocity

u' = intensity of interstitial turbulence

z = position on surface of tube from lower stagnation point

ϵ = void fraction

θ = polar angle from lower stagnation point

ν = kinematic viscosity of gas

Introduction

In Adams and Welty [1], a gas convection model of heat transfer to a tube immersed in a large-particle fluidized bed is presented. Calculations based upon the model have been found to agree well with recent heat transfer measurements in large-particle fluidized beds reported by George, et al. [2] and Catipovic, et al. [3]. The purpose of this note is to summarize an approximate formula for the Nusselt number due to gas convection which has been obtained by correlating intermediate numerical results presented by Adams [4] and Adams and Welty [1].

Discussion

The gas convective Nusselt number is obtained as a result of analysis of the three-dimensional viscous flow within interstitial channels adjacent to the heat transfer surface. This flow is modeled by dividing the flow field into an inviscid core and surrounding viscous boundary layer, with a Stokes' flow approximation near particle contact points. Furthermore, the inviscid flow is assumed to be "stagnation-like" as a result of the presence of a particle at the entrance of the channel and to contain "free-stream" turbulence produced by the wakes of particles. Heat transfer due to the two-dimensional portion of the boundary layer flow is obtained using an integral procedure which includes the effect of the free-stream turbulence. For the Stokes' region, the energy equation reduces to the steady conduction equation which is solved using a numerical conformal mapping. The size of the Stokes' region is established by requiring the Nusselt number be continuous across the channel. Because of the numerical conformal mapping and the inclusion of imposed turbulence, the analytical procedure is quite complicated, but can be simplified by correlating the intermediate numerical results reported by Adams [4] and Adams and Welty [1].

---

[1] Assistant Professor, Department of Mechanical Engineering, Oregon State University, Corvallis, Oregon 97331. Mem. ASME.

Contributed by the Heat Transfer Division for publication in the JOURNAL OF HEAT TRANSFER. Manuscript received by the Heat Transfer Division August 5, 1980.

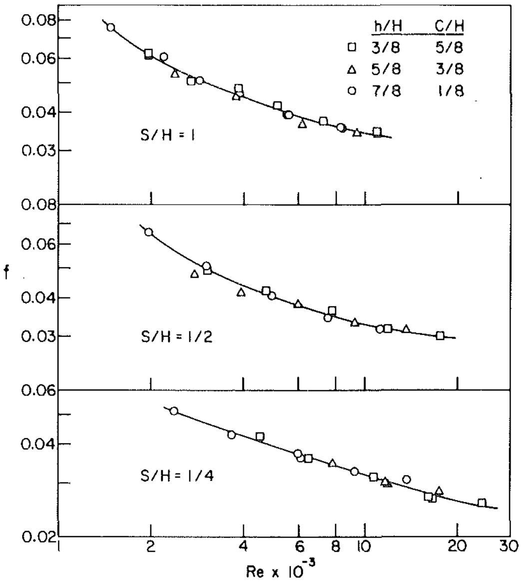

Fig. 4 Friction factor results for logitudinally finned ducts

three graphs of Fig. 4 have been brought together in the lower portion of Fig. 3, where the Prandtl equation is also plotted. From this comparison, it is seen that the spread among the experimental results is no greater than ten percent. At the high Reynolds number end of the range, however, there appears to be a tendency for the friction factors for the $S/H = \frac{1}{2}$ and 1 spacings to decrease more slowly than do the f values for the $S/H = 1/4$ spacing and from the Prandtl equation.

The fact that there is a spread of the experimental results with S/H indicates that the use of the hydraulic diameter is not fully able to eliminate the effects of interfin spacing. On the other hand, the relatively slower decrease of the larger-spacing friction factors at the higher Reynolds numbers is suggestive of possible fluid flow complexities. In this connection, it may be noted that a slowly decreasing friction factor with Reynolds number has been encountered in duct flows where there are significant inertial losses (e.g., roughness). It may be conjectured that in the present flow configuration, inertial-type losses may be induced by secondary flows (i.e., corkscrew-like flows). Such flows are known to exist in rectangular ducts under turbulent conditions. It is to be expected that the more vigorous the secondary flow, the greater the inertial losses. Thus, it would appear that the secondary flows are more constrained when the interfin spacing is small and are more vigorous for larger interfin spacings.

Acknowledgment

This research was performed under the auspices of the Office of Naval Research (contract no. N00014-79-C-0621).

References

1 Carnavos, T. C., "Heat Transfer Performance of Internally Finned Tubes in Turbulent Flow," in *Advances in Enhanced Heat Transfer*, American Society of Mechanical Engineers, New York, 1979, pp. 61–67.

2 Sparrow, E. M., Baliga, B. R., and Patankar, S. V., "Forced Convection Heat Transfer from a Shrouded Fin Array With and Without Tip Clearance," ASME JOURNAL OF HEAT TRANSFER, Vol. 100, 1978, pp. 572–579.

3 Jones, O. C., Jr., "An Improvement in the Calculation of Turbulent Friction in Rectangular Ducts," ASME *Journal of Fluids Engineering*, Vol. 98, 1976, pp. 173–181.

An Approximate Formula for Gas Convection Dominant Heat Transfer in Large-Particle Fluidized Beds

R. L. Adams[1]

Nomenclature

Ar = Archimedes number, $\frac{d_p^3 g}{\nu^2}\left(\frac{\rho_p}{\rho_g} - 1\right)$
D = tube diameter
d_p = particle diameter
k_g = gas thermal conductivity at bed temperature
Nu = Nusselt number, $\frac{\dot{q}'' L}{k_g(T_B - T_w)}$
Nu_p = Nusselt number based upon particle diameter
Nu_{p0} = stokes region contribution to average Nusselt number
$(\text{Nu})_{2D}$ = two-dimensional Nusselt number
$(\text{Nu}_p)_{\text{Total}}$ = total Nusselt number for tube
Q_g^+ = dimensionless average interstitial gas velocity, Q_g/U_{mf}
Re_p = Reynolds number, $\frac{U_{mf} d_p}{\nu}$
r_p = particle radius
s_p = half of particle spacing at wall
T_B = bed temperature
T_w = wall temperature
U_{mf} = minimum fluidizing velocity
u' = intensity of interstitial turbulence
z = position on surface of tube from lower stagnation point
ϵ = void fraction
θ = polar angle from lower stagnation point
ν = kinematic viscosity of gas

Introduction

In Adams and Welty [1], a gas convection model of heat transfer to a tube immersed in a large-particle fluidized bed is presented. Calculations based upon the model have been found to agree well with recent heat transfer measurements in large-particle fluidized beds reported by George, et al. [2] and Catipovic, et al. [3]. The purpose of this note is to summarize an approximate formula for the Nusselt number due to gas convection which has been obtained by correlating intermediate numerical results presented by Adams [4] and Adams and Welty [1].

Discussion

The gas convective Nusselt number is obtained as a result of analysis of the three-dimensional viscous flow within interstitial channels adjacent to the heat transfer surface. This flow is modeled by dividing the flow field into an inviscid core and surrounding viscous boundary layer, with a Stokes' flow approximation near particle contact points. Furthermore, the inviscid flow is assumed to be "stagnation-like" as a result of the presence of a particle at the entrance of the channel and to contain "free-stream" turbulence produced by the wakes of particles. Heat transfer due to the two-dimensional portion of the boundary layer flow is obtained using an integral procedure which includes the effect of the free-stream turbulence. For the Stokes' region, the energy equation reduces to the steady conduction equation which is solved using a numerical conformal mapping. The size of the Stokes' region is established by requiring the Nusselt number be continuous across the channel. Because of the numerical conformal mapping and the inclusion of imposed turbulence, the analytical procedure is quite complicated, but can be simplified by correlating the intermediate numerical results reported by Adams [4] and Adams and Welty [1].

---

[1] Assistant Professor, Department of Mechanical Engineering, Oregon State University, Corvallis, Oregon 97331. Mem. ASME.

Contributed by the Heat Transfer Division for publication in the JOURNAL OF HEAT TRANSFER. Manuscript received by the Heat Transfer Division August 5, 1980.

The Nusselt number for the interstitial channel is

$$\mathrm{Nu}_p = \left(\frac{x_s}{s_p}\right) \mathrm{Nu}_{p2D} + \mathrm{Nu}_{p0} \tag{1}$$

where Nu_{p0} is the Stokes' region contribution. The two-dimensional fraction, x_s/s_p, depends upon both the geometry of the channel and two-dimensional Nusselt number. This parameter, obtained from the numerical solution for the Stokes' region, can be approximated by

$$\frac{x_s}{s_p} \simeq 0.76 - \frac{k_1 S_0}{(\mathrm{Nu}_p)_{2D}} \text{ for } (\mathrm{Nu}_p)_{2D} \geq (\mathrm{Nu}_p)_m \tag{2a}$$

$$\frac{x_s}{s_p} \simeq \frac{k_2}{S_0} (\mathrm{Nu}_p)_{2D} \text{ for } (\mathrm{Nu}_p)_{2D} < (\mathrm{Nu}_p)_m \tag{2b}$$

where

$$k_1 = 7.36 - 10.81 \left(\frac{s_p}{r_p} - 1\right) \tag{3}$$

$$k_2 = 0.00904 + 0.01587 \left(\frac{s_p}{r_p} - 1\right) \tag{4}$$

and

$$(\mathrm{Nu}_p)_m = \frac{2k_1 S_0}{0.76 - (0.578 - 4k_1 k_2)^{1/2}} \tag{5}$$

The agreement with this approximation is within about 15 percent for $1 \leq s_p/r_p \leq 1.27$ or for $0.435 \leq \epsilon \leq 0.65$ where ϵ is the void fraction at the wall and the approximation

$$\frac{s_p}{r_p} = \frac{0.75}{\sqrt{1-\epsilon}} \text{ is used.} \tag{6}$$

Also, when the temperature along the particle surface varies linearly from T_w at the contact point to T_B at the upper edge of the Stokes' region, the numerical results provide the following approximation for the Stokes' region Nusselt number, Nu_{p0}:

$$\mathrm{Nu}_{p0} \simeq \frac{2\, S_0}{\left(\frac{s_p}{r_p}\right)} \left(3.81 - 1.60 \left(\frac{s_p}{r_p} - 1\right)\right) \tag{7}$$

where

$$S_0 = \frac{1}{2}\left(1 + \frac{T_w}{T_B}\right)\left(\frac{T_w}{T_B}\right)^{1/2}\left(\frac{1 + A_1/T_B}{T_w/T_B + A_1/T_B}\right) \tag{8}$$

with

A_1 = Sutherland constant (110K for air).

The two-dimensional Nusselt number obtained from the integral solution is

$$(\mathrm{Nu}_p)_{2D} = \frac{2\sqrt{2}}{N_{Hv}} \left\{\frac{Q_g^+ \mathrm{Re}_p}{\left(\frac{s_p}{r_p}\right)\Omega_v}\right\}^{1/2} \tag{9}$$

where Q_g^+ is the dimensionless interstitial gas velocity, Re_p is the Reynolds number based upon minimum fluidizing velocity and particle diameter, N_{Hv} is a parameter which depends upon Prandtl number and Ω_v is the velocity profile shape parameter. From the numerical results, N_{Hv} is approximately independent of the intensity of interstitial turbulence (varying between 1.5 and 1.6 for a wide range of $\beta_T = 0.13\, \mathrm{u}' \sqrt{2\mathrm{Re}_p Q_g^+}$ and for $\mathrm{Pr} = 0.7$) and Ω_v can be approximated by

$$\Omega_v \simeq 1.405 + 5.6\, e^{-0.462\beta_T} \tag{10}$$

to within 5 percent of the numerical results. It is further suggested that the approximation

$$N_{Hv} \simeq 1.34\, \mathrm{Pr}^{-0.4} \tag{11}$$

be used so that the proper variation in Nusselt number with Prandtl number is obtained (see, e.g., Kays [9]).

After the above approximations are assembled, the Nusselt number for the interstitial channel flow is found to be

$$\mathrm{Nu}_p \simeq \begin{cases} a\sqrt{\mathrm{Re}_p} + b + \mathrm{Nu}_{p0} & \mathrm{Re}_p \geq \mathrm{Re}_{pm} \quad (12a) \\ c\, \mathrm{Re}_p + \mathrm{Nu}_{p0} & \mathrm{Re}_p < \mathrm{Re}_{pm} \quad (12b) \end{cases}$$

where

$$a = 0.76\alpha \tag{13}$$

$$b = -k_1 S_0 \tag{14}$$

$$c = \frac{k_2 \alpha^2}{S_0} \tag{15}$$

$$\alpha = \frac{2.11}{\mathrm{Pr}^{-0.4}} \left[\frac{Q_q^+}{\left(\frac{s_p}{r_p}\right)(1.405 + 5.6e^{-0.0849u'\sqrt{\mathrm{Re}_p}\, Q_g^+}}\right]^{1/2} \tag{16}$$

The maximum Reynolds number, Re_{pm}, for quasi-linear behavior satisfies the nonlinear equation

$$\mathrm{Re}_{pm}\, Q_g^+ = A + B\, e^{-C\sqrt{\mathrm{Re}_{pm} Q_g^+}} \tag{17}$$

where

$$A = 1.405\,\beta \tag{18}$$

$$B = 5.6\,\beta \tag{19}$$

$$C = 0.0849\, u' \tag{20}$$

with

$$\beta = \left[\frac{1.34\, \mathrm{Pr}^{-0.4}\, k_1 S_0 \sqrt{\frac{1}{2}\frac{s_p}{r_p}}}{0.76 - (0.578 - 4k_1 k_2)^{1/2}}\right]^2 \tag{21}$$

Typically, $S_0 \sim 1$, $\mathrm{Pr} \sim 0.7$, $u' \sim 0.2$ so that $\mathrm{Re}_{pm} Q_g^+$ ranges between 5000 and 3500 for void fractions of 0.45 to 0.65 (typical surface values).

Results

The accuracy of the approximate formula for local Nusselt number around a tube is indicated in Fig. 1. For this calculation, the interstitial gas velocity (Q_g^+) was obtained from the potential pressure solution described by Adams and Welty [1] with account for voidage variations around the tube. The main parameters for the calculation are indicated on the figure and the approximate formula is seen to produce

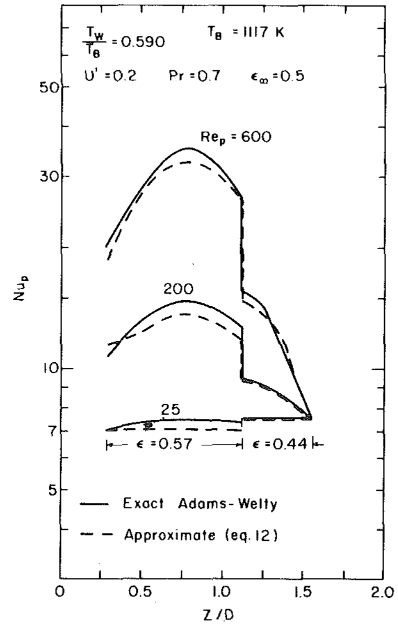

Fig. 1 Local Nusselt number comparison for horizontal tube

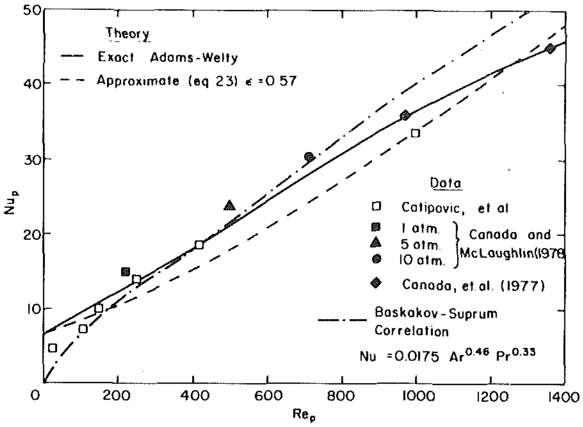

Fig. 2 Total Nusselt number for horizontal tube

results within about 10 percent of the numerical calculation. Note that values for the region $z/D < 0.3$ are not shown because a bubble is normally attached there.

The total Nusselt number for an immersed tube can be approximated using the model by neglecting voidage variations so that the gas velocity is

$$Q_g^+ \simeq \frac{2}{\epsilon} \sin \theta \tag{22}$$

where θ is measured from the lower stagnation point. Then, with $\beta_T \simeq 0.13u' \sqrt{\mathrm{Re}_p/\epsilon}$, integration of equation (12b) gives

$$(\mathrm{Nu}_p)_{\mathrm{Total}} \simeq \frac{\left(0.0917 + 0.154 \left(\frac{s_p}{r_p} - 1\right)\right)\mathrm{Re}_p}{\epsilon S_0 N_{Hv}{}^2 \left(\frac{s_p}{r_p}\right) \left(1.405 + 5.6e^{-0.0849u'\sqrt{\mathrm{Re}/\epsilon}}\right)} + \frac{2\,S_0}{(S_p/r_p)}\left(3.81 - 1.6\left(\frac{S_p}{r_p} - 1\right)\right) \tag{23}$$

Now, considering air (Pr = 0.7) low temperature operation (so that $S_0 = 1.0$), turbulence intensity, $u' = 0.2$, and using the correlation of Wen and Yu [5] for Re_p with $\epsilon = 0.57$ (the average surface value) the variation in total Nusselt number shown in Fig. 2 is obtained. Shown with the approximation are exact numerical results, an experimental correlation developed by Baskakov and Suprum [6] and experimental data obtained by Catipovic [3] and Canada [7] for operation near minimum fluidizing conditions. The major source of error in the approximation is the assumption of constant voidage, but the error is still at most 15 percent for the range of parameters indicated.

Conclusion

The approximate Nusselt number obtained using equation (13) provides a reasonable alternative to the numerical procedure developed by Adams and Welty [1] for local gas convection dominant Nusselt number. Integration of the approximate formula for heat transfer to an immersed horizontal tube with constant voidage provides results which do not match exact results with variable voidage but are within about 15 percent of those results and experimental data.

References

1 Adams, R. L., and Welty, J. R., "A Gas Convection Model of Heat Transfer in Large-Particle Fluidized Beds," *AIChE Journal*, Vol. 25, No. 3, 1979, pp. 395–405.

2 George, A., Welty, J. R., and Catipovic, N. M., "An Analytical Study of Heat Transfer to a Horizontal Cylinder in a Large-Particle Fluidized Bed," ASME Paper 79-HT-78, Aug. 1979.

3 Catipovic, N. M., Fitzgerald, T. J., George, A. H., and Welty, J. R., "Experimental Validation of the Adams-Welty Model for Heat Transfer in Large-Particle Fluidized Beds," to be published, *AIChE Journal*.

4 Adams, R. L., "An Analytical Model of Heat Transfer to a Horizontal Cylinder Immersed in a Gas-Fluidized Bed," Ph.D. Thesis, Oregon State University, Corvallis, 1977.

5 Wen, C. Y. and Yu, Y. H., "A Generalized Method of Predicting the Minimum Fluidization Velocity," *AIChE Journal*, Vol. 12, 1966, p. 610.

6 Baskakov, A. P. and Suprum, V. M., "Determination of the Convective Component of the Heat Transfer Coefficient to a Gas Fluidized Bed," *International Chemical Engineering*, Vol. 12, 1972, pp. 324–326.

7 Canada, G. S. and McLaughlin, M. H., "Large-Particle Fluidization and Heat Transfer at High Pressures," *AIChE Symposium Series*, Vol. 74, No. 176, 1978, pp. 27–37.

8 Canada, G. S., McLaughlin, M. H., and Staub, F. W., "Two-Phase Flow and Heat Transfer in Fluidized Beds," Quarterly Reports prepared for the Electric Power Research Institute (Contract RP-525-1), General Electric Corporate Research and Development, Schenectady, NY, 1977.

9 Kays, W. M., *Convective Heat and Mass Transfer*, McGraw-Hill, New York, 1966.

Application of the Integral Method to Two-Dimensional Transient Heat Conduction Problems

---

W. W. Yuen[1] and R. A. Wessel[1]

Nomenclature

F = function defined by equation (8)
t = time
u = transformed coordinate defined by equation (4)
v = transformed coordinate defined by equation (4)
x = coordinate
y = coordinate
α = thermal diffusivity
δ = one-dimensional penetration depth
$\eta = u/\delta$
θ = temperature

Introduction

In the field of heat transfer, the integral method is one of the most powerful solution techniques. For practical engineering applications, the method is used to generate approximate closed-form solutions. The effect of system parameters and the importance of various dimensionless groups can be readily demonstrated. For many numerical computations, the integral method is used to generate small-time solutions which otherwise are very difficult to obtain. Review of the integral method and its application to both linear and nonlinear heat transfer problems is available in the literature [1].

The objective of this work is to show that the integral method can be generalized to apply to the two-dimensional transient conduction problem. The problem of a rectangular corner with uniform initial temperature is solved as an illustration.

Mathematical Formulation

The physical model and its associated coordinate system for the rectangular-corner problem is shown in Fig. 1(a). For simplicity, all thermal properties are assumed to be constant. The conduction equation is

$$\frac{\partial^2\theta}{\partial x^2} + \frac{\partial^2\theta}{\partial y^2} = \frac{1}{\alpha}\frac{\partial\theta}{\partial t} \tag{1}$$

with θ being the temperature and α the thermal diffusivity. The initial condition is

$$\theta(x,y,t) = 0 \qquad t < 0, \qquad \text{all } x,y \tag{2}$$

---

[1] Department of Mechanical and Environmental Engineering, University of California, Santa Barbara, Calif. 93106.

Contributed by the Heat Transfer Division for publication in the JOURNAL OF HEAT TRANSFER. Manuscript received by the Heat Transfer Division, July 2, 1980.

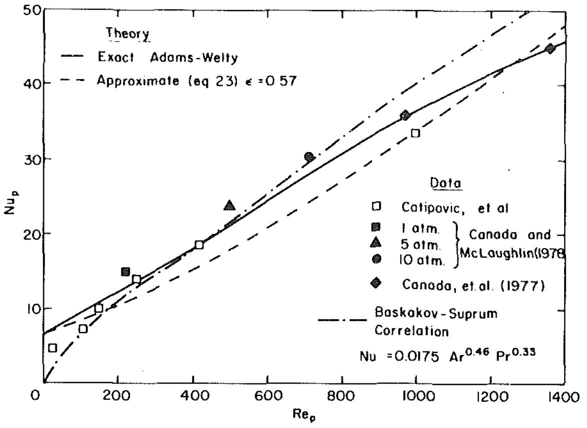

Fig. 2 Total Nusselt number for horizontal tube

results within about 10 percent of the numerical calculation. Note that values for the region $z/D < 0.3$ are not shown because a bubble is normally attached there.

The total Nusselt number for an immersed tube can be approximated using the model by neglecting voidage variations so that the gas velocity is

$$Q_g^+ \simeq \frac{2}{\epsilon} \sin \theta \tag{22}$$

where θ is measured from the lower stagnation point. Then, with $\beta_T \simeq 0.13u' \sqrt{\mathrm{Re}_p/\epsilon}$, integration of equation (12*b*) gives

$$(\mathrm{Nu}_p)_{\mathrm{Total}} \simeq \frac{\left(0.0917 + 0.154\left(\frac{s_p}{r_p} - 1\right)\right)\mathrm{Re}_p}{\epsilon S_0 N_{Hv}{}^2\left(\frac{s_p}{r_p}\right)\left(1.405 + 5.6e^{-0.0849u'\sqrt{\mathrm{Re}/\epsilon}}\right) + \frac{2\,S_0}{(S_p/r_p)}\left(3.81 - 1.6\left(\frac{S_p}{r_p} - 1\right)\right)} \tag{23}$$

Now, considering air ($\mathrm{Pr} = 0.7$) low temperature operation (so that $S_0 = 1.0$), turbulence intensity, $u' = 0.2$, and using the correlation of Wen and Yu [5] for Re_p with $\epsilon = 0.57$ (the average surface value) the variation in total Nusselt number shown in Fig. 2 is obtained. Shown with the approximation are exact numerical results, an experimental correlation developed by Baskakov and Suprum [6] and experimental data obtained by Catipovic [3] and Canada [7] for operation near minimum fluidizing conditions. The major source of error in the approximation is the assumption of constant voidage, but the error is still at most 15 percent for the range of parameters indicated.

Conclusion

The approximate Nusselt number obtained using equation (13) provides a reasonable alternative to the numerical procedure developed by Adams and Welty [1] for local gas convection dominant Nusselt number. Integration of the approximate formula for heat transfer to an immersed horizontal tube with constant voidage provides results which do not match exact results with variable voidage but are within about 15 percent of those results and experimental data.

References

1 Adams, R. L., and Welty, J. R., "A Gas Convection Model of Heat Transfer in Large-Particle Fluidized Beds," *AIChE Journal*, Vol. 25, No. 3, 1979, pp. 395–405.

2 George, A., Welty, J. R., and Catipovic, N. M., "An Analytical Study of Heat Transfer to a Horizontal Cylinder in a Large-Particle Fluidized Bed," ASME Paper 79-HT-78, Aug. 1979.

3 Catipovic, N. M., Fitzgerald, T. J., George, A. H., and Welty, J. R., "Experimental Validation of the Adams-Welty Model for Heat Transfer in Large-Particle Fluidized Beds," to be published, *AIChE Journal*.

4 Adams, R. L., "An Analytical Model of Heat Transfer to a Horizontal Cylinder Immersed in a Gas-Fluidized Bed," Ph.D. Thesis, Oregon State University, Corvallis, 1977.

5 Wen, C. Y. and Yu, Y. H., "A Generalized Method of Predicting the Minimum Fluidization Velocity," *AIChE Journal*, Vol. 12, 1966, p. 610.

6 Baskakov, A. P. and Suprum, V. M., "Determination of the Convective Component of the Heat Transfer Coefficient to a Gas Fluidized Bed," *International Chemical Engineering*, Vol. 12, 1972, pp. 324–326.

7 Canada, G. S. and McLaughlin, M. H., "Large-Particle Fluidization and Heat Transfer at High Pressures," *AIChE Symposium Series*, Vol. 74, No. 176, 1978, pp. 27–37.

8 Canada, G. S., McLaughlin, M. H., and Staub, F. W., "Two-Phase Flow and Heat Transfer in Fluidized Beds," Quarterly Reports prepared for the Electric Power Research Institute (Contract RP-525-1), General Electric Corporate Research and Development, Schenectady, NY, 1977.

9 Kays, W. M., *Convective Heat and Mass Transfer*, McGraw-Hill, New York, 1966.

Application of the Integral Method to Two-Dimensional Transient Heat Conduction Problems

W. W. Yuen[1] and R. A. Wessel[1]

Nomenclature

F = function defined by equation (8)
t = time
u = transformed coordinate defined by equation (4)
v = transformed coordinate defined by equation (4)
x = coordinate
y = coordinate
α = thermal diffusivity
δ = one-dimensional penetration depth
$\eta = u/\delta$
θ = temperature

Introduction

In the field of heat transfer, the integral method is one of the most powerful solution techniques. For practical engineering applications, the method is used to generate approximate closed-form solutions. The effect of system parameters and the importance of various dimensionless groups can be readily demonstrated. For many numerical computations, the integral method is used to generate small-time solutions which otherwise are very difficult to obtain. Review of the integral method and its application to both linear and nonlinear heat transfer problems is available in the literature [1].

The objective of this work is to show that the integral method can be generalized to apply to the two-dimensional transient conduction problem. The problem of a rectangular corner with uniform initial temperature is solved as an illustration.

Mathematical Formulation

The physical model and its associated coordinate system for the rectangular-corner problem is shown in Fig. 1(*a*). For simplicity, all thermal properties are assumed to be constant. The conduction equation is

$$\frac{\partial^2\theta}{\partial x^2} + \frac{\partial^2\theta}{\partial y^2} = \frac{1}{\alpha}\frac{\partial\theta}{\partial t} \tag{1}$$

with θ being the temperature and α the thermal diffusivity. The initial condition is

$$\theta(x,y,t) = 0 \qquad t < 0, \qquad \text{all } x,y \tag{2}$$

---

[1] Department of Mechanical and Environmental Engineering, University of California, Santa Barbara, Calif. 93106.

Contributed by the Heat Transfer Division for publication in the JOURNAL OF HEAT TRANSFER. Manuscript received by the Heat Transfer Division, July 2, 1980.

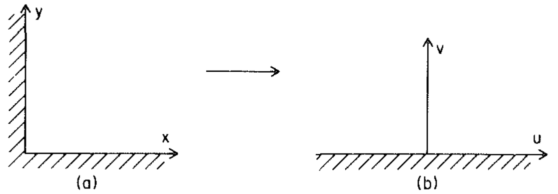

Fig. 1 The original and transformed coordinate system for the present problem

The boundary conditions for the two cases considered in the present work are

$$\begin{aligned}\theta(0,y,t) &= 1 \quad t \geqq 0, \quad y \geqq 0\\ \theta(x,0,t) &= 1 \quad t \geqq 0, \quad x \geqq 0\end{aligned} \tag{3}$$

The above initial and boundary conditions are obviously normalized for simplicity. Since the problem is linear, solutions to problems with unnormalized conditions can be readily generated by superposition of the present results.

As they are, equation (1) together with the initial and boundary conditions are practically impossible to be solved by the integral method. Physically, application of the integral method requires the existence of a characteristic length such that beyond this length, the influence of the wall can be neglected. While it is clear that at any given time there exists a certain interior region of the rectangular corner which is relatively unaffected by the heated wall, the definition of a "length" for the problem under the present geometry appears to be extremely difficult, if not impossible.

This difficulty can be alleviated, however, if the following coordinate transformation is utilized.

$$u = x^2 - y^2 \tag{4}$$

$$v = 2xy \tag{5}$$

Mathematically, equations (4) and (5) represent the familiar conformal transformation [3] which is often used in the solution of the steady state conduction problem. Physically, this transformation maps the rectangular corner into the upper half plane as shown in Fig. 1(*b*). The curves u = const. and v = const. can be interpreted as the flux line and potential line for the rectangular corner in potential theory. In the transformed coordinate, equations (1, 2), and (3) become

$$4(u^2 + v^2)^{1/2}\left[\frac{\partial^2\theta}{\partial u^2} + \frac{\partial^2\theta}{\partial v^2}\right] = \frac{1}{\alpha}\frac{\partial\theta}{\partial t} \tag{1a}$$

$$\theta(u,v,t) = 0 \qquad t < 0, \qquad \text{all } u,v \tag{2a}$$

$$\theta(u,0,t) = 1 \qquad t \geqq 0 \tag{3a}$$

It is interesting to note that the transformed problem can now be interpreted as the problem of transient conduction in a semi-infinite medium with a spatially-dependent thermal diffusivity.

While a complete solution of equation (1*a*) together with its initial and boundary conditions is just as difficult as it is for the original problem, the transformed problem has the advantage that it is more adaptable for the integral method. Physically, it is reasonable to assume that for each value of u at time t, there exists a penetration depth $\delta(u,t)$ such that $\theta = 0$ for all $v > \delta$. As in the traditional integral method for one-dimensional transient conduction problem, a temperature profile can be assumed at each value of u. A differential equation for $\delta(u,t)$ can be generated by an integration of equation (1*a*).

Results

Similar to the one-dimensional transient conduction problem, the temperature profile for the case with constant wall temperature is first assumed to be a second degree polynomial as follows

$$\theta(u,v,t) = \left(1 - \frac{v}{\partial(u,t)}\right)^2 \tag{6}$$

Substitute equation (6) into equation (1*a*) and integrate over v from 0 to δ, the following equation is resulted.

$$\frac{1}{3}\frac{\partial^2\delta}{\partial u^2} + \frac{2}{\delta} = \frac{1}{4\alpha}\frac{\partial F(\delta,u)}{\partial\delta}\frac{\partial\delta}{\partial t} \tag{7}$$

The function $F(u,\delta)$ in the above equation is defined as

$$F(u,\delta) = \left(1 - \frac{1}{2}\eta^2\right)\ln\left[\frac{1 + (1 + \eta^2)^{1/2}}{\eta}\right] - \frac{3}{2}(1 + \eta^2)^{1/2} + 2\eta \tag{8}$$

where $\eta = u/\delta$. The boundary conditions and initial condition for equation (7) are

$$\frac{\partial\delta}{\partial u}(0,t) = 0 \tag{9}$$

$$\lim_{u\to\infty} \delta(u,t) = (48u\alpha t)^{1/2} \tag{10}$$

$$\delta(u,0) = 0 \tag{11}$$

Physically, the problem is symmetric about the origin $u = 0$. Equation (7) is thus needed to be solved only for cases with $u > 0$. Equation (9) is the result of such symmetry. Equation (10) is based on the fact that in the limit of large u, the present result should reduce to the one-dimensional case which yields the following expression for the approximate temperature profile [4].

$$\theta(y,t) = \left(1 - \frac{y}{(12\alpha t)^{1/2}}\right)^2 \tag{12}$$

While an exact numerical solution to equation (7) is not difficult to obtain, a closed-form early-time solution can be readily generated by assuming that the second derivative of δ is negligible. Equation (7) can then be integrated to yield

$$\begin{aligned}\frac{8\alpha t}{\delta} = -\eta^2 \ln\left[\frac{1 + (1 + \eta^2)^{1/2}}{\eta}\right] + \frac{\eta}{2}\ln\\ \times\left[\frac{2(1 + (1 + \eta^2)^{1/2} - \eta)\eta^4}{(1 + (1 + \eta^2)^{1/2} + \eta)(\eta + (\eta^2 + 1)^{1/2})^3}\right]\\ + 1 + \frac{\eta^2}{[1 + (1 + y)^2]^{1/2}}\end{aligned} \tag{13}$$

It is interesting to note that equation (6), utilizing the value of δ generated by equation (13), already yields temperature distributions compared favorably with the exact solution, particularly in the limit of large u. The worst accuracy appears to occur at $u = 0$. Equation (13) gives

$$\delta(0,t) = 8\alpha t \tag{14}$$

Equation (6) becomes

$$\theta(0,v,t) = \left(1 - \frac{v}{8\alpha t}\right)^2 \tag{15}$$

Note that since the line $u = 0$ in the u-v plane corresponds to the line $x = y$ in the x-y plane, the temperature profile is only a function of x. The exact expression of the temperature profile is available [2]. It is

$$\theta(x,t) = 1 - \left[\operatorname{erf}\frac{x}{2(\alpha t)^{1/2}}\right]^2 \tag{16}$$

Compared to equation (16), equation (15) is not very accurate, except in the limit of small x and large t. But it still yields the correct qualitative behavior of the temperature profile.

Since equation (7) is of the same general form as a one-dimensional transient conduction problem, its solution can be readily obtained by any standard numerical computation routine such as the tri-diagonal algorithm. Results of temperature profiles generated by the present integral method compare well with the available exact solution [2]. For the least accurate case at $u = 0$, approximate temperature profiles at two different times are compared with the exact solution in Fig. 2. The agreement is quite acceptable. The numerical solution also suggests that for large values of αt ($\alpha t > 1$), the penetration depth

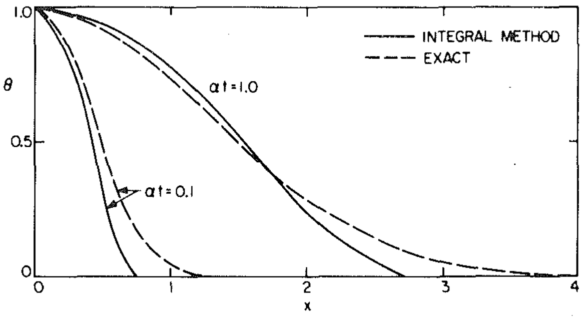

Fig. 2 Comparison between temperature profiles generated by the integral method and the exact result for the problem with a constant wall temperature

at $u = 0$ can be approximated as

$$\lim_{\alpha t \to \infty} \delta(0,t) \to 16\alpha t \tag{17}$$

The temperature profile at $u = 0$ becomes

$$\theta(x,t) = \left(1 - \frac{x^2}{8\alpha t}\right)^2 \tag{18}$$

Equation (18) represents a fairly accurate approximation for equation (16).

Conclusion

Utilizing a simple conformal transformation which maps the region of interest onto the upper half plane, the integral method is generalized to apply to the two-dimensional transient conduction problem. Transient heat conduction in a rectangular corner subjected to a constant temperature boundary conditions is solved as an illustration of the method. Results compare well with the available exact result and they are generated with little effort.

References

1 Goodman, T. R., "Application of Integral Methods to Transient Nonlinear Heat Transfer," *Advances in Heat Transfer*, Vol. 1, 1964, pp. 55–122.

2 Carslaw, H., and Jaeger, J., "*Conduction of Heat Solids*," Oxford Press, 1959.

3 Pennisi, L. L., *Elements of Complex Variables*, Holt, Rinehart and Winston, New York, 1963, pp. 288–393.

4 Eckert, E. R. G., and Drake, R. M., *Analysis of Heat and Mass Transfer*, McGraw-Hill, New York, 1972, pp. 183–188.

The Temperature Distribution of a Sphere Placed in a Directed Uniform Heat Flux

K. A. Werley[1] and J. G. Gilligan[1]

Nomenclature

α = thermal diffusivity $\equiv \dfrac{k}{dc_p}$
β, γ = eigenvalues
c_p = specific heat
d = density
F = heat flux
J = Bessel function
k = thermal conductivity
λ, μ = eigenvalues
m, n = summation indices
P = Legendre polynomial
ρ = radial position in sphere
r = dimensionless position $\equiv \rho/R$
R = radius of sphere
τ = time
t = dimensionless time $\equiv \dfrac{\alpha\tau}{R^2}$
θ = angle
T = temperature
T_0 = initial temperature

Introduction

The purpose of this Technical Note is to solve analytically the time-dependent heat conduction problem of a sphere, with uniform initial temperature, located in a uniform field of directed heat flux. To the authors' knowledge, this solution has not been displayed, but is of interest in the area of magnetic thermonuclear reactor engineering. It has been shown that a "rain" of high speed liquid or solid spheres (e.g., Lithium) can effectively remove over a magnitude larger heat flux than a stationary solid wall while simultaneously gettering large fluxes of particles, thereby acting as a vacuum pump [1–3]. Thus, the importance of this concept requires that an accurate description of the temperature distribution be known so that vaporization rates, thermal stresses, and particle trapping efficiencies can be calculated.

Problem Description

The problem of a sphere with an initial uniform temperature, T_0, located in a field of directed uniform heat flux, F, is described by the heat conduction equation in spherical coordinates (see Fig. 1):

$$\frac{1}{\rho^2}\frac{\partial}{\partial \rho}\left(\rho^2 \frac{\partial T}{\partial \rho}\right) + \frac{1}{\rho^2 \sin\theta}\frac{\partial}{\partial \theta}\left(\sin\theta \frac{\partial T}{\partial \theta}\right) = \frac{1}{\alpha}\frac{\partial T}{\partial \tau}$$
$$\times\; 0 \le \rho \le R;\; 0 \le \theta \le \pi;\; 0 \le \tau \tag{1}$$

It can be shown with simple geometrical arguments, that the directed uniform heat flux transforms to a surface flux which varies as the cosine distribution over the front of the sphere. Thus the initial and boundary conditions can be written:

$$T(\rho, \theta, 0) = T_0 \tag{2}$$

$$T(\rho, \theta, \tau) = \text{finite, for arbitrary } \theta \text{ and } \rho \tag{3}$$

$$\frac{\partial T}{\partial \rho}(R, \theta, \tau) = \begin{cases} \dfrac{F}{k}\cos\theta, & 0 \le \theta \le \dfrac{\pi}{2} \\ 0 & , \dfrac{\pi}{2} \le \theta \le \pi \end{cases} \tag{4}$$

The above set of equations describes the temperature distribution in the sphere provided that the following four assumptions are valid: (*a*) The material has constant, uniform properties (k, α, d, c_p). (*b*) The sphere does not spin relative to the directed flux. (*c*) There are no radiative heat losses. (*d*) There are no convection losses, either from the surface or in the interior (for a liquid sphere).

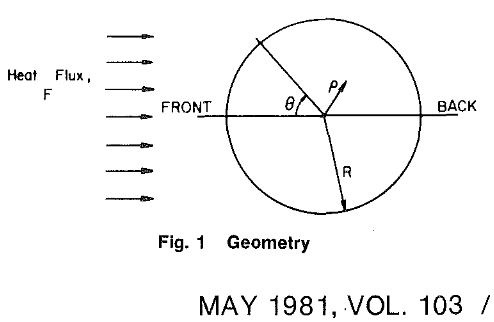

Fig. 1 Geometry

---

[1] Fusion Studies Laboratory, University of Illinois, Urbana, Ill. 61801.

Contributed by the Heat Transfer Division for publication in the JOURNAL OF HEAT TRANSFER. Manuscript received by the Heat Transfer Division July 28, 1980.

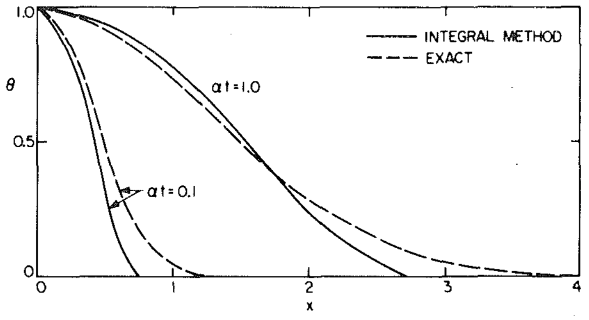

Fig. 2 Comparison between temperature profiles generated by the integral method and the exact result for the problem with a constant wall temperature

at $u = 0$ can be approximated as

$$\lim_{\alpha t\to\infty} \delta(0,t) \to 16\alpha t \qquad (17)$$

The temperature profile at $u = 0$ becomes

$$\theta(x,t) = \left(1-\frac{x^2}{8\alpha t}\right)^2 \qquad (18)$$

Equation (18) represents a fairly accurate approximation for equation (16).

Conclusion

Utilizing a simple conformal transformation which maps the region of interest onto the upper half plane, the integral method is generalized to apply to the two-dimensional transient conduction problem. Transient heat conduction in a rectangular corner subjected to a constant temperature boundary conditions is solved as an illustration of the method. Results compare well with the available exact result and they are generated with little effort.

References

1 Goodman, T. R., "Application of Integral Methods to Transient Nonlinear Heat Transfer," *Advances in Heat Transfer*, Vol. 1, 1964, pp. 55–122.

2 Carslaw, H., and Jaeger, J., "*Conduction of Heat Solids*," Oxford Press, 1959.

3 Pennisi, L. L., *Elements of Complex Variables*, Holt, Rinehart and Winston, New York, 1963, pp. 288–393.

4 Eckert, E. R. G., and Drake, R. M., *Analysis of Heat and Mass Transfer*, McGraw-Hill, New York, 1972, pp. 183–188.

The Temperature Distribution of a Sphere Placed in a Directed Uniform Heat Flux

K. A. Werley[1] and J. G. Gilligan[1]

Nomenclature

α = thermal diffusivity $\equiv \frac{k}{dc_p}$

β, γ = eigenvalues

c_p = specific heat

d = density

F = heat flux

J = Bessel function

k = thermal conductivity

λ, μ = eigenvalues

m, n = summation indices

P = Legendre polynomial

ρ = radial position in sphere

r = dimensionless position $\equiv \rho/R$

R = radius of sphere

τ = time

t = dimensionless time $\equiv \frac{\alpha\tau}{R^2}$

θ = angle

T = temperature

T_0 = initial temperature

Introduction

The purpose of this Technical Note is to solve analytically the time-dependent heat conduction problem of a sphere, with uniform initial temperature, located in a uniform field of directed heat flux. To the authors' knowledge, this solution has not been displayed, but is of interest in the area of magnetic thermonuclear reactor engineering. It has been shown that a "rain" of high speed liquid or solid spheres (e.g., Lithium) can effectively remove over a magnitude larger heat flux than a stationary solid wall while simultaneously gettering large fluxes of particles, thereby acting as a vacuum pump [1–3]. Thus, the importance of this concept requires that an accurate description of the temperature distribution be known so that vaporization rates, thermal stresses, and particle trapping efficiencies can be calculated.

Problem Description

The problem of a sphere with an initial uniform temperature, T_0, located in a field of directed uniform heat flux, F, is described by the heat conduction equation in spherical coordinates (see Fig. 1):

$$\frac{1}{\rho^2}\frac{\partial}{\partial\rho}\left(\rho^2\frac{\partial T}{\partial\rho}\right)+\frac{1}{\rho^2\sin\theta}\frac{\partial}{\partial\theta}\left(\sin\theta\frac{\partial T}{\partial\theta}\right)=\frac{1}{\alpha}\frac{\partial T}{\partial\tau}$$

$$\times\, 0\le\rho\le R;\ 0\le\theta\le\pi;\ 0\le\tau \qquad (1)$$

It can be shown with simple geometrical arguments, that the directed uniform heat flux transforms to a surface flux which varies as the cosine distribution over the front of the sphere. Thus the initial and boundary conditions can be written:

$$T(\rho,\theta,0) = T_0 \qquad (2)$$

$$T(\rho,\theta,\tau) = \text{finite, for arbitrary } \theta \text{ and } \rho \qquad (3)$$

$$\frac{\partial T}{\partial\rho}(R,\theta,\tau) = \begin{cases} \frac{F}{k}\cos\theta, & 0\le\theta\le\frac{\pi}{2} \\ 0 & ,\ \frac{\pi}{2}\le\theta\le\pi \end{cases} \qquad (4)$$

The above set of equations describes the temperature distribution in the sphere provided that the following four assumptions are valid: (*a*) The material has constant, uniform properties (k, α, d, c_p). (*b*) The sphere does not spin relative to the directed flux. (*c*) There are no radiative heat losses. (*d*) There are no convection losses, either from the surface or in the interior (for a liquid sphere).

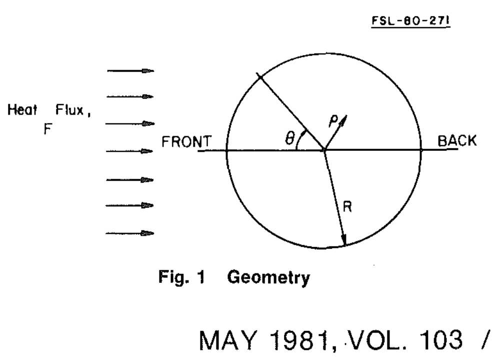

Fig. 1 Geometry

---

[1] Fusion Studies Laboratory, University of Illinois, Urbana, Ill. 61801.

Contributed by the Heat Transfer Division for publication in the JOURNAL OF HEAT TRANSFER. Manuscript received by the Heat Transfer Division July 28, 1980.

Result

The solution is found by making a Laplace transform in time and then using the method of separation of variables to find the spatial dependence. The final result is obtained by evaluating the inverse Laplace transform by contour integration. After considerable manipulation, we can write the final result in terms of dimensionless spatial and time variables:

$$\frac{kT(r,\theta,t)}{RF} = \frac{kT_0}{FR} + \frac{3t}{4} + \frac{5r^2-3}{40} - \frac{1}{2r}\sum_{m=1}^{\infty}\frac{\sin(\beta_m r)e^{-\beta_m^2 t}}{\beta_m^2 \sin(\beta_m)}$$
$$+ \cos\theta\left\{\frac{r}{2} - r^{-1/2}\sum_{m=1}^{\infty}\frac{J_{3/2}(\mu_m r)\,e^{-\mu_m^2 t}}{J_{3/2}(\mu_m)[\mu_m^2-2]}\right\}$$
$$- \sum_{n=1}^{\infty}\frac{2n+1/2}{2n^2+n-1}P_{2n}(0)P_{2n}(\cos\theta)\left\{\frac{r^{2n}}{4n} - r^{-1/2}\sum_{m=1}^{\infty}\right.$$
$$\left.\times\frac{J_{2n+1/2}(\gamma_m r)e^{-\gamma_m^2 t}}{J_{2n+1/2}(\gamma_m)[\gamma_m^2 - 2n(2n+1)]}\right\} \quad (5)$$

Here, β_m, μ_m, γ_m are the roots of $\tan\beta_m = \beta_m$,

$$\frac{d}{d\mu}\,\mu_m{}^{-1/2}\,J_{3/2}(\mu_m) = 0, \quad \text{and}\ \frac{d}{d\gamma}\,\gamma_m{}^{-1/2}\,J_{2n+1/2}(\gamma_m) = 0;$$

$$\beta_0, \mu_0, \gamma_0 = 0.$$

Note, the value of β_m, μ_m, and γ_m can be read from existing tables [4] as they are just the values where the local extrema of spherical Bessel functions occur. Also note that the solution is well behaved, even when r equals zero.

$$\lim_{r\to 0}\frac{\sin(ar)}{r} = a; \quad \lim_{r\to 0} r^{-1/2}\quad J_{n+1/2}(br) = 0, \quad n = 1, 2, 3 \ldots$$

Properties of the Solution

Note that the final result (5) is made up of three distinct parts: terms which are linear in time, independent of time, and exponential in time. Since there are no losses from the sphere, the average sphere temperature is given by $c_p d\,(T_{\text{AVG}} - T_0)\,4/3\,\pi R^3 = F\pi R^2\tau$.

$$T_{\text{AVG}}(t) = T_0 + \frac{3}{4}\frac{F\alpha\tau}{kR} = T_0 + \frac{FR}{k}\frac{3t}{4} \quad (6)$$

Thus, the linear time part of the solution just represents the average temperature rise of the sphere. In the limit of large time, the exponential part approaches zero, so, if we consider $T - T_{\text{AVG}}$, we are left with the time-independent part which represents a static temperature profile that is achieved at large time. This profile is shown as the $t = \infty$ curve in Fig. 2 and 3. The terms containing the exponential behavior express how the initial temperature profile relaxes into the static shape.

If we evaluate the series solution for the changing shape of the temperature profile, we have a complete description of the temperature history of the sphere. Figures 2 and 3 give these results along the diameter of the sphere (which is parallel to the directed heat flux) and on the surface of the sphere. Defining $f(r, \theta, t)$ to be the value of the ordinate of Fig. 2, we can write expressions for the maximum temperature of the sphere, $T_{\text{MAX}}(t)$, and the temperature difference across the sphere, $T_{\text{MAX}}(t) - T_{\text{MIN}}(t)$.

$$T_{\text{MAX}}(t) = T_{\text{AVG}}(t) + f(1, 0, t)\,\frac{FR}{k} \quad (7)$$

$$T_{\text{MAX}}(t) - T_{\text{MIN}}(t) = [f(1, 0, t) - f(1, \pi, t)]\,\frac{FR}{k} \quad (8)$$

Also, from Fig. 2, we see that for $t > 0.5$, the profile is approaching the static shape. In this case we can approximate $f(r, \theta, t)$ by $f(r, \theta, \infty)$, so $f(1, 0, \infty) = 0.689$ and $f(1, \pi, \infty) = -0.311$. Note that the result for the maximum temperature difference across the sphere is equivalent to the case of a slab of thickness $2R$, under a uniform heat load on one side, which has been examined by Carslaw and Jaeger [5].

Previous collector design calculations in references [1] and [2] have assumed that the maximum temperature difference across a sphere is some fraction ($\frac{2}{3}$ and $\frac{1}{2}$, respectively) of the slab wall case. This calculation shows that that assumption underestimates the maximum temperature and temperature difference. A Russian design [3] reports having solved the conduction problem of a sphere with a uniform heat flux over a hemisphere. This model is also fairly crude (compared to the problem of interest of a sphere in a directed flux) and it leads them to the faulty conclusion that a sphere will absorb a higher specific heat flux than a slab. For high flux designs in which $T_{\text{MAX}} - T_{\text{MIN}}$ is large and T_{MAX} is near some acceptable material limit, it is important to use our more precise results for making reliable designs.

Acknowledgments

The authors would like to thank Professor of Mathematics R. G. Langebartel of the University of Illinois at Urbana-Champaign, Kirby Fong, of the Lawrence Livermore Laboratory, and contributions from the Sandia Math Program Library. This work was supported by the Electric Power Research Institute under contract EPRI RP645-1.

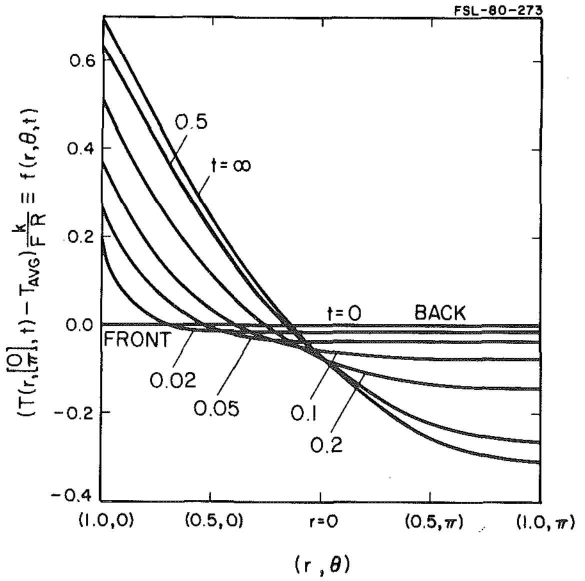

Fig. 2 Temperature profile (above T_{AVG}) in sphere (along the diameter parallel to the external heat flux)

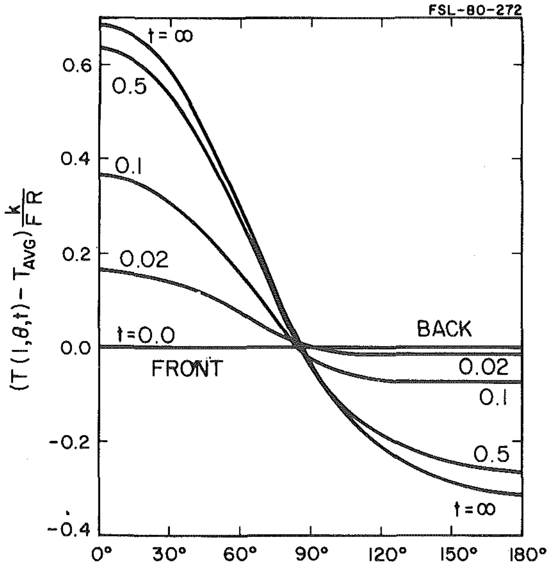

Fig. 3 Sphere surface temperature (above T_{AVG})

References

1 Wells, W. M., "ORNL TNS Program: Evaluation of the Bundle Divertor," ORNL/TM-6727, Oak Ridge Nat. Lab., Oak Ridge, Tenn., Nov. 1979.

2 Werley, K. A., Gilligan, J. G., and Miley, G. H., "A High Flux Energy and Particle Collection Scheme for Divertors," Proc. 11th Symp. on Fusion Technology, Oxford, England, Sept. 1980.

3 Lipov, M. Ku., and Murav'ev., E. V., "The Development of Highly Efficient Divertor Systems for Tokamak Energy Reactors," The I. B. Kurchatov Order of Lenin Institute of Atomic Energy, Moscow, 1979.

4 Tables of Spherical Bessel Functions, Math. Tables Project, Nat. Bureau of Standards, Vol. I & II, Columbia University Press, N.Y., 1947.

5 Carslaw, and Jaeger, *Conduction of Heat in Solids*, Oxford, 1959, p. 112.

Approximate Temperature Distribution for Phase Change of a Semi-Infinite Body

Sung Hwan Cho[1] **and J. Edward Sunderland**[2]

Nomenclature

B = Biot number, B = hL/k
c = specific heat at constant pressure
E = nondimensionalized enthalpy of phase change, $E = H/c\Delta T$
f = dimensionless constant defined by equation (10)
g = dimensionless constant defined by equation (12)
H = enthalpy of fusion
h = surface heat transfer coefficient
k = thermal conductivity
L = reference thickness, $L = \rho\alpha H/q$ for constant heat flux case, and $L = k/h$ for convection case
q = heat flux at the fixed surface
S = phase change position
s = nondimensionalized phase change position, $s = S/L$
T = temperature
t = nondimensionalized time, $t = \alpha\tau/L^2$
T_f = fusion temperature
T_∞ = surrounding temperature
ΔT = reference temperature difference, $\Delta T = H/c$ in Section 2 and $\Delta T = T_f - T_\infty$ in Section 3
t_0 = dimensionless constant defined by equation (10)
u = nondimensionalized temperature, $u = (T - T_f)/\Delta T$
X = distance
x = nondimensionalized distance, $x = X/L$
α = thermal diffusivity
ρ = density
τ = time

1 Introduction

Exact solutions to heat conduction problems with phase change are known only for the cases when phase change thickness is proportional to the square root of time. El-Genk and Cronenberg [1] claim that their solution is the first known exact solution of phase change problem with heat flux boundary condition. Their solution, however, is not exact because equations (8) and (9) do not satisfy the energy equation, equation (1) of reference [1]. In order for their solution to satisfy the energy equation, the quantity A, defined in equation (5) must be a constant. A is not a constant; it is a function of time. A similar method was used by Cho [2] for phase change problems with constant heat flux and convection surface conditions. This paper gives an approximate method of solution to phase change problems with constant heat flux and heat convection to the surroundings from a fixed surface. The initial temperature is assumed to be at the fusion temperature. The solutions for this case give a good approximation for most problems where the initial temperature is different from the fusion temperature because the enthalpy changes with phase change are generally much greater than the enthalpy changes resulting only from temperature changes.

2 Freezing of Liquid in a Semi-Infinite Geometry with Constant Heat Flux at the Surface

This is the same problem studied by El-Genk and Cronenberg [1]. The problem can be written in the following dimensionless form.

$$\frac{\partial^2 u}{\partial x^2} = \frac{\partial u}{\partial t} \quad 0 < x < s(t), \quad t \geq 0 \tag{1}$$

$$\frac{\partial u}{\partial x} = 1 \text{ at } x = 0, \quad t \geq 0 \tag{2}$$

$$u = 0 \text{ at } x = s(t), \quad t \geq 0 \tag{3}$$

$$\frac{\partial u}{\partial x} = E\frac{ds}{dt} \text{ at } x = s(t), \quad t \geq 0 \tag{4}$$

$$s(0) = 0 \tag{5}$$

Symbols are defined in the Nomenclature.

The temperature distribution is assumed to have a similar profile to that without phase change. Thus

$$u = x \operatorname{erfc}\left(\frac{x}{2\sqrt{t + t_0}}\right) - 2\sqrt{\frac{t + t_0}{\pi}}\, e^{-x^2/4(t + t_0)} + f \tag{6}$$

where f and t_0 are constants. Equation (6) satisfies the energy equation (1) and a boundary condition (2). If one chooses the reference temperature difference $\Delta T = H/C$, then $E = 1$.

Subjecting equation (6) to the conditions at the phase change front, equations (3) and (4), one obtains

$$s \operatorname{erfc}\left(\frac{s}{2\sqrt{t + t_0}}\right) - 2\sqrt{\frac{t + t_0}{\pi}}\, e^{-s^2/4(t+t_0)} + f = 0, \quad t \geq 0 \tag{7}$$

and

$$\frac{ds}{dt} = \operatorname{erfc}\left(\frac{s}{2\sqrt{t + t_0}}\right), \quad t \geq 0 \tag{8}$$

Note that equation (8) is the same as equation (11) of reference [1].

If a continuous function $s(t)$ exists which satisfies both equations (7) and (8) simultaneously, then the solution is exact. Unfortunately, no such function exists.

Differentiating equation (7) with respect to t,

$$\frac{ds}{dt} = \frac{1}{\sqrt{\pi(t + t_0)}\, e^{s^2/4(t+t_0)}\, erfc\left(\frac{s}{2\sqrt{t + t_0}}\right)} \tag{9}$$

Equation (9) could also be obtained by substituting equation (8) of reference [1] into the energy equation (equation (1) of reference [1]).

Applying the initial condition (5) to equations (7–9),

$$t_0 = 1/\pi, \quad \text{and} \quad f = 2/\pi \tag{10}$$

The solution obtained from equation (7) is an approximate solution of the problem where the energy balance at the phase change front is relaxed, while the solution obtained from equation (8) is an approximate solution where temperature continuity at the phase change front is relaxed.

Figure 1 shows phase change positions as functions of time obtained from equations (7) and (8), and they are compared with a series solution [3] and a heat balance integral solution [4]. The maximum difference in the approximate solutions for the range shown in Fig. 1 is less than 10 percent. The solution obtained by satisfying the heat flux boundary condition (equation (8)) agrees very well with Goodman's solution [4] which is an approximate solution where the energy equation is satisfied by temperature in the average only.

---

[1] Department of Mechanical Engineering, Korea Military Institute, Seoul, Korea.

[2] Department of Mechanical Engineering, University of Massachusetts, Amherst, Mass. 01003.

Contributed by the Heat Transfer Division for publication in the JOURNAL OF HEAT TRANSFER. Manuscript received by the Heat Transfer Division April 2, 1980.

References

1 Wells, W. M., "ORNL TNS Program: Evaluation of the Bundle Divertor," ORNL/TM-6727, Oak Ridge Nat. Lab., Oak Ridge, Tenn., Nov. 1979.

2 Werley, K. A., Gilligan, J. G., and Miley, G. H., "A High Flux Energy and Particle Collection Scheme for Divertors," Proc. 11th Symp. on Fusion Technology, Oxford, England, Sept. 1980.

3 Lipov, M. Ku., and Murav'ev., E. V., "The Development of Highly Efficient Divertor Systems for Tokamak Energy Reactors," The I. B. Kurchatov Order of Lenin Institute of Atomic Energy, Moscow, 1979.

4 Tables of Spherical Bessel Functions, Math. Tables Project, Nat. Bureau of Standards, Vol. I & II, Columbia University Press, N.Y., 1947.

5 Carslaw, and Jaeger, *Conduction of Heat in Solids*, Oxford, 1959, p. 112.

Approximate Temperature Distribution for Phase Change of a Semi-Infinite Body

Sung Hwan Cho[1] and J. Edward Sunderland[2]

Nomenclature

B = Biot number, B = hL/k
c = specific heat at constant pressure
E = nondimensionalized enthalpy of phase change, $E = H/c\Delta T$
f = dimensionless constant defined by equation (10)
g = dimensionless constant defined by equation (12)
H = enthalpy of fusion
h = surface heat transfer coefficient
k = thermal conductivity
L = reference thickness, $L = \rho\alpha H/q$ for constant heat flux case, and $L = k/h$ for convection case
q = heat flux at the fixed surface
S = phase change position
s = nondimensionalized phase change position, $s = S/L$
T = temperature
t = nondimensionalized time, $t = \alpha\tau/L^2$
T_f = fusion temperature
T_∞ = surrounding temperature
ΔT = reference temperature difference, $\Delta T = H/c$ in Section 2 and $\Delta T = T_f - T_\infty$ in Section 3
t_0 = dimensionless constant defined by equation (10)
u = nondimensionalized temperature, $u = (T - T_f)/\Delta T$
X = distance
x = nondimensionalized distance, $x = X/L$
α = thermal diffusivity
ρ = density
τ = time

1 Introduction

Exact solutions to heat conduction problems with phase change are known only for the cases when phase change thickness is proportional to the square root of time. El-Genk and Cronenberg [1] claim that their solution is the first known exact solution of phase change problem with heat flux boundary condition. Their solution, however, is not exact because equations (8) and (9) do not satisfy the energy equation, equation (1) of reference [1]. In order for their solution to satisfy the energy equation, the quantity A, defined in equation (5) must be a constant. A is not a constant; it is a function of time. A similar method was used by Cho [2] for phase change problems with constant heat flux and convection surface conditions. This paper gives an approximate method of solution to phase change problems with constant heat flux and heat convection to the surroundings from a fixed surface. The initial temperature is assumed to be at the fusion temperature. The solutions for this case give a good approximation for most problems where the initial temperature is different from the fusion temperature because the enthalpy changes with phase change are generally much greater than the enthalpy changes resulting only from temperature changes.

2 Freezing of Liquid in a Semi-Infinite Geometry with Constant Heat Flux at the Surface

This is the same problem studied by El-Genk and Cronenberg [1]. The problem can be written in the following dimensionless form.

$$\frac{\partial^2 u}{\partial x^2} = \frac{\partial u}{\partial t} \quad 0 < x < s(t), \quad t \geq 0 \qquad (1)$$

$$\frac{\partial u}{\partial x} = 1 \text{ at } x = 0, \quad t \geq 0 \qquad (2)$$

$$u = 0 \text{ at } x = s(t), \quad t \geq 0 \qquad (3)$$

$$\frac{\partial u}{\partial x} = E\frac{ds}{dt} \text{ at } x = s(t), \quad t \geq 0 \qquad (4)$$

$$s(0) = 0 \qquad (5)$$

Symbols are defined in the Nomenclature.

The temperature distribution is assumed to have a similar profile to that without phase change. Thus

$$u = x \operatorname{erfc}\left(\frac{x}{2\sqrt{t + t_0}}\right) - 2\sqrt{\frac{t + t_0}{\pi}}\, e^{-x^2/4(t + t_0)} + f \qquad (6)$$

where f and t_0 are constants. Equation (6) satisfies the energy equation (1) and a boundary condition (2). If one chooses the reference temperature difference $\Delta T = H/C$, then $E = 1$.

Subjecting equation (6) to the conditions at the phase change front, equations (3) and (4), one obtains

$$s \operatorname{erfc}\left(\frac{s}{2\sqrt{t + t_0}}\right) - 2\sqrt{\frac{t + t_0}{\pi}}\, e^{-s^2/4(t+t_0)} + f = 0, \quad t \geq 0 \qquad (7)$$

and

$$\frac{ds}{dt} = \operatorname{erfc}\left(\frac{s}{2\sqrt{t + t_0}}\right), \quad t \geq 0 \qquad (8)$$

Note that equation (8) is the same as equation (11) of reference [1].

If a continuous function $s(t)$ exists which satisfies both equations (7) and (8) simultaneously, then the solution is exact. Unfortunately, no such function exists.

Differentiating equation (7) with respect to t,

$$\frac{ds}{dt} = \frac{1}{\sqrt{\pi(t + t_0)}\, e^{s^2/4(t+t_0)}\, erfc\left(\frac{s}{2\sqrt{t + t_0}}\right)} \qquad (9)$$

Equation (9) could also be obtained by substituting equation (8) of reference [1] into the energy equation (equation (1) of reference [1]).

Applying the initial condition (5) to equations (7–9),

$$t_0 = 1/\pi, \quad \text{and} \quad f = 2/\pi \qquad (10)$$

The solution obtained from equation (7) is an approximate solution of the problem where the energy balance at the phase change front is relaxed, while the solution obtained from equation (8) is an approximate solution where temperature continuity at the phase change front is relaxed.

Figure 1 shows phase change positions as functions of time obtained from equations (7) and (8), and they are compared with a series solution [3] and a heat balance integral solution [4]. The maximum difference in the approximate solutions for the range shown in Fig. 1 is less than 10 percent. The solution obtained by satisfying the heat flux boundary condition (equation (8)) agrees very well with Goodman's solution [4] which is an approximate solution where the energy equation is satisfied by temperature in the average only.

---

[1] Department of Mechanical Engineering, Korea Military Institute, Seoul, Korea.

[2] Department of Mechanical Engineering, University of Massachusetts, Amherst, Mass. 01003.

Contributed by the Heat Transfer Division for publication in the JOURNAL OF HEAT TRANSFER. Manuscript received by the Heat Transfer Division April 2, 1980.

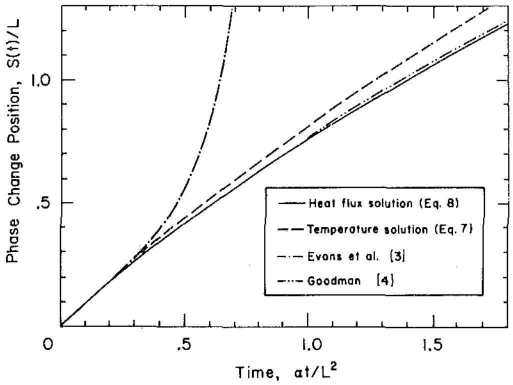

Fig. 1 Phase change position as a function of time with constant heat flux

3 Freezing of Liquid by Surface Heat Convection

The approximate method derived in the previous section is now applied to freezing a semi-infinite liquid body initially at the fusion temperature which is cooled by convection at its free surface. The surface heat transfer coefficient is constant.

The same problem was studied by London and Seban [5] and Kreith and Romie [6] with an electrical analogy; by Goodman [4] with the heat balance integral method; and by Westphal [7] with a series method. Gutowski [8] indicated the existence and uniqueness of the solution for this problem without giving proofs or references. Robertson and Schenk [9] presented some experimental results for this problem. An accurate numerical solution has been presented by Sparrow, et al. [10]. An exact solution has not been published.

The problem can be written in dimensionless form as equations (1–5). Surface condition (2) now becomes

$$\frac{du}{dx} - \mathrm{B}u = \mathrm{B} \quad \text{at} \quad x = 0, t \geq 0 \tag{11}$$

The temperature distribution is assumed to have a similar profile to that without phase change. Thus

$$u = g\left\{\mathrm{erf}\left(\frac{x}{2\sqrt{t+t_0}}\right) + e^{\mathrm{B}x+\mathrm{B}^2(t+t_0)} \times \mathrm{erfc}\left(\frac{x}{2\sqrt{t+t_0}} + \mathrm{B}\sqrt{t+t_0}\right)\right\} - 1 \tag{12}$$

where g and t_0 are constants to be determined later. Equation (12) satisfies equations (1) and (11). Note that when the surface heat transfer coefficient becomes infinite, the Biot number becomes infinite, and equation (12) becomes Neumann's solution which is exact for the limiting problem. When the surface heat transfer coefficient is finite, let

$$L = k/h \tag{13}$$

so that B = 1. Equation (12) now becomes

$$u = g\left\{\mathrm{erf}\left(\frac{x}{2\sqrt{t+t_0}}\right) + e^{(x+t+t_0)}\,\mathrm{erfc}\left(\frac{x}{2\sqrt{t+t_0}} + \sqrt{t+t_0}\right)\right\} - 1 \tag{14}$$

Subjecting equation (14) to the conditions at the phase change front, equations (3) and (4), it follows that

$$g\left\{\mathrm{erf}\left(\frac{x}{2\sqrt{t+t_0}}\right) + e^{(s+t+t_0)}\,\mathrm{erfc}\left(\frac{s}{2\sqrt{t+t_0}} + \sqrt{t+t_0}\right)\right\} = 1 \tag{15}$$

and

$$E\frac{ds}{dt} = ge^{(s+t+t_0)}\,\mathrm{erfc}\left(\frac{s}{2\sqrt{t+t_0}} + \sqrt{t+t_0}\right), \tag{16}$$

respectively. If a continuous function $s(t)$ exists which satisfies equations (15) and (16) simultaneously, the solution is exact. However, this is not the case.

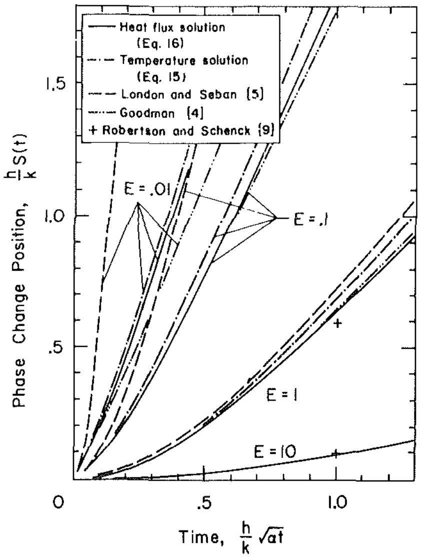

Fig. 2 Phase change position as a function of time with surface heat convection

Differentiating equation (15) with respect to t, one obtains

$$\frac{ds}{dt} = \frac{1}{\sqrt{\pi(t+t_0)}\,\exp\left(\frac{s}{2\sqrt{t+t_0}} + \sqrt{t+t_0}\right)^2 \mathrm{erfc}\left(\frac{s}{2\sqrt{t+t_0}} + \sqrt{t+t_0}\right)} - 1 \tag{17}$$

Applying the initial condition (5) to equations (15–17), it can be shown that

$$g = \frac{1}{e^{t_0}\,\mathrm{erfc}\,(\sqrt{t_0})} \tag{18}$$

where t_0 is now obtained from

$$\sqrt{\pi t_0}\,e^{t_0}\,\mathrm{erfc}\,(\sqrt{t_0}) = \frac{E}{1+E} \tag{19}$$

Now equations (15) and (16) can be solved independently. The solution obtained from equation (15) is an approximate solution where the energy balance at the fusion front is relaxed, while the solution obtained from equation (16) is an approximate solution where temperature continuity at the phase change front is relaxed.

Figure 2 shows results obtained by equations (15) and (16) compared with other approximate methods and experimental data of Robertson and Schenck [9]. The maximum difference between the heat flux and temperature approximations is less than 8 percent for the range shown. The heat flux approximation, equation (16), agrees well with Goodman's solution [4].

London and Seban's solution [5] was obtained by assuming a linear temperature profile in the solid region. The linear temperature profile assumption will always give higher values for the phase change position than actually exist. It can be seen in Fig. 2 that the error becomes larger as E decreases which occurs with rapid freezing.

The results of Fig. 2 were also compared to the numerical solutions obtained by Sparrow, et al. [10] for values of E equal to 0.1 and 1. The numerical results were slightly higher than the heat flux solution (equation (16)) and lie between our two approximate solutions. Comparisons were also made of the nondimensional temperature ratio—u (0) at the free surface defined by

$$u\,(0) = -\frac{T_w - T_f}{T_\infty - T_f} \tag{20}$$

where T_w is the temperature at $x = 0$. This temperature ratio can be determined by letting $x = 0$ in equation (14). Thus

Table 1 Values of t_0 and g to be used in equation (22) to determine surface temperature (note $\mathrm{Ste}_\infty = 1/E$)

E	Ste_∞	t_0	g
0.01	100	3.160146×10^{-5}	1.006352
0.1	10	2.968534×10^{-3}	1.062279
0.2	5	1.113119×10^{-2}	1.122011
1	1	1.872739×10^{-1}	1.534064
10	0.1	4.210264×10^{0}	4.000572
100	0.01	4.901443×10^{1}	12.53491
200	0.005	9.901443×10^{1}	17.72516

Table 2 Values of the surface temperature T_w for convective heating with heat balance satisfied at phase front

Ste_∞	$\mathrm{Ste}_\infty F_0$	$\frac{T_w - T_{\mathrm{sat}}}{T_\infty - T_{\mathrm{sat}}}$	Ste_∞	$\mathrm{Ste}_\infty F_0$	$\frac{T_w - T_{\mathrm{sat}}}{T_\infty - T_{\mathrm{sat}}}$
0.005 (E = 200)	0.130	0.109	5 (E = 0.2)	0.144	0.092
	0.505	0.295		0.744	0.247
	0.755	0.369		3.144	0.451
	1.172	0.453		11.194	0.639
	2.005	0.553		55.500	0.818
	4.505	0.684		124.944	0.876
	9.505	0.776		249.94	0.911
	19.505	0.842		499.94	0.937
	24.505	0.859		999.94	0.955
	49.505	0.900		1249.94	0.960
	99.505	0.929		2499.94	0.972
				4999.94	0.980
1 (E = 1)	0.453	0.250		9999.94	0.986
	0.813	0.344			
	2.063	0.507	10 (E = 0.1)	0.370	0.141
	3.813	0.608		0.870	0.220
	10.924	0.751		2.47	0.346
	24.813	0.830		8.07	0.515
	49.8	0.879		22.47	0.658
	99.8	0.914		39.97	0.882
	199.8	0.934		999.97	0.940
	249.8	0.945		1999.97	0.958
	499.8	0.961		2499.97	0.962
	999.8	0.973		3333.304	0.967
	1999.8	0.981		4999.97	0.973

$$u = g e^{(t+t_0)} \operatorname{erfc} \sqrt{t + t_0} - 1 \quad \text{for} \quad x = 0 \tag{21}$$

With the notation used in [10] equation (21) can be written

$$\frac{T_w - T_{\mathrm{sat}}}{T_\infty - T_{\mathrm{sat}}} = 1 - g \exp\left(\mathrm{Fo} + t_0\right) \operatorname{erfc} \sqrt{\mathrm{Fo} + t_0} \tag{22}$$

where Fo is the Fourier number with k/h as the characteristic dimension and t_0 and g are obtained from equations (18) and (19). Values of t_0 and g are given in Table 1. Table 2 gives the free surface temperature T_w. The values presented in Table 2 coincide with the results presented in Fig. 8 of Sparrow, et al. [10].

4 Discussion

It can be shown that the approximate temperature distribution which satisfies the constant heat flux boundary condition gives an upper limit of the phase change thickness. This can be accomplished by defining Q^* such that

$$Q^* = \frac{ds}{dt} - \left.\frac{\partial u}{\partial x}\right|_{x=s(t)}$$

and by demonstrating that $Q^* \geq 0$. This was accomplished by solving equation (7) for a range of values of $s/2\sqrt{t+t_0}$ between 0.01 and 2.0. $S(\tau)/L$ varied from 0.01149 to 1301.85 (when $s/2\sqrt{t+t_0} = 2$). Q^* varied from 0.00477 (when $s/2\sqrt{t+t_0} = 0.01$ to a maximum value of 0.09569 (when $s/2\sqrt{t+t_0} = 0.45$) and then diminished to 0.00211 (when $s/2\sqrt{t+t_0} = 2$). Thus for this very large range of values Q^* remains positive. Physically, Q^* can be interpreted as the measure of error of the boundary condition given in equation (4).

The writers have not been able to prove rigorously that the exact solution lies between the two approximate solutions. However, we have made numerous calculations and comparisons that show that this is to be anticipated. Furthermore the solution based on the heat flux approximation will be closer to the exact solution than the other approximate solution.

Acknowledgments

The writers wish to express their appreciation to Dr. E. M. Sparrow for making available the original graphs that were used in reference [10].

References

1 El-Genk, M. S. and Cronenberg, A. W., "Solidification in a Semi-Infinite Region With Boundary Conditions of the Second Kind: An Exact Solution," *Letters in Heat and Mass Transfer*, Vol. 6, Pergamon Press, Great Britain, 1979, pp. 321–327.

2 Cho, S. H., "Heat Conduction With Phase Changes," Ph.D. Dissertation, Department of Mechanical and Aerospace Engineering, North Carolina State University, 1969.

3 Evans, G. W. II, Isaacson, E. and McDonald, J. K. L., "Stefan-Like Problems," *Quarterly Journal of Applied Mathematics*, Vol. 8, 1950, pp. 312–319.

4 Goodman, T. R., "The Heat Balance Integral and its Application to Problems Involving Change of Phase," ASME JOURNAL OF HEAT TRANSFER, Vol. 80, 1958, pp. 335–341.

5 London, A. L. and Seban, R. A., "Rate of Ice Formation," *Trans. ASME*, Vol. 65, 1943, pp. 771–778.

6 Kreith, F. and Romie, F. E., "A Study of the Thermal Diffusion Equation With Boundary Conditions Corresponding to Solidification or Melting of Materials Initially at the Fusion Temperature," *Proceedings of Physical Society*, London, Vol. 68(B), 1955, pp. 277–291.

7 Westphal, K. O., "Series Solution of Freezing Problem with the Fixed Surface Radiating into a Medium of Arbitrary Varying Temperature," *International Journal of Heat and Mass Transfer*, Vol. 10, 1967, pp. 195–205.

8 Gutowski, R., "The Problem of Motion of the Freezing Front in Liquids," *Aschwm. Mech. Stosow.*, Vol. 15, 1963, pp. 167–182.

9 Robertson, S. R. and Schenk, H. Jr., "Correcting the London-Seban Equation for the Case of Molten Metal Solidification," ASME JOURNAL OF HEAT TRANSFER, Vol. 89, 1967, pp. 118–119.

10 Sparrow, E. M., Lee, L. and Shamsundar, N., "Convective Instability in a Melt Layer Heated From Below," ASME JOURNAL OF HEAT TRANSFER, Vol. 98, 1976, pp. 88–94.

Gray-Gas Approximation of Carbon Dioxide Standard Emissivity

Ihab H. Farag[1] **and Tarek A. Allam**[1]

Nomenclature

$a_{g,i}$ = weighting factor of the gray-gas i, $i = 0$ clear gas for which the absorption coefficient is zero

$b_{j,i}$ = coefficients of the polymonial of the $a_{g,i}$'s

c_i = coefficients of the polynomial of Z

k_i = absorption coefficient of gray gas i

L = thickness of the gas slab, cm

p = partial pressure of the emitting, or absorbing, gas, atm

pL = optical thickness of gas slab, cm, atm

T = temperature, K

Z = sum of the weighting factors of the gray gases excluding the clear component

ϵ_g = gas emissivity

τ = temperature in K/1000

Introduction

The main mode of heat transfer, at high temperatures, is thermal radiation. Hence, the knowledge of the emissivities of carbon dioxide and water vapor would be very important in burner design and thermal efficiency calculations.

---

[1] Department of Chemical Engineering, University of New Hampshire, Durham, NH 03824

Contributed by the Heat Transfer Division for publication in the JOURNAL OF HEAT TRANSFER. Manuscript received by the Heat Transfer Division May 12, 1980.

Table 1 Values of t_0 and g to be used in equation (22) to determine surface temperature (note $\mathrm{Ste}_\infty = 1/E$)

E	Ste_∞	t_0	g
0.01	100	3.160146×10^{-5}	1.006352
0.1	10	2.968534×10^{-3}	1.062279
0.2	5	1.113119×10^{-2}	1.122011
1	1	1.872739×10^{-1}	1.534064
10	0.1	4.210264×10^{0}	4.000572
100	0.01	4.901443×10^{1}	12.53491
200	0.005	9.901443×10^{1}	17.72516

Table 2 Values of the surface temperature T_w for convective heating with heat balance satisfied at phase front

Ste_∞	$\mathrm{Ste}_\infty F_0$	$\frac{T_w - T_{sat}}{T_\infty - T_{sat}}$	Ste_∞	$\mathrm{Ste}_\infty F_0$	$\frac{T_w - T_{sat}}{T_\infty - T_{sat}}$
	0.130	0.109		0.144	0.092
	0.505	0.295		0.744	0.247
	0.755	0.369		3.144	0.451
	1.172	0.453		11.194	0.639
	2.005	0.553		55.500	0.818
0.005	4.505	0.684	5	124.944	0.876
	9.505	0.776		249.94	0.911
(E = 200)	19.505	0.842	(E = 0.2)	499.94	0.937
	24.505	0.859		999.94	0.955
	49.505	0.900		1249.94	0.960
	99.505	0.929		2499.94	0.972
				4999.94	0.980
	0.453	0.250		9999.94	0.986
	0.813	0.344			
	2.063	0.507		0.370	0.141
	3.813	0.608		0.870	0.220
1	10.924	0.751		2.47	0.346
	24.813	0.830		8.07	0.515
(E = 1)	49.8	0.879	10	22.47	0.658
	99.8	0.914	(E = 0.1)	39.97	0.882
	199.8	0.934		999.97	0.940
	249.8	0.945		1999.97	0.958
	499.8	0.961		2499.97	0.962
	999.8	0.973		3333.304	0.967
	1999.8	0.981		4999.97	0.973

$$u = g e^{(t+t_0)} \operatorname{erfc} \sqrt{t + t_0} - 1 \quad \text{for} \quad x = 0 \qquad (21)$$

With the notation used in [10] equation (21) can be written

$$\frac{T_w - T_{\text{sat}}}{T_\infty - T_{\text{sat}}} = 1 - g \exp(\mathrm{Fo} + t_0) \operatorname{erfc} \sqrt{\mathrm{Fo} + t_0} \qquad (22)$$

where Fo is the Fourier number with k/h as the characteristic dimension and t_0 and g are obtained from equations (18) and (19). Values of t_0 and g are given in Table 1. Table 2 gives the free surface temperature T_w. The values presented in Table 2 coincide with the results presented in Fig. 8 of Sparrow, et al. [10].

4 Discussion

It can be shown that the approximate temperature distribution which satisfies the constant heat flux boundary condition gives an upper limit of the phase change thickness. This can be accomplished by defining Q^* such that

$$Q^* = \frac{ds}{dt} - \left.\frac{\partial u}{\partial x}\right|_{x=s(t)}$$

and by demonstrating that $Q^* \geq 0$. This was accomplished by solving equation (7) for a range of values of $s/2\sqrt{t + t_0}$ between 0.01 and 2.0. $S(\tau)/L$ varied from 0.01149 to 1301.85 (when $s/2\sqrt{t + t_0} = 2$). Q^* varied from 0.00477 (when $s/2\sqrt{t + t_0} = 0.01$ to a maximum value of 0.09569 (when $s/2\sqrt{t + t_0} = 0.45$) and then diminished to 0.00211 (when $s/2\sqrt{t + t_0} = 2$). Thus for this very large range of values Q^* remains positive. Physically, Q^* can be interpreted as the measure of error of the boundary condition given in equation (4).

The writers have not been able to prove rigorously that the exact solution lies between the two approximate solutions. However, we have made numerous calculations and comparisons that show that this is to be anticipated. Furthermore the solution based on the heat flux approximation will be closer to the exact solution than the other approximate solution.

Acknowledgments

The writers wish to express their appreciation to Dr. E. M. Sparrow for making available the original graphs that were used in reference [10].

References

1 El-Genk, M. S. and Cronenberg, A. W., "Solidification in a Semi-Infinite Region With Boundary Conditions of the Second Kind: An Exact Solution," *Letters in Heat and Mass Transfer*, Vol. 6, Pergamon Press, Great Britain, 1979, pp. 321–327.

2 Cho, S. H., "Heat Conduction With Phase Changes," Ph.D. Dissertation, Department of Mechanical and Aerospace Engineering, North Carolina State University, 1969.

3 Evans, G. W. II, Isaacson, E. and McDonald, J. K. L., "Stefan-Like Problems," *Quarterly Journal of Applied Mathematics*, Vol. 8, 1950, pp. 312–319.

4 Goodman, T. R., "The Heat Balance Integral and its Application to Problems Involving Change of Phase," ASME JOURNAL OF HEAT TRANSFER, Vol. 80, 1958, pp. 335–341.

5 London, A. L. and Seban, R. A., "Rate of Ice Formation," *Trans. ASME*, Vol. 65, 1943, pp. 771–778.

6 Kreith, F. and Romie, F. E., "A Study of the Thermal Diffusion Equation With Boundary Conditions Corresponding to Solidification or Melting of Materials Initially at the Fusion Temperature," *Proceedings of Physical Society*, London, Vol. 68(B), 1955, pp. 277–291.

7 Westphal, K. O., "Series Solution of Freezing Problem with the Fixed Surface Radiating into a Medium of Arbitrary Varying Temperature," *International Journal of Heat and Mass Transfer*, Vol. 10, 1967, pp. 195–205.

8 Gutowski, R., "The Problem of Motion of the Freezing Front in Liquids," *Aschwm. Mech. Stosow.*, Vol. 15, 1963, pp. 167–182.

9 Robertson, S. R. and Schenk, H. Jr., "Correcting the London-Seban Equation for the Case of Molten Metal Solidification," ASME JOURNAL OF HEAT TRANSFER, Vol. 89, 1967, pp. 118–119.

10 Sparrow, E. M., Lee, L. and Shamsundar, N., "Convective Instability in a Melt Layer Heated From Below," ASME JOURNAL OF HEAT TRANSFER, Vol. 98, 1976, pp. 88–94.

Gray-Gas Approximation of Carbon Dioxide Standard Emissivity

Ihab H. Farag[1] and Tarek A. Allam[1]

Nomenclature

$a_{g,i}$ = weighting factor of the gray-gas i, $i = 0$ clear gas for which the absorption coefficient is zero

$b_{j,i}$ = coefficients of the polymonial of the $a_{g,i}$'s

c_i = coefficients of the polynomial of Z

k_i = absorption coefficient of gray gas i

L = thickness of the gas slab, cm

p = partial pressure of the emitting, or absorbing, gas, atm

pL = optical thickness of gas slab, cm, atm

T = temperature, K

Z = sum of the weighting factors of the gray gases excluding the clear component

ϵ_g = gas emissivity

τ = temperature in K/1000

Introduction

The main mode of heat transfer, at high temperatures, is thermal radiation. Hence, the knowledge of the emissivities of carbon dioxide and water vapor would be very important in burner design and thermal efficiency calculations.

---

[1] Department of Chemical Engineering, University of New Hampshire, Durham, NH 03824

Contributed by the Heat Transfer Division for publication in the JOURNAL OF HEAT TRANSFER. Manuscript received by the Heat Transfer Division May 12, 1980.

The purpose of the present work was to develop and test a model to predict the carbon dioxide standard emissivity at any given T and pL.

Theory and Approach

The model adopted [2] formulates the real gas emission by gray-plus-clear gases. The emissivity-pL relationship for any real-gas can be approximated by the weighted sum of a sufficient number of gray gases. This can be represented by the following equation,

$$\epsilon_g = \sum_i a_{g,i} (1 - e^{-k_i pL}) \qquad (1)$$

The $a_{g,i}$'s should satisfy the restriction that,

$$\sum_i a_{g,i} = a_{g,0} + a_{g,1} + a_{g,2} + \ldots + a_{g,n} = 1 \qquad (2)$$

because in the limit as $pL \rightarrow \infty$ ϵ_g approaches 1. Meanwhile, all values of the $a_{g,i}$'s have to be positive.

The term Z was defined as the sum of the weighting factors of the gray gases excluding the clear component, i.e., (from equation (2))

$$Z = \sum_{i=1}^{n} a_{g,i} = (1 - a_{g,0}) \qquad (3)$$

Expanding and rearranging equation (1),

$$Z - \epsilon_g = a_{g,1} e^{-k_1 pL} + \ldots + a_{g,n} e^{-k_n pL} \qquad (4)$$

If $k_n > k_{n-1} \ldots k_2 > k_1$, all the right-hand side terms would be negligible at high pL values (200 − 1000 cm atm) except the first term involving k_1, i.e.

$$Z - \epsilon_g = a_{g,1} e^{-k_1 pL} \qquad (5)$$

Therefore, at large pL's, a plot of the logarithm of $Z - \epsilon_g$ versus pL would yield a straight line with a slope of $-k_1$ and an intercept of $a_{g,1}$, using an estimate of Z which is close to the correct value.

Actually a trial-and-error procedure was used to get Z. The value that gave a straight line relation, was used in subsequent calculations.

After the evaluation of the Z's, $a_{g,1}$ and k_1 for the nine different temperatures, the procedure was continued to evaluate all the $a_{g,2}$, $a_{g,3}, \ldots a_{g,6}$ and $k_2, k_3 \ldots k_6$. The calculations were completed when the sixth gray-gas constant was added since $a_{g,1} + \ldots + a_{g,6}$ was equal to the assumed value of Z. Consequently, a total of 13 constants were determined for each given temperature. To include the effect of temperature in the analysis, the absorption coefficients were assumed to be constant and the a_g's were assumed to vary according to the form

$$a_{g,i} = b_{1,i} + b_{2,i}\,\tau + b_{3,i}\,\tau^2. \qquad (6)$$

The b's were evaluated using the Simplex method. An equation containing 27 coefficients resulted from the fitting. These are $6k$'s, $6b_1$'s, $6b_2$'s, $6b_3$'s and three coefficients for Z which was written as

$$Z = c_1 + c_2\,\tau + c_3 \tau^2 \qquad (7)$$

The data were obtained from [7] and [1] who utilized the statistical model and the spectral constants of Ludwig [5, 6] to calculate carbon dioxide emission and compare it with experimental data. They tabulated its standard emissivity for pL range of 0.05 to 1000 cm atm and a temperature range of 300 to 1800 K. Leckner [3, 4] used the spectral data of carbon dioxide to calculate the total emissivity. He compared his results with the data of Hottel and developed a model containing 20 constants. His model was used for comparison.

Results and Discussion

Figure 1 shows the plot of the tabulated standard emissivities of carbon dioxide, the present model and emissivities calculated using Leckner's model [4] at 1800 K.

To judge how good the fit is an "error" is defined as

$$\text{error} = 100 \text{ percent } (\epsilon_{\text{tab}} - \epsilon_{\text{calc}})/\epsilon_{\text{tab}} \qquad (8)$$

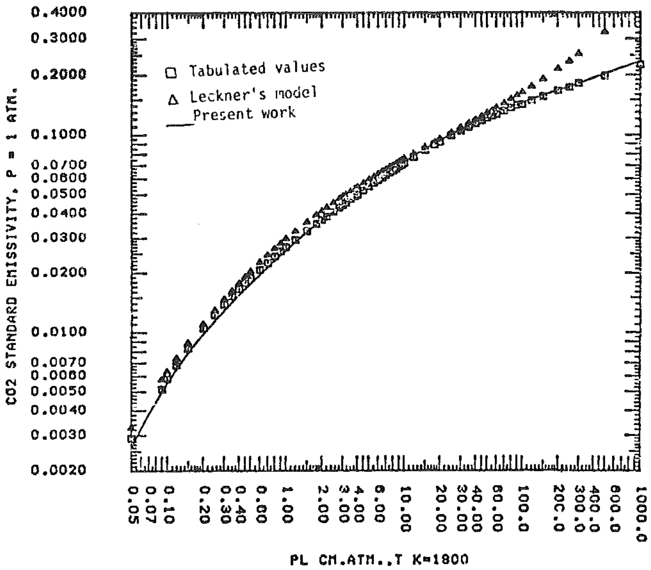

Fig. 1 CO_2 standard emissivity at 1800 K

Table 1 Coefficients of $\Sigma a_{g,i}$, $a_{g,i}$'s and k values

$Z = \Sigma a_{g,i}$	c_1	c_2	c_3
	2.7769×10^{-1}	3.3869×10^{-2}	1.4249×10^{-5}

i	1	2	3	4	5	6
k_i	0.0003647	0.003633	0.0310	0.1496	1.0361	7.806

$a_{g,i}$	$b_{1,i}$	$b_{2,i}$	$b_{3,i}$
1	0.1074	−0.10705	0.072727
2	0.027237	0.10127	−0.043773
3	0.058438	−0.001208	0.0006558
4	0.019078	0.037609	−0.015424
5	0.056993	−0.025412	0.0026167
6	0.0028014	0.038826	−0.020198

In Fig. 1, Leckner's model overestimates the emissivities over the entire range having an error of −109.18 percent. The present model had an error range of −3.68 to 11.30 percent. Similar comparisons and plots were made at temperatures of 300–1600 K. It was noticed that Leckner's model, generally, has a wavy trend with a portion of good agreement changing its location when the temperature is increased. The reason for large errors in Leckner's model was generally due to large calculated emissivities especially at a pL of 1000 cm atm.

From a general consideration of the present model, it can be noticed that, the error ranged between −25.92 and 23.24 percent as the two extremes. Actually these extremes occur at a low pL of 0.05 cm atm. Considering the range from 1.0 to 1000 cm atm would reduce the error extremes at −12.24 to 10.35 percent. Since, for industrial applications, a more realistic range would be from 800 to 1800 K, the limits of the error are reduced to −4.18 and 5.87 percent. It is clear that the present model is much better in calculating the emissivities.

Table 1 includes the coefficients necessary to calculate the standard emissivity of carbon dioxide at any temperature (in K) and pL (in cm atm) within the range.

From the previous arguments the following conclusions could be drawn:

1 The model presented in this work is reliable yet easy to use. It is also stable because it was based on the physical relation between the pL's and the emissivities.

2 The strength of the present model lies in the ease of use, i.e., ease of programmability.

3 The range of error in calculating the emissivities is between −4.18 and 5.87 percent for a temperature range of 800–1800 K and a pL range of 1.0–1000 cm atm.

4 The model represented in this paper gives a good alternative to existing model(s).

Acknowledgments

The authors would like to acknowledge the support from NSF, Grant ENG-77-06679. The senior author would like to acknowledge the support of the UNH Summer Faculty Fellowship Program.

References

1 Farag, I. H., "Radiative Heat Transmission from Non-Luminous Gases. Computational Study of the Emissivities of Water Vapor and Carbon Dioxide," Sc.D. Thesis, M.I.T., Cambridge, Mass., 1976.
2 Hottel, H. C., and Sarofim, A. F., *Radiative Transfer*, McGraw-Hill, New York, 1967.
3 Leckern, B., "The Spectral and Total Emissivity of Carbon Dioxide," *Combustion and Flame*, Vol. 17, 37–44, 1971.
4 Leckner, B., "Spectral and Total Emissivity of Water Vapor and Carbon Dioxide," *Combustion and Flame*, Vol. 19, 1972, pp. 33–48.
5 Ludwig, C. B., Malkmus, W., Reardon, J. E., and Thomson, J. A. L. "Handbook of Infrared Radiation from Combustion Gases," Editors R. Goulard and J. A. L. Thomson, NASA SP-3080, Washington, D.C. 1973.
6 Ludwig, C. B. and Malkmus, W., "Band Model Representations for High Temperature Water Vapor and Carbon Dioxide," *Proceedings of the Special Conference on Molecular Radiation*, Huntsville, Ala., NASA TMX-53711, 1968.
7 Sarofim, A. F., I. H. Farag, and H. C. Hottel, "Radiative Heat Transmission from Non-Luminous Gases. Computational Study of the Emissivities of Carbon Dioxide," presented at the AIAA-ASME Thermophysics & Heat Transfer Conference, Palo Alto, Calif., May 1978.